



pharmaceutics

Special Issue Reprint

Ophthalmic Drug Delivery

2nd Edition

Edited by
Francisco Javier Otero-Espinar and Anxo Fernández Ferreiro

mdpi.com/journal/pharmaceutics



Ophthalmic Drug Delivery, 2nd Edition

Ophthalmic Drug Delivery, 2nd Edition

Editors

Francisco Javier Otero-Espinar

Anxo Fernández Ferreiro



Basel • Beijing • Wuhan • Barcelona • Belgrade • Novi Sad • Cluj • Manchester

Editors

Francisco Javier Otero-Espinar
Department of Pharmacology,
Pharmacy and
Pharmaceutical Technology
University of Santiago de
Compostela (USC)
Santiago de Compostela
Spain

Anxo Fernández Ferreiro
Hospital Pharmacy &
Department and
Pharmacology Group
SERGAS and Health Research
Institute Santiago Compostela
Santiago de Compostela
Spain

Editorial Office

MDPI
St. Alban-Anlage 66
4052 Basel, Switzerland

This is a reprint of articles from the Special Issue published online in the open access journal *Pharmaceutics* (ISSN 1999-4923) (available at: www.mdpi.com/journal/pharmaceutics/special_issues/ophthalmic.drugdelivery_II).

For citation purposes, cite each article independently as indicated on the article page online and as indicated below:

Lastname, A.A.; Lastname, B.B. Article Title. <i>Journal Name</i> Year , <i>Volume Number</i> , Page Range.
--

ISBN 978-3-0365-8799-8 (Hbk)

ISBN 978-3-0365-8798-1 (PDF)

doi.org/10.3390/books978-3-0365-8798-1

© 2023 by the authors. Articles in this book are Open Access and distributed under the Creative Commons Attribution (CC BY) license. The book as a whole is distributed by MDPI under the terms and conditions of the Creative Commons Attribution-NonCommercial-NoDerivs (CC BY-NC-ND) license.

Contents

Preface	vii
Lin Chen, Liangju Kuang, Amy E. Ross, Wissam Farhat, Nikolay Boychev and Sina Sharfi et al. Topical Sustained Delivery of Miltefosine Via Drug-Eluting Contact Lenses to Treat Acanthamoeba Keratitis Reprinted from: <i>Pharmaceutics</i> 2022 , <i>14</i> , 2750, doi:10.3390/pharmaceutics14122750	1
José Izo Santana da Silva de Jesus, Felipe Rebello Lourenço, Kelly Ishida, Thayná Lopes Barreto, Valdir Carlos Avino and Edson dos Santos Neto et al. Besifloxacin Nanocrystal: Towards an Innovative Ophthalmic Preparation Reprinted from: <i>Pharmaceutics</i> 2022 , <i>14</i> , 2221, doi:10.3390/pharmaceutics14102221	15
Ana Castro-Balado, Enrique Bandín-Vilar, Andrea Cuartero-Martínez, Laura García-Quintanilla, Gonzalo Hermelo-Vidal and Xurxo García-Otero et al. Cysteamine Eye Drops in Hyaluronic Acid Packaged in Innovative Single-Dose Systems: Stability and Ocular Biopermanence Reprinted from: <i>Pharmaceutics</i> 2022 , <i>14</i> , 2194, doi:10.3390/pharmaceutics14102194	36
Phatsawee Jansook and Thorsteinn Loftsson Aqueous Prostaglandin Eye Drop Formulations Reprinted from: <i>Pharmaceutics</i> 2022 , <i>14</i> , 2142, doi:10.3390/pharmaceutics14102142	54
Yidong Zhang, Chengshou Zhang, Silong Chen, Jianghua Hu, Lifang Shen and Yibo Yu Research Progress Concerning a Novel Intraocular Lens for the Prevention of Posterior Capsular Opacification Reprinted from: <i>Pharmaceutics</i> 2022 , <i>14</i> , 1343, doi:10.3390/pharmaceutics14071343	67
Rubén Varela-Fernández, Xurxo García-Otero, Victoria Díaz-Tomé, Uxía Regueiro, Maite López-López and Miguel González-Barcia et al. Mucoadhesive PLGA Nanospheres and Nanocapsules for Lactoferrin Controlled Ocular Delivery Reprinted from: <i>Pharmaceutics</i> 2022 , <i>14</i> , 799, doi:10.3390/pharmaceutics14040799	89
Marion Barrieu, Philip Chennell, Mouloud Yessaad, Yassine Bouattour, Mathieu Wasiak and Mireille Jouannet et al. Physicochemical Stability of a Novel Tacrolimus Ophthalmic Formulation for the Treatment of Ophthalmic Inflammatory Diseases Reprinted from: <i>Pharmaceutics</i> 2022 , <i>14</i> , 118, doi:10.3390/pharmaceutics14010118	114
Xurxo García-Otero, Cristina Mondelo-García, Francisco González, Roman Perez-Fernandez, Leandro Avila and Jose Ramón Antúnez-López et al. Anti-Inflammatory Effect of Tacrolimus/Hydroxypropyl- β - Cyclodextrin Eye Drops in an Endotoxin-Induced Uveitis Model Reprinted from: <i>Pharmaceutics</i> 2021 , <i>13</i> , 1737, doi:10.3390/pharmaceutics13101737	137
E Seul Kim, Min Sang Lee, Hayoung Jeong, Su Yeon Lim, Doha Kim and Dahwun Kim et al. Sustained-Release Microspheres of Rivoceranib for the Treatment of Subfoveal Choroidal Neovascularization Reprinted from: <i>Pharmaceutics</i> 2021 , <i>13</i> , 1548, doi:10.3390/pharmaceutics13101548	149

Yusuke Shinozaki, Shin-ichi Akanuma, Yuika Mori, Yoshiyuki Kubo and Ken-ichi Hosoya Comprehensive Evidence of Carrier-Mediated Distribution of Amantadine to the Retina across the Blood–Retinal Barrier in Rats Reprinted from: <i>Pharmaceutics</i> 2021 , <i>13</i> , 1339, doi:10.3390/pharmaceutics13091339	159
Gustav Christensen, Leon Barut, Dileep Urimi, Nicolaas Schipper and François Paquet-Durand Investigating Ex Vivo Animal Models to Test the Performance of Intravitreal Liposomal Drug Delivery Systems Reprinted from: <i>Pharmaceutics</i> 2021 , <i>13</i> , 1013, doi:10.3390/pharmaceutics13071013	172
Tobias Sonntag, Franziska Froemel, W. Daniel Stamer, Andreas Ohlmann, Rudolf Fuchshofer and Miriam Breunig Distribution of Gold Nanoparticles in the Anterior Chamber of the Eye after Intracameral Injection for Glaucoma Therapy Reprinted from: <i>Pharmaceutics</i> 2021 , <i>13</i> , 901, doi:10.3390/pharmaceutics13060901	187
Grace Cooksley, Joseph Lacey, Marcus K. Dymond and Susan Sandeman Factors Affecting Posterior Capsule Opacification in the Development of Intraocular Lens Materials Reprinted from: <i>Pharmaceutics</i> 2021 , <i>13</i> , 860, doi:10.3390/pharmaceutics13060860	204
Hyeong Min Kim, Hyounkoo Han, Hye Kyoung Hong, Ji Hyun Park, Kyu Hyung Park and Hyuncheol Kim et al. Permeability of the Retina and RPE-Choroid-Sclera to Three Ophthalmic Drugs and the Associated Factors Reprinted from: <i>Pharmaceutics</i> 2021 , <i>13</i> , 655, doi:10.3390/pharmaceutics13050655	226
Mariana Morais, Patrícia Coimbra and Maria Eugénia Pina Comparative Analysis of Morphological and Release Profiles in Ocular Implants of Acetazolamide Prepared by Electrospinning Reprinted from: <i>Pharmaceutics</i> 2021 , <i>13</i> , 260, doi:10.3390/pharmaceutics13020260	237
Xurxo García-Otero, Victoria Díaz-Tomé, Rubén Varela-Fernández, Manuel Martín-Pastor, Miguel González-Barcia and José Blanco-Méndez et al. Development and Characterization of a Tacrolimus/ Hydroxypropyl- β -Cyclodextrin Eye Drop Reprinted from: <i>Pharmaceutics</i> 2021 , <i>13</i> , 149, doi:10.3390/pharmaceutics13020149	251
Celia Djayet, Dominique Bremond-Gignac, Justine Touchard, Philippe-Henri Secretan, Fabrice Vidal and Matthieu P. Robert et al. Formulation and Stability of Ataluren Eye Drop Oily Solution for Aniridia Reprinted from: <i>Pharmaceutics</i> 2020 , <i>13</i> , 7, doi:10.3390/pharmaceutics13010007	278
Anna-Kaisa Rimpelä, Michel Garneau, Katja S. Baum-Kroker, Tanja Schönberger, Frank Runge and Achim Sauer Quantification of Drugs in Distinctly Separated Ocular Substructures of Albino and Pigmented Rats Reprinted from: <i>Pharmaceutics</i> 2020 , <i>12</i> , 1174, doi:10.3390/pharmaceutics12121174	289

Preface

Research in ophthalmic drug delivery has developed significant advances in the few last years, and efforts have been made to develop more effective topical formulations to increase drug bioavailability, efficiency, and safety. Drug delivery to the posterior segment of the eye remains a great challenge in the pharmaceutical industry due to the complexity and particularity of the eye's anatomy and physiology. Some advances have been made with the purpose of maintaining constant drug levels in the site of action. The anatomical ocular barriers have a great impact on drug pharmacokinetics and, subsequently, on the pharmacological effect.






Despite the increasing interest in efficiently reaching the posterior segment of the eye with reduced adverse effects, there is still a need to expand the knowledge of ocular pharmacokinetics that allow the development of safer and more innovative drug delivery systems. These novel approaches may greatly improve the lives of patients with ocular pathologies.

Francisco Javier Otero-Espinar and Anxo Fernández Ferreiro

Editors

Article

Topical Sustained Delivery of Miltefosine Via Drug-Eluting Contact Lenses to Treat Acanthamoeba Keratitis

Lin Chen^{1,2,3,†}, Liangju Kuang^{3,*,†}, Amy E. Ross³, Wissam Farhat³, Nikolay Boychev³, Sina Sharfi³, Levi N. Kanu³, Longqian Liu¹, Daniel S. Kohane⁴ and Joseph B. Ciolino^{3,*}

¹ Department of Optometry and Visual Science, West China Hospital, Sichuan University, Chengdu 610041, China

² Department of Ophthalmology, Affiliated Hospital of Zunyi Medical University, Zunyi 563000, China

³ Department of Ophthalmology, Schepens Eye Research Institute of Massachusetts Eye and Ear Infirmary, Harvard Medical School, Boston, MA 02114, USA

⁴ Department of Anesthesia, Boston Children's Hospital, Harvard Medical School, Boston, MA 02115, USA

* Correspondence: liangju_kuang@meei.harvard.edu (L.K.); joseph_ciolino@meei.harvard.edu (J.B.C.)

† These authors contributed equally to this work.

Abstract: This study aimed to develop a miltefosine-eluting contact lens (MLF-CL) device that would allow sustained and localized miltefosine release for the treatment of Acanthamoeba keratitis. MLF-CLs were produced in three different miltefosine doses by solvent-casting a thin miltefosine-polymer film around the periphery of a methafilcon hydrogel, which was then lathed into a contact lens. During seven days of in vitro testing, all three formulations demonstrated sustained release from the lens at theoretically therapeutic levels. Based on the physicochemical characterization of MLF-CLs, MLF-CL's physical properties are not significantly different from commercial contact lenses in terms of light transmittance, water content and wettability. MLF-CLs possessed a slight reduction in compression modulus that was attributed to the inclusion of polymer-drug films but still remain within the optimal range of soft contact lenses. In cytotoxicity studies, MLF-CL indicated up to 91% viability, which decreased proportionally as miltefosine loading increased. A three-day biocompatibility test on New Zealand White rabbits revealed no impact of MLF-CLs on the corneal tissue. The MLF-CLs provided sustained in vitro release of miltefosine for a week while maintaining comparable physical features to a commercial contact lens. MLF-CL has a promising potential to be used as a successful treatment method for Acanthamoeba keratitis.

Citation: Chen, L.; Kuang, L.; Ross, A.E.; Farhat, W.; Boychev, N.; Sharfi, S.; Kanu, L.N.; Liu, L.; Kohane, D.S.; Ciolino, J.B. Topical Sustained Delivery of Miltefosine Via Drug-Eluting Contact Lenses to Treat Acanthamoeba Keratitis.

Pharmaceutics **2022**, *14*, 2750.

<https://doi.org/10.3390/pharmaceutics14122750>

pharmaceutics14122750

Academic Editors: Francisco Javier Otero-Espinar and Anxo Fernández Ferreiro

Received: 12 October 2022

Accepted: 23 November 2022

Published: 8 December 2022

Publisher's Note: MDPI stays neutral with regard to jurisdictional claims in published maps and institutional affiliations.



Copyright: © 2022 by the authors. Licensee MDPI, Basel, Switzerland. This article is an open access article distributed under the terms and conditions of the Creative Commons Attribution (CC BY) license (<https://creativecommons.org/licenses/by/4.0/>).

Keywords: acanthamoeba keratitis; controlled drug delivery; contact lens; miltefosine; PLGA

1. Introduction

Acanthamoeba keratitis (AK) is a rare but potentially blinding corneal infection caused by free-living Acanthamoeba amoebae [1,2]. Inadequate disinfection of commercial contact lenses is one of the most common risks of AK [3–5]. With the increasing number of people wearing contact lenses, the prevalence of Acanthamoeba infections in the world is on the rise [6–10]. AK treatment at present is suboptimal and the prognosis of this condition is often poor [11]. First-line therapies for AK include topical polyhexamethylene biguanide (PHMB), propamide isethionate, chlorhexidine, dibromopropamide, and/or hexamidine [12,13], often requiring two or more drugs. However, the treatment duration is lengthy, complicated, and is often ultimately unsuccessful in complete eradication. Frequent eye drop instillation, as often as hourly throughout the day [14] is used in clinical practice, in part because of the limited bioavailability of topical eye drops [15]. Bioavailability from eye drops is estimated to be less than 5% because of the anatomic barriers in the anterior segment of the eye (e.g., tear film barrier and corneal barrier) [16,17]. In addition, trophozoites and cysts (two forms of Acanthamoeba's lifecycle) can remain in the cornea

for over two years [2,18]. Non-adherence can lead to suboptimal dosing. In general, killing of amoebic trophozoites and cysts is a challenge.

Miltefosine is an alkylphosphocholine agent with a broad spectrum of antiparasitic properties, which has recently been used in AK. This drug is commonly used as an oral medication to treat leishmaniasis [19]. After obtaining orphan drug designation from the FDA in 2016, oral miltefosine has been shown to be effective in refractory AK in several recent case reports [20–23]. However, systemic administration can produce severe inflammatory responses [24,25]. Providing a topical treatment could mitigate or even eliminate miltefosine's systemic side effects. Although miltefosine eye drops were effective in the management of AK in hamster [26] and rat [27] models, a clinical study failed to replicate the results in the humans [28]. The ineffectiveness observed may be attributed to the low bioavailability of eye drops in general and the fact that all studied cases had advanced keratitis at the time of initiation of the topical miltefosine therapy.

Previously, we have described a contact lens drug delivery system involving the incorporation of a thin drug-poly[lactic-co-glycolic acid] (PLGA) film into a poly[hydroxyethyl methacrylate] (pHEMA) hydrogel. This system has previously been used to achieve zero-order release kinetics at therapeutically relevant concentrations with fluorescein and ciprofloxacin for up to one month [29].

In this study, we incorporated miltefosine into this contact lens system to create a therapeutic contact lens (MLF-CL) for the treatment of AK. Miltefosine was loaded at different concentrations and the physicochemical properties (hydration, water contact angle, mechanical strength) of the MLF-CLs were investigated and compared with commercial contact lenses. Drug release kinetics were measured for a period of one week. In addition, the cytocompatibility and in vivo biocompatibility of the MLF-CL was evaluated.

2. Materials and Methods

2.1. Materials

Miltefosine was purchased from Cayman Chemical (Ann Arbor, MI, USA). Liquid methafilcon and methafilcon contact lens blanks were purchased from Kontur Kontakt Lens (Hercules, CA, USA). Poly(lactide-co-glycolide), 85% lactide, 15% glycolide (MW 190 KDa) was purchased from Merck and Cie (Schaffhausen, Switzerland). Hexafluoroisopropanol (HFIP) was purchased from Oakwood Chemical (Estill, NC, USA). Gibco phosphate-buffered saline (PBS), Dulbecco's Modification of Eagle's Medium, penicillin-streptomycin, and L-glutamine were purchased from Thermo Fisher Scientific (Waltham, MA, USA). Biopsy punches were purchased from Sklar Instruments (Westchester, PA, USA). All other reagents were purchased from Millipore-Sigma (St. Louis, MO, USA), except where otherwise noted.

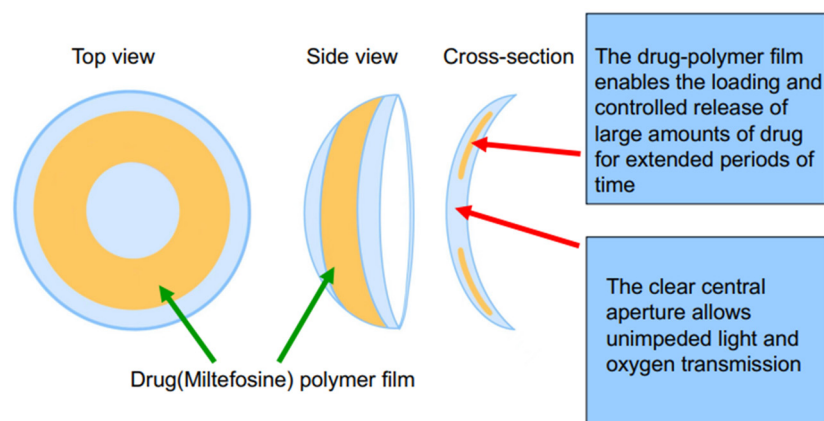
2.2. MLF-CL Fabrication

The drug-polymer solution was created by dissolving miltefosine and PLGA in HFIP, in ratios provided in Table 1. The polymer concentration was kept at 50 mg/mL. The film was created by using solvent casting. 50 μ L of solution was then pipetted into a concavity lathed into a cylinder of dry polymerized methafilcon. After 6 min of rotation on a spin coater (Model SC100, Best Tools LLC, St. Louis, MO, USA), the liquid HFIP evaporated, leaving a drug-polymer film. A 4 mm biopsy punch was used to define and remove the central diameter of the drug-polymer film to create a clear central aperture. The hydrogel blanks containing the films were placed on a desiccator under vacuum for two weeks to remove residual HFIP. The side of the film that was not yet in contact with methafilcon was then encapsulated in methafilcon through ultraviolet (UV) photopolymerization using ethylene glycol dimethacrylate (0.3%, crosslinker), Irgacure[®] 2959 (9 mg/mL, photoinitiator) and 3.5 min of UV light exposure at 120 mW/cm² applied within a Zeta 7401 UV chamber (Loctite, Düsseldorf, Germany) for 3.5 min at 120 mW/cm². The methafilcon cylinder was then lathed into a contact lens that consisted of the drug-PLGA film fully encapsulated

within methafilcon, with the initial cylinder on the front curve and polymerized methafilcon on the back curve (Scheme 1).

Table 1. MLF-CL formulations.

Formulation Name	Drug: Polymer Ratio
Commercial contact lens	N/A
MLF-CL ₂	2:25
MLF-CL ₄	4:25
MLF-CL ₈	8:25



Scheme 1. Schematic illustration of the designed miltefosine-eluting contact lens (MLF-CL).

2.3. Optical Coherence Topography

To evaluate MLF-CL morphology and film thickness, all formulations were imaged using anterior segment optical coherence topography (AS-OCT, RTVue, Optovue, Fremont, CA, USA) to assess the morphology. Non-hydrated MLF-CLs were positioned with the convex side of the lens facing the OCT camera. Raster scanning imaging was used in four segments for each contact lens to obtain cross sectional images of the contact lens and drug-polymer film.

2.4. MLF-CL Release

In vitro release of the MLF-CLs was conducted by hydrating MLF-CLs in 5 mL phosphate buffered saline (PBS) and placing in an incubator shaker at 37 °C at 64 rpm. At predetermined time points, the MLF-CLs were removed from PBS and immersed in fresh PBS. Release buffer aliquots were stored at 4 °C until drug concentration was quantified. Four lenses were used per formulation. Release quantification was performed by a colorimetric method.

2.5. Water Content

Water content of the MLF-CLs was performed by gravimetric method, according to ISO-18369-1 guidelines [30]. MLF-CLs were immersed in PBS until reaching equilibrium swelling, defined by a less than 5% change in mass in a 24 h period. Weight was recorded, then MLF-CLs were dried at 60 °C overnight and re-weighed. Weights were taken immediately after removal from the oven to prevent atmospheric moisture from influencing the results. All weights were recorded in duplicate. Four lenses were used per formulation. Percent water content was calculated by the following formula

$$\frac{W_s - W_d}{W_s} \times 100\%$$

where W_s = weight at equilibrium swelling and W_d = dry weight.

2.6. Light Transmission

Light transmission was measured through commercial contact lenses and the central aperture of the hydrated MLF-CL using SpectraMax M3 [31]. The average light transmission was calculated by averaging the transmission over the visible light spectrum (390–700 nm).

2.7. Water Contact Angle

MLF-CLs were hydrated in PBS until they reached equilibrium swelling. A drop of distilled water (about 5 μ L) onto the surface via a syringe. Then, a high-resolution image was captured from the side using the Dino-Lite Edge camera. The contact angle for each formulation ($n = 4$ and 5 measurements per specimen) was determined using ImageJ software (NIH, Bethesda, MD, USA) as a function of time.

2.8. Mechanical Properties

The mechanical features of the MLF-CLs were determined at room temperature using a Mark-10 ESM 303 motorized test stand (Mark-10 Corporation, Copiague, NY, USA). Before analysis, samples were hydrated by immersing them in PBS for 2 days. The compression test was conducted on rings with 7 mm and 6 mm external and internal diameter, respectively and with a crosshead speed of 1 mm/min. The Compression Modulus was obtained from the linear derivative of the stress–strain curve in the low stiffness range (less than 10% strain). Three independent measurements were conducted for each group.

2.9. Cytotoxicity

L929 murine fibroblasts (American Tissue Culture Collection, Manassas, VA, USA) were used to assess the cytotoxicity of MLF-CLs. L929 cells were grown in Dulbecco's Modification of Eagle's Medium (DMEM), supplemented with 10% fetal bovine serum, 1% penicillin-streptomycin, and 4 mM L-glutamine. Cytotoxicity was measured by the minimum elution media method, described by ISO 10993-5 guidelines [32]. MLF-CLs or vehicle lenses (with the polymer film but no drug) were immersed in supplemented DMEM in a volume of 1.8 mL for each MLF-CL. The MLF-CLs were incubated at 37 °C for 24 h to capture eluted drugs and leachables. The elution media (extract) was applied neat to L929s plated in 96 well plates at 1×10^5 cells/mL the day prior. The cells with extract were incubated for 24 h. Cell viability was measured by CellTiter 96[®] Non-Radioactive Cell Proliferation Assay (MTT) (Promega, Madison, WI, USA). Results were expressed as percentage viability of L929 controls that were not exposed to extract. Four lenses were used for each formulation, with six replicates per lens.

2.10. Animals

The study protocol #2021N000159 was approved on 7 July 2021 by the Institutional Animal Care and Utilization Committee at Schepens Eye Research Institute of Massachusetts Eye and Ear Infirmary (Boston, MA). All animals were treated according to the Association for Research in Vision and Ophthalmology (ARVO) Statement for the Use of Animals in Ophthalmic and Vision Research (ARVO Handbook, 1993). New Zealand white rabbits (NZW) (Charles River Laboratories, Boston, MA, USA) age four months, each weighing 3–5 kg, were used for the biocompatibility study. Only one eye in each NZW was used to prevent bilateral vision restriction. The contralateral eye was untreated and served as a control. NZWs were singly housed in a climate-controlled environment with free access to food and water during acclimation and throughout the experiment. NZWs were acclimated for seven days prior to experiments. In each of the studies, intramuscular injection of 30 mg/kg ketamine, 5 mg/kg xylazine, and 1 mg/kg acepromazine were used for anesthesia. 0.05 mg/kg Buprenorphine HCl was used for pain control prior to tarsorrhaphy.

Only MLF-CL₄ was used for the biocompatibility study. Under anesthesia, NZWs had baseline photos taken by a Topcon DC-3 digital camera attachment for slit lamp. The MLF-CL was placed on the cornea, with care to place it under the nictating membrane. The MLF-CL was evaluated to ensure free movement on the cornea without fluting or bubbling.

To improve lens retention, eyes with contact lenses received a temporary tarsorrhaphy in which the eyelids were closed with one to two 5-0 Nylon sutures. NZWs were evaluated daily for signs of discomfort. After three days, the tarsorrhaphy and MLF-CL and re-imaged. NZW eyes were evaluated for redness, edema, discharge, and fur matting. NZWs were euthanized with 120 mg/kg pentobarbital, and the corneas were removed from both eyes. The eyes were fixed in 10% formalin, embedded in paraffin, and cut into 10-micron sections in an anterior to posterior fashion so that the pupil and the optic nerve were in one section (PO section). Slides were stained with hematoxylin and eosin (H&E) to visualize ocular structures.

2.11. Statistics

For all continuous data, nonparametric descriptive statistics were used to determine statistical significance. Kruskal–Wallis Test was calculated, and if significant, followed by pairwise comparisons to determine significant differences between groups. A *p*-Value of less than 0.05 was considered significant.

3. Results

3.1. MLF-CL Was Successfully Encapsulated in Contact Lens Hydrogels

Three dosages of MLF-CLs were created by changing the drug amount loaded in each lens while keeping PLGA concentration constant (Table 1). Drug-polymer (PLGA) films were created through solvent casting, then encapsulated in methafilcon hydrogel using ultraviolet (UV) polymerization of hydroxyethylmethacrylate (HEMA) (Figure 1). When hydrated, the MLF-CLs expanded from 11.3 mm to 14.5 mm diameter and from 4 mm to 5 mm central aperture diameter and maintained a normal shape (Figure 1a). Anterior segment ocular coherence tomography (AS-OCT) images demonstrated uniform drug-polymer films completely within the methafilcon hydrogel and a clear aperture to preserve light transmission to the visual system (Figure 1b). Film thickness was roughly the same for all groups: MLF-CL₂: $83.30 \pm 6.08 \mu\text{m}$, MLF-CL₄: $81.11 \pm 1.15 \mu\text{m}$, MLF-CL₈: $85.03 \pm 5.62 \mu\text{m}$ ($p = 0.779$, Kruskal–Wallis, $n = 4$). When imaged by OCT, no delamination of the film from the hydrogel was observed before hydration or after the lens was hydrated (Figure S1), indicating the film had sufficient adherence to the hydrogel that allow the film to maintain the same configuration during the hydration process which increased the diameter of the lens.

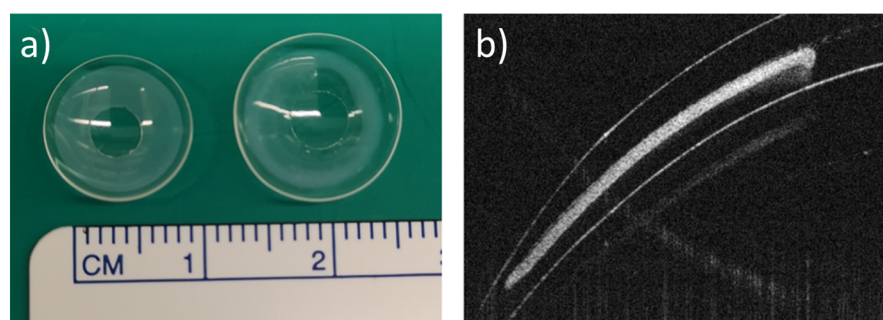


Figure 1. Miltefosine-eluting contact lens (MLF-CL). (a) Photographs of dry (left) and hydrated (right) contact lens. (b) An ocular coherence tomography (OCT) image of a section of a dry MLF-CL showing an encapsulated miltefosine-polymer film and central aperture to allow for unimpeded vision.

Drug release from MLF-CLs was studied in PBS at 37 °C. Because miltefosine aqueous solubility is relatively high (reported as 440 mg/mL [33]), frequent buffer changes were performed to preserve infinite sink conditions. All formulations demonstrated relatively constant state release through seven days (Figure 2). Cumulative 7-day miltefosine release ranged from $156.0 \pm 4.7 \mu\text{g}$ (MLF-CL₂) to $470.3 \pm 39.8 \mu\text{g}$ (MLF-CL₈) (Figure 2). We analyzed the miltefosine release kinetics from the MLF-CL using zero-order, first-order, Higuchi, and Korsmeyer-Peppas mathematical models (Table S1). Considering the highest

value of R^2 -adjusted, the lowest Akaike Information Criterion (AIC) values and the largest Model Selection Criterion (MSC) [34], the release data fit well to the Korsmeyer-Peppas model for all formulations (Figure S2 and Table S1). The predicted release based on Korsmeyer-Peppas model was shown in Figure S2. These results indicated the diffusional release of miltefosine from contact lens, which was consistent with other drugs released from therapeutic contact lenses [31,35].

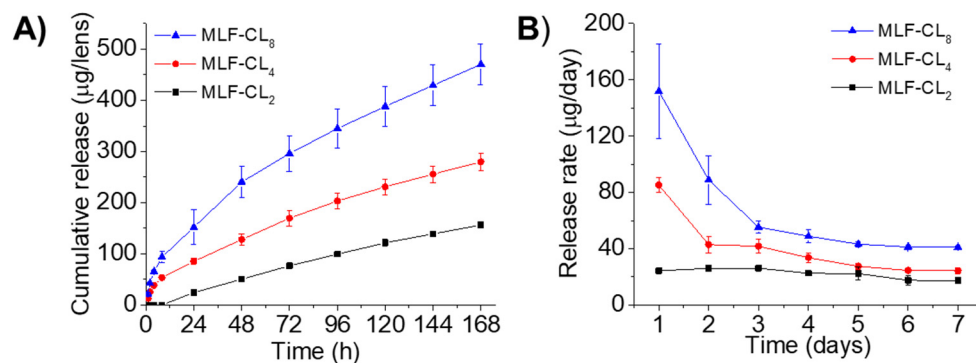


Figure 2. In vitro miltefosine (MLF) release from MLF-CLs. (A) the cumulative release and (B) the daily release rate. Quantitative data are expressed as mean \pm standard deviation (SD), $n = 4$ /group per time point.

3.2. MLF-CL Water Content Was Comparable to Commercial Contact Lenses

The water content of contact lenses is reported to have a significant impact on oxygen permeability and contact lens wearing comfort [36,37]. MLF-CL water content was assessed by the gravimetric method [38] and the results were compared to commercial methafilcon contact lenses (Kontur) ($n = 4$ /group). Commercial contact lens had a water content ($53 \pm 1.6\%$) comparable to the reported value (55%) [39,40]. There was no significant ($p = 0.49$, Kruskal–Wallis Test) difference in the water content between MLF-CLs and commercial methafilcon lenses (Figure 3).

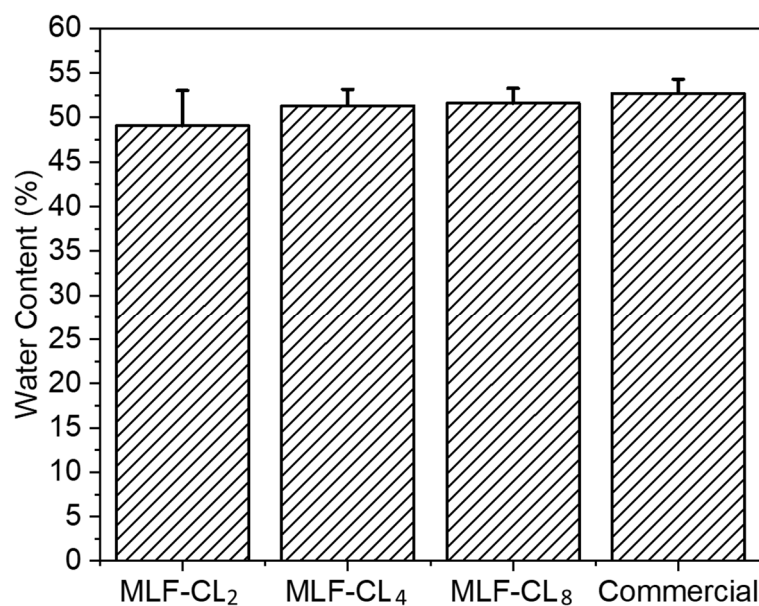


Figure 3. Equilibrium water content for miltefosine-eluting contact lenses (MLF-CLs) compared to commercial contact lenses. Quantitative data are expressed as mean \pm standard deviation (SD). No significant statistical difference among samples by Kruskal–Wallis Test. $p = 0.49$, $n = 4$.

3.3. MLF-CL Light Transmittance Was comparable to Commercial Contact Lenses

The light transmittance properties of contact lenses are clearly important for visual performance. MLF-CL maintained light transmittance >95% through the central aperture between 390 nm to 700 nm (Figure 4A). The difference in average light transmittance between the commercial contact lenses and MLF-CL was negligible ($p = 0.15$, Kruskal–Wallis Test, $n = 4$ per group, Figure 4B), which was in agreement with our previous reports [35,41].

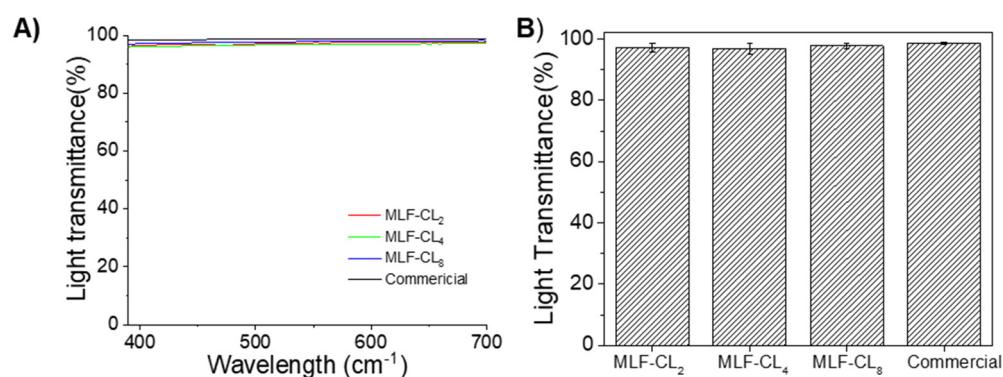


Figure 4. (A) Light transmittance curve of commercial lens and central aperture of MLF-CL through the visible light spectrum (from 390 nm to 700 nm). (B) The average light transmission of MLF-CL, which was calculated by averaging the transmission over the visible light spectrum (390–700 nm). $n = 4$ lens per group. Quantitative data are expressed as mean \pm standard deviation (SD). No significant difference in average light transmittance between the commercial contact lenses and MLF-CL was observed ($p = 0.15$, Kruskal–Wallis Test).

3.4. Compression Modulus Was Similar between MLF-CLs and Commercial Contact Lenses

Excessive stiffness in a contact lens can result in discomfort. Compression tests [42] were performed on the various MLF-CLs formulations to estimate their mechanical properties. The stress–strain curves of the different lenses were plotted, hence providing a visual display, indicating their strength and elasticity. MLF-CLs were compared to commercial CLs ($n = 3$ /group, Figure 5). All groups were compared by Kruskal–Wallis Test. Commercial CLs demonstrated the highest modulus at 491 ± 140 kPa. MLF-CL₂ (220 ± 50 kPa), MLF-CL₄ (296 ± 92 kPa) and MLF-CL₈ (255 ± 30 kPa) with no significant differences among them ($p = 0.1$, Kruskal–Wallis Test).

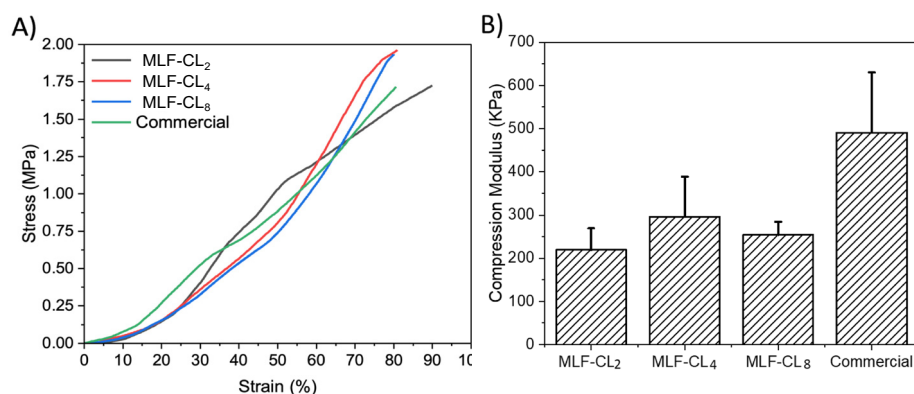


Figure 5. (A) Average stress–strain curves and (B) Compression modulus for miltefosine-eluting contact lenses (MLF-CLs) compared to commercial contact lenses. Quantitative data are expressed as mean \pm standard deviation (SD). No significant statistical difference among samples. by Kruskal–Wallis Test. $p = 0.1$, $n = 3$.

3.5. MLF-CL Surface Wettability was Comparable to Commercial Contact Lenses

Water contact angle is a measure of the wettability of a surface. Poor wettability can break up the tear film, leading to dry eyes [36,43]. Water contact angle was measured in MLF-CLs and commercial contact lenses using sessile drop technique, the most commonly used method for biomaterials [44]. All contact lenses were cut to lie flat to ensure the most accurate measurements. Compared to commercial contact lenses ($26.2 \pm 4.0^\circ$), there were no significant differences ($p = 0.06$, Kruskal–Wallis Test) among the MLF-CL groups ($n = 4$ /group) (Figure 6).

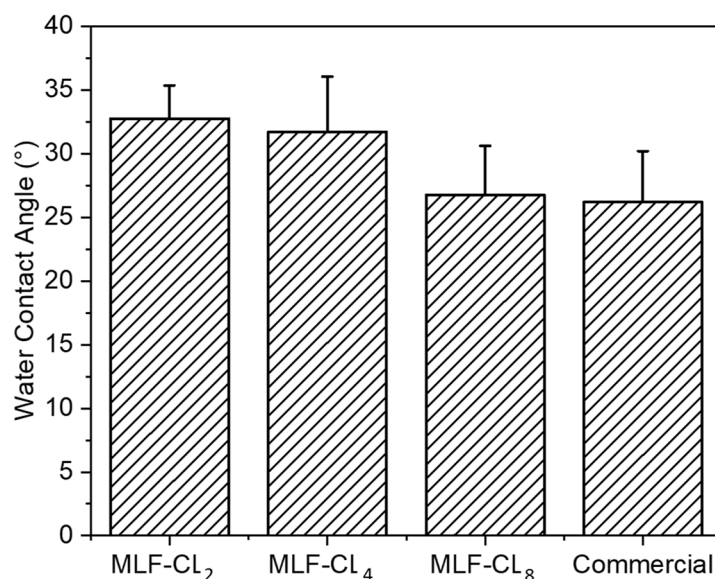


Figure 6. Water contact angle of miltefosine-eluting contact lenses (MLF-CLs) and commercial contact lenses. Quantitative data are expressed as mean \pm standard deviation (SD). No significant statistical difference among samples by Kruskal–Wallis Test. $p = 0.06$, $n = 4$.

3.6. MLF-CL Exhibited Dose-Dependent In Vitro Cytotoxicity to L929 Murine Fibroblasts

Because miltefosine or MLF-CL leachables such as unreacted monomer, photoinitiator, or residual solvent could potentially cause toxicity, we tested the cytotoxicity of MLF-CLs by the minimum elution media method, where the extract from hydrated MLF-TCLs was exposed to L929 murine fibroblasts [45,46]. The L929 murine fibroblast cells are highly proliferative and frequently used in cytotoxicity testing to evaluate cellular viability and proliferation [47]. Results were compared to L929 cells not exposed to extract. Vehicle lenses showed no cytotoxicity ($98.7 \pm 7.3\%$). MLF-CLs showed viability that was inversely proportional to MLF content, with viabilities of $90.6 \pm 3.3\%$, $72.7 \pm 4.8\%$, and $29.8 \pm 1.9\%$ for MLF-CL₂, MLF-CL₄, and MLF-CL₈, respectively (Figure 7).

3.7. MLF-CLs Demonstrated Suitable Biocompatibility In Vivo

Potential risks with contact lens wear include corneal edema, cornea abrasions, and microbial keratitis and there is also the risk of local or systemic toxicity from topically delivered miltefosine. Normal New Zealand White (NZW) rabbits were used to assess biocompatibility as rabbits are the lowest order mammal that can wear a contact lens. In addition, NZW eye dimensions are comparable to those of a human [48]. MLF-CL₄s were chosen to be evaluated in vivo as they had demonstrated suitable physicochemical properties similar to other commercial contact lenses while maintaining an acceptable cytotoxicity level. NZWs ($n = 3$, two females, one male) wore the MLF-CL₄s continuously for three days. One eye showed erythema throughout the conjunctiva, on day 3. In the other two rabbits, no abnormalities were seen in daily observations during the lens wear period. No erythema, discharge, lid edema, or epithelial defects were noted on slit lamp exam after three days of continuous wear.

Pathology revealed normal corneas and irises in all NZWs. No changes in the corneal epithelium, stromal lamellae, Descemet's membrane, and endothelium were observed (Figure 8). Results were compared to the contralateral eyes of each rabbit, showing no difference between eyes that wore the MLF-CL and untreated eyes.

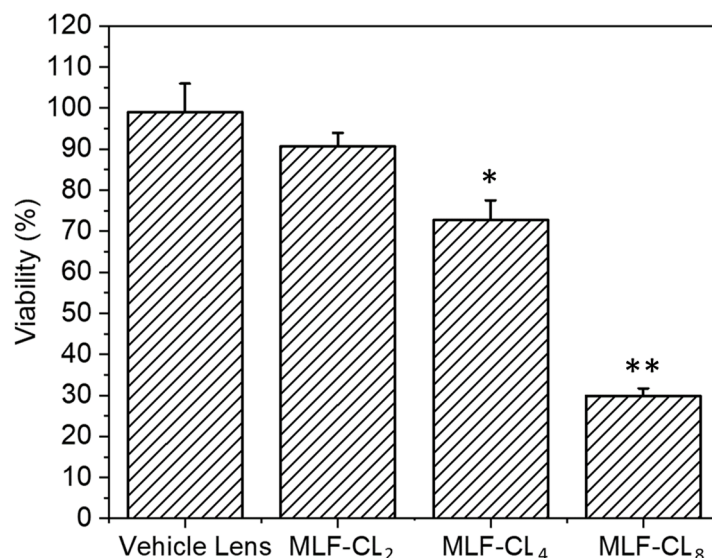


Figure 7. Cell viability of L929s with eluted media from miltefosine-eluting contact lenses (MLF-CLs). Results are expressed as percent viability of untreated L929s. Cell viability for MLF-CLs compared to vehicle lenses. * $p = 0.017$, ** $p < 0.001$ by Kruskal–Wallis Test with Bonferroni correction. $n = 4$.

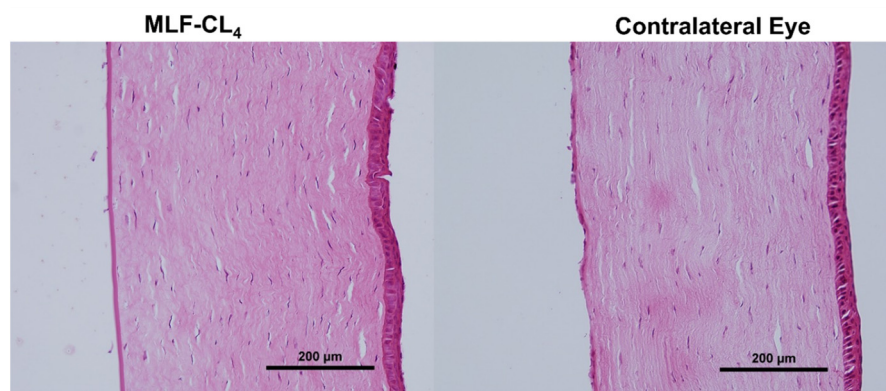


Figure 8. Hematoxylin and Eosin(H&E) stained corneas for New Zealand white rabbits (NZW) eyes wearing miltefosine-eluting contact lenses (MLF-CL₄) compared to the contralateral eye (untreated).

4. Discussion

In this work, we have encapsulated miltefosine in a contact lens hydrogel. This device provides sustained release of miltefosine for one week and may be of use in the treatment of AK. To our knowledge, this is the first report of a miltefosine sustained release system for the treatment of ocular disease.

PLGA was chosen due to its safety and excellent sustained drug release profiles [49]. PLGA is a component of numerous FDA- and European Medicine Agency (EMA)- approved drug delivery devices. The ratio of lactide to glycolide of 85:15 in PLGA was chosen because higher lactide content is associated with a decrease in degradation rate and drug release rate [49]. PLGA can degrade into its two monomeric constituents (lactic acid and glycolic acid) via hydrolysis reactions, which in turn can be easily metabolized via the Krebs cycle. Therefore, PLGA produces minimal systemic toxicity when used in biological applications [50], and showed no toxicity in our studies. The films were made by solvent

casting and lathing, but other approaches could be employed, such as 3D printing of the film and producing contact lenses from molds [51].

In a miltefosine-loaded nanostructured lipid carriers release system [52], most drugs were released within a few hours. Miltefosine-loaded alginate nanoparticles sustained the release of miltefosine for 24 h [53]. In contrast, our MLF-CLs achieved a stable release rate over a period of 7 consecutive days. The sustained release of MLF-CLs may be attributed to the high partition coefficient ($\log P$ of 3.8) of miltefosine and interaction between drug and PLGA [54]. Miltefosine was miscible with PLGA in the drug-polymer film (Figure 1), indicating the interaction between drug and PLGA. Considering the hydrophobic properties of miltefosine and PLGA, this suggests drug-polymer interactions were due to this shared hydrophobicity with charge interactions as a secondary effect. The drug-polymer interaction can be investigated by Fourier-transform infrared spectroscopy (FTIR) and Differential Scanning Calorimeter (DSC) [55,56]. These results were consistent with our previous reports that PLGA films in contact lenses were able to sustain the release of hydrophobic drugs such as dexamethasone and latanoprost [35,41,57,58]. While AK often requires a treatment duration of weeks to months, extended wear of a single contact lens is limited to seven days to prevent complications from contact lens overwear, including corneal edema and microbial keratitis. In practice, a patient with AK could wear consecutive MLF-CLs—exchanged once weekly by an ophthalmologist—until AK is eradicated.

Previous studies have reported a minimum amebicidal concentration (MAC) of 16 $\mu\text{g}/\text{mL}$ for clinical and environmental isolates [59–61]. The formulations MLF-CL₂, MLF-CL₄ and MLF-CL₈ released 24, 85 and 151 μg of miltefosine on the first day, respectively. The daily release rate thereafter ranged from 17–26 $\mu\text{g}/\text{day}$ for MLF-CL₂, 24–42 $\mu\text{g}/\text{day}$ for MLF-CL₄, and ranged from 41–89 $\mu\text{g}/\text{day}$ for MLF-CL₈ (Figure 2B) after one week of testing, well above the MAC. Based on the design of contact lens drug delivery, the fluid exchange in the post-lens tear film that exists between the cornea and the contact lens has been shown to be slower than fluid exchange on the surface of the eye [62,63], which may improve the drug bioavailability compared to topical eye drops. In our previous study with a latanoprost contact lens, we found that contact lenses with drug-polymer films had high correlation coefficients between drug release *in vitro* and drug absorption *in vivo* [57]. We expect that the amount of miltefosine released by MLF-CLs in the eye may reach therapeutic amounts *in vivo*.

The light transmittance of central aperture was above 95% for all three formulation and was comparable to commercial lens, though the film-embedded part of the MLF-CL showed semitransparency (Figure 1). We also have the flexibility to increase the MLF-CL central aperture size to further increase visual performance.

Wettability and mechanical properties of the lenses are critical for the physiological compatibility, handling, durability, and comfort of wearing the lenses. In fact, oxygen diffusivity and water content are key parameters influencing the comfort and safety of a lens [36]. MLF-CLs showed similar water content compared to commercial methafilcon contact lenses of about 53% water uptake. At a range of 26–33°, MLF-CL wettability was also similar to commercial contact lenses. One of the limitations to our study is that we did not directly measure oxygen transmittance, which has been associated with wearing comfort.

The modulus range for the MLF-CLs we measured was between 210 kPa and 300 kPa. We found that MLF-CLs are softer than commercial contact lenses (490 kPa) as they showed a significantly lower modulus. This decrease in modulus is most likely the result of increased chain mobility in the contact lens hydrogel. Nonetheless, the modulus of MLF-CL is still within the acceptable range of values reported in the literature for the currently available contact lens materials (300 to 600 kPa) [64].

MLF-CL showed cell viability inversely proportional to dose: MLF-CL₂ had the highest cell viability (91%) and MLF-CL₈ had the lowest cell viability (36%). Given that the vehicle lens had cell viability of close to 100%, the decreased cell viability is solely associated with

increased miltefosine dose. Nonetheless, MLF-CL₄ had an acceptable level (73%) of cell survival by ISO standards [65]. In addition, Miltefosine was significantly less toxic than 0.02% (200 µg/mL) chlorhexidine, a standard concentration of chlorhexidine drops used to treat AK [66]. In our own studies, chlorhexidine showed significant toxicity at 0.005% (50 µg/mL), compared to miltefosine alone, which did not demonstrate cytotoxicity until 90 µg/mL (Figure S3). This is higher than the believed efficacious dose of 65.12 µg/mL. Previous *in vitro* studies on anti-AK drugs have shown low cell viability of 21% with 0.02% chlorhexidine (CHX) and 38% with both 0.02% polyhexamethylene biguanide (PHMB) and 0.01% (100 µg/mL) propamidine isethionate (PI). Given the favorable physicochemical properties of MLF-CL₄, combined with minor *in vivo* toxicity, additional formulations can be investigated with changing miltefosine concentrations to reduce cytotoxicity. We also have the flexibility to adjust the MLF-CL central aperture size to achieve this purpose.

In the biocompatibility experiment for this study, one of three rabbits exhibited adverse effects after three days of wear. Miltefosine acts as an immunomodulator, activating Type 1 T-helper cells (Th1) which in turn increase the recipient's inflammatory response. Cytokines, particularly interferon gamma and interleukin 12 have been observed to be elevated with oral miltefosine use [67]. However, pathology did not reveal any abnormalities in the cornea and iris, indicating the adverse effects of miltefosine were self-limiting. In clinical practice, the severe inflammation reaction is alleviated by prescribing oral and/or topical steroids [24], though the practice is often contested, as steroids can dampen the body's natural immune response [68,69]. Topical steroids could be prescribed, or potentially include steroids in the MLF-CL. *In vivo* and *in vitro* correlation can be poor, which also supports testing *in vivo* biocompatibility. More research is needed (i.e., evaluating long-term outcomes of MLF-CL wear) to determine the appropriate course of action.

5. Conclusions

We incorporated the miltefosine-PLGA film into a commercially available hydrogel material to form a delivery system that can slowly release miltefosine. MLF-CL's physical properties were not significantly different from commercial contact lenses in terms of light transmittance, water content, and wettability. This ocular drug delivery system provides a slow and steady release of miltefosine over the course of a week and has the safety profile to serve as a promising drug treatment platform for AK. More critical efforts are needed to develop an efficient and safe MLF-CL device that can be validated in animals and clinics. In accordance with the outcomes of this investigation, we envision that the MLF-CL₄ lens is very suitable for further *in vivo* and clinical studies, as it shows comparable physicochemical properties to the commercial contact lens, optimal biocompatibility, and an enhanced and sustained drug release over a period on one week.

Supplementary Materials: The following supporting information can be downloaded at: <https://www.mdpi.com/article/10.3390/pharmaceutics14122750/s1>, Figure S1: The OCT image of hydrated MLF-CL; Figure S2: *In vitro* release profiles (actual cumulative release %) of MLF-CL and mathematical modeling (predicted release %) of the miltefosine release profiles. The *in vitro* release profiles of miltefosine from MLF-CL fit to the Korsmeyer-Peppas model. Data are shown as the means ± SD, n = 4 for each group; Figure S3: Cell viability of L929s subjected to different concentrations of (A) Miltefosine (µg/mL) and (B) Chlorhexidine free base drug (µg/mL); Table S1: Mathematical model examination for the miltefosine release from MLF-CL. R²-adjusted, Akaike Information Criterion (AIC) and the Model Selection Criterion (MSC) employed for model selection (n = 4). The best model possesses the highest value of R²-adjusted, the lowest AIC value and the largest MSC [34].

Author Contributions: Conceptualization: L.C., L.K., A.E.R. and J.B.C. Investigation: L.C., L.K., A.E.R., W.F., N.B., S.S., L.N.K., J.B.C. Analysis: L.C., L.K., A.E.R., W.F., N.B. and J.B.C. Writing—Original draft preparation: L.C., L.K., A.E.R., W.F. Visualization: L.K., W.F., A.E.R., L.C., L.L. Writing—review and editing: L.C., L.K., A.E.R., W.F., N.B., L.N.K., D.S.K., J.B.C. Supervision: J.B.C. Project administration: J.B.C. Funding acquisition: L.C. and J.B.C. All authors have read and agreed to the published version of the manuscript.

Funding: L.C. was supported by the China Scholarship Council and the National Nature Science Foundation of China (No. 81960183). This project was funded by NIH 1R01 EY026640 (JBC) and P30EY003790 (Schepens Eye Research Institute Core).

Institutional Review Board Statement: The animal protocol was approved by the Schepens Eye Research Institute Institutional Animal Care and Use Committee (Protocol 2021N000159, approved on 7 July 2021).

Informed Consent Statement: Not applicable.

Data Availability Statement: Not applicable.

Acknowledgments: The authors would like to thank Miele MacMillan and Honey Thomas for assistance with animal studies, Menglu Yang for cell culture assistance, Mengqiu Huang for assistance with schematic illustration, and Jerry Niederkorn for experimental suggestions.

Conflicts of Interest: J.B.C. and D.S.K. have a financial interest in Theroptix, a company developing a contact lens drug delivery system. They are inventors of the technology, co-founders, and serve as consultants. J.B.C.'s interests were reviewed and are managed by Massachusetts Eye and Ear and Mass General Brigham Healthcare in accordance with their conflict of interest policies. D.S.K.'s interests are managed by Boston Children's Hospital in accordance with their conflict of interest policies.

References

- Panjwani, N. Pathogenesis of Acanthamoeba keratitis. *Ocul. Surf.* **2010**, *8*, 70–79. [CrossRef] [PubMed]
- de Lacerda, A.G.; Lira, M. Acanthamoeba keratitis: A review of biology, pathophysiology and epidemiology. *Ophthalmic Physiol. Opt.* **2021**, *41*, 116–135. [CrossRef] [PubMed]
- Kaufman, A.R.; Tu, E.Y. Advances in the management of Acanthamoeba keratitis: A review of the literature and synthesized algorithmic approach. *Ocul. Surf.* **2022**, *25*, 26–36. [CrossRef]
- Fanselow, N.; Sirajuddin, N.; Yin, X.T.; Huang, A.J.W.; Stuart, P.M. Acanthamoeba Keratitis, Pathology, Diagnosis and Treatment. *Pathogens* **2021**, *10*, 323. [CrossRef]
- Niederkorn, J.Y. The biology of Acanthamoeba keratitis. *Exp. Eye Res.* **2021**, *202*, 108365. [CrossRef] [PubMed]
- Lorenzo-Morales, J.; Khan, N.A.; Walochnik, J. An update on Acanthamoeba keratitis: Diagnosis, pathogenesis and treatment. *Parasite* **2015**, *22*, 10. [CrossRef] [PubMed]
- Alkharashi, M.; Lindsley, K.; Law, H.A.; Sikder, S. Medical interventions for acanthamoeba keratitis. *Cochrane Database Syst. Rev.* **2015**, *2*, CD010792. [CrossRef]
- McKelvie, J.; Alshiakhi, M.; Ziaei, M.; Patel, D.V.; McGhee, C.N. The rising tide of Acanthamoeba keratitis in Auckland, New Zealand: A 7-year review of presentation, diagnosis and outcomes (2009–2016). *Clin. Exp. Ophthalmol.* **2018**, *46*, 600–607. [CrossRef]
- Randag, A.C.; van Rooij, J.; van Goor, A.T.; Verkerk, S.; Wisse, R.P.L.; Saelens, I.E.Y.; Stoutenbeek, R.; van Dooren, B.T.H.; Cheng, Y.Y.Y.; Eggink, C.A. The rising incidence of Acanthamoeba keratitis: A 7-year nationwide survey and clinical assessment of risk factors and functional outcomes. *PLoS ONE* **2019**, *14*, e0222092. [CrossRef]
- Rayamajhee, B.; Willcox, M.D.; Henriquez, F.L.; Petsoglou, C.; Carnt, N. Acanthamoeba keratitis: An increasingly common infectious disease of the cornea. *Lancet Microbe* **2021**, *2*, e345–e346. [CrossRef]
- Maycock, N.J.; Jayaswal, R. Update on Acanthamoeba Keratitis: Diagnosis, Treatment, and Outcomes. *Cornea* **2016**, *35*, 713–720. [CrossRef] [PubMed]
- Carnt, N.; Stapleton, F. Strategies for the prevention of contact lens-related Acanthamoeba keratitis: A review. *Ophthalmic Physiol. Opt.* **2016**, *36*, 77–92. [CrossRef] [PubMed]
- Somani, S.N.; Ronquillo, Y.; Moshirfar, M. Acanthamoeba Keratitis. In *StatPearls [Internet]*; Stat Pearls Publishing: Treasure Island, FL, USA, 2022.
- Garg, P.; Kalra, P.; Joseph, J. Non-contact lens related Acanthamoeba keratitis. *Indian J. Ophthalmol.* **2017**, *65*, 1079. [CrossRef] [PubMed]
- Sharma, A.; Taniguchi, J. Emerging strategies for antimicrobial drug delivery to the ocular surface: Implications for infectious keratitis. *Ocul. Surf.* **2017**, *15*, 670–679. [CrossRef] [PubMed]
- Lanier, O.L.; Manfre, M.G.; Bailey, C.; Liu, Z.; Sparks, Z.; Kulkarni, S.; Chauhan, A. Review of Approaches for Increasing Ophthalmic Bioavailability for Eye Drop Formulations. *AAPS PharmSciTech* **2021**, *22*, 107. [CrossRef] [PubMed]
- Peng, C.; Kuang, L.; Zhao, J.; Ross, A.E.; Wang, Z.; Ciolino, J.B. Bibliometric and visualized analysis of ocular drug delivery from 2001 to 2020. *J. Control Release* **2022**, *345*, 625–645. [CrossRef]
- Kremer, I.; Cohen, E.J.; Eagle Jr, R.C.; Udell, I.; Laibson, P.R. Histopathologic evaluation of stromal inflammation in Acanthamoeba keratitis. *CLAO J. Off. Publ. Contact Lens Assoc. Ophthalmol. Inc* **1994**, *20*, 45–48.
- Palic, S.; Beijnen, J.H.; Dorlo, T.P.C. An update on the clinical pharmacology of miltefosine in the treatment of leishmaniasis. *Int. J. Antimicrob. Agents* **2022**, *59*, 106459. [CrossRef]

20. Avdagic, E.; Chew, H.F.; Veldman, P.; Tu, E.Y.; Jafri, M.; Doshi, R.; Boggild, A.K.; Reidy, J.J.; Farooq, A.V. Resolution of Acanthamoeba Keratitis with Adjunctive Use of Oral Miltefosine. *Ocul. Immunol. Inflamm.* **2021**, *29*, 278–281. [CrossRef]
21. Hirabayashi, K.E.; Lin, C.C.; Ta, C.N. Oral miltefosine for refractory Acanthamoeba keratitis. *Am. J. Ophthalmol. Case Rep.* **2019**, *16*, 100555. [CrossRef]
22. Dewan, N.; Ming, W.; Holland, S.P.; Yeung, S.N.; Iovieno, A. Oral Miltefosine as Adjunctive Treatment for Recalcitrant Acanthamoeba Keratitis. *Cornea* **2019**, *38*, 914–917. [CrossRef] [PubMed]
23. Naranjo, A.; Martinez, J.D.; Miller, D.; Tonk, R.; Amescua, G. Systemic Miltefosine as an Adjunct Treatment of Progressive Acanthamoeba Keratitis. *Ocul. Immunol. Inflamm.* **2021**, *29*, 1576–1584. [CrossRef] [PubMed]
24. Thulasi, P.; Saeed, H.N.; Rapuano, C.J.; Hou, J.H.; Appenheimer, A.B.; Chodosh, J.; Kang, J.J.; Morrill, A.M.; Vyas, N.; Zegans, M.E.; et al. Oral Miltefosine as Salvage Therapy for Refractory Acanthamoeba Keratitis. *Am. J. Ophthalmol.* **2021**, *223*, 75–82. [CrossRef] [PubMed]
25. Si, Z.; Veldman, P.B.; Reidy, J.J.; Farooq, A.V. Severe Inflammatory Response in a Patient on Oral Miltefosine for Acanthamoeba Keratitis. *Ocul. Immunol. Inflamm.* **2021**, *30*, 1027–1028. [CrossRef]
26. Polat, Z.A.; Obwaller, A.; Vural, A.; Walochnik, J. Efficacy of miltefosine for topical treatment of Acanthamoeba keratitis in Syrian hamsters. *Parasitol. Res.* **2012**, *110*, 515–520. [CrossRef]
27. Polat, Z.A.; Walochnik, J.; Obwaller, A.; Vural, A.; Dursun, A.; Arici, M.K. Miltefosine and polyhexamethylene biguanide: A new drug combination for the treatment of Acanthamoeba keratitis. *Clin. Exp. Ophthalmol.* **2014**, *42*, 151–158. [CrossRef]
28. Bagga, B.; Joseph, J.; Garg, P.; Chandran, K.; Jayabhasker, P.; Manjulatha, K.; Sharma, S. Efficacy of Topical Miltefosine in Patients with Acanthamoeba Keratitis: A Pilot Study. *Ophthalmology* **2019**, *126*, 768–770. [CrossRef]
29. Ciolino, J.B.; Hoare, T.R.; Iwata, N.G.; Behlau, I.; Dohlman, C.H.; Langer, R.; Kohane, D.S. A drug-eluting contact lens. *Invest. Ophthalmol. Vis. Sci.* **2009**, *50*, 3346–3352. [CrossRef]
30. ISO 18369-1:2017; Ophthalmic optics—Contact lenses—Part 1: Vocabulary, classification system and recommendations for labelling specifications. International Organization for Standardization: Geneva, Switzerland, 2017.
31. Zhu, Q.; Liu, C.; Sun, Z.; Zhang, X.; Liang, N.; Mao, S. Inner layer-embedded contact lenses for pH-triggered controlled ocular drug delivery. *Eur. J. Pharm. Biopharm.* **2018**, *128*, 220–229. [CrossRef]
32. ISO 10993-5: 2009; Biological evaluation of medical devices—Part 5: Tests for in vitro cytotoxicity. International Organization for Standardization: Geneva, Switzerland, 2009.
33. Van Bocxlaer, K.; Yardley, V.; Murdan, S.; Croft, S.L. Topical formulations of miltefosine for cutaneous leishmaniasis in a BALB/c mouse model. *J. Pharm. Pharmacol.* **2016**, *68*, 862–872. [CrossRef]
34. Jiang, C.; Cano-Vega, M.A.; Yue, F.; Kuang, L.; Narayanan, N.; Uzunalli, G.; Merkel, M.P.; Kuang, S.; Deng, M. Dibenzazepine-loaded nanoparticles induce local browning of white adipose tissue to counteract obesity. *Mol. Ther.* **2017**, *25*, 1718–1729. [CrossRef] [PubMed]
35. Ross, A.E.; Bengani, L.C.; Tulsan, R.; Maidana, D.E.; Salvador-Culla, B.; Kobashi, H.; Kolovou, P.E.; Zhai, H.; Taghizadeh, K.; Kuang, L. Topical sustained drug delivery to the retina with a drug-eluting contact lens. *Biomaterials* **2019**, *217*, 119285. [CrossRef] [PubMed]
36. Sindt, C.W.; Longmuir, R.A. Contact lens strategies for the patient with dry eye. *Ocul. Surf.* **2007**, *5*, 294–307. [CrossRef] [PubMed]
37. Dupre, T.E.; Benjamin, W.J. Relationship of Water Content With Silicon and Fluorine Contents of Silicone-Hydrogel Contact Lens Materials. *Eye Contact Lens* **2019**, *45*, 23–27. [CrossRef]
38. Kim, T.-H.; Ye, K.-H.; Sung, A. A study on the measurement of water content in hydrogel contact lens by gravimetric method. *J. Korean Ophthalmic Opt. Soc.* **2008**, *13*, 59–63.
39. Gonzalez-Mejjome, J.M.; Lira, M.; Lopez-Aleman, A.; Almeida, J.B.; Parafita, M.A.; Refojo, M.F. Refractive index and equilibrium water content of conventional and silicone hydrogel contact lenses. *Ophthalmic Physiol. Opt.* **2006**, *26*, 57–64. [CrossRef]
40. Harissi-Dagher, M.; Beyer, J.; Dohlman, C.H. The role of soft contact lenses as an adjunct to the Boston keratoprosthesis. *Int. Ophthalmol. Clin.* **2008**, *48*, 43–51. [CrossRef]
41. Bengani, L.C.; Kobashi, H.; Ross, A.E.; Zhai, H.; Salvador-Culla, B.; Tulsan, R.; Kolovou, P.E.; Mittal, S.K.; Chauhan, S.K.; Kohane, D.S. Steroid-eluting contact lenses for corneal and intraocular inflammation. *Acta Biomater.* **2020**, *116*, 149–161. [CrossRef]
42. Chen, X.; Dunn, A.C.; Sawyer, W.G.; Sarntinoranont, M. A biphasic model for micro-indentation of a hydrogel-based contact lens. *J. Biomech. Eng.* **2007**, *129*, 156–163. [CrossRef]
43. Keir, N.; Jones, L. Wettability and silicone hydrogel lenses: A review. *Eye Contact Lens* **2013**, *39*, 100–108. [CrossRef]
44. Taylor, M.; Urquhart, A.J.; Zelzer, M.; Davies, M.C.; Alexander, M.R. Picoliter water contact angle measurement on polymers. *Langmuir* **2007**, *23*, 6875–6878. [CrossRef] [PubMed]
45. Farhat, W.; Ayollo, D.; Arakelian, L.; Thierry, B.; Mazari-Arrighi, E.; Caputo, V.; Faivre, L.; Cattani, P.; Larghero, J.; Chatelain, F. Biofabrication of an Esophageal Tissue Construct from a Polymer Blend Using 3D Extrusion-Based Printing. *Adv. Eng. Mater.* **2022**, *24*, 2200096. [CrossRef]
46. Wadajkar, A.S.; Ahn, C.; Nguyen, K.T.; Zhu, Q.; Komabayashi, T. In vitro cytotoxicity evaluation of four vital pulp therapy materials on I929 fibroblasts. *Int. Sch. Res. Not.* **2014**, *2014*, 191068. [CrossRef] [PubMed]
47. Lopes, V.R.; Schmidtke, M.; Fernandes, M.H.; Martins, R.; Vasconcelos, V. Cytotoxicity in I929 fibroblasts and inhibition of herpes simplex virus type 1 Kupka by estuarine cyanobacteria extracts. *Toxicol. In Vitro* **2011**, *25*, 944–950. [CrossRef]

48. Los, L. The rabbit as an animal model for post-natal vitreous matrix differentiation and degeneration. *Eye* **2008**, *22*, 1223–1232. [CrossRef]
49. Makadia, H.K.; Siegel, S.J. Poly lactic-co-glycolic acid (PLGA) as biodegradable controlled drug delivery carrier. *Polymers* **2011**, *3*, 1377–1397. [CrossRef]
50. Kumari, A.; Yadav, S.K.; Yadav, S.C. Biodegradable polymeric nanoparticles based drug delivery systems. *Colloids Surf B Biointerfaces* **2010**, *75*, 1–18. [CrossRef]
51. Ciolino, J.B.; Hudson, S.P.; Mobbs, A.N.; Hoare, T.R.; Iwata, N.G.; Fink, G.R.; Kohane, D.S. A prototype antifungal contact lens. *Invest. Ophthalmol. Vis. Sci.* **2011**, *52*, 6286–6291. [CrossRef]
52. Yu, G.; Ali, Z.; Khan, A.S.; Ullah, K.; Jamshaid, H.; Zeb, A.; Imran, M.; Sarwar, S.; Choi, H.-G.; ud Din, F. Preparation, pharmacokinetics, and antitumor potential of miltefosine-loaded nanostructured lipid carriers. *Int. J. Nanotechnol. Nanomed.* **2021**, *16*, 3255. [CrossRef]
53. de Castro Spadari, C.; Lopes, L.B.; Ishida, K. Alginate nanoparticles as non-toxic delivery system for miltefosine in the treatment of candidiasis and cryptococcosis. *Int. J. Nanotechnol. Nanomed.* **2019**, *14*, 5187.
54. Jimenez-Anton, M.D.; Garcia-Calvo, E.; Gutierrez, C.; Escribano, M.D.; Kayali, N.; Luque-Garcia, J.L.; Olias-Molero, A.I.; Corral, M.J.; Costi, M.P.; Torrado, J.J.; et al. Pharmacokinetics and disposition of miltefosine in healthy mice and hamsters experimentally infected with *Leishmania infantum*. *Eur. J. Pharm. Sci.* **2018**, *121*, 281–286. [CrossRef]
55. Kuang, L.; Damayanti, N.P.; Jiang, C.; Fei, X.; Liu, W.; Narayanan, N.; Irudayaraj, J.; Campanella, O.; Deng, M. Bioinspired glycosaminoglycan hydrogels via click chemistry for 3D dynamic cell encapsulation. *J. Appl. Polym. Sci.* **2019**, *136*, 47212. [CrossRef] [PubMed]
56. Kuang, L.; Goins, J.; Zheng, W.; Eduafo, P.; Ma, H.; Posewitz, M.; Wu, D.T.; Liang, H. Spontaneous microalgae dewatering directed by retrievable, recyclable, and reusable nanoparticle-pinned polymer brushes. *Chem. Mater.* **2019**, *31*, 4657–4672. [CrossRef]
57. Ciolino, J.B.; Stefanescu, C.F.; Ross, A.E.; Salvador-Culla, B.; Cortez, P.; Ford, E.M.; Wymbs, K.A.; Sprague, S.L.; Mascoop, D.R.; Rudina, S.S.; et al. In vivo performance of a drug-eluting contact lens to treat glaucoma for a month. *Biomaterials* **2014**, *35*, 432–439. [CrossRef] [PubMed]
58. Ciolino, J.B.; Ross, A.E.; Tulsan, R.; Watts, A.C.; Wang, R.F.; Zurakowski, D.; Serle, J.B.; Kohane, D.S. Latanoprost-Eluting Contact Lenses in Glaucomatous Monkeys. *Ophthalmology* **2016**, *123*, 2085–2092. [CrossRef]
59. Schuster, F.L.; Guglielmo, B.J.; Visvesvara, G.S. In-vitro activity of miltefosine and voriconazole on clinical isolates of free-living amebas: *Balamuthia mandrillaris*, *Acanthamoeba* spp., and *Naegleria fowleri*. *J. Eukaryot Microbiol.* **2006**, *53*, 121–126. [CrossRef]
60. Walochnik, J.; Duchene, M.; Seifert, K.; Obwaller, A.; Hottkowitz, T.; Wiedermann, G.; Eibl, H.; Aspöck, H. Cytotoxic activities of alkylphosphocholines against clinical isolates of *Acanthamoeba* spp. *Antimicrob. Agents Chemother.* **2002**, *46*, 695–701. [CrossRef]
61. Monogue, M.L.; Watson, D.; Alexander, J.S.; Cavuoti, D.; Doyle, L.M.; Wang, M.Z.; Prokesch, B.C. Minimal Cerebrospinal Fluid Concentration of Miltefosine despite Therapeutic Plasma Levels during the Treatment of Amebic Encephalitis. *Antimicrob. Agents Chemother.* **2019**, *64*, e01127-19. [CrossRef]
62. Paugh, J.R.; Stapleton, F.; Keay, L.; Ho, A. Tear exchange under hydrogel contact lenses: Methodological considerations. *Investig. Ophthalmol. Vis. Sci.* **2001**, *42*, 2813–2820.
63. Lin, M.C.; Soliman, G.N.; Lim, V.A.; Giese, M.L.; Wofford, L.E.; Marmo, C.; Radke, C.; Polse, K.A. Scalloped channels enhance tear mixing under hydrogel contact lenses. *Optom. Vis. Sci.* **2006**, *83*, 874–878. [CrossRef]
64. Bhamra, T.S.; Tighe, B.J. Mechanical properties of contact lenses: The contribution of measurement techniques and clinical feedback to 50 years of materials development. *Cont. Lens Anterior Eye* **2017**, *40*, 70–81. [CrossRef] [PubMed]
65. *ISO 10993-1:2018*; Biological evaluation of medical devices. International Organization for Standardization: Geneva, Switzerland, 2018.
66. Walochnik, J.; Obwaller, A.; Gruber, F.; Mildner, M.; Tschachler, E.; Suchomel, M.; Duchene, M.; Auer, H. Anti-acanthamoeba efficacy and toxicity of miltefosine in an organotypic skin equivalent. *J. Antimicrob. Chemother.* **2009**, *64*, 539–545. [CrossRef] [PubMed]
67. Palic, S.; Bhairosing, P.; Beijnen, J.H.; Dorlo, T.P.C. Systematic Review of Host-Mediated Activity of Miltefosine in Leishmaniasis through Immunomodulation. *Antimicrob. Agents Chemother.* **2019**, *63*, e02507-18. [CrossRef] [PubMed]
68. Nakagawa, H.; Koike, N.; Ehara, T.; Hattori, T.; Narimatsu, A.; Kumakura, S.; Goto, H. Corticosteroid eye drop instillation aggravates the development of *Acanthamoeba* keratitis in rabbit corneas inoculated with *Acanthamoeba* and bacteria. *Sci. Rep.* **2019**, *9*, 12821. [CrossRef]
69. Shimmura-Tomita, M.; Takano, H.; Kinoshita, N.; Toyoda, F.; Tanaka, Y.; Takagi, R.; Kobayashi, M.; Kakehashi, A. Risk factors and clinical signs of severe *Acanthamoeba* keratitis. *Clin. Ophthalmol.* **2018**, *12*, 2567. [CrossRef]

Article

Besifloxacin Nanocrystal: Towards an Innovative Ophthalmic Preparation

José Izo Santana da Silva de Jesus ^{1,†}, Felipe Rebello Lourenço ¹, Kelly Ishida ², Thayná Lopes Barreto ², Valdir Carlos Avino ³, Edson dos Santos Neto ⁴ and Nádia Araci Bou-Chacra ^{1,*,†}

- ¹ Department of Pharmacy, Faculty of Pharmaceutical Sciences, University of São Paulo, Professor Lineu Prestes Av 580, Cidade Universitária, São Paulo 05508-000, Brazil
- ² Department of Microbiology, Institute of Biomedical Sciences, University of São Paulo, Professor Lineu Prestes Av 2415, Cidade Universitária, São Paulo 05508-000, Brazil
- ³ Department of Research and Development, Pearson Saúde Animal S.A., Rua Arizona 491, Edifício Itaporanga, 18° Andar, Conjunto 182, Cidade Monções, São Paulo 04567-001, Brazil
- ⁴ Ophthalmology Division, Clinical Hospital of the Faculty of Medicine, University of São Paulo, Avenida Dr. Eneas de Carvalho Aguiar, 255, Cerqueira César, São Paulo 05403-000, Brazil
- * Correspondence: chacra@usp.br; Tel.: +55-(11)-3091-3628
- † These authors contributed equally to this work.

Abstract: Bacterial conjunctivitis significantly impacts public health, including more than one-third of eye diseases reported worldwide. It is an infection caused by various aerobic and anaerobic bacteria and is highly contagious. Therefore, it has a high incidence of bacterial resistance to the antibiotics commonly used for treatment. Among the most recent antibiotics, besifloxacin is a fourth-generation fluoroquinolone antibiotic indicated exclusively for topical ophthalmic use. Due to its importance in treating bacterial conjunctivitis and its low solubility in water, limiting its efficacy, a nanotechnology-based drug delivery preparation was developed to overcome this hurdle. Besifloxacin nanocrystals were prepared by small-scale wet milling and response surface methodology, using Povacoat[®] as a stabilizer. The particle's average hydrodynamic diameter (Z-ave) was approximately 550 nm (17 times smaller than raw material), with a polydispersity index (PdI) of less than 0.2. The saturation solubility increased about two times compared to the raw material, making it possible to increase the dissolution rate of this drug substance, potentially improving its bioavailability and safety. The optimized preparation was stable under an accelerated stability study (90 days). The Z-ave, PZ, PdI, and content did not alter significantly during this period. Furthermore, the 0.6% m/m besifloxacin nanocrystals at the maximum dose and the Povacoat[®] stabilizer did not show toxicity in *Galleria mellonella* larvae. The innovative ophthalmic preparation minimum inhibitory concentration (MIC) was 0.0960 µg/mL and 1.60 µg/mL against *Staphylococcus aureus* and *Pseudomonas aeruginosa*, respectively, confirming in vitro efficacy. Therefore, besifloxacin nanocrystals revealed the potential for reduced dosing of the drug substance, with a minor occurrence of adverse effects and greater patient adherence to treatment.

Keywords: nanocrystals; conjunctivitis; besifloxacin; Povacoat[®]; fluoroquinolones

Citation: Jesus, J.I.S.d.S.d.; Lourenço, F.R.; Ishida, K.; Barreto, T.L.; Avino, V.C.; Neto, E.d.S.; Bou-Chacra, N.A. Besifloxacin Nanocrystal: Towards an Innovative Ophthalmic Preparation. *Pharmaceutics* **2022**, *14*, 2221. <https://doi.org/10.3390/pharmaceutics14102221>

Academic Editors: Francisco Javier Otero-Espinar and Anxo Fernández Ferreiro

Received: 10 September 2022

Accepted: 5 October 2022

Published: 18 October 2022

Publisher's Note: MDPI stays neutral with regard to jurisdictional claims in published maps and institutional affiliations.



Copyright: © 2022 by the authors. Licensee MDPI, Basel, Switzerland. This article is an open access article distributed under the terms and conditions of the Creative Commons Attribution (CC BY) license (<https://creativecommons.org/licenses/by/4.0/>).

1. Introduction

Conjunctivitis refers to the inflammatory process of the conjunctiva and affects all age groups [1]. Bacterial conjunctivitis is responsible for more than one-third of eye complications worldwide, causing pain and discomfort to patients, decreasing their quality of life, and increasing health care costs [2–5]. Alfonso and colleagues [6] report that the costs of treating conjunctivitis ranged from 377 to 875 million dollars annually in the United States.

Bacterial conjunctivitis is highly contagious and can be caused by aerobic and anaerobic bacteria. It also includes other common species such as *Neisseria gonorrhoeae*, *Neisseria*

meningitides, *Pseudomonas*, *Proteus*, and *Corynebacterium* [1,2,4]. Bacterial infections, if not treated properly, can have potentially serious consequences, including irreversible vision complications such as permanent loss [7]. Furthermore, in some cases, such as after glaucoma surgery, the contagion of bacterial conjunctivitis increases the patient's risk of developing endophthalmitis [8]. This devastating complication can cause permanent vision loss [9,10].

In the case of more severe complications, such as the development of mucopurulent exudate, treatment with antibiotics should be immediate, including several classes of antibiotics, such as aminoglycosides, combinations of polymyxin B, macrolides, sulfonamides, and the fluoroquinolones [2,4]. The indication of the fluoroquinolone class as topical ophthalmic was only from 1990 onwards and brought significant therapeutic advantages, as it has a broad spectrum and low toxicity. However, many of these therapeutic classes are no longer effective or show bacterial resistance [11]. In this context, besifloxacin, a recent member of fourth-generation fluoroquinolones, has significant advantages. This antimicrobial was developed exclusively for topical ophthalmic use. Unlike other fluoroquinolones, besifloxacin is not used for treating other infections, and this drug substance is the only one in its class to present a lower risk of developing resistance [2,5].

The synthesis of besifloxacin was initiated by a Japanese company, and in 2009 it was approved by the Food and Drug Administration (FDA) for the treatment of bacterial conjunctivitis in the United States; two years later, it was approved by ANVISA in Brazil [12,13]. Besifloxacin shows low water solubility (0.143 mg/mL) and is marketed as besifloxacin hydrochloride by Bausch & Lomb Incorporated under the trade name Besivance[®], 0.6% ophthalmic suspension [5,14,15].

Conventional ophthalmic preparations (drops) are rapidly removed from the ocular surface due to eye protection mechanisms. Therefore, the retention time of drugs in the eye is minimal with consequently low bioavailability, generally less than 5% [16,17]. A different nano-based besifloxacin delivery was developed to overcome these challenges [17–20]. However, there are no besifloxacin nanocrystals reported in the literature. Nanocrystal increases the surface area to volume ratio of the drug substance, enhancing its saturation solubility, dissolution velocity, and adhesiveness when compared to the drug on the micro-metric scale, with a consequent increase in bioavailability [21–25]. Given these benefits, the global nanotechnology market for drug delivery is projected to reach US\$ 164.1 billion by 2027 [26], showing that the global nanotechnology market for drug delivery is projected to reach US\$ 164.1 billion by 2027. Nanocrystals alone should reach US\$ 83.1 billion in this period, with a growth of 21.9% for the next years.

In general, drug nanocrystals are prepared in dispersion media with the addition of stabilizers (surfactants and polymers), resulting in a colloidal state referred to as nanosuspensions [21,22]. The choice of stabilizer is complex and critical in the development stage of nanocrystals. Design space, a strategic tool in the QbD concept, allows for understanding and establishing multivariate combinations and interactions of input variables for the proper development of the product or process [27,28].

Therefore, this study aims to develop besifloxacin nanocrystals using a spatial design approach with subsequent physicochemical characterization, in vivo toxicity (*Galleria mellonella model*), and in vitro efficacy by determining the minimum inhibitory concentration against two main bacteria causing conjunctivitis.

2. Materials and Methods

2.1. Materials

Besifloxacin (99.93%, MW 430.301 g/mol, Log P 0.54, water solubility: 0.143 mg/mL) was purchased from Jinan Shengqi Pharmaceutical Co., Ltd. (Jinan China). Povacoat[®] (POVA) was donated from DAIDO Takeshima Nishiyodogawa-Ku, Osaka, Japan). Polysorbate 80, cetylpyridinium chloride (CPC), benzalkonium chloride (BAC), benzyltrimethylhexadecylammonium chloride 16-BAC, and chitosan (CS) were purchased from Sigma-Aldrich (St. Louis, MO, USA). Poloxamer 188 (P188), Poloxamer 407 (P407), Poloxamer HS 15 (HS

15), tocopherol polyethylene glycol succinate (TPGS), and Kollicoat[®] IR (KLT) were purchased from BASF (Ludwigshafen am Rhein, Germany). Triethylamine, phosphoric acid, acetonitrile, and phosphate buffer solution pH 7.0 (Certipur[®]) were purchased from Merck (Darmstadt, Germany). The product Besivance[®] (0.6% ophthalmic suspension) (Bausch & Lomb Incorporated, Bridgewater, NJ, USA) was obtained from a local market. Milli-Q[®] Integral 10 ultrapure water (Merck KGaA, Darmstadt, Germany) was used for analytical purposes.

2.2. Drug Analysis

2.2.1. Particle Size Determination by Laser Diffraction

The particle size of besifloxacin (raw material) was determined and compared with the commercial product (Besivance[®]), for which the Beckman Coulter[™] LS 13 320 laser diffraction particle size analyzer equipped with a ULM module (Universal Liquid Module) was used (Beckman Coulter Inc., Brea, CA, USA). A suspension of the drug was prepared in phosphate buffer pH 7.0, and the commercial product (Besivance[®]) was used directly for analysis. Results represent the average of three readings.

2.2.2. Determination of Minimum Inhibitory Concentration (MIC)

The MIC of besifloxacin (raw material) against *Staphylococcus aureus* ATCC[®] 23235[™] and *Pseudomonas aeruginosa* ATCC[®] 9027[™] were determined by the microdilution method. Posteriorly, tubes containing the serial dilutions (0.125 to 60 µg/mL) were incubated in an oven at 37 °C for 24 h. The determination of the inhibition and/or growth of microorganisms was performed by spectrophotometer [29].

2.3. Preparation of Besifloxacin Nanocrystals Using Small-Scale Wet Bead Milling

2.3.1. Exploratory Tests for Stabilizer and Statistical Variables Selection

The besifloxacin nanocrystals were obtained using a small-scale top-down approach by wet bead milling, according to Romero, Keck, and Müller [30]. The system was composed of three magnetic stirring bars (5 mm each) arranged on top of each other in a 10 mL glass vial, stirred by a magnetic stirring plate (IKA[®]-WERKE, Staufen im Breisgau, Germany). In the first exploratory assay, the proposed formulation consisted of 0.6 wt% of besifloxacin (BSF) and 0.6 wt% of conventional stabilizers (1:1 wt ratio). In the second part, the same drug concentration was maintained (0.6 wt%); however, new stabilizers and different proportions were tested. All formulations had their total weight adjusted to 10 g with buffer solution pH 7.0 (dipotassium hydrogen phosphate/disodium hydrogen phosphate). Additionally, 30% of the vial volume was filled with 3.0 g (*w/w*) zirconium beads (size of 0.1 mm) (Retsch, Germany).

Initially, each tested stabilizer was weighed and transferred to the vial containing half of the planned buffer solution, and the system was stirred for 10 min to ensure total solubilization. In sequence, the besifloxacin was weighed and added to the formulation and the remaining buffer solution to complete 10 g of nanosuspension. The milling process was at 1200 rpm for 4 days for all stabilizers. The measurements of average hydrodynamic diameter (*Z-ave*) and polydispersity index (*PdI*) were determined within 24 h of the milling process.

The formulations whose stabilizers allowed particle size reduction to nanometer-scale were kept at room temperature. *Z-ave* and *PdI* measurements were determined after 7 and 15 days to verify the maintenance of particle size stability. Additionally, as a part of the third preliminary study, the processing time (24 and 96 h) and the number of magnetic bars (2 and 3) were tested with the stabilizer Povacoat[®], chosen for the optimization step.

2.3.2. Nanosuspension Optimization Process Applying Box–Behnken Experiment Design

The Box–Behnken design refers to a response surface design without considering the built-in full factorial or fractional design (Minitab[®] 18). For this model, at least three factors were considered. In this sense, the exploratory studies allowed to establish the agitation speed as a critical parameter of the process, as well as the stabilizer (Povacoat[®]), the drug

(besifloxacin), and their concentrations, to optimize the formulation. These independent variables were selected for the experiment, as follows in Table 1. Thus, this experiment was used to evaluate the responses of the dependent variable, average hydrodynamic diameter ($Z\text{-ave}$).

Table 1. Independent variables and levels selected for Box–Behnken design.

Level	Besifloxacin (wt%)	Stabilizer (Povacoat®) (wt%)	Stirring Speed (rpm)
Minimum (−1)	0.4	0.6	800
Central point (0)	0.6	0.8	1000
Maximum (+1)	0.8	1.0	1200

2.3.3. Mathematical Model Verification

The mathematical equation derived from the response surface analysis determined the besifloxacin nanosuspensions formulations for the statistical model verification. These formulations were prepared using the conditions described in this section on the nanosuspension optimization process applying a Box–Behnken experiment design. The $Z\text{-ave}$ measurement was determined at the end of this period.

2.4. Dynamic Light Scattering and Zeta Potential

The nanocrystals $Z\text{-ave}$ and polydispersity indexes (PDI) were determined by photon correlation spectroscopy using Zetasizer Nano SZ90 (Malvern Instruments, Malvern, UK). Light scattering was monitored at 25 °C at an angle of 90°. The samples were previously diluted in the besifloxacin saturated solution (ratio of 1:24) for a total of 1 mL, considering an instrument sensitivity range. The measurements used disposable polystyrene cells. The analysis was performed once for each nanosuspension, and the software performed three runs.

The ZP was carried out by electrophoretic light scattering using the same equipment. Three measurements were taken for each sample, each comprising 14 accumulations. The measurements were taken at 25 °C before dilution with buffer solution pH 7.0 (conductivity = 2238 $\mu\text{S}/\text{cm}$). The applied field force was 20 V/cm, and the results were obtained from a Henry equation [31].

2.5. Distribution and Particle Size by Laser Diffraction (LD)

The distribution and particle size of the besifloxacin nanosuspension (0.6 w%) were performed by low-angle laser scattering using the Mastersizer 2000 equipment (Malvern Instruments, Malvern, UK), equipped with a Hydro 2000MU module (Malvern Instruments), Malvern, UK). The equipment was programmed for the wet method with a measurement range from 50 nm to 1 mm, using pH 7.0 phosphate buffer for dispersion. Granule refractive index: 1.67. The results were presented based on the volume distribution (D10, D50 and D90), which indicates the percentage of existing particles below the given size (nm).

2.6. Density, Viscosity, and pH

The density was determined using a DMA 4500 M densimeter (Anton Paar GmbH, Graz, Austria). For the measurement, the sample was placed directly in the equipment, in enough quantity to fill the hose/channel. The density was determined concerning water at 25 °C.

The viscosity was performed using an LVDV-I PRIME viscometer (Brookfield, Middleboro, MA, USA), equipped with an LV-3 spindle (63), and the speed was 50 rpm. For testing, 15 mL of the nanosuspension was transferred to the SC4-13RPY sample container (Brookfield, Middleboro, MA, USA).

The pH was determined with an Orion™ Versa Star Pro™ potentiometer (Thermo Fisher Scientific, Waltham, MA, USA). All these analyses were performed directly on besifloxacin nanosuspension samples, without dilution, in triplicate at 25 °C.

2.7. Osmolality

The osmolality of the optimized formulation was determined using the A₂O Advanced Automated Osmometer (Advanced Instruments, Norwood, MA, USA). For this, 1 mL of the nanosuspension was transferred to a glass tube and placed on the disk of the equipment that performs the injection automatically. In this equipment, measurements were determined from the freezing point depression of the sample. The sample injection volume was 100 µL, and the temperature range for determining the freezing point was −40 °C to +45 °C. Measurements were performed in triplicate.

2.8. Validation of the Method by High-Performance Liquid Chromatography (HPLC)

The reference method was developed by COSTA and colleagues using the commercial product Besivance[®] (0.6% ophthalmic suspension) [12]. The following performance characteristics were determined: linearity, selectivity, precision, accuracy, and system suitability [32,33]. The excipients of the commercial product were measured during a validation study (selectivity) in the reference method [12]. Additionally, a placebo was prepared to contain Povacoat[®] (9 mg/mL), glycerol (10 mg/mL), and benzalkonium chloride (1 mg/mL) to evaluate possible interferences in the analytical responses of this method.

2.8.1. HPLC System and Apparatus

The Dionex[™] UltiMate[™] 3000 UHPLC⁺ liquid chromatography (Thermo Fisher Scientific, Waltham, MA, USA) was used, consisting of a DGP-3600 quaternary pump, ACC-3000 autosampler (with sample thermostat), ACC-3000 column compartment, and DAD detector 3000 (RS) equipped with Chromeleon[™] software version 6.80. The C18 Eclipse Plus 150 mm × 4.6 mm × 3.5 µm column (Agilent Technologies, Santa Clara, CA, USA) was used. The mobile phase consisted of a mixture of 0.5% (*v/v*) triethylamine solution (pH adjusted to 3.0 with dilute phosphoric acid (10% *v/v*)) and acetonitrile (74:26 *v/v*) at a flow rate of 1.0 mL/min. The injection volume of the solutions was 20 µL, with a column temperature of 25 °C, UV detection at 295 nm, using a diode matrix (DAD) [12].

2.8.2. Solutions

Stock solutions of the standard (SQR) and samples containing 500 µg/mL of besifloxacin were prepared. From these solutions, aliquots were diluted using the mobile phase to obtain adequate concentrations to determine the performance characteristics of the method. The solutions were transferred to a 2 mL vial using a Millex[®]-HV-PVDF filter 13 mm in diameter, 0.45 µm pore size, and then analyzed. Additionally, a filter test was performed to assess the compatibility and possible interference in the analytical responses [34].

The density of the besifloxacin nanosuspension (0.6 wt%) was determined as 1.0081 g/mL. This result was considered for weighing the aliquot of the nanosuspension. Afterwards, a sample solution was prepared with a concentration of 50 µg/mL of besifloxacin.

2.9. Scanning Electron Microscopy (SEM)

The raw material (besifloxacin hydrochloride) and nanocrystals (lyophilized nanosuspension) were analyzed using a Quanta[™] 650 FEG scanning electron microscope (SEM) (FEI Company, Hillsboro, OR, USA). The samples were plated with platinum using a metallizer MED-020 high-vacuum coating system (Baltic, Pfäffikon, Switzerland). This metallization (the layer between 10–15 nm thick) guarantees the conduction of the electron beam in the analyzed sample. For analysis, 10 kV of electron acceleration voltage was applied. The raw material besifloxacin was analyzed at 5000 to 30,000 times magnification, and the nanocrystal was analyzed at 5000 to 100,000 times magnification.

2.10. Lyophilization

The lyophilized samples were used for the analyses that needed dry samples (lyophilized powder), which was obtained by drying the nanosuspension using the

lyophilization process using a Christ Alpha 2-4 LSC (Martin Christ Gefriertrocknungsanlagen GmbH, Osterode am Harz, Germany). For this, 1.5 mL aliquots of nanosuspension were frozen at $-45\text{ }^{\circ}\text{C}$ with a pressure of 0.120 mbar for 48 h. After lyophilization, the besifloxacin nanocrystals were resuspended in the same volume of pH 7.0 buffer (proportional to the volume of the initial formulation), and the Z-ave, IP, and PZ were determined to verify the efficiency of lyophilization.

2.11. Thermal Analysis

Differential scanning calorimetry (DSC) analysis was performed using DSC 7020 equipment (Hitachi High-Tech Corporation, Tokyo, Japan). All measurements were performed under a dynamic nitrogen atmosphere (50 mL min^{-1}). The weight of the samples was approximately 2 mg. DSC curves were obtained by heating at a rate of $10\text{ }^{\circ}\text{C min}^{-1}$ from 25 to $300\text{ }^{\circ}\text{C}$. As a reference, an empty sealed aluminum crucible was used.

The thermogravimetry and derived thermogravimetry (TG/DTG) curves were obtained using an STA 7200 analyzer (Hitachi High-Tech Corporation, Tokyo, Japan), with a sample weight of approximately 2 mg in the temperature range from 30 to $600\text{ }^{\circ}\text{C}$, at a rate of $10\text{ }^{\circ}\text{C min}^{-1}$ under a dynamic nitrogen atmosphere (100 mL min^{-1}). The lyophilized nanosuspension, besifloxacin (raw material), Povacoat[®], benzalkonium chloride, and a mixture of both (same proportion of the formulation) were characterized.

2.12. X-ray Diffraction (XRD)

X-ray diffraction analyses were performed using a Rigaku Miniflex 600-C diffractometer (Rigaku Corporation, Tokyo, Japan). For this, the samples were ground to obtain a fine powder. Next, the powder was spread evenly in the rotating glass sample holder (zero background) with the aid of a glass slide. The equipment was configured in reflection mode with a scan range from 2.3° to $50^{\circ} 2\Theta$, and a speed of $10^{\circ}/\text{min}$ (0.02° step) was applied. The diffractograms were generated by the SmartLab Studio II software (Rigaku Corporation, Tokyo, Japan).

2.13. Saturation Solubility

The saturation solubility was evaluated using the shake-flask method [35], using a Tecnal TE 4080 (Tecnal, São Paulo Brazil) stirring oven at $37 \pm 1\text{ }^{\circ}\text{C}$ with stirring 150 RPM. For the study, the following media were considered: ultrapure water Milli-Q[®] Integral 10 (Merck KGaA, Darmstadt, Germany), pH 4.0 phosphate buffer (citric acid/sodium hydroxide/hydrogen chloride), Certipur[®] (Merck KGaA, Darmstadt, Germany), phosphate buffer pH 6.8, and phosphate buffer pH 7.0 (disodium dipotassium hydrogen phosphate hydrogen phosphate) Certipur[®] (Merck KGaA, Darmstadt, Germany).

To prepare the saturated solution of the drug, 250 mg of besifloxacin (raw material) was weighed and transferred to an Erlenmeyer flask containing 250 mL of the previously described media (concentration 1 mg/mL). Similarly, 4130 mg of the besifloxacin nanosuspension (equivalent to 25 mg of besifloxacin, density 1.0081 g/mL) was transferred to Erlenmeyer of 25 mL containing 25 mL of the media (concentration 1 mg/mL). For these preparations, the declared solubility of besifloxacin of 0.143 mg/mL was considered [5].

The samples were incubated, and after 24 and 48 h, an aliquot of 1 mL was removed, filtered Millex[®]-HV-PVDF 13 mm in diameter, with a pore size of 0.45 μm . From this filtrate, solutions with a theoretical concentration of 50 $\mu\text{g/mL}$ were prepared using the respective media (ultrapure water, pH 4.0 buffer, pH 6.8 buffer, and pH 7.0 buffer). Afterwards, the sample solutions were transferred to a 2 mL vial using Millex[®]-HV-PVDF filters 13 mm in diameter, pore size 0.45 μm , and quantified in triplicate (three injections) by HPLC.

2.14. In Vivo Toxicity

Larvae of *Galleria mellonella* ranging from 2.0 to 2.5 cm in length and 150 to 200 mg in weight were used to determine the toxicity of besifloxacin nanocrystals and the Povacoat[®]. Doses of 500 mg/kg of besifloxacin nanocrystals (0.06 mg/larvae) and 750 mg/kg of

Povacoat[®] (0,09 mg/larvae) were injected (10 µL) in the last left pro-leg of larvae ($n = 16$ larvae per group). In addition, sterile phosphate-buffered saline (pH 7.0) was also injected into a larval group to control mechanical injury and vehicle. The larvae were maintained at 37 °C, and the survival of all groups was monitored daily for 5 days [36].

2.15. Determination of Minimum Inhibitory Concentration (MIC)

The minimum inhibitory concentration (MIC) was determined for besifloxacin hydrochloride (raw material) and for besifloxacin nanosuspension 0.6 wt% against *Staphylococcus aureus* and *Pseudomonas aeruginosa*. Similarly, a serial dilution method was used, according to item 2.2.2 [29].

2.16. Stability Study

The accelerated stability study of the besifloxacin nanosuspension was conducted in a Climacell Eco-Line climate chamber (MMM Medcenter Einrichtungen GmbH, Planegg, Germany) considering the main regulatory guidelines [37,38]. For this purpose, three batches of the formulation were prepared, and the samples were transferred to type I amber glass vials, closed with butyl caps, sealed with an aluminum seal, and conditioned for accelerated stability for 90 days at the condition: 40 °C ± 2 °C / 75%RH ± 5%RH.

Monthly, Z-ave, PdI, ZP, pH, and aspect were determined. In addition, the besifloxacin content was determined at time 0 and after 90 days. Analysis of variance (ANOVA) was performed using Excel software.

3. Results and Discussion

3.1. Drug Analysis

3.1.1. Particle Size Determination by Laser Diffraction

The initial particle size distribution for besifloxacin hydrochloride (raw material) and commercial product (Besivance[®] 0.6% ophthalmic suspension) was determined as a preliminary analysis. The particle size distribution (Figure 1) shows the same bimodal formation for both product and raw material samples. The central peak presents the most extensive distribution of particles, with a diameter $9.33 \pm 3.22 \mu\text{m}$ and $10.62 \pm 1.76 \mu\text{m}$ for raw material and Besivance[®], respectively. In addition, the D90 shows that 90% of the particles have a diameter smaller than 13 µm for both samples.

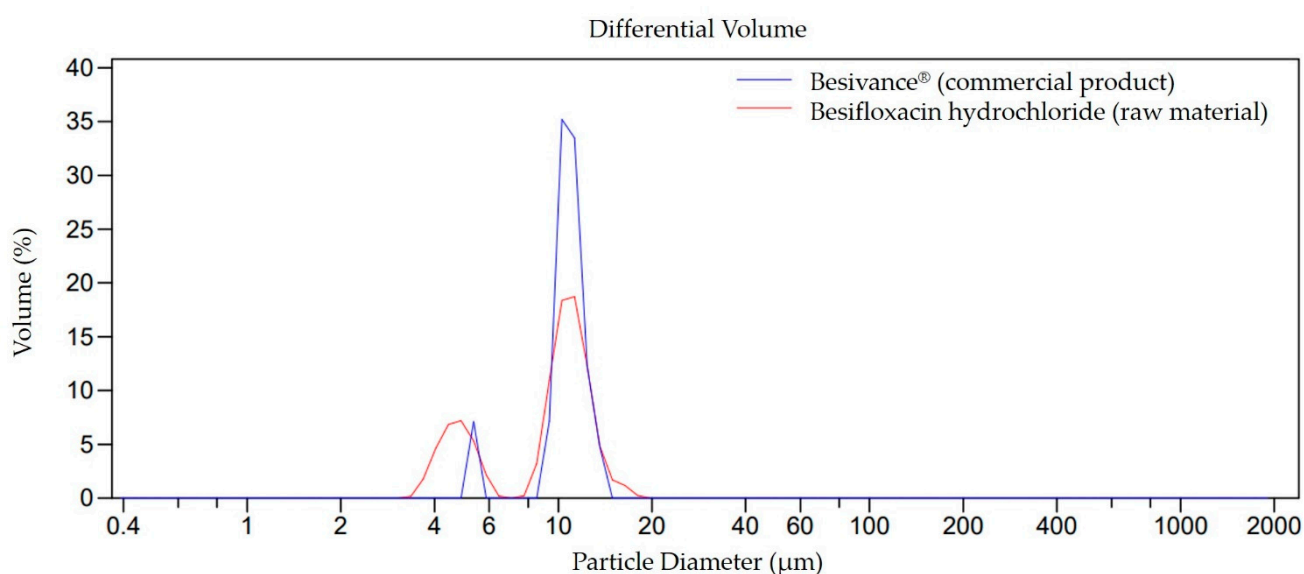


Figure 1. Particle size distribution for the commercial product Besivance[®] and besifloxacin hydrochloride. The peaks represent the average of three readings.

Therefore, the raw material besifloxacin hydrochloride is presented on a micrometric scale, close to the reference values (commercial product). Drug nanocrystal prepared using small-scale wet bead milling can overcome the low water solubility hurdle of the raw material, which potentially improves drug bioavailability justifying the present study.

3.1.2. Determination of Minimum Inhibitory Concentration (MIC)

Likewise, the *in vitro* antimicrobial activity of besifloxacin hydrochloride (raw material) and Besivance[®] were determined using microorganisms that frequently cause bacterial conjunctivitis.

MIC for *Pseudomonas aeruginosa* against besifloxacin hydrochloride and the product Besivance[®] was 1.58 and 0.99 µg/mL, respectively. The values reported in the literature are between 0.5 and 4 µg/mL [8,29,39]. Against *Staphylococcus aureus*, the MIC was 0.0957 and 0.0959 µg/mL for besifloxacin hydrochloride and the product Besivance[®], respectively. The literature reported values between 0.008 and 8 µg/mL [8,29,39]. Thus, the raw material met the requirements for use in the drug nanocrystal development process.

3.2. Preparation of Besifloxacin Nanocrystals Using Small-Scale Wet Bead Milling

3.2.1. Exploratory Tests for Stabilizer and Nanosuspension Optimization Process Applying Box–Behnken Experiment Design

The choice of stabilizer is complex and critical in the development stage of nanocrystals. In the present study, 11 stabilizers were tested to obtain nanocrystals. These stabilizers were compared considering their efficiency in particle size reduction and the preliminary results for their physical stability. For this, 24 formulations were evaluated with a single stabilizer or combinations, divided into three stages.

In the first exploratory study, the stabilizers conventionally used to obtain nanocrystals were tested (Figure S1), and no significant size reduction or no physical stability was observed. In the second part, formulations with new and promising stabilizers were prepared (Figure S2). Therefore, a study was carried out to evaluate the stability of the formulations with the stabilizers that reduced the size of the particles to the nanometric scale in the first and second exploratory studies (Table S1).

From the exploratory study, it was found that the stabilizer Povacoat[®] allowed us to obtain an innovative formulation for treating bacterial conjunctivitis. Figure 2 shows formulas F1, F3, F7, and F8 selected from preliminary studies. However, after 15 days, F1 containing Povacoat[®] presented physical stability. Developed as a pharmaceutical excipient, Povacoat[®], with consolidated use for coating and wet granulation processes, has a pKa of 3.56 in strong acid and 9.5 in strong base, with a load of 0.03 in pH 6.5. This copolymer is established as a stabilizing agent for obtaining nanocrystals, preventing aggregations, and improving the saturation solubility of nanosuspensions with drugs with nanometer-scale particles [28,40–46].

The concept of design space has been consolidated as a fundamental step in pharmaceutical development. This approach allows the understanding and establishing multivariate combinations and interactions of input variables for the proper development of the product or process [28,47,48]. The main variables found in exploratory studies were considered in this optimization.

The concentration of Povacoat[®] (1.0 wt%) obtained in the preliminary investigation was considered to establish the maximum concentration of this stabilizer for the experimental design (+1). The central level (0) was 0.8 wt% and the minimum concentration (−1) established was 0.6 wt%, with the prospect of obtaining the same concentration concerning the drug (1:1). This concentration was also tested in preliminary trials. Although non-ionic stabilizers are less toxic than cationic, these should be used with as little as possible concentration to avoid patient risks [48].

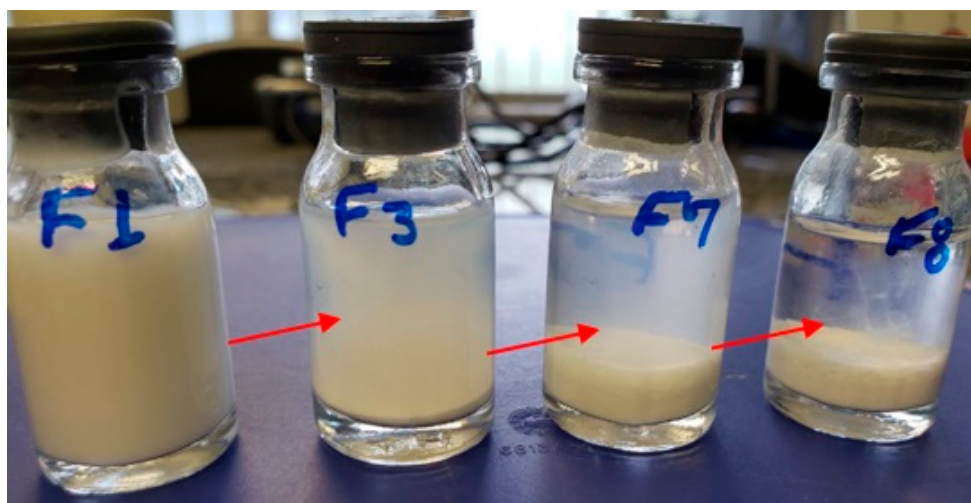


Figure 2. Aspect of the formulas containing the stabilizers Povacoat[®] 1.0 wt% (F1), Kollicoat[®] 0.3 wt% + Chitosan 0.3 wt% (F3), Poloxamer[®] 407 0.5 wt% + Chitosan 0.5 wt% (F7), and Poloxamer[®] 407 0.3 wt% + Chitosan 0.3 wt% (F8). Stability after 15 days (25 °C).

For drug substance concentration, the following levels were considered: (−1), central (0) and (+1), 0.4, 0.6, and 0.8 (wt%), respectively, aiming to evaluate a possible synergistic effect in the reduction of Z-ave. Speed is also a critical parameter of the process; therefore, in the experiment (−1), central (0), and (+1) were 800, 1000, and 1200 rpm, respectively. The measurement of Z-ave was taken after 24 h of preparation (Table 2).

Table 2. Box–Behnken experimental design and observed responses. Average hydrodynamic diameter (Z-ave) in nm was obtained for the besifloxacin nanocrystal preparations. Conditions: 30% (m/m) zirconium beads and 2 magnetic bars, 25 °C.

Formula	Order	Central Point	Besifloxacin (wt%)	Povacoat [®] (wt%)	Speed (rpm)	Z-ave (nm)	PdI
1	1	2	0.4	0.6	1000	641.2 ± 45.2	0.110 ± 0.123
2	12	2	0.6	1.0	1200	596.7 ± 27.6	0.199 ± 0.137
3	11	2	0.6	0.6	1200	651.7 ± 61.8	0.131 ± 0.174
4	8	2	0.8	0.8	1200	677.5 ± 78.4	0.145 ± 0.137
5	5	2	0.4	0.8	800	638.6 ± 33.0	0.204 ± 0.166
6	13	0	0.6	0.8	1000	585.3 ± 21.7	0.168 ± 0.069
7	4	2	0.8	1.0	1000	592.9 ± 28.1	0.199 ± 0.187
8	10	2	0.6	1.0	800	608.3 ± 18.6	0.198 ± 0.186
9	2	2	0.8	0.6	1000	748.4 ± 47.6	0.183 ± 0.107
10	7	2	0.4	0.8	1200	595.4 ± 35.2	0.139 ± 0.070
11	3	2	0.4	1.0	1000	666.7 ± 37.6	0.310 ± 0.217
12	9	2	0.6	0.6	800	666.7 ± 51.6	0.197 ± 0.141
13	6	2	0.8	0.8	800	661.5 ± 35.4	0.162 ± 0.104
14	15	0	0.6	0.8	1000	587.6 ± 30.1	0.110 ± 0.103
15	14	0	0.6	0.8	1000	578.9 ± 12.3	0.158 ± 0.039

According to Table 2, it is possible to observe that the maximum and minimum values of Z-ave were 748.4 ± 47.6 nm and 578.9 ± 12.3 nm, respectively, and that IP values were less than 0.2. For this optimization, the analysis of variance (Table 3) showed that the quadratic model was significant (*p*-value less than 0.05; $\alpha < 0.05$) and presented a non-significant value for lack of fit (*p*-value = 0.154). The variables showed significant quadratic terms: besifloxacin*besifloxacin, Povacoat[®]*Povacoat[®], speed*speed. In addition, interactions between besifloxacin and Povacoat[®] and besifloxacin and rate were observed. The interaction between besifloxacin and Povacoat[®] reduced particle size, while the interaction

between besifloxacin and velocity favored its increase (Equation (1)). Additionally, the quadratic terms influence the Z-ave (increasing). These impacts are also shown in the Z-ave contour plots (Figure 3).

Table 3. Analysis of variance to test the significance of the terms obtained for the particle Z-ave variation of the besifloxacin nanocrystal preparations. The variables are besifloxacin concentration (wt%), Povacoat® concentration (wt%), and velocity (rpm).

Source	DF	Adj. SS	Adj. MS	F-Value	p-Value
Model	8	30,471.9	3808.99	45.16	0.0001
Linear	3	9902.4	3300.82	39.14	0.0001
Besifloxacin	1	2791.2	2791.17	33.09	0.001
Povacoat®	1	6749.5	6749.48	80.03	0.0001
Speed	1	361.8	361.81	4.29	0.084
Square	3	10,474.4	3491.47	41.40	0.0001
Besifloxacin * Besifloxacin	1	7149.8	7149.80	84.77	0.0001
Povacoat® * Povacoat®	1	3688.1	3688.06	43.73	0.001
Speed * Speed	1	865.7	865.70	10.26	0.019
Interaction between 2 factors	2	10,095.0	5047.52	59.85	0.0001
Besifloxacin * Povacoat®	1	9218.9	9218.88	109.30	0.0001
Besifloxacin * Speed	1	876.2	876.16	10.39	0.018
Error	6	506.1	84.34		
Lack-of-fit	4	465.4	116.35	5.72	0.154
Pure error	2	40.6	20.32	*	*
Total	14	30,977.9			

DF: degree of freedom; Adj. SS: Sum of the adjusted squares; Adj. MS: Adjusted quadratic mean, F-value: F statistic; p-value: significance level; (*): not calculated. Besifloxacin square (Besifloxacin * Besifloxacin); Povacoat®square (Povacoat®* Povacoat®); Speed square (Speed * Speed); interaction between Besifloxacin and Povacoat®(Besifloxacin * Povacoat®), and interaction between Besifloxacin and Speed (Besifloxacin * Speed).

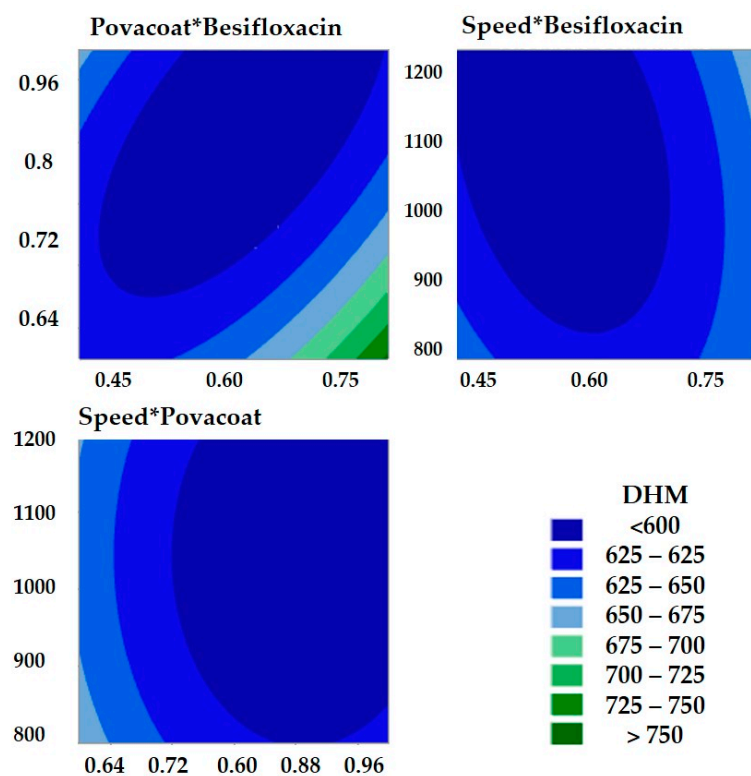


Figure 3. Contour graph related to the Z-ave evaluation of the besifloxacin nanocrystal, whose variables are besifloxacin concentration (wt%), Povacoat® concentration (wt%), and velocity (rpm).

The regression equation obtained for the mathematical model of the experiment is described in Equation (1).

$$Z - \text{ave} = 1608 - 637 \text{ Besifloxacin} - 689 \text{ Povacoat} - 1.021 \text{ Speed} + 1100 \text{ Besifloxacin} * \text{Besifloxacin} + 790 \text{ Povacoat} * \text{Povacoat} + 0.000383 \text{ Speed} * \text{Speed} - 1200 \text{ Besifloxacin} * \text{Povacoat} + 0.370 \text{ Besifloxacin} * \text{Speed}. \quad (1)$$

where Z-ave: average hydrodynamic diameter.

The coefficient of determination and the adjusted coefficient of determination ($R^2 = 98.37\%$ and R^2 (Adj.) = 96.16%) are close, allowing the conclusion that nonsignificant values were not considered for the model (Table 4). The predicted R-squared indicates how well a regression model predicts responses to new observations. In this case, the R^2 (pred) was 75.85% . Generally, values above 70% indicate an excellent forecast.

Table 4. Significance of coded regression coefficients and fit index of the selected model in evaluating Z-ave nanocrystals of besifloxacin.

Term	Coef	SE Coef	t-Value	p-Value	VIF
Constant	583.93	5.30	110.13	0.0001	
Besifloxacin	18.68	3.25	5.75	0.001	1.00
Povacoat®	−29.05	3.25	−8.95	0.000	1.00
Speed	−6.72	3.25	−2.07	0.084	1.00
Besifloxacin * Besifloxacin	44.00	4.78	9.21	0.0001	1.01
Povacoat® * Povacoat®	31.60	4.78	6.61	0.001	1.01
Speed * Speed	15.31	4.78	3.20	0.019	1.01
Besifloxacin * Povacoat®	−48.01	4.59	−10.45	0.0001	1.00
Besifloxacin * Speed	14.80	4.59	3.22	0.018	1.00

S: 9.18% R^2 : 98.37% R^2 (adj.): 96.16% R^2 (pred): 75.85%

Coef: Coefficient; SE Coef: Standard deviation coefficient; t-value: size of the difference relative to the variation; p-value: level of significance of terms; VIF: variance inflation factor; S: standard deviation; R^2 : coefficient of determination; R^2 (adj.): Adjusted coefficient of determination; R^2 (pred): Coefficient of prediction determination of the adjusted model. Besifloxacin square (Besifloxacin * Besifloxacin); Povacoat®square (Povacoat®* Povacoat®); Speed square (Speed * Speed); interaction between Besifloxacin and Povacoat®(Besifloxacin * Povacoat®), and interaction between Besifloxacin and Speed (Besifloxacin * Speed).

3.2.2. Mathematical Model Verification

Two formulations with target particle sizes were prepared (F1: target 600 nm, F2: target 576 nm). The same concentration of the reference product was used in this study (0.6% m/m), which is essential to guarantee the minimum inhibitory concentration (MIC). For the formulations, the same conditions were maintained: 30% zirconium spheres and two magnetic bars, with the total amount adjusted to 10 g with phosphate buffer (pH 7.0). The experimental Z-ave (F1 and F2) are close to the theoretical values of each formulation. Therefore, they show the validity of the model (Table 5). Thus, the besifloxacin nanosuspension 0.6 wt% (F2) was selected for posterior analysis due to its reduced particle size (560.3 ± 4.2 nm).

Table 5. Variables obtained in the Box–Behnken experimental design for the optimized nanocrystal preparations and respective theoretical and experimental Z-ave values.

Formula	Besifloxacin (wt%)	Povacoat® (wt%)	Speed (rpm)	Theoretical Z-ave (nm)	Experimental Z-ave (nm)	PdI	ZP (mV)
F1	0.6	0.8	834	600	639.9 ± 30.3	0.101 ± 0.056	-10.10 ± 0.15
F2	0.6	0.9	1044	576	560.3 ± 4.2	0.098 ± 0.067	-10.20 ± 0.10

3.3. Distribution and Particle Size by Laser Diffraction (LD)

Nanotechnology-based materials or final products are those designed to exhibit properties or phenomena, including physical, chemical, or biological effects that are attributable to its dimensions, even if they are smaller than 1 μm (1000 nm) in size [49].

Given the importance of particle size in nanosuspensions, one of the main characteristics of nanoscale products [50], it is essential to verify particle size by two different techniques. Therefore, a new batch of besifloxacin nanosuspension 0.6 wt% was prepared and analyzed by laser diffraction (LD) and dynamic light scattering (DLS), the latter being the primary technique used during this study. The determination by DLS is related to the Brownian motion of the particles, which promotes the scattering of laser light at different intensities. Consequently, the particle size was determined using the Stokes–Einstein relationship. The particle size distribution by LD is related to the modification of the scattered light intensity as a function of the scattering angle, based on Mie’s theory [31,51].

A saturated drug solution was used for dispersion in the DLS technique and phosphate buffer (pH 7.0) for the LD technique. These precautions are essential to maintain the physical characteristics of the nanocrystals during measurements [42].

The DLS analysis showed $Z\text{-ave} = 531.1 \pm 2.7 \text{ nm}$ and $\text{PdI} = 0.102 \pm 0.031$ (Figure S3), while the LD analysis showed $D_{90} = 0.309 \pm 0.003 \mu\text{m}$, where 95.08% of the particles have a size $\leq 0.564 \pm 0.005 \mu\text{m}$, as shown in Figure 4. Thus, the nanosuspension of besifloxacin 0.6% wt% has a particle size approximately 17 times smaller compared to the average particle size of besifloxacin hydrochloride (raw material) and the commercial product (Besivance[®]) (approximately 10 μm). Furthermore, the similarity between the results of the two techniques (DLS and DL) showed that the milling process was adequate.

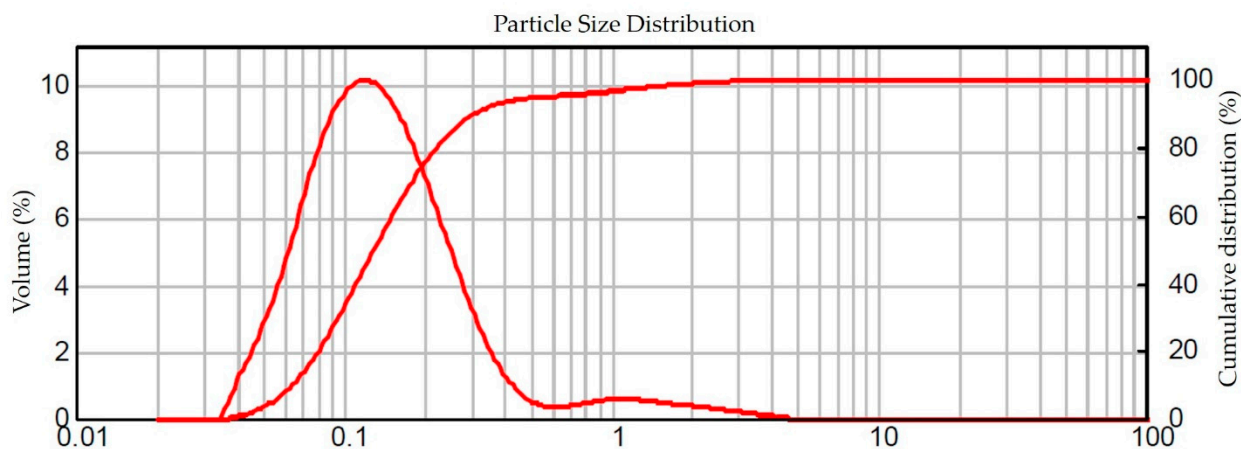


Figure 4. Particle size distribution of besifloxacin nanosuspension 0.6 wt% by laser diffraction (LD). Representative of three runs ($n = 3$).

3.4. pH, Density, and Viscosity

The pH for the optimized formulation (besifloxacin nanosuspension 0.6 wt%) was 6.52 using phosphate buffer (pH = 7.0) as diluent. In this condition, the drug is not solubilized, unlike the manufacturing process of the reference product (Besivance[®]). In this case, besifloxacin hydrochloride is dissolved, and after dissolution, the drug is precipitated at pH 6.5 (zwitterion form of the active) [52]. Thus, more steps are required to obtain the commercial product than the besifloxacin nanosuspension.

Therefore, this pH value (pH = 6.5) is within the reference of the United States Pharmacopoeia [53], which establishes that pH between 3.0 and 8.6 is tolerable for ophthalmic formulations. Furthermore, this result can be considered ideal without causing discomfort to patients since tear pH ranges from 6.5 to 7.6, with a mean value of 7.0 [54]. Still, the nanosuspension is suitably buffered, avoiding pH fluctuations and contributing to its stability.

The density of nanosuspension was 1.0081 g/mL, with an average viscosity of 2.40 ± 0.01 cP. These values are within the range of tear fluid viscosity, varying from 1.05 to 5.97 cP. In addition, preparations with a viscosity below 20 cP do not cause discomfort to patients [55]. Determining the viscosity of ophthalmic preparations is not a compendial requirement but must be considered for product specifications, and depends on the proposed formulation [53].

Adequate viscosity allows better Z-ave stability, avoiding aggregation/agglomeration. The Povacoat[®] is likely adsorbed on the nanocrystal surface, reducing the risk of agglomeration of nanoparticles related to the Ostwald ripening phenomenon [22,56]. In addition, the increase in viscosity favors an increase in the residence time of the drug in the eye, improving bioavailability. However, high viscosity can inhibit the diffusion of drugs from the formulation to the eye [53]. Additionally, high viscosity can increase patient discomfort (pain and blurred vision) and result in dose variability [17]. In the case of the commercial product (Besivance[®]), DuraSite[™] technology offers a viscosity of approximately 1500 cps [14].

3.5. Osmolality

The mean osmolality obtained for the besifloxacin nanosuspension (0.6 wt%) was 164.3 ± 1.5 mOsmol/kg. The United States Pharmacopeia establishes that the default value for the isosmotic solution is 0.9 wt% sodium chloride (NaCl) solution, which has an osmolality of 285 mOsmol/kg and an osmolarity of 284 mOsmol/L [57]. Therefore, it was proposed to adjust the osmolality of the nanosuspension of besifloxacin 0.6 wt% (optimized formula). Usually, osmolality adjustment can be performed with 0.9 wt% sodium chloride solution; however, this is not recommended for the adjustment of nanosuspensions, as it can change the zeta potential and destabilize the formulation. For this, glycerol was considered, which is a neutral osmotic agent [58].

After adding 1.0 wt% of glycerol, an average osmolality of 303.7 ± 0.6 mOsmol/kg was obtained, close to the typical values of 0.9% sodium chloride solution, as recommended by the United States Pharmacopoeia. Values between 171 and 1711 mOsmol/kg can be tolerated without discomfort to the patient [57]. In addition, these values are like those declared for the reference product Besivance[®] (290 mOsmol/kg) [5,14].

3.6. Validation of the Method by High Performance Liquid Chromatography (HPLC)

For specificity, a placebo containing Povacoat[®] (stabilizer), glycerol (isotonizing agent), and benzalkonium chloride (preservative), used in the optimized formulation, did not interfere with the analytical responses. In addition, a test was performed using Millex[®]-HV-PVDF filters 13 mm in diameter, with 0.45 μ m pores, which had no influence on the analytical responses from the filtering of the solutions.

The method was linear, presenting a correlation coefficient of $r = 0.9996$ ($R^2 = 99.96\%$) for drug concentrations ranging from 20 to 80 μ g/mL. In the precision by repeatability (intraday), the following values of relative standard deviation (RSD) were obtained: 1.20% on the first day, 0.84% on the second day, and 0.39% on the third day. Regarding intermediate precision, the analyses provided an RSD of 0.94%. The accuracy was evaluated by the recovery method (addition of the standard) and was shown to be satisfactory (99.03%). Therefore, the method is adequate, like the one validated by COSTA and colleagues [12], meeting the recommendations of the ICH guide and United States Pharmacopeia [32,33].

3.7. Scanning Electron Microscopy (SEM)

Scanning electron microscopy (SEM) showed the morphology of the raw material besifloxacin (Figure 5a) and the besifloxacin nanocrystals (Figure 5b). Microphotographs showed a change from the irregular prismatic crystal to an approximately spherical shape after the milling process. Furthermore, the micrographs showed that the nanocrystals are involved in a light layer, likely related to the Povacoat[®] stabilizer [42].

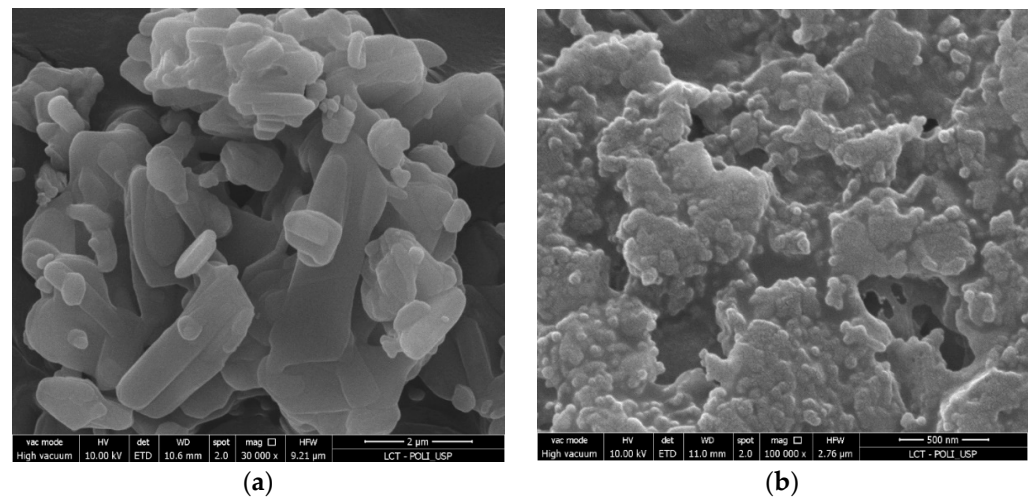


Figure 5. Microphotography of raw material besifloxacin (a) and besifloxacin nanocrystals (b).

3.8. Lyophilization

The lyophilized samples were used for the analyses that needed dry samples. The samples before lyophilization showed $Z\text{-ave} = 510.5 \pm 8.5$ nm, $PdI = 0.052 \pm 0.060$ and $PZ = -9.66 \pm 0.27$. After the drying process, these characteristics did not change, presenting $Z\text{-ave} = 514.4 \pm 27.0$ nm, $PdI = 0.153 \pm 0.118$, and $PZ = -8.66 \pm 0.68$. Therefore, the lyophilization method was adequate and did not change the characteristics of the nanocrystals. In addition, we verified that the redispersion time of the nanocrystals was fast, and no apparent aggregates were observed. Unlike other lyophilization processes [42], the besifloxacin nanocrystals were successfully dried without adding a cryoprotectant substance. Avoiding the need to add substances is essential due to the restriction of using substances in ophthalmic preparations [59].

3.9. Thermal Analysis

The differential scanning calorimetry (DSC) (Figure 6) showed the expected thermal temperature profile for each formulation component analyzed individually. Regarding besifloxacin (raw material), no thermal events were observed in the temperature range studied, consistent with Santos and colleagues [17].

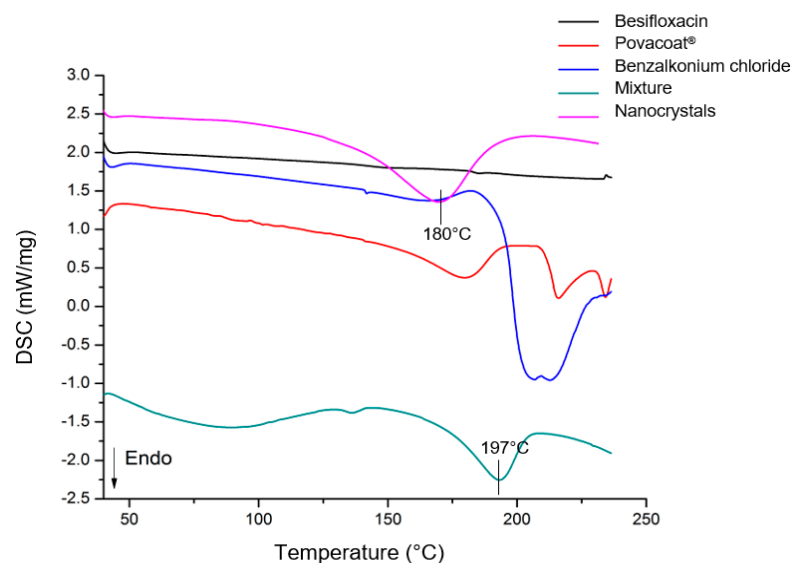


Figure 6. DSC curves of formulation components, mixture (same proportion as formulation), and besifloxacin nanocrystals.

For the nanocrystals, an endothermic curve was observed at approximately 180 °C; in this case, it shifted at a previous temperature with the mixture (197 °C). However, it is possible to show that this curve is related to the sum of the thermal events of the individual components, mainly Povacoat[®] (Figure 6). Therefore, the analysis showed the thermal stability of the nanocrystals, since no degradation events were observed up to 180 °C. Furthermore, the similarity of the DSC curves of the nanocrystals and the mixture shows that the crystalline form was probably maintained. Additionally, this guarantees the compatibility of the components.

3.10. X-ray Diffraction (XRD)

According to the XRD obtained for the nanocrystals (Figure 7), it is possible to observe the prominent peaks of besifloxacin in the 2Θ angles of 10.6, 19.7, and 21.1°, revealing that the crystalline form is likely predominant in the lyophilized formulation. The besifloxacin peaks are also shown in Figure S4. Similar results were presented by Harry [60], where besifloxacin hydrochloride is characterized by diffractograms with peaks at 2Θ angles of 10.6, 15, 19.7, 21.1, and $22^\circ \pm 0.2$.

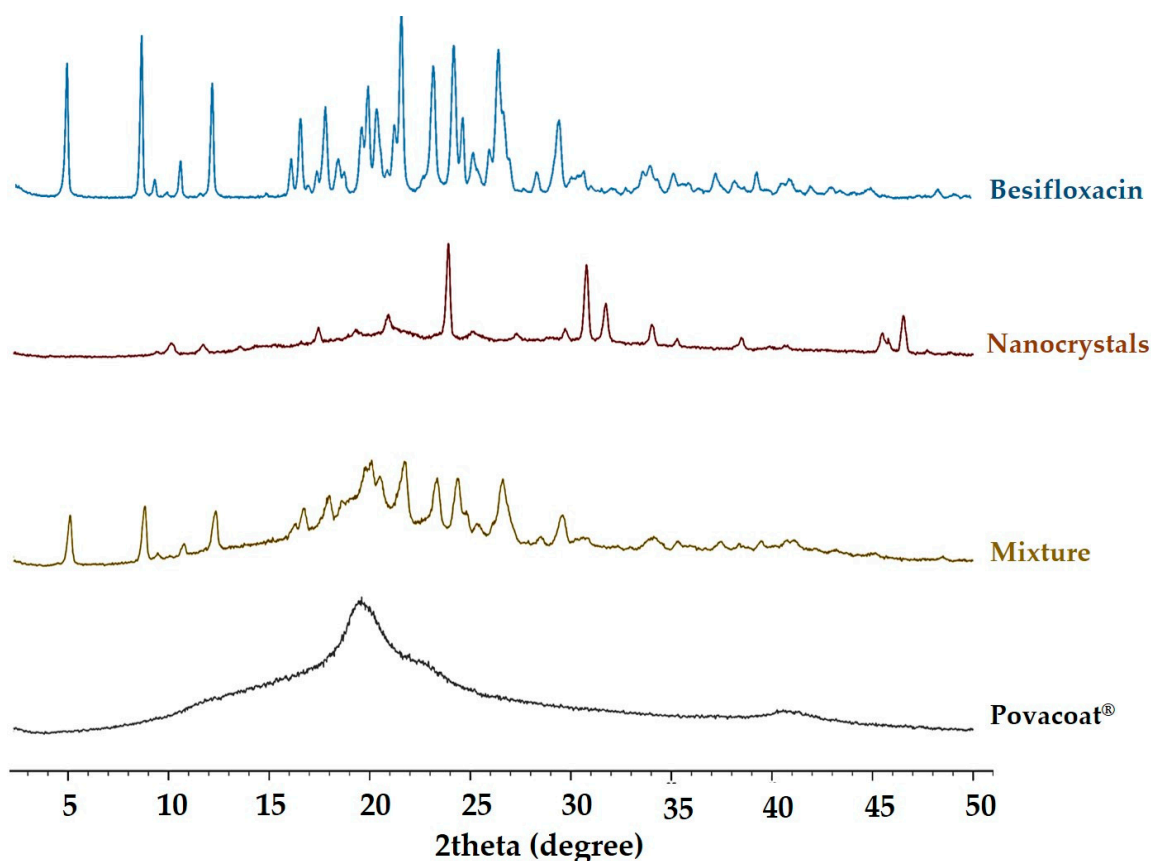


Figure 7. X-ray diffraction of besifloxacin (raw material), nanocrystals, mixture (besifloxacin and Povacoat[®]), and Povacoat[®]. $n = 3$.

Regarding the peaks formed after the angle 2Θ 30°, these are mainly related to the free base of besifloxacin, which present low solubility at pH 6.5, condition of the milling process, and nanosuspension. The same characteristics were observed during the manufacturing process of the Besivance[®] product, where the HCl salt is converted into the free base [60]. Still, these peaks may be related to the interaction of the drug's free base with the Povacoat[®] stabilizer (Figure 7) for the formation of the nanocrystal. Therefore, the crystalline phase is possibly predominant in the nanosuspension.

3.11. Saturation Solubility

Analyses to determine the saturation solubility were conducted under 4 pH conditions (ultrapure water, phosphate buffer pH 4.0, pH 6.0, and pH 7.0) [35]. The concentration of besifloxacin dissolved in each medium was determined by HPLC, using the validated method for quantification and indicative of stability. The tests were performed in three replicates with a theoretical concentration of 50 µg/mL for each condition and showed a relative standard deviation below 1.5% for the media, meeting the Brazilian regulatory requirement [35].

Figure 8 shows the saturation solubility of besifloxacin hydrochloride (raw material) and nanosuspension. Regarding the incubation time, no significant changes were observed after 24 h (Figure 8a) and 48 h (Figure 8b). For nanocrystals, the solubility increases approximately twice in phosphate buffer at pH 6.8 and 7.0, relative to the raw material. This performance allows to increase the bioavailability of the drug substance [21–24,42]. The decrease in the particle radius with a consequent increase in the curvature of their surface causing an increase in the dissolution pressure, according to the Ostwald-Freundlich equation [25]. The reference product (Besivance[®]) presents the same pH range [52]. Furthermore, this is the ideal pH range for ophthalmic formulations, considering the tear pH [54].

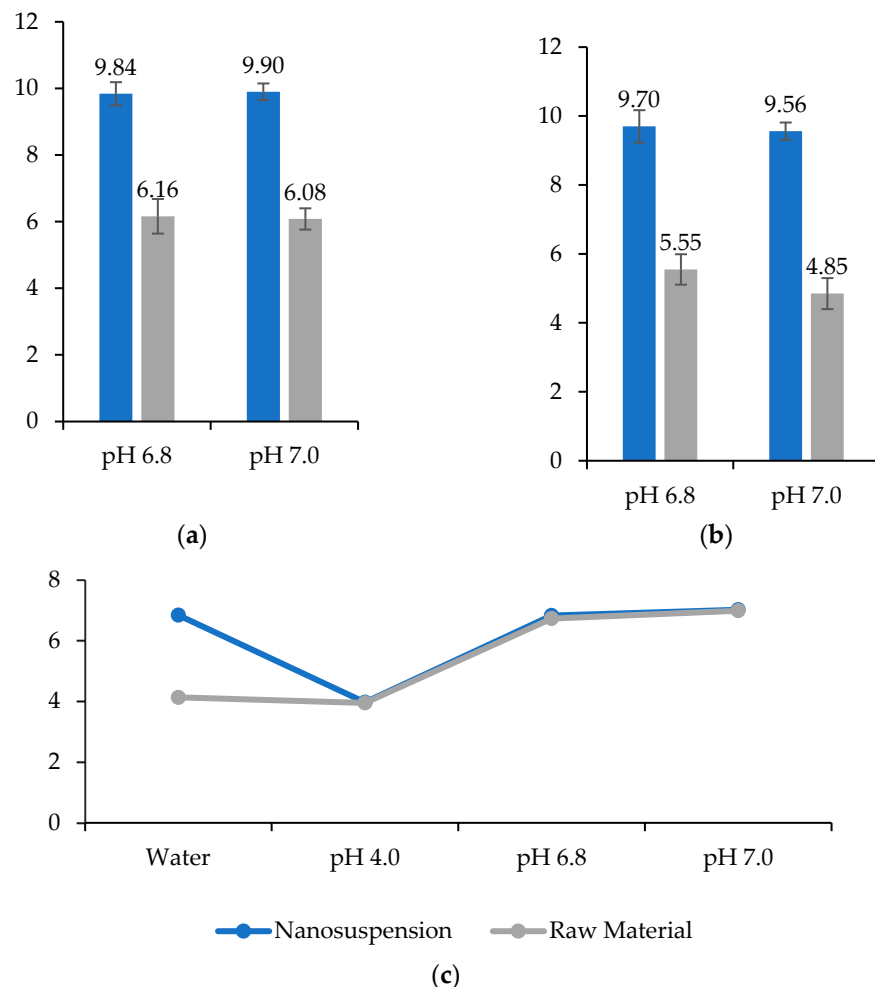


Figure 8. Saturation solubility of besifloxacin (raw material) and nanosuspension (besifloxacin 0.6 wt%). (a) Solubility after 24 h of incubation. (b) Solubility after 48 h of incubation. (c) pH of the samples at the end of the incubation. Theoretical concentration: 50 µg/mL. $n = 3$.

The solubility of the raw material in water follows the literature (0.143 mg/mL) [5]. However, the nanosuspension showed lower solubility in this medium (11.11 ± 0.43 µg/mL).

This is due to the increase in pH to neutrality when the nanosuspension (buffered at pH 7.0) is added to this medium at the beginning of the tests (Figure 8c). In buffer pH 4.0, raw material and nanosuspension showed solubility $50.65 \pm 0.94 \mu\text{g/mL}$ and $51.50 \pm 0.19 \mu\text{g/mL}$, respectively.

3.12. Determination of Minimum Inhibitory Concentration (MIC)

The MIC values were determined as a function of the presence/absence of microbial growth for the test tubes containing the serial dilutions (0.125 to 60 $\mu\text{g/mL}$). The MIC for besifloxacin hydrochloride (raw material) and the nanosuspension against *Pseudomonas aeruginosa* was 1.60 $\mu\text{g/mL}$. Against *Staphylococcus aureus*, the MIC for besifloxacin (raw material) and the nanosuspension were 0.0958 and 0.0960 $\mu\text{g/mL}$, respectively. These values are like those observed in the preliminary analyses of the raw material and the product (item 3.3). Furthermore, they agree with the literature [8,29,39]. Thus, the milling process did not interfere with the in vitro antibiotic efficacy. Similar results were reported for different nano-based besifloxacin delivery: liposome [17], nanoemulsion [18], nanostructured lipid carrier [19], and nanofibrous [20] (Table S2).

3.13. In Vivo Toxicity

Larvae of *Galleria mellonella* ($n = 16$) were injected using a maximal dose of besifloxacin nanosuspension, Povacoat[®], and the phosphate buffer (vehicle control). Besifloxacin nanosuspension (500 mg/kg) and the Povacoat[®] (750 mg/kg) did not show toxicity (Figure S5). The three groups presented 100% larvae survival at the end of the experiment (5 days). An in vivo toxicity study in this model has been used [36,61], mainly because conventional in vitro methods show limitations that make it difficult to simulate physiological responses [62]. Furthermore, this method can support preliminary decisions, reducing the number of tests in mammals [63].

3.14. Stability Study

An accelerated stability study was carried out in order to evaluate possible physico-chemical changes in the nanosuspension, and samples were incubated at $40 \text{ }^\circ\text{C} \pm 2 \text{ }^\circ\text{C}/75\% \text{ RH} \pm 5\% \text{ RH}$. As for the aspect, evaluation of the samples carried out at each time point of the study indicate homogeneity, without change in color, odor, phase separation, and significant sample sedimentation. At each moment, slight sediment of approximately 1 mm in thickness was seen at the bottom of the flasks; this sediment is broken up easily through manual homogenization.

About Z-ave, an increase above 50 nm was observed between the initial analysis (time 0) and 30 days for the three batches (Figure 9). Therefore, the analysis of variance (ANOVA) showed a statistically significant change (p -value = 0.00033; $\alpha = 0.05$) for the period evaluated. This may be related to the small sediment (≈ 1 mm thick) observed in the visual analysis. However, in the later periods, Z-ave stability was observed, and between 30 and 90 days, there was no statistically significant difference (p -value = 0.94; $\alpha = 0.05$). Therefore, its stability can be improved by increasing the viscosity of the formulation and/or adding components that increase the steric hindrance of the formulation, such as ammonium quaternary.

Additionally, a monomodal distribution was observed (Figure S6) after 90 days of incubation, with $\text{PdI} \leq 0.2$, and no statistically significant change (p -value = 0.22239; $\alpha = 0.05$) (Figure 9). Similarly, no significant changes were observed in pH (p -value = 0.78369; $\alpha = 0.05$) and zeta potential (p -value = 0.18212; $\alpha = 0.05$) (Figure 10). Additionally, the content was stable at the end of the period.

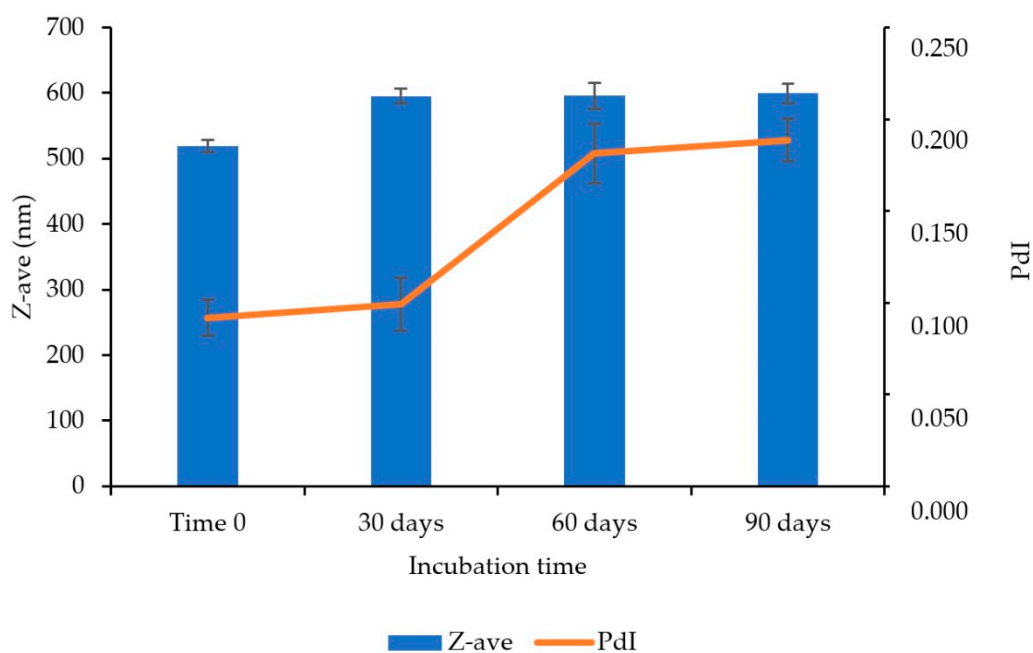


Figure 9. Determination of the average hydrodynamic diameter (Z-ave) in nm and polydispersion index (PdI), for the accelerated stability study of the nanosuspension of besifloxacin 0.6 wt%, in the time intervals: T0, 30, 60, and 90 days. Study condition: $40\text{ }^{\circ}\text{C} \pm 2\text{ }^{\circ}\text{C}/75\% \text{ RH} \pm 5\% \text{ RH}$. $n = 3$ batch.

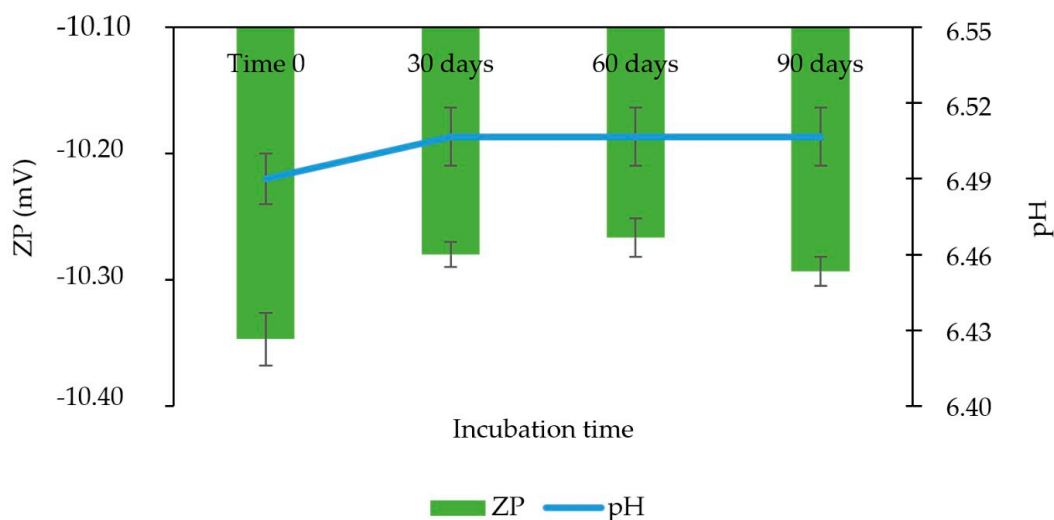


Figure 10. Determination of zeta potential (ZP) and pH for the accelerated stability study of the nanosuspension of besifloxacin 0.6 wt%, in the time intervals: T0, 30, 60, and 90 days. Study condition: $40\text{ }^{\circ}\text{C} \pm 2\text{ }^{\circ}\text{C}/75\% \text{ RH} \pm 5\% \text{ RH}$. $n = 3$ batch.

4. Conclusions

The besifloxacin nanocrystals were successfully prepared using small-scale bed milling and response surface methodology. Povacoat[®] 0.9 wt% reduced the particle size of besifloxacin hydrochloride (550 nm) 17 times, which increased the saturation solubility by approximately two times concerning the raw material. The besifloxacin nanocrystal 0.6 wt% showed in vitro efficacy and did not show toxicity in a larval model. In addition, it presented satisfactory physical and chemical stability, and was able to meet the requirements of a commercial product. Thus, besifloxacin nanocrystals revealed the potential for reduced doses of the drug substance, with the minor occurrence of adverse effects and greater patient adherence to treatment.

Supplementary Materials: The following supporting information can be downloaded at: <https://www.mdpi.com/article/10.3390/pharmaceutics14102221/s1>. Figure S1: Determination of Z-ave (nm) for the first exploratory study; Figure S2: Determination of Z-ave (nm) for the second exploratory study; Figure S3: Freeze-dried besifloxacin nanosuspension DLS measurements: (a) Size distribution by intensity; (b) Size distribution by volume; (c) Correlogram; (d) Z-average trend; (e) Statistics graph $n = 3$; Figure S4: X-ray diffraction of besifloxacin (raw material) and nanocrystals (freeze-dried). Figure S5: Toxicity of besifloxacin nanocrystals (500 mg/kg) and Povacoat[®] (750 mg/kg) in a larval model of *Galleria mellonella*; Figure S6: Particle distribution (monomodal), accelerated stability: 90 days. Study condition: $40^{\circ}\text{C} \pm 2^{\circ}\text{C}/75\% \text{RH} \pm 5\% \text{RH}$; Table S1: Stability of the average hydrodynamic diameter (Z-ave) in nm, in the time intervals: immediately after milling (T0), 7 days, 15 days and 30 days. Process time 4 days. Storage condition: 25°C . Table S2: Nano-based besifloxacin delivery: type, composition, properties, antimicrobial activity and, physical-chemical stability condition.

Author Contributions: Conceptualization, J.I.S.d.S.d.J. and N.A.B.-C.; methodology, J.I.S.d.S.d.J.; formal analysis, F.R.L., J.I.S.d.S.d.J., K.I. and T.L.B.; resources, E.d.S.N., N.A.B.-C. and V.C.A.; data curation, J.I.S.d.S.d.J. and N.A.B.-C.; writing—original draft preparation, J.I.S.d.S.d.J.; writing—review and editing, J.I.S.d.S.d.J. and N.A.B.-C.; supervision, N.A.B.-C.; project administration, N.A.B.-C. All authors have read and agreed to the published version of the manuscript.

Funding: This research received no external funding.

Institutional Review Board Statement: Not applicable.

Informed Consent Statement: Not applicable.

Data Availability Statement: The data presented in this study are available on request from the corresponding author.

Acknowledgments: We thank all the sample donors and researchers. Jim Hesson copyedited the manuscript <https://www.academicenglishsolutions.com/blank> (accessed on 2 September 2022).

Conflicts of Interest: The authors declare no conflict of interest.

References









1. Azari, A.A.; Barney, N.P. Conjunctivitis: A Systematic Review of Diagnosis and Treatment. *JAMA* **2013**, *310*, 1721–1729. [CrossRef] [PubMed]
2. Khimdas, S.; Visscher, K.L.; Hutnik, C.M.L. Besifloxacin Ophthalmic Suspension: Emerging Evidence of Its Therapeutic Value in Bacterial Conjunctivitis. *Ophthalmol. Eye Dis.* **2011**, *3*, 7–12. [CrossRef] [PubMed]
3. Mejia-Lopez, H.; Alberto, C.; Climent-Flores, A.; Bautista-de Lucio, V.M. Epidemiological Aspects of Infectious Conjunctivitis. In *Conjunctivitis—A Complex and Multifaceted Disorder*; Intech Open: London, UK, 2011.
4. Saher, O.; Ghorab, D.M.; Mursi, N.M. Levofloxacin Hemihydrate Ocular Semi-Sponges for Topical Treatment of Bacterial Conjunctivitis: Formulation and in-Vitro/in-Vivo Characterization. *J. Drug Deliv. Sci. Technol.* **2016**, *31*, 22–34. [CrossRef]
5. Tótolí, E.G.; Salgado, H.R.N. Besifloxacin: A Critical Review of Its Characteristics, Properties, and Analytical Methods. *Crit. Rev. Anal. Chem.* **2018**, *48*, 132–142. [CrossRef]
6. Alfonso, S.A.; Fawley, J.D.; Lu, X.A. Conjunctivitis. *Prim. Care Clin. Off. Pract.* **2015**, *42*, 325–345. [CrossRef]
7. Asbell, P.A.; Sanfilippo, C.M.; Pillar, C.M.; DeCory, H.H.; Sahm, D.F.; Morris, T.W. Antibiotic Resistance among Ocular Pathogens in the United States Five-Year Results from the Antibiotic Resistance Monitoring in Ocular Microorganisms (ARMOR) Surveillance Study. *JAMA Ophthalmol.* **2015**, *133*, 1445–1454. [CrossRef]
8. Comstock, T.L.; Karpecki, P.M.; Morris, T.W.; Zhang, J.Z. Besifloxacin: A Novel Anti-Infective for the Treatment of Bacterial Conjunctivitis. *Clin. Ophthalmol.* **2010**, *4*, 215–225. [CrossRef]
9. Kirstahler, P.; Bjerrum, S.S.; Friis-Møller, A.; La Cour, M.; Aarestrup, F.M.; Westh, H.; Pamp, S.J. Genomics-Based Identification of Microorganisms in Human Ocular Body Fluid. *Sci. Rep.* **2018**, *8*, 4126. [CrossRef]
10. Lipsky, L.; Barrett, G. Intracameral Antibiotics for Prophylaxis of Postoperative Endophthalmitis in Australia: A Review. *Clin. Exp. Ophthalmol.* **2019**, *47*, 537–541. [CrossRef]
11. Seiple, I.B.; Zhang, Z.; Jakubec, P.; Langlois-Mercier, A.; Wright, P.M.; Hog, D.T.; Yabu, K.; Allu, S.R.; Fukuzaki, T.; Carlsen, P.N.; et al. A Platform for the Discovery of New Macrolide Antibiotics. *Nature* **2016**, *533*, 338–345. [CrossRef]
12. Costa, M.C.N.; Barden, A.T.; Andrade, J.M.M.; Oppe, T.P.; Schapoval, E.E.S. Quantitative Evaluation of Besifloxacin Ophthalmic Suspension by HPLC, Application to Bioassay Method and Cytotoxicity Studies. *Talanta* **2014**, *119*, 367–374. [CrossRef] [PubMed]
13. Hughes, B. 2009 FDA Drug Approvals. *Nat. Rev. Drug Discov.* **2010**, *9*, 89–93. [CrossRef] [PubMed]

14. Bausch & Lomb Incorporated Besivance™ Material Safety Data Sheet. Available online: [//s3-us-west-2.amazonaws.com/drugbank/msds/DB06771.pdf?1365982762](https://s3-us-west-2.amazonaws.com/drugbank/msds/DB06771.pdf?1365982762) (accessed on 6 September 2022).
15. Achouri, D.; Alhanout, K.; Piccerelle, P.; Andrieu, V. Recent Advances in Ocular Drug Delivery. *Drug Dev. Ind. Pharm.* **2013**, *39*, 1599–1617. [CrossRef]
16. Gao, L.; Liu, G.; Ma, J.; Wang, X.; Zhou, L.; Li, X. Drug Nanocrystals: In Vivo Performances. *J. Control. Release* **2012**, *160*, 418–430. [CrossRef] [PubMed]
17. dos Santos, G.A.; Ferreira-Nunes, R.; Dalmolin, L.F.; dos Santos Ré, A.C.; Anjos, J.L.V.; Mendanha, S.A.; Aires, C.P.; Lopez, R.F.V.; Cunha-Filho, M.; Gelfuso, G.M.; et al. Besifloxacin Liposomes with Positively Charged Additives for an Improved Topical Ocular Delivery. *Sci. Rep.* **2020**, *10*, 19285. [CrossRef] [PubMed]
18. Kassaei, S.N.; Mahboobian, M.M. Besifloxacin-Loaded Ocular Nanoemulsions: Design, Formulation and Efficacy Evaluation. *Drug Deliv. Transl. Res.* **2022**, *12*, 229–239. [CrossRef]
19. Polat, H.K.; Kurt, N.; Aytakin, E.; Akdağ Çaylı, Y.; Bozdağ Pehlivan, S.; Çalıř, S. Design of Besifloxacin HCl-Loaded Nanostructured Lipid Carriers: In Vitro and Ex Vivo Evaluation. *J. Ocul. Pharmacol. Ther.* **2022**, *38*, 412–423. [CrossRef] [PubMed]
20. Polat, H.K.; Bozdağ Pehlivan, S.; Özkul, C.; Çalamak, S.; Öztürk, N.; Aytakin, E.; Fırat, A.; Ulubayram, K.; Kocabeyođlu, S.; İrkeç, M.; et al. Development of Besifloxacin HCl Loaded Nanofibrous Ocular Inserts for the Treatment of Bacterial Keratitis: In Vitro, Ex Vivo and in Vivo Evaluation. *Int. J. Pharm.* **2020**, *585*, 119552. [CrossRef]
21. Barbosa, S.F.; Takatsuka, T.; Tavares, G.D.; Araújo, G.L.B.; Wang, H.; Vehring, R.; Löbenberg, R.; Bou-Chacra, N.A. Physical–Chemical Properties of Furosemide Nanocrystals Developed Using Rotation Revolution Mixer. *Pharm. Dev. Technol.* **2016**, *21*, 812–822. [CrossRef]
22. Chen, M.-L.; John, M.; Lee, S.L.; Tyner, K.M. Development Considerations for Nanocrystal Drug Products. *AAPS J.* **2017**, *19*, 642–651. [CrossRef]
23. Davis, B.M.; Pahlitzsch, M.; Guo, L.; Balendra, S.; Shah, P.; Ravindran, N.; Malaguarnera, G.; Sisa, C.; Shamsher, E.; Hamze, H.; et al. Topical Curcumin Nanocarriers Are Neuroprotective in Eye Disease. *Sci. Rep.* **2018**, *8*, 6712. [CrossRef] [PubMed]
24. Tyner, K.M.; Zheng, N.; Choi, S.; Xu, X.; Zou, P.; Jiang, W.; Guo, C.; Cruz, C.N. How Has CDER Prepared for the Nano Revolution? A Review of Risk Assessment, Regulatory Research, and Guidance Activities. *AAPS J.* **2017**, *19*, 1071–1083. [CrossRef] [PubMed]
25. Williams, H.D.; Trevaskis, N.L.; Charman, S.A.; Shanker, R.M.; Charman, W.N.; Pouton, C.W.; Porter, C.J.H. Strategies to Address Low Drug Solubility in Discovery and Development. *Pharmacol. Rev.* **2013**, *65*, 315–499. [CrossRef] [PubMed]
26. Markets, R. *Nanotechnology—Global Market Trajectory & Analytics*; Global Industry Analysts, Inc.: San Jose, CA, USA, 2020.
27. Peters, M.C.C.; de Oliveira, I.F.; Machado, M.G.M.; Ferreira, D.C.; Zanin, M.H.A.; Bou-Chacra, N. The Glucocorticoid Derivative with the Phthalimide Group Cationic Nanocrystal for Ophthalmic Application: A Design Space Development Approach. *Mater. Today Chem.* **2021**, *19*, 100396. [CrossRef]
28. Zuo, J.; de Araujo, G.L.B.; Stephano, M.A.; Zuo, Z.; Bou-Chacra, N.A.; Löbenberg, R. Design Space Approach in the Development of Esculetin Nanocrystals by a Small-Scale Wet-Bead Milling Process. *J. Drug Deliv. Sci. Technol.* **2020**, *55*, 101486. [CrossRef]
29. Haas, W.; Pillar, C.M.; Hesje, C.K.; Sanfilippo, C.M.; Morris, T.W. Bactericidal Activity of Besifloxacin against Staphylococci, Streptococcus Pneumoniae and Haemophilus Influenzae. *J. Antimicrob. Chemother.* **2010**, *65*, 1441–1447. [CrossRef]
30. Romero, G.B.; Keck, C.M.; Müller, R.H.; Bou-Chacra, N.A. Development of Cationic Nanocrystals for Ocular Delivery. *Eur. J. Pharm. Biopharm.* **2016**, *107*, 215–222. [CrossRef] [PubMed]
31. MALVERN Zetasizer Nano Series—Performance, Simplicity, Versatility. Malvern Instruments Ltd. 2014. Available online: https://www.malvernpanalytical.com/en/assets/MRK1839_tcm50-17228.pdf (accessed on 10 August 2022).
32. VICH ICH Topic Q2 (R1) Validation of Analytical Procedures: Text and Methodology. 2005. Available online: https://www.ema.europa.eu/en/documents/scientific-guideline/ich-q-2-r1-validation-analytical-procedures-text-methodology-step-5_en.pdf (accessed on 6 September 2022).
33. United States Pharmacopeia. *<1225> Validation of Compendial Procedures*; USP 43-NF 38; Pharmacopeial: Rockville Convention, MD, USA, 2021.
34. Brazilian Health Surveillance Agency (ANVISA). Resolução da Diretoria Colegiada RDC Nº 166, de 24 de Julho de 2017. Dispõe sobre a validação de métodos analíticos e dá outras providências. Available online: https://www.in.gov.br/materia/-/asset_publisher/Kujrw0TZC2Mb/content/id/19194581/do1-2017-07-25-resolucao-rdc-n-166-de-24-de-julho-de-2017-19194412 (accessed on 6 September 2022).
35. Brazilian Health Surveillance Agency (ANVISA). Resolução da Diretoria Colegiada RDC Nº 37, de 03 de Agosto de 2011. Dispõe Sobre o Guia Para Isenção e Substituição de Estudos de Biodisponibilidade Relativa/Bioequivalência e Dá Outras Providências. Available online: https://bvsm.saudef.gov.br/bvs/saudeflegis/anvisa/2011/res0037_03_08_2011.html (accessed on 6 September 2022).
36. de Spadari, C.; de Bastiani, F.W.M.d.S.; Lopes, L.B.; Ishida, K. Alginate Nanoparticles as Non-Toxic Delivery System for Miltefosine in the Treatment of Candidiasis and Cryptococcosis. *Int. J. Nanomed.* **2019**, *14*, 5187–5199. [CrossRef]
37. ICH Q1—Evaluation of Stability Data. Guideline 2003. Available online: https://www.ema.europa.eu/en/documents/scientific-guideline/ich-q-1-r2-stability-testing-new-drug-substances-products-step-5_en.pdf (accessed on 6 September 2022).

38. Brazilian Health Surveillance Agency (ANVISA). Resolução da Diretoria Colegiada RDC N° 318, de 6 de Novembro de 2019. Estabelece os critérios para a realização de Estudos de Estabilidade de insumos farmacêuticos ativos e medicamentos, exceto biológicos, e dá outras providências. Available online: <https://www.in.gov.br/web/dou/-/resolucao-rdc-n-318-de-6-de-novembro-de-2019-226513805> (accessed on 26 August 2022).
39. Silverstein, B.E.; Morris, T.W.; Gearing, L.S.; DeCory, H.H.; Comstock, T.L. Besifloxacin Ophthalmic Suspension 0.6% in the Treatment of Bacterial Conjunctivitis Patients with Pseudomonas Aeruginosa Infections. *Clin. Ophthalmol.* **2012**, *6*, 1987–1996. [CrossRef]
40. de Cássia Zaghi Compri, J.; Andres Felli, V.M.; Lourenço, F.R.; Takatsuka, T.; Fotaki, N.; Löbenberg, R.; Bou-Chacra, N.A.; Barros de Araujo, G.L. Highly Water-Soluble Orotic Acid Nanocrystals Produced by High-Energy Milling. *J. Pharm. Sci.* **2019**, *108*, 1848–1856. [CrossRef]
41. Lin, S.Y.; Lin, H.L.; Chi, Y.T.; Hung, R.Y.; Huang, Y.T.; Kao, C.Y.; Hsieh, W.H. Povacoat Affecting Solid-State Polymorphic Changes of Indomethacin after Co-Evaporation from Different Types of Solvents via Conventional and Microwave Drying Techniques. *Asian J. Pharm. Sci.* **2016**, *11*, 376–384. [CrossRef]
42. Melo, K.J.C.; Henostroza, M.A.B.; Löbenberg, R.; Bou-Chacra, N.A. Rifampicin Nanocrystals: Towards an Innovative Approach to Treat Tuberculosis. *Mater. Sci. Eng. C* **2020**, *112*, 110895. [CrossRef] [PubMed]
43. Ochi, M.; Kawachi, T.; Toita, E.; Hashimoto, I.; Yuminoki, K.; Onoue, S.; Hashimoto, N. Development of Nanocrystal Formulation of Meloxicam with Improved Dissolution and Pharmacokinetic Behaviors. *Int. J. Pharm.* **2014**, *474*, 151–156. [CrossRef] [PubMed]
44. Ueda, H.; Aikawa, S.; Kashima, Y.; Kikuchi, J.; Ida, Y.; Tanino, T.; Kadota, K.; Tozuka, Y. Anti-Plasticizing Effect of Amorphous Indomethacin Induced by Specific Intermolecular Interactions with PVA Copolymer. *J. Pharm. Sci.* **2014**, *103*, 2829–2838. [CrossRef] [PubMed]
45. Yuminoki, K.; Seko, F.; Horii, S.; Takeuchi, H.; Teramoto, K.; Nakada, Y.; Hashimoto, N. Preparation and Evaluation of High Dispersion Stable Nanocrystal Formulation of Poorly Water-Soluble Compounds by Using Povacoat. *J. Pharm. Sci.* **2014**, *103*, 3772–3781. [CrossRef] [PubMed]
46. Yuminoki, K.; Seko, F.; Horii, S.; Takeuchi, H.; Teramoto, K.; Nakada, Y.; Hashimoto, N. Application of Povacoat as Dispersion Stabilizer of Nanocrystal Formulation. *Asian J. Pharm. Sci.* **2016**, *11*, 48–49. [CrossRef]
47. ICH Q8(R2). Pharmaceutical Development. Guideline. 2009. Available online: <https://www.ema.europa.eu/en/ich-q8-r2-pharmaceutical-development> (accessed on 6 September 2022).
48. Peters, M.C.C.; dos Santos Neto, E.; Monteiro, L.M.; Yukuyama, M.N.; Machado, M.G.M.; de Oliveira, I.F.; Zanin, M.H.A.; Löbenberg, R.; Bou-Chacra, N. Advances in Ophthalmic Preparation: The Role of Drug Nanocrystals and Lipid-Based Nanosystems. *J. Drug Target.* **2020**, *28*, 259–270. [CrossRef]
49. U.S. Food and Drug Administration Food and Drug Administration—Guidance for Industry Considering Whether an FDA-Regulated Product Involves the Application of Nanotechnology. *Biotechnol. Law Rep.* **2014**, *30*, 613–616. [CrossRef]
50. Kornecki, M.; Strube, J. Process Analytical Technology for Advanced Process Control in Biologics Manufacturing with the Aid of Microscopic Kinetic Modeling. *Bioengineering* **2018**, *5*, 25. [CrossRef]
51. HORIBA A Guidebook to Particle Size Analysis. Available online: https://static.horiba.com/fileadmin/Horiba/Products/Scientific/Particle_Characterization/Particle_Guidebook_06-2021.pdf (accessed on 2 August 2022).
52. Australian Government Department of Health and Ageing AusPAR: Besifloxacin Hydrochloride. Available online: <https://www.tga.gov.au/resources/auspar/auspar-besifloxacin-hydrochloride> (accessed on 2 August 2022).
53. Pharmacopeia, U.S. (771) *Ophthalmic Products—Quality Tests*; USP 43-NF 38; Pharmacopeial: Rockville Convention, MD, USA, 2021.
54. Abelson, M.B.; Udell, I.J.; Weston, J.H. Normal Human Tear Ph by Direct Measurement. *Arch. Ophthalmol.* **1981**, *99*, 301. [CrossRef]
55. Aldrich, D.S.; Bach, C.M.; Brown, W.; Chambers, W.; Fleitman, J.; Hunt, D.; Marques, M.R.C.; Mille, Y.; Mitra, A.K.; Platzer, S.M.; et al. Ophthalmic Preparations. *Pharmacop. Forum* **2013**, *39*, 1–21.
56. Skrdla, P.J.; Yang, H. On the Stability of Nano-Formulations Prepared by Direct Synthesis: Simulated Ostwald Ripening of a Typical Nanocrystal Distribution Post-Nucleation. *AAPS PharmSciTech* **2019**, *20*, 34. [CrossRef] [PubMed]
57. United States Pharmacopeia. (785) *Osmolality and Osmolarity*; USP 43-NF 38; Pharmacopeial: Rockville Convention, MD, USA, 2021.
58. Bazán Henostroza, M.A.; Curo Melo, K.J.; Nishitani Yukuyama, M.; Löbenberg, R.; Araci Bou-Chacra, N. Cationic Rifampicin Nanoemulsion for the Treatment of Ocular Tuberculosis. *Colloids Surf. A: Physicochem. Eng. Asp.* **2020**, *597*, 124755. [CrossRef]
59. Food and Drug Administration 2018 NEW DRUG THERAPY APPROVALS. Available online: https://www.fda.gov/files/drugs/published/New-Drug-Therapy-Approvals-2018_3.pdf (accessed on 2 August 2022).
60. Harry, M.; King, J. Fluoroquinolone Carboxylic Acid Molecular Crystals. U.S. Patent No. 8,481,526, 9 July 2013.
61. Piatek, M.; Sheehan, G.; Kavanagh, K. Galleria Mellonella: The Versatile Host for Drug Discovery, in Vivo Toxicity Testing and Characterising Host-Pathogen Interactions. *Antibiotics* **2021**, *10*, 1545. [CrossRef] [PubMed]
62. Moya-Andérico, L.; Vukomanovic, M.; del Cendra, M.; Segura-Feliu, M.; Gil, V.; del Río, J.A.; Torrents, E. Utility of Galleria Mellonella Larvae for Evaluating Nanoparticle Toxicology. *Chemosphere* **2021**, *266*, 129235. [CrossRef]
63. Mikulak, E.; Gliniewicz, A.; Przygodzka, M.; Solecka, J. Galleria Mellonella L. as Model Organism Used in Biomedical and Other Studies. *Prz. Epidemiol.* **2018**, *72*, 57–73.

Article

Cysteamine Eye Drops in Hyaluronic Acid Packaged in Innovative Single-Dose Systems: Stability and Ocular Biopermanence

Ana Castro-Balado ^{1,2,3,†} , Enrique Bandín-Vilar ^{1,2,3,†} , Andrea Cuartero-Martínez ^{2,†},
Laura García-Quintanilla ^{1,2,3}, Gonzalo Hermelo-Vidal ², Xurxo García-Otero ^{3,4} , Lorena Rodríguez-Martínez ²,
Jesús Mateos ² , Manuela Hernández-Blanco ⁵, Pablo Aguiar ⁴ , Irene Zarra-Ferro ^{1,2}, Miguel González-Barcia ^{1,2},
Cristina Mondelo-García ^{1,2,*} , Francisco J. Otero-Espinar ^{3,*}  and Anxo Fernández-Ferreiro ^{1,2,*} 

¹ Pharmacy Department, University Clinical Hospital of Santiago de Compostela (SERGAS), 15706 Santiago de Compostela, Spain

² Clinical Pharmacology Group, Health Research Institute of Santiago de Compostela (IDIS), 15706 Santiago de Compostela, Spain

³ Pharmacology, Pharmacy and Pharmaceutical Technology Department, Faculty of Pharmacy, University of Santiago de Compostela (USC), 15782 Santiago de Compostela, Spain

⁴ Molecular Imaging Group, Health Research Institute of Santiago de Compostela (IDIS), 15706 Santiago de Compostela, Spain

⁵ Microbiology Department, University Clinical Hospital of Santiago de Compostela (SERGAS), 15706 Santiago de Compostela, Spain

* Correspondence: crismondelo1@gmail.com (C.M.-G.); francisco.otero@usc.es (F.J.O.-E.); anxordes@gmail.com (A.F.-F.)

† These authors contributed equally to this work.

Citation: Castro-Balado, A.;

Bandín-Vilar, E.; Cuartero-Martínez,

A.; García-Quintanilla, L.;

Hermelo-Vidal, G.; García-Otero, X.;

Rodríguez-Martínez, L.; Mateos, J.;

Hernández-Blanco, M.; Aguiar, P.;

et al. Cysteamine Eye Drops in

Hyaluronic Acid Packaged in

Innovative Single-Dose Systems:

Stability and Ocular Biopermanence.

Pharmaceutics **2022**, *14*, 2194.

[https://doi.org/10.3390/](https://doi.org/10.3390/pharmaceutics14102194)

[pharmaceutics14102194](https://doi.org/10.3390/pharmaceutics14102194)

Academic Editor: Raid Alany

Received: 23 September 2022

Accepted: 12 October 2022

Published: 15 October 2022

Publisher's Note: MDPI stays neutral with regard to jurisdictional claims in published maps and institutional affiliations.



Copyright: © 2022 by the authors. Licensee MDPI, Basel, Switzerland. This article is an open access article distributed under the terms and conditions of the Creative Commons Attribution (CC BY) license (<https://creativecommons.org/licenses/by/4.0/>).

Abstract: Cystinosis is a rare genetic disorder characterized by the accumulation of cystine crystals in different tissues and organs causing, among other symptoms, severe ocular manifestations. Cysteamine eye drops are prepared in hospital pharmacy departments to facilitate access to treatment, for which vehicles that provide adequate biopermanence, as well as adaptable containers that maintain its stability, are required. Difficulties related to cysteamine preparation, as well as its tendency to oxidize to cystamine, show the importance of conducting rigorous galenic characterization studies. This work aims to develop and characterize an ophthalmic compounded formulation of cysteamine prepared with hyaluronic acid and packaged in innovative single-dose systems. For this task, the effect of different storage temperatures and the presence/absence of nitrogen on the physicochemical stability of the formulation and its packaging was studied in a scaled manner, until reaching the optimal storage conditions. The results showed that 0.55% cysteamine, prepared with hyaluronic acid and packaged in single-dose containers, is stable for 30 days when stored at $-20\text{ }^{\circ}\text{C}$. In addition, opening vials every 4 h at room temperature after 30 days of freezing maintains the stability of the cysteamine formulation for up to 16 h. Moreover, ocular biopermanence studies were conducted using molecular imaging, concluding that the biopermanence offered by the vehicle is not affected by the freezing process, where a half-life of 31.11 min for a hyaluronic acid formulation stored for 30 days at $-20\text{ }^{\circ}\text{C}$ was obtained, compared with 14.63 min for 0.9% sodium chloride eye drops.

Keywords: cystinosis; ophthalmic administration; cysteamine; compounded formulation; PET

1. Introduction

Cystinosis is considered a rare autosomal recessive lysosomal disease that affects approximately 100,000–200,000 people in the general population [1,2]. It is characterized by the lysosomal accumulation of cystine crystals, the disulfide of the amino acid cysteine, with low solubility in water. Mutations in the CTNS gene, which encodes cystinosisin, the carrier that transports cystine from the lysosome, are responsible for this cumulative

process [3]. The presence of cystine crystals in different tissues leads to the progressive damage and dysfunction of multiple organs, such as the pancreas, brain, thyroid, kidneys, and eyes [4]. The most frequently described ocular manifestation is the deposition of cystine crystals in the cornea, but it also affects other eye structures, causing visual impairment and eventually, blindness [5–7].

Currently, the aminothiols cysteamine remains the only available treatment of cystinosis [8], although other pathways have been recently explored to expand therapeutic options [9–12]. Cysteamine lowers intracellular levels of cystine by forming a cysteamine–cysteine mixed disulfide, which resembles lysine and leaves the lysosome using a “lysine transport system” [8,13]. The authorization of oral cysteamine (Cystagon[®]) in 2012 by the Food and Drug Administration (FDA), followed by the delayed-release formulation years later (Procysbi[®]), has completely changed the management and prognosis of cystinosis [14–16]. However, systemic cysteamine has a low ocular bioavailability due to the lack of corneal vascularization, so it must be administered by the ophthalmic route. Cystaran[®] 0.44% eye drops received FDA approval in 2012 as an orphan drug, requiring administration of one drop per eye every waking hour [17], which complicates patient compliance. To improve this aspect, Cystadrops[®] 0.55% was subsequently approved by the European Medicines Agency (EMA) and the FDA in 2017 and 2021, respectively [18,19]. This formulation contains sodium carboxymethylcellulose that provides high viscosity, thus achieving a longer residence time on the ocular surface and allowing its administration four times a day [19].

Commercial cysteamine preparations are not available in most countries, as access is sometimes delayed due to mandatory procedures and authorizations. In this scenario, hospital pharmacy departments (HPD) are responsible for preparing cysteamine ophthalmic compounded formulations as a therapeutic alternative [20]. These formulations need to be properly developed with appropriate galenic characterization studies prior to their translation into clinical practice [21]. Cysteamine is an easily oxidizable molecule whose exposure to the air reduces its shelf life, since the thiol functional group immediately reacts with oxygen to form a disulfide called cystamine, which is ineffective in the treatment of cystinosis [21–23]. This process occurs quickly in air and solution [24], making it difficult to develop adequate determination methods that allow the simultaneous detection of cysteamine and cystamine [25]. Strategies such as packaging under a nitrogen atmosphere, adding antioxidants, reducing the pH, and lowering the temperature in storage, effectively increase its stability [26–28].

Classical compounded formulations of cysteamine eye drops are produced in HPD with 0.9% sodium chloride (NaCl), but these require frequent instillations while the patient is awake due to its low ocular biopermanence. To optimize the formulation and avoid these difficult dosage schedules, our group developed and characterized a bioadhesive cysteamine hydrogel with high ocular permanence, using hyaluronic acid 0.4% as a vehicle [6,20,29]. However, after four years of producing this formulation in our center, we have detected in the internal quality controls that important parameters, such as the molecular weight of the sodium hyaluronate used (supplied by the same distributor authorized by the Spanish Agency of Medicines and Medical Devices), exhibited important variations of up to 40% in the different batches produced. In addition, other substances, including proteins, nucleic acids, metals, and chlorate content, have been detected [30,31]. According to previous publications, this could significantly interfere with compounding and stability studies using different batches, as they would no longer be reproducible [32–35]. To overcome this problem, we have decided to use commercialized eye drops that contain 0.4% hyaluronic acid (Aquoral[®]). This choice offers the advantages of a constant source, a dependable purification technique, and a certified molecular weight in the hyaluronate used.

When transferring compounded formulations to clinical practice, it is important to take into account the comfort of the patient and the pharmacy staff in charge of the preparation. Therefore, packaging in single-dose systems would allow the use of one disposable container per day, while the rest of the dispensed batch could be kept at low-temperature

conditions that favor the stability of the active ingredient, in this case, cysteamine. The use of one single-dose container per day would facilitate its handling and transportation by patients, also reducing the number of visits to the hospital for dispensing treatment. When using these single-dose containers, it is necessary to devise a system that allows easy and fast filling, but without entailing a workload in the formulation production circuit. At the same time, it is important to consider whether storage at low temperatures can negatively affect the physical properties of the compounded formulation, or the properties of the container.

The objective of this work is to develop and characterize an ophthalmic compounded formulation of 0.55% cysteamine, packaged in single-dose containers, for its elaboration from HPD. The stability study of the formulation and its final container was carried out in a scaled manner under different storage conditions (with/without nitrogen saturation, refrigerated or frozen) for 30 days to achieve the most optimal form of conservation. Their chemical (cysteamine and cystamine content, pH), physical (osmolality and viscosity), and microbiological stability, as well as packaging elasticity after storage at low temperatures, were evaluated. An in-use stability study was also conducted at room temperature to simulate conditions for opening the eye drops prior to administration. Finally, a preclinical ocular biopermanence study was carried out by PET/CT imaging.

2. Materials and Methods

2.1. Materials

Cysteamine hydrochloride (cysteamine purity 97%) was obtained from Apollo Scientific (Stockport, UK) and 1-Heptanesulphonic acid sodium salt was obtained from Sigma Aldrich (St. Louis, MO, USA). Cystamine dihydrochloride (Cystamine purity 97%) was obtained from Thermo Fisher Scientific (Geel, Belgium). Aquoral[®] eye drops (0.4% w/v % hyaluronic acid (HA), sodium chloride, sodium citrate, citric acid monohydrate, water for injectable preparations) were purchased from Esteve (Barcelona, Spain). Acetonitrile UHPLC-MS grade and acetic acid were purchased from VWR Chemicals (Radnor, PA, USA). Balanced Salt Solution (BSS[®]) was purchased from Alcon (Geneva, Switzerland). Ultrapure water from MilliQ, Merck Millipore (Madrid, Spain) was used. As a packaging material, COL Eye Drops System[®] made with polyvinyl chloride (PVC) and di-n-octyl phthalate/di(2-ethylhexyl) phthalate (DOP/DEHP), free from Biomed Device (Modena, Italy), were used as single-dose containers.

2.2. Elaboration and Packaging of Cysteamine Hydrochloride Sterile Solutions

Initially, 275 mg of cysteamine were dissolved in 10 mL of BSS via magnetic stirring. To achieve a cysteamine concentration of 0.55%, sufficient Aquoral[®] (AQ) was used as a diluent. Finally, sterilizing filtration was performed with a 0.22 µm membrane filter (Stericup[®] Merck Millipore ExpressTM PLUS) under vacuum. The compounded formulation was produced in triplicate.

Single-dose systems were filled under aseptic conditions in a horizontal laminar flow cabinet by generating an initial vacuum using the coupled syringe, connections, and filters, according to the manufacturer's instructions [36,37]. Successive aspirations and expulsions of the air contained inside the system were carried out until the complete collapse of the single-dose containers was achieved. Through the lateral connection, 30 mL of each of the formulations were aspirated with the syringe incorporated in the system. The previously generated vacuum enables a homogeneous filling of the single-dose units (approximately 1.3–1.5 mL per vial) once the corresponding stopcocks are opened. In the case of single-dose vials saturated with nitrogen, an epidural needle was immersed in the 30 mL formulation contained in the syringe after the plunger was withdrawn. Nitrogen sparging was performed through the needle connected to a 0.22 µm filter for a total of 5 min per system, plugging the syringe opening with the plunger as much as possible. The filling of the vials was carried out as mentioned above.

Finally, each single-dose container was individually sealed with a heat-sealing gun provided by the manufacturer, and its correct closure was individually checked.

2.3. Cysteamine and Cystamine Quantification

The quantification of cysteamine and cystamine in the compounded formulations was analyzed by ultra-high-performance liquid chromatography (UHPLC) using a modified version of the method proposed by Kim et al. [38]. The analysis was performed with a UHPLC coupled with photodiode array detection (PDA), using an ACQUITY UPLC H-Class System (Waters®) with ACQUITY PDA detector (Waters®).

We employed an ACQUITY® BEH C18 column (2.1 × 50 mm, 1.7 μm, Waters®) at a temperature of 45 °C. The mobile phase was a mixture of aqueous 4 mM sodium 1-heptane sulfonate:acetonitrile in gradient mode, as shown in Table 1. The wavelengths used for the detection of cysteamine and cystamine were 215 nm and 244 nm, respectively. Data were collected and processed with Empower 3 Software (2002–2019 Waters®) Application Manager.

Table 1. Gradient UHPLC quantification method for cysteamine and cystamine. The mobile phase A was an aqueous solution of 4 mM sodium heptane sulfonate, and the mobile phase B was acetonitrile.

Time	Mobile Phase A (%)	Mobile Phase B (%)
0	95.0	5.0
0.50	95.0	5.0
2.50	70.0	30.0
3.20	95.0	5.0
6.0	95.0	5.0

All test samples were diluted 1:50 with 0.1% acetic acid and analyzed by UHPLC, setting the injection volume to 5 μL.

2.4. Storage Stability Study

Single-dose vials, with and without nitrogen saturation, were stored, protected from light, in a refrigerator (2–8 °C) or freezer (−20 °C). Initially, the storage stability study was carried out for a period of 30 days. Storage stability tests were performed in triplicate and conducted on days 0, 3, 7, 15, 21, and 30. All samples were kept at room temperature for at least 30 min prior to analysis to avoid measurement errors due to temperature variations.

Based on the most stable storage conditions, an in-use stability study was carried out once the vials were opened.

2.4.1. Determination of pH and Osmolarity

The pH of the formulations was determined with a BasiC20® pH meter, while the osmolarity was measured with a cryoscopic freezing point osmometer (OsmoSpecial1®) in 150 μL aliquots. Each determination was carried out in triplicate on days 0, 3, 7, 15, 21, and 30.

2.4.2. Viscosity Tests

The viscosity of cysteamine compounded formulations was determined on days 0, 15, and 30 in triplicate, with a rotational viscometer (Anton Paar ViscoQC 300® with PTD 80 Peltier Temperature). For this, 2 mL of each formulation were introduced into the equipment, and the measurement was carried out at 25 °C and 100 revolutions per minute (rpm). A one-way ANOVA was carried out to determine if there were significant differences.

In addition, a viscosity speed-scan test was also performed at different rpm in order to analyze the rheological behavior of cysteamine eye drops in hyaluronic acid.

2.4.3. Microbiological Stability

Each formulation was analyzed on days 0 and 30 to determine microbiological stability. Aliquots of 1.5 mL were added to plates containing blood agar, Sabouraud agar, and fluid

thioglycolate medium. Subsequently, plates were cultured at 37 °C for 48 h, 15 days, and 10 days, respectively. At the end of each incubation period, the plates were inspected for any signs of microbiological growth.

2.4.4. Statistical Analysis

The Pharmaceutical Codex was used to establish the expiry date of the compounded formulations, which was set at a reduction $\geq 10\%$ of cysteamine with respect to the initial concentration [39]. Changes in pH and osmolality were considered unacceptable if their values exceeded the acceptance criteria for ophthalmic applications [40,41]. Microbiological stability was considered acceptable when no microbial growth occurred in the cultured samples.

The results of the different assays were compared by multivariate analysis of variance using Graph Pad Prism[®] v.9.0.1 software.

2.4.5. Elasticity of Single-Dose Containers

The effect of refrigerated and frozen storage on the mechanical strength of single-dose containers was studied in triplicate, measuring its elastic properties using a precision universal testing machine, Shimadzu Autograph AGS-X Series, with a load cell of 1 kN using Trapezium X material testing operation software (Shimadzu corporation, Kyoto, Japan). Measurements were made at time 0 and after 30 days of storage in the refrigerator or freezer. After emptying the content, the head of the single dose was cut and positioned with the help of adjustable clamps in the press at each of its ends. The tensile test speed was 0.2 cm/s, and force-displacement curves were recorded during the experiment to determine elastic modulus (Young's modulus). A one-way ANOVA was carried out to determine whether there were significant differences.

2.5. In-Use Stability Study

Once the storage stability data was known, the in-use assay was carried out using vials previously stored under the best conditions. These vials were opened at room temperature, protected from light, every 4 h for 24 h, removing two drops per opening, except for during 8 h of sleep. The concentration of cysteamine and cystamine was measured at each of the openings.

2.6. In Vivo Evaluation of the Residence Time on the Ocular Surface

In vivo studies were carried after storage stability data were available, using vials previously stored under optimal conditions. The aim of this assay was to determine whether the freezing/thawing process significantly affects the ocular biopermanence properties of the formulation. An initial measurement was made on the day of preparation, followed by a measurement at day 30 of vials stored in the freezer. In addition, NaCl 0.9%, without bioadhesive properties, was used as a control formulation.

These studies were performed on four male Sprague Dawley rats (8 eyes), with an average weight of 250 g, supplied by the University of Santiago de Compostela (Santiago, Spain). The animals were kept in individual cages, with free access to food and water, in a room under controlled temperature (22 ± 1 °C) and humidity ($60 \pm 5\%$) and with day-night cycles regulated by artificial light (12/12 h). The animals were treated according to the guidelines for laboratory animals (National Research Council (US) Committee for the Update of the Guide for the Care and Use of Laboratory Animals, 2011; The Association for Research in Vision and Ophthalmology, 2014). Experiments were approved by the Animal Experimentation Ethics Committee of the Health Research Institute of Santiago de Compostela (2021/430700).

To quantitatively evaluate ocular permanence, radiolabeling of the formulation was performed following the method described in previous works of our group [6,42]. Positron emission tomography (PET) images were acquired using the ALBIRA PET/CT preclinical imaging system (Bruker Biospin, Woodbridge, CT, USA). Prior to image acquisition, the

animals were anesthetized in a gas chamber with an administration of 3% isoflurane in oxygen, an anesthetic method that continued during acquisition through an inhalation mask. Throughout the procedure, the respiratory rate was monitored, and after each examination, the animals were awakened.

Once asleep, 7.5 μL of each formulation previously labeled with ^{18}F -fluorodeoxyglucose (^{18}F -FDG) (formulation:FDG ratio 10:1) was instilled with an automatic micropipette into the conjunctival fornix. The range of radioactivity administered in each eye was between 0.15–0.25 MBq. Immediately after instillation, a 10 min individual PET was acquired, and at 30, 60, 90, and 120 min. Once the images were reconstructed using 6 iterations, they were analyzed with Amide's Medical Image Data Analysis Tool [43], manually drawing regions of interest (ROI) with a spherical shape of $15 \times 15 \times 15$ mm delimiting the signal area in each eye. Finally, the percentage of activity (%) at a certain time was corrected for radioactive decay with the help of a one compartment model using GraphPad Prism® 8 v.8.2.1 software. A non-compartmental analysis was also performed by calculating the remaining percentage of the formulations versus time.

3. Results

3.1. Cysteamine and Cystamine Quantification

The UHPLC-PDA determination method employed is highly specific and allows for the simultaneous detection of both cysteamine and cystamine, in only 6 min. A narrow, symmetrical, and well-defined chromatographic peak of cysteamine was obtained with an elution time of 1.12 min, while for cystamine, it was obtained at minute 2.46 (Figure 1). The analytical method was validated for linearity, accuracy, precision, and detection and quantification limits for cysteamine and cystamine. A linear calibration curve was obtained over a cysteamine and cystamine concentration range of 0.5–10 mg/mL ($R^2 = 0.999$). The limit of detection (LOD) and limit of quantitation (LOQ) were 0.25 mg/L and 0.5 mg/L, respectively, for both compounds. Compliance with the analytical validation standards of the European Medicines Agency (EMA) was also ascertained [44].

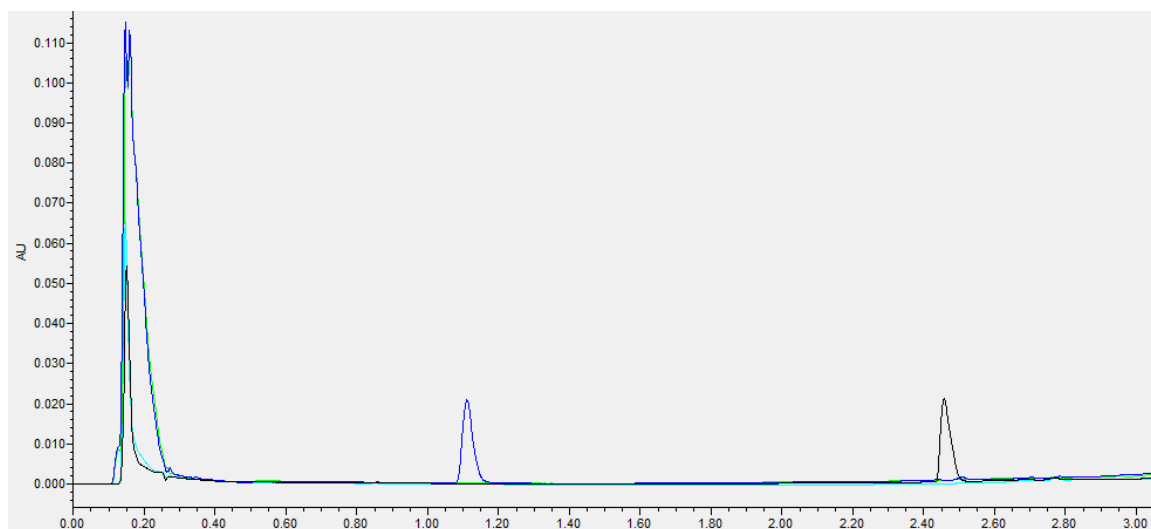


Figure 1. UHPLC chromatogram overlays showing the elution profiles of cysteamine at 215 nm (dark blue) and its oxidation product cystamine at 244 nm (black) in the studied matrix, Aquoral® (green at 215 nm, light blue at 244 nm). Data were collected and processed with Empower® 3 Software Application Manager.

3.2. Storage Stability Study

The variation in the cysteamine concentration of the compounded formulations made with AQ and packaged in single-dose containers over time under the different experimental conditions is shown in Figure 2. Cysteamine concentrations fell below 90% after day 7

when kept refrigerated, without noting any relevant differences in terms of saturation with nitrogen (n.s., two-way ANOVA followed by Tukey's multiple comparison test). On the other hand, stability increased considerably when single-dose containers were stored in the freezer, having a physicochemical stability of up to 30 days prior to opening. As observed for storage in the refrigerator, saturation with nitrogen did not affect the concentration of cysteamine. In parallel to the decrease in cysteamine concentration, there was an increase in cystamine concentration throughout the study, as shown in Figure S2 of the Supplementary Material.

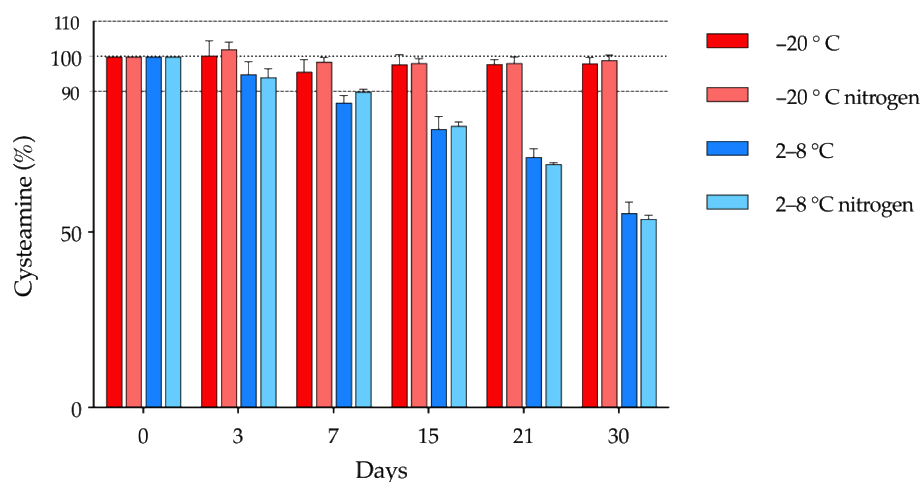


Figure 2. Cysteamine content with respect to the initial concentration throughout the study for each of the temperature settings (refrigeration/freezing) and in the presence/absence of nitrogen.

Cysteamine showed zero-order degradation kinetics, since the rate of reaction was independent of drug concentration. The degradation rate constants (K) of formulations preserved at 2–8 °C, in which significant degradation occurred, were calculated using the Arrhenius Equation (1):

$$K = A \cdot e^{-Ea/R \cdot T} \quad (1)$$

where K is the degradation rate constant; A is the frequency factor assumed independent of temperature, which represents the frequency of collisions between reactant molecules at a standard concentration; Ea is the activation energy (J/mol); R is the gas constant (8.314 J/mol·K); and T is the temperature expressed in Kelvin. Results are shown in Table 2.

Table 2. Degradation rate constants (K) from storage stability studies. SDk : standard deviation of K ; r^2 : goodness-of-fit measure for linear regression models.

Storage Conditions	K (%/Day)	SDk (%/Day)	r^2
2–8 °C	1.414	0.05502	0.9270
2–8 °C nitrogen	1.496	0.02904	0.9808

3.2.1. pH and Osmolality

Variations in the pH of the cysteamine compounded formulations under the two preservation conditions over time are depicted in Figure 3a. With the use of the AQ as a vehicle, the pH remained stable (6.5–6.8) throughout the stability study under freezing or refrigeration. Likewise, nitrogen saturation did not cause variations with respect to the vials that contained oxygen. These constant pH values are probably due to some buffering effect exerted by the excipients (sodium citrate and citric acid monohydrate) present in the AQ eye drops [45].

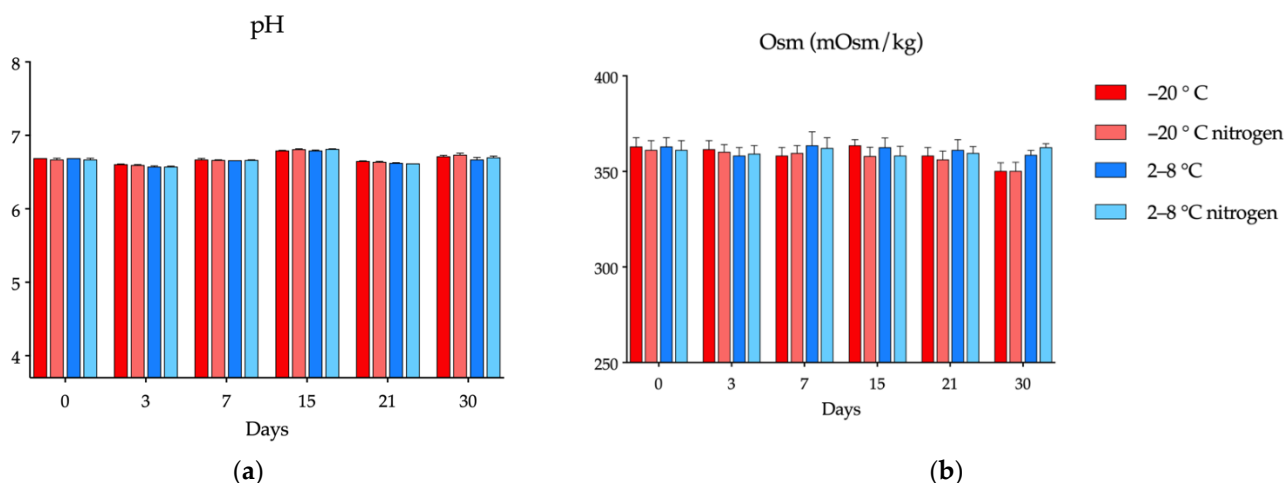


Figure 3. Variation in pH and osmolality (mOsm/kg) of the 5.5 mg/mL cysteamine formulation in Aquoral[®] on days 0, 3, 7, 15, 21, and 30: (a) pH; (b) osmolality.

Osmolality values (around 350 mOsm/Kg) of the formulations under the four experimental conditions remained between $\pm 5\%$ of the initial values over the study period (Figure 3b), being the dispersion of the values greater at day 30.

3.2.2. Viscosity tests

The initial viscosity of the formulations, measured at 25 °C and 100 rpm, was found to be around 30 mPa·s, as seen in Figure 4. On day 15 of the study, single-dose vials stored in the freezer showed a statistically significant drop in viscosity ($p = 0.0098$) with respect to that measured at day 0. On day 30, no statistically significant changes were observed with respect to the previous measurement on day 15, although the differences with respect to day 0 were maintained ($p = 0.0057$). On the other hand, for samples preserved in the refrigerator, viscosity hardly varied between days 0, 15, and 30. It was also observed that saturation with nitrogen did not introduce variations in the viscosity of the formulation when comparing vials kept at the same temperature.

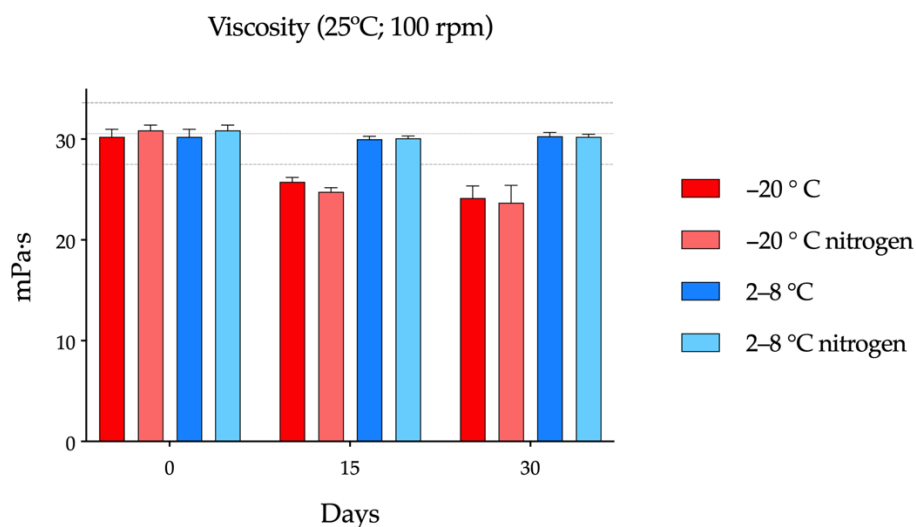


Figure 4. Viscosity variation measured at 25 °C and 100 revolutions per minute throughout the study period of the cysteamine formulations in Aquoral[®] stored in a freezer (−20 °C)/refrigerator (2–8 °C) and with/without nitrogen saturation.

The pseudoplastic behavior of HA has been observed regarding the present results, since the viscosity values decrease as the shear force increases. The viscosity values with respect to different rpm in all the formulations are represented in Figures S3–S5.

3.2.3. Microbiological Stability

No microbial growth was observed in any of the compounded formulations during the storage period, which indicates that adequate storage of the samples was maintained under all study conditions.

3.2.4. Elasticity of Single-Dose Containers

Young's modulus (E) is the ratio between the tensile stress (force per unit area) and the deformation of the solid material in the linear elastic region of the force-displacement curve. It is calculated using the following Equation (2):

$$E = \frac{\sigma}{\varepsilon} \quad (2)$$

where E is the Young's modulus, σ is the force per unit area, and ε is the proportional deformation. Young's modulus values were obtained in this study by Trapezium X software directly from the slope of the tensile stress-deformation curve in the initial linear elastic region of the trace, considering the dimension of the probe used in the experiment. The results showed no statistically significant differences between the two storage temperatures of the containers over time (Figure 5). In addition, the change in volume of the content with freezing did not cause modifications in its elastic properties.

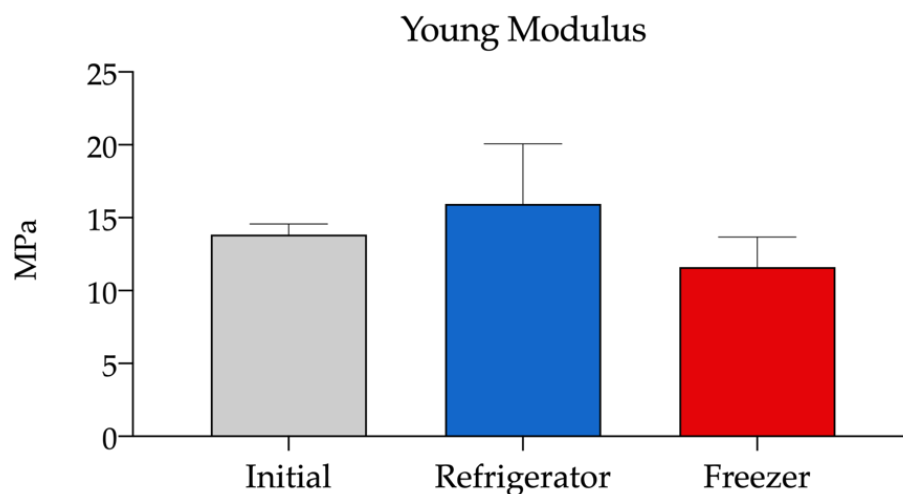


Figure 5. Young's modulus of the COL Eye Drops® vials used for the stability study at the initial time and after 30 days stored in the refrigerator (2–8 °C) and freezer (−20 °C).

Considering these results, freezing without nitrogen is postulated as the best and most practical storage condition. With vials stored under these conditions for 30 days, the in-use stability study was evaluated, with the aim of determining their chemical stability after being opened, simulating their real-life use.

3.3. In-Use Stability Study

As in the storage assay, while the concentration of cysteamine decreased, cystamine concentration increased throughout the study. At the time of opening, a slight decrease in the cysteamine concentration was already observed, as well as a slight increase in the cystamine concentration, which is consistent with the degradation detected after 30 days of storage at −20 °C (Figure 2). After opening each single-dose container 5 times every 4 h at room temperature (16 h after removal from the freezer and initial opening), the

concentration of cysteamine remained above 90% with respect to the initial concentration on day on which the formulation was prepared. These results indicate that single-dose vials stored for up to 30 days in the freezer can be used throughout a day, excluding the 8 h of sleep, once thawed and opened.

3.4. In Vivo Evaluation of the Residence Time on the Ocular Surface

The residence time on the ocular surface of the pharmaceutical compounding was calculated immediately after its preparation and after being stored in the freezer for 30 days using small-animal PET imaging in rats. Figure 6 shows the permanence of these formulations from the eye compared to NaCl 0.9% (control). A strong signal immediately after instillation was observed and, after 120 min of contact, a considerable percentage of hydrogel remained on the ocular surface. This behavior is observed in a similar way, with no statistically significant differences, throughout the different PET images, for day 0 after formulation and day 30 after formulation, when stored at $-20\text{ }^{\circ}\text{C}$.

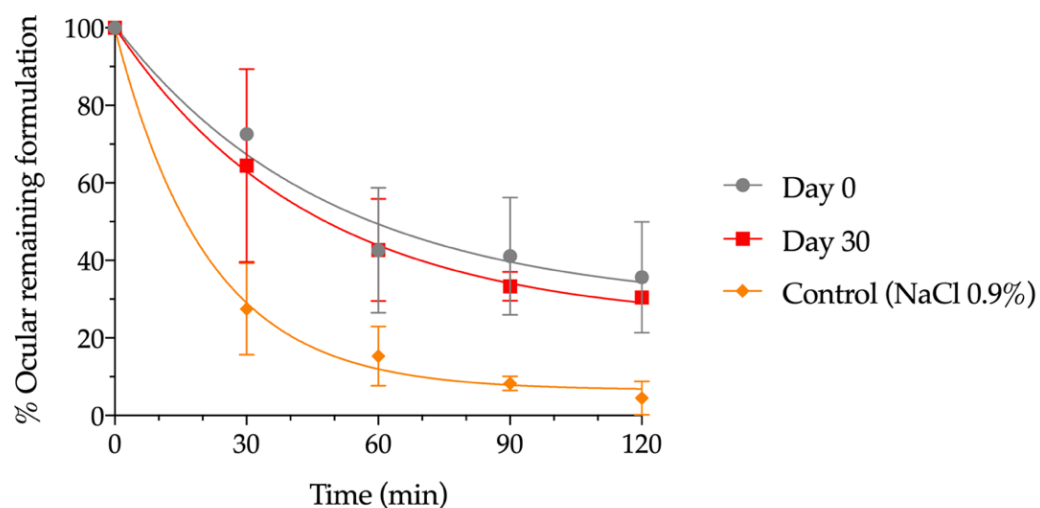


Figure 6. Percentage of formulation remaining on the ocular surface with respect to time zero determined by PET at day 0 and day 30 after storage in the freezer, as compared with NaCl 0.9%.

Data were fitted to a mono exponential equation dependent on time, as shown in Figure 6, and the pharmacokinetic parameters obtained by fitting to the one-compartmental model. A half-life of 33.86 min for day 0 after formulation and 31.11 min for day 30 after formulation, when stored at $-20\text{ }^{\circ}\text{C}$, was obtained, demonstrating no influence of freezing on this parameter and showing an ocular residence time more than two-fold higher than for NaCl 0.9%, whose half-life was 14.63 min.

Figure 7 shows an axial view of the PET registration images of animal heads immediately after administration and 30, 60, 90, and 120 min after instillation, showing the distribution of the labelled formulation. Initially, the formulation is located on the surface of the eye. After 2 h, the concentration in the eye was still significant, indicating a long retention time on the ocular surface. An additional radiotracer signal was detected in the nasolacrimal duct and nasal cavity, as part of the formulation entered the nasal cavity from the lacrimal sac.

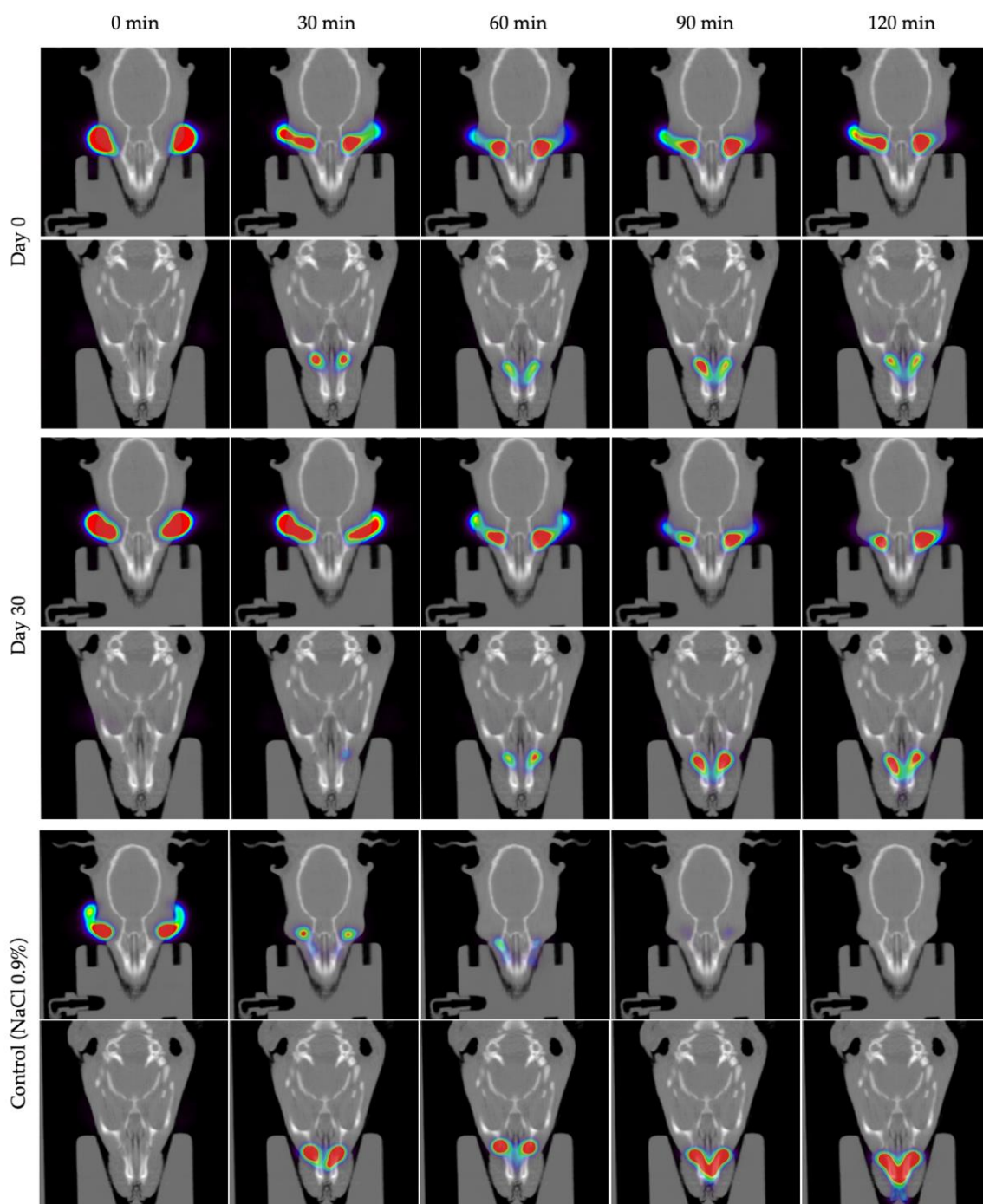


Figure 7. Positron emission tomography (PET) images (maximum intensity projections, coronal views) obtained at different time points after ocular administration of eye drops labelled with ^{18}F -fluorodeoxyglucose (^{18}F -FDG).

4. Discussion

Currently, only two commercial ophthalmic presentations of cysteamine (Cystaran[®] and Cystadrops[®]) are authorized for the treatment of cystinosis, but they are not commercialized in all countries [25]. Thus, pharmaceutical compounding from HPD can constitute a therapeutic alternative, avoiding the difficulty of access to treatment by some patients [46].

Undoubtedly, the physicochemical instability of cysteamine has been one of the greatest challenges when developing ophthalmic formulations with an acceptable period of validity that allows for adequate therapeutic compliance and avoids numerous hospital

visits to collect the medication. Cysteamine is very unstable in a solution, where it rapidly converts to cystamine, a non-toxic molecule, but without therapeutic effect. Several strategies have been shown to effectively reduce cysteamine oxidation, such as oxygen removal, decreasing temperature, the addition of antioxidant compounds—such as ascorbic acid or disodium edetate (EDTA)—or solution acidification [24,25,47]. To date, several stability studies of cysteamine formulations have been published [6,20,21,25,48], but the lack of uniformity in their preparation (vehicles, excipients, packaging, storage conditions, etc.) and the different determination methods used have led to irreproducible results.

The aim of the present work is to find a simple method of elaboration and conservation of an ophthalmic compounded formulation of cysteamine for an adequate translation to clinical practice. This is intended to offer a practical solution to processing services and to facilitate dispensing of the drug to patients. Our results showed that the new vehicle and single-dose packaging system used in this work allowed the treatment to be dispensed for a long period of time, as long as the containers were stored under low-temperature conditions. With this innovative system, it is possible to use one vial per day with the possibility of closing it, while the rest of the batch can be kept at a low temperature. On the contrary, the use of multidose vials is associated with greater contact with oxygen after opening, since the air contained inside the container is renewed with each opening, favoring the oxidation of cysteamine. A compounded formulation of 0.55% cysteamine, produced with a commercial preparation of 0.4% HA, was stored under refrigeration (2–8 °C) or freezing (−20 °C). To prevent oxidation, saturation with nitrogen was also studied. Physicochemical, microbiological, and mechanical studies were carried out for a period of 30 days, discarding those storage conditions that were inadequate in achieving a long period of validity, until optimal conditions were achieved. Considering all these data, an in-use stability study was carried out.

For this study, a new determination method was developed based on the one previously proposed by Kim et al. [38], which allows for the detection of both cysteamine and cystamine, in a short analysis period of just 6 min. Our results showed that the cysteamine compounded formulation was not stable beyond 7 days when stored at 2–8 °C in single dose vials, which is impractical for patients and HPDs daily work, but when preserved at −20 °C, a stability of at least 30 days was achieved. These findings are consistent with those previously published in the literature reporting that oxidation to cystamine is favored at high temperatures [21,47,49–51]. Reda et al. previously showed the effects of storage in the refrigerator and freezer for up to 52 weeks, where it was seen that conservation at −20 °C guaranteed a longer period of validity [21]. Although the results differ slightly from those of the present work, it is important to consider the differences in terms of the composition of the mixture, final packaging, and determination method.

In addition to temperature, the presence of oxygen has also been described as a relevant factor that plays an important role in the chemical stability of cysteamine [48]. Therefore, in order to prevent oxidation, the saturation of the formulation with nitrogen was also studied. However, in the present study, this strategy did not provide less degradation at any of the temperatures or times studied with respect to formulations without nitrogen, as can be seen in Figure 2. This result can possibly be explained due to the material that makes up the single-dose COL containers, PVC, with known oxygen permeability [52]. This permeability may allow for the passage of oxygen through the material, losing the beneficial effect that the initial saturation of the formulations with nitrogen may have had. For this reason, it is important to consider the functionality and composition of the containers in which cysteamine formulations are packaged. In this regard, Cystaran[®] is supplied in an opaque, white, low-density polyethylene (LDPE) bottle with a LDPE-controlled dropper tip and closed with a polypropylene screw cap. As LDPE is permeable to oxygen, Cystaran[®] must be stored frozen between −25 °C and −15 °C to remain stable for over one year [21]. After thawing the bottle, it must be stored at 2 °C to 25 °C and discarded after one week [17]. Regarding Cystadrops[®], it can be stored for six months refrigerated prior to opening, with no need of being frozen. This is possible due to its packaging, which consist of a sealed

amber vial with a bromobutyl stopper and an aluminium seal, which have a very low permeability to oxygen [28,49]. Before opening the bottle, the seal and stopper must be removed and replaced by a PVC dropper with a high-density polyethylene (HDPE) closure, which mandates that the bottle must be discarded after one week once opened (storage temperature <25 °C) [19]. Regarding the single-dose PVC system used in the present study, its oxygen permeability does not entail a problem for the stability of the formulation when it is frozen. For this reason, nitrogen saturation is ruled out to increase stability in the monodose vials. Furthermore, nitrogen is a resource that is scarcely available in HPDs, adding significant complexity to the manufacturing process.

Regarding the vehicle used for the elaboration, HA was chosen because it has several advantages. On the one hand, it alleviates part of the irritative symptomatology previously described in other cysteamine formulations [53–56]. This is achieved due to its restorative properties that enhance corneal epithelium healing, improve the function of the ocular surface, increase the stability of the precorneal tear film, and protect/restore the morphology and distribution of the goblet cells responsible for the secretion of mucins [57–60]. On the other hand, HA reduces the ocular clearance of cysteamine by increasing its retention time on the ocular surface, favoring its ocular bioavailability, as has been demonstrated in previous works [6,7]. According to Sandri et al. [61], hyaluronic acid, especially that of low molecular weight (<202 kDa), exhibits penetration enhancement properties comparable to, or even better than, chitosan hydrochloride, depending on the compound. In this way, cysteamine permeates into the cornea and reaches the lysosomes of the corneal cells where cystine crystals accumulate [14]. Aquoral[®] has been selected in this study as a source of HA because it is classified as a medical device used for the treatment of dry eye, which allows for keeping both the origin and the molecular weight of HA constant, something that would be more difficult to achieve if HA was obtained as a raw material due to the high variability reported between different manufacturers and batches [32,57]. According to previous publications, these variations may seriously interfere with compounding and stability studies, as they would no longer be reproducible [32–35].

Pescina et al. showed that cysteamine oxidation decreases at an acidic pH of 4.2, being a pH-dependent reaction, while corneal penetration was found to be poor at pH 4.2, but enhanced at pH 7 [47]. With this reasoning, it might be hypothesized that better cysteamine stability results could be achieved by lowering the pH of ophthalmic preparations, but it is necessary to consider that ocular administration of solutions with a pH too far from the tear pH (7.4–7.7) could cause discomfort in the eye. Formulated with a pH of 4.1–4.5, Cystaran[®] used this strategy to reduce cysteamine degradation [17,47,62]. This correlation between pH and cysteamine stability agrees with the European Assessment report regarding Cystadrops[®] (pH 4.6–5.4), which states that low buffered pH, along with high viscosity, are the contributing factors to ocular irritation and inflammation, but this has to be weighed against the benefits of the stability of the active substance [53]. Both presentations use benzalkonium chloride as a preservative and as a trans-corneal permeation enhancer, which can produce toxic effects [40]. The most reported ocular adverse events (incidence around 10% or greater) were eye pain, blurred vision, eye irritation, ocular hyperaemia, eye pruritus, increased lacrimation, eye deposit, and instillation site discomfort [2,22,54,55], many of which are related to the pathology itself. In the case of commercial presentations, pH reduction below physiological values was chosen in order to improve the stability of cysteamine with the consequent problems that this entails. On the contrary, in the present work, a pH value to the physiological value has been chosen, with constant values around 6.7. These values are achieved because of the citric acid/citrate buffer system present in the Aquoral[®] commercial formulation [45], avoiding the excessive tearing associated with formulations with a lower pH [40]. The present proposal for distribution in single-dose containers allows us to maintain acceptable cysteamine stability at a physiological pH due to freezing effects, which also favors the corneal permeation of the active ingredient [47].

Regarding osmolality, it remained practically constant throughout the study in all formulations, with values around 350 mOsm/Kg, similar to those previously published [50].

Although these values are higher than the 289 ± 21 mOsm/L reported for tears, considerably higher values are found in the commercial formulations of other active ingredients used in the treatment of chronic ocular pathologies, such as Travatan[®] (travoprost) or Vividrin iso EDO[®] (chromoglicin acid), with 368.5 and 341 mOsm/L, respectively [41,63].

Although freezing provides chemical stability to cysteamine, preventing its rapid degradation, it is unknown if this process can affect the physical properties of the formulation itself or of the final packaging. To determine whether this process significantly affected the properties of HA, viscosity studies were carried out on the day of its preparation, as well as after 15 and 30 days of storage in the refrigerator/freezer. From these data, it was possible to see that the viscosity remained practically constant at 2–8 °C, while on days 15 and 30, a drop was observed in those stored at –20 °C. This may be explained due to changes in polymer conformation during the freeze/thaw processes [64]. The present cysteamine compounded formulation maintained the pseudoplastic behavior of HA previously described in the literature [65–67] during all storage times and conditions, by decreasing its viscosity with increasing shear force, as seen in Figures S3–S5.

The clinical implications that the drop in viscosity of the frozen formulations may have on ocular biopermanence is unknown, so we decided to carry out a study using an *in vivo* molecular imaging technique with the most promising formulation in terms of stability. For determination, 0.9% NaCl was used as a control, as it is one of the most widely used vehicles in the preparation of eye drops compounded formulations produced in HPD [40,68]. Our results showed that the decrease in the viscosity of the frozen formulations did not translate into relevant clinical changes, and their bioadhesive properties were maintained. This was demonstrated by the lack of relevant differences in ocular biopermanence between the formulations made with AQ before and after thawing. These ocular biopermanence results are in line with those previously published [6]. Another relevant aspect that we wanted to assess with this work was whether the single-dose container could be altered by the freezing/thawing process. We observed that the elasticity of the single-dose vials remained constant after 30 days of storage, both in the refrigerator and in the freezer, despite the increase in the internal volume caused by the freezing of the content inside the containers.

After characterizing the formulation under different storage conditions for 30 days, its chemical stability *in-use* after opening was determined. Conditions were established to simulate its use in real life, opening the single-dose container 5 times a day and storing it at room temperature. We have confirmed that the vial can be used within the first 16 h of the day after 30 days of storage in the freezer. This allows for convenient transport, thanks to its portability, with no need for refrigeration, thus facilitating the administration of the drops throughout the day, therefore increasing the therapeutic adherence of the patients. These results cannot be compared with those previously published by Martín-Sabroso et al. due to methodological differences. The previous work used a different vehicle and final containers and performed the stability study using vials stored in the refrigerator and opened 4 times a day for 7 days, where degradation ranging from 30% to 60% was observed for all the formulations after 7 days of use [48].

Regarding the limitations of the present study, some aspects of the formulation and the vials used have not been characterized in depth. For instance, the behavior of HA after the freeze/thaw process requires further studies to better characterize the vehicle. A cryoprotective compound could be used as an excipient in future formulations to prevent the properties from being modified by freezing [69]. Moreover, measuring the oxygen permeability of the single-dose container would explain why bubbling with nitrogen provides scarcely any improvement in the chemical stability of cysteamine. Finally, it would also be interesting to know whether this parameter is affected by the freezing/thawing processes.

5. Conclusions

Hospital pharmacy departments play a relevant role in facilitating access to drugs when these are not readily available in all countries, such as orphan drugs. Cysteamine eye drops are used to treat ocular cystinosis, which is an easily oxidizable molecule that requires

rigorous stability studies to establish an adequate period of validity. With the aim to find a simple method of preparation and conservation of an ophthalmic compounded formulation of 0.55% cysteamine in HA, packaging in single-dose containers and subsequent freezing for 30 days, protected from light, are proposed. These conditions preserved the stability and biopermanence of the formulation and the integrity of the packaging material, which was scarcely affected by the low temperatures. Once thawed, vials can be used for 16 h, allowing for the administration of cysteamine every 4 h. These results favor a quick and easy transfer to clinical practice, eluding complex production processes such as nitrogen saturation, and avoiding numerous hospital visits to collect the compounded formulation, facilitating better therapeutic adherence of patients to treatment.

Supplementary Materials: The following are available online at <https://www.mdpi.com/article/10.3390/pharmaceutics14102194/s1>, Figure S1: COL Eye Drops System[®] used in the stability study, provided from Biomed Device; Figure S2. Cystamine content with respect to the initial concentration throughout the study for each of the temperature settings (refrigeration/freezing) and presence/absence of nitrogen; Figure S3. Speed-scan test of the cysteamine formulations at 25 °C with the presence/absence of nitrogen at day 0, where the viscosity is measured at different revolutions per minute (rpm); Figure S4. Speed-scan test at 25 °C of the cysteamine formulations stored at different temperature conditions and in the presence/absence of nitrogen at day 15, where the viscosity is measured at different rpm; Figure S5. Speed-scan test at 25 °C of the cysteamine formulations stored at different temperature conditions and in the presence/absence of nitrogen at day 30, where the viscosity is measured at different rpm.

Author Contributions: Conceptualization, M.G.-B., F.J.O.-E., P.A. and A.F.-F.; methodology, G.H.-V. and E.B.-V.; software, E.B.-V. and G.H.-V.; validation, G.H.-V. and E.B.-V.; formal analysis, A.C.-B., A.C.-M., G.H.-V., J.M., X.G.-O. and L.R.-M.; investigation, A.C.-B., A.C.-M., X.G.-O., P.A., M.H.-B. and G.H.-V.; resources, F.J.O.-E., I.Z.-F. and A.F.-F.; data curation, A.C.-B., E.B.-V., A.C.-M., X.G.-O., L.R.-M., J.M. and G.H.-V.; writing—original draft preparation, A.C.-B., A.C.-M. and C.M.-G.; writing—review and editing L.G.-Q., E.B.-V., L.R.-M., C.M.-G. and A.F.-F.; visualization, M.G.-B., F.J.O.-E. and A.F.-F.; supervision, C.M.-G. and A.F.-F.; project administration, C.M.-G. and A.F.-F.; funding acquisition, F.J.O.-E., I.Z.-F. and A.F.-F. All authors have read and agreed to the published version of the manuscript.

Funding: This research was funded by the Fundación Española de Farmacia Hospitalaria (FEFH 18–19), the Fundación Mutua Madrileña (XIX Convocatoria de Ayudas a la Investigación en Salud 2022) and the “Asociación La Lucha de Iker.” A.F.-F., C.M.-G., E.B.-V., L.G.-Q. and A.C.B. are grateful to ISCIII for financing in the form of the JR18/00014, JR20/00026, CM20/00135, CM20/00024 and CM21/00114 personnel contracts. J.M. acknowledges the support of Xunta de Galicia (GAIN) by Talent Senior research grant 11_IN858A_2021_1141142.

Institutional Review Board Statement: The animal study protocol was approved by Animal Experimentation Ethics Committee of the Health Research Institute of Santiago de Compostela (2021/430700).

Informed Consent Statement: Not applicable.

Data Availability Statement: Not applicable.

Acknowledgments: The graphical abstract image was created with BioRender.com. We thank the Biomed Device Company, developer of the monodose COL system, and its distributor, BexenMedical, for supplying, free of charge, the containers for the realization of this study.

Conflicts of Interest: The authors declare no conflict of interest.

References

1. Orphanet: Cystinosis. Available online: https://www.orpha.net/consor/cgi-bin/OC_Exp.php?lng=en&Expert=213 (accessed on 2 July 2022).
2. Liang, H.; Labbé, A.; Baudouin, C.; Plisson, C.; Giordano, V. Long-Term Follow-up of Cystinosis Patients Treated with 0.55% Cysteamine Hydrochloride. *Br. J. Ophthalmol.* **2020**, *105*, 608–613. [CrossRef] [PubMed]
3. Cherqui, S.; Kalatzis, V.; Trugnan, G.; Antignac, C. The Targeting of Cystinosin to the Lysosomal Membrane Requires a Tyrosine-Based Signal and a Novel Sorting Motif*. *J. Biol. Chem.* **2001**, *276*, 13314–13321. [CrossRef] [PubMed]

4. Syres, K.; Harrison, F.; Tadlock, M.; Jester, J.V.; Simpson, J.; Roy, S.; Salomon, D.R.; Cherqui, S. Successful Treatment of the Murine Model of Cystinosis Using Bone Marrow Cell Transplantation. *Blood* **2009**, *114*, 2542–2552. [CrossRef] [PubMed]
5. Nesterova, G.; Gahl, W.A. Cystinosis: The Evolution of a Treatable Disease. *Pediatric Nephrol.* **2013**, *28*, 51–59. [CrossRef] [PubMed]
6. Luaces-Rodríguez, A.; Díaz-Tomé, V.; González-Barcia, M.; Silva-Rodríguez, J.; Herranz, M.; Gil-Martínez, M.; Rodríguez-Ares, M.T.; García-Mazás, C.; Blanco-Mendez, J.; Lamas, M.J.; et al. Cysteamine Polysaccharide Hydrogels: Study of Extended Ocular Delivery and Biopermanence Time by PET Imaging. *Int. J. Pharm.* **2017**, *528*, 714–722. [CrossRef]
7. McKenzie, B.; Kay, G.; Matthews, K.H.; Knott, R.; Cairns, D. Preformulation of Cysteamine Gels for Treatment of the Ophthalmic Complications in Cystinosis. *Int. J. Pharm.* **2016**, *515*, 575–582. [CrossRef]
8. Kaur, S.; Sarma, P.; Kaur, H.; Prajapat, M.; Shekhar, N.; Bhattacharyya, J.; Kaur, H.; Kumar, S.; Medhi, B.; Ram, J.; et al. Efficacy and Safety of Topical Cysteamine in Corneal Cystinosis: A Systematic Review and Meta- Analysis. *Am. J. Ophthalmol.* **2020**, *223*, 275–285. [CrossRef]
9. Andrzejewska, Z.; Nevo, N.; Thomas, L.; Chhuon, C.; Bailleux, A.; Chauvet, V.; Courtoy, P.J.; Chol, M.; Guerrero, I.C.; Antignac, C. Cystinosis Is a Component of the Vacuolar H⁺-ATPase-Ragulator-Rag Complex Controlling Mammalian Target of Rapamycin Complex 1 Signaling. *J. Am. Soc. Nephrol.* **2016**, *27*, 1678–1688. [CrossRef]
10. Thoene, J.G.; DelMonte, M.A.; Mullet, J. Microvesicle Delivery of a Lysosomal Transport Protein to Ex Vivo Rabbit Cornea. *Mol. Genet. Metab. Rep.* **2020**, *23*, 100587. [CrossRef]
11. Hollywood, J.A.; Przepiorski, A.; D'Souza, R.F.; Sreebhavan, S.; Wolvetang, E.J.; Harrison, P.T.; Davidson, A.J.; Holm, T.M. Use of Human Induced Pluripotent Stem Cells and Kidney Organoids to Develop a Cysteamine/Mtor Inhibition Combination Therapy for Cystinosis. *J. Am. Soc. Nephrol.* **2020**, *31*, 962–982. [CrossRef]
12. Liu, Z.; Kompella, U.B.; Chauhan, A. Gold Nanoparticle Synthesis in Contact Lenses for Drug-Less Ocular Cystinosis Treatment. *Eur. J. Pharm. Biopharm.* **2021**, *165*, 271–278. [CrossRef] [PubMed]
13. Pisoni, R.L.; Thoene, J.G.; Christensen, H.N. Detection and Characterization of Carrier-Mediated Cationic Amino Acid Transport in Lysosomes of Normal and Cystinotic Human Fibroblasts. Role in Therapeutic Cystine Removal? *J. Biol. Chem.* **1985**, *260*, 4791–4798. [CrossRef]
14. Gahl, W.A.; Kuehl, E.M.; Iwata, F.; Lindblad, A.; Kaiser-Kupfer, M.I. Corneal Crystals in Nephropathic Cystinosis: Natural History and Treatment with Cysteamine Eyedrops. *Mol. Genet. Metab.* **2000**, *71*, 100–120. [CrossRef] [PubMed]
15. European Medicines Agency. Cystagon® Prescribing Information. 1997. Available online: <https://www.ema.europa.eu/en/medicines/human/EPAR/cystagon> (accessed on 5 August 2022).
16. Schneider, J.A. Approval of Cysteamine for Patients with Cystinosis. *Pediatric Nephrol.* **1995**, *9*, 254. [CrossRef]
17. Food and Drug Administration. Cystaran® Prescribing Information. 2012. Available online: https://www.accessdata.fda.gov/drugsatfda_docs/label/2012/200740s000lbl.pdf (accessed on 20 August 2022).
18. Food and Drug Administration. Cystadrops® Prescribing Information. 2012. Available online: https://www.accessdata.fda.gov/drugsatfda_docs/label/2020/211302s000lbl.pdf (accessed on 20 August 2022).
19. European Medicines Agency. Cystadrops® Prescribing Information. 2016. Available online: https://www.ema.europa.eu/en/documents/product-information/cystadrops-epar-product-information_es.pdf (accessed on 20 August 2022).
20. Fernández-Ferreiro, A.; Luaces-Rodríguez, A.; Díaz-Tomé, V.; Gil-Martínez, M.; Ares, M.T.R.; Peralba, R.T.; Blanco-Méndez, J.; González-Barcia, M.; Otero-Espinar, F.J.; Lamas, M.J. Cysteamine ophthalmic hydrogel for the treatment of ocular cystinosis. *Farm. Hosp.* **2017**, *41*, 678–687. [CrossRef]
21. Reda, A.; van Schepdael, A.; Adams, E.; Paul, P.; Devolder, D.; Elmonem, M.A.; Veys, K.; Casteels, I.; van den Heuvel, L.; Levtschenko, E. Effect of Storage Conditions on Stability of Ophthalmological Compounded Cysteamine Eye Drops. In *JIMD Reports*; Springer: Berlin/Heidelberg, Germany, 2017; Volume 42, pp. 47–51. [CrossRef]
22. Labbé, A.; Baudouin, C.; Deschênes, G.; Loirat, C.; Charbit, M.; Guest, G.; Niaudet, P. A New Gel Formulation of Topical Cysteamine for the Treatment of Corneal Cystine Crystals in Cystinosis: The Cystadrops OCT-1 Study. *Mol. Genet. Metab.* **2014**, *111*, 314–320. [CrossRef]
23. Jimenez, J.; Washington, M.A.; Resnick, J.L.; Nischal, K.K.; Fedorchak, M.V. A Sustained Release Cysteamine Microsphere/Thermoresponsive Gel Eyedrop for Corneal Cystinosis Improves Drug Stability. *Drug Deliv. Transl. Res.* **2021**, *11*, 2224–2238. [CrossRef]
24. Atallah, C.; Charcosset, C.; Greige-Gerges, H. Challenges for Cysteamine Stabilization, Quantification, and Biological Effects Improvement. *J. Pharm. Anal.* **2020**, *10*, 499–516. [CrossRef]
25. Castro-Balado, A.; Mondelo-García, C.; Varela-Rey, I.; Moreda-Vizcaíno, B.; Sierra-Sánchez, J.F.; Rodríguez-Ares, M.T.; Hermelo-Vidal, G.; Zarra-Ferro, I.; González-Barcia, M.; Yebra-Pimentel, E.; et al. Recent Research in Ocular Cystinosis: Drug Delivery Systems, Cysteamine Detection Methods and Future Perspectives. *Pharmaceutics* **2020**, *12*, 1177. [CrossRef]
26. Purkiss, R. Stability of Cysteamine Hydrochloride in Solution. *J. Clin. Pharm. Ther.* **1977**, *2*, 199–203. [CrossRef]
27. Brodrick, A.; Broughton, H.M.; Oakley, R.M. The Stability of an Oral Liquid Formulation of Cysteamine. *J. Clin. Hosp. Pharm.* **1981**, *6*, 67–70. [CrossRef] [PubMed]
28. Dixon, P.; Powell, K.; Chauhan, A. Novel Approaches for Improving Stability of Cysteamine Formulations. *Int. J. Pharm.* **2018**, *549*, 466–475. [CrossRef]
29. Carracedo, G.; Pastrana, C.; Serramito, M.; Rodríguez-Pomar, C. Evaluation of Tear Meniscus by Optical Coherence Tomography after Different Sodium Hyaluronate Eyedrops Instillation. *Acta Ophthalmol.* **2019**, *97*, e162–e169. [CrossRef] [PubMed]

30. Acofarma Fórmulas Magistrales. Distribuidor de Productos para Farmacias Analysis Bulletin—Sodium Hyaluronate. Available online: <https://productoquimico.acofarma.com> (accessed on 5 August 2022).
31. Agencia Española de Medicamentos y Productos Sanitarios. Registro Unificado de Empresas de Sustancias Activas. Available online: <https://labofar.aemps.es/labofar/registro/ruesa/consulta.do#nav-no> (accessed on 5 August 2022).
32. Snetkov, P.; Zakharova, K.; Morozkina, S.; Olekhnovich, R.; Uspenskaya, M. Hyaluronic Acid: The Influence of Molecular Weight on Structural, Physical, Physico-Chemical, and Degradable Properties of Biopolymer. *Polymers* **2020**, *12*, 1800. [CrossRef]
33. Olejnik, A.; Goscianska, J.; Zielinska, A.; Nowak, I. Stability determination of the formulations containing hyaluronic acid. *Int. J. Cosmet. Sci.* **2015**, *37*, 401–407. [CrossRef]
34. Falcone, S.J.; Palmeri, D.M.; Berg, R.A. Rheological and cohesive properties of hyaluronic acid. *J. Biomed. Mater. Res. Part A* **2006**, *76A*, 721–728. [CrossRef]
35. Bothner, H.; Wik, O. Rheology of Hyaluronate. *Acta Oto-Laryngol.* **1987**, *104*, 25–30. [CrossRef]
36. Biomed Device-Care in a Revolutionary Way. COL®Video-Kit for the Preparation of Aliquots of Eye Drops with Hemocomponents. Available online: <https://www.youtube.com/watch?v=FCorvJXkUZw> (accessed on 5 August 2022).
37. Biomed Device-Care in a Revolutionary Way. COL®Eye Drops System. Available online: <http://col-eyedrops.com/index.php/it/eye-drops-system/col> (accessed on 5 August 2022).
38. Kim, Y.; Na, D.H. Simultaneous Determination of Cysteamine and Cystamine in Cosmetics by Ion-Pairing Reversed-Phase High-Performance Liquid Chromatography. *Toxicol. Res.* **2019**, *35*, 161–165. [CrossRef]
39. Lund, W. *The Pharmaceutical Codex: Principles and Practice of Pharmaceutics*; The Pharmaceutical Press: London, UK, 1994; ISBN 0-85369-290-4.
40. Fernández-Ferreiro, A.; Castro-Balado, A.; García Quintanilla, L.; Lamas, M.; Otero-Espinar, F.; Mendez, J.; Gómez-Ulla, F.; Gil-Martínez, M.; Tomé, V.; Luaces-Rodríguez, A.; et al. *Formulación Magistral Oftálmica Antiinfecciosa*; SEFH Sociedad Española de Farmacia Hospitalaria: Madrid, Spain, 2019; ISBN 978-84-09-10764-3.
41. Dutescu, R.M.; Panfil, C.; Schrage, N. Osmolarity of Prevalent Eye Drops, Side Effects, and Therapeutic Approaches. *Cornea* **2015**, *34*, 560–566. [CrossRef]
42. Fernández-Ferreiro, A.; Silva-Rodríguez, J.; Otero-Espinar, F.J.; González-Barcia, M.; Lamas, M.J.; Ruibal, A.; Luaces-Rodríguez, A.; Vieites-Prado, A.; Sobrino, T.; Herranz, M.; et al. Positron Emission Tomography for the Development and Characterization of Corneal Permanence of Ophthalmic Pharmaceutical Formulations. *Investig. Ophthalmol. Vis. Sci.* **2017**, *58*, 772–780. [CrossRef]
43. Loening, A.M.; Gambhir, S.S. AMIDE: A Free Software Tool for Multimodality Medical Image Analysis. *Mol. Imaging* **2003**, *2*, 131–137. [CrossRef] [PubMed]
44. Committee for Medicinal Products for Human Use (CHMP). European Medicines Agency Guideline on Bioanalytical Method Validation. Available online: https://www.ema.europa.eu/en/documents/scientific-guideline/guideline-bioanalytical-method-validation_en.pdf (accessed on 22 September 2022).
45. Esteve Aquoral®. Available online: <https://aquoral.es/aquoral-lagrimas-artificiales-alivio-rapido-y-duradero/aquoral/> (accessed on 5 August 2022).
46. Abbas, N.; Hasan, S.S.; Curley, L.; Babar, Z.-U.-D. Access to Medicines—A Systematic Review of the Literature. *Res. Soc. Adm. Pharm.* **2020**, *16*, 1166–1176. [CrossRef] [PubMed]
47. Pescina, S.; Carra, F.; Padula, C.; Santi, P.; Nicoli, S. Effect of PH and Penetration Enhancers on Cysteamine Stability and Trans-Corneal Transport. *Eur. J. Pharm. Biopharm.* **2016**, *107*, 171–179. [CrossRef] [PubMed]
48. Martín-Sabroso, C.; Alonso-González, M.; Fernández-Carballido, A.; Aparicio-Blanco, J.; Córdoba-Díaz, D.; Navarro-García, F.; Córdoba-Díaz, M.; Torres-Suárez, A.I. Limitations and Challenges in the Stability of Cysteamine Eye Drop Compounded Formulations. *Pharmaceutics* **2022**, *15*, 2. [CrossRef]
49. Makuloluwa, A.K.; Shams, F. Cysteamine Hydrochloride Eye Drop Solution for the Treatment of Corneal Cystine Crystal Deposits in Patients with Cystinosis: An Evidence-Based Review. *Clin. Ophthalmol.* **2018**, *12*, 227–236. [CrossRef]
50. Bozdog, S.; Gumus, K.; Gumus, O.; Unlu, N. Formulation and in Vitro Evaluation of Cysteamine Hydrochloride Viscous Solutions for the Treatment of Corneal Cystinosis. *Eur. J. Pharm. Biopharm.* **2008**, *70*, 260–269. [CrossRef]
51. U.S. Cysteamine Eye Drop Development. Available online: <http://www.cystinosis.com/Documents/EyeDropPaper.html> (accessed on 5 August 2022).
52. Bastarrachea, L.; Dhawan, S.; Sablani, S.S. Engineering Properties of Polymeric-Based Antimicrobial Films for Food Packaging: A Review. *Food Eng. Rev.* **2011**, *3*, 79–93. [CrossRef]
53. European Medicines Agency. European Public Assessment Report (EPAR) for Cystadrops. Available online: <https://www.ema.europa.eu/en/medicines/human/EPAR/cystadrops> (accessed on 5 August 2022).
54. Food and Drug Administration. FDA Drug Approval Package: CYSTADROPS. Available online: https://www.accessdata.fda.gov/drugsatfda_docs/nda/2020/211302Orig1s000TOC.cfm (accessed on 5 August 2022).
55. Liang, H.; Labbé, A.; Le Mouhaër, J.; Plisson, C.; Baudouin, C. A New Viscous Cysteamine Eye Drops Treatment for Ophthalmic Cystinosis: An Open-Label Randomized Comparative Phase III Pivotal Study. *Investig. Ophthalmol. Vis. Sci.* **2017**, *58*, 2275. [CrossRef]
56. Yang, Y.-J.; Lee, W.-Y.; Kim, Y.-J.; Hong, Y.-P. A Meta-Analysis of the Efficacy of Hyaluronic Acid Eye Drops for the Treatment of Dry Eye Syndrome. *Int. J. Environ. Res. Public Health* **2021**, *18*, 2383. [CrossRef]

57. Aragona, P.; Simmons, P.A.; Wang, H.; Wang, T. Physicochemical Properties of Hyaluronic Acid-Based Lubricant Eye Drops. *Transl. Vis. Sci. Technol.* **2019**, *8*, 2. [CrossRef]
58. Posarelli, C.; Passani, A.; Del Re, M.; Fogli, S.; Toro, M.D.; Ferreras, A.; Figus, M. Cross-Linked Hyaluronic Acid as Tear Film Substitute. *J. Ocul. Pharmacol. Ther.* **2019**, *35*, 381–387. [CrossRef] [PubMed]
59. Troiano, P.; Monaco, G. Effect of Hypotonic 0.4% Hyaluronic Acid Drops in Dry Eye Patients: A Cross-over Study. *Cornea* **2008**, *27*, 1126–1130. [CrossRef] [PubMed]
60. Ang, B.C.H.; Sng, J.J.; Wang, P.X.H.; Htoon, H.M.; Tong, L.H.T. Sodium Hyaluronate in the Treatment of Dry Eye Syndrome: A Systematic Review and Meta-Analysis. *Sci. Rep.* **2017**, *7*, 9013. [CrossRef] [PubMed]
61. Sandri, G.; Rossi, S.; Ferrari, F.; Bonferoni, M.C.; Zerrouk, N.; Caramella, C. Mucoadhesive and Penetration Enhancement Properties of Three Grades of Hyaluronic Acid Using Porcine Buccal and Vaginal Tissue, Caco-2 Cell Lines, and Rat Jejunum. *J. Pharm. Pharmacol.* **2004**, *56*, 1083–1090. [CrossRef]
62. Datta, S.; Baudouin, C.; Brignole-Baudouin, F.; Denoyer, A.; Cortopassi, G.A. The Eye Drop Preservative Benzalkonium Chloride Potently Induces Mitochondrial Dysfunction and Preferentially Affects LHON Mutant Cells. *Investig. Ophthalmol. Vis. Sci.* **2017**, *58*, 2406–2412. [CrossRef] [PubMed]
63. Özalp, O.; Atalay, E.; Alataş, İ.Ö.; Küskü Kiraz, Z.; Yıldırım, N. Assessment of Phosphate and Osmolarity Levels in Chronically Administered Eye Drops. *Turk. J. Ophthalmol.* **2019**, *49*, 123–129. [CrossRef]
64. Casey-Power, S.; Ryan, R.; Behl, G.; McLoughlin, P.; Byrne, M.E.; Fitzhenry, L. Hyaluronic Acid: Its Versatile Use in Ocular Drug Delivery with a Specific Focus on Hyaluronic Acid-Based Polyelectrolyte Complexes. *Pharmaceutics* **2022**, *14*, 1479. [CrossRef]
65. Johnson, R.S.; Niedermeier, W.; Bobo, P. The Pseudoplastic Behavior of Aqueous Solutions of Hyaluronic Acid. *Biorheology* **1971**, *7*, 177–187. [CrossRef]
66. Ahumada, L.A.C.; González, M.X.R.; Sandoval, O.L.H.; Olmedo, J.J.S. Evaluation of Hyaluronic Acid Dilutions at Different Concentrations Using a Quartz Crystal Resonator (QCR) for the Potential Diagnosis of Arthritic Diseases. *Sensors* **2016**, *16*, 1959. [CrossRef]
67. García-Abuín, A.; Gómez-Díaz, D.; Navaza, J.M.; Regueiro, L.; Vidal-Tato, I. Viscosimetric Behaviour of Hyaluronic Acid in Different Aqueous Solutions. *Carbohydr. Polym.* **2011**, *85*, 500–505. [CrossRef]
68. Klang, M.G. Sterile Preparation Formulation. In *Compounding Sterile Preparations*, 4th ed.; American Society of Health-System Pharmacists (ASHP): Bethesda, MD, USA, 2018; pp. 51–66. ISBN 978-1-58528-484-9.
69. ScienceDirect Topics. Cryoprotective Agent—An Overview. Available online: <https://www.sciencedirect.com/topics/pharmacology-toxicology-and-pharmaceutical-science/cryoprotective-agent> (accessed on 24 August 2022).

Review

Aqueous Prostaglandin Eye Drop Formulations

Phatsawee Jansook ^{1,*}  and Thorsteinn Loftsson ² 

¹ Faculty of Pharmaceutical Sciences, Chulalongkorn University, 254 Phyathai Road, Pathumwan, Bangkok 10330, Thailand

² Faculty of Pharmaceutical Sciences, University of Iceland, Hofsvallagata 53, IS-107 Reykjavik, Iceland

* Correspondence: phatsawee.j@chula.ac.th; Tel.: +66-2-218-8273

Abstract: Glaucoma is one of the leading causes of irreversible blindness worldwide. It is characterized by progressive optic neuropathy in association with damage to the optic nerve head and, subsequently, visual loss if it is left untreated. Among the drug classes used for the long-term treatment of open-angle glaucoma, prostaglandin analogues (PGAs) are the first-line treatment and are available as marketed eye drop formulations for intraocular pressure (IOP) reduction by increasing the trabecular and uveoscleral outflow. PGAs have low aqueous solubility and are very unstable (i.e., hydrolysis) in aqueous solutions, which may hamper their ocular bioavailability and decrease their chemical stability. Additionally, treatment with PGA in conventional eye drops is associated with adverse effects, such as conjunctival hyperemia and trichiasis. It has been a very challenging for formulation scientists to develop stable aqueous eye drop formulations that increase the PGAs' solubility and enhance their therapeutic efficacy while simultaneously lowering their ocular side effects. Here the physicochemical properties and chemical stabilities of the commercially available PGAs are reviewed, and the compositions of their eye drop formulations are discussed. Furthermore, the novel PGA formulations for glaucoma treatment are reviewed.

Keywords: ocular hypertension; prostaglandin analogues; aqueous solubility; chemical stability; drug delivery; intraocular pressure

Citation: Jansook, P.; Loftsson, T. Aqueous Prostaglandin Eye Drop Formulations. *Pharmaceutics* **2022**, *14*, 2142. <https://doi.org/10.3390/pharmaceutics14102142>

Academic Editors: Francisco Javier Otero-Espinar and Anxo Fernández Ferreiro

Received: 24 August 2022

Accepted: 7 October 2022

Published: 9 October 2022

Publisher's Note: MDPI stays neutral with regard to jurisdictional claims in published maps and institutional affiliations.



Copyright: © 2022 by the authors. Licensee MDPI, Basel, Switzerland. This article is an open access article distributed under the terms and conditions of the Creative Commons Attribution (CC BY) license (<https://creativecommons.org/licenses/by/4.0/>).

1. Introduction

Glaucoma is a group of eye diseases that causes the progressive degeneration of the retinal ganglion cells and the retinal nerve fiber layer. The most common type of glaucoma is primary open-angle glaucoma (POAG), representing 74% of all glaucoma cases [1]. POAG is caused by the obstruction of the aqueous humor outflow within the trabecular network which increases the intraocular pressure (IOP) with consequent optic nerve damage [1,2]. Prostaglandins (PGs) are eicosanoids derived from arachidonic acid and other polyunsaturated fatty acids which have diverse biological activities, including the relaxation of smooth muscles. In general, PGs are lipophilic, chemically unstable, and poorly water-soluble compounds composed of a cyclopentane ring with two side chains [3,4].

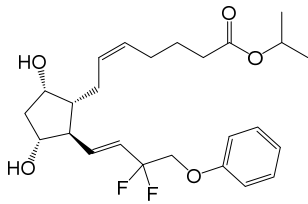
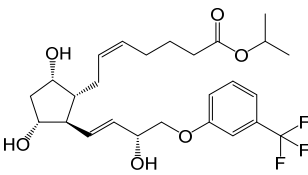
In 1977, Camras, Bito and Eakins [5] showed that $\text{PGF}_{2\alpha}$ lowered the IOP in rabbits. It was discovered that PGs reduce the IOP by enhancing the aqueous humor outflow, and the first antiglaucoma prostaglandin analog (PGA), latanoprost, received the Food and Drug Administration's approval between August 2000 and March 2001 [6]. Now PGAs are considered the drugs of choice for the treatment of POAG [7,8]. Currently there are five PGAs marketed as aqueous eye drops. These are 0.01% bimatoprost ophthalmic solution (Lumigan[®], Allergan, Irvine, CA, USA), 0.005% latanoprost ophthalmic solution (Xalatan[®], Pfizer, New York, NY, USA) and emulsion (Xelpros[®], Sun Ophthalmics, Cranbury, NJ, USA), 0.024% latanoprostene bunod ophthalmic solution (Vyzulta[®], Bausch & Lomb, Bridgewater, NJ, USA), 0.0015% tafluprost ophthalmic solution (Taflotan[®], Santen, Osaka, Japan, and Zioptan[®], Akron, Lake Forest, IL, USA/Merck, Kenilworth, NJ, USA), 0.004%

travoprost ophthalmic solution (Travatan[®], in Europe) and Travatan Z[®] (in the USA, Novartis, Cambridge, MA, USA). All these PGA are PGF_{2α} derivatives; four are ester prodrugs of the corresponding acids, while one, bimatoprost, is an amide prodrug (Table 1). For example, latanoprost is an isopropyl ester (i.e., a prodrug) of latanoprost acid, which is a PGF_{2α} analog. Likewise, tafluprost and travoprost are isopropyl ester prodrugs of tafluprost acid and travoprost acid, respectively. Latanoprost is hydrolyzed by the corneal esterase to yield the biologically active agent latanoprost acid [6]. Bimatoprost is also rapidly hydrolyzed by ocular esterase to the biologically active bimatoprost acid [9].

Table 1. Structure and physicochemical properties of prostaglandin F_{2α} and its analogs, which are currently used in ophthalmology.

Prostaglandin Analog	Structure	Molecular Weight	Calculated Values ^a	
			LogP _(o/w) ^b	Solubility in Water ^c
Prostaglandin F _{2α} (pKa 4.76)		354.48	2.6 (LogD _{7.0} 0.4)	30 mg/mL (at pH 7.0)
Latanoprost acid		390.51	2.8 (LogD _{7.0} 0.6)	7 mg/mL (at pH 7.0)
Bimatoprost (Lumigan [®])		415.57	2.8	40 µg/mL
Latanoprost (Xalatan [®] , Xelpros [®])		432.59	4.3	6 µg/mL
Latanoprostene bunod (Vyzulta [®])		507.62	4.8	1 µg/mL

Table 1. Cont.

Prostaglandin Analog	Structure	Molecular Weight	Calculated Values ^a	
			LogP _(o/w) ^b	Solubility in Water ^c
Tafluprost (Taflotan [®] , Zioptan [®])		452.53	3.8	10 µg/mL
Travoprost (Travatan Z [®])		500.55	4.1	4 µg/mL

^a Calculated using Advanced Chemistry Development (ACD/Labs) Software V11.02 (Advanced Chemistry Development Inc., Toronto, ON, Canada). ^b The 10-logarithm of the calculated 1-octanol/water partition coefficient.

^c The calculated solubility in pure water at pH 7.0 and 25 °C.

Bimatoprost, latanoprost, tafluprost and travoprost appear to have very comparable efficacy regarding IOP reduction in patients with primary open-angle glaucoma [10]. Latanoprostene bunod is a prodrug of two active entities, latanoprost acid and butanediol mononitrate, which yields nitric oxide [11]. Nitric oxide lowers the IOP and improves the ocular blood flow, both of which can result in neuroprotection [12]. Thus, latanoprostene bunod might have some therapeutic advantages over the other PGAs, although the difference was shown to be insignificant with regard to the reduction in IOP [13]. An enhanced therapeutic efficacy has been obtained by combining the PGAs with non-prostaglandin IOP-lowering drugs. Examples of such combinations are 0.005% latanoprost with 0.02% netarsudil (Roclanda[®], Aerie Pharmaceuticals, Durham, NC, USA), 0.005% latanoprost with 0.5% timolol (Xalacom[®], Pfizer, New York, NY, USA), 0.03% bimatoprost with 0.5% timolol (Ganfort[®], Allergan, Irvine, CA, USA), 0.004% travoprost with 0.5% timolol (DuoTrav[®], Novartis, Basel, Switzerland) and 0.0015% tafluprost with 0.5% timolol (Taptiqom[®], Santen, Osaka, Japan).

The monographs for latanoprost, latanoprost compounded topical solution, travoprost and travoprost ophthalmic solution are in the USP43-NF38, while the Ph. Eur. 10.3 only has a monograph for latanoprost. The following is a review of the physicochemical properties of the PGAs currently used in ophthalmology, their solubilization and stability in aqueous solutions and the composition of their eye drop formulations.

2. Physicochemical Properties and Eye Drop Formulations

PGAs reduce the IOP by ciliary muscle relaxation and increased aqueous humor outflow [14]. Thus, when applied topically to the eye, the PGA molecules must permeate the cornea into the aqueous humor to access their receptors. $P_{o/w}$ is the partition coefficient (i.e., the concentration ratio at equilibrium) of an uncharged molecule between 1-octanol and water, while $D_{o/w}$ is the partition coefficient of an ionizable compound at some fixed pH or ionization. Compounds with low $P_{o/w}$ are hydrophilic and, in general, water-soluble, while compounds with high $P_{o/w}$ are lipophilic and poorly soluble in water. The optimal $\text{Log}P_{o/w}$ value (i.e., 10-logarithm of $P_{o/w}$) for drug permeation from the aqueous tear fluid, through the cornea and into the aqueous humor is between 1 and 3, in which the drugs with $\text{Log}P_{o/w}$ values less than 1 or greater than about 3 display a decreased ability to permeate the lipophilic cornea [15]. Prostaglandin $F_{2\alpha}$ and latanoprost acid are fully ionized in the tear fluid with a $\text{Log}D_{o/w}$ value much less than unity, while their PGAs (i.e., ester prodrug analogues) have $\text{Log}P_{o/w}$ values between 3.8 and 4.8, except bimatoprost (i.e., the amide

prodrug analog) which has a $\text{LogP}_{o/w}$ value of 2.8 (Table 1). Accordingly, bimatoprost has the optimal $\text{LogP}_{o/w}$ value for transcorneal permeation, while the acids are too hydrophilic at a physiologic pH and the other PGAs a bit too lipophilic.

All the PGAs in Table 1 are practically insoluble in water, although bimatoprost appears to be slightly more soluble than the other PGAs in the table. The more optimal lipophilicity and slightly greater solubility increases the ability of bimatoprost to permeate from the aqueous tear fluid into the eye and can explain the slightly greater efficacy of bimatoprost compared to the other PGAs [10,13]. The PGAs are very potent drugs with low aqueous solubility which are administered topically to the eye in close to PGA saturated aqueous eye drop solutions. In other words, the dissolved PGA molecules will possess a high level of thermodynamic activity in the aqueous exterior and, thus, the molecules will have the maximum tendency to partition from the aqueous tear fluid into the lipophilic cornea [16,17]. This enhances their ability to permeate into the eye in spite of their greater than optimum $\text{LogP}_{o/w}$ value.

The PGs are derivatives of long chain fatty acids containing a substituted cyclopentane ring which are rapidly dehydrated in aqueous solutions and known to form epimers under strong acidic and alkaline conditions [18–20]. Additionally, PGs and their analogs contain one or more double bonds and, thus, are sensitive towards oxidation. While PGE_2 and related PGs are very unstable in aqueous environment, $\text{PGF}_{2\alpha}$ and its derivatives are, in general, less susceptible to chemical degradation. The major degradation pathways of PGAs in aqueous media are hydrolysis to form the PG acids (i.e., the active form of the PGAs), epimerization, trans isomerization and oxidation. For example, known degradation products of latanoprost in aqueous solutions are latanoprost acid, the latanoprost 15-epi diastereomer and the latanoprost 5,6-*trans* isomer, as well as oxidation products, such as the latanoprost 5-keto and 15-keto derivatives (Figure 1). Latanoprost undergoes photoinduced degradation and the highly lipophilicity drug is absorbed into plastic containers [21–23].

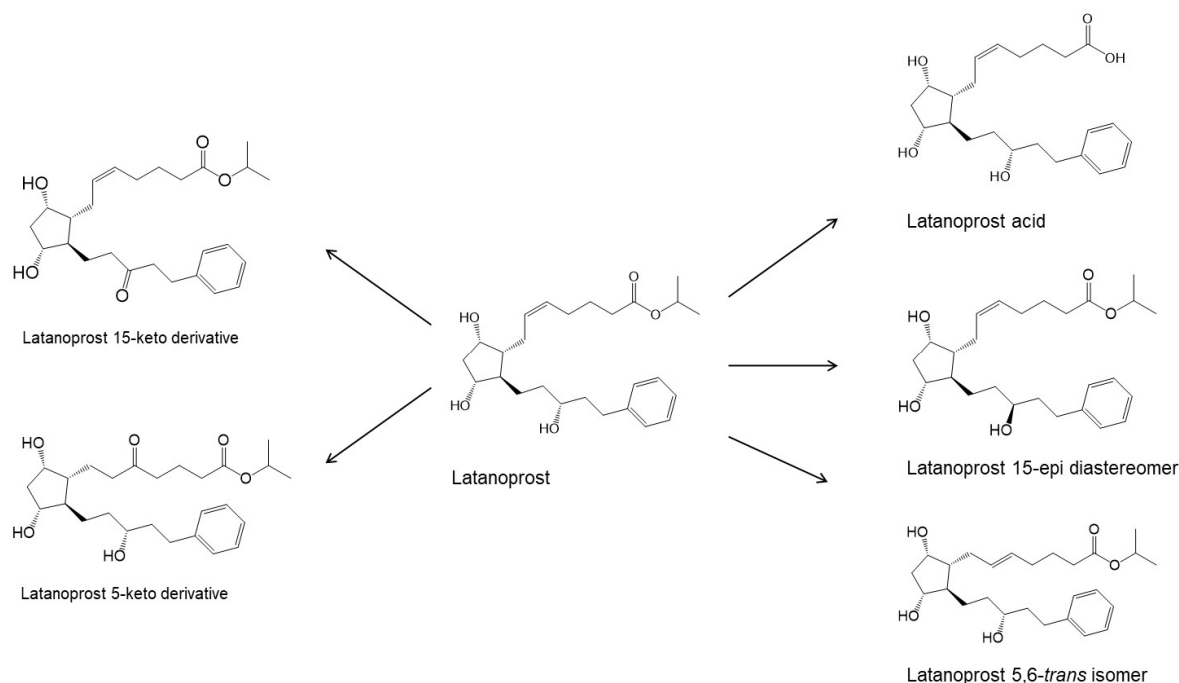


Figure 1. The main degradation products of latanoprost. Based on USP43-NF38 and Ph. Eur. 10.3, as well as reference [22]. Other degradation products have also been identified during forced degradation under somewhat extreme conditions [22].

Xalatan[®] contains 0.05 mg/mL of latanoprost in an aqueous solution of benzalkonium chloride (0.02%) as a preservative, sodium chloride for adjustment of the tonicity, a pH 6.7 phosphate buffer (sodium dihydrogen phosphate monohydrate 4.60 mg/mL and anhy-

drous disodium phosphate 4.74 mg/mL) and water for injection. In an unopened original package, the eye drops have a shelf-life of 36 months when stored in a refrigerator (2–8 °C) protected from light. The addition of non-ionic surfactants, such as polyoxyl 40 stearate and polyethylene glycol monostearate 25, and cyclodextrins to the aqueous eye drop media will increase the shelf-life of the latanoprost eye drops [23–27]. It was reported that latanoprost eye drops in the presence of 2-hydroxypropyl- β -cyclodextrin were stable at 25 °C and 60% relative humidity for at least six months, while the one containing a non-ionic surfactant remained stable for up to 24 months under the same storage conditions [23,24]. The proposed mechanism is that the interaction between the ester group of latanoprost and the complex micelle of those non-ionic surfactants results in hydrolysis being inhibited [27]. For the role of cyclodextrin, it shields the ester group of latanoprost inside the cavity, providing degradation protection [26].

The degradation profile of travoprost (Figure 2) is very similar to that of latanoprost, and in aqueous solutions, travoprost is most stable at pH 6.0 ± 0.2 [28]. Travatan[®] contains 0.04 mg/mL of travoprost, polyquaternium-1 (0.01 mg/mL) as preservative, polyethylene glycol 40 hydrogenated castor oil (2 mg/mL) which increases the chemical stability and solubility of travoprost, boric acid, propylene glycol (7.5 mg/mL), mannitol and sodium chloride in purified water. Travatan Z[®] contains 0.04 mg/mL of travoprost in an aqueous solution containing polyethylene glycol 40 hydrogenated castor oil, and a pH 5.7 buffer-preservative system (sofZia[®]) which is composed of boric acid, propylene glycol, sorbitol, zinc chloride and purified water [29].

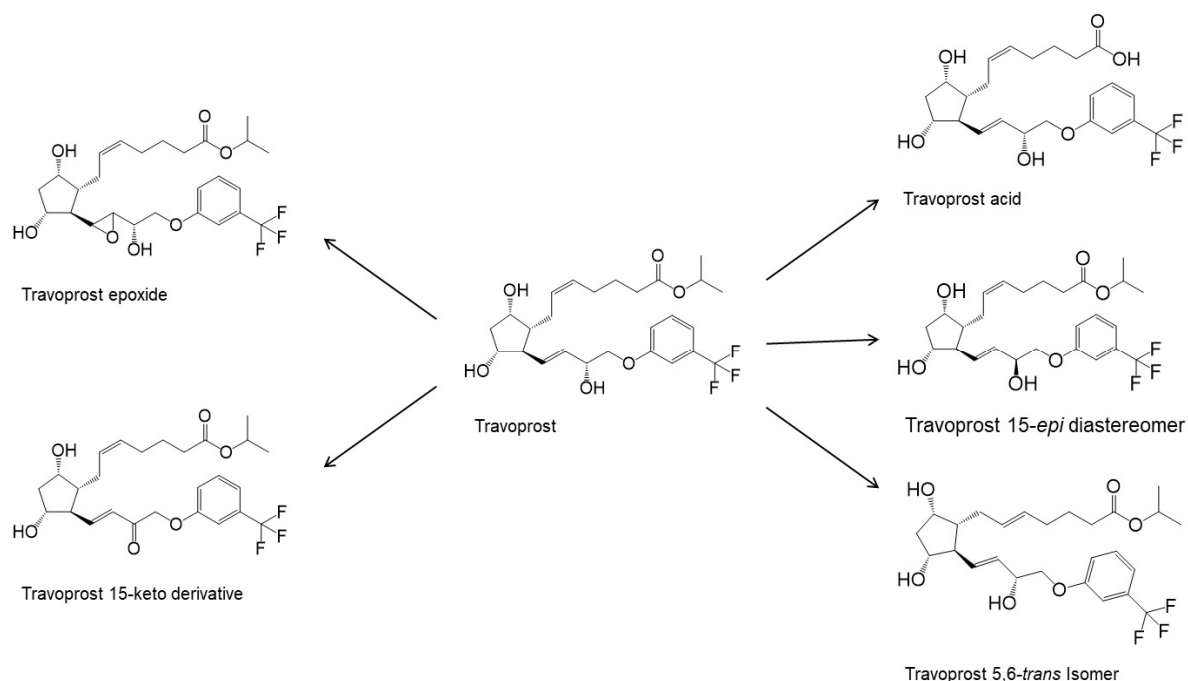


Figure 2. Degradation products of travoprost. Based on USP43-NF38 and reference [30].

The aqueous eye drops compositions of tafluprost and bimatoprost are also simple aqueous buffer solutions. Tafluprost is, like latanoprost and travoprost, an isopropyl ester with its maximum stability at pH between 5.5 and 6.7, while bimatoprost is an amide with its maximum stability between pH 6.8 and 7.8. In general, amides are more chemically stable than esters of comparable structures and studies have shown that bimatoprost eye drops are more stable than, for example, latanoprost and travoprost eye drops [31,32]. Tafluprost is the first preservative-free commercially available PGA (Zioptan[®]) containing 0.015 mg/mL of tafluprost in an aqueous solution containing polysorbate 80 as a solubilizer, glycerol, phosphate buffer and disodium edetate. Unopened cartons and foil pouches should be stored in the refrigerator (2–8 °C). After the foil pouch is opened, the unit-dose

containers may be stored in the opened pouch for up to 28 days at room temperature (20–25 °C) [33].

Latanoprostene bunod is a double ester prodrug releasing two active drugs upon hydrolysis (Figure 3). Thus, one would expect that this double ester would be more chemically unstable than the other monoester prodrugs, such as latanoprost. However, the shelf-life of Vyzulta[®] in unopened containers is similar to those of the other ester PGAs. Vyzulta[®] contains 0.24 mg/mL of latanoprostene bunod in an aqueous solution containing polysorbate 80, glycerol, 0.2 mg/mL of benzalkonium chloride, pH 5.5 citrate buffer and disodium edetate. The shelf-life of Vyzulta[®] unopened containers is up to 3 years at 2 to 8 °C.

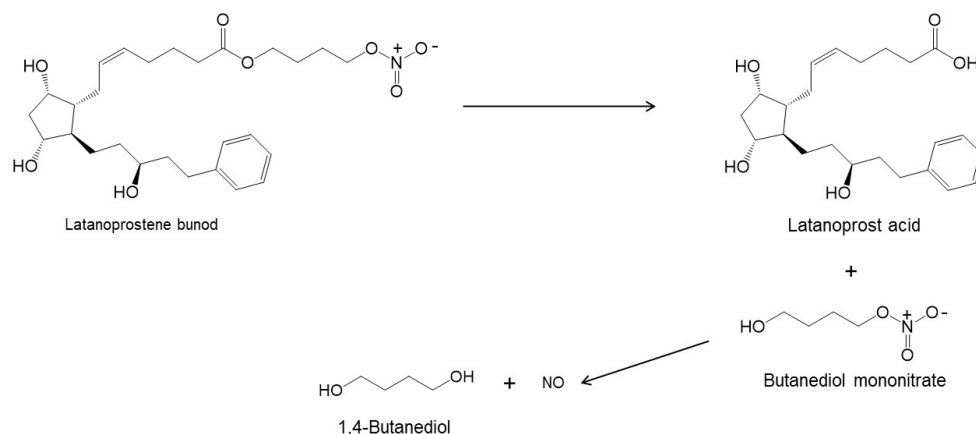


Figure 3. Hydrolysis of latanoprostene bunod [11,34].

Most of the commercially marketed PGA eye drops mentioned above contain benzalkonium chloride as a preservative. The concentration of benzalkonium chloride in eye drops ranges from 0.004% to 0.02% [35]. Its bactericidal activity is effective against both Gram-positive and Gram-negative bacteria, including fungi. It has been reported that benzalkonium chloride can act as a penetration enhancer, increasing the penetration of drug molecules from the surface into ocular tissues [36]. However, most in vivo studies do not support these findings [37]. To decrease the overall adverse effects of 0.03% bimatoprost, mainly conjunctival hyperemia, while maintaining the IOP-lowering effect, 0.01% bimatoprost was introduced and the concentration of benzalkonium chloride was increased from 0.005% to 0.02% [38]. However, it is well-known that the common side effects of benzalkonium chloride are conjunctival hyperemia, superficial punctate keratitis and a decrease in tear production which results in ocular discomfort and inflammation [39]. Consequently, the higher benzalkonium chloride concentration in the new bimatoprost eye drops (0.01% Lumigan, Allergan, Inc.) should result in not decreased but increased side effects, such as hyperemia, which is not the case [38]. Some studies have reported that the preserved and preservative-free PGA eye drops do not differ significantly in IOP lowering efficacy [40–42]. This observation might promote the marketing of novel preservative-free PGA eye drops.

3. Novel PGA Formulations

Cyclodextrins can solubilize and stabilize PGF_{2α} and other PGs in both aqueous solutions and solid phases [43–47]. Likewise, cyclodextrins are known to increase both the aqueous solubility and chemical stability of the PGAs. For example, 2-hydroxypropyl-β-cyclodextrin forms a water-soluble complex with latanoprost without decreasing the IOP-lowering effect of the drug in a rabbit model [24]. According to the investigators, the eye drop solution was stable when stored at 25 °C for at least 6 months. 2-Hydroxypropyl-β-cyclodextrin has also been shown to solubilize and stabilize tafluprost [48]. Through the formation of inclusion complexes, it has been shown that propylamino-β-cyclodextrin increases the solubilization and chemical stability of latanoprost. The in vivo ocular tolerance

study in rabbits revealed that the latanoprost/propylamino- β -cyclodextrin complex eye drop formulation decreases ocular irritation when compared to the commercially available latanoprost 0.005% formulation (Xalatan[®], Pfizer Inc., New York, NY, USA) [26]. Gonzalez et al. (2007) [49] investigated the efficacy, safety and chemical stability of a novel cyclodextrin-containing latanoprost eye drop in comparison to Xalatan[®]. The efficacy and toxicological profiles of the two latanoprost eye drops were comparable, but the eye drops containing cyclodextrin displayed improved chemical stability at 25 °C and 40 °C. Latanoprost has been formulated as an aqueous eye drop microsuspension in which the microparticles consisted of solid latanoprost/ γ -cyclodextrin complexes [25]. In vitro and in vivo studies in rabbits showed that the aqueous eye drop microsuspension resulted in an almost four-fold increase in topical bioavailability and a significant enhancement in the chemical stability of the drug compared to the commercial eye drops (Xalatan[®]).

Biocompatible lipid-based nanocarriers have emerged as a potential alternative to conventional ocular drug delivery systems [50,51]. These include micro- and nanoemulsions deliver lipophilic and poorly water-soluble drugs to the ocular surface [52–54]. The preservative-free 0.005% latanoprost cationic emulsion (Catioprost[®]) is formulated using Novasorb[®] technology. The cationic nanoemulsion of latanoprost was as effective as Xalatan[®] for lowering IOP and was well tolerated by the rabbit ocular surface. Additionally, it was able to promote a healing process of the injured cornea which boosted the compliance of long-term patients [55–57]. When compared to Travasan[®]Z in Phase II clinical data, Catioprost[®] decreased the IOP to the same level as Travatan[®]Z and caused less conjunctival hyperemia [58]. Ismail et al. (2020) [59] developed travoprost eye drop nanoemulsions composed of labrafac lipophile[®] and tween 80 and studied the eye drops in vivo in rabbits. The eye drops showed prolonged IOP-lowering effects, a good level of safety and no irritation in the rabbit ocular tissues. Recently, a novel ophthalmic latanoprost 0.005% nanoemulsion was prepared and the cytotoxicity on human epithelial conjunctival cells was reported by Tau et al. (2022). It revealed that the new latanoprost nanoemulsion might cause less discomfort on the eye surface than currently available latanoprost solutions [60].

Liposomes and lipids for ocular delivery of prostaglandins have also been investigated [51,61]. Latanoprost loaded unilamellar liposomes were prepared and evaluated in eye drops. However, latanoprost could not permeate from this vehicle through the corneal epithelium, and thus it did not show any IOP reduction in vivo in rabbits. After a single subconjunctival injection, the resulting liposome formulation had an IOP-lowering effect that was sustained for up to 50 days without toxic side effects [62]. Later, the same group developed a new latanoprost-loaded egg-phosphatidylcholine liposome that resulted in the sustained delivery of latanoprost for up to 90 days and 120 days in vivo in rabbits and nonhuman primates, respectively, after a single subconjunctival injection [63,64]. Niosomes are promising ocular delivery systems formed by the self-assembly of nonionic surfactants in aqueous solutions [65,66]. A novel latanoprost niosome loaded into a poloxamer gel system had a prolonged drug release and an effective reduction in the IOP of normotensive rabbits for 3 days with no ocular irritation [67].

A thermosensitive latanoprost-loaded hydrogel composed of chitosan, gelatin and glycerol phosphate demonstrated significant IOP-lowering effects in rabbits [68]. Another thermosensitive pluronic based in situ gel for latanoprost was investigated and it was found that the optimum formulation enhanced the transcorneal permeation, resulting in a rapid decrease in IOP and a high therapeutic response compared to the reference eye drops. Furthermore, latanoprost loaded in situ gelling formulation was found to be more stable under storage conditions at 4 and 25 °C than the conventional eye drops [69]. Various types of minitables have been developed for topical drug delivery to the eye [70]. Minitables containing bimatoprost have been successfully developed and tested in humans (Biophta, France; www.biophta.com, accessed on 11 July 2022). After its administration to the cul de sac, the tablet transforms into an in-situ gel which releases the drug continuously for 7 days. The PGA-loaded nanotechnology platforms and other ocular biomaterials for the treatment of glaucoma are summarized in Table 2.

Table 2. Case examples of PGA-loaded nanotechnology-based formulations and ocular biomaterial containing PGA for treatment of glaucoma.

Prostaglandin Analog	Ophthalmic Preparation	Study	Main Observation	Refs.
Nanotechnology platforms				
Latanoprost	Niosome loaded in situ gel	In vitro release and in vivo in rabbits	<ul style="list-style-type: none"> • Prolonged drug release • Effective IOP reduction in normotensive rabbits for 3 days with no ocular irritation 	[67]
	Liposome	In vitro release, in vivo in rabbits and in human primate model	<ul style="list-style-type: none"> • Sustained drug release • No localized inflammatory and toxicity • Not effective for IOP reduction after topical administration • Successfully decreased IOP and sustained drug release after single subconjunctival injection 	[62–64]
	Hyaluronic acid-chitosan nanoparticles	In vivo in albino rats.	<ul style="list-style-type: none"> • A greater IOP-lowering effect in comparison to the plain drug and Xalatan® eye drops 	[71]
	Poly(lactic-co-glycolic acid) nanoparticles	In vitro release and in vivo in rabbits	<ul style="list-style-type: none"> • Sustained drug release– • Increasing in the drug efficacy period after applied iontophoresis • Extended the period of IOP reduction for up to a week 	[72]
Travoprost	DNA nanoparticles	Ex vivo in porcine cornea, in vivo in rats and mice	<ul style="list-style-type: none"> • A long-lasting residence time on the cornea for over 60 min • Enhanced the ocular drug bioavailability 	[73]
	Liposome	In vitro release and in vivo in rabbits	<ul style="list-style-type: none"> • Faster onset, longer duration and greater reduction in IOP than commercial formulation 	[74]
Ocular biomaterials				
Latanoprost	Poly(lactic-co-glycolic acid) film contact lens	In vitro release and in vivo in rabbits	<ul style="list-style-type: none"> • Initial burst release followed by sustained release • Safety profile and providing a therapeutic amount of drug into aqueous humor for at least one month 	[75]
	Niosome laden contact lens	In vitro release and in vivo in rabbits	<ul style="list-style-type: none"> • Increased the drug loading capacity and prolonged drug release up to 48–96 h. • Approximately three-fold enhancement in ocular bioavailability when compared to conventional contact lens 	[76]
	PEGylated solid lipid nanoparticle-laden soft contact lens	In vitro release and in vivo in rabbits	<ul style="list-style-type: none"> • Improved the drug-loading capacity and sustained drug release • High drug concentrations in lower conjunctival sac compared to conventional soaked lens and drug solution 	[77]

Table 2. Cont.

Prostaglandin Analog	Ophthalmic Preparation	Study	Main Observation	Refs.
Bimatoprost	Molecular imprinted silicone contact lens	In vitro release and in vivo in rabbits	<ul style="list-style-type: none"> • Reduced burst release and prolonged drug release • Improved uptake and release kinetics of drug from the contact lens in comparison to the conventional soaking methodology 	[78]
	Chitosan polymeric inserts	In vitro release and in vivo in Wistar rats	<ul style="list-style-type: none"> • Sustained drug release • IOP reduction for four weeks after application 	[79]
	Ocular insert	Phase II clinical study	<ul style="list-style-type: none"> • A greater sustained IOP-lowering effect with no adverse effects up to 6 months 	[80]
Travoprost	Spanlastic nano-vesicles ocular insert	In vitro release and in vivo pharmacokinetic in rabbits	<ul style="list-style-type: none"> • Sustained drug release • Enhanced bioavailability of drug compared to marketed eye drop 	[81]

4. Conclusions

Nowadays, the only therapeutic approach to treating glaucoma is lowering the IOP. Non-invasive methods for delivering antiglaucoma drugs are preferred, especially topical administration in the form of aqueous eye drops. Five PGAs, i.e., latanoprost, bimatoprost, travoprost, tafluprost and latanoprostene bunod, are currently available as topical eye drops. Most of the PGA preparations contain preservatives that can result in side effects and local irritation. The use of non-preservative eye drop formulations has improved the ocular tolerance profile. Glaucoma patients are often on chronic therapies with multiple antiglaucoma drugs prescribed by their physicians. Fixed drug combinations (i.e., more than one active compounds in the same medication) in preservative-free eye drop formulations help to reduce the number of instillations, which leads to a reduction in the adverse reactions and an improvement the patient's compliance. The low aqueous solubility of PGA compounds and their chemical instability in aqueous media are the main drawbacks of PGA eye drop formulation development. Thus, novel and patient-friendly PGA eye drop formulations with fewer side effects, including enhanced physical and chemical stability at room temperature, need to be developed. Among the drug delivery systems mentioned above, aqueous cyclodextrin-based nanoemulsions and in situ gel systems are potential nanocarriers for PGA formulations. These systems use biocompatible and biodegradable excipients and are suitable for large-scale production, easily applied to the site of action, and improve the ocular drug bioavailability, resulting in a greater IOP reduction compared to conventional eye drop formulations.

The development of PGA ophthalmic formulations is still challenging. The various PGAs possess different physicochemical properties which may require different formulation approaches, but in general PGAs are potent drugs that possess low aqueous solubility and poor chemical stability in aqueous-based eye drops.

Author Contributions: Conceptualization, T.L.; writing—original draft preparation, T.L. and P.J.; writing—review and editing, T.L. and P.J. All authors have read and agreed to the published version of the manuscript.

Funding: This work was financially supported by Faculty of Pharmaceutical Sciences, Chulalongkorn University.

Institutional Review Board Statement: Not applicable.

Informed Consent Statement: Not applicable.

Data Availability Statement: Not applicable.

Conflicts of Interest: The authors declare no conflict of interest.

References

- Zukerman, R.; Harris, A.; Vercellin, A.V.; Siesky, B.; Pasquale, L.R.; Ciulla, T.A. Molecular genetics of glaucoma: Subtype and ethnicity considerations. *Genes* **2021**, *12*, 55. [CrossRef] [PubMed]
- Leske, M.C.; Heijl, A.; Hussein, M.; Bengtsson, B.; Hyman, L.; Komaroff, E. Factors for glaucoma progression and the effect of treatment: The early manifest glaucoma trial. *Arch. Ophthalmol.* **2003**, *121*, 48–56. [CrossRef] [PubMed]
- Sali, T. Prostaglandins. In *Encyclopedic Reference of Immunotoxicology*; Assenmacher, M., Avraham, H.K., Avraham, S., Bala, S., Barnett, J., Basketter, D., Ben-David, Y., Berek, C., Blümel, J., Bolliger, A.P., et al., Eds.; Springer: Berlin/Heidelberg, Germany, 2005; pp. 537–540.
- Shaw, J.E.; Ramwell, P.W. Prostaglandins: A general review. *Res. Prostaglandins* **1971**, *1*, 1–8. [PubMed]
- Camras, C.B.; Bitó, L.Z.; Eakins, K.E. Reduction of intraocular pressure by prostaglandins applied topically to the eyes of conscious rabbits. *Investig. Ophthalmol. Vis. Sci.* **1977**, *16*, 1125–1134.
- Russo, A.; Riva, I.; Pizzolante, T.; Noto, F.; Quaranta, L. Latanoprost ophthalmic solution in the treatment of open angle glaucoma or raised intraocular pressure: A review. *Clin. Ophthalmol.* **2008**, *2*, 897–905. [PubMed]
- Wang, T.; Cao, L.; Jiang, Q.; Zhang, T. Topical medication therapy for glaucoma and ocular hypertension. *Front. Pharmacol.* **2021**, *12*, 749858. [CrossRef] [PubMed]
- Katsanos, A.; Riva, I.; Bozkurt, B.; Holló, G.; Quaranta, L.; Oddone, F.; Irkeç, M.; Dutton, G.N.; Konstas, A.G. A new look at the safety and tolerability of prostaglandin analogue eyedrops in glaucoma and ocular hypertension. *Expert Opin. Drug Saf.* **2022**, *21*, 525–539. [CrossRef] [PubMed]
- Davies, S.S.; Ju, W.-K.; Neufeld, A.H.; Abran, D.; Chemtob, S.; Roberts, L.J. Hydrolysis of Bimatoprost (Lumigan) to its free acid by ocular tissue in vitro. *J. Ocul. Pharmacol. Ther.* **2003**, *19*, 45–54. [CrossRef] [PubMed]
- Moussa, W.G.E.H.; Farhat, R.G.; Nehme, J.C.; Sahyoun, M.A.; Schakal, A.R.; Jalkh, A.E.; Karam, M.P.A.; Azar, G.G. Comparison of efficacy and ocular surface disease index score between bimatoprost, latanoprost, travoprost, and tafluprost in glaucoma patients. *J. Ophthalmol.* **2018**, 1319628. [CrossRef]
- Najjar, A.; Najjar, A.; Karaman, R. Newly developed prodrugs and prodrugs in development; an insight of the recent years. *Molecules* **2020**, *25*, 884. [CrossRef]
- Samaha, D.; Diaconu, V.; Bouchard, J.F.; Desalliers, C.; Dupont, A. Effect of latanoprostene bunod on optic nerve head blood flow. *Optom. Vis. Sci.* **2022**, *99*, 172–176. [CrossRef]
- Harasymowycz, P.; Royer, C.; Mathurin, K.; Lachaine, J.; Beauchemin, C.; Cui, A.X.; Barbeau, M.; Jobin-Gervais, K.; Mathurin, K.; Lachaine, J.; et al. Short-term efficacy of latanoprostene bunod for the treatment of open-angle glaucoma and ocular hypertension: A systematic literature review and a network meta-analysis. *Br. J. Ophthalmol.* **2022**, *106*, 640–647. [CrossRef] [PubMed]
- Winkler, N.S.; Fautsch, M.P. Effects of prostaglandin analogues on aqueous humor outflow pathways. *J. Ocul. Pharmacol. Ther.* **2014**, *30*, 102–109. [CrossRef] [PubMed]
- Yoshida, F.; Topliss, J.G. Unified model for the corneal permeability of related and diverse compounds with respect to their physicochemical properties. *J. Pharm. Sci.* **1996**, *85*, 819–823. [CrossRef] [PubMed]
- Loftsson, T. Topical drug delivery to the retina: Obstacles and routes to success. *Expert Opin. Drug Deliv.* **2022**, *19*, 9–21. [CrossRef] [PubMed]
- Sripetch, S.; Loftsson, T. Topical drug delivery to the posterior segment of the eye: Thermodynamic considerations. *Int. J. Pharm.* **2021**, *597*, 120332. [CrossRef]
- Hageman, M.J. Prostaglandin E₂. In *Chemical Stability of Pharmaceuticals: A Handbook for Pharmacists*, 2nd ed.; Connors, K.A., Amidon, G.L., Stella, V.J., Eds.; John Wiley & Sons: New York, NY, USA, 1986; pp. 719–727.
- Oesterling, T.O.; Morozowich, W.; Roseman, T.J. Prostaglandins. *J. Pharm. Sci.* **1972**, *61*, 1861–1895. [CrossRef] [PubMed]
- Stehle, R.G. Physical chemistry, stability, and handling of prostaglandins E₂, F_{2α}, D₂, and I₂: A critical summary. *Methods Enzymol.* **1982**, *86*, 436–458.
- Morgan, P.V.; Proniuk, S.; Blanchard, J.; Noecker, R.J. Effect of temperature and light on the stability of latanoprost and its clinical relevance. *J. Glaucoma* **2001**, *10*, 401–405. [CrossRef]
- Velpandian, T.; Kotnala, A.; Halder, N.; Ravi, A.K.; Archunan, V.; Sihota, R. Stability of latanoprost in generic formulations using controlled degradation and patient usage simulation studies. *Curr. Eye Res.* **2015**, *40*, 561–571. [CrossRef]
- Ochiai, A.; Iida, K.; Takabe, H.; Kawamura, E.; Sato, Y.; Kato, Y.; Ohkuma, M.; Danjo, K. Formulation design of latanoprost eye drops to improve the stability at room temperature. *J. Pharm. Sci. Technol.* **2010**, *70*, 324–332.
- Sawatdee, S.; Phetmung, H.; Srichana, T. Development of a stable latanoprost solution for use as eye drops. *Chiang Mai J. Sci.* **2013**, *40*, 656–668.
- Zhou, X.; Li, X.; Xu, J.; Cheng, Y.; Cao, F. Latanoprost-loaded cyclodextrin microaggregate suspension eye drops for enhanced bioavailability and stability. *Eur. J. Pharm. Sci.* **2021**, *160*, 105758. [CrossRef] [PubMed]



26. Rodriguez-Aller, M.; Guinchard, S.; Guillarme, D.; Pupier, M.; Jeannerat, D.; Rivara-Minten, E.; Veuthey, J.-L.; Gurny, R. New prostaglandin analog formulation for glaucoma treatment containing cyclodextrins for improved stability, solubility and ocular tolerance. *Eur. J. Pharm. Biopharm.* **2015**, *95*, 203–214. [CrossRef]
27. Ochiai, A.; Danjo, K. The stabilization mechanism of latanoprost. *Int. J. Pharm.* **2011**, *410*, 23–30. [CrossRef] [PubMed]
28. Airy, S.; Chiou, J.; Nguyen, H.; Jani, R.; Gan, O.; Kabra, B.; Nguyen, H.; Weiner, A. Developmental preformulation studies in the design of travoprost ophthalmic solution 0.004% (TRAVANTAN®). In Proceedings of the American Association of Pharmaceutical Scientists (AAPS) Annual Meeting, Toronto, ON, Canada, 16–29 October 2002.
29. Kahook, M.Y. Travoprost Z ophthalmic solution with sofZia: Clinical safety and efficacy. *Expert Rev. Ophthalmol.* **2007**, *2*, 363–368. [CrossRef]
30. Alviset, G.; Corvis, Y.; Hammad, K.; Lemut, J.; Maury, M.; Mignet, N.; Boudy, V. New preservative-free formulation for the enhanced ocular bioavailability of prostaglandin analogues in glaucoma. *Pharmaceutics* **2022**, *14*, 453. [CrossRef]
31. Loftson, T. *Drug Stability for Pharmaceutical Scientists*; Academic Press: Cambridge, CA, USA, 2014; p. 170.
32. Johnson, T.V.; Gupta, P.K.; Vudathala, D.K.; Blair, I.A.; Tanna, A.P. Thermal stability of bimatoprost, latanoprost, and travoprost under simulated daily use. *J. Ocul. Pharmacol. Ther.* **2011**, *27*, 51–59. [CrossRef]
33. Swymer, C.; Neville, M.W. Tafluprost: The first preservative-free prostaglandin to treat open-angle glaucoma and ocular hypertension. *Ann. Pharmacother.* **2012**, *46*, 1506–1510. [CrossRef]
34. Kaufman, P.L. Latanoprostene bunod ophthalmic solution 0.024% for IOP lowering in glaucoma and ocular hypertension. *Expert Opin. Pharmacother.* **2017**, *18*, 433–444. [CrossRef]
35. Baudouin, C.; Labbé, A.; Liang, H.; Pauly, A.; Brignole-Baudouin, F. Preservatives in eyedrops: The good, the bad and the ugly. *Prog. Retin. Eye Res.* **2010**, *29*, 312–334. [CrossRef]
36. Goldstein, M.H.; Silva, F.Q.; Blender, N.; Tran, T.; Vantipalli, S. Ocular benzalkonium chloride exposure: Problems and solutions. *Eye* **2022**, *36*, 361–368. [CrossRef] [PubMed]
37. Johannsdottir, S.; Jansook, P.; Stefansson, E.; Kristinsdottir, I.M.; Asgrimsdottir, G.M.; Loftsson, T. Topical drug delivery to the posterior segment of the eye: The effect of benzalkonium chloride on topical dexamethasone penetration into the eye in vivo. *J. Drug Deliv. Sci. Technol.* **2018**, *48*, 125–127. [CrossRef]
38. Xu, K.M.; Cho, R.; Chan, T.Y.B. Retrospective analysis of switching bimatoprost 0.01% to bimatoprost 0.03% in patients with various types of glaucoma and ocular hypertension. *Clin. Ophthalmol.* **2022**, *16*, 2385–2390. [CrossRef] [PubMed]
39. Rosin, L.M.; Bell, N.P. Preservative toxicity in glaucoma medication: Clinical evaluation of benzalkonium chloride-free 0.5% timolol eye drops. *Clin. Ophthalmol.* **2013**, *7*, 2131–2135. [CrossRef]
40. Pellinen, P.; Lökkilä, J. Corneal penetration into rabbit aqueous humor is comparable between preserved and preservative-free tafluprost. *Ophthalmic Res.* **2009**, *41*, 118–122. [CrossRef] [PubMed]
41. Economou, M.A.; Laukeland, H.K.; Grabska-Liberek, I.; Rouland, J.F. Better tolerance of preservative-free latanoprost compared to preserved glaucoma eye drops: The 12-month real-life FREE study. *Clin. Ophthalmol.* **2018**, *12*, 2399–2407. [CrossRef] [PubMed]
42. Kim, J.M.; Park, S.W.; Seong, M.; Ha, S.J.; Lee, J.W.; Rho, S.; Lee, C.E.; Kim, K.N.; Kim, T.W.; Sung, K.R.; et al. Comparison of the safety and efficacy between preserved and preservative-free latanoprost and preservative-free tafluprost. *Pharmaceutics* **2021**, *14*, 501. [CrossRef]
43. Uekama, K.; Hirayama, F.; Fujise, A.; Otagiri, M.; Inaba, K.; Saito, H. Inclusion complexation of prostaglandin F2 alpha with gamma-cyclodextrin in solution and solid phases. *J. Pharm. Sci.* **1984**, *73*, 382–384. [CrossRef]
44. Gu, F.-G.; Cui, F.-D.; Gao, Y.-L. Effect of complexation with hydroxypropyl-β-cyclodextrin on solubility, dissolution rate and chemical stability of prostaglandin E1. *J. Chin. Pharm. Sci.* **2004**, *13*, 158–165.
45. Uekama, K.; Hirayama, F.; Yamada, Y.; Inaba, K.; Ikeda, K. Improvements of dissolution characteristics and chemical stability of 16,16-dimethyl-trans-Δ²-prostaglandin E1 methyl ester by cyclodextrin complexation. *J. Pharm. Sci.* **1979**, *68*, 1059–1060. [CrossRef]
46. Inaba, K.; Wakuda, T.; Uekama, K. Prostaglandins and their cyclodextrin complexes. *J. Incl. Phenom.* **1984**, *2*, 467–474. [CrossRef]
47. Uekama, K.; Hieda, Y.; Hirayama, F.; Arima, H.; Sudoh, M.; Yagi, A.; Terashima, H. Stabilizing and solubilizing effects of sulfobutyl ether β-cyclodextrin on prostaglandin E1 analog. *Pharm. Res.* **2001**, *18*, 1578–1585. [CrossRef]
48. Kumar, P.V.T.; Kumar, A.A.; Rao, N.S. Formulation and evaluation of tafluprost ophthalmic solution. *J. Drug Deliv. Ther.* **2019**, *9*, 18–24. [CrossRef]
49. Gonzalez, J.R.; Baiza-Duran, L.; Quintana-Hau, J.; Tornero-Montaño, R.; Castaneda-Hernandez, G.; Ortiz, M.; Alarcon-Oceguera, F.; Beltran-Loustaunau, M.; Cortez-Gastelum, M.; Garcidueñas-Mejia, J.; et al. Comparison of the stability, efficacy, and adverse effect profile of the innovator 0.005% latanoprost ophthalmic solution and a novel cyclodextrin-containing formulation. *J. Clin. Pharmacol.* **2007**, *47*, 121–126. [CrossRef]
50. Battaglia, L.; Serpe, L.; Foglietta, F.; Muntoni, E.; Gallarate, M.; Del Pozo Rodriguez, A.; Solinis, M.A. Application of lipid nanoparticles to ocular drug delivery. *Expert Opin. Drug Deliv.* **2016**, *13*, 1743–1757. [CrossRef] [PubMed]
51. Jacob, S.; Nair, A.B.; Shah, J.; Gupta, S.; Boddu, S.H.S.; Sreeharsha, N.; Joseph, A.; Shinu, P.; Morsy, M.A. Lipid nanoparticles as a promising drug delivery carrier for topical ocular therapy-An overview on recent advances. *Pharmaceutics* **2022**, *14*, 533. [CrossRef]
52. Habib, F.; El-Mahdy, M.; Maher, S. Microemulsions for ocular delivery: Evaluation and characterization. *J. Drug Deliv. Sci. Technol.* **2011**, *21*, 485–489. [CrossRef]

53. Singh, M.; Bharadwaj, S.; Lee, K.E.; Kang, S.G. Therapeutic nanoemulsions in ophthalmic drug administration: Concept in formulations and characterization techniques for ocular drug delivery. *J. Control. Release* **2020**, *328*, 895–916. [CrossRef] [PubMed]
54. Tamilvanan, S.; Benita, S. The potential of lipid emulsion for ocular delivery of lipophilic drugs. *Eur. J. Pharm. Biopharm.* **2004**, *58*, 357–368. [CrossRef]
55. Liang, H.; Baudouin, C.; Faure, M.O.; Lambert, G.; Brignole-Baudouin, F. Comparison of the ocular tolerability of a latanoprost cationic emulsion versus conventional formulations of prostaglandins: An in vivo toxicity assay. *Mol. Vis.* **2009**, *15*, 1690–1699.
56. Daull, P.; Buggage, R.; Lambert, G.; Faure, M.O.; Serle, J.; Wang, R.F.; Garrigue, J.S. A comparative study of a preservative-free latanoprost cationic emulsion (Catioprost) and a BAK-preserved latanoprost solution in animal models. *J. Ocul. Pharmacol. Ther.* **2012**, *28*, 515–523. [CrossRef]
57. Liang, H.; Baudouin, C.; Daull, P.; Garrigue, J.-S.; Buggage, R.; Brignole-Baudouin, F. In vitro and In vivo evaluation of a preservative-free cationic emulsion of latanoprost in corneal wound healing models. *Cornea* **2012**, *31*, 1319–1329. [CrossRef] [PubMed]
58. Daull, P.; Amrane, M.; Garrigue, J.-S. Novasorb® cationic nanoemulsion and latanoprost: The ideal combination for glaucoma management? *Glaucoma* **2017**, *2*, 107. [CrossRef]
59. Ismail, A.; Nasr, M.; Sammour, O. Nanoemulsion as a feasible and biocompatible carrier for ocular delivery of travoprost: Improved pharmacokinetic/pharmacodynamic properties. *Int. J. Pharm.* **2020**, *583*, 119402. [CrossRef]
60. Tau, J.; Passerini, M.S.; Del Papa, M.; Aguilar, A.; Berra, A. A novel ophthalmic latanoprost 0.005% nanoemulsion: A cytotoxicity study. *Graefes Arch. Clin. Exp. Ophthalmol.* **2022**, *260*, 1941–1946. [CrossRef]
61. Agarwal, R.; Iezhitsu, I.; Agarwal, P.; Abdul Nasir, N.A.; Razali, N.; Alyautdin, R.; Ismail, N.M. Liposomes in topical ophthalmic drug delivery: An update. *Drug Deliv.* **2016**, *23*, 1075–1091. [CrossRef] [PubMed]
62. Natarajan, J.V.; Chattopadhyay, S.; Ang, M.; Darwitan, A.; Foo, S.; Zhen, M.; Koo, M.; Wong, T.T.; Venkatraman, S.S. Sustained release of an anti-glaucoma drug: Demonstration of efficacy of a liposomal formulation in the rabbit eye. *PLoS ONE* **2011**, *6*, e24513. [CrossRef]
63. Natarajan, J.V.; Ang, M.; Darwitan, A.; Chattopadhyay, S.; Wong, T.T.; Venkatraman, S.S. Nanomedicine for glaucoma: Liposomes provide sustained release of latanoprost in the eye. *Int. J. Nanomed.* **2012**, *7*, 123–131. [CrossRef]
64. Natarajan, J.V.; Darwitan, A.; Barathi, V.A.; Ang, M.; Htoon, H.M.; Boey, F.; Tam, K.C.; Wong, T.T.; Venkatraman, S.S. Sustained Drug Release in Nanomedicine: A Long-Acting Nanocarrier-Based Formulation for Glaucoma. *ACS Nano* **2014**, *8*, 419–429. [CrossRef] [PubMed]
65. Verma, A.; Tiwari, A.; Saraf, S.; Panda, P.K.; Jain, A.; Jain, S.K. Emerging potential of niosomes in ocular delivery. *Expert Opin. Drug Deliv.* **2021**, *18*, 55–71. [CrossRef] [PubMed]
66. Durak, S.; Esmaeili Rad, M.; Alp Yetisgin, A.; Eda Sutova, H.; Kutlu, O.; Cetinel, S.; Zarrabi, A. Niosomal drug delivery systems for ocular disease-recent advances and future prospects. *Nanomaterials* **2020**, *10*, 1191. [CrossRef]
67. Fathalla, D.; Fouad, E.A.; Soliman, G.M. Latanoprost niosomes as a sustained release ocular delivery system for the management of glaucoma. *Drug Dev. Ind. Pharm.* **2020**, *46*, 806–813. [CrossRef]
68. Cheng, Y.-H.; Tsai, T.-H.; Jhan, Y.-Y.; Chiu, A.W.-H.; Tsai, K.-L.; Chien, C.-S.; Chiou, S.-H.; Liu, C.J.-L. Thermosensitive chitosan-based hydrogel as a topical ocular drug delivery system of latanoprost for glaucoma treatment. *Carbohydr. Polym.* **2016**, *144*, 390–399. [CrossRef]
69. Khattab, A.; Marzok, S.; Ibrahim, M. Development of optimized mucoadhesive thermosensitive pluronic based in situ gel for controlled delivery of Latanoprost: Antiglaucoma efficacy and stability approaches. *J. Drug Deliv. Sci. Technol.* **2019**, *53*, 101134. [CrossRef]
70. Moosa, R.M.; Choonara, Y.E.; du Toit, L.C.; Kumar, P.; Carmichael, T.; Tomar, L.K.; Tyagi, C.; Pillay, V. A review of topically administered mini-tablets for drug delivery to the anterior segment of the eye. *J. Pharm. Pharmacol.* **2014**, *66*, 490–506. [CrossRef]
71. Rubenicia, A.M.L.; Cubillan, L.D.P.; Sicam, V.A.D.P.; Macabeo, A.P.G.; Villaflores, O.B.; Castillo, A.L. Intraocular pressure reduction effect of 0.005% latanoprost eye drops in a hyaluronic acid-chitosan nanoparticle drug delivery system in albino rabbits. *Transl. Vis. Sci. Technol.* **2021**, *10*, 2. [CrossRef]
72. Kim, S.N.; Min, C.H.; Kim, Y.K.; Ha, A.; Park, C.G.; Lee, S.H.; Park, K.H.; Choy, Y.B. Iontophoretic ocular delivery of latanoprost-loaded nanoparticles via skin-attached electrodes. *Acta Biomater.* **2022**, *144*, 32–41. [CrossRef]
73. Schnichels, S.; Hurst, J.; de Vries, J.W.; Ullah, S.; Gruszka, A.; Kwak, M.; Löscher, M.; Dammeyer, S.; Bartz-Schmidt, K.-U.; Spitzer, M.S.; et al. Self-assembled DNA nanoparticles loaded with travoprost for glaucoma-treatment. *Nanomed. Nanotechnol. Biol. Med.* **2020**, *29*, 102260. [CrossRef]
74. González-Cela-Casamayor, M.A.; López-Cano, J.J.; Bravo-Osuna, I.; Andrés-Guerrero, V.; Vicario-de-la-Torre, M.; Guzmán-Navarro, M.; Benítez-Del-Castillo, J.M.; Herrero-Vanrell, R.; Molina-Martínez, I.T. Novel osmoprotective DOPC-DMPC liposomes loaded with antihypertensive drugs as potential strategy for glaucoma treatment. *Pharmaceutics* **2022**, *14*, 1405. [CrossRef]
75. Ciolino, J.B.; Stefanescu, C.F.; Ross, A.E.; Salvador-Culla, B.; Cortez, P.; Ford, E.M.; Wymbs, K.A.; Sprague, S.L.; Mascoop, D.R.; Rudina, S.S.; et al. In vivo performance of a drug-eluting contact lens to treat glaucoma for a month. *Biomaterials* **2014**, *35*, 432–439. [CrossRef] [PubMed]
76. Xue, Y.; Gao, Q.; Zhang, L. Extended ocular delivery of latanoprost from niosome-laden contact lenses: In vitro characterization and in vivo studies. *J. Drug Deliv. Sci. Technol.* **2022**, *68*, 103044. [CrossRef]

77. Dang, H.; Dong, C.; Zhang, L. Sustained latanoprost release from PEGylated solid lipid nanoparticle-laden soft contact lens to treat glaucoma. *Pharm. Dev. Technol.* **2022**, *27*, 127–133. [CrossRef] [PubMed]
78. Yan, F.; Liu, Y.; Han, S.; Zhao, Q.; Liu, N. Bimatoprost imprinted silicone contact lens to treat glaucoma. *AAPS PharmSciTech* **2020**, *21*, 63. [CrossRef] [PubMed]
79. Franca, J.R.; Foureaux, G.; Fuscaldi, L.L.; Ribeiro, T.G.; Rodrigues, L.B.; Bravo, R.; Castilho, R.O.; Yoshida, M.I.; Cardoso, V.N.; Fernandes, S.O.; et al. Bimatoprost-loaded ocular inserts as sustained release drug delivery systems for glaucoma treatment: In vitro and in vivo evaluation. *PLoS ONE* **2014**, *9*, e95461. [CrossRef]
80. Brandt, J.D.; Sall, K.; DuBiner, H.; Benza, R.; Alster, Y.; Walker, G.; Semba, C.P. Six-month intraocular pressure reduction with a topical bimatoprost ocular insert: Results of a Phase II Randomized Controlled study. *Ophthalmology* **2016**, *123*, 1685–1694. [CrossRef]
81. Shukr, M.H.; Ismail, S.; El-Hossary, G.G.; El-Shazly, A.H. Spanlastics nanovesicular ocular insert as a novel ocular delivery of travoprost: Optimization using Box-Behnken design and in vivo evaluation. *J. Liposome Res.* **2022**, 1–11. [CrossRef]

Review

Research Progress Concerning a Novel Intraocular Lens for the Prevention of Posterior Capsular Opacification

Yidong Zhang ^{1,†}, Chengshou Zhang ^{1,†}, Silong Chen ^{1,†} , Jianghua Hu ^{1,2} , Lifang Shen ¹ and Yibo Yu ^{1,*}

¹ Eye Center, The Second Affiliated Hospital, School of Medicine, Zhejiang University, Hangzhou 310058, China; yidongzhang@zju.edu.cn (Y.Z.); zhangchengshou@zju.edu.cn (C.Z.); cshelo@zju.edu.cn (S.C.); laurel_hu@163.com (J.H.); y214180453@163.com (L.S.)

² Jiande Branch, The Second Affiliated Hospital, School of Medicine, Zhejiang University, Hangzhou 310058, China

* Correspondence: yuyibo@zju.edu.cn

† These authors contributed equally to this work.

Abstract: Posterior capsular opacification (PCO) is the most common complication resulting from cataract surgery and limits the long-term postoperative visual outcome. Using Nd:YAG laser-assisted posterior capsulotomy for the clinical treatment of symptomatic PCO increases the risks of complications, such as glaucoma, retinal diseases, uveitis, and intraocular lens (IOL) pitting. Therefore, finding how to prevent PCO development is the subject of active investigations. As a replacement organ, the IOL is implanted into the lens capsule after cataract surgery, but it is also associated with the occurrence of PCO. Using IOL as a medium for PCO prophylaxis is a more facile and efficient method that has demonstrated various clinical application prospects. Thus, scientists have conducted a lot of research on new intraocular lens fabrication methods, such as optimizing IOL materials and design, and IOL surface modification (including plasma/ultraviolet/ozone treatment, chemical grafting, drug loading, coating modification, and layer-by-layer self-assembly methods). This paper summarizes the research progress for different types of intraocular lenses prepared by different surface modifications, including anti-biofouling IOLs, enhanced-adhesion IOLs, micro-patterned IOLs, photothermal IOLs, photodynamic IOLs, and drug-loading IOLs. These modified intraocular lenses inhibit PCO development by reducing the residual intraoperative lens epithelial cells or by regulating the cellular behavior of lens epithelial cells. In the future, more works are needed to improve the biosecurity and therapeutic efficacy of these modified IOLs.

Keywords: posterior capsular opacification; intraocular lens; surface modification; drug delivery; photothermal therapy; photodynamic therapy; micro-pattern; anti-biofouling

Citation: Zhang, Y.; Zhang, C.; Chen, S.; Hu, J.; Shen, L.; Yu, Y. Research Progress Concerning a Novel Intraocular Lens for the Prevention of Posterior Capsular Opacification. *Pharmaceutics* **2022**, *14*, 1343. <https://doi.org/10.3390/pharmaceutics14071343>

Academic Editors: Francisco Javier Otero-Espinar and Anxo Fernández Ferreiro

Received: 15 May 2022

Accepted: 23 June 2022

Published: 25 June 2022

Publisher's Note: MDPI stays neutral with regard to jurisdictional claims in published maps and institutional affiliations.



Copyright: © 2022 by the authors. Licensee MDPI, Basel, Switzerland. This article is an open access article distributed under the terms and conditions of the Creative Commons Attribution (CC BY) license (<https://creativecommons.org/licenses/by/4.0/>).

1. Introduction

Cataracts, the leading cause of blindness globally, is a disease that results in color changes or opacification of a transparent ocular lens and leads to a series of visual defects [1]. Nowadays, researchers consider cataract lens removal surgery combined with intraocular lens (IOL) implantation as the only effective treatment for vision-limiting cataracts [2,3]. Although cataract phacoemulsification surgery is mature, post-surgical complications, such as posterior capsular opacification (PCO), limit the long-term postoperative visual outcomes [4]. PCO incidence ranges from 20% to 40% within five years after cataract surgery in adults, while in children, the incidence is as high as 100% [5,6]. Using Nd:YAG laser-assisted posterior capsulotomy, the clinical management of symptomatic PCO, may lead to several risks, such as glaucoma, retinal diseases, uveitis, and intraocular lens (IOL) pitting [7–9]. Therefore, PCO prevention is still the subject of active investigation.

1.1. Pathophysiology of PCO

The lens sits behind the iris inside the eye and is attached to the ciliary body through zonules [10] (Figure 1a). Histologically, it is composed of the lens capsule (including the anterior capsule, the equatorial region, the acellular posterior capsule), fibers, and single-layer lens epithelium [1]. Lens fibers are transformed from the lens epithelium and compacted from the periphery to the center. Thus, older lens fibers make up the core (nucleus) of the lens, and newly formed lens fibers make up the outer layer of the lens, the cortex (Figure 1b).

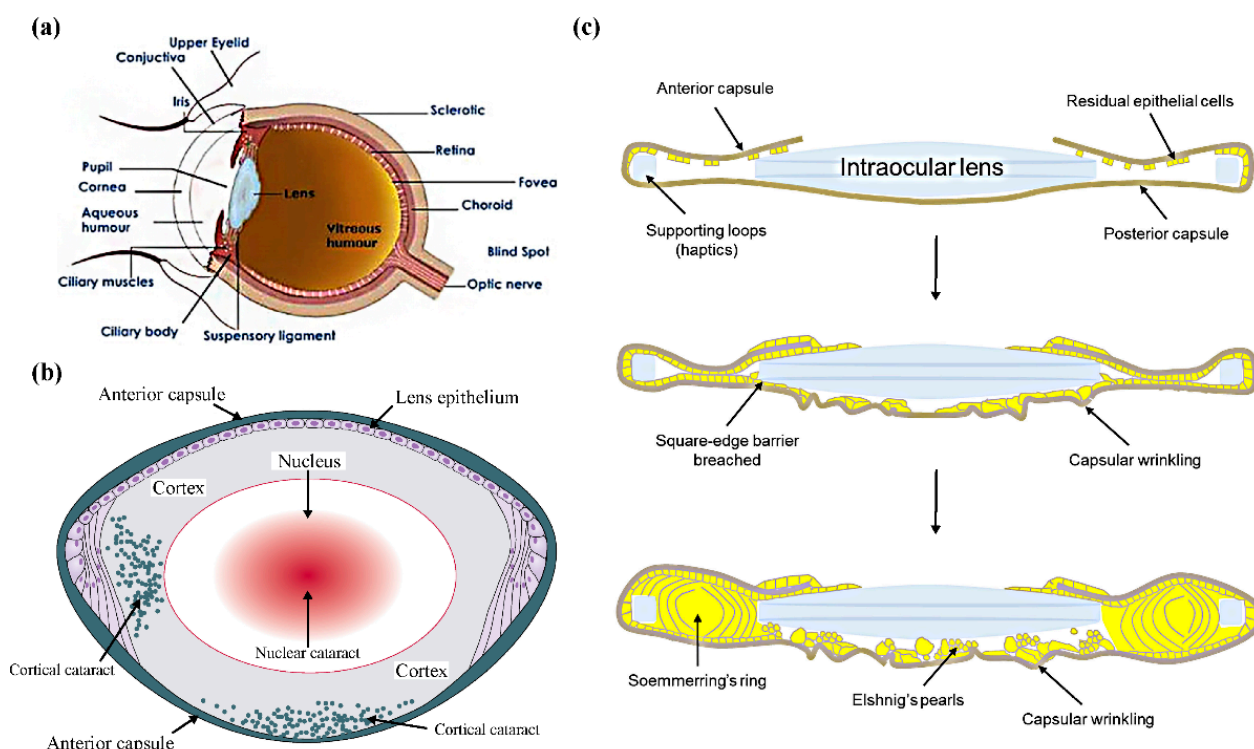


Figure 1. (a) The structure of a human eye. Adapted with permission from Ref. [10]. Copyright 2015 Elsevier. (b) The structure of a human lens. Adapted with permission from Ref. [1]. Copyright 2017 Elsevier. (c) The PCO development following cataract surgery. Adapted with permission from Ref. [5]. Copyright 2021 Elsevier.

The pathophysiology of PCO is still not fully elucidated. Through the surgery of the extracapsular cataract extraction (including the phacoemulsification surgery), the nucleus and cortex were removed, and the lens capsule retains for the IOL implantation [2,3]. Despite the initial success of cataract surgery, there are always residual lens epithelial cells (LECs), as well as the postoperative inflammation, in the capsular bag (Figure 1c). Since cataract surgery initiates a wound-healing response, these living LECs start to proliferate and migrate over all available surfaces, including regions below or outer of the anterior capsule; IOL surfaces; and of primary importance the previously acellular posterior capsule, ultimately encroaching on the visual axis [4,5]. Furthermore, LECs undergo transdifferentiation into myofibroblasts and the process of epithelial–mesenchymal transformation (EMT). In addition, aberrant differentiation is considered to result in swollen globular cells, shown as the structure of Elschnig's pearls. Additionally, the structure of Soemmerring's ring is formed by lens fiber differentiation in the peripheral capsular bag (outside the IOLs). Thus, matrix deposition, capsular wrinkling, increased cell aggregation, and Elschnig's pearls collectively cause significant visual disruption [11]. Moreover, changes in growth factors (such as transforming growth factor, fibroblast growth factor, epidermal growth factor, and insulin-like growth factor), cell adhesion molecules (such as intracellular adhesion molecule-1, various integrin ligands, and CD44), extracellular matrix (ECM)

components (such as fibronectin, vitronectin, and collagen), other signaling molecules, and signal pathways play a critical role in regulating residual LEC functions and behaviors [5].

1.2. The Role of IOLs in PCO Prevention

According to the pathogenesis of PCO, the current research on PCO prevention has focused on reducing the residue of LECs or regulating their cellular behaviors. The cellular behaviors of LECs and the development of PCO are closely related to IOL biocompatibility. Amon et al. [12] have proposed for the first time that the IOL biocompatibility can be divided into the uveal and capsular biocompatibility. The uveal biocompatibility refers to the foreign body inflammatory response of uveal tissue to the IOL. The disruption of the blood–aqueous humor barrier during cataract surgery causes the influx of proteins and cells into the anterior chamber and their adhesion to the IOL surface. This protein adhesion plays a dramatic role in accumulating other cells, and the inflammatory cells convert into macrophages and giant cells, inducing a foreign body response. Capsular biocompatibility mainly refers to the opacification of the anterior and posterior capsule because of the proliferation and migration of LECs or the growth of LECs on the anterior surface of the IOL [13].

The IOL biocompatibility is influenced by several factors, including the IOL material, the optical edge design, and surface properties [14]. A more hydrophilic IOL surface is generally considered for better uveal biocompatibility, while a more hydrophobic IOL surface means better capsular biocompatibility [14]. The hydrophilic IOL surface reduces the adhesion of proteins and cells, which results in an alleviated postoperative inflammatory response, but it provides a suitable interface for the proliferation and migration of LECs. Numerous studies have demonstrated that constructing the hydrophilic anti-biofouling coatings on the IOL surface could reduce PCO incidence by inhibiting the adhesion, proliferation, or migration of LECs on the IOL surface [15–18]. Conversely, PCO has also been regarded as a unique form of an inflammatory response in which inflammatory cells (such as macrophages and giant cells) secrete cytokines and, in turn, regulate cellular behaviors of LECs, leading to severe PCO [13,19,20]. Therefore, the uveal and capsular biocompatibility of the IOL is not separate but closely related properties, and the effect of IOL surface hydrophobicity on PCO formation should also be treated critically. Improving the IOL biocompatibility through surface modification is a potential method for PCO prevention [14,21].

As the replacement organ is directly implanted in the eye, the IOL can serve as a medium to reduce postoperative residual LECs or regulate their behaviors through physical or biochemical means. This is a more facile and efficient method with clinical application prospects for PCO prophylaxis. For example, the IOL can be a drug delivery device that delivers anti-inflammatory, cytotoxic, and antiproliferative drugs that prevent PCO. This has the advantage of improving drugs and prolonging the time of action of drugs [22,23]. A significant benefit of drug-loaded IOLs is ensuring continuous drug delivery, better drug bioavailability, and patient compliance.

In addition to optimizing cataract surgery techniques and the intraoperative irrigation of drug solution in the capsule, scientists have conducted lots of research on using the intraocular lens to prevent PCO formation. They have focused on optimizing the IOL materials, design, and modifying surface properties (such as plasma/ultraviolet/ozone treatment, chemical grafting, drug loading, layer-by-layer self-assembly methods, and coating modification) [22–25].

This article mainly places greater focus on the different intraocular lenses prepared by IOL surface modification for PCO prevention, including anti-biofouling IOLs, enhanced-adhesion IOLs, micro-patterned IOLs, photothermal IOLs, photodynamic IOLs, and drug-loading IOLs. We summarize their brief mechanisms for PCO prevention in Figure 2.

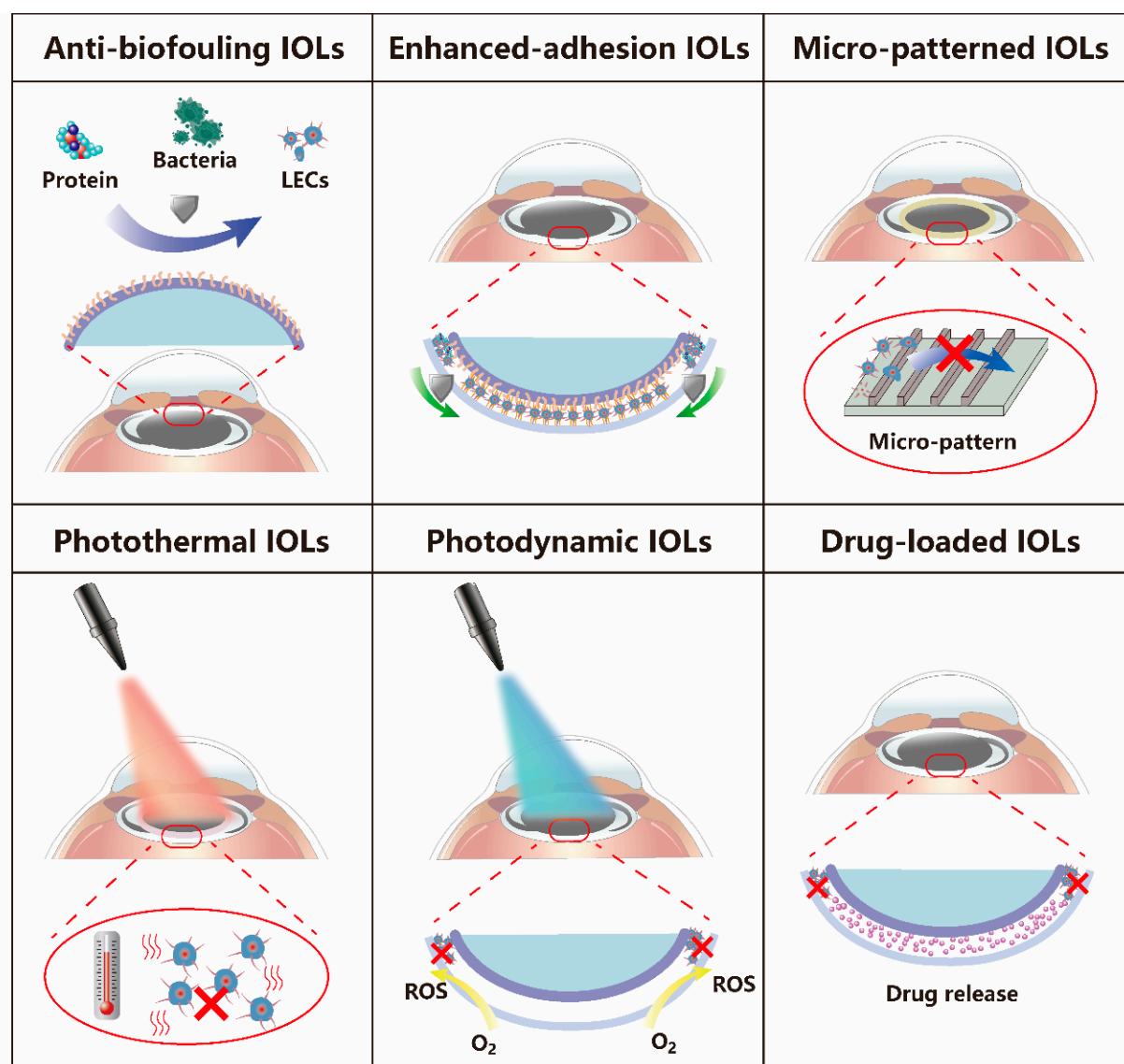


Figure 2. Schematic illustration of the main types of IOLs used for PCO prophylaxis.

2. The Main Types of IOLs Used for PCO Prophylaxis

2.1. Anti-Biofouling IOLs

Biofouling means the undesired adsorption and adhesion of biomolecules, cells, or microorganisms, and the formation of microbial films on material surfaces [26]. Since these biofouling components would induce inflammatory responses and potentially cause infection and/or immunologic rejection, the property of anti-biofouling is significantly relevant to the durability and security of medical applications, for example, medical implants, contact lenses, catheters, hemodialyzers, biosensors, and respirators [26–29]. Antifouling polymers or coatings modified onto these medical devices change their surface characteristics and thus improve biocompatibility and the performance in resisting biofouling.

The fabrication of anti-biofouling IOLs aims to alleviate the inflammatory response and decrease the LEC number on the IOL surface. This is performed by reducing the adhesion of proteins, bacteria, and cells, resulting in the inhibition of PCO formation. Previous studies have induced hydrophilic groups into IOL surfaces, such as heparin, vinyl pyrrolidone, and α -allyl glucoside, and enhanced the anti-biofouling and anti-inflammation ability of IOLs [21]. Nevertheless, in a clinical trial, heparin-surface-modified (HSM) hydrophilic acrylic IOLs and hydrophobic acrylic IOLs were implanted in cataract patients

for 12 months of investigation [30]. In the uncomplicated cataract patients, the respective PCO areas and PCO severity scores were 6.12% and 0.081 in the HSM IOLs group and 5.91% and 0.075 in the control group, respectively. There was no statistically significant difference in the PCO area or the PCO severity score between the two IOLs, demonstrating no superiority of HSM IOLs in preventing PCO. Thus, these anti-fouling IOLs require more investigation to improve the PCO prevention effect before the final clinical application. The reviewed literature of anti-fouling IOLs for PCO prophylaxis with *in vivo* results is summarized in Table 1.

Poly(ethylene glycol) (PEG), a neutral and hydrophilic polymer with low PEG–water interface energy and no immunogenicity, is a commonly used anti-biofouling material. Lee et al. [31] applied PEG molecules for the surface modification of acrylic IOL with a square edge design. The PEG-IOLs were implanted in the rabbit models and found to reduce PCO severity at 36 weeks significantly. Scanning electron microscopy showed more LECs tightly adhered to the IOL surface without PEG modification. However, PEG-IOLs did not substantially inhibit PCO formation after seven weeks. Xu et al. [32] immobilized the hydrophilic PEG onto the IOL surface via a plasma-aided chemical grafting procedure without influencing the optical properties. This PEG-modified IOL had good biocompatibility in the rabbit model and exerted a PCO inhibition effect for more than four months. Subsequently, the research group fabricated the hydrophilic poly(poly(ethylene glycol) methacrylate) (PPEGMA) brush on the IOL surface using reversible addition fragmentation chain-transfer (RAFT) technology, which was an even more stable modification of the PEG. The anti-biofouling coating was sufficient to inhibit LEC adhesion and proliferation on the IOL, thereby reducing the incidence of PCO [17].

The compound 2-Methacryloyloxyethyl Phosphorylcholine (MPC) is an amphoteric material with excellent hydrophilicity, biocompatibility, and a specific bionic structure that provides the artificial cell membrane interface. These features allow for various applications in biological implants, tissue engineering, and drug delivery systems [33]. MPC forms a membrane-like structure and traps water molecules on the acrylic or silicone IOL, resulting in significantly improved surface hydrophilicity and anti-adhesion of proteins, cells, and bacteria [34–36].

Han et al. [37] prepared amphoteric MPC brushes on the surface of IOL acrylic acid by the bottom-up grafting method, and this alleviated the PCO severity after implanting MPC-modified IOL into rabbit eyes. Similarly, Tan et al. [38] synthesized the hydrophilic copolymer P (MPC-MAA) from the negatively charged hydrophilic methyl acrylic acid (MAA) and MPC, and they covalently grafted the copolymer onto the hydrophobic acrylic IOL surface after ammonia plasma treatment. However, the MPC-MAA modification could inhibit postoperative inflammation and anterior capsular opacification (ACO) rather than PCO. In another study, a polymer containing the amphoteric betaine group was used by Wang et al. [39] for surface modification because of its good biocompatibility, lubricity, and anti-biofouling properties in the hydration state. The hydrophilic poly(sulfobetaine methacrylate) (PSBRMA) brush coating was prepared on the IOL using the RAFT method. This decreased LEC adhesion and proliferation *in vitro* and significantly reduced the turbidity of the posterior capsule *in vivo*.

The natural polysaccharide is extensively used in the surface modification of bio-materials, such as hyaluronic acid (HA) and chitosan (CHI). HA is a negatively-charged polysaccharide, naturally existing in the vitreous body, joint, and skin. However, CHI is the only cationic natural polysaccharide [40,41]. Considering the advantages of the hydration property of polysaccharides, Lin et al. [42] constructed a hydrogel-like polyelectrolyte multilayer coating composed of HA and CHI components on the surface of the silicone IOL using the electrostatic layer-by-layer (LBL) self-assembly method. The anti-biofouling coating of HA/CHI inhibited LEC adhesion and proliferation. For the *in vivo* experiments, modified IOLs prevented the central PCO (3 mm diameter), but the severity of peripheral PCO and Soemmerring's ring was not significantly different between the control and modified IOL groups.

The modified IOLs mentioned above were rarely resistant to biofouling while maintaining tight contact with the posterior capsule. Thus, Wu et al. [43] fabricated a new type of IOL with a hydrophobic anti-biofouling coating (Figure 3). After functionalizing the nanomorphology of the hydrophobic IOL surface and covalently conjugating it with a “liquid-like” polydimethylsiloxane brush, the resulting (NT + LLL)-IOL exhibited strong resistance to biological fouling, including proteins, cells, and bacteria, because of the low surface energy of the modified surface. The hydrophobic surface of the (NT + LLL)-IOL had a better attachment to the posterior capsule, thus preventing residual LEC migration. Therefore, the (NT + LLL)-IOL implantation alleviated the intraocular inflammation response postoperatively and PCO formation. Despite having a liquid-like layered coating, the (NT + LLL)-IOL still had advantages of optical transparency, good biocompatibility, and mechanical robustness.

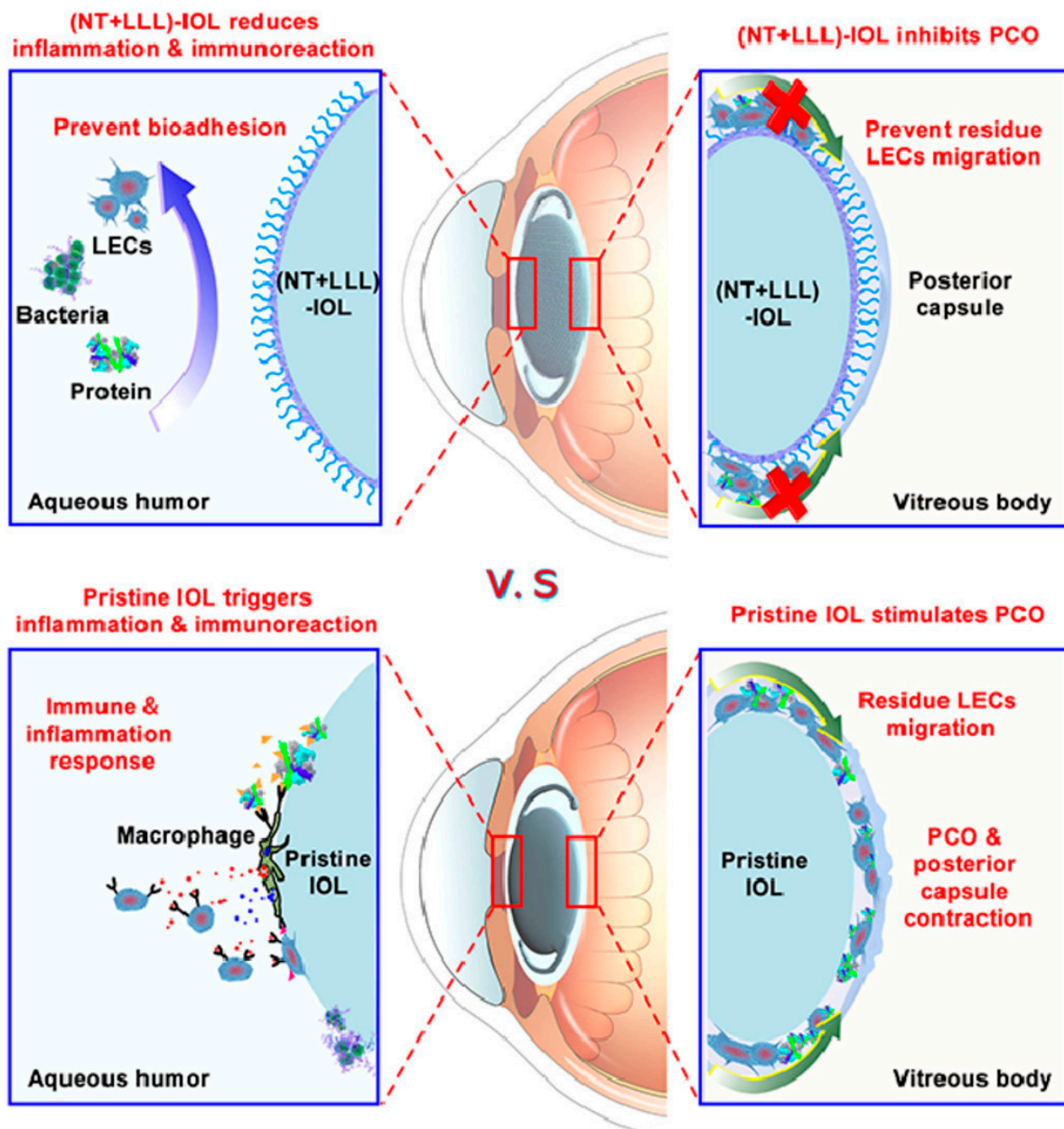


Figure 3. Schematic illustration of the (NT + LLL)-IOL with advantages of anti-bio-adhesion and PCO inhibition, compared to the pristine IOL. Adapted with permission from Ref. [43]. Copyright 2021 Elsevier.

Table 1. Summary of reviewed literature of anti-biofouling IOLs for PCO prophylaxis with in vivo results.

Composition	Main Fabrication Method	IOL Type	Observation	Prophylaxis Effect	Ref.
PEG	oxygen plasma-aided activation and grafting polymerization	acrylic IOL (SA60AT, Alcon)	eight weeks in rabbit model	alleviate PCO formation for six weeks, but had no effect afterwards	[31]
PPEGMA	oxygen and argon plasma-aided activation and grafting polymerization	acrylic IOL (SN60WF, Alcon)	four months in rabbit model	alleviate PCO formation	[32]
PPEGMA	oxygen plasma-aided activation and RAFT grafting polymerization	acrylic IOL (SN60WF, Alcon)	six months in rabbit model	alleviate PCO formation	[17]
MPC	RAFT grafting polymerization	acrylic IOL (SN60WF, Alcon)	one month in rabbit model	alleviate PCO formation	[37]
MPC/MAA	ammonia plasma-aided activation and grafting polymerization	acrylic IOL (Eyegood Medical Tech.)	eight weeks in rabbit model	alleviate anterior capsular opacification formation, but did not alleviate PCO formation	[38]
PSBMA	RAFT grafting polymerization	acrylic IOL (66Vision Tech.)	six months in rabbit model	alleviate PCO formation	[39]
HA/CHI	layer-by-layer assembly	acrylic IOL (Alcon)	one month in rabbit model	alleviate CPCO formation not PPCO	[42]
PDMS	oxygen plasma-aided activation and chemical vapor deposition	acrylic IOL (Eyebright Medical Tech.)	two months in rabbit model	alleviate PCO formation	[43]

2.2. Enhanced-Adhesion IOLs

According to the “sandwich” theory proposed by Linnola et al. [44–47], the IOL surface with biological adhesion properties allows the LECs to adhere to the IOL, forming the three-tier structure of the IOL, monolayer LECs, and posterior capsule membrane. The sealed sandwich structure prevents further LEC proliferation and migration, thereby reducing the incidence of PCO. The monolayer LEC’s proliferation probably only slightly influences the contrast sensitivity and not transparency of posterior capsules. In addition to LECs, the proteins that make up the extracellular matrix, including fibronectin, vimentin, laminin, and collagen IV, can play a role in this adhesion mode [45,46].

Thus, the molecular basis of relatively lower PCO incidences in hydrophobic IOL than hydrophilic IOL has been speculated by protein adsorption behaviors [48,49]. The hydrophobic surface is considered more bio-sticky to the posterior capsule than hydrophilic one via adsorbing more proteins and via the adsorbed adhesion protein-induced cell layer [44–46]. On the other hand, the similarly shaped hydrophobic acrylic IOLs with stronger adhesive force were shown to inhibit LEC migration and PCO more than IOLs with weaker adhesive force [50]. Arjun et al. [51] proved fibronectin adsorption of simulated posterior capsules significantly reduced simulated LEC infiltration between hydrophobic acrylic IOLs and the posterior capsules by increasing adhesion forces compared with fibronectin-free controls. Additionally, LECs slow down the rate of the differentiation once they are well attached [52].

Previous studies have shown that the ultraviolet/ozone (UV/O₃) or argon plasma-treated IOL surfaces could enhance LEC and protein adhesion, thereby solidifying the binding between the IOL and posterior capsule membrane [53]. Both UV/O₃ treatment and argon plasma treatment increased nitrogen substituents and functional OH and COOH functional groups, thus improve surface characteristics (e.g., wettability and adhesion).

Additionally, the COOH groups are highly adhesive to protein fibronectin [54]. The post-treated IOLs significantly inhibited PCO formation in comparison to control IOLs, and the UV/O₃ treatment was more effective than the argon plasma treatment [53]. Additionally, UV/O₃ treatment causes little damage to the IOL surface, whereas argon plasma may promote surface deterioration through an etching effect. Farukhi et al. [55] used UV/O₃ treatment to modify the posterior surface of IOLs, which achieved similar PCO prevention effects in in vivo animal experiments.

The RGD peptide (Arg-Gly-Asp sequence) is the primary functional motif of fibronectin that promotes cell adhesion [45,46,56]. The RGD modification method has been widely studied for promoting cell adhesion onto material surfaces in cancer therapy and diagnosis [57]. The biomimetic strategy of RGD peptide-grafting on the IOL surface has been demonstrated superiority in enhancing the LEC adhesion without inducing the EMT process of LECs in vitro experiments [58]. The surface modification did not produce a significant change in the optical and mechanical properties of IOLs. The IOL with RGD peptide-functionalization has the potential to reconstruct the sandwich structure of the IOL-LEC capsule biomaterial. However, the effect of PCO prophylaxis should be further confirmed by in vivo experiments. On the other hand, macrophages, fibroblastic cells, and other types of cells will recognize the RGD peptide via their surficial integrins and attach to RGD-functionalized surfaces non-discriminatorily [56,59]. The RGD-based strategy lacks biological specificity and thereby has no direct regulation effect on other cell processes, for example, cell differentiation.

2.3. Micro-Patterned IOLs

The edge design of IOLs is closely related to cell migration and PCO formation. Nishi et al. [60] first demonstrated that the sharp-edge design of IOLs could decrease PCO incidence in clinical practice by inhibiting LEC migration from the IOL edge to the central optical axis [61,62].

In fact, cell migration is based on the interaction of focal adhesions (proteins embedded in the cell membrane) with biomaterial interfaces. Additionally, the unique micro-surface or micro-patterned topography could direct specific biological behaviors, such as cell migration in the eyes, by regulating the placement of focal adhesions [63,64]. Magin et al. [65] reported that silicone protective membrane (PM) with different Sharklet micro-patterns could inhibit LEC migration on its surface in an in vitro PCO model compared to the PM without micro-patterns. Additionally, the micro-patterns protruding from the surface reduced migration more than the recessed features. Thus, Kramer et al. [66] implanted the Sharklet micro-patterned PM in the capsule after cataract surgery and then embedded the IOL in the PM device, which resulted in PCO inhibition. Subsequently, the research group directly incorporated a Sharklet micro-patterned membrane on the posterior surface of the IOL peripheral rim to effectively alleviate PCO severity [67].

The femtosecond laser (FL) processing of materials, known as laser ablation, is a facile and efficient technique for creating desired micro-patterned interfaces that control focal cell adhesion, migration, differentiation, and other behaviors [68–72]. For example, the FS-ablated electrospun scaffolds facilitate endothelial cell ingrowth and increase the M2 macrophage and overall cell infiltration [69]. Additionally, FL-patterned silicon substrates with micro-cone arrays were shown to work as a potential and valuable platform for patterning neurons into artificial networks [71]. Another study also investigated the effect of periodic nano-textured patterns on LEC behaviors. Here, the researchers innovatively prepared the micro-patterned IOL samples of poly(HEMA) using femtosecond laser (FL) microfabrication (Figure 4). These groove/ridge patterns inhibited the migration of the single and collective LECs in a width-dependent mode. The groove with a size comparable to the size of cells exhibited the most significant inhibition effect [73]. Additionally, the proliferative rates of LECs were also slightly decreased on the nano-textured patterned surface. Experiments in vivo demonstrated that the implantation of commercially available IOLs modified by the FL ablation did not induce intraocular inflammation, but effectively

reduced PCO severity for eight weeks. Furthermore, the FL induced ablation uses ultrashort laser pulses (~100 fs) to minimize thermal stress and collateral damage to materials, such as metal, ceramic, silicon, and polymer, resulting in stable and reproducible patterning processing. This facile and precise strategy for FL microfabrication is free of chemical treatment and allows for potential application in various biomaterials for regulating cell behaviors in biomedical devices and implants.

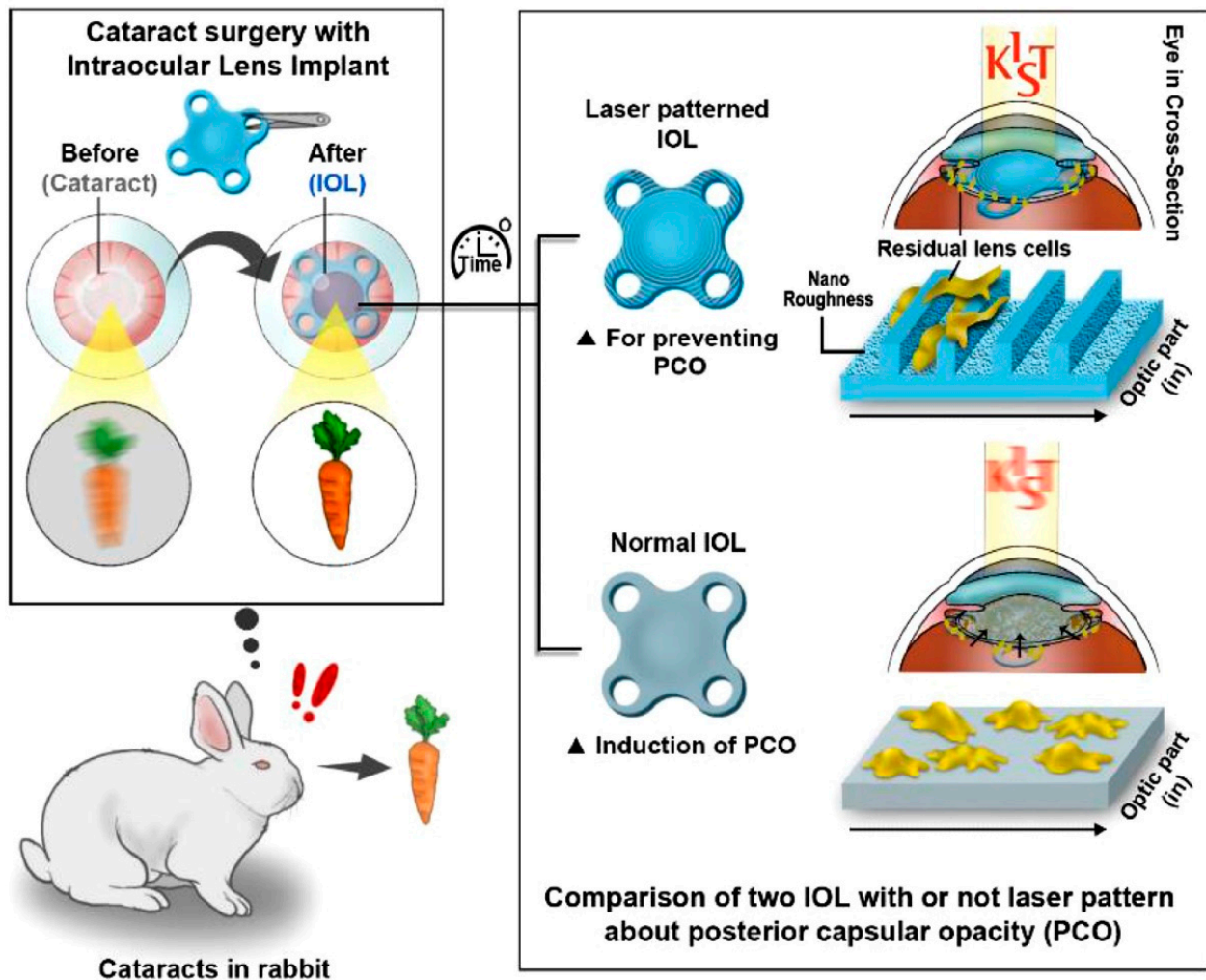


Figure 4. Schematic illustration of nano-textured micro-patterning on intraocular lens to suppress posterior capsular opacification by regulating cell behavior, such as adhesion, migration, and proliferation. Adapted with permission from Ref. [73]. Copyright 2020 Elsevier.

2.4. Photothermal IOLs

As a non-invasive treatment method, near-infrared (NIR) photothermal therapy (PTT) has been widely studied and used in the treatment of many diseases [74–76]. Nanomaterials with photothermal conversion properties can have a therapeutic role when converting light energy into heat energy under the irradiation of near-infrared light (700–1400 nm wavelength). Compared with drug treatment, PTT treatment minimizes collateral damage to other tissues through controllable nanomaterial distribution and laser irradiation. Carbon-based nanocomposites (such as graphene derivatives and carbon nanotubes), metal nanomaterials (such as Au nanorods), polymers, and other nanocomposites (such as polydopamine) are often used in the development of PTT because of their excellent photothermal conversion properties [77].

Recent literature of photothermal IOLs for PCO prophylaxis with in vivo results is summarized in Table 2. Lin et al. [76] took the lead in applying PTT to remove residual

LECs in the eye and prevent PCO (Figure 5). SiO₂-coated Au nanorods (Au@SiO₂) were integrated into the edge of the IOL using the activation immersion method to obtain nanostructured photothermal ring-modified IOLs. The photothermal IOL has excellent biocompatibility and optical properties, and has a regional restrictive photothermal effect. This allows it to accurately eliminate LECs in vivo and in vitro without affecting other tissues in the eye, thus inhibiting the progress of PCO.

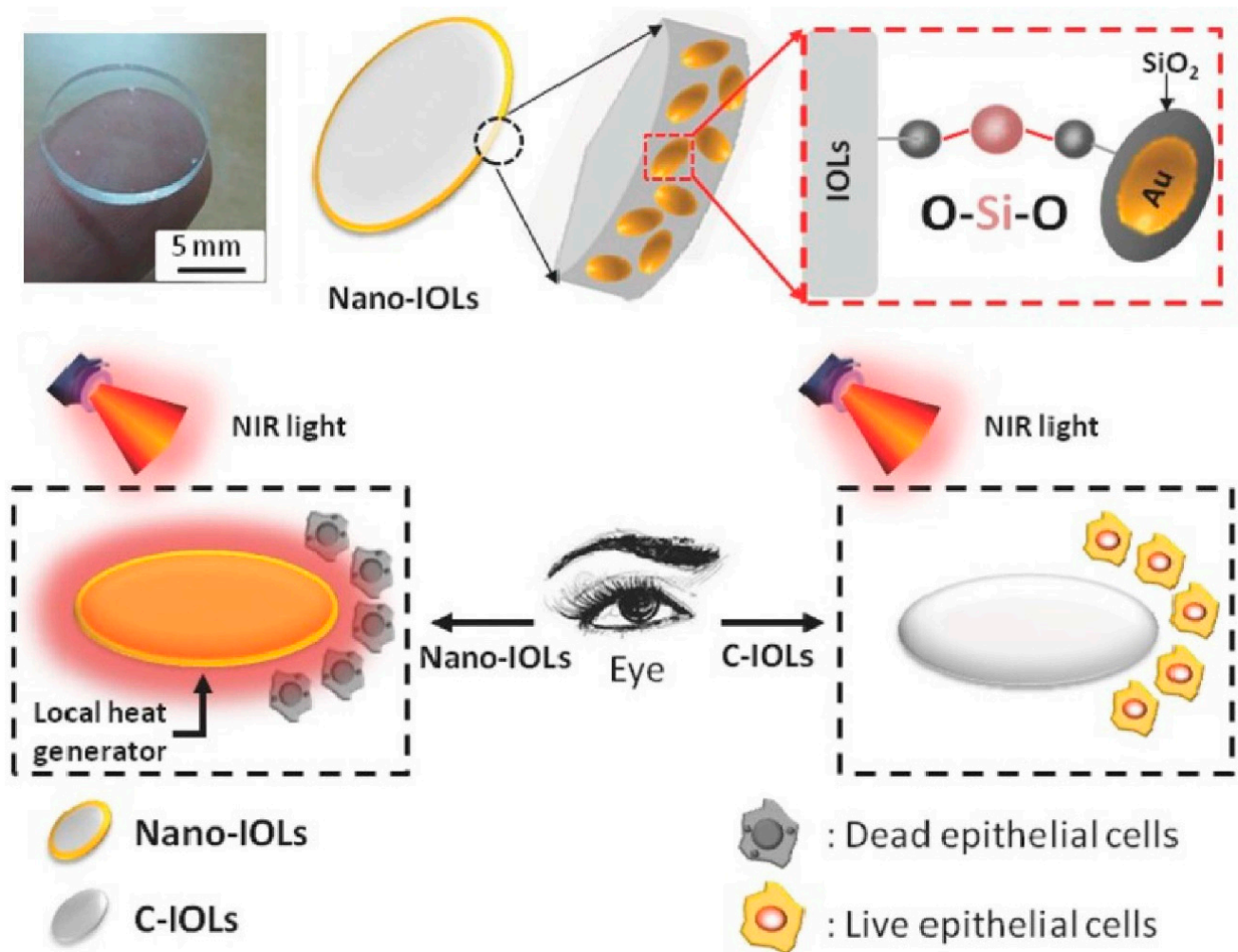


Figure 5. The schematic illustration of nano-IOLs with nanostructured Au@SiO₂ outer rim for prevention of posterior capsule opacification. Adapted with permission from Ref. [76]. Copyright 2017 John Wiley and Sons.

Because of the high cost, complex synthesis, and potential long-term cytotoxicity of gold nanomaterials, Xu et al. [78] used polydopamine (PDA) as the photothermal modification material for IOLs because it is easier to obtain and prepare and has better biocompatibility. The PDA coating was deposited on the surface of the rim annulus of the IOL by a CuSO₄/H₂O₂-triggered PDA rapid deposition technique. Compared with normal IOLs, the modified IOLs could play an influential role in sterilization and PCO prevention under NIR light irradiation. Reduced graphene oxide (rGO)-based nanocomposites have been widely used in PPT for advantages of pronounced photothermal conversion effect, facile synthesis, good biocompatibility, and low cost [79–81]. A previous study proved that repeated rGO exposure did not cause eye toxicity in mouse models [82]. Thus, our team fabricated a polyethyleneimine (PEI)/reduced graphene oxide (rGO) thin film coatings on IOL surface by controllable layer-by-layer self-assembly. The rGO@IOL implant with post-operative NIR irradiation showed promise for clinical applications in PCO prophylaxis [83].

Moreover, carboxylated CuInS/ZnS nano-quantum dots without toxic heavy metals have also been used to develop photothermal IOLs [84].

To enhance the efficiency of photothermal IOLs, Mao et al. [85] introduced a combined photothermal therapy and chemotherapy strategy for PCO prevention (Figure 6). BP-DOX@IOL was prepared by assembling the antiproliferative drug doxorubicin (DOX)-loaded black phosphorus (BP) nanosheets onto the non-optical section of the commercial IOL. The NIR light irradiation triggered the release of DOX loaded by BP-DOX@IOL and led to the area-limited heating of the IOL-modified area through the photothermal conversion effect, which jointly destroyed LECs efficiently. Although the BP-DOX@IOL inhibited the progress of PCO to a certain extent after implantation in the eye, the superposition of postoperative near-infrared light treatment achieved a more excellent PCO prevention effect.

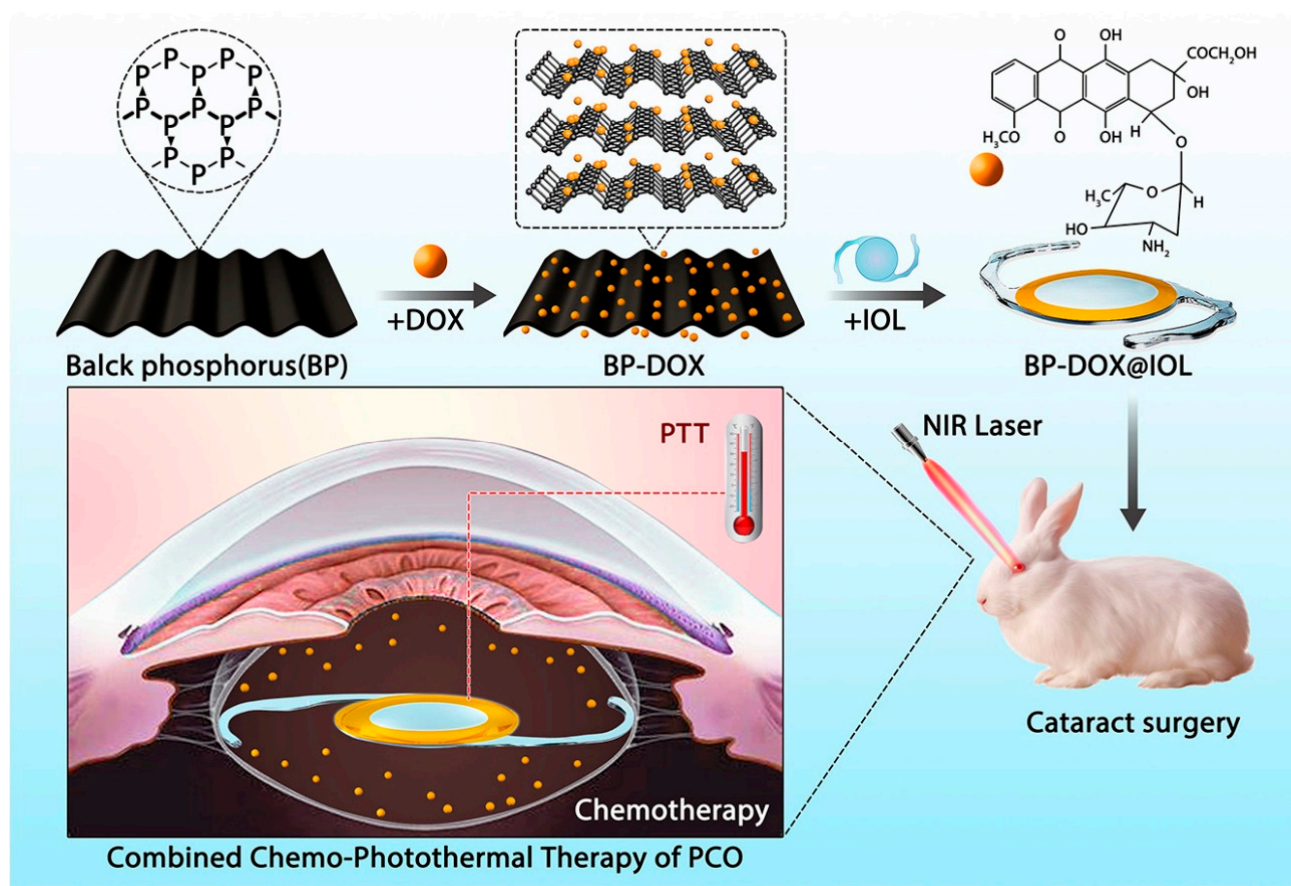


Figure 6. The schematic illustration of BP-based drug delivery system for synergistic chemo-photothermal therapy of PCO. Adapted with permission from Ref. [85]. Copyright 2021 Elsevier.

Table 2. Summary of reviewed literature of photothermal and photodynamic IOLs for PCO prophylaxis with in vivo results.

Composition	Mechanism	Main Fabrication Method	IOL Type	Observation	Irradiation Protocol In Vivo	Ref.
Au nanorods/SiO ₂	PTT	oxygen plasma-aided activation and immersion	commercial acrylic IOL	thirty days in rabbit model	808 nm, 3.3 W/cm ² , 10 min; once a week	[76]

Table 2. Cont.

Composition	Mechanism	Main Fabrication Method	IOL Type	Observation	Irradiation Protocol In Vivo	Ref.
PDA/PEI	PTT	CuSO ₄ /H ₂ O ₂ -triggered rapid deposition	acrylic IOL (66Vision Tech.)	four weeks in rabbit model	808 nm, 0.3 W/cm ² , 10 min; at day 1, 3, 5, 7, 14, 21, and 28	[78]
rGO/PEI	PTT	plasma-aided activation and layer-by-layer self-assembly	acrylic IOL (66Vision Tech.)	four weeks in rabbit model	808 nm, 2.5 W/cm ² , 10 min; three times in the first week, twice in the second week, and once a week in subsequent weeks	[84]
BP/DOX	PTT and chemotherapy	facial activation and immersion	acrylic IOL (Eyebright Medical Tech.)	four weeks in rabbit model	808 nm, 1 W/cm ² , 3 min; once a week from the second week	[85]
ICG/PLGA	PDT	facial activation, electrostatic attraction and immersion	commercial IOL	eight weeks in rabbit model	785 nm, 120 mW/cm ² , 10 min; every day for one month	[86]
α-CD-Ce-6/PPEGMA	PDT	RAFT technology and supramolecular self-assembly	acrylic IOL (66Vision Tech.)	two months in rabbit model	660 nm, 2.4 W/cm ² , 2 min; once a day in the first week	[87]
Ce-6/PDA	PDT	self-polymerization	acrylic IOL (66Vision Tech.)	four weeks in rabbit model	660 nm, 2.4 W/cm ² , 2 min; once a day for two weeks	[88]

2.5. Photodynamic IOLs

Photodynamic therapy (PDT) uses photosensitizers (PSs) under the irradiation of specific wavelengths of light to convert oxygen into reactive oxygen species (ROS), thereby inducing cell apoptosis. PDT therapy has been widely used to treat diseases with abnormal cell proliferation, such as cancer [89]. Similar to PTT treatment, PDT can minimize collateral damage to other tissues through controlled illumination and the distribution of photosensitive materials.

Previous PDT regimens that used photosensitizer solution directly perfuse the capsular bag followed by light exposure, which may induce potential ocular toxicity [90,91]. Therefore, modifying photosensitizer materials on the surface of IOL is a feasible approach (summarized in Table 2). Indocyanine green (ICG), a non-toxic and water-soluble dye, is a commonly used reagent in ophthalmic clinical applications and a photosensitizer material. Zhang et al. [86] prepared the photodynamic IOLs by adsorbing ICG molecules with positively-charged IOLs and sealing them with polylactic-co-glycolic acid (PLGA). Because of the presence of ICG, the light transmittance of the assembled ICG-IOL decreases. However, after implantation into the eye, with the gradual degradation of the PLGA, the water-soluble ICG is released from the IOL, and the light transmittance of the IOL can be restored. ICG-IOL combined with laser irradiation (785 nm) effectively reduced LEC activity and inhibited LEC proliferation and migration. In vivo implantation experiments showed that the ICG-IOL-based PDT system could significantly prevent the occurrence of PCO and had good biocompatibility.

Tang et al. [87] used chlorin e6 (Ce6) as a model photosensitizer and grafted it onto α-cyclodextrin (α-CD) molecules to synthesize α-CD-Ce6 (Figure 7). Subsequently, utilizing

the host–guest interaction between PEGMA and α -CD, a PEGMA- α -CD-Ce6 coating with photodynamic therapy function was constructed on the surface of the previously PEGMA brush-modified IOL [17,87]. In vitro experiments confirmed that the photodynamic IOL could generate a large amount of ROS under 660 nm laser irradiation, effectively inducing the apoptosis of LECs and inhibiting PCO development in vivo. In other research, this group attached Ce6 to the IOL surface when fabricating highly viscous PDA coatings via the rapid self-polymerization of dopamine. It also proved that the PDT coating based on the Ce6 photosensitizer could eliminate residual LECs significantly and prevent PCO formation [88].

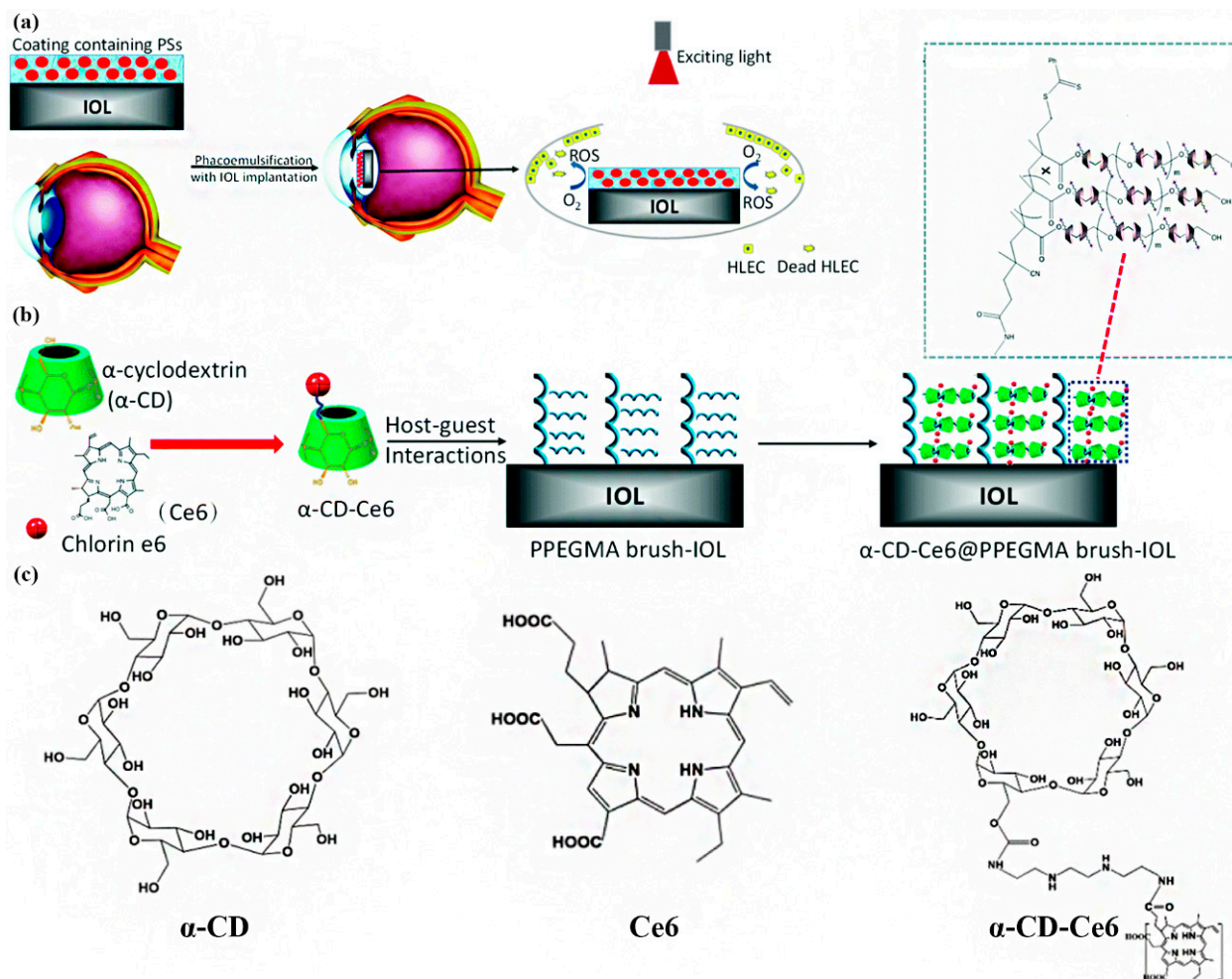


Figure 7. (a) Schematic illustration of an IOL with PS-containing coating and the process of PDT. (b) Schematic of the surface coating structure of the IOL. (c) Chemical structure of α -CD, Ce6, and α -CD-Ce6. Adapted with permission from Ref. [87]. Copyright 2021 Royal Society of Chemistry.

2.6. Drug-Loaded IOLs

As drug delivery devices for handling postoperative cataract complications, IOLs can improve drug bioavailability, ensure sustained drug release, and enhance patient compliance, with broad clinical application prospects [22]. Drug-loaded IOLs can be constructed using direct drug solution soaking, supercritical impregnation, drug reservoir attachment, and surface modification. To prevent the PCO, drug-loaded IOLs can transport anti-inflammatory, antineoplastic, anti-cell migration, or anti-EMT drugs into the capsular bag [22,23]. Thus, the reviewed literature of drug-loaded IOLs for PCO prophylaxis with in vivo results is summarized in Table 3.

It has been suggested that the inflammatory response after cataract surgery induces LEC proliferation, migration, EMT, and other cell behaviors, which may accelerate the

process of PCO [92]. The cyclooxygenase-2 (COX-2) level in LECs is associated with PCO development, and it is often elevated by injury or inflammatory cytokines [93]. Nonsteroidal anti-inflammatory drugs (NSAIDs) exert anti-inflammatory effects by inhibiting COX-2. After finding that the selective NSAIDs Celecoxib (CXB) inhibited the proliferation of LECs in vitro [94], Brookshire et al. [95] implanted IOLs into the eyes of experimental dogs after incubating IOLs in CXB solution, and this effectively reduced the postoperative inflammation. In the fourth week, the CXB-IOL group showed a better PCO prevention effect than the group treated by another COX-2 inhibitor, namely, bromfenac (BF) eye drops. However, the long-term (56 weeks) PCO prevention effect was significantly lower than the BF eye drops-treated group. Zhang et al. [96] pointed out that BF can inhibit the transforming growth factor- β 2 (TGF- β 2) through the signal-regulated kinase (ERK)/glycogen synthase kinase-3 β (GSK-3 β)/Snail signaling pathway. The team fabricated BF-loaded PLGA coatings on the haptic region of the IOL by ultrasonic spraying. BF-PLGA-IOL inhibited PCO formation in rabbit PCO models, which was more effective than the BF drops-treated group.

Antitumor drugs can generally be divided into cytotoxic drugs (such as 5-Fluorouracil (5-FU), DOX, and paclitaxel (PAC)) and non-cytotoxic drugs (such as gefitinib and erlotinib) [23]. However, the safety and efficacy of antineoplastic drugs used in the eyes require close attention. To reduce the toxicity of 5-FU, Huang et al. [97] prepared 5-FU-loaded CHI nanoparticles (NPs) and surface-modified IOLs with drug-loaded nanoparticles, which could sustainably release 5-FU after being implanted into the eye. The released 5-FU then inhibited LEC proliferation and promoted LEC apoptosis. Han et al. [98] prepared DOX-incorporated chitosan (CHI) NPs using a sodium tripolyphosphate (TPP) gel method. The positively charged CHI-TPP-DOX nanoparticles (CTDNPs) and the negatively charged heparin (HEP) self-assembled layer-by-layer on the IOL surface through electrostatic interaction to obtain the (HEP/CTDNP)_n multilayer-modified IOL. The LEC adhesion, proliferation, and migration on the modified IOL surface were significantly inhibited because of the surface hydrophilic modification combined with the drug-loading modification. This IOL effectively reduced the formation of PCO and the Soemmerring's ring (SR). Similar studies focused on IOL modification by hydrophilic anti-biofouling coatings loaded with DOX or PAC have also confirmed that such multifunctional IOLs may have great potential in preventing PCO. This makes up for the shortcomings of simple hydrophilic anti-biofouling IOLs with poor long-term PCO prevention [99,100]. In another study, drug-eluting IOLs loaded with the EGF inhibitors, gefitinib or erlotinib, could effectively slow LEC proliferation in ex vivo models of the human lens capsular bag. Additionally, sustainable drug release showed no toxicity to corneal endothelial cells [101,102].

Immunosuppressants, such as cyclosporin A (CsA) and rapamycin (RAPA), also have the potential to inhibit cellular proliferation and PCO formation [23]. For example, the CsA-loaded PLGA (CsA@PLGA) coating-modified IOL prepared by Teng et al. [103] reduced the degree of PCO within six months after implantation in rabbit models. Using the spin-coating technique, Lu et al. [104] designed and fabricated a centrifugally concentric ring-patterned drug-loaded PLGA coating (Figure 8). The concentric ring morphology, drug loading, and release properties were investigated, and the spin-coating parameters were optimized. Then, they created a concentric coating with a thin center and a thick rim, which is especially suitable for the surface modification of the intraocular lens without affecting the optical quality of the IOL. The CsA@PLGA coating-modified IOLs significantly inhibited cell proliferation and induced cell death via the autophagy-mediated cell death pathway. In vivo intraocular implant results confirmed its inhibitory effect on PCO. In another study, the researchers compared the preventive effects of RAPA intraoperative capsular bag perfusion, postoperative RAPA eye drops, and PLGA coating-modified IOLs loaded with RAPA on PCO prevention [105]. The results showed that in the RAPA-PLGA-IOL group, the anterior RAPA concentration reached a peak at 4 days after surgery and continued to release RAPA for up to 8 weeks. Compared with the control group, only the

RAPA-PLGA-IOL group can greatly reduce the degree of posterior capsular opacity, and there is no statistical difference in the degree of PCO among the other groups.

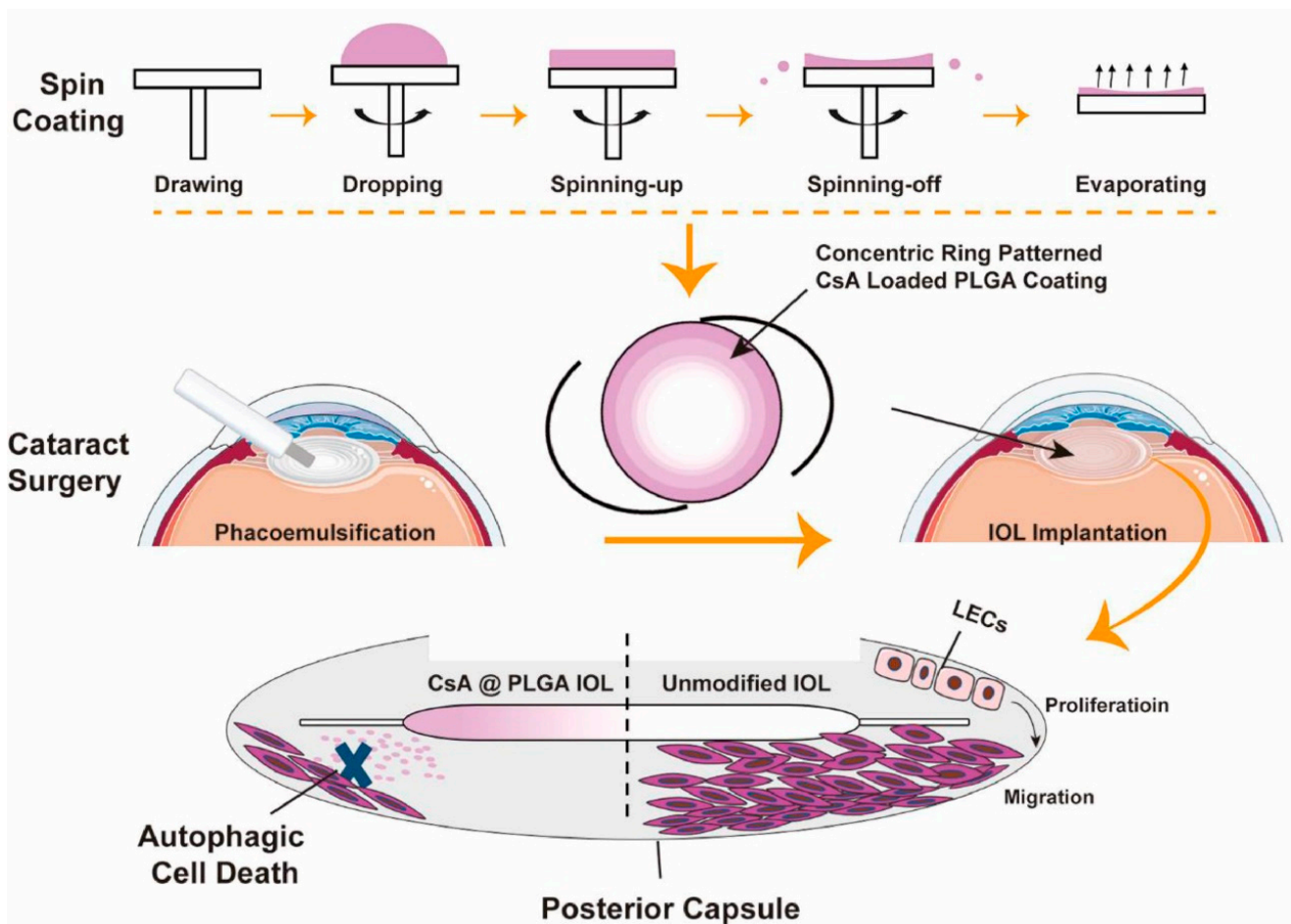


Figure 8. Schematic illustration of intraocular lens modified by centrifugally concentric ring-patterned drug-loaded PLGA coating for posterior capsular opacification prevention. Adapted with permission from Ref. [104]. Copyright 2022 Elsevier.

EMT usually demonstrates the loss of cell polarity and adhesion and the acquisition of migration and invasion capabilities. This is accompanied by the production of large amounts of extracellular matrix and the inhibition of cell apoptosis simultaneously. Furthermore, the cell migration and EMT process play essential roles in PCO pathogenesis. Methotrexate intraocular lenses prepared by supercritical impregnation reduce cellular fibrosis by inhibiting the EMT process [106]. Moreover, TGF- β is a key signaling molecule that induces LEC migration and the EMT process, which is usually used to construct EMT models [107]. The occurrence and development of PCO are expected to be inhibited by targeting TGF- β , TGF- β receptors, and their upstream and downstream signaling pathways. Sun et al. [108] successfully immobilized the anti-TGF- β 2 antibody on the IOL surface by plasma pretreatment and layer-by-layer self-assembly technology. These IOLs maintained stability and immune activity for at least three months. Anti-TGF- β 2 antibody-functionalized IOLs can directly target and bind TGF- β 2 molecules after implantation in the capsular bag, thereby inhibiting the TGF- β 2-induced LEC migration and EMT process after cataract surgery. As mentioned above, the molecular mechanism of bromfenac sodium targeting the TGF- β 2 signaling pathway is used to inhibit the cell migration and EMT process of LECs [96].

Table 3. Summary of reviewed literature of drug-loaded IOLs for PCO prophylaxis with in vivo results.

Drug	Other Composition	Mechanism	Main Loading Method	Loading Dosage	IOL Type	Observation	Ref.
CXB	none	not verified in the article	immersion	unclear	acrylic IOL	56 weeks in dog model	[95]
BF	PLGA	inhibit cell migration and TGF- β 2-induced EMT	ultrasonic spray technique	$\approx 100 \mu\text{g}/\text{IOL}$ of BF	acrylic IOL (Wuxi Vision PRO)	four weeks in rabbit model	[96]
5-FU	CHI	inhibit cell proliferation and promote cell apoptosis	fluorine ion beam-aided activation and immersion	$\approx 19.55 \pm 1.31 \text{ mg}/\text{IOL}$ of 5-FU	PMMA IOL (CJ55, Rafi Systems)	four weeks in rabbit model	[97]
DOX	CHI/TPP/HEP	inhibit cell adhesion, proliferation, and migration	ionic gelation, surficial activation, and layer-by-layer self-assembly	unclear	acrylic IOL (66Vision Tech.)	two months in rabbit model	[98]
DOX	PDA/MPC	inhibit cell adhesion, proliferation	self-polymerization and immersion	$\approx 2.8 \mu\text{g}/\text{IOL}$ of DOX	acrylic IOL (66Vision Tech.)	six weeks in rabbit model	[99]
CsA	PLGA	inhibit cell proliferation and promote autophagy-mediated cell death	spin-coating technique	unclear	acrylic IOL (66Vision Tech.)	four weeks in rabbit model	[104]
RAPA	PLGA	not verified in the article	proprietary spray technique	unclear	PMMA IOL (Suzhou Medical Instrument)	three months in rabbit model	[105]

3. Biosecurity of IOLs in PCO Prophylaxis

Biosecurity issues of modified IOLs using different strategies for PCO prevention still need more attention and exploration. Researchers usually perform histopathology examinations of other eye tissues, including cornea, iris, and retina, to illustrate the biosecurity in IOLs. Nonetheless, they should also attach more importance to detections of intraocular pressure (IOP), corneal endothelial cells, and visual electrophysiology in vivo experiments. The IOP reflects the circulation situation of aqueous humor. Corneal endothelial cells are vital for keeping the cornea transparent. Additionally, visual electrophysiology (such as electroretinogram) demonstrates the retinal function.

Photothermal IOLs have nowadays been shown to exert a local heating effect and kill LECs in a limited field, as demonstrated by in vitro and in vivo experiments [76,78,83,84]. Since ROS generated in the PDT strategy has a short action distance (<20 nm) and limited lifetime (<40 ns), photodynamic IOLs were effective in killing adherent LECs on the surface and alleviated toxicity to other eye tissues [86,87]. Approaches of PTT and PDT for PCO prevention caused no significant changes in IOP and corneal endothelial cell count [85,86]. However, researchers have not achieved direct and accurate monitoring of intraocular temperature change. Additionally, new temperature monitoring technology is needed to help researchers optimize the assembling of photothermal materials and the use of illumination power. Nevertheless, retinal toxicity is a significant issue when applying photothermal or photodynamic IOLs with light irradiation. Mao et al. performed an electroretinogram test and found the retinal function stayed normal in the group of BP-

DOX@IOL implantation with 808 nm laser irradiation treatment [85]. The drug-loaded IOLs are not yet used in clinical studies since it is vital to ensure that those pharmacological agents cause no effect on other ocular tissues. More specifically, toxicity to the corneal endothelium leads to the decompensation and opacification of the cornea [5,22,23]. Thus, we recommend that functional and structural analyses for evaluating the biocompatibility and biosecurity of modified IOLs be combined with specific treatments.

4. Conclusions and Future Perspectives

Scientists have developed different surface-modified IOLs using different strategies to disrupt PCO formation. Anti-biofouling IOLs can effectively resist the adhesion of proteins, cells, and even bacteria to reduce the intraocular inflammatory response after cataract surgery. Decreased LEC adhesion and migration on the IOL surface can reduce PCO incidence. Adhesion-enhanced IOLs can adhere more closely to the posterior capsule to form a sandwich structure of the IOL, monolayer LECs, and posterior capsule membrane, promoting LEC adhesion to inhibit LEC proliferation and differentiation, thereby preventing PCO. The surface micro-patterned IOL utilizes the specially designed surface topography to regulate LEC migration behavior to the center of the posterior capsule, effectively suppressing the opacity of the posterior capsule. Photothermal and photodynamic IOLs have introduced PTT and PDT therapy, which can safely and effectively remove residual LECs. Through controllable irradiation of specific wavelength light and distribution of photothermal materials or photosensitizers, PTT and PDT strategies will not damage other ocular tissues outside IOLs. Drug-loaded IOLs inhibit PCO development by loading various drugs that regulate the proliferation, migration, EMT, and other behaviors of residual LECs.

However, there are still some problems waiting to be solved in the future if we want to apply these new types of IOLs for PCO prevention in the clinical. The first one is biosecurity, discussed in Section 3. Researchers should perform rigorous and precise approaches to evaluating the use of laser or light irradiation and establish relatively uniform standards for the ophthalmic treatment of PCO. Certain issues, such as controlled and sustained release and ocular toxicity of drugs, require more in-depth research to ensure intraocular safety and the effectiveness of PCO prevention. The pharmaceuticals will ultimately be released from drug-loaded IOLs and lose their effect once the concentration in the lens capsule decreases below the effective concentration. Nonetheless, PTT and PDT strategies can be performed repeatedly under unlimited time constraints since the photothermal and photodynamic coatings can be stable on IOL surfaces. Additionally, anti-biofouling, enhance-adhesive, or micro-patterned modifications are also retained for a longer period of time than the drug-loading modification. Pharmacotherapy can be combined with other non-pharmaceutical strategies. On the other hand, methods for only regulating LECs behaviors, not killing, can be combined with methods for eliminating residual LECs. A single functional IOL may be less effective in long-term PCO prevention; thus, developing multifunctional IOLs united with different surface modifications can generate a more effective PCO prevention system. In vitro cell experiments and in vivo animal PCO model experiments have confirmed that many surface-modified IOLs have excellent biocompatibility and PCO prevention effects. However, there is still a lack of more reliable, clinically relevant research data, which requires further investigation.

The surface-modified intraocular lenses with different functions require the cross-integration of multidisciplinary theoretical knowledge, such as materials science, medicine, pharmacology, and cell biology. They have broad clinical application prospects in the future prevention and treatment of PCO.

Author Contributions: Y.Z., C.Z. and S.C. collected the information and drafted and revised the manuscript. J.H. contributed to collecting information and editing the manuscript. L.S. contributed to revised the manuscript. Y.Y. directed the work and finalized the manuscript. All authors have read and agreed to the published version of the manuscript.

Funding: This project was supported by the National Natural Science Foundation of China (Grant No. 82070938) and Natural Science Foundation of Zhejiang Province (Grant No. LY20H120011).

Institutional Review Board Statement: Not applicable.

Informed Consent Statement: Not applicable.

Data Availability Statement: Not applicable.

Conflicts of Interest: The authors declare no conflict of interest.

References

- Liu, Y.; Wilkins, M.; Kim, T.; Malyugin, B.; Mehta, J.S. Cataracts. *Lancet* **2017**, *390*, 600–612. [CrossRef]
- Chen, X.; Xu, J.; Chen, X.; Yao, K. Cataract: Advances in Surgery and Whether Surgery Remains the Only Treatment in Future. *Adv. Ophthalmol. Pract. Res.* **2021**, *1*, 100008. [CrossRef]
- Allen, D.; Vasavada, A. Cataract and Surgery for Cataract. *BMJ* **2006**, *333*, 128–132. [CrossRef] [PubMed]
- Wormstone, I.M.; Wang, L.; Liu, C.S.C. Posterior Capsule Opacification. *Exp. Eye Res.* **2009**, *88*, 257–269. [CrossRef]
- Nibourg, L.M.; Gelens, E.; Kuijjer, R.; Hooymans, J.M.M.; van Kooten, T.G.; Koopmans, S.A. Prevention of Posterior Capsular Opacification. *Exp. Eye Res.* **2015**, *136*, 100–115. [CrossRef]
- Medsinge, A.; Nischal, K.K. Pediatric Cataract: Challenges and Future Directions. *Clin. Ophthalmol.* **2015**, *9*, 77–90. [CrossRef]
- Karahan, E.; Er, D.; Kaynak, S. An Overview of Nd:YAG Laser Capsulotomy. *Med. Hypothesis Discov. Innov. Ophthalmol.* **2014**, *3*, 45–50.
- Steinert, R.F.; Puliafito, C.A.; Kumar, S.R.; Dudak, S.D.; Patel, S. Cystoid Macular Edema, Retinal Detachment, and Glaucoma after Nd:YAG Laser Posterior Capsulotomy. *Am. J. Ophthalmol.* **1991**, *112*, 373–380. [CrossRef]
- Wesolosky, J.D.; Tennant, M.; Rudnisky, C.J. Rate of Retinal Tear and Detachment after Neodymium:YAG Capsulotomy. *J. Cataract Refract. Surg.* **2017**, *43*, 923–928. [CrossRef]
- Thompson, J.; Lakhani, N. Cataracts. *Prim. Care Clin. Off. Pract.* **2015**, *42*, 409–423. [CrossRef]
- Wormstone, I.M.; Wormstone, Y.M.; Smith, A.J.O.; Eldred, J.A. Posterior Capsule Opacification: What’s in the Bag? *Prog. Retin. Eye Res.* **2021**, *82*, 100905. [CrossRef]
- Amon, M. Biocompatibility of Intraocular Lenses. *J. Cataract Refract. Surg.* **2001**, *27*, 178–179. [CrossRef]
- Saika, S. Relationship between Posterior Capsule Opacification and Intraocular Lens Biocompatibility. *Prog. Retin. Eye Res.* **2004**, *23*, 283–305. [CrossRef]
- Özyol, P.; Özyol, E.; Karel, F. Biocompatibility of Intraocular Lenses. *Turk. J. Ophthalmol.* **2017**, *47*, 221–225. [CrossRef]
- Krall, E.M.; Arlt, E.M.; Jell, G.; Strohmaier, C.; Moussa, S.; Dexl, A.K. Prospective Randomized Intraindividual Comparison of Posterior Capsule Opacification after Implantation of an IOL with and without Heparin Surface Modification. *J. Refract. Surg.* **2015**, *31*, 466–472. [CrossRef]
- Bozukova, D.; Pagnoulle, C.; De Pauw-Gillet, M.-C.; Desbief, S.; Lazzaroni, R.; Ruth, N.; Jérôme, R.; Jérôme, C. Improved Performances of Intraocular Lenses by Poly(Ethylene Glycol) Chemical Coatings. *Biomacromolecules* **2007**, *8*, 2379–2387. [CrossRef]
- Lin, Q.; Tang, J.; Han, Y.; Xu, X.; Hao, X.; Chen, H. Hydrophilic Modification of Intraocular Lens via Surface Initiated Reversible Addition-Fragmentation Chain Transfer Polymerization for Reduced Posterior Capsular Opacification. *Colloids Surf. B Biointerfaces* **2017**, *151*, 271–279. [CrossRef]
- Lan, X.; Lei, Y.; He, Z.; Yin, A.; Li, L.; Tang, Z.; Li, M.; Wang, Y. A Transparent Hydrophilic Anti-Biofouling Coating for Intraocular Lens Materials Prepared by “Bridging” of the Intermediate Adhesive Layer. *J. Mater. Chem. B* **2021**, *9*, 3696–3704. [CrossRef]
- Barbour, W.; Saika, S.; Miyamoto, T.; Ohnishi, Y. Biological Compatibility of Polymethyl Methacrylate, Hydrophilic Acrylic and Hydrophobic Acrylic Intraocular Lenses. *Ophthalmic Res.* **2005**, *37*, 255–261. [CrossRef]
- Lewis, A.C. Interleukin-6 in the Pathogenesis of Posterior Capsule Opacification and the Potential Role for Interleukin-6 Inhibition in the Future of Cataract Surgery. *Med. Hypotheses* **2013**, *80*, 466–474. [CrossRef]
- Huang, Q.; Cheng, G.P.-M.; Chiu, K.; Wang, G. Surface Modification of Intraocular Lenses. *Chin. Med. J.* **2016**, *129*, 206–214. [CrossRef]
- Topete, A.; Saramago, B.; Serro, A.P. Intraocular Lenses as Drug Delivery Devices. *Int. J. Pharm.* **2021**, *602*, 120613. [CrossRef]
- Zhang, R.; Xie, Z. Research Progress of Drug Prophylaxis for Lens Capsule Opacification after Cataract Surgery. *J. Ophthalmol.* **2020**, *2020*, 2181685. [CrossRef]
- Mylona, I.; Tsinopoulos, I. A Critical Appraisal of New Developments in Intraocular Lens Modifications and Drug Delivery Systems for the Prevention of Cataract Surgery Complications. *Pharmaceutics* **2020**, *13*, 448. [CrossRef]
- Cooksley, G.; Lacey, J.; Dymond, M.K.; Sandeman, S. Factors Affecting Posterior Capsule Opacification in the Development of Intraocular Lens Materials. *Pharmaceutics* **2021**, *13*, 860. [CrossRef]
- Sanchez-Cano, C.; Carril, M. Recent Developments in the Design of Non-Biofouling Coatings for Nanoparticles and Surfaces. *Int. J. Mol. Sci.* **2020**, *21*, 1007. [CrossRef]
- Leslie, D.C.; Waterhouse, A.; Berthet, J.B.; Valentin, T.M.; Watters, A.L.; Jain, A.; Kim, P.; Hatton, B.D.; Nedder, A.; Donovan, K.; et al. A Bioinspired Omniphobic Surface Coating on Medical Devices Prevents Thrombosis and Biofouling. *Nat. Biotechnol.* **2014**, *32*, 1134–1140. [CrossRef]

28. He, Z.; Yang, X.; Wang, N.; Mu, L.; Pan, J.; Lan, X.; Li, H.; Deng, F. Anti-Biofouling Polymers with Special Surface Wettability for Biomedical Applications. *Front. Bioeng. Biotechnol.* **2021**, *9*, 807357. [CrossRef]
29. Chan, H.-M.; Erathodiyil, N.; Wu, H.; Lu, H.; Zheng, Y.; Ying, J.Y. Calcium Cross-Linked Zwitterionic Hydrogels as Antifouling Materials. *Mater. Today Commun.* **2020**, *23*, 100950. [CrossRef]
30. Kang, S.; Choi, J.A.; Joo, C.-K. Comparison of Posterior Capsular Opacification in Heparin-Surface-Modified Hydrophilic Acrylic and Hydrophobic Acrylic Intraocular Lenses. *Jpn. J. Ophthalmol.* **2009**, *53*, 204–208. [CrossRef] [PubMed]
31. Lee, H.I.; Kim, M.K.; Ko, J.H.; Lee, H.J.; Wee, W.R.; Lee, J.H. The Efficacy of an Acrylic Intraocular Lens Surface Modified with Polyethylene Glycol in Posterior Capsular Opacification. *J. Korean Med. Sci.* **2007**, *22*, 502. [CrossRef]
32. Xu, X.; Tang, J.; Han, Y.; Wang, W.; Chen, H.; Lin, Q. Surface PEGylation of Intraocular Lens for PCO Prevention: An In Vivo Evaluation. *J. Biomater. Appl.* **2016**, *31*, 68–76. [CrossRef]
33. Monge, S.; Canticcioni, B.; Graillot, A.; Robin, J.-J. Phosphorus-Containing Polymers: A Great Opportunity for the Biomedical Field. *Biomacromolecules* **2011**, *12*, 1973–1982. [CrossRef]
34. Shigeta, M.; Tanaka, T.; Koike, N.; Yamakawa, N.; Usui, M. Suppression of Fibroblast and Bacterial Adhesion by MPC Coating on Acrylic Intraocular Lenses. *J. Cataract Refract. Surg.* **2006**, *32*, 859–866. [CrossRef]
35. Huang, X.; Yao, K.; Zhang, Z.; Zhang, Y.; Wang, Y. Uveal and Capsular Biocompatibility of an Intraocular Lens with a Hydrophilic Anterior Surface and a Hydrophobic Posterior Surface. *J. Cataract Refract. Surg.* **2010**, *36*, 290–298. [CrossRef]
36. Huang, X.; Li, H.; Lin, L.; Yao, K. Reduced Silicone Oil Adherence to Silicone Intraocular Lens by Surface Modification with 2-Methacryloyloxyethyl Phosphoryl-Choline. *Curr. Eye Res.* **2013**, *38*, 91–96. [CrossRef]
37. Han, Y.; Xu, X.; Tang, J.; Shen, C.; Lin, Q.; Chen, H. Bottom-up Fabrication of Zwitterionic Polymer Brushes on Intraocular Lens for Improved Biocompatibility. *Int. J. Nanomed.* **2016**, *12*, 127–135. [CrossRef]
38. Tan, X.; Zhan, J.; Zhu, Y.; Cao, J.; Wang, L.; Liu, S.; Wang, Y.; Liu, Z.; Qin, Y.; Wu, M.; et al. Improvement of Uveal and Capsular Biocompatibility of Hydrophobic Acrylic Intraocular Lens by Surface Grafting with 2-Methacryloyloxyethyl Phosphorylcholine-Methacrylic Acid Copolymer. *Sci. Rep.* **2017**, *7*, 40462. [CrossRef]
39. Wang, R.; Xia, J.; Tang, J.; Liu, D.; Zhu, S.; Wen, S.; Lin, Q. Surface Modification of Intraocular Lens with Hydrophilic Poly(Sulfobetaine Methacrylate) Brush for Posterior Capsular Opacification Prevention. *J. Ocul. Pharmacol. Ther.* **2021**, *37*, 172–180. [CrossRef]
40. Necas, J.; Bartosikova, L.; Brauner, P.; Kolar, J. Hyaluronic Acid (Hyaluronan): A Review. *Vet. Med.* **2008**, *53*, 397–411. [CrossRef]
41. Ravi Kumar, M.N.V. A Review of Chitin and Chitosan Applications. *React. Funct. Polym.* **2000**, *46*, 1–27. [CrossRef]
42. Lin, Q.; Xu, X.; Wang, B.; Shen, C.; Tang, J.; Han, Y.; Chen, H. Hydrated Polysaccharide Multilayer as an Intraocular Lens Surface Coating for Biocompatibility Improvements. *J. Mater. Chem. B* **2015**, *3*, 3695–3703. [CrossRef]
43. Wu, Q.; Liu, D.; Chen, W.; Chen, H.; Yang, C.; Li, X.; Yang, C.; Lin, H.; Chen, S.; Hu, N.; et al. Liquid-like Layer Coated Intraocular Lens for Posterior Capsular Opacification Prevention. *Appl. Mater. Today* **2021**, *23*, 100981. [CrossRef]
44. Linnola, R.J.; Holst, A. Evaluation of a 3-Piece Silicone Intraocular Lens with Poly(Methyl Methacrylate) Haptics. *J. Cataract Refract. Surg.* **1998**, *24*, 1509–1514. [CrossRef]
45. Linnola, R.J.; Werner, L.; Pandey, S.K.; Escobar-Gomez, M.; Znoiko, S.L.; Apple, D.J. Adhesion of Fibronectin, Vitronectin, Laminin, and Collagen Type IV to Intraocular Lens Materials in Pseudophakic Human Autopsy Eyes. Part 2: Explanted Intraocular Lenses. *J. Cataract Refract. Surg.* **2000**, *26*, 1807–1818. [CrossRef]
46. Linnola, R.J.; Werner, L.; Pandey, S.K.; Escobar-Gomez, M.; Znoiko, S.L.; Apple, D.J. Adhesion of Fibronectin, Vitronectin, Laminin, and Collagen Type IV to Intraocular Lens Materials in Pseudophakic Human Autopsy Eyes. Part 1: Histological Sections. *J. Cataract Refract. Surg.* **2000**, *26*, 1792–1806. [CrossRef]
47. Linnola, R.J. Sandwich Theory: Bioactivity-Based Explanation for Posterior Capsule Opacification. *J. Cataract Refract. Surg.* **1997**, *23*, 1539–1542. [CrossRef]
48. Heatley, C.J.; Spalton, D.J.; Kumar, A.; Jose, R.; Boyce, J.; Bender, L.E. Comparison of Posterior Capsule Opacification Rates between Hydrophilic and Hydrophobic Single-Piece Acrylic Intraocular Lenses. *J. Cataract Refract. Surg.* **2005**, *31*, 718–724. [CrossRef]
49. Bertrand, V.; Bozukova, D.; Svaldo Lanero, T.; Huang, Y.-S.; Schol, D.; Rosière, N.; Grauwels, M.; Duwez, A.-S.; Jérôme, C.; Pagnouille, C.; et al. Biointerface Multiparametric Study of Intraocular Lens Acrylic Materials. *J. Cataract Refract. Surg.* **2014**, *40*, 1536–1544. [CrossRef]
50. Katayama, Y.; Kobayakawa, S.; Yanagawa, H.; Tochikubo, T. The Relationship between the Adhesion Characteristics of Acrylic Intraocular Lens Materials and Posterior Capsule Opacification. *Ophthalmic Res.* **2007**, *39*, 276–281. [CrossRef]
51. Jaitli, A.; Roy, J.; Chatila, A.; Liao, J.; Tang, L. Role of Fibronectin and IOL Surface Modification in IOL: Lens Capsule Interactions. *Exp. Eye Res.* **2022**, *221*, 109135. [CrossRef]
52. Arita, T.; Lin, L.R.; Susan, S.R.; Reddy, V.N. Enhancement of Differentiation of Human Lens Epithelium in Tissue Culture by Changes in Cell-Substrate Adhesion. *Investig. Ophthalmol. Vis. Sci.* **1990**, *31*, 2395–2404.
53. Matsushima, H.; Iwamoto, H.; Mukai, K.; Obara, Y. Active Oxygen Processing for Acrylic Intraocular Lenses to Prevent Posterior Capsule Opacification. *J. Cataract Refract. Surg.* **2006**, *32*, 1035–1040. [CrossRef]
54. Nakanishi, J.; Kikuchi, Y.; Takarada, T.; Nakayama, H.; Yamaguchi, K.; Maeda, M. Photoactivation of a Substrate for Cell Adhesion under Standard Fluorescence Microscopes. *J. Am. Chem. Soc.* **2004**, *126*, 16314–16315. [CrossRef]

55. Farukhi, A.M.; Werner, L.; Kohl, J.C.; Gardiner, G.L.; Ford, J.R.; Cole, S.C.; Vasavada, S.A.; Noristani, R.; Mamalis, N. Evaluation of Uveal and Capsule Biocompatibility of a Single-Piece Hydrophobic Acrylic Intraocular Lens with Ultraviolet–Ozone Treatment on the Posterior Surface. *J. Cataract Refract. Surg.* **2015**, *41*, 1081–1087. [CrossRef]
56. Ruoslahti, E.; Pierschbacher, M.D. New Perspectives in Cell Adhesion: RGD and Integrins. *Science* **1987**, *238*, 491–497. [CrossRef]
57. Danhier, F.; Le Breton, A.; Pr eat, V. RGD-Based Strategies to Target Alpha(v) Beta(3) Integrin in Cancer Therapy and Diagnosis. *Mol. Pharm.* **2012**, *9*, 2961–2973. [CrossRef]
58. Huang, Y.-S.; Bertrand, V.; Bozukova, D.; Pagnouille, C.; Labrug ere, C.; De Pauw, E.; De Pauw-Gillet, M.-C.; Durrieu, M.-C. RGD Surface Functionalization of the Hydrophilic Acrylic Intraocular Lens Material to Control Posterior Capsular Opacification. *PLoS ONE* **2014**, *9*, e114973. [CrossRef]
59. Ruoslahti, E. RGD and Other Recognition Sequences for Integrins. *Annu. Rev. Cell. Dev. Biol.* **1996**, *12*, 697–715. [CrossRef]
60. Nishi, O.; Nishi, K.; Wickstr om, K. Preventing Lens Epithelial Cell Migration Using Intraocular Lenses with Sharp Rectangular Edges. *J. Cataract Refract. Surg.* **2000**, *26*, 1543–1549. [CrossRef]
61. Cheng, J.; Wei, R.; Cai, J.; Xi, G.; Zhu, H.; Li, Y.; Ma, X. Efficacy of Different Intraocular Lens Materials and Optic Edge Designs in Preventing Posterior Capsular Opacification: A Meta-Analysis. *Am. J. Ophthalmol.* **2007**, *143*, 428–436. [CrossRef]
62. Kohnen, T.; Fabian, E.; Gerl, R.; Hunold, W.; H utz, W.; Strobel, J.; Hoyer, H.; Mester, U. Optic Edge Design as Long-Term Factor for Posterior Capsular Opacification Rates. *Ophthalmology* **2008**, *115*, 1308–1313, 1314.e1–3. [CrossRef]
63. McHugh, K.J.; Saint-Geniez, M.; Tao, S.L. Topographical Control of Ocular Cell Types for Tissue Engineering: Topographical Control of Ocular Cell Types. *J. Biomed. Mater. Res.* **2013**, *101*, 1571–1584. [CrossRef]
64. Xia, N.; Thodeti, C.K.; Hunt, T.P.; Xu, Q.; Ho, M.; Whitesides, G.M.; Westervelt, R.; Ingber, D.E. Directional Control of Cell Motility through Focal Adhesion Positioning and Spatial Control of Rac Activation. *FASEB J.* **2008**, *22*, 1649–1659. [CrossRef]
65. Magin, C.M.; May, R.M.; Drinker, M.C.; Cuevas, K.H.; Brennan, A.B.; Reddy, S.T. Micropatterned Protective Membranes Inhibit Lens Epithelial Cell Migration in Posterior Capsule Opacification Model. *Trans. Vis. Sci. Technol.* **2015**, *4*, 9. [CrossRef]
66. Kramer, G.D.; Werner, L.; MacLean, K.; Farukhi, A.; Gardiner, G.L.; Mamalis, N. Evaluation of Stability and Capsular Bag Opacification with a Foldable Intraocular Lens Coupled with a Protective Membrane in the Rabbit Model. *J. Cataract Refract. Surg.* **2015**, *41*, 1738–1744. [CrossRef]
67. Ellis, N.; Werner, L.; Balendiran, V.; Shumway, C.; Jiang, B.; Mamalis, N. Posterior Capsule Opacification Prevention by an Intraocular Lens Incorporating a Micropatterned Membrane on the Posterior Surface. *J. Cataract Refract. Surg.* **2020**, *46*, 6. [CrossRef]
68. Ranella, A.; Barberoglou, M.; Bakogianni, S.; Fotakis, C.; Stratakis, E. Tuning Cell Adhesion by Controlling the Roughness and Wettability of 3D Micro/Nano Silicon Structures. *Acta Biomater.* **2010**, *6*, 2711–2720. [CrossRef]
69. Lee, B.L.-P.; Jeon, H.; Wang, A.; Yan, Z.; Yu, J.; Grigoropoulos, C.; Li, S. Femtosecond Laser Ablation Enhances Cell Infiltration into Three-Dimensional Electrospun Scaffolds. *Acta Biomater.* **2012**, *8*, 2648–2658. [CrossRef]
70. Jeon, H.; Koo, S.; Reese, W.M.; Loskill, P.; Grigoropoulos, C.P.; Healy, K.E. Directing Cell Migration and Organization via Nanocrater-Patterned Cell-Repellent Interfaces. *Nat. Mater.* **2015**, *14*, 918–923. [CrossRef]
71. Simitzi, C.; Efsthathopoulos, P.; Kourgiantaki, A.; Ranella, A.; Charalampopoulos, I.; Fotakis, C.; Athanassakis, I.; Stratakis, E.; Gravanis, A. Laser Fabricated Discontinuous Anisotropic Microconical Substrates as a New Model Scaffold to Control the Directionality of Neuronal Network Outgrowth. *Biomaterials* **2015**, *67*, 115–128. [CrossRef] [PubMed]
72. Jun, I.; Chung, Y.-W.; Heo, Y.-H.; Han, H.-S.; Park, J.; Jeong, H.; Lee, H.; Lee, Y.B.; Kim, Y.-C.; Seok, H.-K.; et al. Creating Hierarchical Topographies on Fibrous Platforms Using Femtosecond Laser Ablation for Directing Myoblasts Behavior. *ACS Appl. Mater. Interfaces* **2016**, *8*, 3407–3417. [CrossRef] [PubMed]
73. Seo, Y.; Kim, S.; Lee, H.S.; Park, J.; Lee, K.; Jun, I.; Seo, H.; Kim, Y.J.; Yoo, Y.; Choi, B.C.; et al. Femtosecond Laser Induced Nano-Textured Micropatterning to Regulate Cell Functions on Implanted Biomaterials. *Acta Biomater.* **2020**, *116*, 138–148. [CrossRef] [PubMed]
74. Li, J.; Zhang, W.; Ji, W.; Wang, J.; Wang, N.; Wu, W.; Wu, Q.; Hou, X.; Hu, W.; Li, L. Near Infrared Photothermal Conversion Materials: Mechanism, Preparation, and Photothermal Cancer Therapy Applications. *J. Mater. Chem. B* **2021**, *9*, 7909–7926. [CrossRef]
75. Ye, Y.; He, J.; Qiao, Y.; Qi, Y.; Zhang, H.; Santos, H.A.; Zhong, D.; Li, W.; Hua, S.; Wang, W.; et al. Mild Temperature Photothermal Assisted Anti-Bacterial and Anti-Inflammatory Nanosystem for Synergistic Treatment of Post-Cataract Surgery Endophthalmitis. *Theranostics* **2020**, *10*, 8541–8557. [CrossRef]
76. Lin, Y.-X.; Hu, X.-F.; Zhao, Y.; Gao, Y.-J.; Yang, C.; Qiao, S.-L.; Wang, Y.; Yang, P.-P.; Yan, J.; Sui, X.-C.; et al. Photothermal Ring Integrated Intraocular Lens for High-Efficient Eye Disease Treatment-Supply. *Adv. Mater.* **2017**, *29*, 1701617. [CrossRef]
77. Xu, J.; Yao, K.; Xu, Z. Nanomaterials with a Photothermal Effect for Antibacterial Activities: An Overview. *Nanoscale* **2019**, *11*, 8680–8691. [CrossRef]
78. Xu, J.; Li, H.; Hu, D.; Zhang, X.; Wang, W.; Ji, J.; Xu, Z.; Yao, K. Intraocular Lens with Mussel-Inspired Coating for Preventing Posterior Capsule Opacification via Photothermal Effect. *ACS Appl. Bio Mater.* **2021**, *4*, 3579–3586. [CrossRef]
79. Yang, K.; Feng, L.; Shi, X.; Liu, Z. Nano-Graphene in Biomedicine: Theranostic Applications. *Chem. Soc. Rev.* **2013**, *42*, 530–547. [CrossRef]
80. Dash, B.S.; Jose, G.; Lu, Y.-J.; Chen, J.-P. Functionalized Reduced Graphene Oxide as a Versatile Tool for Cancer Therapy. *Int. J. Mol. Sci.* **2021**, *22*, 2989. [CrossRef]

81. Robinson, J.T.; Tabakman, S.M.; Liang, Y.; Wang, H.; Casalongue, H.S.; Vinh, D.; Dai, H. Ultrasmall Reduced Graphene Oxide with High Near-Infrared Absorbance for Photothermal Therapy. *J. Am. Chem. Soc.* **2011**, *133*, 6825–6831. [CrossRef]
82. An, W.; Zhang, Y.; Zhang, X.; Li, K.; Kang, Y.; Akhtar, S.; Sha, X.; Gao, L. Ocular Toxicity of Reduced Graphene Oxide or Graphene Oxide Exposure in Mouse Eyes. *Exp. Eye Res.* **2018**, *174*, 59–69. [CrossRef]
83. Zhang, C.; Guo, Q.; Tong, Z.; Chen, S.; Mao, Z.; Yu, Y. Thin Film Nanoarchitectonics of Layer-by-Layer Assembly with Reduced Graphene Oxide on Intraocular Lens for Photothermal Therapy of Posterior Capsular Opacification. *J. Colloid Interface Sci.* **2022**, *619*, 348–358. [CrossRef]
84. Mao, Y.; Yu, S.; Kang, Y.; Zhang, D.; Wu, S.; Zhang, J.; Xiong, Y.; Li, M.; Zhang, J.; Wang, J.; et al. CuInS/ZnS Quantum Dots Modified Intraocular Lens for Photothermal Therapy of Posterior Capsule Opacification. *Exp. Eye Res.* **2021**, *202*, 108282. [CrossRef]
85. Mao, Y.; Li, M.; Wang, J.; Wang, K.; Zhang, J.; Chen, S.; Liu, X.; Liang, Q.; Gao, F.; Wan, X. NIR-Triggered Drug Delivery System for Chemo-Photothermal Therapy of Posterior Capsule Opacification. *J. Control. Release* **2021**, *339*, 391–402. [CrossRef]
86. Zhang, Z.; Huang, W.; Lei, M.; He, Y.; Yan, M.; Zhang, X.; Zhao, C. Laser-Triggered Intraocular Implant to Induce Photodynamic Therapy for Posterior Capsule Opacification Prevention. *Int. J. Pharm.* **2016**, *498*, 1–11. [CrossRef]
87. Tang, J.; Liu, S.; Han, Y.; Wang, R.; Xia, J.; Chen, H.; Lin, Q. Surface Modification of Intraocular Lenses via Photodynamic Coating for Safe and Effective PCO Prevention. *J. Mater. Chem. B* **2021**, *9*, 1546–1556. [CrossRef]
88. Qie, J.; Wen, S.; Han, Y.; Liu, S.; Shen, L.; Chen, H.; Lin, Q. A Polydopamine-Based Photodynamic Coating on the Intraocular Lens Surface for Safer Posterior Capsule Opacification Conquering. *Biomater. Sci.* **2022**, *10*, 2188–2197. [CrossRef]
89. Correia, J.H.; Rodrigues, J.A.; Pimenta, S.; Dong, T.; Yang, Z. Photodynamic Therapy Review: Principles, Photosensitizers, Applications, and Future Directions. *Pharmaceutics* **2021**, *13*, 1332. [CrossRef]
90. Koh, H.J.; Kang, S.J.; Lim, S.J.; Chu, Y.K.; Lee, S.C.; Kwon, O.W.; Kim, H.B. The Effect of Photodynamic Therapy with Rose Bengal on Posterior Capsule Opacification in Rabbit Eyes. *Ophthalmic Res.* **2002**, *34*, 107–112. [CrossRef]
91. Van Tenten, Y.; Schuitmaker, H.J.; De Groot, V.; Willekens, B.; Vrensen, G.F.J.M.; Tassignon, M.-J. A Preliminary Study on the Prevention of Posterior Capsule Opacification by Photodynamic Therapy with Bacteriochlorin A in Rabbits. *Ophthalmic Res.* **2002**, *34*, 113–118. [CrossRef]
92. Jiang, J.; Shihan, M.H.; Wang, Y.; Duncan, M.K. Lens Epithelial Cells Initiate an Inflammatory Response Following Cataract Surgery. *Investig. Ophthalmol. Vis. Sci.* **2018**, *59*, 4986–4997. [CrossRef]
93. Chandler, H.L.; Barden, C.A.; Lu, P.; Kusewitt, D.F.; Colitz, C.M.H. Prevention of Posterior Capsular Opacification through Cyclooxygenase-2 Inhibition. *Mol. Vis.* **2007**, *13*, 677–691.
94. Davis, J.L.; Yi, N.Y.; Salmon, J.H.; Charlton, A.N.; Colitz, C.M.H.; Gilger, B.C. Sustained-Release Celecoxib from Incubated Acrylic Intraocular Lenses Suppresses Lens Epithelial Cell Growth in an Ex Vivo Model of Posterior Capsule Opacity. *J. Ocul. Pharmacol. Ther.* **2012**, *28*, 359–368. [CrossRef]
95. Brookshire, H.L.; English, R.V.; Nadelstein, B.; Weigt, A.K.; Gift, B.W.; Gilger, B.C. Efficacy of COX-2 Inhibitors in Controlling Inflammation and Capsular Opacification after Phacoemulsification Cataract Removal. *Vet. Ophthalmol.* **2015**, *18*, 175–185. [CrossRef]
96. Zhang, X.; Lai, K.; Li, S.; Wang, J.; Li, J.; Wang, W.; Ni, S.; Lu, B.; Grzybowski, A.; Ji, J.; et al. Drug-Eluting Intraocular Lens with Sustained Bromfenac Release for Conquering Posterior Capsular Opacification. *Bioact. Mater.* **2021**, *9*, 343–357. [CrossRef]
97. Huang, X.; Wang, Y.; Cai, J.; Ma, X.; Li, Y.; Cheng, J.; Wei, R. Sustained Release of 5-Fluorouracil from Chitosan Nanoparticles Surface Modified Intra Ocular Lens to Prevent Posterior Capsule Opacification: An In Vitro and In Vivo Study. *J. Ocul. Pharmacol. Ther.* **2013**, *29*, 208–215. [CrossRef]
98. Han, Y.; Tang, J.; Xia, J.; Wang, R.; Qin, C.; Liu, S.; Zhao, X.; Chen, H.; Lin, Q. Anti-Adhesive and Antiproliferative Synergistic Surface Modification of Intraocular Lens for Reduced Posterior Capsular Opacification. *Int. J. Nanomed.* **2019**, *14*, 9047–9061. [CrossRef]
99. Liu, S.; Zhao, X.; Tang, J.; Han, Y.; Lin, Q. Drug-Eluting Hydrophilic Coating Modification of Intraocular Lens via Facile Dopamine Self-Polymerization for Posterior Capsular Opacification Prevention. *ACS Biomater. Sci. Eng.* **2021**, *7*, 1065–1073. [CrossRef]
100. Huang, H.; Zhu, S.; Liu, D.; Wen, S.; Lin, Q. Antiproliferative Drug-Loaded Multi-Functionalized Intraocular Lens for Reducing Posterior Capsular Opacification. *J. Biomater. Sci. Polym. Ed.* **2021**, *32*, 735–748. [CrossRef]
101. Wertheimer, C.; Kueres, A.; Siedlecki, J.; Braun, C.; Kassumeh, S.; Wolf, A.; Mayer, W.; Priglinger, C.; Priglinger, S.; Eibl-Lindner, K. The Intraocular Lens as a Drug Delivery Device for an Epidermal Growth Factor–Receptor Inhibitor for Prophylaxis of Posterior Capsule Opacification. *Acta Ophthalmol.* **2018**, *96*, e874–e882. [CrossRef] [PubMed]
102. Kassumeh, S.; Kueres, A.; Hillenmayer, A.; von Studnitz, A.; Elhardt, C.; Ohlmann, A.; Priglinger, S.G.; Wertheimer, C.M. Development of a Drug-Eluting Intraocular Lens to Deliver Epidermal Growth Factor Receptor Inhibitor Gefitinib for Posterior Capsule Opacification Prophylaxis. *Eur. J. Ophthalmol.* **2021**, *31*, 436–444. [CrossRef] [PubMed]
103. Teng, H.; Zhang, H.; Tian, F.; Gu, H.Q.; Liu, X.; Sun, J. The study of cyclosporin A modified intraocular lens preventing posterior capsular opacification in rabbit eyes. *Zhonghua Yan Ke Za Zhi* **2016**, *52*, 110–116. [CrossRef] [PubMed]
104. Lu, D.; Han, Y.; Liu, D.; Chen, S.; Qie, J.; Qu, J.; Lin, Q. Centrifugally Concentric Ring-Patterned Drug-Loaded Polymeric Coating as an Intraocular Lens Surface Modification for Efficient Prevention of Posterior Capsular Opacification. *Acta Biomater.* **2021**, *128*, 327–341. [CrossRef] [PubMed]

105. Liu, H.; Zhang, Y.; Ma, H.; Zhang, C.; Fu, S. Comparison of Posterior Capsule Opacification in Rabbit Eyes Receiving Different Administrations of Rapamycin. *Graefe's Arch. Clin. Exp. Ophthalmol.* **2014**, *252*, 1111–1118. [CrossRef]
106. Ongkasin, K.; Masmoudi, Y.; Wertheimer, C.M.; Hillenmayer, A.; Eibl-Lindner, K.H.; Badens, E. Supercritical Fluid Technology for the Development of Innovative Ophthalmic Medical Devices: Drug Loaded Intraocular Lenses to Mitigate Posterior Capsule Opacification. *Eur. J. Pharm. Biopharm.* **2020**, *149*, 248–256. [CrossRef]
107. Lee, E.H.; Joo, C.K. Role of Transforming Growth Factor-Beta in Transdifferentiation and Fibrosis of Lens Epithelial Cells. *Investig. Ophthalmol. Vis. Sci.* **1999**, *40*, 2025–2032.
108. Sun, C.; Teng, W.; Cui, J.; Huang, X.; Yao, K. The Effect of Anti-TGF-B2 Antibody Functionalized Intraocular Lens on Lens Epithelial Cell Migration and Epithelial–Mesenchymal Transition. *Colloids Surf. B Biointerfaces* **2014**, *113*, 33–42. [CrossRef]

Article

Mucoadhesive PLGA Nanospheres and Nanocapsules for Lactoferrin Controlled Ocular Delivery

Rubén Varela-Fernández^{1,2}, Xurxo García-Otero^{1,3}, Victoria Díaz-Tomé¹, Uxía Regueiro², Maite López-López², Miguel González-Barcia⁴, María Isabel Lema^{5,*} and Francisco Javier Otero-Espinar^{1,6,7,*}

- ¹ Department of Pharmacology, Pharmacy and Pharmaceutical Technology, University of Santiago de Compostela (USC), Campus Vida, 15782 Santiago de Compostela, Spain; rubenvf1@gmail.com (R.V.-F.); xurxo.garcia.otero@gmail.com (X.G.-O.); victoriadiazto@gmail.com (V.D.-T.)
- ² Clinical Neurosciences Group, University Clinical Hospital, Health Research Institute of Santiago de Compostela (IDIS), 15706 Santiago de Compostela, Spain; uxia.regueiro@usc.es (U.R.); maite.lopez.lopez@rai.usc.es (M.L.-L.)
- ³ Molecular Imaging Group, University Clinical Hospital, Health Research Institute of Santiago de Compostela (IDIS), 15706 Santiago de Compostela, Spain
- ⁴ Clinical Pharmacology Group, University Clinical Hospital, Health Research Institute of Santiago de Compostela (IDIS), 15706 Santiago de Compostela, Spain; miguel.gonzalez.barcia@sergas.es
- ⁵ Department of Surgery and Medical-Surgical Specialties, Ophthalmology Area, University of Santiago de Compostela (USC), Campus Vida, 15706 Santiago de Compostela, Spain
- ⁶ Institute of Materials Imatus, University of Santiago de Compostela (USC), Campus Vida, 15782 Santiago de Compostela, Spain
- ⁷ Paraquasil Group, University Clinical Hospital, Health Research Institute of Santiago de Compostela (IDIS), 15706 Santiago de Compostela, Spain
- * Correspondence: mariaisabel.lema@usc.es (M.I.L.); francisco.otero@usc.es (F.J.O.-E.)

Citation: Varela-Fernández, R.; García-Otero, X.; Díaz-Tomé, V.; Regueiro, U.; López-López, M.; González-Barcia, M.; Isabel Lema, M.; Otero-Espinar, F.J. Mucoadhesive PLGA Nanospheres and Nanocapsules for Lactoferrin Controlled Ocular Delivery. *Pharmaceutics* **2022**, *14*, 799. <https://doi.org/10.3390/pharmaceutics14040799>

Academic Editor: Juan José Torrado

Received: 21 February 2022

Accepted: 1 April 2022

Published: 6 April 2022

Publisher's Note: MDPI stays neutral with regard to jurisdictional claims in published maps and institutional affiliations.



Copyright: © 2022 by the authors. Licensee MDPI, Basel, Switzerland. This article is an open access article distributed under the terms and conditions of the Creative Commons Attribution (CC BY) license (<https://creativecommons.org/licenses/by/4.0/>).

Abstract: Background: the present work describes the preparation, characterization and optimization of eight types of PLGA-based nanosystems (nanospheres and nanocapsules) as innovative mucoadhesive drug delivery systems of lactoferrin, in order to achieve a preclinical consistent base as an alternative pharmacological treatment to different ocular syndromes and diseases. Methods: All different nanoparticles were prepared via two modified nanoprecipitation techniques, using a three-component mixture of drug/polymer/surfactant (Lf/PLGA/Poloxamer), as a way to overcome the inherent limitations of conventional PLGA NPs. These modified polymeric nanocarriers, intended for topical ophthalmic administration, were subjected to in vitro characterization, surface modification and in vitro and in vivo assessments. Results: An appropriate size range, uniform size distribution and negative ζ potential values were obtained for all types of formulations. Lactoferrin could be effectively included into all types of nanoparticles with appropriate encapsulation efficiency and loading capacity values. A greater, extended, and controlled delivery of Lf from the polymeric matrix was observed through the in vitro release studies. No instability or cytotoxicity was proved for all the formulations by means of organotypic models. Additionally, mucoadhesive in vitro and in vivo experiments show a significant increase in the residence time of the nanoparticles in the eye surface. Conclusions: all types of prepared PLGA nanoparticles might be a potential alternative for the topical ophthalmic administration of lactoferrin.

Keywords: nanoparticles; PLGA; lactoferrin; topical ophthalmic administration; nanoprecipitation; protein nanocarriers; keratoconus; corneal ecstasic disorder

1. Introduction

The eye is an airtight organ and presents a high resistance to the absorption of xenobiotics [1,2]. In the past few decades, different strategies have been deeply studied to improve ocular drug retention, ameliorate topical ophthalmic therapeutic effects and minimize the limitations of conventional drug-delivery systems (DDS). At present, several drug-loaded

colloidal systems, intended for ophthalmic applications, are reported to provide controlled drug release, as well as better retention in the eye surface as opposed to well-known typical eye drops [3].

Biodegradable polymers, such as poly (lactic-co-glycolic) acid (PLGA), are broadly used as novel DDS due to their compliance with the desirable requirements intended for topical ophthalmic administration (safety, biodegradability, biocompatibility, non-toxicity, sustained drug release and drug site-specific targeting) [4]. PLGA is composed of lactic acid and glycolic acid, providing a large range of physicochemical properties depending on the lactic/glycolic acid ratio.

PLGA nanocarriers may be generally prepared by using different techniques, where nanoprecipitation is one of the most common. Nanoprecipitation involves the addition of a water-miscible organic solution, where a hydrophobic polymer is dispersed into an aqueous solution, prompting a diffusion process that promotes the polymer precipitation [5]. Homogenous and identical particle size distribution is obtained with this technique, leading to an enhanced colloidal stability [6–8], reduced production times and expenditures [9,10], and high production yields [11]. Depending on the preparation process, the nanoparticle structure may differ. The drug may be either entrapped into the matrix or adsorbed on the surface [12,13].

The resultant nanosystems present a controlled drug release based on the polymer degradation rate, as well as the diffusion processes of the encapsulated drug [14]. During design and development procedure, the selection of the most appropriate type of PLGA is the main key factor to achieve an effective drug delivery [15]. The lack of mucoadhesiveness hinders its use in topical ophthalmic administration, although PLGA nanoparticles reached good results as DDS [16].

Lactoferrin (Lf) is an iron-binding single-chain glycoprotein composed of two lobes to which Fe^{3+} ions may strongly bind. Lf is acknowledged as a first-line defense protein with a pleiotropic functional pattern in humans, including anti-inflammatory [17,18], antibacterial [19–21], antiviral [22–24] and antitumoral [25,26] actions, among others. Unlike other iron-binding proteins, Lf was observed to promote iron retention in inflamed tissue, as well as stimulate corneal epithelial wound healing [27,28], thereby restricting free radical production and avoiding oxidative damage and inflammation. As consequence of the functions of this glycoprotein, Lf has been proposed for the treatment of different surface ocular pathologies [29], such as (I) dry eye, including Sjögren syndrome and idiopathic dry eye, (II) keratoconjunctivitis, (III) giant papillary conjunctivitis, (IV) irritative and vernal conjunctivitis or (V) viral and bacterial ocular infections, among others.

Additionally, Lf has been identified as a candidate to inhibit hypoxia-inducible factors (HIFs), whose main objective is based on the expression regulation of various genes, including VEGF and, consequently, they are considered as a target for treatment of neovascular ocular diseases such as age-related macular degeneration (AMD), diabetic retinopathy and diabetic macular edema [30].

Likewise, Lf has also been recognized as a key molecule in the pathogenesis of Keratoconus (KC). KC is a progressive and bilateral degenerative ectatic disorder, characterized by a disorder distinguished by stromal thinning, corneal steepening and irregular astigmatism, which lead to great visual acuity and impaired social health and life quality that affects young adults causing, worsening over time [31]. KC affects all ethnicities and both genders in the same way, whose initial prevalence (1/2000) has significantly increased in the last few years due to new diagnosis techniques [32]. The etiology of KC remains unclear, where environmental, genetic, and behavioral factors act as the main pathophysiological contributors [33,34], not existing approved treatment to prevent or decrease its progression [35], only aimed to slow down its progress [36].

Furthermore, numerous research have recognized the role of oxidative stress and lipid peroxidation pathways in the KC pathogenesis [37–39]. Under physiological conditions, the generation of reactive oxygen species (ROS) during metabolism is counteracted by the action of antioxidant enzymes, particularly catalase, superoxide dismutase and glu-

tathione peroxidase, among others. Thus, any alteration in this balance would promote the generation of an oxidative stress phenomenon [40]. Likewise, increased oxidative stress is also associated with several types of non-apoptotic cell death, one of them being ferroptosis (an iron-dependent cell death process). Ferroptosis induced by the malfunction of the glutathione-dependent antioxidant shield, resulting in the accumulation of lipid peroxidation products [41]. Nevertheless, lipophilic antioxidants (e.g., α -tocopherol, butylated hydroxytoluene or β -carotene) and iron chelators have proven efficacy as strong suppressors in the ferroptosis cell death prevention [42,43].

In recent years, different works were published aiming to improve the Lf ocular bioavailability due to its great potential in the treatment of several ophthalmic diseases [44]. This improvement may be achieved by increasing the permanence of Lf on the ocular surface or improving Lf corneal permeation. In the present work, Lf-loaded PLGA nanoparticles were prepared by two different modified nanoprecipitation techniques, using a three-component mixture of drug/polymer/surfactant (Lf/PLGA/Poloxamer), as a way to overcome the inherent limitations of conventional PLGA NPs (high initial burst, incomplete release and instability of the encapsulated proteins, among others). These modified polymeric nanocarriers, intended for topical ophthalmic administration, were subjected to *in vitro* characterization, surface-modification, and *in vitro* and *in vivo* assessments.

2. Materials

Resomer[®] RG 502 (Mw: 10,000 Da; lactide:glycolide = 50:50), Resomer[®] RG 502H (Mw: 17,000 Da; lactide:glycolide = 50:50), Resomer[®] RG 503 (Mw: 24,000 Da; lactide:glycolide = 50:50) and Resomer[®] RG 503 H (Mw: 38,000 Da; lactide:glycolide = 50:50) were purchased from Evonik (Essen, Germany). Hydrochloric acid (HCl) and sodium hydroxide (NaOH) and were acquired from Merck (Darmstadt, Germany). Lactoferrin, Polyvinyl Alcohol (PVA) and Pluronic[®] F68 were acquired from Sigma-Aldrich (St Louis, MI, USA). Visking dialysis tubing cellulose membrane (14,000 g/mol molecular weight cutoff) was purchased from Sigma-Aldrich (St. Louis, MI, USA). All other chemicals and reagents were of the highest purity grade commercially available.

3. Methods

3.1. Preparation of PLGA Nanoparticles

3.1.1. One-Step Nanoprecipitation Method: Nanospheres

The preparation of PLGA nanospheres (NSs) was performed by a modified nanoprecipitation method, based on the elaboration procedure previously developed by Bilati et al. [45], with minor modifications. The polymer was firstly dissolved in DMSO ($v = 4$ mL). This solution was injected by a syringe/needle system, introducing the needle into the dispersing solution, an 0.5% (w/v) Pluronic[®] F68 aqueous solution ($v = 40$ mL), under magnetic stirring (up to 750 rpm) at room temperature for 30 min. A 1:10 organic:aqueous phase ratio was established for the nanoparticles preparation. Nanoprecipitation immediately occurred when the organic solution was in contact with the aqueous phase. Resulting suspensions were centrifuged 3 times at 4 °C and 50,000 rpm for 1-h cycles and washed with double-distilled water to eliminate the residual DMSO, gradually replacing it with water for subsequent freeze-drying, using trehalose as cryoprotectant (0.5% w/v). Lactoferrin-loaded PLGA NSs were prepared following the same procedure used for blank nanoparticles, although adding the protein to the aqueous solution before the addition of the organic solution and the subsequently nanoparticle's formation (see Figure 1). A 1:10 (w/w) protein:polymer ratio was established for the drug-loaded nanospheres preparation.

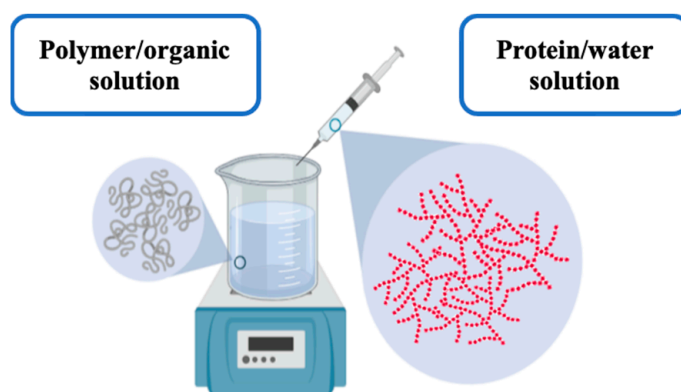


Figure 1. Simplified representation of the PLGA-based nanospheres elaboration process.

3.1.2. Two-Step Nanoprecipitation Method: Nanocapsules

The preparation of PLGA nanocapsules (NCs) was performed by a modified two-step nanoprecipitation method, using a method as developed by Weber et al. [46] and subsequently described by Morales-Cruz et al. [47], with negligible changes. Briefly, Lf was dissolved in an aqueous phase (0.01% *w/v*) and then solvent-precipitated by adding acetonitrile at a 1:4 (*v/v*) ratio. The resultant protein suspension was stirred for 5 min at room temperature.

Furthermore, PLGA was also dissolved in acetonitrile ($C_{PLGA} = 5 \text{ mg/mL}$) under magnetic stirring (500 rpm) at $25 \pm 2 \text{ }^\circ\text{C}$, and subsequently added to the Lf suspension drop wisely. The resulting mixture was finally added into a maturation medium in a 1:10 (*v/v*) ratio, composed of a 1% (*w/v*) PVA solution, under vigorous stirring (>750 rpm) and room temperature to promote the nanoparticle formation.

Polymer nanoprecipitation instantaneously occurred upon infusion of the Lf suspension. The resulting lactoferrin-loaded PLGA NCs were centrifuged for 1 h at 14,000 rpm, the supernatant discarded, and the sediment resuspended in an ocular buffer saline (PBS). A thrice washing step was applied prior to the samples freeze-dried using trehalose as cryoprotectant (0.5% *w/v*) (see Figure 2). A 1:10 (*w/w*) protein:polymer ratio was established for the drug-loaded nanocapsules preparation.

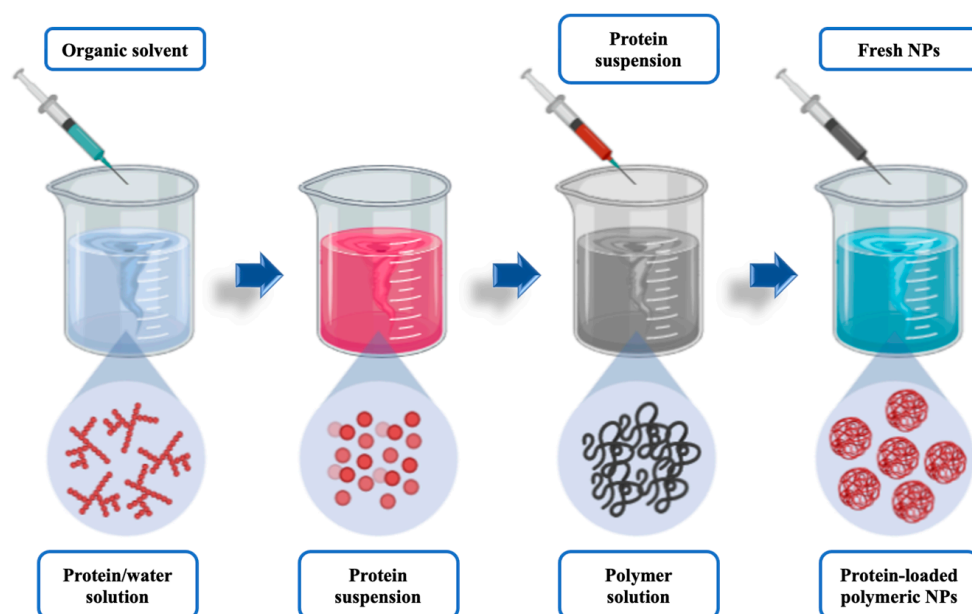


Figure 2. Simplified representation of the PLGA-based nanocapsules elaboration process.

3.2. Physicochemical Characterization of the Nanoparticles

3.2.1. Particle Size, Polydispersity, and Surface Charge

The average particle size, size distribution, and surface potential of the nanoparticles were determined by Dynamic Light Scattering with non-invasive back scattering (DLS-NIBS) at 25 °C. PLGA NPs were 1:10 diluted prior to the analysis. DLS subsets were defined as previously described [44,48]. Each batch was thrice assessed.

3.2.2. Morphological Evaluation

PLGA NSs and NCs were morphologically analyzed two different microscopical techniques, these being: (I) Scanning Electron Microscopy (SEM), and (II) Transmission Electron Microscopy (TEM). An appropriate sample preparation was made prior to the SEM and TEM analysis, as previously described [44,48]. Different batches were used for both types of analysis.

3.2.3. Production Yield (PY)

The PY values of the PLGA NPs were acquired by a centrifugation technique [49], with slight changes. Concisely, predefined volumes of the PLGA NSs or NCs were centrifuged (14,000 rpm, 25 °C, 1 h), the supernatants were discarded, and the sediment was vacuum-dried until constant weight. The PY values were finally estimated as follows (Equation (1)):

$$\text{PY (\%)} = (\text{NPs weight}) / (\text{Total initial solids weight}) \times 100 \quad (1)$$

3.2.4. Encapsulation Efficiency (EE) and Loading Capacity (LC)

Encapsulation efficiency and loading capacity of the PLGA NPs were determined by following a centrifugation/spectrophotometry procedure, as previously described [44,48]. EE and LC values were obtained by a centrifugation technique, trailed by the free-drug measurement by UV-Vis spectrophotometry, after polymer precipitation. Briefly, 20 mg of PLGA-based nanoparticles were dissolved into 2.5 mL dichloromethane, followed by a mechanic stirring process (Vortex[®], VWR International) (Darmstadt, Germany) to promote the polymer dissolution. Later, 5 mL of methanol were appended, and samples were subsequently vortexed for 1 min to foster polymer precipitation. Samples were then centrifuged (5000 rpm, 10 min) and the supernatant was subsequently collected. Unbound Lf was quantified by UV-Vis spectrophotometry at a 280.0 nm wavelength, using a method previously validated by our group. This procedure was repeated using 9 randomized batches for each formulation. The EE (Equation (2)) and LC (Equation (3)) of Lf were respectively calculated as follows:

$$\text{EE} = (\text{Total amount of drug} - \text{Amount of unbound drug}) / (\text{Total amount of drug}) \times 100 \quad (2)$$

$$\text{LC} = (\text{Total amount of drug} - \text{Amount of unbound drug}) / (\text{NPs weight}) \times 100 \quad (3)$$

3.3. Stability Studies

3.3.1. Stability to Storage

ICH guidelines were followed to design the procedure for determining storage stability [50], with negligible adjustments. PLGA NSs and NCs were freshly prepared, isolated by centrifugation, and resuspended in PBS (pH 7.4, v = 10 mL). Samples (1 mL) were incubated at different temperature environments: (a) 4 ± 2 °C, (b) 25 ± 2 °C, and (c) 37 ± 2 °C for two different periods: 8 h (short-time stability) and 3 months (long-term stability), at 100 rpm and protected from light. Size and size distribution were studied in triplicate for each batch.

3.3.2. Stability to pH

A complete pH interval (2, 4, 6, 7, 8, 10, and 12) was pre-established for the stability study of PLGA NSs and NCs, as previously described [44]. Samples (500 µL) were 1:10

diluted in Milli-Q[®] water and consequently refrigerated for 24 h. Size, polydispersity, and surface charge were finally analyzed by DLS, as mentioned in previous sections.

3.3.3. Stability to Ionic Strength

A complete ionic strength interval (0.2, 0.4, 0.6, 0.8, 1.2, 1.4, 1.6, and 2 M) was pre-established for the stability study of PLGA NSs and NCs, as previously described [44,48]. Samples (500 μ L) were 1:10 diluted in Milli-Q[®] water and then refrigerated for 24 h. Size, size distribution, and surface charge were finally analyzed by DLS, as mentioned in previous sections.

3.4. In Vitro Release Study

The Lf delivery from PLGA NSs and NCs was determined following the dialysis fundamentals previously described as a way to establish the drug diffusion and kinetic behavior from these colloidal systems in a simulated physiological environment. Henceforward, freshly prepared lactoferrin-loaded PLGA NSs and NCs were suspended in PBS (pH 7.4 and ionic strength 0.075 M) for a physiological background proof-of-concept test [51]. The experimental procedure was extensively described in previous works [44,48], where a 1.5 mg/mL NPs concentration ([Lf] = 0.15 mg/mL) was adjusted to fill the donor chamber of the Franz diffusion cells ($v = 3$ mL). The protein release rate from PLGA NSs and NCs was determined at predetermined times by UV-Vis spectrophotometry at a 280.0 nm wavelength.

3.5. Cytotoxicity Analysis

3.5.1. Bovine Corneal Opacity and Permeability Test (BCOP)

The BCOP test is an organotypic model commonly employed in the assessment of a great variety of formulations with potential ocular irritancy to fulfill the animal replacement bases.

The BCOP test fundamentals were based on the methodology earlier protocolized by Tchao et al. [52] and improved by Gautheron et al. [53], with minimal adjustments. A standardized procedure for PLGA NPs addition, as well as the permeability and opacity measurements, were established and considerably described in previous works [44]. In this test, corneal opacity changes were estimated by two different experimental techniques (luxmetry and the UV-VIS spectrophotometry), while permeability data was exclusively obtained by UV-Vis spectrophotometry (490.0 nm wavelength). Each formulation was evaluated in triplicate. The resulting permeability and opacity values were used to calculate an in vitro score value (if necessary, see Equation (4)) [53,54]. Furthermore, the classification of PLGA NPs may be performed agreeing to the Kay and Calandra rating [53].

$$\text{IVIS} = \text{mean opacity value} + (15 \times \text{mean permeability OD}_{490} \text{ value}) \quad (4)$$

3.5.2. Hen's Egg Test on the Chorioallantoic Membrane (HET-CAM)

The HET-CAM test has turned into a universal standard test for the assessment of acute eye irritation and corrosion phenomena [55,56], where three potential consequences may be observed in the CAM vasculature and subsequently measured following the Kalweit et al. criteria [57]. The experimental procedure was extensively described in previous works [44]. Briefly, viable eggs were employed after 9 days of incubation under specific environmental conditions [44], using the CAM as the target tissue. Once the formulation was placed onto the CAM, a 5 min inspection period was carried out, taking frames from the beginning to the end of the assay. Results were both individually and combined analyzed. Each formulation was thrice appraised.

3.6. Ocular Surface Retention Study

3.6.1. Ex Vivo Corneal Surface Retention

The ex vivo corneal surface retention assay was based on the method firstly defined by Belgamwar et al. and Gradauer et al. [58,59], with minimal adjustments. The experimental procedure was extensively described in previous works [44]. Briefly, freshly excised eyes were placed upwards on specifically designed holders. Fluorescein-stained PLGA NSs and NCs were then added, where the formulation's excess was collected and reapplied. The residual formulation volume was finally quantified for fluorescence intensity by UV-Vis spectrophotometry at a 490.0 nm wavelength. Each preparation was examined in triplicate. Resulting data was compared with the initial intensity values, and the ex vivo corneal mucoadhesion values were subsequently quantified as follows (Equation (5)):

$$\text{Mucoadhesion (\%)} = \left[\frac{((\text{Abs}_0 - V_0) - (\text{Abs}_F - V_F))}{(\text{Abs}_0 - V_0)} \right] \times 100 \quad (5)$$

where Abs_0 and Abs_F indicate the absorbance value for the initial and final fluorescein-stained PLGA NPs, V_0 denotes the volume instilled to the eyes, and V_F designates the final volume of the formulations that was not adsorbed to the mucosa.

3.6.2. In Vivo Corneal Surface Retention Study

Evaluation of the Radiolabeling Stability and Efficiency of PLGA-Based Nanoparticles

Radioactive fluoride (^{18}F) and gallium (^{68}Ga) are two of the most commonly used positron emitters due to their optimal positron features (see details in Table 1), making them suitable for the Positron Emission Tomography (PET) imaging technique. In any case, ^{18}F is mostly used in different conjugates, where 2- ^{18}F -fluoro-2-deoxy-D-glucose (^{18}F -FDG) and ^{18}F -Choline are the most commonly used, while ^{68}Ga is mainly used in binary or ternary complexes, such as the ^{68}Ga -DOTA (1,4,7,10-tetraazacyclododecane-tetraacetic acid).

Table 1. Physicochemical characteristics of different radiotracers (^{18}F and ^{68}Ga).

Radiotracer	$t_{1/2}$ (min)	$E_{\beta^+, \max}$ (KeV)	β^+ Intensity (%)
^{18}F	109.7	635	97
^{68}Ga	67.71	1899	89

Lately, several methodologies have been investigated to trace a variety of nanosized systems using the aforementioned radiotracers' labeling [60–63]. The assessment of PLGA-based NPs radiolabeling efficiency and stability was performed by an incubation procedure, as previously described [44,48]. It must be considered that ^{18}F -FDG and ^{18}F -Choline were provided by the Cyclotron unit of the University Hospital of Santiago de Compostela (CHUS), while and ^{68}Ga -DOTA was provided by the Galician Radiopharmacy Unit. The radiolabeling efficiency of PLGA-based nanoparticles was quantify by the radiotracer activity, both in the supernatant and the remnant vials, considering the incubation interval and the radiotracer decay. Statistical analysis was later employed to acquire the radiolabeling efficiency and labeling stability data.

Experimental In Vivo Evaluation of the Ocular Biopermanence of PLGA-Based Nanoparticles

The PET/CT combined technique was used for the in vivo estimation of the PLGA NPs retention time on the ocular surface, as previously described [64]. The in vivo experimental procedure was performed in male Sprague-Dawley rats, whose environmental and feeding conditions were controlled throughout the procedure, according to the ARVO approved guidelines for laboratory animals [65]. The PET/CT acquisition and data processing were extensively described in previous works [44,48]. Each formulation was tested in quadruplicate (two animals, four eyes) to fulfill the laboratory animal regulatory outlines [66].

The PLGA NPs radioactivity versus time diagrams were finally acquired, comparing the resulting data against a control solution (^{18}F -Choline buffered solution). A monoex-

ponential decay equation based on a single compartmental model was applied for the remaining formulation versus time fitting by means of the GraphPad Prism[®] v. 8.41 software (San Diego, CA, USA) and pKSolver[®], a solver add-in for Excel[®] (Microsoft, Redmond, WA, USA) [67].

3.7. Data Analysis

Pairs of groups were compared by carrying out one-tailed Student's *t*-test and multiple group comparison was conducted by one-way or two-way analysis of variance, with a 95% significance level ($p < 0.05$), using the GraphPad Prism[®] v. 8.41 software (San Diego, CA, USA). All data were presented as a mean and standard deviation (mean \pm SD). Tukey's or Bonferroni's tests were also used for post-hoc contrast.

4. Results and Discussion

4.1. Preparation of Lactoferrin-Loaded PLGA Nanoparticles

4.1.1. One-Step Nanoprecipitation Method: Lactoferrin-Loaded PLGA Nanospheres

The conventional nanoprecipitation technique is usually based on a solvent displacement phenomenon, where a suitable solvent condition shifted into an inappropriate solvent condition [68]. Nevertheless, the modified one-step nanoprecipitation methodology applied in the present work made it possible to successfully entrap Lf into PLGA nanospheres. Certainly, both protein and polymer were individually dissolved into two different proper solvents. Then, both were changed to a single unsuitable solvent in a one-step mixing process. The obtention of lactoferrin-loaded PLGA NSs was based on the interfacial deposition of the nanoparticle components by a solvent displacement phenomenon between two dissimilar solvents [69].

4.1.2. Two-Step Nanoprecipitation Method: Lactoferrin-Loaded PLGA Nanocapsules

The modified two-step nanoprecipitation method designed for the obtention of lactoferrin-loaded PLGA NCs was successfully applied. This method was based on the assumptions previously described by Giteau et al. [70].

The modified two-step nanoprecipitation method previously described (see Section 3.1.2) was based on a double solvent displacement process, by using a desolvating agent (acetonitrile) to promote the protein precipitation and the polymer dissolution. The original methodology was also slightly changed to assure the obtention of nanosized PLGA nanocarriers with high Lf content, avoiding enzyme inactivation or aggregation phenomena.

4.2. Physicochemical Characterization of the Nanoparticles

4.2.1. Particle Size Distribution and ζ Potential

Nano-sized particles are known to affect different biological parameters, such as the in vivo tissue distribution, drug content, or stability, among others [71–74].

Figure 3 shows the average size and ζ potential for PLGA NSs and NCs, respectively. The PDI index was minimum for all formulations, suggesting that a homogeneous population of nanoparticles was obtained. Regarding the surface charge, high negatively ζ potential values were obtained, presumably due to the PLGA presence in the surface [75]. This negatively charged net might indicate that these colloidal systems would remain stable over time, which is desirable in order to prevent particle aggregation or coalescence [76].

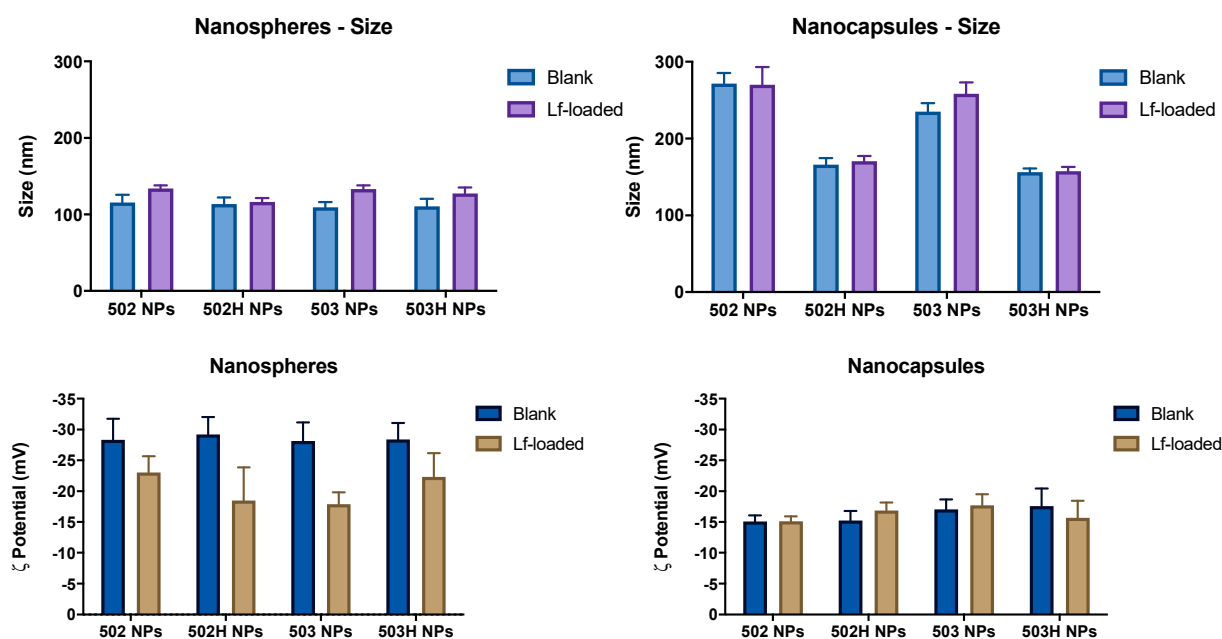


Figure 3. Comparison of size and ζ potential differences for blank and lactoferrin-loaded PLGA-based nanoparticles. A one-way ANOVA statistical analysis was applied, and no statistically significant differences were found among the formulations ($p > 0.05$), regardless of the polymer used.

4.2.2. Effect of Protein Loading on Particle Size and ζ Potential

Figure 3 displays the mean size for blank and lactoferrin-loaded PLGA-based nanoparticles. The resulting data suggest that Lf hardly has any influence on particle size. However, it must be taken into account that the drug:polymer ratio was 1:40, so its impact may be camouflaged by the component proportions in the final formulation. A one-way ANOVA statistical analysis was applied, and no statistically significant differences were found among the formulations (α n.s.), regardless of the polymer used.

On the other hand, surface charge values of Lf-loaded PLGA NSs were lower than blank PLGA NSs (see Figure 3), suggesting that the Lf might not be just encapsulated into the nanocarriers, but also adsorbed to the nanoparticle surface. A one-way ANOVA statistical analysis was carried out, and no statistically significant differences were found among the formulations ($\alpha < 0.001$), regardless of the polymer used.

These results are supported by previous studies [77], where the surface potential of the nanoparticles was affected by the molecular distribution of all the compounds and the net formed by the chemical positions. Nevertheless, these ζ potential differences are not significantly observed in the lactoferrin-loaded PLGA NCs (α n.s.) (see Figure 3), supporting the idea that Lf is encapsulated and protected by a polymeric shell, typical of a reservoir colloidal system, without being massively adhered to the polymeric surface.

4.2.3. Morphological Evaluation

SEM and TEM images were scanned both before and after the vacuum-drying process to prove that the physical and morphological characteristics of the PLGA NPs remained unchanged after the dehydration process. Resultant images confirmed the presence of homogenous populations of spherical shape and size below 300 nm. Hence, the vacuum-dried PLGA NPs presumably guarantee the nanoscale size, where size and morphology results were aligned with the morphological evaluation data.

The microstructural analysis by TEM also set that PLGA-based nanoparticles were observed as individual spherical entities, with a homogeneous distribution, spherical in shape and irregular surface particles with well-defined sizes (see Figure 4). These results agree well with previous studies [78–80], clearly differentiating the structure of the NSs from the NCs.

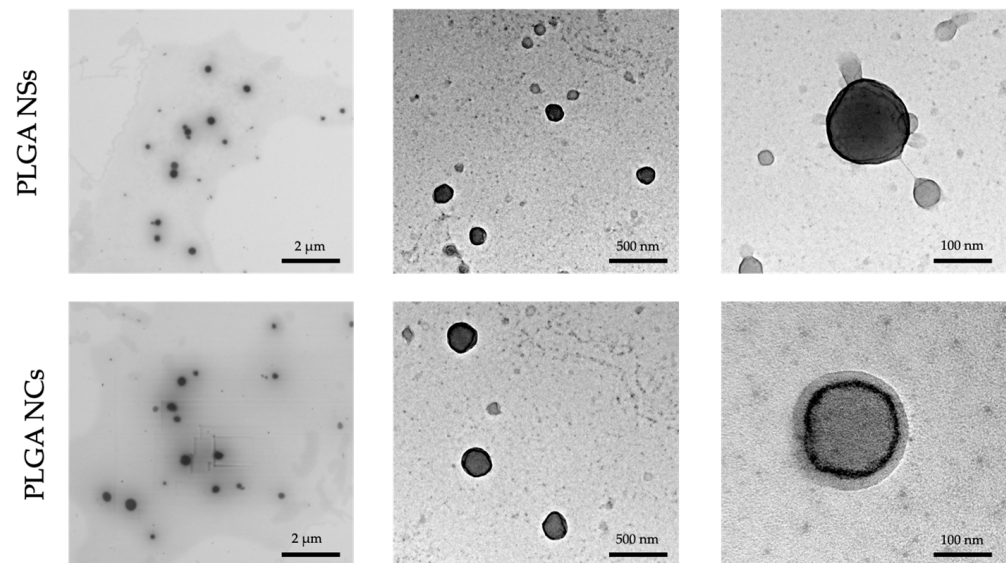


Figure 4. TEM images of lactoferrin-loaded PLGA NSs and lactoferrin-loaded PLGA NCs.

4.2.4. Production Yield (PY), Encapsulation Efficiency (EE) and Loading Capacity (LC) of Nanoparticles

Two different types of PLGA-based NPs were developed for Lf encapsulation. Figure 5 shows the PY, EE and LC of resulting lactoferrin-loaded PLGA-based NPs. The EE determination proved that the nanoprecipitation technique was reproducible and useful, supported by appropriate PY values (above 80%). A one-way ANOVA analysis was performed to assess the existence of dissimilarities among the prepared formulations. The resultant data indicate that no statistically significant differences were found in terms of PY and EE. Nevertheless, considerable differences were observed for LC values, where NCs-based formulations permitted the obtention of high Lf-embedded content into the polymer matrix, compared to the NSs-based formulations, which barely showed any loading capacity (less than 10%). These data are consistent with the nanoparticle preparation method, where NCs show a large amount of drug inside the polymer matrix while, in the NSs, the drug is mostly adhered to the polymeric matrix surface, presumably by electrostatic bonds.

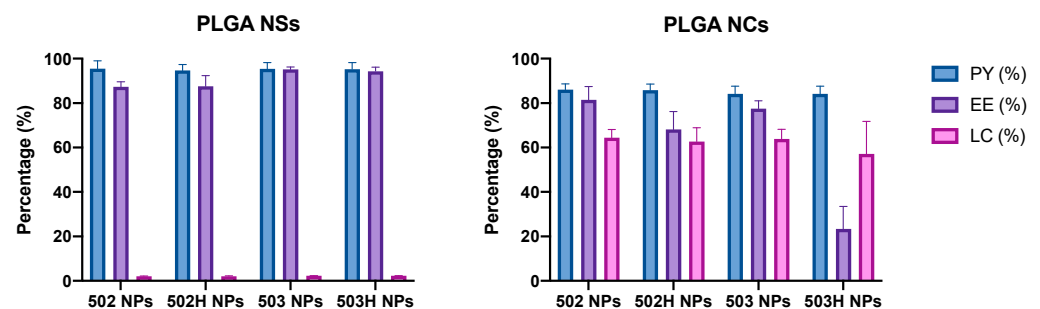


Figure 5. PY, EE, and LC values for PLGA-nanoparticles. No statistically significant differences were found in terms of PY and EE ($p > 0.05$). Nevertheless, considerable differences were observed for LC values, where NCs-based formulations permitted the obtention of higher Lf-embedded content into the polymer matrix, compared to the NSs-based formulations ($p < 0.0001$).

4.3. Stability Studies

4.3.1. Stability to Storage

The resultant data for the long-term stability study proved that both PLGA NPs did not experience any significant modification in their size over a 3-month period (see Figures 6 and 7) for two different temperature sets (4 ± 2 °C and 25 ± 2 °C). Nevertheless,

aggregation phenomena were observed in the third temperature set ($37 \pm 2 \text{ }^\circ\text{C}/60 \pm 5\% \text{ RH}$) as of the second month. This process may be associated with the glass transition temperature of the PLGA, which varies from 40 to $60 \text{ }^\circ\text{C}$ (near the studied temperature), leading to an increase in the brittle characteristics of the polymer in physiological-like conditions [81].

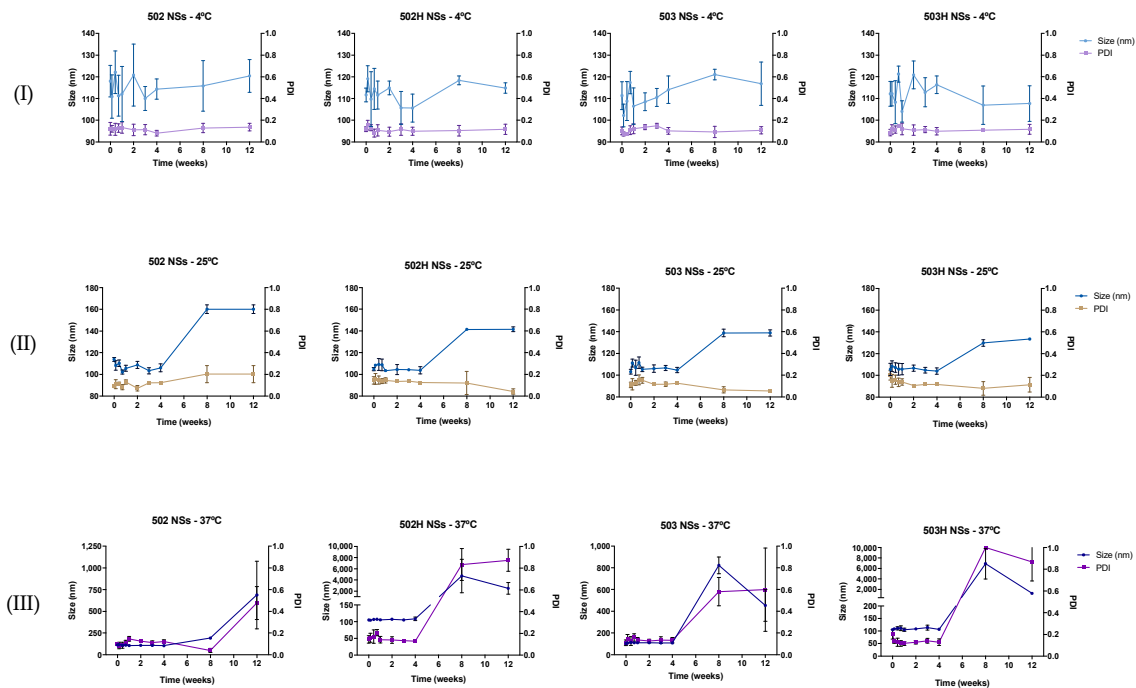


Figure 6. Stability-to-storage study for PLGA-based NSs at three different temperature conditions: (I) $4 \pm 2 \text{ }^\circ\text{C}$, (II) $25 \pm 2 \text{ }^\circ\text{C}$ and (III) $37 \pm 2 \text{ }^\circ\text{C}$, respectively.

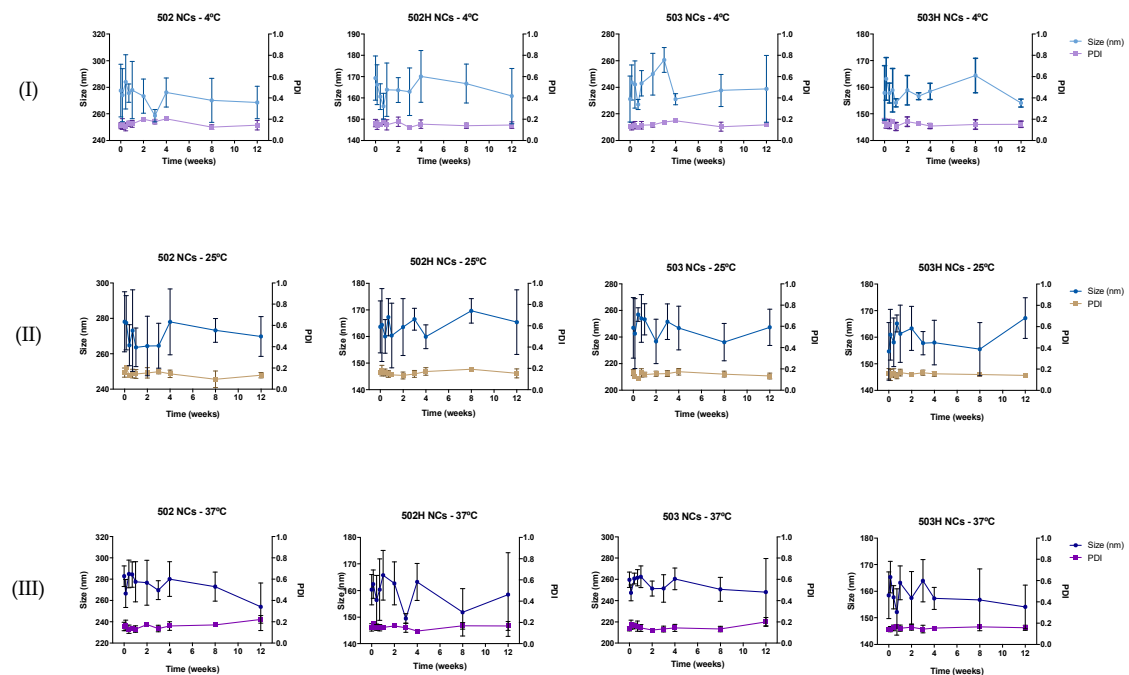


Figure 7. Stability-to-storage study for PLGA-based NCs at three different temperature conditions: (I) $4 \pm 2 \text{ }^\circ\text{C}$, (II) $25 \pm 2 \text{ }^\circ\text{C}$ and (III) $37 \pm 2 \text{ }^\circ\text{C}$, respectively.

4.3.2. Stability to pH

Collapse, rupture, or aggregation of nanoparticles may appear as a consequence of pH media variations. Figures 8 and 9 show the variations in the physical magnitudes for both PLGA-based nanoparticles along the studied pH interval.

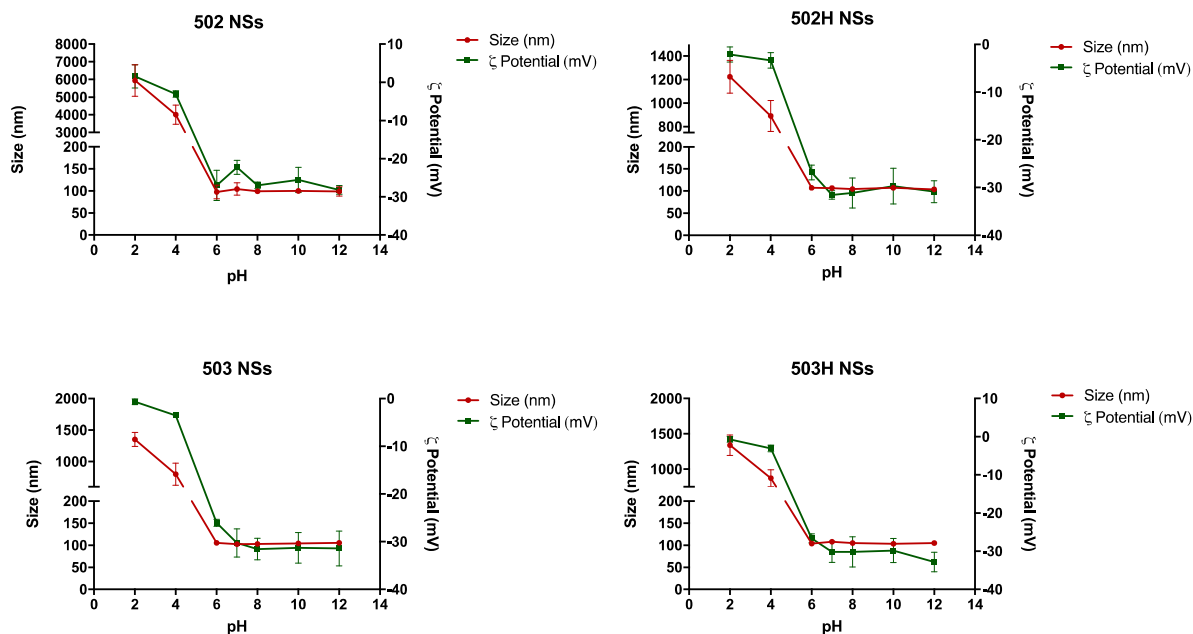


Figure 8. Changes in size and ζ potential values of lactoferrin-loaded PLGA NSs over the studied pH interval.

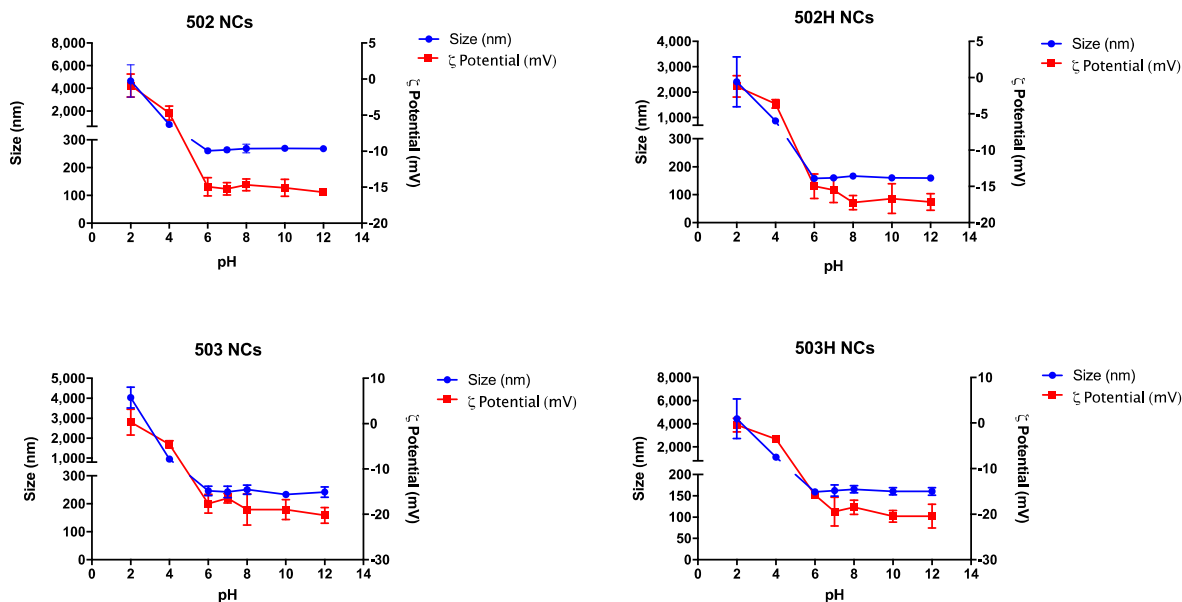


Figure 9. Changes in size and ζ potential values of lactoferrin-loaded PLGA NCs over the studied pH interval.

The same pattern was observed along the pH interval in terms of size and ζ potential values for both types of PLGA nanoparticles. These changes are apparently related to the polymeric nature of the resultant nano-sized particles, where PLGA determines the nanoparticle's ζ potential. Therefore, extremely acidic pH values promoted the nanoparticle's aggregation due to the interaction between the protonated medium (positive charge) and the carboxyl groups of the polymer (negative charge), where a nullification of the NPs

surface charge was observed. Nonetheless, PLGA-based nanoparticles remained stable in the rest of the pH interval. Hence, PLGA-based colloidal systems would be suitable for topical ophthalmic administration [82].

4.3.3. Stability to Ionic Strength

Collapse, rupture, or aggregation of nanoparticles may appear because of ionic strength media variations. Figures 10 and 11 show the resultant data for both types of Lf-loaded PLGA nanoparticles over the studied ionic strength interval, respectively.

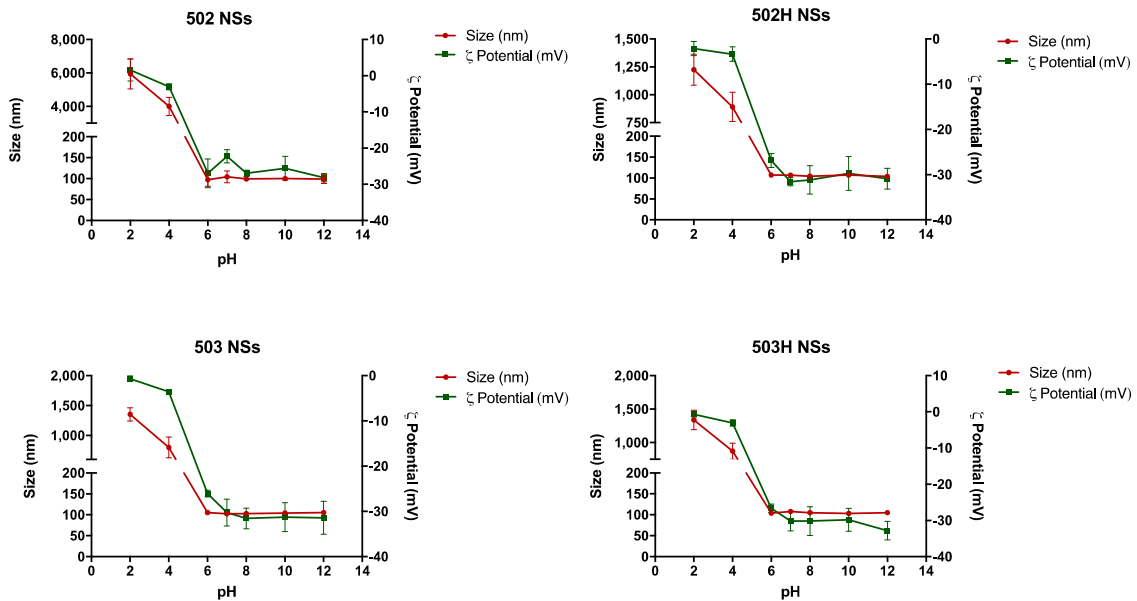


Figure 10. Changes in size and ζ potential values of lactoferrin-loaded PLGA NSs over the studied ionic strength interval.

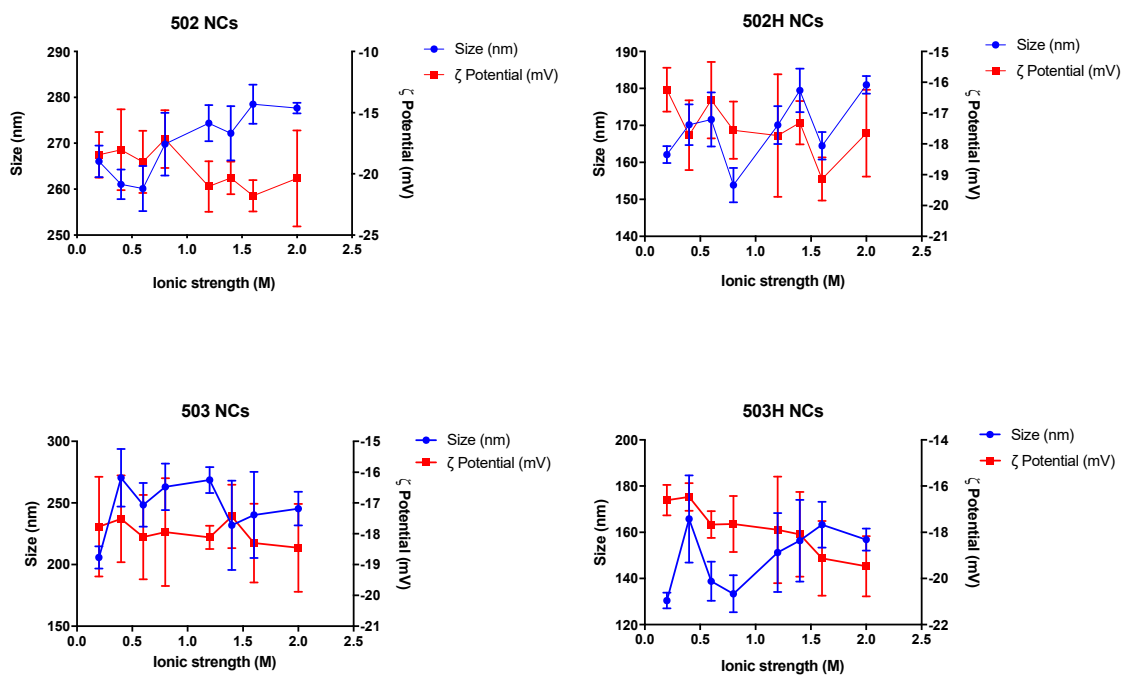


Figure 11. Changes in size and ζ potential values of lactoferrin-loaded PLGA NCs over the studied ionic strength interval.

The colloidal steadiness of both types of nanoparticles remained stable in spite of dys-physiological conditions due to variations in the ionic strength values of the medium, where a surface charge rise seemed to be directly related to an increase in the NaCl concentration.

Ionic strength may condition the physical stability of PLGA nanoparticles by promoting possible time-dependent precipitation, sedimentation, or aggregation phenomena [83]. Nonetheless, Lf-loaded PLGA NPs remained stable in terms of changes in size, turbidity, and particle compactness in spite of changes in the ionic strength values of the media over the studied period.

4.4. In Vitro Release Study

The two key release mechanisms linked to drug-loaded PLGA nanosystems are usually diffusion and bioerosion/degradation. The release rate is initially controlled by the diffusion mechanism while the bioerosion/degradation processes modulate the final stage of the release period. Preceding studies have also proven the influence of drug release mechanisms and many other factors (porosity, water content, polymer–drug and drug–drug interactions, among others) in drug diffusion and degradation kinetics from PLGA-based DDS [83].

The pilot in vitro release study of lactoferrin from the PLGA NPs evidenced that both nanospheres and nanocapsules exhibited a controlled release profile, compared to a Lf aqueous solution (control solution), as observed in Figure 12. The in vitro lactoferrin release profiles allow the elucidation of a biphasic pattern, as follows: (I) a first initial burst release due to the lactoferrin desorption from the particle surface, and (II) an asintotic release phase, resulting from the lactoferrin diffusion from the polymer matrix because of the polymer erosion processes. It must be considered that the polymer's autocatalytic degradation is based on the excision of ester bonds, resulting in a decrease in the molecular weight, being faster in the matrix center and becoming more pronounced in larger systems [84].

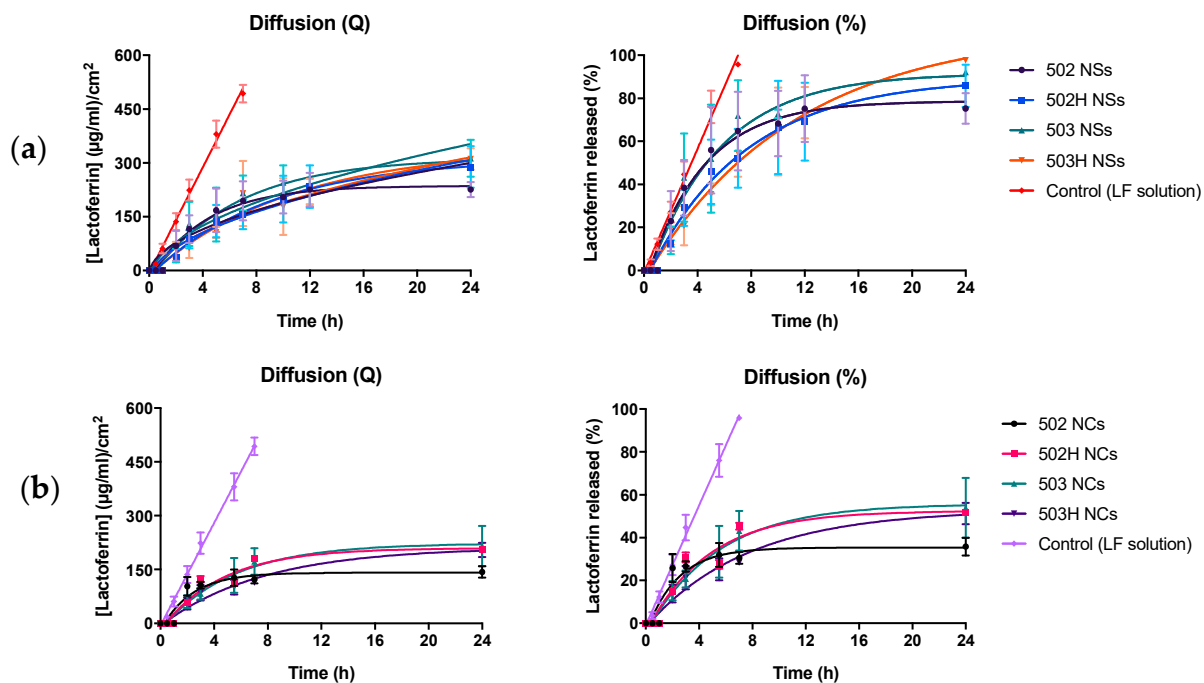


Figure 12. In vitro release study of Lf from PLGA NSs (a) and NCs (b). The first graph embodies the raw amount of Lf corrected by the available surface released from the PLGA NSs over the 24 h period. The second graph represents the percentage of Lf released from the PLGA NSs over the 24 h period. No statistically significant differences were observed among all the PLGA-based formulations ($p > 0.05$).

On the other hand, a lower molecular weight leads to less hydrophobia and therefore a higher water absorption capability, increasing their hydrolysis and bioerosion rate. Thus, the release of Lf was expected to be faster in the nanoparticles made with Resomer[®] RG 502 and Resomer[®] RG 502H, compared to those made with Resomer[®] RG 503 and Resomer[®] RG 503H. Nevertheless, no statistically significant differences were observed among all the formulations.

In addition, the release rate can be also affected by interactions between the drug and the polymer. These interactions and their impact on the subsequent release profiles have been deeply examined in previous studies [81–83]. However, no statistically significant differences were noticed among all the formulations despite differences in the hydrophobicity of the polymers, possibly due to the similarity on the lactic and glycolic acids' content.

The resulting in vitro release profiles were adjusted to different kinetic models. The best correlation was obtained with the Hopfenberg and Peppas-and-Korsmeyer kinetic models (with n values in the range of 0.57–0.93), suggesting that the surface erosion of both NSs and NCs was caused by the dissolution, swelling and polymer chain scission processes [85–87], and the protein diffusion was the predominant release mechanism (Table 2). These results were supported by data previously published in other scientific articles [88–90].

Table 2. Release data of Lf-loaded PLGA NSs and NCs into the Hopfenberg ($M_t/M_\infty = 1 - [kt]^n$), Higuchi ($M_t/M_\infty = k\sqrt{t}$), Peppas and Korsmeyer ($M_t/M_\infty = kt^n$), and monoexponential diffusion kinetics models.

Formulation	Hopfenberg			Higuchi		Peppas and Korsmeyer		
	k	n	R	k	R	k	n	R
502 NSs	0.0377	3	0.9418	26.04	0.9265	50.57	0.58	0.9326
502H NSs	0.0302	3	0.9679	23.99	0.9363	14.21	0.70	0.9610
503 NSs	0.0394	3	0.9340	27.42	0.9061	20.09	0.92	0.9163
503H NSs	0.0293	3	0.9789	24.00	0.9364	11.12	0.80	0.9787
502 NCs	0.0215	3	0.7839	14.85	0.7924	0.57	0.57	0.7965
502H NCs	0.0243	3	0.8798	17.85	0.8336	0.81	0.81	0.8826
503 NCs	0.0237	3	0.9639	17.82	0.8909	0.93	0.93	0.9722
503H NCs	0.0170	3	0.8914	12.76	0.8756	0.70	0.70	0.9043

4.5. Cytotoxicity Analysis

4.5.1. Bovine Corneal Opacity and Permeability Test (BCOP)

The BCOP test is an appropriate ex vivo tissue model that allows the depth of injury assessment by distinguishing the moderate, severe, and extremely severe ocular irritant substances. Figure 13a show the transparency variations measured by UV-Vis spectrophotometry for the lactoferrin-loaded PLGA NSs and NCs. Figure 13b show the transparency variations measured by luxmetry for the lactoferrin-loaded PLGA NSs and NCs, respectively.

All PLGA-based formulations showed an in vitro IS of 0 (IS = 0), exhibiting no cytotoxicity effects in terms of transparency modification, compared to control formulations. These results are also supported by the fluorescein permeability data (see Figure 13c), where no fluorescein passage was observed through the corneas after the administration of the formulations.

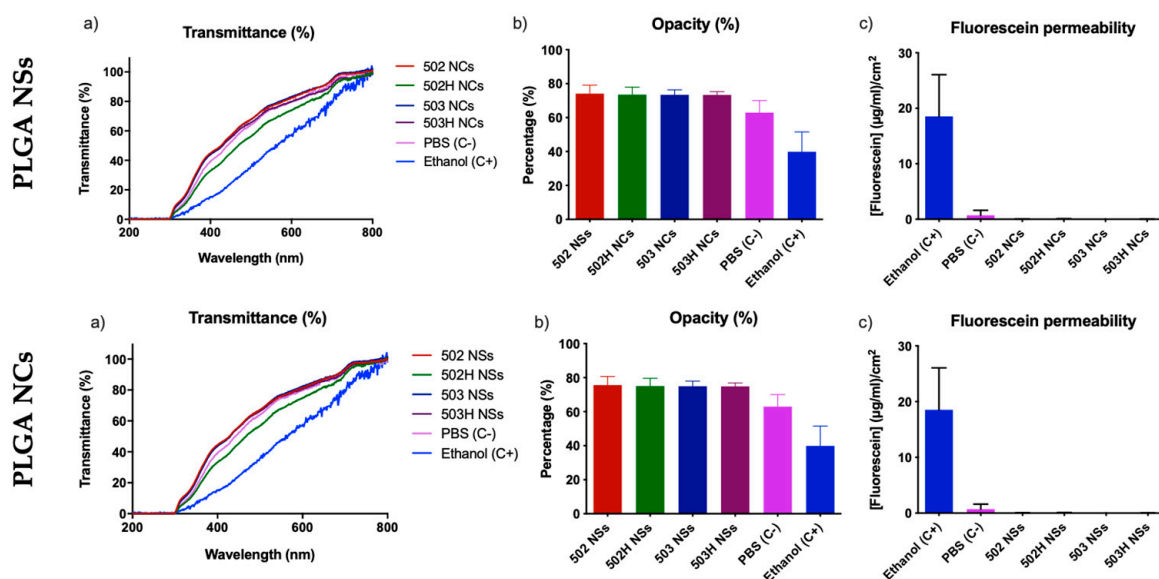


Figure 13. Resulting data of the BCOP test for PLGA-based NSs (top) and NCS (bottom). (a) final corneal transparency values measured by UV-Vis spectrophotometry; (b) final corneal transparency values measured by luxmetry, and (c) fluorescein permeability measured by UV-Vis spectrophotometry.

4.5.2. Hen’s Egg Test on the Chorioallantoic Membrane (HET-CAM)

The CAM is a non-innervated tissue and constitutes a well-developed vascularization model and an easy-to-study alternative strategy for ocular irritation assessment due to the complete inflammatory process response, similar to that induced in the Draize test, as it can be performed with greater efficiency and faster measurements than other in vivo tests [91–93]. Thus, the HET-CAM assay was used to assess the cytotoxicity and biocompatibility of the prepared nanoparticles.

PLGA-based NPs showed no cytotoxicity effects (IS = 0) (see Figure 14), comparing them with control formulations (0.9% (w/v) NaCl and 1.8% (w/v) NaOH aqueous solutions, used as negative and positive control formulations). These results are in accordance with formerly published studies [94] and agree with the results previously obtained by the BCOP test (see Section 4.5.1) confirming that these nanoparticles are biocompatible and non-toxic.

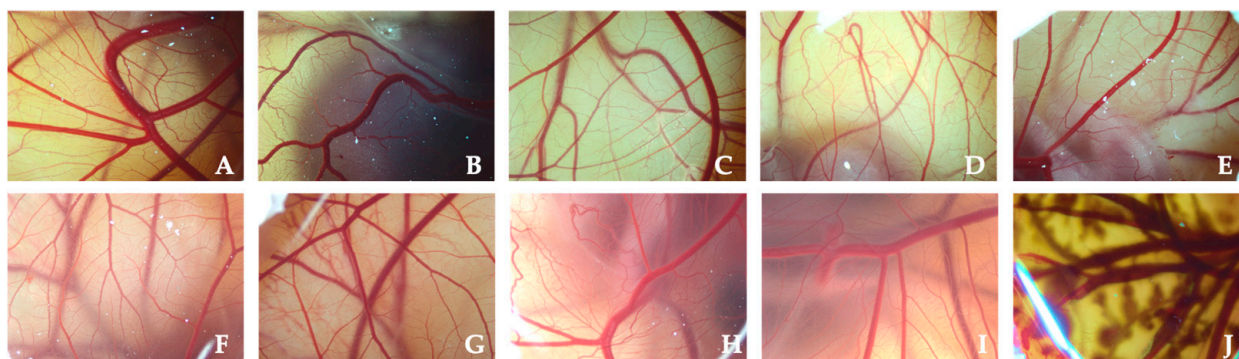


Figure 14. Resulting images of CAM membranes after the PLGA-based nanoparticles administration during the HET-CAM test, compared to the control solutions: (A) 502 PLGA NSs; (B) 502H PLGA NSs; (C) 503 PLGA NSs; (D) 503H PLGA NSs; (E) 502 PLGA NCS; (F) 502H PLGA NCS; (G) 503 PLGA NCS; (H) 503H PLGA NCS; (I) NaCl aqueous solution; and (J) NaOH aqueous solution.

4.6. Ocular Surface Retention Study

4.6.1. Ex Vivo Corneal Surface Model

The ex vivo corneal surface bioadhesion determination was adapted from the previous works described by Belgamwar et al. (2009) and Gradauer et al. (2012) [58,59], with minor modifications. Figure 15 displays the mucoadhesion percentage for all the PLGA-based NPs. The resulting data reinforce the possibility of using PLGA-based nanoparticles as an alternative technological strategy for the topical ophthalmic administration of Lf.

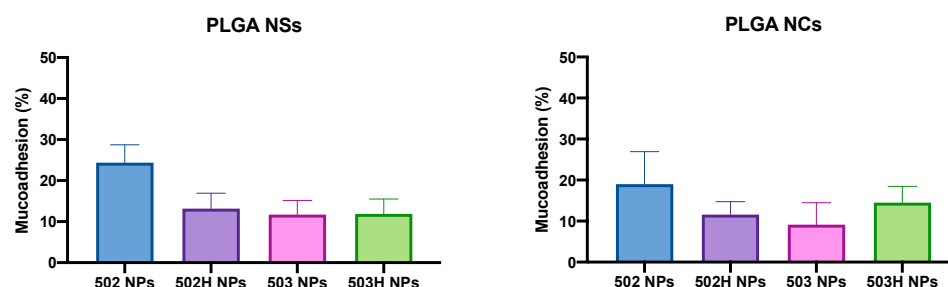


Figure 15. Ex vivo mucoadhesion data for PLGA-based nanoparticles. A one-way ANOVA analysis was applied for the PLGA NSs, showing no differences among the formulations ($p > 0.05$), except for the 502 PLGA NSs, which showed a higher mucoadhesion than the rest, being statistically significant ($p < 0.02$). Nevertheless, the same one-way ANOVA analysis was applied for the PLGA NCs, and no significant differences were observed between the prepared formulations, even for the 502 PLGA NCs compared to the others ($p > 0.05$).

A one-way ANOVA analysis was applied for the PLGA NSs, showing no differences among the formulations, except for the 502 PLGA NSs, which showed a higher mucoadhesion than the rest, being statistically significant. Nevertheless, the same one-way ANOVA analysis was applied for the PLGA NCs, and no significant differences were observed between the prepared formulations, even for the 502 PLGA NCs compared to the others.

The PLGA NSs and NCs ex vivo mucoadhesion values are lower than observed in our group for previous studies made with chitosan and sulfobutylether- β -cyclodextrin/chitosan nanoparticles [44] and nanostructured lipid carriers [48], so it seems that PLGA-based nanoparticles have less mucoadhesiveness. This is presumably associated with the surface charge of the nanoparticles, where chitosan-based NPs showed a positive surface charge, which allowed electrostatic interactions with the sialic acid groups of mucin, whereas PLGA nanoparticles showed a negative surface charge, so that their main mechanism of ocular adhesion may be associated with ease of permeation through the corneal layers. Likewise, it must be considered that the ex vivo conditions directly correlate with in vivo conditions, where different factors are involved and influence the pharmaceutical form administration, such as tearing and blinking, among others (see details in Section 4.6.2).

4.6.2. In Vivo Ocular Surface Permanence Study

Evaluation of the Radiolabeling Stability and Efficiency of PLGA-Based Nanoparticles

Figure 16 shows the ^{18}F -FDG, ^{18}F -Choline and ^{68}Ga -DOTA radiolabeling stability and efficiency for PLGA-based NPs, respectively. As observed, ^{18}F -FDG and ^{68}Ga -DOTA led to low radiolabeling efficiency (under 50%), although a radiolabeling stability was observed along the studied interval time, while ^{18}F -Choline displayed a great radiolabeling efficiency (over 80%) and stability over the assayed period (up to 3 h), assuring suitable properties for PLGA NPs radiolabeling study. Based on these results, ^{18}F -Choline was chosen as the radiotracer for subsequent in vivo radiolabeling studies.

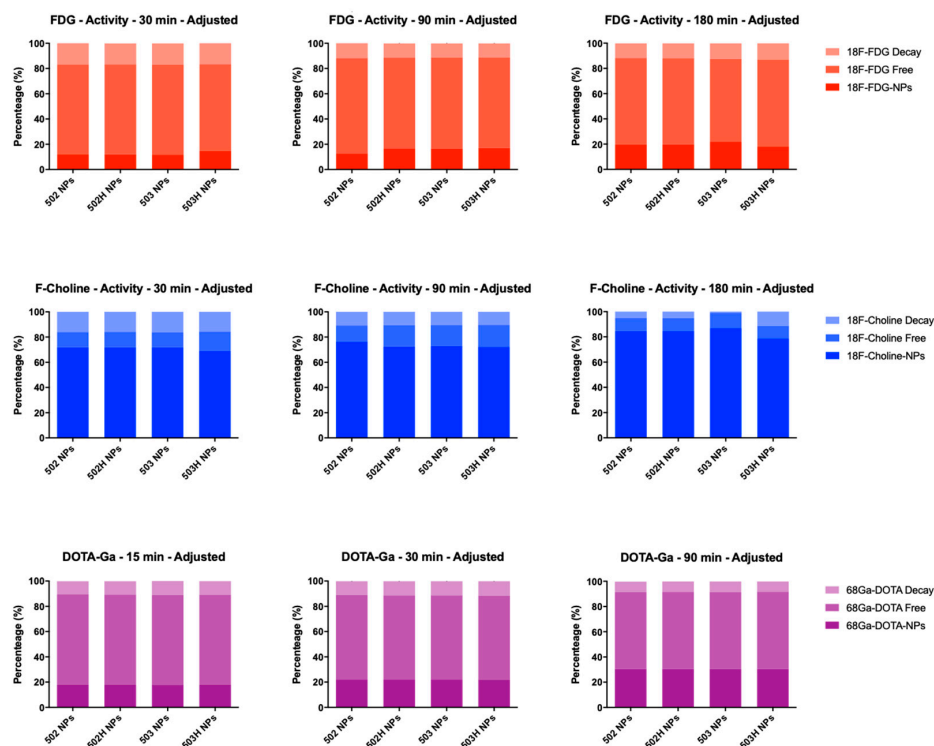


Figure 16. ^{18}F -Choline (top), ^{18}F -FDG (middle) and ^{68}Ga -DOTA (bottom) radiolabeling stability and efficiency for PLGA-based nanoparticles over time.

The labeling efficiency of the studied radiotracers are closely related with the radiotracer charge and the ζ potential of the nanoparticles. PLGA nanoparticles, similarly to the nanostructured lipid carriers (NLCs) developed in previous works [48], have a negative surface charge and, therefore, have a maximum radiolabeling efficiency with ^{18}F -Choline, which has a positively charged net. On the contrary, chitosan-based nanoparticles [44] that showed a positively charged surface, better radiolabeling performance was obtained with the ^{18}F -FDG that has a negatively charged net. In the case of ^{68}Ga -DOTA, the radiotracer is also negatively charged, although the radiolabeling efficiency of PLGA NPs was lower, presumably due to the larger size of the radiotracer.

Experimental In Vivo Evaluation of Ocular Surface Permanence

Figure 17 shows the ocular surface permanence of the ^{18}F -Choline-radiolabeled PLGA-based nanoparticles for a 300-min period, compared to the ^{18}F -FDG solution, used as control. A ^{18}F -FDG solution was used as a standard due to the fact that the ^{18}F -Choline is positively charged in its free form, so that it would ionically interact with the negative charge of the sialic acid groups of the mucin layer, resulting in erroneous biodistribution values. On the contrary, ^{18}F -FDG, presenting a free negative charge, would not bind to the mucin layer, perfectly simulating the administration of a control substance. For the sake of clarification, an analysis of the ^{18}F -Choline-labeled PLGA nanoparticles was carried out to see if this radiotracer modified the size and surface charge, and the results showed that there was no change in either parameter (unpublished data), ensuring that the labeling procedure is suitable for this type of delivery system. The corneal surface retention study of the PLGA-based NPs was measured by the ^{18}F -Choline radioactivity assessment in a PET system.

The ocular surface permanence of the PLGA-based nanoparticles was carried out on rats using ^{18}F -Choline as a radiotracer. A PET equipment was employed in order to trail the radioactivity evaluation over the studied time (Figure 18). In the present work, a longer $t_{1/2}$ was observed for both Lf-loaded PLGA NSs and NCs, compared to the ^{18}F -FDG control solution, despite the fact that both formulations presented a tear-like composition [94].

Resultant data were precisely adjusted to a monoexponential decline outline by a single compartmental model ($R = 0.9875$ for Lf-loaded PLGA NSs, $R = 0.9977$ for Lf-loaded PLGA NCs, and $R = 0.9930$ for the ^{18}F -FDG solution) (see Figure 17). The resultant data are in accordance with PET data of previous studies [95], and suggest that PLGA-based nanoparticles showed mucoadhesive, cell uptake and corneal penetration characteristics.

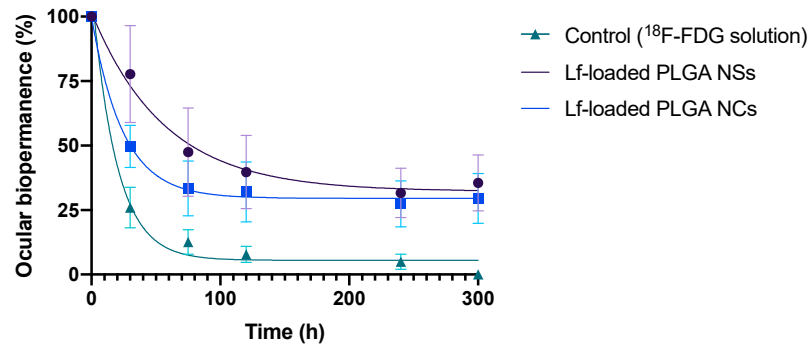


Figure 17. Ocular biopermanence of a ^{18}F -Choline radiolabeled PLGA-based nanoparticles and a ^{18}F -FDG aqueous solution (control), assessed pondering the primary biopermanence data (%) in the ROI. Statistically significant differences ($p < 0.05$) were observed regarding PLGA-based formulations and ^{18}F -FDG solution.

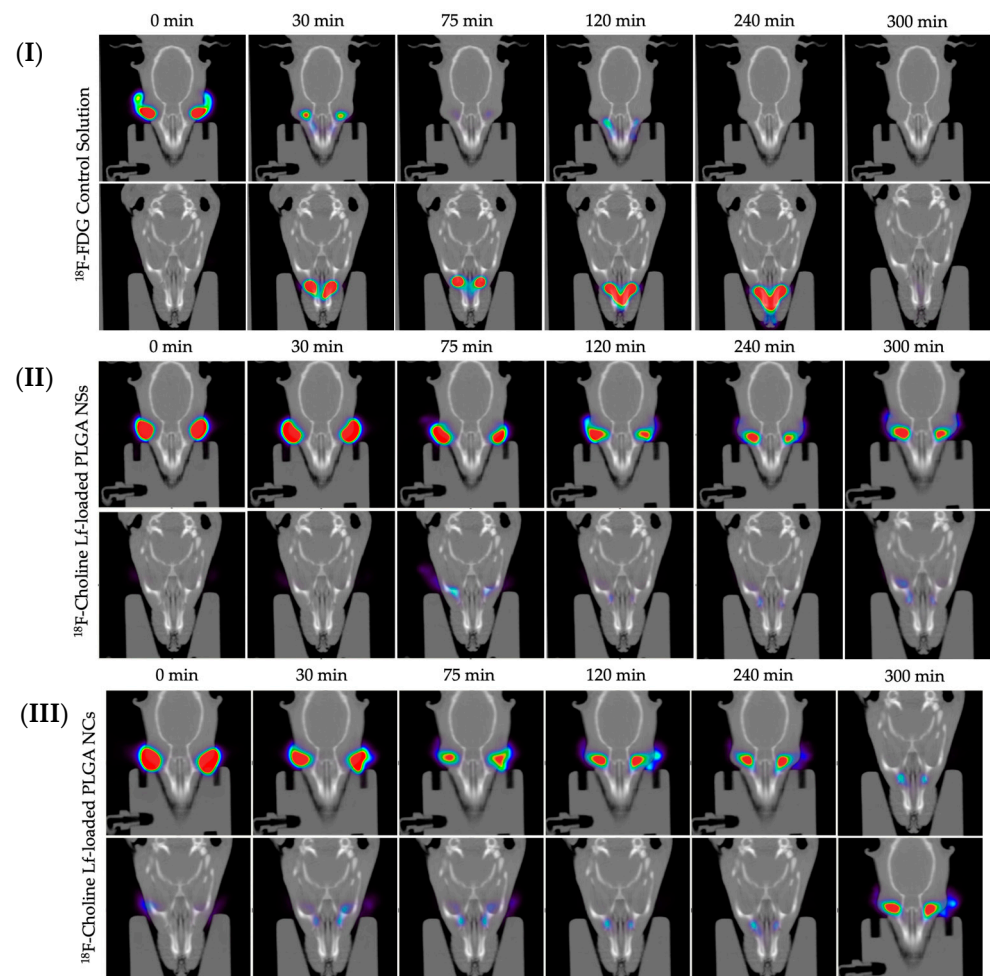


Figure 18. Fused PET/CT images during the 5 h studied interval. (I) ^{18}F -FDG buffered aqueous solution, (II) ^{18}F -Choline radiolabeled PLGA NSs and (III) ^{18}F -Choline radiolabeled PLGA NCs.

Table 3 shows the pharmacokinetics factors (k , $t_{1/2}$, MRT, AUC, and % dose 30 min) of the ^{18}F -Choline radiolabeled PLGA-based nanoparticles and ^{18}F -FDG standard solution. Statistically significant differences ($p < 0.05$) were observed regarding PLGA-based formulations and ^{18}F -FDG solution for the studied period, where Lf-loaded polymeric nanoparticles exhibited a better ocular retention outline.

Table 3. Ocular biopermanence parameters for ^{18}F -Choline radiolabeled PLGA-based nanoparticles and ^{18}F -FDG control (named as “control” in the table) formulations.

Formulation	K (min^{-1})		$t_{1/2}$ (min)		% Dose 30 min	
	Mean	SD	Mean	SD	Mean	SD
PLGA NSs	0.008	0.0092	93.31	37.71	77.73	18.78
PLGA NCs	0.014	0.0107	51.32	17.45	49.72	8.19
^{18}F -FDG control	0.044	0.012	16.27	3.81	23.31	5.89
^{18}F -Choline control	0.013	0.012	53.19	11.28	42.90	5.33

The ocular permanence of the PLGA-based nanoparticles obtained by the PET technique followed the same pattern that the mucoadhesive Lf-loaded CS/TPP and CS/SBE- β -CD NPs, as well as the Lf-loaded NLC [44]. Corneally, chitosan-based NPs displayed a $t_{1/2}$ of 114 ± 72 h for CS/TPP NPs, and 60 ± 20 h for CS/SBE- β -CD NPs, respectively, while Lf-loaded NLC showed a $t_{1/2}$ of 107.82 ± 38.10 h. Thus, results confirmed the great bioadhesive capability of the PLGA-based formulations in the ocular mucosa.

5. Conclusions

In recent decades, polymeric nanoparticles have risen as promising alternatives for drug delivery in the biomedical field. Indeed, PLGA-based formulations have turned into promising DDS for topical ophthalmic administration, compared to the conventional pharmaceutical forms. This is mainly associated with their numerous advantages, such as their versatility, ease of scale, high stability, biodegradability and biocompatibility, among others.

The present work reports the design, development and physicochemical characterization of tunable-size Lf-loaded PLGA-based nanoparticles by modified nanoprecipitation methods. Lf-loaded PLGA-based nanoparticles showed appropriate average particle size, size distribution and ζ potential, as well as a spherical and uniform shape. Different drug:polymer ratios were tested in order to obtain the lowest particle size with maximum production yield, encapsulation efficiency, and loading capacity values. Analogously, all formulations showed good stability to storage, pH and ionic strength in the studied ranges. A controlled lactoferrin release was also confirmed, confirming their use as suitable DDS for topical ophthalmic delivery. Resultant data also demonstrated that both nanosystems (NSs and NCs) interact with ocular surface, guaranteeing an optimal contact between the formulation and the corneal mucosa for at least 5 h, with no evidence of tissue cytotoxicity.

In conclusion, different PLGA-based NPs were proposed as biocompatible DDS for the lactoferrin administration via topical ophthalmic route, reinforced by several preclinical studies in order to accomplish a reliable base as a new pharmacological alternative for the keratoconus treatment over the invasive surgical procedures. Despite this, better in vitro/in vivo correlations should be made in order to broaden the knowledge of the potential of these nanosystems as a new approach for the keratoconus treatment, as well as establish its reproducibility with the backdrop of other biological features.

Author Contributions: Conceptualization, R.V.-F., M.I.L. and F.J.O.-E.; methodology, R.V.-F.; software, R.V.-F. and F.J.O.-E.; validation, F.J.O.-E., M.I.L. and M.G.-B.; formal analysis, R.V.-F. and F.J.O.-E.; investigation, R.V.-F.; resources, R.V.-F.; data curation, X.G.-O., V.D.-T.; writing—original draft preparation, R.V.-F.; writing—review and editing, R.V.-F., X.G.-O., V.D.-T. and F.J.O.-E.; visualization, U.R. and M.L.-L.; supervision, F.J.O.-E., M.I.L. and M.G.-B.; project administration, F.J.O.-E., M.I.L. and M.G.-B.; funding acquisition, F.J.O.-E., M.I.L. and M.G.-B. All authors have read and agreed to the published version of the manuscript.

Funding: This project has been awarded a grant from the Spanish Ministry of Economy and Competitiveness (Instituto de Salud Carlos III: PI18/00159), and partially supported by the Spanish Ministry of Science, Innovation and Universities (RTI2018-099597-B-100).

Institutional Review Board Statement: The study was conducted according to the guidelines of the Declaration of Helsinki and approved by the Ethics Committee of Health Research Institute of Santiago de Compostela (IDIS) (C007, 15 October 2020).

Informed Consent Statement: Not applicable.

Data Availability Statement: Not applicable.

Acknowledgments: R.V.F. and X.G.O. acknowledge the financial support of the FIDIS (Health Research Institute of Santiago de Compostela Foundation). Similarly, U.R. and M.L.L. recognize the support from Xunta de Galicia (Galician Innovation Agency GAIN: IN607A2018/3) and Spanish Research Network on Cerebrovascular Diseases INVICTUS PLUS (RD16/0019) fellowships.

Conflicts of Interest: The authors declare no conflict of interest. The authors are only responsible for the content and writing of this article. The funders had no role in the design of the study; in the collection, analyses, or interpretation of data; in the writing of the manuscript, or in the decision to publish the results.

References

1. Bucolo, C.; Drago, F.; Salomone, S. Ocular drug delivery: A clue from nanotechnology. *Front. Pharmacol.* **2012**, *3*, 188. [CrossRef] [PubMed]
2. Sahoo, S.K.; Dilnawaz, F.; Krishnakumar, S. Nanotechnology in ocular drug delivery. *Drug Discov. Today* **2008**, *13*, 144–151. [CrossRef]
3. Nagarwal, R.C.; Kant, S.; Singh, P.N.; Maiti, P.; Pandit, J.K. Polymeric nanoparticulate system: A potential approach for ocular drug delivery. *J. Control. Release* **2009**, *136*, 2–13. [CrossRef] [PubMed]
4. Danhier, F.; Ansorena, E.; Silva, J.M.; Coco, R.; Le Breton, A.; Préat, V. PLGA-based nanoparticles: An overview of biomedical applications. *J. Control. Release* **2012**, *161*, 505–522. [CrossRef] [PubMed]
5. Fessi, H.; Puisieux, F.; Devissaguet, J.P.; Ammoury, N.; Benita, S. Nanocapsule formation by interfacial polymer deposition following solvent displacement. *Int. J. Pharm.* **1989**, *55*, R1–R4. [CrossRef]
6. Lepeltier, E.; Bourgaux, C.; Couvreur, P. Nanoprecipitation and the “Ouzo effect”: Application to drug delivery devices. *Adv. Drug Deliv. Rev.* **2014**, *71*, 86–97. [CrossRef] [PubMed]
7. Beck-Broichsitter, M.; Nicolas, J.; Couvreur, P. Solvent selection causes remarkable shifts of the “Ouzo region” for poly(lactide-co-glycolide) nanoparticles prepared by nanoprecipitation. *Nanoscale* **2015**, *7*, 9215–9221. [CrossRef] [PubMed]
8. Vitale, S.A.; Katz, J.L. Liquid Droplet Dispersions Formed by Homogeneous Liquid–Liquid Nucleation: “The Ouzo Effect”. *Langmuir* **2003**, *19*, 4105–4110. [CrossRef]
9. Aubry, J.; Ganachaud, F.; Addad, J.-P.C.; Cabane, B. Nanoprecipitation of Polymethylmethacrylate by Solvent Shifting: 1. Boundaries. *Langmuir* **2009**, *25*, 1970–1979. [CrossRef]
10. Legrand, P.; Lesieur, S.; Bochot, A.; Gref, R.; Raatjes, W.; Barratt, G.; Vauthier, C. Influence of polymer behaviour in organic solution on the production of polylactide nanoparticles by nanoprecipitation. *Int. J. Pharm.* **2007**, *344*, 33–43. [CrossRef] [PubMed]
11. Yang, Z.; Foster, D.; Dhinojwala, A. Continuous production of polymer nanoparticles using a membrane-based flow cell. *J. Colloid Interface Sci.* **2017**, *501*, 150–155. [CrossRef]
12. Hans, M.L.; Lowman, A.M. Biodegradable nanoparticles for drug delivery and targeting. *Curr. Opin. Solid State Mater. Sci.* **2002**, *6*, 319–327. [CrossRef]
13. Soppimath, K.S.; Aminabhavi, T.M.; Kulkarni, A.R.; Rudzinski, W.E. Biodegradable polymeric nanoparticles as drug delivery devices. *J. Control. Release* **2001**, *70*, 1–20. [CrossRef]
14. Corrigan, O.I.; Li, X. Quantifying drug release from PLGA nanoparticulates. *Eur. J. Pharm. Sci.* **2009**, *37*, 477–485. [CrossRef] [PubMed]
15. Mu, L.; Feng, S.S. A novel controlled release formulation for the anticancer drug paclitaxel (Taxol[®]): PLGA nanoparticles containing vitamin E TPGS. *J. Control. Release* **2003**, *86*, 33–48. [CrossRef]

16. Lemoine, D.; Pr at, V. Polymeric nanoparticles as delivery system for influenza virus glycoproteins. *J. Control. Release* **1998**, *54*, 15–27. [CrossRef]
17. Appelmelk, B.J.; An, Y.Q.; Geerts, M.; Thijs, B.G.; De Boer, H.A.; MacLaren, D.M.; De Graaff, J.; Nuijens, J.H. Lactoferrin is a lipid A-binding protein. *Infect. Immun.* **1994**, *62*, 2628–2632. [CrossRef] [PubMed]
18. Hayashida, K.-I.; Kaneko, T.; Takeuchi, T.; Shimizu, H.; Ando, K.; Harada, E. Oral Administration of Lactoferrin Inhibits Inflammation and Nociception in Rat Adjuvant-Induced Arthritis. *J. Veter. Med. Sci.* **2004**, *66*, 149–154. [CrossRef] [PubMed]
19. Schryvers, A.B.; Morris, L.J. Identification and characterization of the human lactoferrin-binding protein from *Neisseria meningitidis*. *Infect. Immun.* **1988**, *56*, 1144–1149. [CrossRef] [PubMed]
20. Ellison, R.T.; Giehl, T.J. Killing of gram-negative bacteria by lactoferrin and lysozyme. *J. Clin. Investig.* **1991**, *88*, 1080–1091. [CrossRef] [PubMed]
21. Takakura, N.; Wakabayashi, H.; Ishibashi, H.; Teraguchi, S.; Tamura, Y.; Yamaguchi, H.; Abe, S. Oral Lactoferrin Treatment of Experimental Oral Candidiasis in Mice. *Antimicrob. Agents Chemother.* **2003**, *47*, 2619–2623. [CrossRef] [PubMed]
22. Marchetti, M.; Superti, F.; Ammendolia, M.G.; Rossi, P.; Valenti, P.; Seganti, L. Inhibition of poliovirus type 1 infection by iron-, manganese- and zinc-saturated lactoferrin. *Med. Microbiol. Immunol.* **1999**, *187*, 199–204. [CrossRef]
23. Murphy, M.E.; Kariwa, H.; Mizutani, T.; Tanabe, H.; Yoshimatsu, K.; Arikawa, J.; Takashima, I. Characterization of in vitro and in vivo Antiviral Activity of Lactoferrin and Ribavirin upon Hantavirus. *J. Veter. Med. Sci.* **2001**, *63*, 637–645. [CrossRef] [PubMed]
24. Berkhout, B.; Floris, R.; Recio, I.; Visser, S. The antiviral activity of the milk protein lactoferrin against the human immunodeficiency virus type 1. *BioMetals* **2004**, *17*, 291–294. [CrossRef]
25. Eliassen, L.T.; Berge, G.; Sveinbj rnsson, B.; Svendsen, J.S.; Vorland, L.H.; Rekdal,  . Evidence for a Direct Antitumor Mechanism of Action of Bovine Lactoferricin. *Anticancer Res.* **2002**, *22*, 2703–2710.
26. Tsuda, H.; Sekine, K.; Fujita, K.-I.; Iigo, M. Cancer prevention by bovine lactoferrin and underlying mechanisms—A review of experimental and clinical studies. *Biochem. Cell Biol.* **2002**, *80*, 131–136. [CrossRef]
27. Pattamatta, U.; Willcox, M.; Stapleton, F.; Cole, N.; Garrett, Q. Bovine Lactoferrin Stimulates Human Corneal Epithelial Alkali Wound Healing In Vitro. *Investig. Ophthalmol. Vis. Sci.* **2009**, *50*, 1636–1643. [CrossRef] [PubMed]
28. Flanagan, J.L.; Willcox, M.D.P. Role of lactoferrin in the tear film. *Biochimie* **2009**, *91*, 35–43. [CrossRef] [PubMed]
29. Vagge, A.; Senni, C.; Bernabei, F.; Pellegrini, M.; Scorcia, V.; Traverso, C.E.; Giannaccare, G. Therapeutic Effects of Lactoferrin in Ocular Diseases: From Dry Eye Disease to Infections. *Int. J. Mol. Sci.* **2020**, *21*, 6668. [CrossRef] [PubMed]
30. Ibuki, M.; Shoda, C.; Miwa, Y.; Ishida, A.; Tsubota, K.; Kurihara, T. Lactoferrin Has a Therapeutic Effect via HIF Inhibition in a Murine Model of Choroidal Neovascularization. *Front. Pharmacol.* **2020**, *11*, 174. [CrossRef] [PubMed]
31. Kymes, S.M.; Walline, J.; Zadnik, K.; Sterling, J.; Gordon, M.O.; Collaborative Longitudinal Evaluation of Keratoconus Study Group. Changes in the Quality-of-Life of People with Keratoconus. *Am. J. Ophthalmol.* **2008**, *145*, 611–617.e1. [CrossRef] [PubMed]
32. Godefrooij, D.A.; de Wit, G.A.; Uiterwaal, C.S.; Imhof, S.M.; Wisse, R.P. Age-specific Incidence and Prevalence of Keratoconus: A Nationwide Registration Study. *Am. J. Ophthalmol.* **2017**, *175*, 169–172. [CrossRef] [PubMed]
33. Sharif, R.; Bak-Nielsen, S.; Hjortdal, J.; Karamichos, D. Pathogenesis of Keratoconus: The intriguing therapeutic potential of prolactin-inducible protein. *Prog. Retin. Eye Res.* **2018**, *67*, 150–167. [CrossRef]
34. Tur, V.M.; MacGregor, C.; Jayaswal, R.; O’Brart, D.; Maycock, N. A review of keratoconus: Diagnosis, pathophysiology, and genetics. *Surv. Ophthalmol.* **2017**, *62*, 770–783. [CrossRef]
35. Romero-Jim nez, M.; Santodomingo-Rubido, J.; Wolffsohn, J. Keratoconus: A review. *Contact Lens Anterior Eye* **2010**, *33*, 157–166. [CrossRef] [PubMed]
36. Meiri, Z.; Keren, S.; Rosenblatt, A.; Sarig, T.; Shenhav, L.; Varssano, D. Efficacy of Corneal Collagen Cross-Linking for the Treatment of Keratoconus: A Systematic Review and Meta-Analysis. *Cornea* **2016**, *35*, 417–428. [CrossRef]
37. Buddi, R.; Lin, B.; Atilano, S.; Zorapapel, N.C.; Kenney, M.C.; Brown, D.J. Evidence of Oxidative Stress in Human Corneal Diseases. *J. Histochem. Cytochem.* **2002**, *50*, 341–351. [CrossRef]
38. Gondhowiardjo, T.D.; Van Haeringen, N.J.; V lker-Dieben, H.J.; Beekhuis, H.W.; Kok, J.H.; Van Rij, G.; Pels, L.; Kijlstra, A. Analysis of Corneal Aldehyde Dehydrogenase Patterns in Pathologic Corneas. *Cornea* **1993**, *12*, 146–154. [CrossRef]
39. Atilano, S.R.; Coskun, E.P.; Chwa, M.; Jordan, N.; Reddy, V.; Le, K.; Wallace, D.C.; Kenney, M.C. Accumulation of Mitochondrial DNA Damage in Keratoconus Corneas. *Investig. Ophthalmol. Vis. Sci.* **2005**, *46*, 1256–1263. [CrossRef]
40. Lubrano, S.B.V.; Balzan, S. Enzymatic antioxidant system in vascular inflammation and coronary artery disease. *World J. Exp. Med.* **2015**, *5*, 218–224. [CrossRef]
41. Cao, J.Y.; Dixon, S.J. Mechanisms of ferroptosis. *Cell. Mol. Life Sci.* **2016**, *73*, 2195–2209. [CrossRef]
42. Zilka, O.; Shah, R.; Li, B.; Angeli, J.P.F.; Griesser, M.; Conrad, M.; Pratt, D.A. On the Mechanism of Cytoprotection by Ferrostatin-1 and Liproxstatin-1 and the Role of Lipid Peroxidation in Ferroptotic Cell Death. *ACS Cent. Sci.* **2017**, *3*, 232–243. [CrossRef] [PubMed]
43. Dixon, S.J.; Lemberg, K.M.; Lamprecht, M.R.; Skouta, R.; Zaitsev, E.M.; Gleason, C.E.; Patel, D.N.; Bauer, A.J.; Cantley, A.M.; Yang, W.S.; et al. Ferroptosis: An Iron-Dependent Form of Nonapoptotic Cell Death. *Cell* **2012**, *149*, 1060–1072. [CrossRef] [PubMed]

44. Varela-Fernández, R.; García-Otero, X.; Díaz-Tomé, V.; Regueiro, U.; López-López, M.; González-Barcia, M.; Lema, M.I.; Otero-Espinar, F.J. Design, Optimization, and Characterization of Lactoferrin-Loaded Chitosan/TPP and Chitosan/Sulfobutylether- β -cyclodextrin Nanoparticles as a Pharmacological Alternative for Keratoconus Treatment. *ACS Appl. Mater. Interfaces* **2021**, *13*, 3559–3575. [CrossRef] [PubMed]
45. Bilati, U.; Allémann, E.; Doelker, E. Nanoprecipitation versus emulsion-based techniques for the encapsulation of proteins into biodegradable nanoparticles and process-related stability issues. *AAPS PharmSciTech* **2005**, *6*, E594–E604. [CrossRef] [PubMed]
46. Weber, C.; Coester, C.; Kreuter, J.; Langer, K. Desolvation process and surface characterisation of protein nanoparticles. *Int. J. Pharm.* **2000**, *194*, 91–102. [CrossRef]
47. Morales-Cruz, M.; Flores-Fernández, G.M.; Morales-Cruz, M.; Orellano, E.A.; Rodriguez-Martinez, J.A.; Ruiz, M.; Griebenow, K. Two-step nanoprecipitation for the production of protein-loaded PLGA nanospheres. *Results Pharma Sci.* **2012**, *2*, 79–85. [CrossRef] [PubMed]
48. Varela-Fernández, R.; García-Otero, X.; Díaz-Tomé, V.; Regueiro, U.; López-López, M.; González-Barcia, M.; Lema, M.I.; Otero-Espinar, F.J. Lactoferrin-loaded nanostructured lipid carriers (NLCs) as a new formulation for optimized ocular drug delivery. *Eur. J. Pharm. Biopharm.* **2022**, *172*, 144–156. [CrossRef]
49. Jithan, A.; Madhavi, K.; Madhavi, M.; Prabhakar, K. Preparation and characterization of albumin nanoparticles encapsulating curcumin intended for the treatment of breast cancer. *Int. J. Pharm. Investig.* **2011**, *1*, 119–125. [CrossRef]
50. IHT Guideline. Stability Testing of New Drug Substances and Products. Q1A (R2) Current Step 4. 2003. pp. 1–24. Available online: [file:///C:/Users/MDPI/Desktop/Q1A\(R2\)%20Guideline.pdf](file:///C:/Users/MDPI/Desktop/Q1A(R2)%20Guideline.pdf) (accessed on 20 February 2022).
51. Orthner, M.P.; Lin, G.; Avula, M.; Buetefisch, S.; Magda, J.; Rieth, L.W.; Solzbacher, F. Hydrogel Based Sensor Arrays (2 × 2) with Perforated Piezoresistive Diaphragms for Metabolic Monitoring (In Vitro). *Sens. Actuators B Chem.* **2010**, *145*, 807–816. [CrossRef] [PubMed]
52. Salem, H.; Katz, S.A. *Alternative Toxicological Methods*; CRC Press: Boca Raton, FL, USA, 2003; ISBN 978-0-203-00879-9.
53. Eskes, C.; Bessou, S.; Bruner, L.; Curren, R.; Jones, P.; Kreiling, R.; Liebsch, M.; McNamee, P.; Pape, W.; Prinsen, M.K.; et al. Subgroup 3. Eye Irritation. 76. *Altern. Lab. Anim. ATLA* **2005**, *33*, 47–81. [CrossRef]
54. Sina, J.F.; Galer, D.M.; Sussman, R.G.; Gautheron, P.D.; Sargent, E.V.; Leong, B.; Shah, P.V.; Curren, R.D.; Miller, K. A Collaborative Evaluation of Seven Alternatives to the Draize Eye Irritation Test Using Pharmaceutical Intermediates. *Fundam. Appl. Toxicol.* **1995**, *26*, 20–31. [CrossRef] [PubMed]
55. Wallig, M.A.; Haschek, W.M.; Rous-Seaux, C.G.; Bolon, B. (Eds.) Chapter 22-Special Senses. In *Fundamentals of Toxicologic Pathology*, 3rd ed.; Academic Press: Cambridge, MA, USA, 2018; pp. 673–747, ISBN 978-0-12-809841-7.
56. Luepke, N. Hen's egg chorioallantoic membrane test for irritation potential. *Food Chem. Toxicol.* **1985**, *23*, 287–291. [CrossRef]
57. Kalweit, S.; Besoke, R.; Gerner, I.; Spielmann, H. A national validation project of alternative methods to the Draize rabbit eye test. *Toxicol. Vitro.* **1990**, *4*, 702–706. [CrossRef]
58. Belgamwar, V.; Shah, V.; Surana, S.J. Formulation and evaluation of oral mucoadhesive multiparticulate system containing metoprolol tartarate: An in vitro-ex vivo characterization. *Curr. Drug Deliv.* **2009**, *6*, 113–121. [CrossRef]
59. Prassl, R.; Gradauer, K.; Vonach, C.; Leitinger, G.; Kolb, D.; Fröhlich, E.; Roblegg, E.; Bernkop-Schnürch, A.; Prassl, R. Chemical coupling of thiolated chitosan to preformed liposomes improves mucoadhesive properties. *Int. J. Nanomed.* **2012**, *7*, 2523–2534. [CrossRef] [PubMed]
60. Rojas, S.; Gispert, J.D.; Abad, S.; Buaki-Sogo, M.; Victor, V.M.; Garcia, H.; Herance, J.R. In Vivo Biodistribution of Amino-Functionalized Ceria Nanoparticles in Rats Using Positron Emission Tomography. *Mol. Pharm.* **2012**, *9*, 3543–3550. [CrossRef] [PubMed]
61. Pérez-Campaña, C.; Gómez-Vallejo, V.; Martín, A.; Sebastián, E.S.; Moya, S.E.; Reese, T.; Ziolo, R.F.; Llop, J. Tracing nanoparticles in vivo: A new general synthesis of positron emitting metal oxide nanoparticles by proton beam activation. *Analyst* **2012**, *137*, 4902–4906. [CrossRef] [PubMed]
62. Allmeroth, M.; Moderegger, D.; Biesalski, B.; Koynov, K.; Rösch, F.; Thews, O.; Zentel, R. Modifying the Body Distribution of HPMA-Based Copolymers by Molecular Weight and Aggregate Formation. *Biomacromolecules* **2011**, *12*, 2841–2849. [CrossRef] [PubMed]
63. Allmeroth, M.; Moderegger, D.; Gündel, D.; Buchholz, H.-G.; Mohr, N.; Koynov, K.; Rösch, F.; Thews, O.; Zentel, R. PEGylation of HPMA-based block copolymers enhances tumor accumulation in vivo: A quantitative study using radiolabeling and positron emission tomography. *J. Control. Release* **2013**, *172*, 77–85. [CrossRef] [PubMed]
64. Fernández-Ferreiro, A.; Silva-Rodríguez, J.; Otero-Espinar, F.J.; González-Barcia, M.; Lamas, M.J.; Ruibal, A.; Luaces-Rodríguez, A.; Vieites-Prado, A.; Sobrino, T.; Herranz, M.; et al. Positron Emission Tomography for the Development and Characterization of Corneal Permanence of Ophthalmic Pharmaceutical Formulations. *Investig. Ophthalmol. Vis. Sci.* **2017**, *58*, 772–780. [CrossRef]
65. The Association for Research in Vision and Ophthalmology-Statement for the Use of Animals in Ophthalmic and Vision Research. Available online: <https://www.arvo.org/About/policies/statement-for-the-use-of-animals-in-ophthalmic-and-vision-research/> (accessed on 22 July 2020).
66. Burden, N.; Aschberger, K.; Chaudhry, Q.; Clift, M.J.D.; Doak, S.H.; Fowler, P.; Johnston, H.; Landsiedel, R.; Rowland, J.; Stone, V. The 3Rs as a framework to support a 21st century approach for nanosafety assessment. *Nanotoday* **2017**, *12*, 10–13. [CrossRef]

67. Zhang, Y.; Huo, M.; Zhou, J.; Xie, S. PKSolver: An add-in program for pharmacokinetic and pharmacodynamic data analysis in Microsoft Excel. *Comput. Methods Programs Biomed.* **2010**, *99*, 306–314. [CrossRef] [PubMed]
68. Capretto, L.; Cheng, W.; Carugo, D.; Katsamenis, O.L.; Hill, M.; Zhang, X. Mechanism of co-nanoprecipitation of organic actives and block copolymers in a microfluidic environment. *Nanotechnology* **2012**, *23*, 375602. [CrossRef] [PubMed]
69. Othman, R.; Vladisavljević, G.T.; Shahmohamadi, H.; Nagy, Z.K.; Holdich, R.G. Formation of size-tuneable biodegradable polymeric nanoparticles by solvent displacement method using micro-engineered membranes fabricated by laser drilling and electroforming. *Chem. Eng. J.* **2016**, *304*, 703–713. [CrossRef]
70. Giteau, A.; Venier-Julienne, M.-C.; Marchal, S.; Courthaudon, J.-L.; Sergent, M.; Montero-Menei, C.; Verdier, J.-M.; Benoit, J.-P. Reversible protein precipitation to ensure stability during encapsulation within PLGA microspheres. *Eur. J. Pharm. Biopharm.* **2008**, *70*, 127–136. [CrossRef] [PubMed]
71. Csaba, N.; Garcia-Fuentes, M.; Alonso, M.J. The performance of nanocarriers for transmucosal drug delivery. *Expert Opin. Drug Deliv.* **2006**, *3*, 463–478. [CrossRef] [PubMed]
72. Varela-Fernández, R.; Díaz-Tomé, V.; Luaces-Rodríguez, A.; Conde-Penedo, A.; García-Otero, X.; Luzardo-Álvarez, A.; Fernández-Ferreiro, A.; Otero-Espinar, F.J. Drug Delivery to the Posterior Segment of the Eye: Biopharmaceutic and Pharmacokinetic Considerations. *Pharmaceutics* **2020**, *12*, 269. [CrossRef] [PubMed]
73. Kumari, A.; Yadav, S.K.; Pakade, Y.B.; Singh, B.; Yadav, S.C. Development of biodegradable nanoparticles for delivery of quercetin. *Colloids Surf. B Biointerfaces* **2010**, *80*, 184–192. [CrossRef] [PubMed]
74. Mohanraj, V.J.; Chen, Y. Nanoparticles—A review. *Trop. J. Pharm. Res.* **2006**, *5*, 561–573. [CrossRef]
75. Oyarzun-Ampuero, F.; Brea, J.; Loza, M.; Torres, D.; Alonso, M. Chitosan–hyaluronic acid nanoparticles loaded with heparin for the treatment of asthma. *Int. J. Pharm.* **2009**, *381*, 122–129. [CrossRef]
76. Schiffelers, R.M.; Woodle, M.C.; Scaria, P. Pharmaceutical Prospects for RNA Interference. *Pharm. Res.* **2004**, *21*, 1–7. [CrossRef] [PubMed]
77. Tantra, R.; Tompkins, J.; Quincey, P. Characterisation of the de-agglomeration effects of bovine serum albumin on nanoparticles in aqueous suspension. *Colloids Surf. B Biointerfaces* **2010**, *75*, 275–281. [CrossRef]
78. Parveen, S.; Sahoo, S.K. Long circulating chitosan/PEG blended PLGA nanoparticle for tumor drug delivery. *Eur. J. Pharmacol.* **2011**, *670*, 372–383. [CrossRef] [PubMed]
79. Zahr, A.S.; Davis, C.A.; Pishko, M.V. Macrophage Uptake of Core–Shell Nanoparticles Surface Modified with Poly(ethylene glycol). *Langmuir* **2006**, *22*, 8178–8185. [CrossRef]
80. Prego, C.; Torres, D.; Fernandez-Megia, E.; Novoa-Carballal, R.; Quiñoá, E.; Alonso, M.J. Chitosan–PEG nanocapsules as new carriers for oral peptide delivery: Effect of chitosan pegylation degree. *J. Control. Release* **2006**, *111*, 299–308. [CrossRef] [PubMed]
81. Park, P.I.P.; Jonnalagadda, S. Predictors of glass transition in the biodegradable poly-lactide and poly-lactide-co-glycolide polymers. *J. Appl. Polym. Sci.* **2006**, *100*, 1983–1987. [CrossRef]
82. Abdelkader, H.; Fathalla, Z.; Moharram, H.; Ali, T.; Pierscionek, B. Cyclodextrin Enhances Corneal Tolerability and Reduces Ocular Toxicity Caused by Diclofenac. *Oxidative Med. Cell. Longev.* **2018**, *2018*, 5260976. [CrossRef] [PubMed]
83. Sreekumar, S.; Goycoolea, F.M.; Moerschbacher, B.M.; Rivera-Rodríguez, G.R. Parameters influencing the size of chitosan-TPP nano- and microparticles. *Sci. Rep.* **2018**, *8*, 4695. [CrossRef] [PubMed]
84. Fredenberg, S.; Wahlgren, M.; Reslow, M.; Axelsson, A. The mechanisms of drug release in poly(lactic-co-glycolic acid)-based drug delivery systems—A review. *Int. J. Pharm.* **2011**, *415*, 34–52. [CrossRef] [PubMed]
85. Budhian, A.; Siegel, S.J.; Winey, K.I. Controlling the in vitro release profiles for a system of haloperidol-loaded PLGA nanoparticles. *Int. J. Pharm.* **2008**, *346*, 151–159. [CrossRef]
86. Gaspar, M.M.; Blanco, D.; Cruz, M.E.; Alonso, M.J. Formulation of l-asparaginase-loaded poly(lactide-co-glycolide) nanoparticles: Influence of polymer properties on enzyme loading, activity and in vitro release. *J. Control. Release* **1998**, *52*, 53–62. [CrossRef]
87. Holgado, M.; Cózar-Bernal, M.; Salas, S.; Arias, J.L.; Alvarez-Fuentes, J.; Fernández-Arévalo, M.; Villafuerte, M.D.L.A.H. Protein-loaded PLGA microparticles engineered by flow focusing: Physicochemical characterization and protein detection by reversed-phase HPLC. *Int. J. Pharm.* **2009**, *380*, 147–154. [CrossRef] [PubMed]
88. Mircioiu, C.; Voicu, V.; Anuta, V.; Tudose, A.; Celia, C.; Paolino, D.; Fresta, M.; Sandulovici, R.; Mircioiu, I. Mathematical Modeling of Release Kinetics from Supramolecular Drug Delivery Systems. *Pharmaceutics* **2019**, *11*, 140. [CrossRef] [PubMed]
89. Lee, P.I. Modeling of drug release from matrix systems involving moving boundaries: Approximate analytical solutions. *Int. J. Pharm.* **2011**, *418*, 18–27. [CrossRef] [PubMed]
90. Martins, S.; Sarmiento, B.; Ferreira, D.C.; Souto, E.B. Lipid-based colloidal carriers for peptide and protein delivery-liposomes versus lipid nanoparticles. *Int. J. Nanomed.* **2007**, *2*, 595–607.
91. Saw, C.L.L.; Heng, P.W.S.; Liew, C.V. Chick Chorioallantoic Membrane as an In Situ Biological Membrane for Pharmaceutical Formulation Development: A Review. *Drug Dev. Ind. Pharm.* **2008**, *34*, 1168–1177. [CrossRef] [PubMed]
92. Vargas, A.; Zeisser-Labouèbe, M.; Lange, N.; Gurny, R.; Delie, F. The chick embryo and its chorioallantoic membrane (CAM) for the in vivo evaluation of drug delivery systems. *Adv. Drug Deliv. Rev.* **2007**, *59*, 1162–1176. [CrossRef] [PubMed]
93. Schoubben, A.; Blasi, P.; Marenzoni, M.L.; Barberini, L.; Giovagnoli, S.; Cirotto, C.; Ricci, M. Capreomycin supergenerics for pulmonary tuberculosis treatment: Preparation, in vitro, and in vivo characterization. *Eur. J. Pharm. Biopharm.* **2013**, *83*, 388–395. [CrossRef] [PubMed]

94. Kean, T.; Thanou, M. Biodegradation, biodistribution and toxicity of chitosan. *Adv. Drug Deliv. Rev.* **2010**, *62*, 3–11. [CrossRef] [PubMed]
95. Luaces-Rodríguez, A.; Touriño-Peralba, R.; Alonso-Rodríguez, I.; García-Otero, X.; González-Barcia, M.; Rodríguez-Ares, M.T.; Martínez-Pérez, L.; Aguiar, P.; Gómez-Lado, N.; Silva-Rodríguez, J.; et al. Preclinical Characterization and Clinical Evaluation of Tacrolimus Eye Drops. *Eur. J. Pharm. Sci.* **2018**, *120*, 152–161. [CrossRef]

Article

Physicochemical Stability of a Novel Tacrolimus Ophthalmic Formulation for the Treatment of Ophthalmic Inflammatory Diseases

Marion Barrieu ¹, Philip Chennell ^{2,*}, Mouloud Yessaad ¹, Yassine Bouattour ², Mathieu Wasiak ¹, Mireille Jouannet ¹, Yoann Le Basle ² and Valérie Sautou ²

- ¹ CHU Clermont-Ferrand, Pôle Pharmacie, F-63003 Clermont-Ferrand, France; mbarrieu@chu-clermontferrand.fr (M.B.); myessaad@chu-clermontferrand.fr (M.Y.); mwasiak@chu-clermontferrand.fr (M.W.); mjouannet@chu-clermontferrand.fr (M.J.)
- ² Université Clermont Auvergne, CHU Clermont Ferrand, Clermont Auvergne INP, CNRS, ICCF, F-63000 Clermont-Ferrand, France; ybouattour@chu-clermontferrand.fr (Y.B.); ylebasle@chu-clermontferrand.fr (Y.L.B.); vsautou@chu-clermontferrand.fr (V.S.)
- * Correspondence: pchennell@chu-clermontferrand.fr

Citation: Barrieu, M.; Chennell, P.; Yessaad, M.; Bouattour, Y.; Wasiak, M.; Jouannet, M.; Le Basle, Y.; Sautou, V. Physicochemical Stability of a Novel Tacrolimus Ophthalmic Formulation for the Treatment of Ophthalmic Inflammatory Diseases. *Pharmaceutics* **2022**, *14*, 118. <https://doi.org/10.3390/pharmaceutics14010118>

Academic Editors: Francisco Javier Otero-Espinar and Anxo Fernández Ferreiro

Received: 5 December 2021

Accepted: 29 December 2021

Published: 4 January 2022

Publisher's Note: MDPI stays neutral with regard to jurisdictional claims in published maps and institutional affiliations.



Copyright: © 2022 by the authors. Licensee MDPI, Basel, Switzerland. This article is an open access article distributed under the terms and conditions of the Creative Commons Attribution (CC BY) license (<https://creativecommons.org/licenses/by/4.0/>).

Abstract: Tacrolimus is an immunosuppressant used to treat a large variety of inflammatory or immunity-mediated ophthalmic diseases. However, there are currently no commercial industrial forms available that can provide relief to patients. Various ophthalmic formulations have been reported in the literature, but their stability has only been tested over short periods. The objective of this study was to evaluate the physicochemical stability of a preservative-free tacrolimus formulation (0.2 and 1 mg/mL) at three storage temperatures (5 °C, 25 °C and 35 °C) for up to nine months in a multidose eyedropper. Analyses performed were the following: visual inspection and chromaticity, turbidity, viscosity, size of micelles, osmolality and pH measurements, tacrolimus quantification by a stability-indicating liquid chromatography method, breakdown product research, and sterility assay. In an in-use study, tacrolimus quantification was also performed on the drops emitted from the eyedroppers. All tested parameters remained stable during the nine month period when the eyedrops were stored at 5 °C. However, during storage at 25 °C and 35 °C, several signs of chemical instability were detected. Furthermore, a leachable compound originating from a silicone part of the eyedropper was detected during the in-use assay. Overall, the 0.2 mg/mL and 1 mg/mL tacrolimus ophthalmic solutions were physicochemically stable for up to nine months when stored at 5 °C.

Keywords: tacrolimus; ophthalmic solution; physicochemical stability; container-content interaction; leachable compound

1. Introduction

Tacrolimus (TAC), also named FK-506, is a macrolide immunosuppressant of the calcineurin inhibitor pharmacological class that binds to a specific cytosolic protein FKBP12 immunophilin (also named FK506 binding protein) [1,2], forming a complex that binds to calcineurin and inhibits it. Inhibiting calcineurin blocks the dephosphorylation of NFAT (nuclear factor of activated T cells), preventing it from crossing the nuclear envelope and entering the nucleus. Therefore, NFAT will not bind to gene promoter regions, thus decreasing the transcription of cytokines like IL-2 which have an essential role in T cell activation [3]. In addition to use in the field of transplantation to prevent graft rejection, TAC is also used to treat a large variety of inflammatory or immunity-mediated ophthalmic diseases such as dry eye syndrome (caused by Sjögren's syndrome [4] or by graft versus host disease (GVHD) [5]), corneal or conjunctive immunological diseases [6], chronic follicular conjunctivitis or severe vernal and atopic keratoconjunctivitis [7–9]. Because of its mechanism of action, which is similar to cyclosporine, and its strong immunosuppressive

power, tacrolimus is a good candidate to manage ophthalmic pathologies [6] for which cyclosporine is not tolerated or no longer effective. Moreover, it expands the therapeutic arsenal, particularly for vernal keratoconjunctivitis (VKC) and allergic eye diseases, the management of which is complex. According to the literature, ophthalmic TAC is used at various concentrations, depending on the disease, varying from 0.003% to 0.1% (*m/v*). Indeed, tested concentrations generally ranged from 0.003% to 0.03% for the treatment of VKC, and from 0.02% to 0.1% for the treatment of allergic eye diseases [10,11]. The administration can fluctuate from once to several times a day according to the concentration and for a duration of treatment which can range from a few days to several months or years for chronic diseases [8].

Tacrolimus is a hydrophobic molecule with a calculated log P of 2.7 [12]. Thus, its low solubility in aqueous solutions at clinically relevant concentrations makes the development of a stable ophthalmic formulation complex. To date, there is no tacrolimus-based ophthalmic medication commercially available that is well tolerated and that can provide relief to patients. Talymus, which is a 1 mg/mL (0.1%) tacrolimus suspension, has been marketed since 2008 in Japan, but is not available in USA or in Europe, except in France under a special nominative temporary use authorization [13]. However, this medication can also cause numerous adverse effects such as burning or foreign body sensation in the eye (40% of patients), eye irritation (more than 20% of patients) eye pain, ocular hyperaemia, photophobia, etc. [14]. In addition, and despite the fact that medications from the treatment of chronic ophthalmic diseases are ideal candidates for preservative-free formulations [15], Talymus contains a preservative (benzalkonium chloride which is a quaternary ammonium compound), which is well known to cause cytotoxic damage to conjunctival and corneal epithelial cells, resulting in signs and symptoms of ocular surface disease, at concentrations starting at 0.005% [16]. Whilst the concentration of benzalkonium chloride in Talymus is not disclosed in the available Product Information, commonly used concentrations in ophthalmic medications range between 0.004 and 0.025%, and numerous studies have shown that eye drops with this preservative cause sometimes severe clinical consequences for the patients, comparatively to unpreserved medications [16,17]. This has led to numerous formulations being developed and tested by the pharmaceutical and medical communities. Some ophthalmic formulations based on castor oil [18] or olive oil [19] have been reported in the literature, but numerous adverse effects such as redness, burning, itching have been identified due to the use of these oily excipients. Other formulations have been tested, but their long-term stability (more than three months) is either insufficient [20] or was not evaluated [21]. These galenic and chemical issues make it complicated for compounding pharmacies to develop and produce tacrolimus ophthalmic solutions. The objective of this study was therefore to develop a physicochemically stable, preservative-free formulation of tacrolimus, at two different concentrations, 0.2 mg/mL (0.02% *m/v*) and 1 mg/mL (0.1% *m/v*), in order to cover a wide therapeutic spectrum of ophthalmic illnesses (VKC and allergic eye diseases).

2. Materials and Methods

2.1. Preparation and Storage of TAC Formulation

Tacrolimus ophthalmic solutions were prepared at two concentrations: 0.2 mg/mL (0.02% *m/v*) and 1 mg/mL (0.1% *m/v*). Tacrolimus powder was dissolved into absolute ethanol at room temperature under gentle agitation. The Kolliphor EL[®] (KEL) was then added and mixed under vigorous mechanical agitation. In order to stabilize the pH, the hydrogenophosphate–hyaluronate buffer solution was added. The quantities used are summarized in Table 1. The final concentrations of ethanol were of 3.76 mg/mL (0.08 µmol/mL) and 18.79 mg/mL (0.41 µmol/mL) for, respectively, the 0.2 and 1 mg/mL tacrolimus formulation.

Table 1. Composition of the tacrolimus ophthalmic formulations. Q.S: Quantity Sufficient.

Chemical Compounds	Formulation	
	0.2 mg/mL = 0.02%	1 mg/mL = 0.1%
Tacrolimus monohydrate Batch 70312001218, exp 01/10/2023, Inresa, France	200 mg	1000 mg
KEL: Macrogol 35 glycerol ricinoleate (Kolliphor EL [®]) Batch 192835002, exp 30/04/2021, Inresa, France	16 g	80 g
Absolute ethanol Batch 20010089/B, exp 01/24, Cooper, France	4.76 mL	23.81 mL
Buffer solution (composition described below)	Q.S. 1 L	Q.S. 1 L
Buffer Solution		
Sodium dihydrogenophosphate dihydrate (NaH ₂ PO ₄) Batch 190298040, exp. 30/11/2021, Inresa, France	500 mg	
Disodic monohydrogenophosphate dodecahydrate (Na ₂ HPO ₄) Batch 18129611, exp. 30/04/2023, Inresa, France	37 mg	
Hyaluronate sodium Batch PH13560S02, exp 01/12/2023, Inresa, France	1500 mg	
Sodium chloride (NaCl) 0.9% Versylene [®] ; Fresenius Kabi France, Louviers, France	Q.S. 1 L	

The final solutions of tacrolimus were filtered through a 0.22 µm filter Stericup[®] Sterile Vacuum Filtration Systems (Merck Millipore, MC2, Clermont-Ferrand, France) and then an aseptic repartition was realized under the laminar airflow of an ISO 4.8 microbiological safety cabinet using a conditioning pump (Repeater[®] pump, Baxter, Guyancourt, France). The low-density polyethylene multidose eyedroppers (reference VPL28B10N02, Laboratoire CAT, Lorris, France), possessing a sterility preserving system (Novelia[®] nozzle) using silicones parts to hermetically release the eye drops, were filled with 5 mL and stored until analysed.

2.2. Study Design

The stability of the tacrolimus formulations was studied in unopened eyedroppers stored in the dark vertically for nine months at different storage temperatures: 5 ± 3 °C (Liebherr refrigerator), at 25 ± 1 °C and 35 ± 1 °C with 60 ± 5% residual humidity in a validated climate chamber (Binder GmbH, Tuttlingen, Germany). A simulated used study was also performed during 28 days at 5 °C after 8 months of storage at 5 °C for both concentrations.

2.3. Stability of Tacrolimus in Unopened Multidose Eyedroppers

Immediately after the preparation (Day 0 = D0) and at months 1 (M1), 2 (M2), 3 (M3), 4 (M4), 6 (M6), 8 (M8) and 9 (M9), four units ($n = 4$) of each concentration and each storage temperature condition were taken for analysis. The different parameters that were evaluated during the study are summarized in Table 2. At the initial day (D0), the analyses were performed immediately after conditioning in order to have the most representative results of the initial conditions (with the least degradation or modification of parameters).

2.4. Stability of Tacrolimus in Opened Multidose Eyedroppers (Simulated Use Study)

A simulation of patient use was performed after eight months of storage at 5 °C. Eight units of each concentration were opened and one drop from each eyedropper was manually emitted out of the bottle and collected for analysis every day (except weekends) twice a day (morning and evening) for one month and tacrolimus concentration was measured in the emitted drops. To ensure that a sufficient volume was collected to allow tacrolimus quantification, at each analysis time the drops were pooled by two (each time from the same

two vials, which remained associated throughout the analysis). Thus, the results of these analyses were returned with $n = 4$. The units were stored vertically at 5 ± 2 °C between drops gathering. Moreover, after the 28 days, units were opened and remaining solution was subjected to tacrolimus quantification as well as pH and osmolality measurements.

Table 2. Summary of analyses at each analysis time (X: assessed parameters). TAC: tacrolimus; BPr: breakdown product research.

Months	Studied Parameters					
	Visual Aspect, pH, Osmolality, TAC quantification & BPr	Chromaticity	Viscosity	Turbidity	Micelle Size	Sterility Assay
0	X	X	X	X	X	X
1	X			X		
2	X			X		
3	X	X	X	X	X	X
4	X					
6	X	X	X	X	X	X
8	X					
9	X	X	X	X	X	X

2.5. Analyses Performed on the Tacrolimus Solution

2.5.1. Visual Inspection

The multidose eyedroppers were emptied into glass test tubes without passing through the delivery device, and the tacrolimus solutions were visually inspected under daylight and under polarized white light from an inspection station (LV28, Allen and Co., Liverpool, UK). Aspect and colour of the solutions were noted, and a screening for visible particles, haziness, or gas development was performed.

2.5.2. Chromaticity and Luminance Analysis

Chromaticity and luminance were measured with a UV-visible spectrophotometer (V670, Jasco Corporation®, Lisses, France) using the mode Colour Diagnosis of the built-in software (Spectra Manager®, version 2.12.00, Jasco Corporation®, Lisses, France) with a quartz measuring cell. The CIE $L^*a^*b^*$ colour parameters were used to represent the colour changes [22,23]. Transmittance spectra were obtained by using a light source D65 (wavelength between 780 and 380 nm), data pitch 5 nm, colour matching JIS Z8701-1999 and scan speed 400 nm/min. The difference of colour perception (ΔE) was calculated using the following equations for the spectrophotometric analysis [24]:

$$\Delta a = a^* - a_0^* \quad (1)$$

$$\Delta b^* = b^* - b_0^* \quad (2)$$

$$\Delta L^* = L^* - L_0^* \quad (3)$$

$$\Delta E = ((\Delta L^*)^2 + (\Delta a^*)^2 + (\Delta b^*)^2)/0.5 \quad (4)$$

a_0^* , b_0^* and L_0^* were the initial values at day 0 and Δa^* , Δb^* and ΔL^* were the difference in chromatic coordinates and lightness. The values of each colour parameter are expressed as the mean of four different samples.

2.5.3. Tacrolimus Quantification and Breakdown Products (BP) Research

- Chemicals and instrumentation

The quantification method used was directly transposed from the stability indicating ultra-high performance liquid chromatography (UHPLC) method published by Peterka et al. [25], after minor adaptations from UHPLC to high performance liquid chromatography (HPLC). The HPLC separation column used was a Kinetex® Core-Shell 2.6 μm EVO C18 100 Å, 100 mm \times 3 mm, reference 00D-4725-Y0, (Phenomenex, Le Pecq, France), with an associated security guard ULTRA EVO-C18 sub2 μm -Coreshell reference AJ0-9296 (Phenomenex, Le Pecq, France). This column has an equivalent stationary phase to that

used by Peterka et al. [25] (C18 phase, USP L1 classification). Due to the modification of the column granulometry, the flow rate was increased to 1 mL/min and the mobile phase gradient was lengthened. The method was validated on a reverse-phase HPLC Prominence-I LC2030C 3D with diode array detection (Shimadzu France SAS, Marne La Vallée, France), and the associated software used to record and interpret chromatograms was LabSolutions® version 5.82 (Shimadzu France SAS, Marne La Vallée, France). The mobile phase was a gradient mixture of phases A and B. Mobile phase A was an aqueous ortho-phosphoric acid solution at 85% (0.1 %, *v/v*). Mobile phase B was prepared by mixing 500 mL of ACN (Acetonitrile for HPLC, 99.95% ref 412342 2.5L) and 47 mL of MTBE (tert-Butyl methyl ether for HPLC, $\geq 99.8\%$, Sigma Aldrich, Saint Quentin Fallavier, France), ref 34875-1L). The column oven was set at 70 °C and the mobile phase was stored at ambient temperature before reaching the column. The gradient used is presented in Table 3. In order to verify the correct transposition of the method and to allow the identification as proposed in the original method of tacrolimus and its equilibrium compounds I and II, related substances and byproducts (ascomycin) and breakdown products (tacrolimus alpha-hydroxy acid and tacrolimus regioisomer), the relative retention times of tacrolimus and ascomycin (impurity A) were checked against those obtained by Peterka et al. [25]. These compounds were analysed as recommended by the tacrolimus European Pharmacopoeia monography [26].

Table 3. Gradient used for the liquid chromatography mobile phase.

Time (minutes)	Mobile Phase	
	A (%)	B (%)
0	63	37
1	63	37
12	60	40
17	45	55
19	10	90
22.5	10	90
23	63	37
27	63	37

- Method validation

Linearity was verified by preparing one calibration curve daily for three days using five concentrations of tacrolimus (European Pharmacopoeia reference standard Y0001925) at 2.5, 5, 20, 50 and 100 µg/mL, diluted with a solvent consisting of ACN-water (70:30, *v/v*). Each calibration curve was considered acceptable if it had a determination coefficient R^2 equal or higher than 0.999. Variance homogeneity of the curves was verified using a Cochran test. ANOVA tests were applied to determine the applicability of the linear model. Each day for three days, six solutions of tacrolimus 30 µg/mL were prepared, analysed, and quantified using a calibration curve prepared the same day [27]. To verify the method precision, repeatability was estimated by calculating relative standard deviation (RSD) of intraday analysis and intermediate precision was evaluated using an RSD of interdays analysis [27]. Both RSDs were considered acceptable if they were lower than 5%. Method accuracy was verified by evaluating the recovery of five theoretical concentrations to experimental values found using mean curve equation, and results were considered acceptable if found within the range of 90–110%. The overall accuracy profile was constructed according to Hubert et al. [28–30]. An evaluation of the matrix effect was performed by reproducing the previous methodology in the presence of all excipients included in the formulation and by comparing the calibration curves and intercepts. Specificity was also assessed by comparing the UV spectra obtained with the DAD detector for tacrolimus with and without the excipients.

2.5.4. pH

For each unit, pH measurements were made using a Seven Multi TM pH-meter with an In Lab Micro Pro ISM glass electrode (Mettler-Toledo, Viroflay, France). Measures were preceded by an instrument validation using standard buffer solution of pH 1.68, pH 4.01, pH 7.01 and pH 10.01 (Mettler-Toledo, Viroflay, France).

2.5.5. Osmolality

The osmolality was measured on 20 μ L samples using a freezing point osmometer Model 2020 Osmometer[®] (Advanced instruments Inc., Radiometer, SAS, Neuilly Plaisance, France). Measurements were preceded by an instrument validation performed using a calibrated osmolality standard of 290 mOsmol/kg.

2.5.6. Turbidity

Turbidity of the different solutions was measured using a 2100Q Portable Turbidimeter (Hach Lange, Marne La Vallée, France). In order to obtain the necessary volume for each analysis (>15 mL), four samples per analysed experimental condition and assay time have to be pooled. The results were expressed in Formazin Nephelometric Units (FNU).

2.5.7. Viscosity Measurements

Viscosity was measured using a Brookfield DV1 viscosimeter Labomat associated with a circulation thermostat Julabo, at 25 °C. In order to obtain the necessary volume for each analysis (>20 mL), four samples per analysed experimental condition and assay time have to be pooled. The results were expressed in cP.

2.5.8. Micelle Size Measurements

The size of the tacrolimus micelles was determined by dynamic light scattering measurements using a Zetasizer Nano ZS (Malvern Instruments SARL, Orsay Cedex, France). Each sample (1 mL conditioned a in clear disposable polystyrene cell) was automatically screened 3 times and the results were then averaged. The size distribution by intensity was converted into a size distribution by volume by the instrument's software after use of the solution's refractive index as indicated by the user manual. Comparatively, samples of each formulation containing just the excipients (no tacrolimus) were also submitted to this analysis.

2.5.9. Sterility Assay

The sterility of the solutions was assessed as indicated in the European Pharmacopoeia sterility assay (2.6.1) [31]. Under the laminar air flow of an ISO 4.8 microbiological safety cabinet, each analysed eyedropper was opened, and its contents were filtered under vacuum using a Nalgene[®] analytical test filter funnel onto a 47 mm diameter cellulose nitrate membrane with a pore size of 0.45 μ m (ref 147-0045, Thermo Scientific, purchased from MC2, Clermont-Ferrand, France). The membranes were then rinsed with 500 mL deionized water (Versylene[®]; Fresenius Kabi, Louviers, France) and divided into two equal parts. Each individual part was transferred to each of a growth medium of fluid thioglycolate and soya trypticase. Each culture medium was then incubated for 14 days at 30–35 °C (thioglycolate broth) or 20–25 °C (soya trypticase broth) and visually examined for any signs of microbial growth.

2.5.10. Determination of the Volume of an Eye Drop

To determine an average density, 200 μ L of the prepared solution was weighed ten times. Then ten drops emitted from the eyedroppers were weighed six times to determine the volume of one drop from the previously determined density. This operation was performed for both concentrations of eye drops.

2.6. Degradation Kinetics during Storage

In order to be able to estimate the potential impact of temperature excursions during storage, an evaluation of the degradation kinetics was investigated. Because the study was performed with three different temperatures (5 °C, 25 °C, and 35 °C), it was possible to evaluate the value of the reaction coefficient for an unstudied temperature using the Arrhenius equation [32]:

$$k = A \times \exp\left(-\frac{E_a}{RT}\right) \quad (5)$$

With k the reaction rate coefficient, A the pre-exponential factor, E_a the activation energy, R the universal gas constant = $8.314 \text{ J}\cdot\text{mol}^{-1}\cdot\text{K}^{-1}$ and T the temperature in Kelvin.

First, the degradation rate k for each storage temperature was calculated after verification that the concentration (C) decreased following a first order reaction (i.e., $C = C_0 e^{-kt}$), by plotting $\ln(C)$ as function of the time. Then, each $\ln(k)$ value that was obtained was plotted as a function of $1/T$. The curve has a slope value equal to $-E_a/R$ and an intercept of $\ln(A)$:

$$\ln k = \ln A - \left(\frac{E_a}{R} \times \frac{1}{T}\right) \quad (6)$$

It is then possible to extrapolate, for different temperatures, the k value to determine a stability time such as the time (t) for which the concentration declined below 90% of the initial concentration, for this given different temperature. Once the new k is obtained for a given temperature, it is injected into the integrated equation of a reaction of order 1 and t determined using the following equation:

$$\ln(C_0 \times 0.9) = \ln C_0 - (k \times t_{90}) \quad (7)$$

Which means $t = -\ln 0.9/k$.

2.7. Data Analysis—Acceptability Criteria

The stability of the tested tacrolimus formulations was evaluated using the following physicochemical parameters: visual aspect of the solution, turbidity and micelle size, viscosity, pH and osmolality, tacrolimus concentration and a research of BPs. The study was conducted following methodological guidelines issued by the International Conference on Harmonisation for stability studies [33] and recommendations issued by the French Society of Clinical Pharmacy (SFPC) and by the Evaluation and Research Group on Protection in Controlled Atmosphere (GERPAC) [34]. A variation of concentration outside the 90–110% range of initial concentration (including the limits of a 95% confidence interval of the measurements) was considered as a sign of instability. The presence of BPs and the variation of the physicochemical parameters were also considered a sign of tacrolimus instability. For the sake of comparison, they were also checked against quantities found in a commercial tacrolimus injectable solution (Prograf® 5 mg/mL, Astellas Pharma, Levallois Perret, France). The observed solutions must be of unchanged aspect with regards to the initial aspect. Because there are no standards that define acceptable pH or osmolality variation, pH measures were considered acceptable if they did not vary by more than one pH unit from the initial value [34], and osmolality results were interpreted considering clinical tolerance of the preparation.

2.8. Complementary Study: Analysis of a Suspected Leachable Compound

In a complementary study aimed at analysing a suspected leachable compound detected during the simulated use study in the emitted drops, the following experiments were performed. Firstly, to confirm that the detected compound was not linked in any way to the presence of tacrolimus, the silicone part of the Novelia® (blue valve that is in contact last with the eye drop) device was put in contact with 3 mL a KEL-ethanol (tacrolimus free) mixture and left in contact for 10 days at $25 \pm 2 \text{ °C}$ and $60 \pm 5\%$ residual humidity (Binder GmbH, Tuttlingen, Germany) and the solutions were then analysed ($n = 3$). In

parallel, in order to know if the extracted compound possessed more of a hydrophilic or hydrophobic affinity, the pieces were put in contact independently with 3 mL of water, 3 mL of an ethanol-water mixture (50/50: *v/v*) and 3 mL of ethanol and left in contact also for 10 days in the same storage conditions and the solutions were analysed by HPLC. Secondly, in order to try to identify the leachable compound, the ethanol solution in contact with the valves was analysed by Gas Chromatography coupled to a Mass Spectrometer (GC-MS) on a Clarus 500 GC-MS chromatograph (Perkin Elmer, Boston, MA, USA) using electronic impact ionization tuned to 70 eV and an Optima 5 Accent, 5% diphenyl 95% dimethylpolysiloxane (30 m × 0.25 μm × 0.25 mm ID) capillary column (Macherey-Nagel, Düren, Germany). The vector gas was helium at a flow rate of 0.8 mL/min. The injection volume was 1 μL and the injector temperature was set at 300 °C. The split ratio was 25:1. A temperature gradient was performed: at t_0 min the temperature was fixed at 100 °C and it was increased to 15°/min to 160 °C for 1min, then it was increased to 25 °C/min until 300 °C until the 30 min of analysis. The transfer line was set at 300 °C, the source temperature at 230 °C, and the quadrupole temperature at 150 °C. Electronic impact spectra were recorded in the m/z 50 to 500 range for the scan cycles. Tentative identification of observed peaks was performed with NIST library. When necessary, it was confirmed by analysis of the corresponding chromatographic standard solution. The most plausible candidate compounds (2,4-Di-*tert*-butylphenol, CAS 96-76-4 and 1,3-Di-*tert*-butylbenzene, CAS number 1014-60-4) were then also tested using the GC-MS and tacrolimus HPLC method and the retention times and spectra were compared with those of the leachable compound.

3. Results

3.1. Quantification of Tacrolimus: HPLC Method Validation

Tacrolimus presented a retention time of 10.4 ± 0.3 min and a relative retention time of 22.2 (relative to the solvent front), thus being nearly identical to the one found in the method published by Peterka et al. [25], which was of 22.1. The calibration curve used is linear for concentrations ranging from 2.5 to 100 μg/mL, with a mean linear regression equation of $Y = 5644.959X - 3552.581$, where X is the tacrolimus concentration in μg/mL and Y the surface area of the tacrolimus peak. The intercept was not statistically significantly different from zero, and the mean determination coefficient R^2 of three calibration curves was of 0.9998. No matrix effect was detected. The relative mean relative bias coefficients were less than 3.0% for the calibration points, except for the 2.5 μg/mL, for which it was 9.0%. The mean repeatability RSD coefficient and mean intermediate precision RSD coefficient were less than 5.0%. The accuracy profile constructed with the data showed that the limits of 95% confidence interval coefficients were all within 5.8% of the expected value, except for the 2.5 μg/mL calibration point, for which the upper range limit was 9.7% (see Supplementary Data File S1). The limit of detection was evaluated at 1 μg/mL, and the limit of quantification was fixed at 2.5 μg/mL. Figure 1 presents the chromatograms of a blank solution, a solution containing only excipients but no tacrolimus, and a tacrolimus formulation diluted to 50 μg/mL in ACN-water (70:30, *v/v*).

3.2. Stability of Tacrolimus in Unopened Multidose Eyedroppers

3.2.1. Physical Stability

- Visual inspection and chromaticity measurements

All samples stayed limpid and with a slight yellow tinge throughout the study, for both tested concentrations and conservation temperatures, and there was no appearance of any visible particulate matter, haziness or gas development. For the chromaticity measurements, the initial parameters at day 0 were of 98.79 ± 0.06 , -0.30 ± 0.03 and 2.23 ± 0.03 for respectively L^* , a^* and b^* for the 1 mg/mL formulation and 99.71 ± 0.02 , -0.11 ± 0.06 and 0.72 ± 0.05 for the 0.2 mg/mL formulation (mean ± standard deviation, $n = 4$). These parameters did not vary significantly throughout the study (see Supplementary Materials File S1).

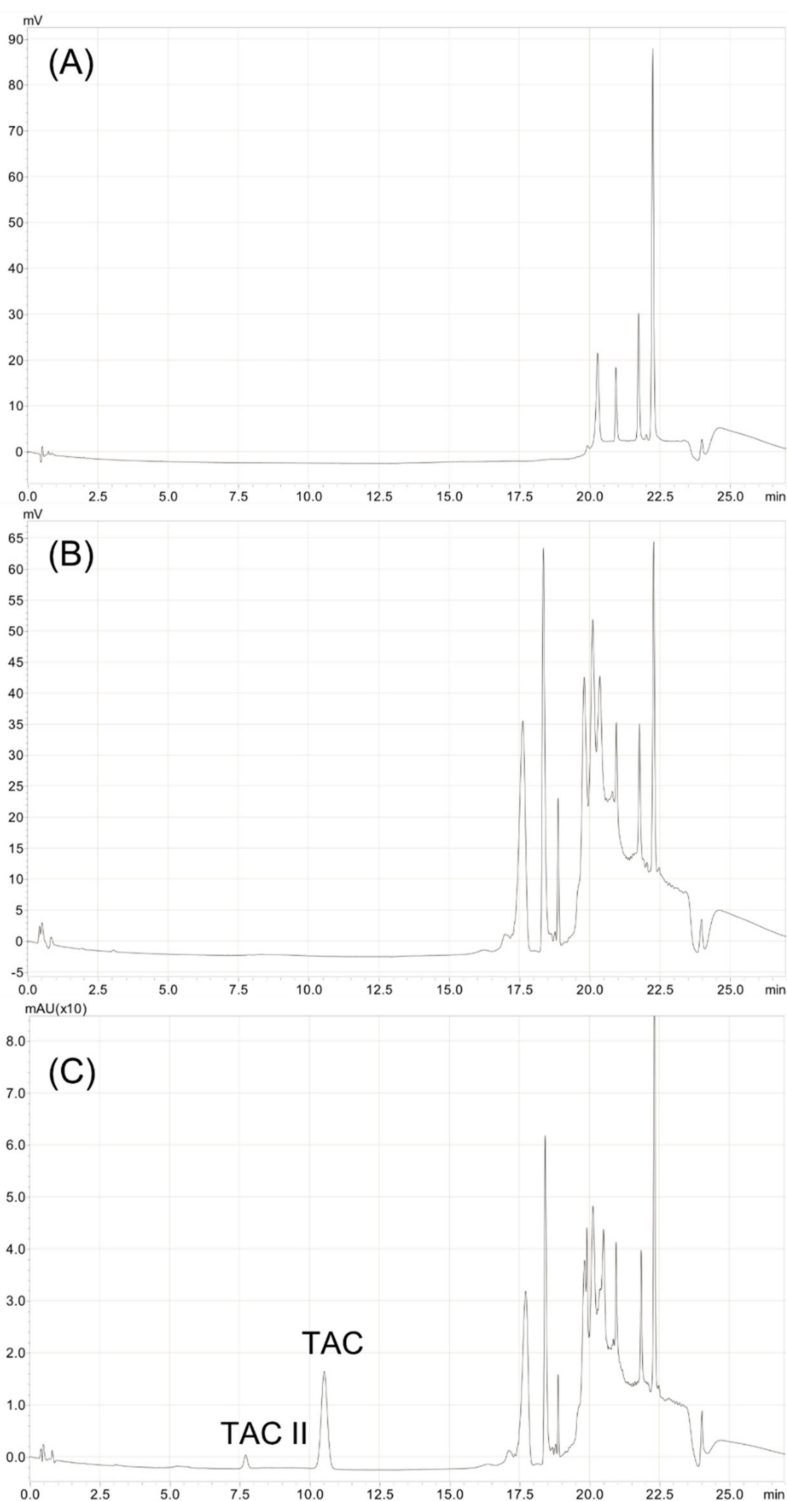


Figure 1. Chromatograms of (A) water blank, (B) Excipients (formulation without tacrolimus) diluted 1/20th and (C) 1 mg/mL tacrolimus formulation diluted 1/20th to 50 µg/mL in acetonitrile-water (70:30, *v/v*). TAC: tacrolimus. TAC II: tacrolimus compound II (equilibrium compound).

- Turbidity

The initial turbidity was of 10 and 3.5 FNU for, respectively, the 1 mg/mL and 0.2 mg/mL tacrolimus concentration. Throughout the study, turbidity did not vary by more than 0.4 FNU when stored at 5 °C and 1 FNU for the 25 °C and 35 °C storage temperature conditions for the 1 mg/mL concentration. For the 0.2 mg/mL concentration, turbidity did

not vary by more than 0.7 FNU, 1.4 FNU and 0.4 FNU for, respectively, the 5 °C 25 °C and 35 °C storage conditions.

- Viscosity

The initial viscosity was of 4.97 and 3.56 cP, respectively, for the 1 mg/mL and 0.2 mg/mL tacrolimus concentration. Throughout the study, the viscosity did not vary by more than 0.36 cP for both concentrations and all three storage temperatures.

- Micelle size

At day 0, for the 1 mg/mL formulation, the micelles were divided into two populations (size distribution): 99.85% had an average size of 1.96 ± 0.66 nm and 0.15% had an average size of 15.31 ± 6.22 nm, while for 0.2 mg/mL formulation, the micelles formed a single population with an average size of 3.01 ± 1.12 nm. During the nine months of storage, the micelle size did not vary by more than 0.03 nm, 0.03 nm and 0.04 nm for the storage condition at 5 °C, 25 °C and 35 °C, respectively, for the 1 mg/mL eye drops and by more than 0.53 nm, 0.54 nm and 0.61 nm for the storage condition at 5 °C, 25 °C and 35 °C, respectively, for the 0.2 mg/mL eye drops. The micelle size for a tacrolimus-free formulation was similar to that of the tacrolimus formulations.

3.2.2. Chemical Stability

- Tacrolimus quantification and BPr

At the beginning of the study, the tacrolimus concentrations were of 1.02 ± 0.02 and 0.20 ± 0.01 mg/mL (mean \pm 95% confidence interval) for the 1 mg/mL and 0.2 mg/mL formulations. Throughout the study, the concentrations remained well within the 90–110% concentration range when the formulations were stored at 5 °C (after nine months of storage, tacrolimus concentrations were of $98.80 \pm 1.88\%$ and $100.03 \pm 0.76\%$, respectively, for the 0.2 mg/mL and 1 mg/mL formulations), but the concentrations decreased when stored and 25 °C and 35 °C, as presented in Figure 2.

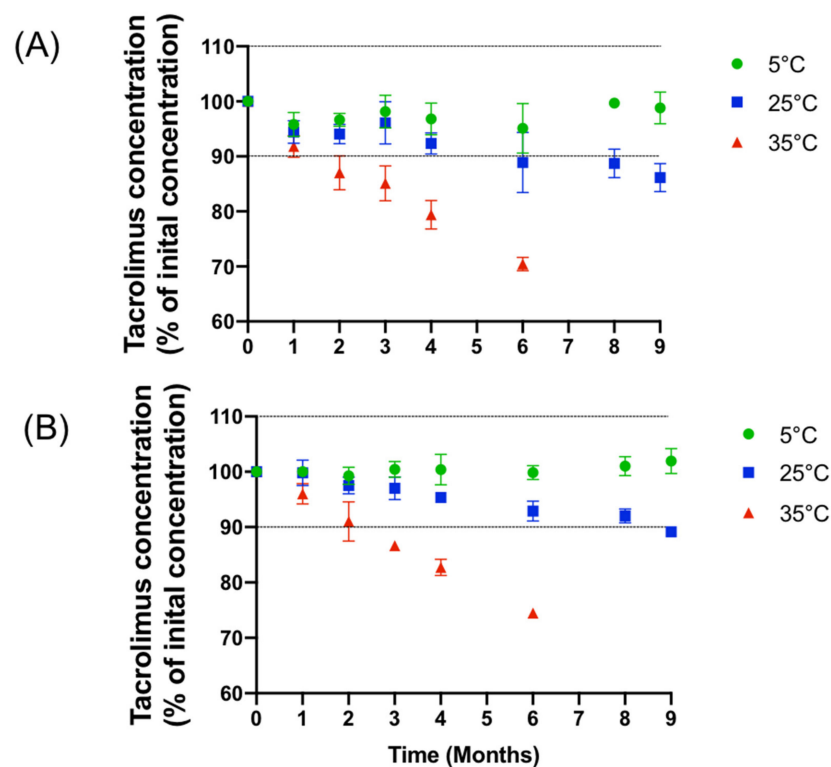


Figure 2. Evolution of the mean concentration of (A): 1 mg/mL and (B): 0.2 mg/mL formulation with IC 95% during nine months at various storage temperature.

This decrease correlates well with the appearance of multiple breakdown products, especially at 35 °C, but also to a lesser degree at 25 °C (Figure 3). Due to the important decrease in tacrolimus concentrations at 35 °C and the appearance of several degradation products, the analyses were stopped after six months of monitoring for both concentrations stored at 35 °C.

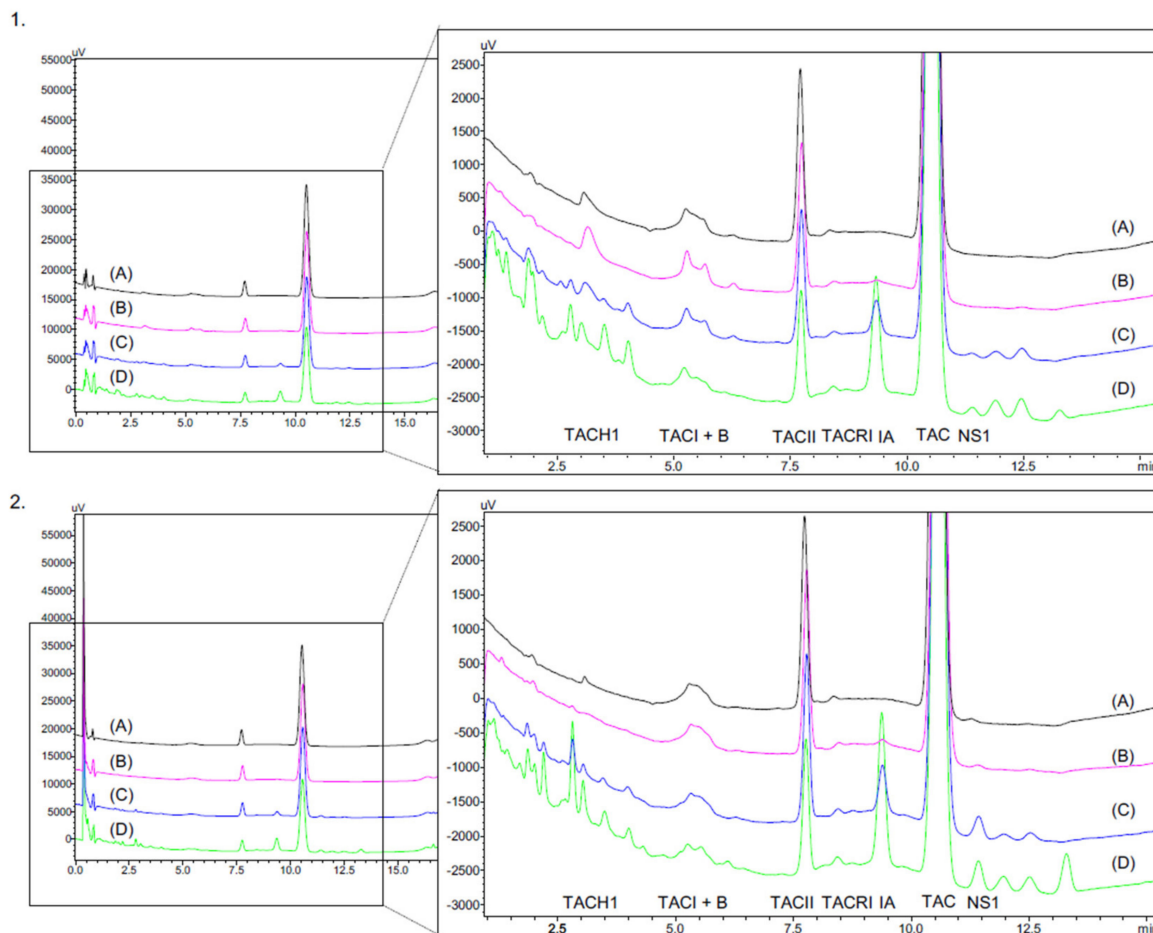


Figure 3. Chromatogram of 1mg/mL (1) and 0.2 mg/mL (2) tacrolimus formulations at day 0 (D0) (A) and after six months of storage at various temperature: (B) at 5 °C/M6; (C) at 25 °C/M6; (D) at 25 °C/M6. TAC-H1: tacrolimus alpha-hydroxy acid; TAC I: tacrolimus compound I (diol); B: impurity B; TAC II: Tacrolimus compound II (10-epimer) TAC: Tacrolimus; TAC-RI: tacrolimus regioisomer; IA: impurity A (ascomycin); NS: nonspecified compound.

In the initial tacrolimus solution, the impurities specified by the European Pharmacopeia were detected at 220 nm and identified. Table 4 presents the ratio of areas under the curve and the relative retention times of the principal's impurities and breakdown products found in formulations stored at 5 °C compared to the other storage temperatures. In the formulations stored for nine months at 5 °C, the content of impurity A was found in similar quantities to those found in Prograf[®] and did not exceed the 0.5%. The amounts of TAC H1 in the formulations were lower than in the Prograf[®] solution. TAC RI compounds and the unspecified impurity (NS1) were not present in Prograf[®]. However, these compounds were present in the formulations at the initiation of the study. Overall, the appearance of breakdown products and impurities was significantly accelerated by increased storage temperatures.

Table 4. Follow-up of the principal tacrolimus impurities and degradation (expressed as the ratio of the area of the peaks observed over the area of tacrolimus at the initial time and comparison with the impurities found in Prograf®. NS: non-specified impurity; RRT: relative retention time, based on tacrolimus retention time, ND: not detected.

Impurities and BP		TAC H1		NS1		TAC RI		Impurity A		NS2	
		%	RRT	%	RRT	%	RRT	%	RRT	%	RRT
Initial condition	1 mg/mL	1.157	0.293	0.110	0.596	0.189	0.794	ND	ND	ND	ND
	0.2 mg/mL	0.180	0.292	ND	ND	0.211	0.793	ND	ND	0.140	1.069
Study endpoint	1 mg/mL 5 °C	0.309	0.299	ND	ND	0.243	0.811	0.230	0.887	ND	ND
	1 mg/mL 25 °C	1.000	0.252	ND	ND	0.259	0.810	3.126	0.887	0.198	1.100
	1 mg/mL 35 °C	1.045	0.265	ND	ND	0.258	0.800	7.263	0.887	0.466	1.083
	0.2 mg/mL 5 °C	0.076	0.269	ND	ND	0.261	0.810	0.328	0.888	0.446	1.098
	0.2 mg/mL 25 °C	1.047	0.269	ND	ND	0.337	0.808	4.251	0.887	1.406	1.099
	0.2 mg/mL 35 °C	2.346	0.267	0.196	0.578	0.374	0.799	9.418	0.887	1.890	1.081
Injectable tacrolimus (Prograf®) 5 mg/mL		0.572	0.291	0.050	0.592	ND	ND	0.326	0.892	ND	ND

- pH

Initial mean pH was of $5.97 \pm 2.05\%$ and $5.56 \pm 5.03\%$, respectively, for the 1 mg/mL and 0.2 mg/mL tacrolimus formulations. As shown in Figure 4, a decrease in pH over time was observed for both concentrations when stored at 25 °C and 35 °C. The drop in pH was more important for the 35 °C and 1 mg/mL conditions. When stored at 5 °C, the pH did not vary by more than 0.04 and 0.08 units, respectively, for the 1 mg/mL and 0.2 mg/mL concentration.

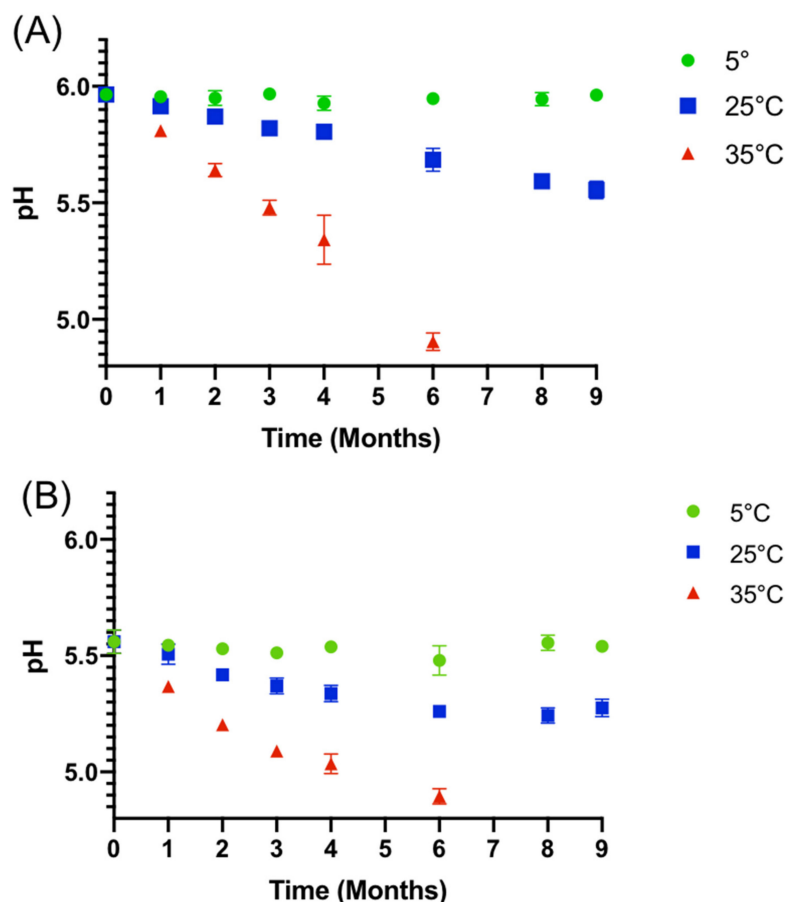


Figure 4. Evolution of the mean pH (\pm IC 95%) for nine months of storage at various temperatures with (A) 1 mg/mL tacrolimus formulation and (B) 0.2 mg/mL tacrolimus formulation.

- Osmolality

Initial mean osmolality was of 769 and 364 mOsm/kg, respectively, for the 1 mg/mL and 0.2 mg/mL tacrolimus formulation. Regarding the 0.2 mg/mL formulation, osmolality did not vary by more than 4.6% (18.75 mOsm/kg) and 3.16% (11.5 mOsm/kg) from the initial mean osmolality during the nine months of storage at, respectively, 5 °C and 25 °C and no more than 4.26% (15.5 mOsm/kg) during the six months of storage at 35 °C. In a similar way, the osmolality of the 1 mg/mL formulation did not vary by more than 7.06% (54.25 mOsm/kg) and 7.25% (55.75 mOsm/kg) of the initial mean osmolality during the nine months of storage at, respectively, 5 °C and 25 °C and no more than 10.8% (83 mOsm/kg) during the six months of storage at 35 °C.

3.2.3. Sterility Assay

None of the four analysed solutions conserved in unopened eyedroppers at day 0, month 3, month 6 and month 9 showed any signs of microbial growth.

3.2.4. Tacrolimus Degradation Kinetics during Storage

Plotting $\ln(C)$, with C in mol/L, as a function of time (seconds), as presented in Figure 5 for the 1 mg/mL formulation, yielded a value of k corresponding to the slope for each storage temperature.

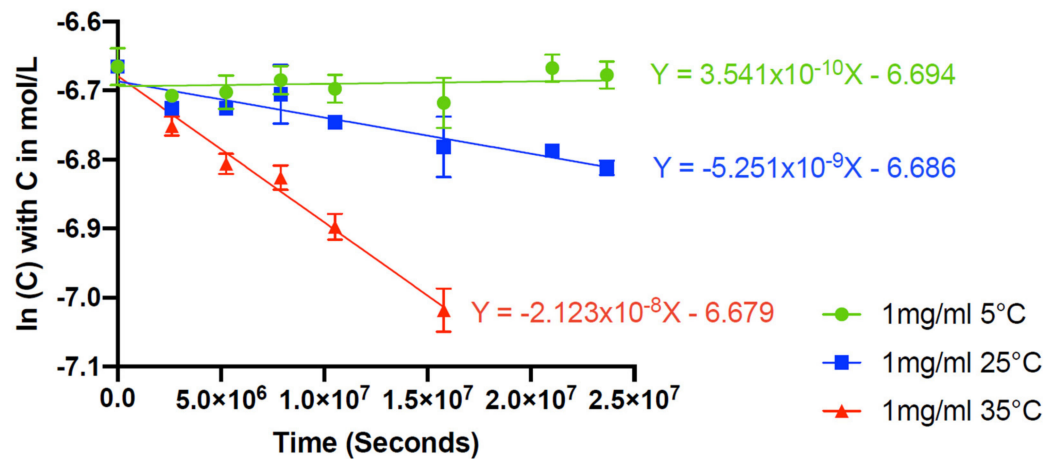


Figure 5. Graphic determination of the rate constant (k).

The plot of $\ln(k)$ as a function of $1/T$, with T in Kelvin, was linear (see Supplementary Data File S1), thus verifying that the reaction obeyed the Arrhenius law. According to Equation (6), the resulting linear regression equation of the three $\ln(k)$ values versus their $1/T$ values was

$$\ln k = 20.429 - (11754 \times \frac{1}{T})$$

With $E_a = 1413.624$ J/mol and $A = 745005719.4$ s⁻¹

If a temperature of 30 °C is selected,

$$\ln k_{30} = 20.429 - (11754 \times 0.003299)$$

$$\ln k_{30} = -18.34259$$

$$k_{30} = 1.08123 \times 10^{-8} \text{ s}^{-1}$$

According to Equation (7), the time to fall to 90% of initial tacrolimus concentration at 30 °C would be

$$t_{90} = \frac{\ln(0.9)}{k_{30}}$$

$$t_{90} = 9744544.18 \text{ s} = 3.71 \text{ months}$$

This information thus allows the estimation of an impact of potential temperature excursions during storage on tacrolimus concentrations. As another example, tacrolimus concentration would decrease by 5% in only five days when stored at 50 °C for the 1 mg/mL formulation (not taking into account other factors like potential physical instability). An estimation of tacrolimus chemical stability during long-term storage can also be made: it would take approximatively 58 months for tacrolimus concentrations to decrease by 5% when stored at 5 °C.

3.3. Tacrolimus Concentrations in Eye Drops during Simulated Use

The simulated test was performed on formulations having been stored for eight months (M8) at 5 °C, and the storage temperature was maintained at 5 °C during the test, except for drop emission. No variation exceeding $\pm 10\%$ of the mean concentration measured at M8 was found for the 1 mg/mL eye drops as seen in the Figure 6A. However, for the 0.2 mg/mL concentration, a greater variability in tacrolimus concentrations was observed (Figure 6B). pH and osmolality remained unchanged.

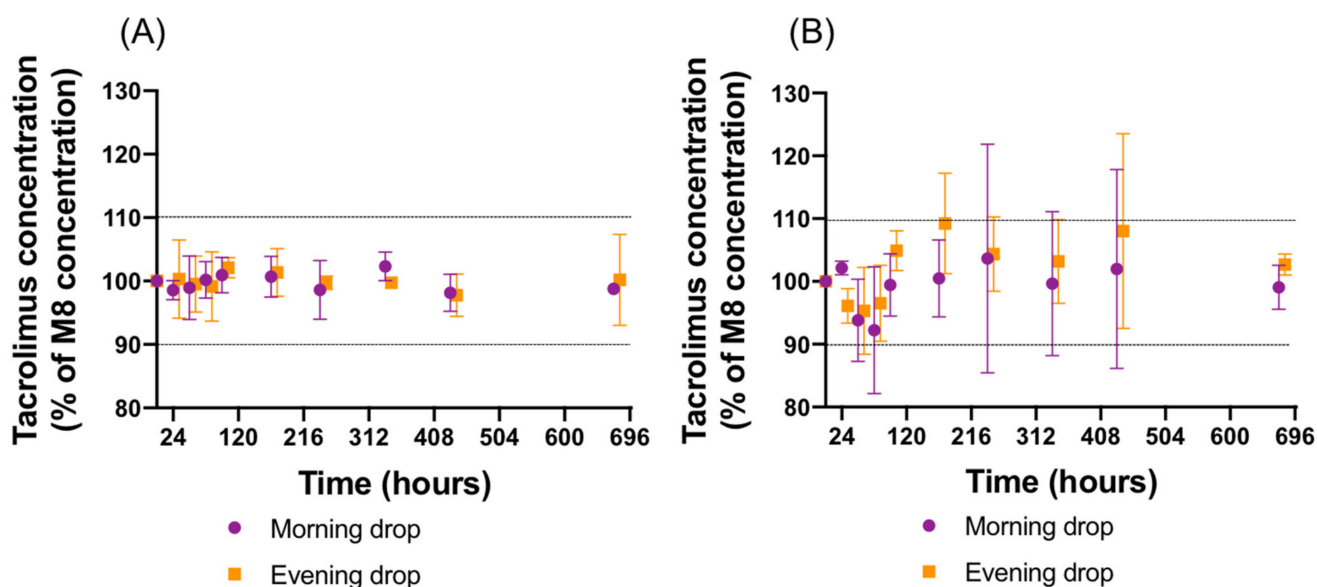


Figure 6. Evolution of the mean concentration (\pm IC 95%) in opened eyedroppers during one month of storage at 5 °C after eight months of storage at 5 °C with (A) 1 mg/mL tacrolimus formulation and (B) 0.2 mg/mL tacrolimus formulation.

During the simulated test, an additional peak appeared in the 1 mg/mL tacrolimus drops emitted from the eyedroppers. This peak was not detected in the tacrolimus solutions in unopened eyedroppers. Figure 7 presents the chromatograms of a formulation stored unopened for eight months at 5 °C without having been in contact with the Novelia[®] delivery nozzle versus with the same formulation after contact with the delivery nozzle. Immediately after the first drop, an increase in the AUC of this compound was observed, before it decreased over time to reach a plateau (see Supplementary Data File S1). The AUC of the compound was higher in the 0.2 mg/mL formulation than in the 1 mg/mL formulation.

This additional compound presented a very similar retention time as one of the breakdown products observed at other storage temperatures and in the 0.2 mg/mL formulation. To ensure that it was not a tacrolimus degradation product, the different parts of the silicone membrane of the ophthalmic multidose device (Novelia[®] nozzle) were put in contact with tacrolimus-free formulation containing only the excipients and compared with a control solution without silicone membrane. As seen in Figure 8, the compound appeared as soon as the solutions were put into contact with the silicone parts of the multidose device, and this despite the absence of tacrolimus, which indicated that it was not a tacrolimus breakdown product and more probably a leachable compound.

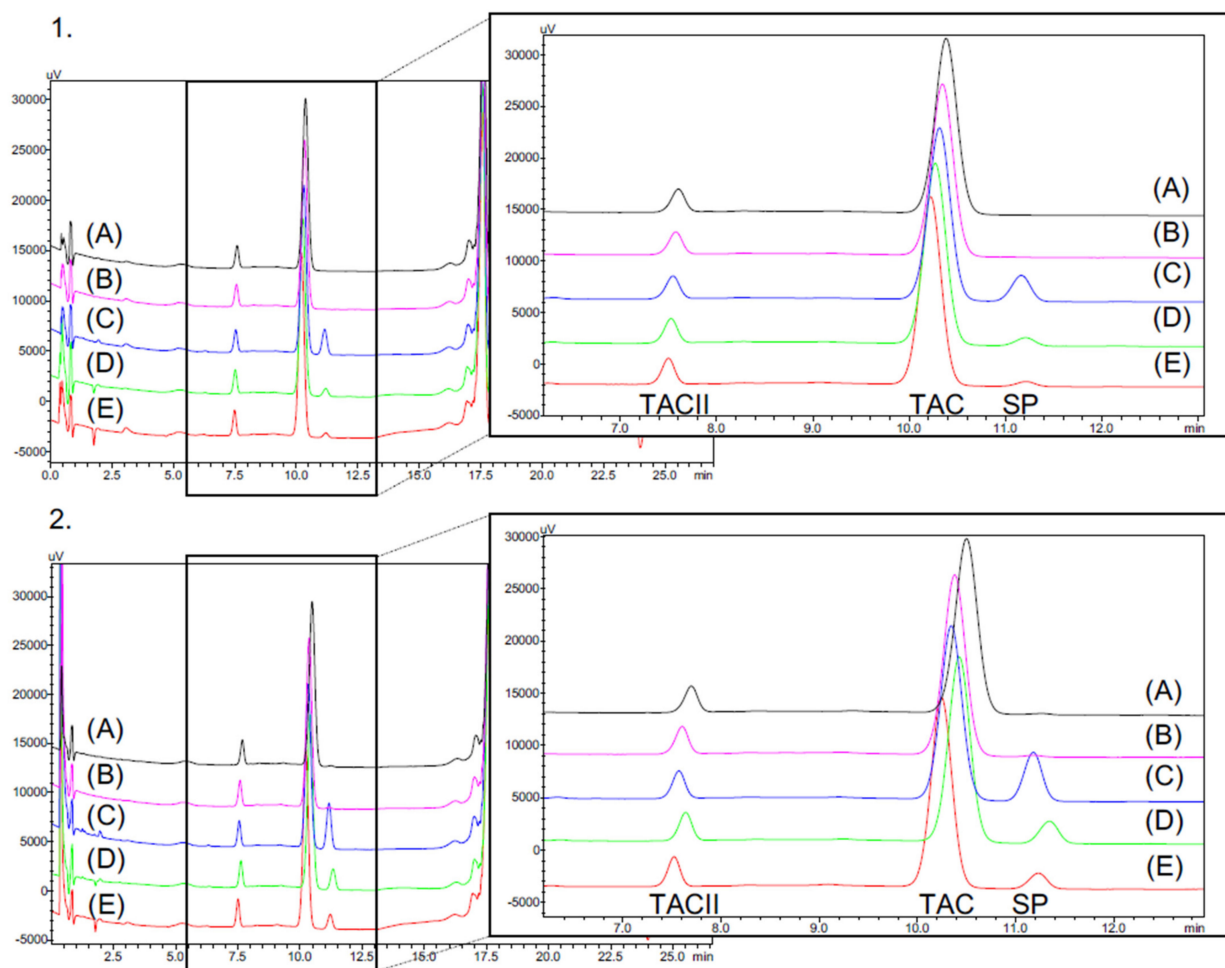


Figure 7. In use assay on the 1 mg/mL (1) and 0.2 mg/mL (2) formulations with (A): formulation stored eight months at 5 °C, (B): Day 0 = first drop, (C): Day 0 = second drop, (D): Day 14= 28th drop and (E): 56th drop after 28 days of analysis. SP = Supplementary peak.

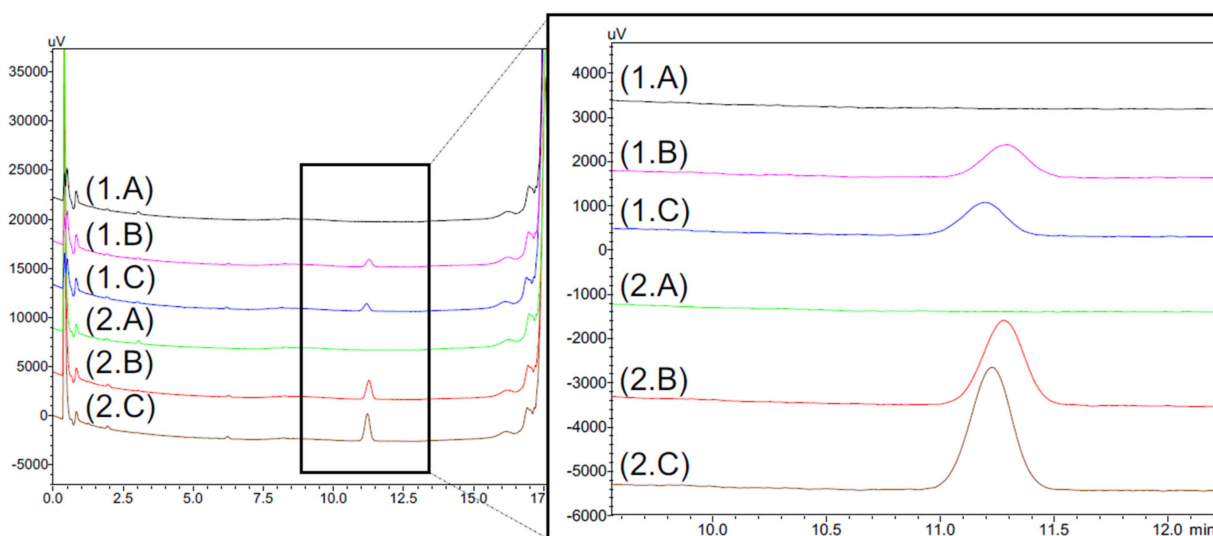


Figure 8. Chromatograms of excipients formulation (TAC-free) of 1 mg/mL (1) and 0.2 mg/mL (2) formulations without contact with the silicone membrane of the ophthalmic multidose delivery system (A) compared with formulations which remained in contact one day (B) and seven days (C) with the silicone membrane.

3.4. Eye Drop Volume

The mean volume of a drop was determined to be 25.0 μL and 25.7 μL , respectively, for the 1 mg/mL and 0.2 mg/mL formulation, with the density being of 0.9815 and 0.98805.

3.5. Complementary Study: Identification of the Leachable Compound

The peak of the leachable compound was detected after 10 days of contact when the silicone parts were put in contact with water-ethanol, ethanol and excipients. This compound can be seen in the absence of tacrolimus, thus confirming that the leachable compound was not linked in any way to tacrolimus. No peaks were seen when silicone parts were put into contact with only water.

Figure 9 shows the chromatograms of the GC-MS analysis obtained from an ethanol solution having been left in contact with the silicone valves for 10 days. Two compounds are clearly visible before 10 min, with retention times of 4.95, 7.43 and multiple compounds between 11.07 min and 17.59 min. Mass analysis of the 4.95 min compound indicated a similarity with 1,3-Di-tert-butylbenzene (CAS number 1014-60-4) or 1,4-Di-tert-butylbenzene (CAS number 1012-72-2), according to the MS NIST library. The compound at 7.43 min was found possibly to be 3,5-Di-tert-butylphenol (CAS number 1138-52-9) or 2,4-Di-tert-butylphenol (CAS number 96-76-4). The peaks detected between 11.07 and 17.59 min seem to belong to the siloxane family. All these peaks presented common m/z values of 73, 147, 221 or 207, 281, 355, with a difference of 74 m/z units between the fragments.

Analytical standards of 1,3-Di-tert-butylbenzene and 2,4-Di-tert-butylphenol were analysed using the tacrolimus HPLC method and the retention times and UV spectra of these products were compared with those of the leachable compound observed during the in-use assay. 2,4-Di-tert-butylphenol possessed a quasi-identical relative retention time (1.069, relative to tacrolimus) and UV spectrum. In order to support the hypothesis that it is the same compound as that observed during the GC-MS analysis, 2,4-Di-tert-butylphenol was also reanalysed by GC-MS and was found to correspond (see Supplementary Data File S1).

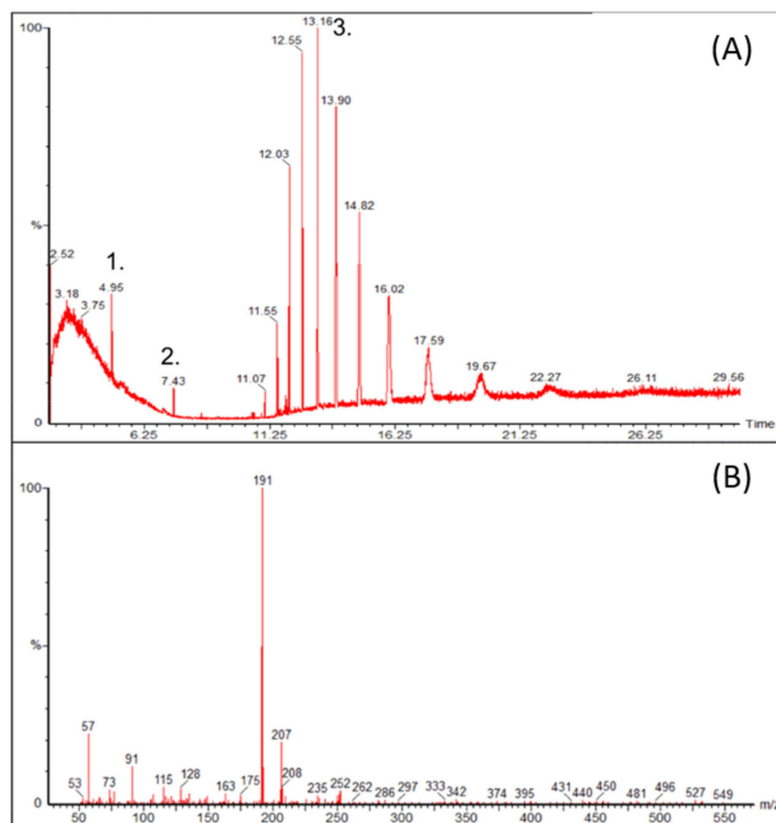


Figure 9. Cont.

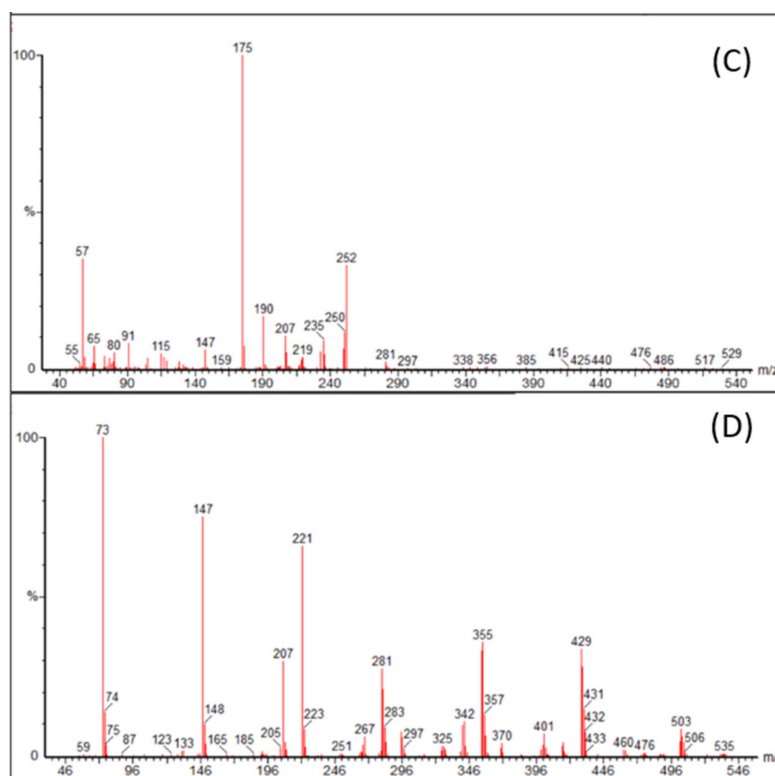


Figure 9. GC-MS analysis of two valves put in contact with absolute ethanol with (A) the total scan and (B–D) the respective m/z of the peaks 1, 2, and 3 isolated in the total scan.

4. Discussion

In this study, we investigated the physicochemical stability of a novel formulation of tacrolimus, at two concentrations (0.2 and 1 mg/mL) at three different storage conditions for nine months (including one month of simulated patient use). For both concentrations, the results showed that the tacrolimus formulation remained stable throughout the study when stored at 5 °C, but tacrolimus degradation occurred when the formulations were stored at 25 °C and 35 °C.

The analytical method used for the quantification of tacrolimus was reproduced from the stability-indicating method published recently by Peterka et al. [25], who performed an in-depth analysis of tacrolimus and its equilibrium compounds, related substances, byproducts and degradation products. In order to transpose this UHPLC method using the HPLC equipment at our disposal, we used a Kinetex[®] Core-Shell 2.6 µm EVO C18 100 × 3 mm column. The length and stationary phase composition were the same as the column used by Peterka et al., which was an AQUITY UPLC BEH C18 column [25]. However, the granulometry was slightly higher (2.6 µm versus 1.7 µm) in order to deal with the increased precolumn pressure, but the Core-Shell technology [35] allowed the system to maintain an equivalent separation to the one obtained by Peterka et al. [25], but for a longer method. Indeed, the flow rate had to be increased by 0.25 mL/min, and the gradient lengthened in order to obtain an equivalent retention of tacrolimus, with a relative retention time (relative to the solvent front) of 22.24 in our method compared to 22.08 in the original method. Overall, the method used allowed an accurate and precise quantification of tacrolimus and the identification of nine other compounds, including ascomycin (impurity A described in the European Pharmacopoeia). During the forced degradation tests they conducted, Peterka et al. [25] found that tacrolimus was highly labile under alkaline conditions, and relatively stable under acidic conditions. This is coherent with the data reported by Prajapati et al. [36], who found that tacrolimus was most stable in a narrow pH range of 4 to 6.

This information justified the choice of pH for the buffer used in our formulation, ranging from about 5.5 to 6 for the 0.2 and 1 mg/mL formulations, respectively. The physiological pH of tears is around 7.5 [37]; however, it has been proven that their buffer capacity is quite important (with regards to the small drop volume administered), and that the eye can tolerate products over a range of pH values from about 3.0 to about 8.6, depending on the buffering capacity of the formulation [38]. The formulation process used is similar to one previously published for the compounding of high concentration cyclosporine formulations [39]. The tacrolimus powder was solubilized first in ethanol then added to macrogol 35 glycerol ricinoleate before being incorporated into the aqueous buffer, thus forming micelles. Sodium hyaluronate was also included as an excipient because it can help epithelial healing thanks to its lubricating capacity but also allows the migration and proliferation of epithelial cells [40,41]. Ethanol can be toxic for the ocular surface, especially at concentrations higher than 13.8% (138 mg/mL) like those used for ocular surface surgeries such as photorefractive keratectomy or pterygium excision [42,43]. However, much lower concentrations like 2.5% (25 mg/mL) can be tolerated, as shown in a retrospective analysis of 20 mg/mL cyclosporine eye drops containing 25 mg/mL of ethanol, yet even so, 37% of patients treated complained of side effects, the main one being a burning sensation [44,45]. The tacrolimus formulations presented in this work contained even less ethanol (3.76 mg/mL and 18.79 mg/mL for the 0.2 and 1 mg/mL tacrolimus formulation, respectively), representing only 15% and 75% of the ethanol present in the 20 mg/mL cyclosporine formulation, and thus the ophthalmic tolerance should therefore be improved even further, especially for the 0.2 mg/mL formulation.

For both tested concentrations, all parameters were in favour of a physicochemical stability of nine months when stored at 5 °C. Visual aspect, colour, turbidity, micelle size and viscosity all remained unchanged through the study, as did the pH and osmolality of the solutions. Tacrolimus concentrations remained well within specifications and overall related compounds, and potential breakdown products levels remained consistent with levels found at the start of the study. Because tacrolimus is considered as a drug with a narrow therapeutic range, the choice of accepting a 90–110% range of the initial concentration can be debatable. However, the United States Pharmacopoeia allows this interval for a tacrolimus compounded oral solution [46], and other authors have proposed an even larger acceptability range, accepting an unusual 20% of loss of tacrolimus [20]. In our case, when the formulations were stored at 5 °C, tacrolimus concentrations decreased by less than 5%, thus guaranteeing stable tacrolimus concentrations throughout the proposed shelf life. However, during storage at higher temperatures (25 °C and 35 °C), several signs of chemical instability were detected (for both concentrations): decrease in tacrolimus concentrations, increase in related compounds and breakdown products and an acidification of the media (especially for the 1 mg/mL formulation and at 35 °C). This is coherent with other previously published studies. In 2013, a 0.6 mg/mL tacrolimus eyedrop prepared in castor oil and stored at ambient temperature showed a decrease in tacrolimus concentrations after four months of storage [18]. In 2017, Ezquer-Garin et al. published a stability study on a 0.3 mg/mL tacrolimus ophthalmic solution prepared by diluting I.V. tacrolimus ampules (5 mg/mL) with Liquifilm sterile ophthalmic eye drops, stored at three different temperatures (frozen, refrigerated and 25 °C) during 85 days [21]. They showed that tacrolimus concentrations remained stable throughout the 85 days when frozen or refrigerated, but that the percentage of the initial tacrolimus concentration remaining had decreased to less than 90% after 1 month when stored at 25 °C [21]. Recently, Ghiglionni et al. [20] followed the tacrolimus concentrations in a novel ethanol-free formulation they developed, using polyethoxylated castor oil as a solvent for tacrolimus at 1 mg/mL. Even if their published data is difficult to interpret, they reported a loss of tacrolimus of up to 20% after 60 days unopened refrigerated storage [20]. However, neither of these studies followed the pH or reported any breakdown products, possibly because of an insufficiently specific chromatographic method. Two studies investigated the stability of tacrolimus solutions solubilized in 2-hydroxypropyl- β -cyclodextrins [36,47]. As stated

previously, Prajapati et al. showed that the tacrolimus had maximum stability between pH 4 and 6 and that hydrolysis was the main cause of degradation in their aqueous media into which they also added various surfactants [36]. The characteristics and stability of the tacrolimus/hydroxypropyl- β -cyclodextrin eye drops were subsequently further evaluated by an excellent study by García-Otero et al. [47]. In this study, the authors followed the tacrolimus concentrations, osmolality, pH and also performed microbiological tests on a 0.2 mg/mL tacrolimus formulation, stored at 4 °C, 25 °C and 40 °C for three months. They also noticed a temperature-dependent degradation, but even when stored at 4 °C, the two formulations they tested lost 10% of the initial tacrolimus in 120 days. This could be explained by the choice of pH (pH 7) which is outside the tacrolimus chemical stability range. Another interesting galenic formulation, using a thin-film hydration method to encapsulate tacrolimus within a chitosan-based amphiphile derivative containing 1 mg/mL of tacrolimus, was also studied [48]. They evaluated the drug concentration, size distribution, zeta potential, pH, osmolality and viscosity during one month at 5 °C, 25 °C, and 40 °C. After one month, tacrolimus concentrations had decreased by 6%, 59% and 99.97% at those temperatures, but again the initial pH was outside optimum stability range. Interestingly, like in our study, the pH also decreased in the formulations stored at 25 °C and 40 °C, by 0.6 and 0.8 pH units, respectively. This phenomenon could be because of the leaching of acids (such as propionic acid) from the gamma-sterilized low density polyethylene surface of the eyedropper, as was hypothesized during a stability study in the same eyedroppers of an ophthalmic formulation of polyhexamethylene biguanide [49]. Alternatively, the acidification could be caused by the appearance of an acid breakdown product, like the acid proposed by Prajapati et al., possessing a m/z of 844 $[M+Na]^+$ [36]. However, as this compound was not referenced by the method developed by Peterka et al. [25], it is possible that it might not be isolated from other compounds (for example, if hidden beneath the impurity A/ascomycin peak, which increased significantly at 35 °C) and thus not detectable as such. Moreover, neither monographies in the USP nor in the European Pharmacopoeia describe this product [26,50]. Because there are no publically available recommendations concerning the acceptable limits of breakdown products in tacrolimus ophthalmic solutions, more studies are needed to be able to evaluate clearly the tolerable limits. Until then, pharmacists and clinicians will have to use their best judgement, taking into account all aspects in order to provide a safe and effective treatment for their patients. The ideal shelf life depends on the intended use of the medication. Most commercialized medications have shelf lives of at least two years; however, for hospital compounded preparation, which is implemented in the absence of a commercial alternative, a shelf life of several months allows the preparation to be compounded in advance, quality checked, stored, transported, dispensed and used by the patients.

This work also used the Arrhenius equation to be able to estimate the impact of various temperatures on tacrolimus degradation. This equation is commonly used to estimate and predict degradation rates at various temperatures for different stability studies of pharmaceutical products [51–53]. In fact, even if this method is not explicitly mentioned in the ICH Q1A(R2) guidelines [33], the Arrhenius equation underpins the general principles of these guidelines [54]. However, many precautions need to be taken into consideration for its application to the developed formulation: (1) the Arrhenius equation can only predict chemical degradations and does not consider possible physical instabilities [54], and (2) the used model postulates that no variation of the estimated activation energy will occur over time, which needs to be confirmed. The information that can be computed from its use must therefore be treated as indicative only until consolidated.

During the simulated test, the overall concentrations remained stable, yet variations in tacrolimus concentrations were observed in the emitted drops, especially with the 0.2 mg/mL formulation. This could be attributed to the sorption of tacrolimus to the surface of the silicone parts in contact with the fluid path inside the Novelia[®] nozzle, similar to what has already been shown for other lipophilic substances like latanoprost, and to a lesser extent, cyclosporine [55]. These variations must, however, be compared

to the variable and small quantity actually absorbed by the eye after instillation [56], and they are quite possibly clinically insignificant. Moreover, the appearance of an additional compound in the chromatographic analysis, which was proven to be independent of the presence of tacrolimus and therefore not a degradation product, suggested the presence of a container–content interaction. The variation of concentration could be caused by tacrolimus sorption to the silicone parts composing the Novelia[®] nozzle and in contact with the fluid path because some studies have reported the sorption of tacrolimus on different types of materials such as PVC [57–59] or silicone [60] during parenteral administration. However, in our case, this phenomenon seems variable but limited in intensity. More notable was the appearance of the additional compound that could be associated to a leaching phenomenon. The first analyses on ethanol extracts with GC-MS narrowed candidate substances to 2,4-Di-tert-butylphenol and 1,3-Di-tert-butylbenzene (or corresponding constitutional isomers) through tentative identification with NIST library. Further investigation with corresponding analytical standards showed 2,4-Di-tert-butylphenol to have identical retention time (with both HPLC and GC) and mass and UV spectra to those of the detected leachable compound. This chemical belongs to the phenol antioxidants class used in polymers as do, for example, butylated hydroxytoluene or molecules commercialized under the Irganox[®] brand. It is used itself or as a precursor for the production of more complex molecules [61]. It is lipophilic (with a LogP of 5.19), thus poorly soluble in water in opposition to organic solvents [62]. Kolliphor[®] EL and ethanol in the eye drops formulation may have favoured leaching from silicon pieces to the solution. The leaching of 2,4-Di-tert-butylphenol in the solution may possibly be a concern for patients, considering that this compound is currently listed as “under evaluation” for endocrine disruption under EU legislation [63]. However, the quantities the patient would be in contact with would be very low, as the volume of a drop was measured to be of about 20 µL, which in our case is also close to the optimum volume [56]. However, this illustrates once again the importance of checking container–content interactions between medications and the administration devices used, which is a factor very rarely studied in the published literature. Indeed, amongst the previous studies mentioned, only García-Otero et al. evaluated, if only in a preliminary way, the use of the proposed container (polypropylene eyedropper bottles), by determining the squeezing force necessary to dispense a drop, yet without evaluating actual container–content interactions [47]. Upfront anticipation of the type of container is of paramount importance, even more so in ophthalmology, because it could impact formulation (with or without microbial preservatives) and device choice (compatibility of the medication’s active substance or excipients with the materials of the device).

5. Conclusions

Tacrolimus ophthalmic micellar solutions at 0.2 mg/mL and 1 mg/mL are physico-chemically stable for up to nine months when stored at 5 °C, but additional studies are still needed to evaluate in-depth the container–content interactions that were detected, especially the impact of a compound leaching out of the used eyedropper bottle.

Supplementary Materials: The following are available online at <https://www.mdpi.com/article/10.3390/pharmaceutics14010118/s1>, Supplementary Data File S1: containing all raw data and Figure S1: Accuracy profile of tacrolimus validation. ARB: Average relative trueness bias. CI: confidence interval, Figure S2: Evolution of chromaticity and luminance for the 1 mg/mL (1) and the 0.2 mg/mL formulation (2) with a* (A), b* (B), L*(C) and ΔE (D) during the 9 month stability study, Figure S3: Applicability of the Arrhenius law, Figure S4: Evolution of the AUC of the leachable compound during the in-use assay at 5 °C, Figure S5: Comparison of the spectra UV of the leachable compound found in the in-use assay for the 1 mg/mL formulation after the delivery of the third drop (A) with the spectra UV of 2,4-Di-tert-butylphenol (B), 1,3-Di-tert-butylbenzene (C) and 1,4-Di-tert-butylbenzene (D).

Author Contributions: Conceptualization: M.B., M.W., M.J. and P.C.; Methodology: M.B., Y.B., Y.L.B., P.C. and V.S.; Investigation: M.B., Y.L.B. and P.C.; Verification: M.Y., Y.B. and P.C.; Writing—original draft: M.B., Y.L.B. and P.C.; Writing—review & editing: all authors. All authors have read and agreed to the published version of the manuscript.

Funding: This research received no external funding.

Institutional Review Board Statement: Not applicable.

Informed Consent Statement: Not applicable.

Data Availability Statement: Raw data is available in the Supplementary Materials.

Acknowledgments: The authors would like to thank Lauralee Wnuk, Marie Mula and Françoise Picq for their help in performing the sterility assays, and Valentine Vannaire for her help during the simulated use study. The authors also gratefully acknowledge Stephen Chennell for his help in double checking the English.

Conflicts of Interest: The authors declare no conflict of interest.

References

1. Siekierka, J.J.; Hung, S.H.; Poe, M.; Lin, C.S.; Sigal, N.H. A Cytosolic Binding Protein for the Immunosuppressant FK506 Has Peptidyl-Prolyl Isomerase Activity but Is Distinct from Cyclophilin. *Nature* **1989**, *341*, 755–757. [CrossRef]
2. Harding, M.W.; Galat, A.; Uehling, D.E.; Schreiber, S.L. A Receptor for the Immuno-Suppressant FK506 Is a Cis-Trans Peptidyl-Prolyl Isomerase. *Nature* **1989**, *341*, 758–760. [CrossRef]
3. Shaw, K.T.; Ho, A.M.; Raghavan, A.; Kim, J.; Jain, J.; Park, J.; Sharma, S.; Rao, A.; Hogan, P.G. Immunosuppressive Drugs Prevent a Rapid Dephosphorylation of Transcription Factor NFAT1 in Stimulated Immune Cells. *Proc. Natl. Acad. Sci. USA* **1995**, *92*, 11205–11209. [CrossRef]
4. Moscovici, B.K.; Holzchuh, R.; Sakasagawa-Naves, F.E.; Hoshino-Ruiz, D.R.; Albers, M.B.V.; Santo, R.M.; Hida, R.Y. Treatment of Sjögren’s Syndrome Dry Eye Using 0.03% Tacrolimus Eye Drop: Prospective Double-Blind Randomized Study. *Cont. Lens Anterior Eye* **2015**, *38*, 373–378. [CrossRef]
5. Sanz-Marco, E.; Udaondo, P.; García-Delpech, S.; Vazquez, A.; Diaz-Llopis, M. Treatment of Refractory Dry Eye Associated with Graft Versus Host Disease with 0.03% Tacrolimus Eyedrops. *J. Ocul. Pharmacol. Ther.* **2013**, *29*, 776–783. [CrossRef]
6. Zhai, J.; Gu, J.; Yuan, J.; Chen, J. Tacrolimus in the Treatment of Ocular Diseases. *BioDrugs* **2011**, *25*, 89–103. [CrossRef]
7. Wan, Q.; Tang, J.; Han, Y.; Wang, D.; Ye, H. Therapeutic Effect of 0.1% Tacrolimus Eye Drops in the Tarsal Form of Vernal Keratoconjunctivitis. *Ophthalmic Res.* **2018**, *59*, 126–134. [CrossRef]
8. Roumeau, I.; Coutu, A.; Navel, V.; Pereira, B.; Baker, J.S.; Chiambaretta, F.; Bremond-Gignac, D.; Dutheil, F. Efficacy of Medical Treatments for Vernal Keratoconjunctivitis: A Systematic Review and Meta-Analysis. *J. Allergy Clin. Immunol.* **2021**, *148*, 822–834. [CrossRef]
9. Kheirkhah, A.; Zavareh, M.K.; Farzbod, F.; Mahbod, M.; Behrouz, M.J. Topical 0.005% Tacrolimus Eye Drop for Refractory Vernal Keratoconjunctivitis. *Eye* **2011**, *25*, 872–880. [CrossRef]
10. Erdinest, N.; Ben-Eli, H.; Solomon, A. Topical Tacrolimus for Allergic Eye Diseases. *Curr. Opin. Allergy Clin. Immunol.* **2019**, *19*, 535–543. [CrossRef]
11. Koh, K.; Jun, I.; Kim, T.-I.; Kim, E.K.; Seo, K.Y. Long-Term Results of Topical 0.02% Tacrolimus Ointment for Refractory Ocular Surface Inflammation in Pediatric Patients. *BMC Ophthalmol.* **2021**, *21*, 247. [CrossRef]
12. National Center for Biotechnology Information PubChem Compound Summary for CID 445643, Tacrolimus. Available online: <https://pubchem.ncbi.nlm.nih.gov/compound/445643> (accessed on 29 November 2021).
13. Mazet, R.; Yaméogo, J.B.G.; Wouessidjewe, D.; Choisnard, L.; Gèze, A. Recent Advances in the Design of Topical Ophthalmic Delivery Systems in the Treatment of Ocular Surface Inflammation and Their Biopharmaceutical Evaluation. *Pharmaceutics* **2020**, *12*, 570. [CrossRef]
14. Senju Pharmaceutical Co., Ltd. *Marketing Authorization Holder Talymus®. Ophthalmic Suspension 0.1%*; Senju Pharmaceutical, Co., Ltd.: Osaka, Japan, 2018.
15. Figus, M.; Agnifili, L.; Lanzini, M.; Brescia, L.; Sartini, F.; Mastropasqua, L.; Posarelli, C. Topical Preservative-Free Ophthalmic Treatments: An Unmet Clinical Need. *Expert Opin. Drug Deliv.* **2020**, *18*, 655–672. [CrossRef]
16. Baudouin, C.; Labbé, A.; Liang, H.; Pauly, A.; Brignole-Baudouin, F. Preservatives in Eyedrops: The Good, the Bad and the Ugly. *Prog. Retin. Eye Res.* **2010**, *29*, 312–334. [CrossRef]
17. Goldstein, M.H.; Silva, F.Q.; Blender, N.; Tran, T.; Vantipalli, S. Ocular Benzalkonium Chloride Exposure: Problems and Solutions. *Eye* **2021**, 1–8. [CrossRef]
18. Gauthier, A.-S.; Rival, B.; Sahler, J.; Fagnoni-Legat, C.; Limat, S.; Guillaume, Y.; Delbosc, B. Développement galénique et analytique d’un collyre à base de tacrolimus 0.06%. *J. Français d’Ophtalmologie* **2013**, *36*, 408–413. [CrossRef]
19. Zulim, L.F.d.C.; Nai, G.A.; Giuffrida, R.; Pereira, C.S.G.; Benguella, H.; Cruz, A.G.; Foglia, B.T.D.; Batista, A.D.S.; Andrade, S.F. Comparison of the Efficacy of 0.03% Tacrolimus Eye Drops Diluted in Olive Oil and Linseed Oil for the Treatment of Keratoconjunctivitis Sicca in Dogs. *Arq. Bras. Oftalmol.* **2018**, *81*, 293–301. [CrossRef]
20. Ghigliani, D.G.; Martino, P.A.; Bruschi, G.; Vitali, D.; Osnaghi, S.; Corti, M.G.; Beretta, G. Stability and Safety Traits of Novel Cyclosporine A and Tacrolimus Ophthalmic Galenic Formulations Involved in Vernal Keratoconjunctivitis Treatment by a High-Resolution Mass Spectrometry Approach. *Pharmaceutics* **2020**, *12*, 378. [CrossRef]

21. Ezquer-Garin, C.; Ferriols-Lisart, R.; Alós-Almiñana, M. Stability of Tacrolimus Ophthalmic Solution. *Am. J. Health Syst. Pharm.* **2017**, *74*, 1002–1006. [CrossRef]
22. Choudhury, A.K.R. *Using Instruments to Quantify Colour*. In *Principles of Colour and Appearance Measurement*; Elsevier: Cham, Switzerland, 2014; pp. 270–317; ISBN 978-0-85709-229-8.
23. United States Pharmacopeia. *USP <631> Color and Achromicity, USPNF 2021 Issue 2 2021*; United States Pharmacopeia and National Formulary: New York, NY, USA, 2021.
24. Hunt, R.W.G.; Pointer, M.R. *Measuring Colour*, 4th ed.; John Wiley & Sons: Hoboken, NJ, USA, 2011; ISBN 978-1-119-97537-3.
25. Peterka, T.R.; Lušin, T.T.; Bergles, J.; Ham, Z.; Grahek, R.; Urleb, U. Forced Degradation of Tacrolimus and the Development of a UHPLC Method for Impurities Determination. *Acta Pharm.* **2019**, *69*, 363–380. [CrossRef]
26. European Pharmacopeia. *Tacrolimus Monohydrate Monograph 01/2018:2244 Corrected 10.0 2021*, 10.2 ed.; European Directorate for the Quality of Medicines and Healthcare: Strasbourg, France, 2021.
27. U.S. Department of Health and Human Services; Food and Drug Administration; Center for Drug Evaluation and Research (CDER); Center for Biologics Evaluation and Research (CBER); International Council for Harmonization of Technical Requirements for Pharmaceuticals for Human Use ICH Q2 (R1). *Guidance for Industry: Validation of Analytical Procedures: Text and Methodology*; ICH: Rockville, MD, USA, 1996.
28. Hubert, P.H.; Nguyen-Huu, J.-J.; Boulanger, B.; Chapuzet, E.; Chiap, P.; Cohen, N.; Compagnon, P.-A.; Dewé, W.; Feinberg, M.; Lallier, M.; et al. Harmonization of Strategies for the Validation of Quantitative Analytical Procedures: A SFSTP Proposal—Part I. *J. Pharm. Biomed. Anal.* **2004**, *36*, 579–586. [CrossRef]
29. Hubert, P.H.; Nguyen-Huu, J.-J.; Boulanger, B.; Chapuzet, E.; Chiap, P.; Cohen, N.; Compagnon, P.-A.; Dewé, W.; Feinberg, M.; Lallier, M.; et al. Harmonization of Strategies for the Validation of Quantitative Analytical Procedures: A SFSTP Proposal—Part II. *J. Pharm. Biomed. Anal.* **2007**, *45*, 70–81. [CrossRef]
30. Hubert, P.H.; Nguyen-Huu, J.-J.; Boulanger, B.; Chapuzet, E.; Cohen, N.; Compagnon, P.-A.; Dewé, W.; Feinberg, M.; Laurentie, M.; Mercier, N.; et al. Harmonization of Strategies for the Validation of Quantitative Analytical Procedures: A SFSTP Proposal—Part III. *J. Pharm. Biomed. Anal.* **2007**, *45*, 82–96. [CrossRef]
31. European Pharmacopoeia. *Monograph 2.6.1 Sterility 10.2 2020*; European Directorate for the Quality of Medicines and Healthcare: Strasbourg, France, 2020.
32. Newton, D.W. Mean Kinetic Temperature for Controlled Room Temperature Drug Storage: Official Definitions and Example Calculations. *Int. J. Pharm. Compd.* **2019**, *23*, 281–287.
33. International Conference of Harmonization (ICH) Quality Guidelines: Guidelines for Stability Q1A to Q1f. Available online: <http://www.ich.org/products/guidelines/%20quality/article/quality-guidelines.html> (accessed on 18 June 2020).
34. French Society of Clinical Pharmacy (SFPC) and Evaluation and Research Group on Protection in Controlled Atmosphere (GERPAC). *Methodological Guidelines for Stability Studies of Hospital Pharmaceutical Preparations*; Société Française de Pharmacie Clinique, Groupe d’Evaluation et de Recherche sur la Protection en Atmosphère Contrôlée: Paris, France, 2013.
35. Hayes, R.; Ahmed, A.; Edge, T.; Zhang, H. Core–Shell Particles: Preparation, Fundamentals and Applications in High Performance Liquid Chromatography. *J. Chromatogr. A* **2014**, *1357*, 36–52. [CrossRef]
36. Prajapati, M.; Eiriksson, F.F.; Loftsson, T. Stability Characterization, Kinetics and Mechanism of Tacrolimus Degradation in Cyclodextrin Solutions. *Int. J. Pharm.* **2020**, *586*, 119579. [CrossRef]
37. Yamada, M.; Mochizuki, H.; Kawai, M.; Yoshino, M.; Mashima, Y. Fluorophotometric Measurement of PH of Human Tears in Vivo. *Curr. Eye Res.* **1997**, *16*, 482–486. [CrossRef]
38. United States Pharmacopeia. *USP <771> Ophthalmic Products—Quality Tests, USPNF 2021 Issue 2 2021*; United States Pharmacopeia and National Formulary: New York, NY, USA, 2021.
39. Chennell, P.; Delaborde, L.; Wasiaak, M.; Jouannet, M.; Feschet-Chassot, E.; Chiambaretta, F.; Sautou, V. Stability of an Ophthalmic Micellar Formulation of Cyclosporine A in Unopened Multidose Eyedroppers and in Simulated Use Conditions. *Eur. J. Pharm. Sci.* **2017**, *100*, 230–237. [CrossRef]
40. Gomes, J.A.P.; Amankwah, R.; Powell-Richards, A.; Dua, H.S. Sodium Hyaluronate (Hyaluronic Acid) Promotes Migration of Human Corneal Epithelial Cells in Vitro. *Br. J. Ophthalmol.* **2004**, *88*, 821–825. [CrossRef]
41. Lee, J.S.; Lee, S.U.; Che, C.-Y.; Lee, J.-E. Comparison of Cytotoxicity and Wound Healing Effect of Carboxymethylcellulose and Hyaluronic Acid on Human Corneal Epithelial Cells. *Int. J. Ophthalmol.* **2015**, *8*, 215–221. [CrossRef]
42. Behrens-Baumann, W.; Theuring, S.; Brewitt, H. The Effect of Topical Cyclosporin A on the Rabbit Cornea. *Graefe’s Arch. Clin. Exp. Ophthalmol.* **1986**, *224*, 520–524. [CrossRef]
43. Oh, J.Y.; Yu, J.M.; Ko, J.H. Analysis of Ethanol Effects on Corneal Epithelium. *Investig. Ophthalmol. Vis. Sci.* **2013**, *54*, 3852–3856. [CrossRef]
44. Chast, F.; Lemare, F.; Legeais, J.-M.; Batista, R.; Bardin, C.; Renard, G. Préparation d’un Collyre de Ciclosporine à 2%. *J. Français d’Ophtalmologie* **2004**, *27*, 567–576. [CrossRef]
45. Kauss Hornecker, M.; Charles Weber, S.; Brandely Piat, M.-L.; Darrodes, M.; Jomaa, K.; Chast, F. Cyclosporine eye drops: A 4-year retrospective study (2009–2013). *J. Français d’Ophtalmologie* **2015**, *38*, 700–708. [CrossRef]
46. United States Pharmacopeia. *Tacrolimus Compounded Oral Suspension, USPNF 2021 Issue 2 2021*; United States Pharmacopeia and National Formulary: New York, NY, USA, 2021.

47. García-Otero, X.; Díaz-Tomé, V.; Varela-Fernández, R.; Martín-Pastor, M.; González-Barcia, M.; Blanco-Méndez, J.; Mondelo-García, C.; Bermudez, M.A.; Gonzalez, F.; Aguiar, P.; et al. Development and Characterization of a Tacrolimus/Hydroxy propyl- β -Cyclodextrin Eye Drop. *Pharmaceutics* **2021**, *13*, 149. [CrossRef]
48. Badr, M.Y.; Abdulrahman, N.S.; Schatzlein, A.G.; Uchegbu, I.F. A Polymeric Aqueous Tacrolimus Formulation for Topical Ocular Delivery. *Int. J. Pharm.* **2021**, *599*, 120364. [CrossRef]
49. Bouattour, Y.; Chennell, P.; Wasiak, M.; Jouannet, M.; Sautou, V. Stability of an Ophthalmic Formulation of Polyhexamethylene Biguanide in Gamma-Sterilized and Ethylene Oxide Sterilized Low Density Polyethylene Multidose Eyedroppers. *PeerJ* **2018**, *6*, e4549. [CrossRef]
50. United States Pharmacopeia. *Tacrolimus, USPNF 2021 Issue 2 2021*; United States Pharmacopeia and National Formulary: New York, NY, USA, 2021.
51. Fan, Z.; Zhang, L. One- and Two-Stage Arrhenius Models for Pharmaceutical Shelf Life Prediction. *J. Biopharm. Stat.* **2015**, *25*, 307–316. [CrossRef]
52. Waterman, K.C. The Application of the Accelerated Stability Assessment Program (ASAP) to Quality by Design (QbD) for Drug Product Stability. *AAPS PharmSciTech* **2011**, *12*, 932. [CrossRef]
53. Waterman, K.C.; Adami, R.C. Accelerated Aging: Prediction of Chemical Stability of Pharmaceuticals. *Int. J. Pharm.* **2005**, *293*, 101–125. [CrossRef]
54. Teasdale, A.; Elder, D.; Nims, R.W. *ICH Quality Guidelines: An Implementation Guide*; Wiley: Hoboken, NJ, USA, 2017; ISBN 9781118971116.
55. Le Basle, Y.; Chennell, P.; Sautou, V. A Sorption Study between Ophthalmic Drugs and Multi Dose Eyedroppers in Simulated Use Conditions. *Pharm. Technol. Hosp. Pharm.* **2017**, *2*, 181–191. [CrossRef]
56. Van Santvliet, L.; Ludwig, A. Determinants of Eye Drop Size. *Surv. Ophthalmol.* **2004**, *49*, 197–213. [CrossRef]
57. Taormina, D.; Abdallah, H.Y.; Venkataramanan, R.; Logue, L.; Burckart, G.J.; Ptachcinski, R.J.; Todo, S.; Fung, J.J.; Starzl, T.E. Stability and Sorption of FK 506 in 5% Dextrose Injection and 0.9% Sodium Chloride Injection in Glass, Polyvinyl Chloride, and Polyolefin Containers. *Am. J. Hosp. Pharm.* **1992**, *49*, 119–122. [CrossRef]
58. Suzuki, M.; Takamatsu, S.; Muramatsu, E.; Nakajima, S.-I.; Tanaka, M.; Kawano, K. Loss of Tacrolimus Solution Content and Leaching of Di-2-Ethylhexyl Phtalate in Practice Injection of Precision Continuous Drip Infusion. *Jpn. J. Hosp. Pharm.* **2000**, *26*, 7–12. [CrossRef]
59. Jin, S.-E.; Jeon, S.; Byon, H.-J.; Hwang, S.-J. Evaluation of Tacrolimus Sorption to PVC- and Non-PVC-Based Tubes in Administration Sets: Pump Method vs. Drip Method. *Int. J. Pharm.* **2017**, *528*, 172–179. [CrossRef]
60. Hacker, C.; Verbeek, M.; Schneider, H.; Steimer, W. Falsely Elevated Cyclosporin and Tacrolimus Concentrations over Prolonged Periods of Time Due to Reversible Adsorption to Central Venous Catheters. *Clin. Chim. Acta* **2014**, *433*, 62–68. [CrossRef]
61. Fiege, H.; Voges, H.-W.; Hamamoto, T.; Umemura, S.; Iwata, T.; Miki, H.; Fujita, Y.; Buysch, H.-J.; Garbe, D.; Paulus, W. Phenol Derivatives. In *Ullmann's Encyclopedia of Industrial Chemistry*; John Wiley & Sons: Hoboken, NJ, USA, 2000; ISBN 9783527306732.
62. National Center for Biotechnology Information. PubChem Compound Summary for CID 7311, 2,4-Di-Tert-Butylphenol. Available online: <https://pubchem.ncbi.nlm.nih.gov/compound/7311> (accessed on 3 December 2021).
63. Endocrine Disruptor List. Available online: <https://edlists.org/> (accessed on 29 November 2021).



Article

Anti-Inflammatory Effect of Tacrolimus/Hydroxypropyl- β -Cyclodextrin Eye Drops in an Endotoxin-Induced Uveitis Model

Xurxo García-Otero ^{1,2,†}, Cristina Mondelo-García ^{3,4,†} , Francisco González ^{5,6,†}, Roman Perez-Fernandez ⁷, Leandro Avila ⁷, Jose Ramón Antúnez-López ⁸, Miguel González-Barcia ^{3,4}, Alfredo Adan ⁹, Pablo Aguiar ² , Francisco J. Otero-Espinar ^{1,10,*} , Maria A. Bermúdez ^{7,*} and Anxo Fernández-Ferreiro ^{3,4,*}

- ¹ Pharmacology, Pharmacy and Pharmaceutical Technology Department, Faculty of Pharmacy, University of Santiago de Compostela (USC), 15705 Santiago de Compostela, Spain; xurxo.garcia@rai.usc.es
- ² Molecular Imaging Group, University Clinical Hospital, Health Research Institute of Santiago de Compostela (IDIS), 15706 Santiago de Compostela, Spain; pablo.aguiar.fernandez@sergas.es
- ³ Pharmacy Department, University Clinical Hospital of Santiago de Compostela (SERGAS), 15706 Santiago de Compostela, Spain; cristina.mondelo.garcia@sergas.es (C.M.-G.); miguel.gonzalez.barcia@sergas.es (M.G.-B.)
- ⁴ Clinical Pharmacology Group, University Clinical Hospital, Health Research Institute of Santiago de Compostela (IDIS), 15706 Santiago de Compostela, Spain
- ⁵ Surgery Department–CIMUS, University of Santiago de Compostela (USC), 15706 Santiago de Compostela, Spain; francisco.gonzalez@usc.es
- ⁶ Ophthalmology Service, University Clinical Hospital, Health Research Institute of Santiago de Compostela (IDIS), 15782 Santiago de Compostela, Spain
- ⁷ Department of Physiology, Center for Research in Molecular Medicine and Chronic Diseases (CIMUS), University of Santiago de Compostela, 15706 Santiago de Compostela, Spain; roman.perez.fernandez@usc.es (R.P.-F.); leandro.avila@usc.es (L.A.)
- ⁸ Pathological Anatomy Department, University Clinical Hospital of Santiago de Compostela (SERGAS), 15706 Santiago de Compostela, Spain; jose.ramon.antunez.lopez@sergas.es
- ⁹ Department of Ophthalmology, Hospital Clinic of Barcelona, 08036 Barcelona, Spain; amadan@clinic.cat
- ¹⁰ Paraquasil Group, Health Research Institute of Santiago de Compostela (IDIS), 15706 Santiago de Compostela, Spain
- * Correspondence: francisco.otero@usc.es (F.J.O.-E.); maria.alvarez.bermudez@udc.es (M.A.B.); anxordes@gmail.com (A.F.-F.)
- † The authors contributed equally to this work.

Citation: García-Otero, X.; Mondelo-García, C.; González, F.; Perez-Fernandez, R.; Avila, L.; Antúnez-López, J.R.; González-Barcia, M.; Adan, A.; Aguiar, P.; Otero-Espinar, F.J.; et al. Anti-Inflammatory Effect of Tacrolimus/Hydroxypropyl- β -Cyclodextrin Eye Drops in an Endotoxin-Induced Uveitis Model. *Pharmaceutics* **2021**, *13*, 1737. <https://doi.org/10.3390/pharmaceutics13101737>

Academic Editor: Marzia Cirri

Received: 1 September 2021

Accepted: 14 October 2021

Published: 19 October 2021

Publisher's Note: MDPI stays neutral with regard to jurisdictional claims in published maps and institutional affiliations.



Copyright: © 2021 by the authors. Licensee MDPI, Basel, Switzerland. This article is an open access article distributed under the terms and conditions of the Creative Commons Attribution (CC BY) license (<https://creativecommons.org/licenses/by/4.0/>).

Abstract: Background: Uveitis is an infrequent disease which constitutes a major cause of ocular morbidity. Correct management is essential, being corticosteroids its cornerstone. In case of contraindication to corticosteroids or treatment failure, the use of topical tacrolimus (TAC) could be an alternative which has already demonstrated safety and effectiveness in other ocular pathologies. However, TAC eye drops are not marketed, thus their elaboration must be carried out in Hospital Pharmacy Departments (HPDs). Methods: 32 Sprague-Dawley rats were divided into 4 groups of 8 rats each: (a) untreated healthy rats (Healthy); (b) untreated Endotoxin-Induced Uveitis model-rats (EIU); (c) EIU-rats treated with standard treatment of dexamethasone ophthalmic drops (DXM) and (d) EIU-rats treated with TAC-hydroxypropyl- β -cyclodextrin eye drops previously developed by our group (TAC-HP β CD). The mRNA expression levels of IL-6, IL-8, MIP-1 α and TNF- α , quantitative analysis of leucocytes in aqueous humor and histological evaluation were performed. Results: TAC-HP β CD eye drops demonstrated to reduce ocular inflammation, expression of IL-6, TNF- α , MIP-1 α and leukocyte infiltration in aqueous humor. Conclusions: TAC-HP β CD eye drops showed beneficial effect in EIU model in rats, positioning as an alternative for uveitis treatment in case of corticosteroids resistance or intolerance.

Keywords: endotoxin-induced uveitis; tacrolimus; eye drops; hydroxypropyl- β -cyclodextrin; interleukins; immunosuppressants

1. Introduction

Uveitis constitutes a heterogeneous group of intraocular inflammatory diseases which is defined as inflammation of the uveal tract that can secondarily affect adjacent structures, such as the retina or the optical nerve [1,2]. The overall prevalence and incidence of these conditions range from 5.81 to 19.42 per 10,000 subjects, and 2.51 to 11.12 per 10,000 person-years, respectively. [3,4]. Even though it is an infrequent disease, it constitutes a major cause of ocular morbidity, since it is the third cause of blindness in developed countries, representing an important health problem [5,6].

From the pathophysiological point of view, the immune system plays a fundamental role in the development of uveitis, whether or not it is secondary to infectious processes [7]. In this sense, the origin of inflammation can be attributed to an endogenous mechanism, either as part of autoimmune systemic diseases or as an isolated ocular condition [8]. Concerning the etiology of non-infectious uveitis, in recent years there have been significant advances in the understanding of their pathogenic mechanisms, pointing to the interaction between environmental factors and a complex genetic background, triggering a deregulated immune response able to overcome the ocular immune privilege [9,10]. In this regard, different proinflammatory molecules are increased depending on the specific origin of the disease [11,12]. In addition, several genetic determinants which might predispose to uveitis have been reported, either focusing on a particular disease [9,13,14], or analyzing the shared genomic basis, regardless the diagnosis [15].

Uveitis correct management is essential for preserving visual function and avoiding ocular and extra-ocular morbidity [16]. In this way, patients are usually treated based on the presence of signs of inflammatory activity, being corticosteroids its cornerstone, due to their immediate efficacy [17]. Location and severity of the inflammation will influence the change from topical to oral administration route. However, long-term administration of these agents can cause serious systemic and ocular adverse effects, such as hypertension, diabetes, and glaucoma [18]. In addition, when patients do not respond to this therapy or have a contraindication for the use of corticosteroids, it is necessary to resort to ophthalmic topical immunosuppressants in order to achieve a sustained control of the inflammatory process [17,19]. In this context, the use of topical tacrolimus (TAC) could be an alternative which has already demonstrated safety and effectiveness in other ocular pathologies including corneal graft rejection [20], vernal keratoconjunctivitis (VKC) [21–24], dry eye [25] or scleritis [26,27] among others.

TAC is a calcineurin inhibitor with a potent immunosuppressive effect which has a mechanism of action similar to that of cyclosporine, but it is 10–50 times more potent, having demonstrated in clinical studies more effectiveness at lower concentrations and a better safety profile [19,28,29].

Regarding uveitis, TAC has showed a positive effect on the progression of the disease through reduction of inflammatory activity and suppression of the entire pathogenic pathway of the disease [28]. It inhibits the expression of Toll-like receptors (TLRs), macrophage inflammatory protein-1 alpha (MIP-1 α), T-cell proliferation and the release of inflammatory cytokines such as interleukine-6 (IL-6), interleukine-8 (IL-8), and tumor necrosis factor alpha (TNF α), which have a key role in the development of uveitis [7,28,30–32]. Even though TAC has demonstrated to be effective in patients with refractory uveitis through oral [33] or intravitreal administration [34,35], topical application would be preferred because it avoids adverse effects related to systemic exposition to this drug and local complications after intraocular injections.

Despite all the above, the use of topical TAC for the treatment of uveitis has been limited because, nowadays TAC eye drops are not globally marketed. Consequently, this elaboration must be carried out in Hospital Pharmacy Departments (HPDs). Due to the deficient physicochemical properties of TAC, including low aqueous solubility and high molecular weight (804.02 g/mol), TAC eye drops must be prepared by reformulation from intravenous drug presentation (Prograf[®]) which contains ethanol and other compounds which usually cause discomfort and unpleasantness to patients [22].

In the last decade, several formulations of TAC for topical ophthalmic administration have been synthesized, including niosomes [36], nanovesicles [37], micelles [38] and nanocapsules [39]. However, it is not possible their translation to clinical practice because their synthesis is very complex to be carried out in HPDs. Most services do not have the necessary infrastructure to be able to develop these systems. The absence of specific equipment in production and quality control makes it impossible to produce these formulations optimally, and the personnel in charge of their production are not adequately trained to perform the necessary techniques in these processes.

In this sense, our group has previously developed and characterized a topical ophthalmic formulation of tacrolimus-hydroxypropyl- β -cyclodextrin (TAC-HP β CD) eye drops containing a 0.02% (*w/v*) of tacrolimus and a 40% (*w/v*) of HP β CD in Liquifilm[®], demonstrating positive effects in terms of drug solubility, stability in aqueous solution and retention time on the ocular surface [40]. This formulation improves the currently prepared eyedrops in HPDs by replacing the irritating compounds of the intravenous drug presentation for HP β CD, which is the most appropriated cyclodextrin for topical ophthalmic administration according to the European Medicines Agency (EMA) [40,41].

The aim of this work is to demonstrate the anti-inflammatory effect of a TAC-HP β CD eye drops formulation, previously developed by our group, in an endotoxin-induced uveitis model in rats to provide for the first time a translational alternative for the elaboration of TAC eyedrops in HPDs.

2. Materials and Methods

Tacrolimus powder was acquired from Guinama[®] S.L.U. (La Pobla de Vallbona, Spain), 2-hydroxypropyl- β -cyclodextrin Kleptose[®] HPB (HPCD; MW = 1399 Da, substitution degree = 0.65 molar ratio) was provided from Roquette Laisa S.A.[®] (Valencia, Spain), Liquifilm[®] was purchased from Allergan[®] Pharmaceuticals Ireland (Mayo, Ireland), Maxidex[®] (1 mg/mL, eye drops) was purchased from Alcon Cusí, S.A.[®] (Barcelona, Spain) and Lipopolysaccharide endotoxin (LPS; *Escherichia coli.*) was obtained from Sigma-Aldrich (San Louis, MO, USA). All other chemicals and reagents were of the highest purity grade commercially available.

2.1. Formulation Elaboration Procedure

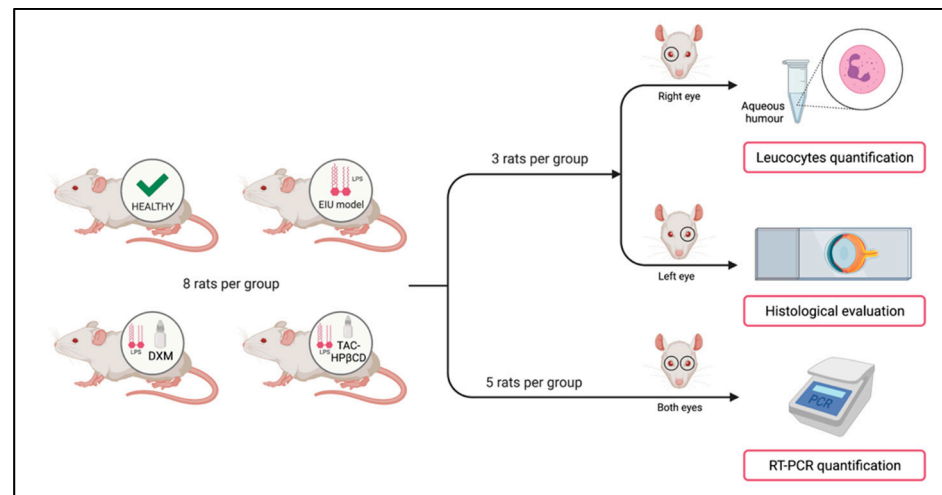
The entire elaboration process of TAC-HP β CD ophthalmic eyedrops was carried out under sterile conditions in a flow laminar cabinet in the HPD of the University Clinical Hospital of Santiago de Compostela. First, the indicated proportion of hydroxypropyl- β -cyclodextrin (40% *w/v*) is dissolved in Liquifilm[®] by stirring, when it was completely solubilized tacrolimus powder was added at a proportion of 0.02% (*w/v*) and left for 72 h under agitation (>750 rpm). Once this time has elapsed, the formulation is filtered through a 0.2 μ m polyether sulfone (PES) filter (Stericup filtration system), and then packaged in sterilized polypropylene eyedropper bottles, showing to be stable for at least 3 months under refrigeration [40].

2.2. In Vivo Endotoxin-Induced Uveitis Model (EIU Model)

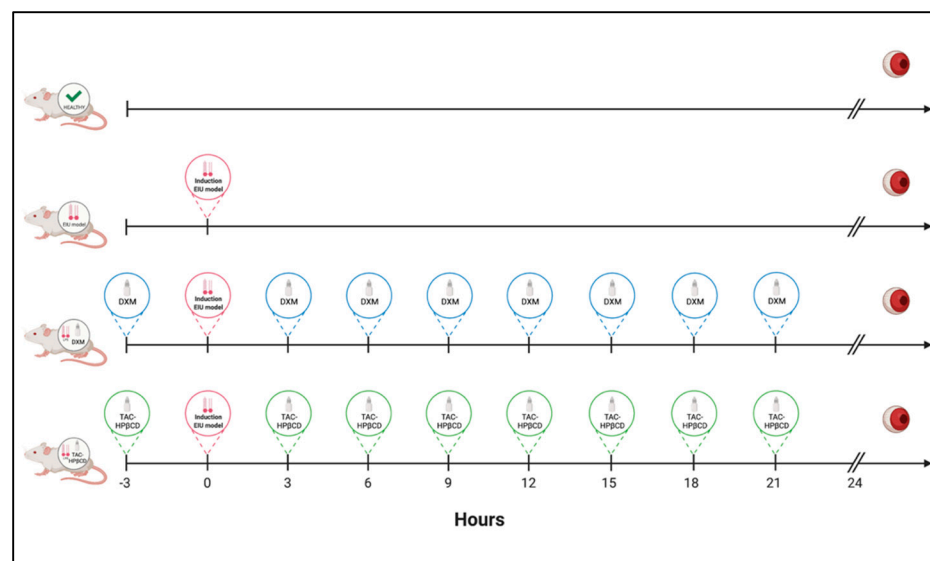
In vivo studies were carried out on male Sprague-Dawley rats with an average weight of 250 g supplied by the animal facility at the University of Santiago de Compostela (CE-BEGA) (Santiago de Compostela, Spain). The animals were kept in cages under controlled temperature (22 ± 1 °C) and humidity ($60 \pm 5\%$), with day–night cycles regulated by artificial light (12/12 h) and feeding ad libitum. The animals were treated according to the ARVO statement for the use of animals in ophthalmic and vision research as well as the approved guidelines for laboratory animals [42,43].

The EIU was induced inoculating 1 mg/kg *Escherichia coli.* LPS diluted in 0.1 mL balance salt solution (BSS) into the rat's right paw as previously described by other authors [44,45]. Once injected, the ocular inflammation peak reaches the maximum after 24 h [46].

In this case, 32 rats were divided into 4 groups of 8 rats each, as indicated in Figure 1. (a) untreated healthy rats (Healthy); (b) untreated EIU-rats (EIU); (c) EIU-rats treated with standard treatment of dexamethasone ophthalmic drops (DXM) (Maxidex[®], dexamethasone 1 mg/mL, Alcon Cusí, Barcelona, Spain) and d) EIU-rats treated with TAC-HP β CD eye drops (TAC-HP β CD). Animals were anesthetized with 2.5% (*v/v*) isoflurane/oxygen and treatments were topically instilled (20 μ L) on each eye 3 h before EIU model induction and every 3 h until 24 h later. Then, rats were euthanized with carbon dioxide and all required samples were extracted.



(A)



(B)

Figure 1. (A) Study groups scheme and distribution of eyes for their posterior analysis. (B) Study timeline: Induction EIU model, treatments, euthanasia and eyes removal. Created with BioRender.com.

2.3. RNA Isolation and Real-Time PCR Analysis

The mRNA expression levels of IL-6, IL-8, MIP-1 α and TNF- α were evaluated in both eyes of the remaining 5 rats of each group by real time-PCR. After extraction, eyeballs were frozen at -20°C and total RNA was isolated using TRIzol reagent (Invitrogen, Barcelona, Spain). Real-time PCR was made with 2 μ g cDNA in a 20 μ L volume using Luminaris Color HiGreenqPCR Master Mix (Fisher Scientific, Rockford, IL, USA). Samples were denatured at 94°C for 10 s, annealed at 58°C for 10 s and extended at 72°C for 10 s for a total of 35 cycles. The amount of PCR products formed in each cycle was evaluated based on SYBR

Green fluorescence with 18S as the endogenous control. Oligonucleotide sequences are detailed in Table 1.

Table 1. Primer sets for real-time PCR.

Primers	Forward (5'-3')	Reverse (5'-3')
IL-6	CTTCAGGCCAAGTTCAGGAG	AGTGG ATCGTGGTTCGTCTTC
IL-8	TCCAGCCAGTTGCCTTCTTG	GGTCTGTTGTGGGTGGTATCC
MIP-1 α	CGTCCTCATCCTGATCACCT	GATACATCCCCGTGAACACC
TNF- α	CCAGATGGTCACCCTCAGAT	CCTTGACCG CTGAAGAGAAC
18S	GTAACCGCTTGAACCCATT	CCATCCAATCGCTAGTAGCG

2.4. Quantitative Analysis of Leucocytes in Aqueous Humor

For leucocyte determination, an expert ophthalmologist collected aqueous humor (10 μ L) from the anterior chamber of the left eye of 3 rats from each group using a 28-gauge needle. Aqueous humor was stained (1:5) with Turk's solution (Merk, Darmstadt, Germany) for leucocyte counting in a Neubauer chamber (Brand GMBH p CO KG, Wertheim, Germany). Each aqueous humor sample was evaluated in triplicate.

2.5. Histological Evaluation

For histological evaluation, right eyes of 3 rats of each group were fixed in 10% neutral buffered formalin for 24 h and embedded in paraffin routinely. Sections of 4 μ m thick were stained with hematoxylin and eosin using a CoverStainer system (Dako-Agilent, Glostrup, Denmark). Six sections from each eye were examined to perform semiquantitative analysis by an anatomopathologist expert. Leucocytes surrounded ciliary processes were taken into account for counting and photographed using an Olympus BX51 microscope equipped with a MC170 camera (Leica, Wetzlar, Germany).

2.6. Statistical Analysis

Values were expressed as mean \pm standard error of the mean (SEM) or standard deviation (SD). Average values were compared using one-way ANOVA with Tukey's multiple comparison test. *p* values of less than 0.05 were considered statistically significant. Graph Pad Prism (Version 8.0.1) software (GraphPad Software, San Diego, CA, USA) was used for all calculations.

3. Results

3.1. Evaluation of the Effect of Tacrolimus on IL-6, IL-8, MIP-1 α , and TNF- α

The mRNA presence of the pro-inflammatory cytokines (IL-6, IL-8, MIP-1 α , and TNF- α) in the eye tissues was assessed by real time-PCR in order to evaluate the effect of TAC-HP β CD on factors involved in the inflammatory process. The levels of cytokines in the eye tissues of healthy, EIU, DXM and TAC-HP β CD groups are shown in Figure 2 and the statistical significance of the different levels detected among groups is depicted in Table 2.

EIU group had considerable high levels of IL-6 (138.89 \pm 89.71), IL-8 (6.53 \pm 5.36), MIP-1 α (217.37 \pm 113.15), and TNF- α (12.58 \pm 3.25) compared to healthy group [IL-6 (0.78 \pm 0.68), IL-8 (1.14 \pm 0.14), MIP-1 α (1.20 \pm 0.18) and TNF- α (1.22 \pm 0.34)]. Consequently, the augmentation of all these factors was statistically significant in the untreated EIU group as compared with healthy rats, which means that the EIU model was properly induced.

On the other hand, DXM group [IL-6 (1.29 \pm 1.59), IL-8 (5.18 \pm 5.09), MIP-1 α (56.88 \pm 54.70); TNF- α (7.31 \pm 5.52)] and TAC-HP β CD group [IL-6 (28.69 \pm 21.24); IL-8 (2.92 \pm 2.73); MIP-1 α (59.26 \pm 41.43); TNF- α (3.57 \pm 2.74)] had substantial fewer values of all the analyzed pro-inflammatory cytokines compared to EIU group. Hence, treatment with TAC-HP β CD and DMX significantly decreased levels of all these factors as compared

with EIU group except for IL-8 whose reduction did not achieve statistical significance neither TAC-HP β CD group nor DMX.

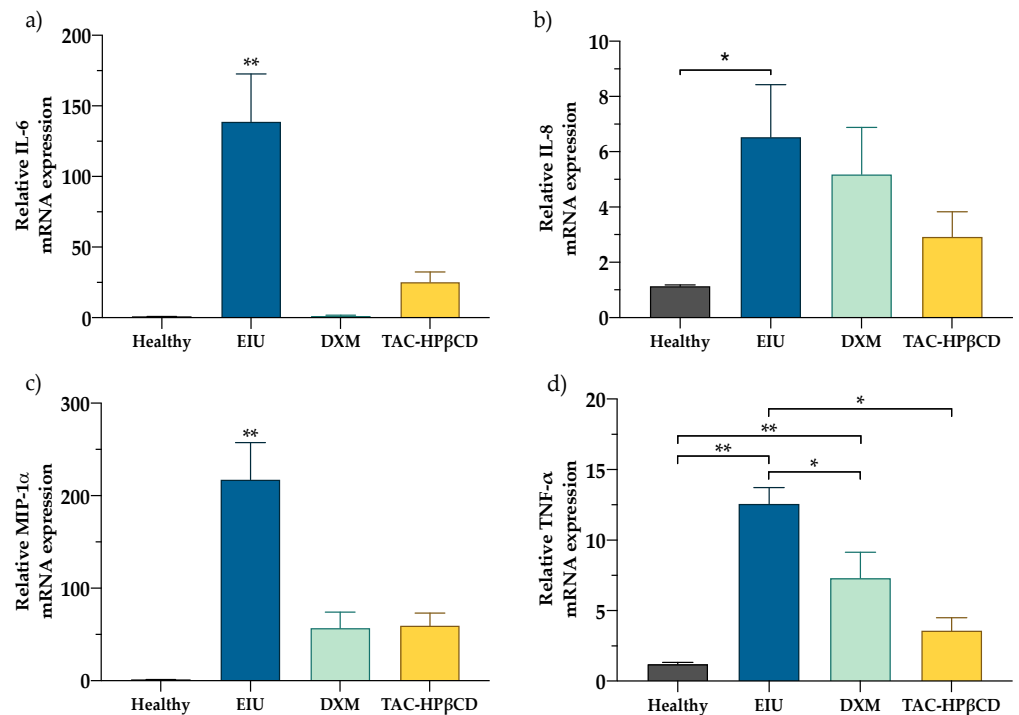


Figure 2. Anti-inflammatory in vivo effect (a) IL-6 (b) IL-8 (c) MIP-1 α and (d) TNF- α mRNA expression in healthy eyes (Healthy), EIU untreated rats (EIU), EIU rats treated with dexamethasone (DXM) and EIU rats treated with TAC-HP β CD (TAC-HP β CD). ($n = 10$ eyes per group). Bars represent mean \pm SD (* $p < 0.05$; ** $p < 0.005$).

Table 2. Existence (YES) or absence (NO) of statistical significance calculated through a Tukey's multiple comparison test among Healthy, EIU, DXM and TAC-HP β CD groups (* $p < 0.05$; ** $p < 0.005$).

Tukey's Multiple Comparison Test	IL-6	IL-8	MIP-1 α	TNF- α
Healthy vs. EIU	YES **	YES *	YES **	YES **
Healthy vs. TAC-HP β CD	NO	NO	NO	NO
Healthy vs. DXM	NO	NO	NO	YES **
EIU vs. TAC-HP β CD	YES **	NO	YES **	YES **
EIU vs. DXM	YES **	NO	YES **	YES *
TAC-HP β CD vs. DXM	NO	NO	NO	NO

Regarding the comparison of the detected levels of pro-inflammatory cytokines between healthy rats and TAC-HP β CD no statistically significant differences were found for IL-6, IL-8, MIP-1 α levels, as well as between healthy rats and DMX group. This, along with the fact that no statistically significant differences were neither found among pro-inflammatory cytokines levels of TAC-HP β CD and DXM group demonstrate that TAC-HP β CD eye drops could be an alternative to topical corticosteroid therapy in the treatment of this model of EIU and their clinical translational use should be studied in future studies. In addition, it should be highlighted that with regard to TNF- α , statistically significant differences were detected between healthy rats and DXM group but no between healthy rats and TAC-HP β CD group. This fact suggest that TAC could be a better option than DXM when the uveitis is related with an elevation of TNF- α .

3.2. Quantitative Analysis of Leucocytes in Aqueous Humor

Leukocyte counts in aqueous humor of healthy, EIU, DXM and TAC-HP β CD groups are depicted in Figures 3 and 4. In this sense, EIU group showed a significantly higher number of leukocytes (44.9 ± 11.0 cells/mL) compared to healthy group (0.2 ± 0.4 cells/mL) ($p < 0.005$), supporting the adequate development of the uveitis model. On the other hand, regarding leukocytes count of TAC-HP β CD group (27.55 ± 5.19 cells/mL), there is a considerable reduction in the number of leukocytes as compared with EIU group, being this difference statistically significant ($p < 0.005$) and positioning this therapy as a possible alternative to DXM treatment in uveitis. However, the decrease in the number of leukocytes is significantly greater in DXM group with regard to TAC-HP β CD group ($p < 0.005$), achieving a number of leukocytes comparable to healthy group.

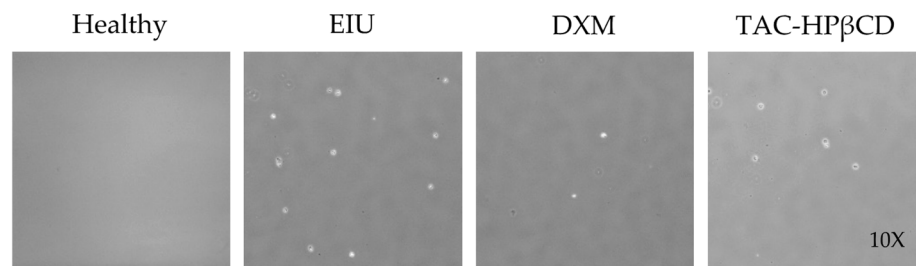


Figure 3. Leucocyte counting in aqueous humor 24 h after LPS injection in a Neubauer chamber. Groups were healthy eyes (Healthy), EIU untreated rats (EIU), EIU rats treated with dexamethasone (DXM) and EIU rats treated with TAC-HP β CD (TAC-HP β CD) ($n = 3$ eyes).

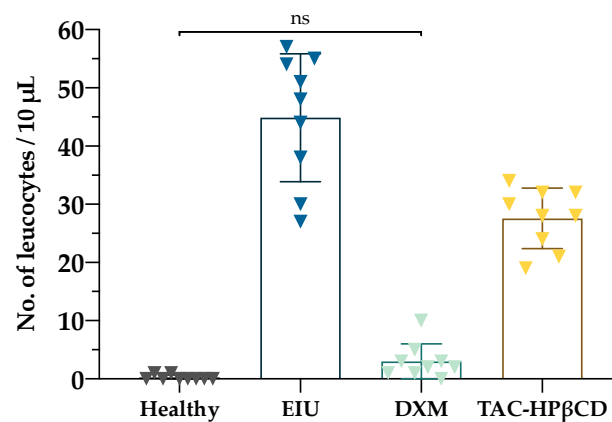


Figure 4. Quantitative analysis of leucocytes in aqueous humor. Groups were healthy eyes (Healthy), EIU untreated rats (EIU), EIU rats treated with dexamethasone (DXM) and EIU rats treated with TAC-HP β CD (TAC-HP β CD) ($n = 3$ eyes per group measured in triplicate). Bars represent mean \pm SD. There are statistically significant differences among all groups except between Healthy and DXM group whose difference is non-significant (ns).

3.3. Histological Evaluation

As it can be seen in Figure 5, the histological evaluation of retinas and ciliary processes showed no infiltration of leucocytes in healthy rats with no LPS injection. Very few or no leucocytes were found in DXM group while some leucocytes can be observed in TAC-HP β CD group. However, there was a considerable higher infiltration of leucocytes in untreated EIU-rats as compared with DXM and TAC-HP β CD groups.

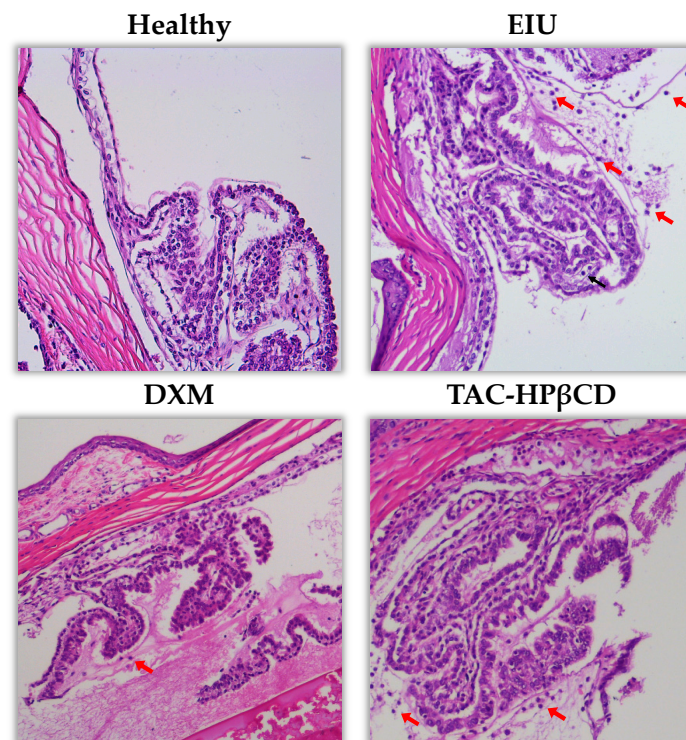


Figure 5. Representative hematoxylin-eosin staining showing infiltrated leucocytes (marked with arrows) in retina and ciliary processes of healthy, EIU, DXM and TAC-HP β CD groups. The histology was carried out 24 h after LPS injection.

4. Discussion

Nowadays, TAC is commercially available in oral and intravenous formulations, used in transplanted patients, and as an ointment for the treatment of atopic dermatitis [47]. TAC eyedrops can constitute an alternative in the treatment of uveitis [48,49] because it has been successfully used for various immune-mediated ocular disorders such as graft rejection [20], vernal keratoconjunctivitis (VKC) [21–24], dry eye [25] or scleritis [26,27]. However, TAC eyedrops are not marketed and they must be elaborated in HPDs. In this sense, it is necessary to highlight that TAC is a highly lipophilic macrolide lactone with a very poor water-solubility (1–2 $\mu\text{g}/\text{mL}$) [50]. This fact constitutes an important hurdle because TAC must be dissolved to allow efficient transport or permeation and reach the target site to become therapeutically effective [51].

Another inconvenience of TAC is that it has a high susceptibility to hydrolysis which leads to a very low stability in aqueous solutions [28,29]. For these reasons, TAC eye drops must be elaborated in HPDs by reformulation of the intravenous drug presentation (Prograf[®]), containing ethanol which have showed to disrupt the integrity of corneal epithelium and induce inflammation in corneal cells [52]. Based on this situation, in recent years several formulations of TAC for topical ophthalmic administration have been developed. In this sense, niosomes [29] and micelles [31] have been synthesized but they were not tested *in vivo*. However, positive effects of ophthalmic TAC were recently reported for nanovesicles [30] and nanocapsules [32].

Our group has previously developed a formulation of TAC-HP β CD eye drops containing a 0.02% (*w/v*) of TAC and a 40% (*w/v*) of HP β CD in Liquifilm[®], which can be safely prepared in HPDs and showed to be stable for at least 3 months under refrigeration [40]. The major advantage of TAC-HP β CD eye drops is that there is no need of using irritating excipients since our formulation strategy increases the solubilization of poorly soluble active ingredients and reduces the use of toxic products. In order to evaluate our formulation, a EIU model was selected because it is easily reproducible, quantifiable and clinical changes are similar to those of human acute uveitis [37]. Some authors stated that after

LPS administration there is an activation of TLRs, increasing levels of proinflammatory mediators, developing inflammation of anterior uvea, choroid and retina and producing the breakdown of blood-humor barrier, with exudation of leukocytes into the aqueous humor [53,54]. In this sense, significantly higher levels of TNF- α , IL-6, IL-8, MIP-1 α and leukocytes, as well as histological evaluation of EIU group, compared to healthy group confirmed the correct development of the uveitis model.

According to its mechanism of action, TAC inhibits calcineurin, blocks the production of proinflammatory cytokines and leads to inhibition of Th1 and Th2 cell activation [28,55]. In this regard, significantly lower levels of TNF- α , IL-6, MIP-1 α and leukocytes, as well as histological evaluation of TAC-HP β CD compared to EIU group confirms the effectiveness of this formulation in the treatment of uveitis. Other authors stated that ophthalmic treatment with TAC solution in light mineral oil, a vehicle where this active substance is not adequately dissolved, was not able to improve any parameter related with clinical manifestation of uveitis comparing to a EIU model [37]. Consequently, our positive therapeutic effects using TAC-HP β CD demonstrate the proper solubilization of TAC in our formulation.

Similarly, TAC proglycosome nanovesicles were synthesized by Garg et al., showing promising results in a rabbit EIU model since they achieved suppression of expression of TNF- α and IL-6 in aqueous humor, and reduction in ocular inflammation, leukocyte infiltration and protein leakage into aqueous humor comparing with the administration of ophthalmic TAC solution [30]. Furthermore, Rebibo et al. elaborated TAC-loaded nanocapsules enabling a superior anti-inflammatory effect on an anterior chamber LPS-induced murine model of keratitis in comparison to the drug in oil solution and with a significant decrease in macrophage inflammatory protein 2 and IL-6, among other evaluated inflammatory markers [32].

Regarding the comparison between the efficacy of our formulation and the standard treatment with dexamethasone, no statistically significant differences were found among pro-inflammatory cytokines levels of TAC-HP β CD and DXM group demonstrating that TAC-HP β CD eye drops could be an alternative to topical corticosteroid therapy in the treatment of this model of EIU and their clinical translational use should be studied in future studies. It is necessary to highlight that Rebibo et al. and Garg et al., in contrast with us, did not compare their formulations with corticosteroid standard treatment [30,32].

In addition, concerning TNF- α mRNA expression, its reduction is statistically significant only between TAC-HP β CD and EIU group but no between DXM and EIU group, which is consistent with TAC mechanism of action [56] and could be especially beneficial in uveitis related to the augmentation of this factor, such as HLA-B27-associated uveitis, sarcoid uveitis and uveitis associated with Behcet's disease among other noninfectious uveitis entities [11,12,57]. This possible personalization of the therapy based on the elevation of certain proinflammatory molecules could constitute an important advance, above all if this local increase could be correlated with systemic increases and detected through a blood test.

With respect to the limitations of our study, the fact that EIU model achieves the maximum inflammation 24 h after injection [36,37] makes necessary to carry out an accelerated dosage regimen and only permits a short-term evaluation which could constitute a hurdle regarding the translation of these results to the clinical setting. Another limitation is the lack of knowledge of the amount and rate of tacrolimus transcorneal permeation. Therefore, it will be necessary to study the intraocular pharmacokinetics of the TAC-HP β CD formulation with a suitable analytical method.

In spite of the fact that other ophthalmic TAC formulations have shown *in vivo* efficacy [37,39], as long as they are not commercialized, their translation to clinical practice is very difficult because of the high complexity of their synthesis. However, our TAC-HP β CD formulation has demonstrated *in vivo* efficacy and it can be easily elaborated in HPDs due to the simplicity of the elaboration process. Regarding the difference of cost associated between TAC eye drops usually prepared in HPDs by reformulation of Prograf[®]

and TAC-HP β CD eye drops, an estimate of the expenditure has been made in the Hospital Pharmacy Service for the two formulations in which the cost would be reduced by 200 euros for each patient and year with the implementation of the TAC-HP β CD formulation.

Future studies are needed to confirm the clinical effectiveness of TAC-HP β CD in order to consider this formulation as an alternative for the treatment of some forms of uveitis. The next step will be to conduct a study with patients in which the TAC-HP β CD formulation will be tested by comparing it with the results obtained in this group's previous work [22] with the TAC formulation used in HPDs.

5. Conclusions

TAC-HP β CD eyedrops showed beneficial effect in EIU model in rats, thus they could be considered an alternative for uveitis treatment in case of corticosteroids resistance or intolerance. This formulation demonstrated to reduce ocular inflammation, expression of IL-6, TNF- α , MIP-1 α and leukocyte infiltration in aqueous humor. In addition, the simple elaboration process of TAC-HP β CD makes possible to prepare this formulation in HDPs, improving in terms of safety the current elaborated TAC eyedrops by reformulation from intravenous drug presentation which contains ethanol and other irritating excipients. Further clinical studies are needed in order to evaluate long-term effectiveness of TAC-HP β CD.

Author Contributions: Conceptualization, A.F.-F., F.J.O.-E. and M.A.B.; methodology, X.G.-O., C.M.-G., F.G., R.P.-F., J.R.A.-L. and L.A.; validation, A.A., M.G.-B. and R.P.-F.; formal analysis, J.R.A.-L. and A.A.; investigation, X.G.-O., C.M.-G., L.A. and J.R.A.-L., resources, X.G.-O., C.M.-G., and M.A.B.; data curation, F.G., A.A., R.P.-F. and L.A.; writing—original draft preparation, X.G.-O., C.M.-G. and F.G.; writing—review and editing, M.G.-B., P.A., A.F.-F., F.J.O.-E. and M.A.B.; visualization, F.G., M.G.-B., J.R.A.-L., A.A. and P.A.; supervision, P.A., A.F.-F., F.J.O.-E. and M.A.B.; project administration, A.F.-F., P.A. and F.J.O.-E.; funding acquisition, A.F.-F. and F.G. All authors have read and agreed to the published version of the manuscript.

Funding: This project was partially funded by Health Research Institute Carlos III (PI20/00719, RETICS RD16/0008/0003), FEDER, Axencia Galega Innovación (Grupos de Potencial Crecimiento IN607B2020/11 y Grupo de Referencia Competitiva ED431C2021/01) and Spanish Ministry of Science, Innovation and Universities (RTI2018-099597-B-100). X. García-Otero is grateful to the IDIS (Health Research Institute of Santiago de Compostela) for financing his predoctoral research fellowship. C. Mondelo-García and A. Fernández-Ferreiro are grateful to the Carlos III Health Institute for financing their personnel contracts: JR20/00026 and JR18/00014.

Institutional Review Board Statement: The study was conducted according to the ARVO statement for the use of animals in ophthalmic and vision research and the approved guidelines for laboratory animals. It was approved by the (Health Research Institute of Santiago de Compostela's (IDIS) Animal Experimentation Ethics Committee (15010/2019/006, approval date: 25 September 2019).

Informed Consent Statement: Not applicable.

Data Availability Statement: Not applicable.

Acknowledgments: Not applicable.

Conflicts of Interest: The authors declare no conflict of interest. The funders had no role in the design of the study; in the collection, analyses, or interpretation of data; in the writing of the manuscript, or in the decision to publish the results.

References

1. Tsirouki, T.; Dastiridou, A.; Dastiridou, O.; Brazitikou, I.; Kalogeropoulos, C.; Androudi, S. A Focus on the Epidemiology of Uveitis. *Ocul. Immunol. Inflamm.* **2018**, *26*, 2–16. [CrossRef] [PubMed]
2. Fonollosa, A.; Adán, A. Uveitis: A multidisciplinary approach. *Arch. Soc. Esp. Ophthalmol.* **2011**, *86*, 393–394. [CrossRef]
3. Acharya, N.R.; Tham, V.M.; Esterberg, E.; Borkar, D.S.; Parker, J.V.; Vinoya, A.C.; Uchida, A. Incidence and Prevalence of Uveitis: Results from the Pacific Ocular Inflammation Study. *JAMA Ophthalmol.* **2013**, *131*, 1405–1412. [CrossRef]
4. Hwang, D.-K.; Chou, Y.-J.; Pu, C.-Y.; Chou, P. Epidemiology of Uveitis among the Chinese Population in Taiwan: A Population-Based Study. *Ophthalmology* **2012**, *119*, 2371–2376. [CrossRef]

5. Hart, C.T.; Zhu, E.Y.; Crock, C.; Rogers, S.L.; Lim, L.L. Epidemiology of Uveitis in Urban Australia. *Clin. Exp. Ophthalmol.* **2019**, *47*, 733–740. [CrossRef] [PubMed]
6. Fanlo, P.; Heras, H.; Espinosa, G.; Adan, A. Complications and Visual Acuity of Patients with Uveitis: Epidemiological Study in a Reference Unit in Northern Spain. *Arch. Soc. Esp. Ophthalmol.* **2019**, *94*, 419–425. [CrossRef]
7. Weinstein, J.E.; Pepple, K.L. Cytokines in Uveitis. *Curr. Opin. Ophthalmol.* **2018**, *29*, 267–274. [CrossRef]
8. De Smet, M.D.; Taylor, S.R.J.; Bodaghi, B.; Miserocchi, E.; Murray, P.I.; Pleyer, U.; Zierhut, M.; Barisani-Asenbauer, T.; LeHoang, P.; Lightman, S. Understanding Uveitis: The Impact of Research on Visual Outcomes. *Prog. Retin. Eye Res.* **2011**, *30*, 452–470. [CrossRef] [PubMed]
9. Lee, R.W.; Nicholson, L.B.; Sen, H.N.; Chan, C.-C.; Wei, L.; Nussenblatt, R.B.; Dick, A.D. Autoimmune and Autoinflammatory Mechanisms in Uveitis. *Semin. Immunopathol.* **2014**, *36*, 581–594. [CrossRef] [PubMed]
10. Taylor, A.W. Ocular Immune Privilege. *Eye* **2009**, *23*, 1885–1889. [CrossRef]
11. Balamurugan, S.; Das, D.; Hasanreisoglu, M.; Toy, B.C.; Akhter, M.; Anuradha, V.K.; Anthony, E.; Gurnani, B.; Kaur, K. Interleukins and Cytokine Biomarkers in Uveitis. *Indian J. Ophthalmol.* **2020**, *68*, 1750–1763. [CrossRef]
12. Curnow, S.J.; Falciani, F.; Durrani, O.M.; Cheung, C.M.G.; Ross, E.J.; Wloka, K.; Rauz, S.; Wallace, G.R.; Salmon, M.; Murray, P.I. Multiplex Bead Immunoassay Analysis of Aqueous Humor Reveals Distinct Cytokine Profiles in Uveitis. *Investig. Ophthalmol. Vis. Sci.* **2005**, *46*, 4251–4259. [CrossRef]
13. Kirino, Y.; Bertias, G.; Ishigatsubo, Y.; Mizuki, N.; Tugal-Tutkun, I.; Seyahi, E.; Ozyazgan, Y.; Sacli, F.S.; Erer, B.; Inoko, H.; et al. Genome-Wide Association Analysis Identifies New Susceptibility Loci for Behçet’s Disease and Epistasis between HLA-B*51 and ERAP1. *Nat. Genet.* **2013**, *45*, 202–207. [CrossRef]
14. Medawar, P.B. Immunity to Homologous Grafted Skin; the Fate of Skin Homografts Transplanted to the Brain, to Subcutaneous Tissue, and to the Anterior Chamber of the Eye. *Br. J. Exp. Pathol.* **1948**, *29*, 58–69. [PubMed]
15. Hou, S.; Du, L.; Lei, B.; Pang, C.P.; Zhang, M.; Zhuang, W.; Zhang, M.; Huang, L.; Gong, B.; Wang, M.; et al. Genome-Wide Association Analysis of Vogt-Koyanagi-Harada Syndrome Identifies Two New Susceptibility Loci at 1p31.2 and 10q21.3. *Nat. Genet.* **2014**, *46*, 1007–1011. [CrossRef]
16. Dick, A.D.; Rosenbaum, J.T.; Al-Dhibi, H.A.; Belfort, R.; Brézin, A.P.; Chee, S.P.; Davis, J.L.; Ramanan, A.V.; Sonoda, K.-H.; Carreño, E.; et al. Guidance on Noncorticosteroid Systemic Immunomodulatory Therapy in Noninfectious Uveitis. *Ophthalmology* **2018**, *125*, 757–773. [CrossRef] [PubMed]
17. Shahab, M.A.; Mir, T.A.; Zafar, S. Optimising Drug Therapy for Non-Infectious Uveitis. *Int. Ophthalmol.* **2019**, *39*, 1633–1650. [CrossRef] [PubMed]
18. Valdes, L.M.; Sobrin, L. Uveitis Therapy: The Corticosteroid Options. *Drugs* **2020**, *80*, 765–773. [CrossRef] [PubMed]
19. Jabs, D.A.; Rosenbaum, J.T.; Foster, C.S.; Holland, G.N.; Jaffe, G.J.; Louie, J.S.; Nussenblatt, R.B.; Stiehm, E.R.; Tessler, H.; Gelder, R.N.V.; et al. Guidelines for the Use of Immunosuppressive Drugs in Patients with Ocular Inflammatory Disorders: Recommendations of an Expert Panel. *Am. J. Ophthalmol.* **2000**, *130*, 492–513. [CrossRef]
20. Joseph, A.; Raj, D.; Shanmuganathan, V.; Powell, R.J.; Dua, H.S. Tacrolimus Immunosuppression in High-Risk Corneal Grafts. *Br. J. Ophthalmol.* **2007**, *91*, 51–55. [CrossRef] [PubMed]
21. Caputo, R.; Marziali, E.; de Libero, C.; Di Grande, L.; Danti, G.; Virgili, G.; Villani, E.; Mori, F.; Bacci, G.M.; Lucenteforte, E.; et al. Long-Term Safety and Efficacy of Tacrolimus 0.1% in Severe Pediatric Vernal Keratoconjunctivitis. *Cornea* **2021**, *40*, 1395–1401. [CrossRef]
22. Luaces-Rodríguez, A.; Touriño-Peralba, R.; Alonso-Rodríguez, I.; García-Otero, X.; González-Barcia, M.; Rodríguez-Ares, M.T.; Martínez-Pérez, L.; Aguiar, P.; Gómez-Lado, N.; Silva-Rodríguez, J.; et al. Preclinical Characterization and Clinical Evaluation of Tacrolimus Eye Drops. *Eur. J. Pharm. Sci. Off. J. Eur. Fed. Pharm. Sci.* **2018**, *120*, 152–161. [CrossRef] [PubMed]
23. Shoughy, S.S.; Jaroudi, M.O.; Tabbara, K.F. Efficacy and Safety of Low-Dose Topical Tacrolimus in Vernal Keratoconjunctivitis. *Clin. Ophthalmol. Auckl. NZ* **2016**, *10*, 643–647. [CrossRef] [PubMed]
24. Astellas Pharma Inc A Randomized, Placebo-Controlled, Double-Masked Study of 0.1% Tacrolimus (FK506) Ophthalmic Suspension in Vernal Keratoconjunctivitis. Available online: clinicaltrials.gov (accessed on 17 August 2021).
25. Moawad, P.; Shamma, R.; Hassanein, D.; Ragab, G.; El Zawahry, O. Evaluation of the Effect of Topical Tacrolimus 0.03% versus Cyclosporine 0.05% in the Treatment of Dry Eye Secondary to Sjogren Syndrome. *Eur. J. Ophthalmol.* **2021**. [CrossRef] [PubMed]
26. Young, A.L.; Wong, S.M.; Leung, A.T.S.; Leung, G.Y.S.; Cheng, L.L.; Lam, D.S.C. Successful Treatment of Surgically Induced Necrotizing Scleritis with Tacrolimus. *Clin. Exp. Ophthalmol.* **2005**, *33*, 98–99. [CrossRef]
27. Lee, Y.J.; Kim, S.W.; Seo, K.Y. Application for Tacrolimus Ointment in Treating Refractory Inflammatory Ocular Surface Diseases. *Am. J. Ophthalmol.* **2013**, *155*, 804–813. [CrossRef] [PubMed]
28. Thomson, A.W.; Bonham, C.A.; Zeevi, A. Mode of Action of Tacrolimus (FK506): Molecular and Cellular Mechanisms. *Ther. Drug Monit.* **1995**, *17*, 584–591. [CrossRef]
29. Murphy, C.C.; Greiner, K.; Plskova, J.; Duncan, L.; Frost, N.A.; Forrester, J.V.; Dick, A.D. Cyclosporine vs. Tacrolimus Therapy for Posterior and Intermediate Uveitis. *Arch. Ophthalmol. Chic.* **2005**, *123*, 634–641. [CrossRef] [PubMed]
30. Horai, R.; Caspi, R.R. Cytokines in Autoimmune Uveitis. *J. Interferon Cytokine Res. Off. J. Int. Soc. Interferon Cytokine Res.* **2011**, *31*, 733–744. [CrossRef]
31. Sakamoto, T. Cell biology of hyalocytes. *Nippon Ganka Gakkai Zasshi* **2003**, *107*, 866–882.

32. Mesquida, M.; Molins, B.; Llorenç, V.; de la Maza, M.S.; Adán, A. Targeting Interleukin-6 in Autoimmune Uveitis. *Autoimmun. Rev.* **2017**, *16*, 1079–1089. [CrossRef] [PubMed]
33. Sloper, C.M.; Powell, R.J.; Dua, H.S. Tacrolimus (FK506) in the Treatment of Posterior Uveitis Refractory to Cyclosporine. *Ophthalmology* **1999**, *106*, 723–728. [CrossRef]
34. Oh-i, K.; Keino, H.; Goto, H.; Yamakawa, N.; Murase, K.; Usui, Y.; Kezuka, T.; Sakai, J.-I.; Takeuchi, M.; Usui, M. Intravitreal Injection of Tacrolimus (FK506) Suppresses Ongoing Experimental Autoimmune Uveoretinitis in Rats. *Br. J. Ophthalmol.* **2007**, *91*, 237–242. [CrossRef]
35. Ishikawa, T.; Hokama, H.; Katagiri, Y.; Goto, H.; Usui, M. Effects of Intravitreal Injection of Tacrolimus (FK506) in Experimental Uveitis. *Curr. Eye Res.* **2005**, *30*, 93–101. [CrossRef] [PubMed]
36. Zeng, W.; Li, Q.; Wan, T.; Liu, C.; Pan, W.; Wu, Z.; Zhang, G.; Pan, J.; Qin, M.; Lin, Y.; et al. Hyaluronic Acid-Coated Niosomes Facilitate Tacrolimus Ocular Delivery: Mucoadhesion, Precorneal Retention, Aqueous Humor Pharmacokinetics, and Transcorneal Permeability. *Colloids Surf. B Biointerfaces* **2016**, *141*, 28–35. [CrossRef]
37. Garg, V.; Nirmal, J.; Riadi, Y.; Kesharwani, P.; Kohli, K.; Jain, G.K. Amelioration of Endotoxin-Induced Uveitis in Rabbit by Topical Administration of Tacrolimus Proglycosome Nano-Vesicles. *J. Pharm. Sci.* **2021**, *110*, 871–875. [CrossRef] [PubMed]
38. Siegl, C.; König-Schuster, M.; Nakowitsch, S.; Koller, C.; Graf, P.; Unger-Manhart, N.; Schindlegger, Y.; Kirchoff, N.; Knecht, C.; Prieschl-Grassauer, E.; et al. Pharmacokinetics of Topically Applied Tacrolimus Dissolved in Marinosolv, a Novel Aqueous Eye Drop Formulation. *Eur. J. Pharm. Biopharm.* **2019**, *134*, 88–95. [CrossRef] [PubMed]
39. Rebibo, L.; Tam, C.; Sun, Y.; Shoshani, E.; Badihi, A.; Nassar, T.; Benita, S. Topical Tacrolimus Nanocapsules Eye Drops for Therapeutic Effect Enhancement in Both Anterior and Posterior Ocular Inflammation Models. *J. Control. Release* **2021**, *333*, 283–297. [CrossRef]
40. García-Otero, X.; Díaz-Tomé, V.; Varela-Fernández, R.; Martín-Pastor, M.; González-Barcia, M.; Blanco-Méndez, J.; Mondelo-García, C.; Bermudez, M.A.; Gonzalez, F.; Aguiar, P.; et al. Development and Characterization of a Tacrolimus/Hydroxypropyl- β -Cyclodextrin Eye Drop. *Pharmaceutics* **2021**, *13*, 149. [CrossRef] [PubMed]
41. European Medicines Agency (EMA). Cyclodextrins Used as Excipients. Available online: <https://www.ema.europa.eu/en/cyclodextrins> (accessed on 17 August 2021).
42. The Association for Research in Vision and Ophthalmology-Statement for the Use of Animals in Ophthalmic and Vision Research. Available online: <https://www.arvo.org/About/policies/statement-for-the-use-of-animals-in-ophthalmic-and-vision-research/> (accessed on 5 May 2021).
43. National Research Council (US). Committee for the Update of the Guide for the Care and Use of Laboratory Animals Guide for the Care and Use of Laboratory Animals. In *The National Academies Collection: Reports Funded by National Institutes of Health*, 8th ed.; National Academies Press (US): Washington, DC, USA, 2011; ISBN 978-0-309-15400-0.
44. Da Silva, P.S.; Girol, A.P.; Oliani, S.M. Mast Cells Modulate the Inflammatory Process in Endotoxin-Induced Uveitis. *Mol. Vis.* **2011**, *17*, 1310–1319.
45. Girol, A.P.; Mimura, K.K.O.; Drewes, C.C.; Bolonheis, S.M.; Solito, E.; Farsky, S.H.P.; Gil, C.D.; Oliani, S.M. Anti-Inflammatory Mechanisms of the Annexin A1 Protein and Its Mimetic Peptide Ac2-26 in Models of Ocular Inflammation in Vivo and in Vitro. *J. Immunol.* **2013**, *190*, 5689–5701. [CrossRef] [PubMed]
46. Bermudez, M.A.; Sendon-Lago, J.; Seoane, S.; Eiro, N.; Gonzalez, F.; Saa, J.; Vizoso, F.; Perez-Fernandez, R. Anti-Inflammatory Effect of Conditioned Medium from Human Uterine Cervical Stem Cells in Uveitis. *Exp. Eye Res.* **2016**, *149*, 84–92. [CrossRef]
47. Cury Martins, J.; Martins, C.; Aoki, V.; Gois, A.F.T.; Ishii, H.A.; da Silva, E.M.K. Topical Tacrolimus for Atopic Dermatitis. *Cochrane Database Syst. Rev.* **2015**, CD009864. [CrossRef]
48. Gamalero, L.; Simonini, G.; Ferrara, G.; Polizzi, S.; Giani, T.; Cimaz, R. Evidence-Based Treatment for Uveitis. *Isr. Med. Assoc. J. IMAJ* **2019**, *21*, 475–479.
49. Hogan, A.C.; McAvoy, C.E.; Dick, A.D.; Lee, R.W.J. Long-Term Efficacy and Tolerance of Tacrolimus for the Treatment of Uveitis. *Ophthalmology* **2007**, *114*, 1000–1006. [CrossRef] [PubMed]
50. Kwon, M.; Yeom, D.; Kim, N.A.; Choi, D.H.; Park, J.; Wang, H.; Yoo, S.D.; Jeong, S.H. Bioequivalence of Tacrolimus Formulations with Different Dynamic Solubility and In-Vitro Dissolution Profiles. *Arch. Pharm. Res.* **2015**, *38*, 73–80. [CrossRef]
51. Loftsson, T.; Muellertz, A.; Siepmann, J. For the Special IJP Issue “Poorly Soluble Drugs”. *Int. J. Pharm.* **2013**, *453*, 1–2. [CrossRef] [PubMed]
52. Oh, J.Y.; Yu, J.M.; Ko, J.H. Analysis of Ethanol Effects on Corneal Epithelium. *Investig. Ophthalmol. Vis. Sci.* **2013**, *54*, 3852–3856. [CrossRef]
53. Yadav, U.C.S.; Ramana, K.V. Endotoxin-Induced Uveitis in Rodents. *Methods Mol. Biol.* **2019**, *1960*, 161–168. [CrossRef]
54. Fox, A.; Hammer, M.E.; Lill, P.; Burch, T.G.; Burrish, G. Experimental Uveitis. Elicited by Peptidoglycan-Polysaccharide Complexes, Lipopolysaccharide, and Muramyl Dipeptide. *Arch. Ophthalmol. Chic.* **1984**, *102*, 1063–1067. [CrossRef] [PubMed]
55. Vafadari, R.; Kraaijeveld, R.; Weimar, W.; Baan, C.C. Tacrolimus Inhibits NF-KB Activation in Peripheral Human T Cells. *PLoS ONE* **2013**, *8*, e60784. [CrossRef] [PubMed]
56. Hikita, N.; Chan, C.C.; Whitcup, S.M.; Nussenblatt, R.B.; Mochizuki, M. Effects of Topical FK506 on Endotoxin-Induced Uveitis (EIU) in the Lewis Rat. *Curr. Eye Res.* **1995**, *14*, 209–214. [CrossRef] [PubMed]
57. Mesquida, M.; Molins, B.; Llorenç, V.; Sainz de la Maza, M.; Hernandez, M.V.; Espinosa, G.; Adán, A. Proinflammatory Cytokines and C-Reactive Protein in Uveitis Associated with Behçet’s Disease. *Mediat. Inflamm.* **2014**, *2014*, e396204. [CrossRef] [PubMed]



Article

Sustained-Release Microspheres of Rivoceranib for the Treatment of Subfoveal Choroidal Neovascularization

E Seul Kim ^{1,†}, Min Sang Lee ^{1,†}, Hayoung Jeong ^{2,3}, Su Yeon Lim ¹, Doha Kim ^{2,3}, Dahwun Kim ¹, Jaeback Jung ¹, Siyan Lyu ¹, Hee Joo Cho ¹, Dong Min Kim ¹, Wonhee Suh ^{2,3,*} and Ji Hoon Jeong ^{1,*}

¹ School of Pharmacy, Sungkyunkwan University, Suwon 16419, Korea; seul4146@skku.edu (E.S.K.); lminsa@skku.edu (M.S.L.); kally37@naver.com (S.Y.L.); gnjs0219@naver.com (D.K.); domonde@naver.com (J.J.); lsy2018dd@hotmail.com (S.L.); chojh823@naver.com (H.J.C.); eastjade@g.skku.edu (D.M.K.)

² Department of Global Innovative Drug, Graduate School of Chung-Ang University, Seoul 06974, Korea; gkdud819@naver.com (H.J.); summerflow02@gmail.com (D.K.)

³ College of Pharmacy, Chung-Ang University, Seoul 06974, Korea

* Correspondence: wsuh@cau.ac.kr (W.S.); jhjeong@skku.edu (J.H.J.); Tel.: +82-02-820-5960 (W.S.); +82-31-290-7783 (J.H.J.)

† These authors contributed equally to this work.

Abstract: The wet type of age-related macular degeneration (AMD) accompanies the subfoveal choroidal neovascularization (CNV) caused by the abnormal extension or remodeling of blood vessels to the macula and retinal pigment epithelium (RPE). Vascular endothelial growth factor (VEGF) is known to play a crucial role in the pathogenesis of the disease. In this study, we tried to repurpose an investigational anticancer drug, rivoceranib, which is a selective inhibitor of VEGF receptor-2 (VEGFR2), and evaluate the therapeutic potential of the drug for the treatment of wet-type AMD in a laser-induced CNV mouse model using microsphere-based sustained drug release formulations. The PLGA-based rivoceranib microsphere can carry out a sustained delivery of rivoceranib for 50 days. When administered intravitreally, the sustained microsphere formulation of rivoceranib effectively inhibited the formation of subfoveal neovascular lesions in mice.

Keywords: rivoceranib; drug repositioning; microsphere; subfoveal choroidal neovascularization; macular degeneration

Citation: Kim, E.S.; Lee, M.S.; Jeong, H.; Lim, S.Y.; Kim, D.; Kim, D.; Jung, J.; Lyu, S.; Cho, H.J.; Kim, D.M.; et al. Sustained-Release Microspheres of Rivoceranib for the Treatment of Subfoveal Choroidal Neovascularization. *Pharmaceutics* **2021**, *13*, 1548. <https://doi.org/10.3390/pharmaceutics13101548>

Academic Editor: Monica M. Jablonski

Received: 18 August 2021
Accepted: 19 September 2021
Published: 24 September 2021

Publisher's Note: MDPI stays neutral with regard to jurisdictional claims in published maps and institutional affiliations.



Copyright: © 2021 by the authors. Licensee MDPI, Basel, Switzerland. This article is an open access article distributed under the terms and conditions of the Creative Commons Attribution (CC BY) license (<https://creativecommons.org/licenses/by/4.0/>).

1. Introduction

The eye is a representative organ, exhibiting the fastest signs of aging, and visual problems are generally more noticeable than other age-related disorders [1]. Age-related macular degeneration (AMD) is a leading cause of irreversible visual loss in older adults [2]. The impaired vision and blindness associated with AMD are due to atrophic and neovascular complications [3]. Although the dry or non-neovascular type of AMD is more prevalent than wet or neovascular AMD, wet AMD is often involved with severely reduced vision acuity and vision loss which occurs when the outgrowth of blood vessels in the choroidal region extends underneath the foveal avascular zone (subfoveal choroidal neovascularization (CNV)) [4,5]. Vascular endothelial growth factor (VEGF) is one of the most critical factors for the vascular proliferation and migration of endothelial cells in the neovascularization process [6]. Therefore, blocking the VEGF signaling pathway to prevent CNV has been popularly employed for the treatment of wet AMD [7]. Monoclonal antibodies targeting VEGF receptors (VEGFR) such as bevacizumab and ranibizumab are frequently used for CNV due to their desirable effectiveness and low incidence of serious ocular and systemic adverse events [8]. However, the lack of a proper delivery system and the high cost of antibody therapy have remained a limitation [9].

Corticosteroids are also widely used for ocular disorders involving CNV and macular edema, owing to their anti-inflammatory and anti-angiogenic properties [10]. Intravitreal

injectable implants containing corticosteroids such as dexamethasone and fluocinolone acetamide could achieve sustained drug release in vitreous space for an extended period. However, steroid therapy is often associated with adverse events, including cataract formation, ocular hypertension, and glaucoma [11–13].

Biodegradable microspheres have been used for the extended release of various active substances including small molecules, polypeptides, and nucleic acids, since they are injectable and biodegradable, so additional surgical procedures for implant removal are not required [14]. In addition, microspheres can be formulated with hydrophobic as well as hydrophilic drugs and deliver the active substances for a longer period compared to nanoparticles [15]. Microspheres containing a small molecular protein kinase C inhibitor (PKC412, Novartis Pharma) and fasudil were developed for CNV and glaucoma, respectively [16,17]. A sustained-release microsphere for an anti-VEGF RNA aptamer was also designed for the treatment of AMD [18].

Rivoceranib is a selective receptor tyrosine kinase inhibitor targeting the intracellular ATP-binding site of VEGFR2. Since VEGFR2 plays a crucial role in VEGF-mediated endothelial cell proliferation, migration, and permeabilization [19], rivoceranib was developed for antiangiogenic cancer therapy, and is in clinical trials for metastatic gastric cancer and metastatic adenoid cystic carcinoma [20]. We hypothesized that rivoceranib, a selective inhibitor of VEGFR tyrosine kinase, could be repositioned as a candidate for an anti-VEGF therapy for CNV. In our previous studies, human albumin-polyethyleneglycol (HSA-PEG) conjugate-based nanoparticles containing rivoceranib effectively reduced retinal vascular leakage and corneal neovascularization by blocking VEGF/VEGFR2 signaling [21,22]. In this study, injectable microsphere dosage forms of rivoceranib were developed for extended drug release in the vitreous space. The potential therapeutic effect of the rivoceranib microspheres for wet AMD was evaluated in a laser-induced CNV animal model.

2. Materials and Methods

2.1. Materials

Rivoceranib was obtained from HLB Bio (Seoul, Korea). Poly(D,L-lactic-co-glycolic acid) (PLGA) copolymers (Resomer RG502 (50:50, Mw 7000–17,000), Resomer RG502H (50:50, Mw 7000–17,000) and Resomer RG503H (50:50, Mw 24,000–38,000)), polyvinyl alcohol (PVA), and Tween 20 were purchased from Sigma (St. Louis, MO, USA). Methylene chloride, acetonitrile, and methanol were of analytical grade and used without purification (J. T. Baker, Phillipsburg, NJ, USA). All the liquid solutions were sterilized by autoclave or filtration (0.45 µm filter unit, Millipore, Billerica, MA, USA).

2.2. Preparation and Characterization of Rivoceranib Microspheres

Microspheres containing rivoceranib were fabricated using an oil-in-water emulsification method. PLGA (360 mg) and rivoceranib (40 mg) were dissolved in methylene chloride/methanol (9:1 *v/v*, 1 mL). The solution was slowly added to 0.5% PVA solution (*w/v*, 300 mL) and emulsified with a high-speed dispersion homogenizer (HG-15D, Daihan Scientific, Seoul, Korea) at either 1500 or 2000 rpm for 2 min. The resulting microspheres were centrifuged at 2000 rpm at 4 °C and the supernatant was removed. The microspheres were resuspended in cold deionized water and washed three times by the centrifugation method. The collected microspheres were freeze-dried at −70 °C and stored at −20 °C until use. The drug loading and encapsulation efficiency of the microspheres were determined using a Waters 626 HPLC pump equipped with a UV detector (Waters, Milford, MA, USA) and C18 reversed-phase column (5 µm particle size; Millipore, Billerica, MA, USA). The mobile phase (acetonitrile and 0.01 M KH₂PO₄ in deionized water, 70:30 *v/v*) was delivered at a flow rate of 1 mL/min. The detection wavelength was set at 260 nm. The morphology and size distribution of the rivoceranib microspheres were observed using scanning electron microscopy (SEM, JSM7600F, JEOL, Tokyo, Japan) and dynamic light scattering (Mastersizer 2000, Malvern Panalytical, Malvern, UK).

2.3. Differential Scanning Calorimetric (DSC) and Fourier-Transform Infrared (FTIR) Spectral Studies

A mixture of PLGA and rivoceranib (1:1, *w/w*) was dissolved in a cosolvent of methylene chloride/methanol (9:1, *v/v*) and the solvent was evaporated to form a film. For DSC analysis, one milligram of the film sample was placed in an aluminum pan and its thermal behavior was monitored by applying heat from 25 °C to 200 °C at a heating rate of 5 °C/min (DSC 6100, Seiko Instruments, Chiba, Japan). For FTIR analysis, the spectral profile of PLGA/rivoceranib film was observed in the range of 400 to 4000 cm^{-1} using FTIR spectrophotometer (IFS66v-S, Bruker, Billerica, MA, USA).

2.4. Drug Release Profiles of PLGA/Rivoceranib Microspheres

The PLGA/rivoceranib microspheres (5 mg) were suspended in 1 mL of deionized water. The suspension was transferred to a dialysis bag (MWCO 5000, Spectrum, Gardena, CA, USA) and drug release was carried out in a 10 mL release medium (0.1% polysorbate 80 in PBS pH 7.4) at 37 °C. The samples were taken at a predetermined period and the release medium was replenished. The amount of released drug was analyzed using HPLC.

2.5. Animals

The animals were cared for in accordance with the Guide for the Care and Use of Laboratory Animals published by the United States National Institutes of Health. The protocols were also approved by the Institutional Animal Care and Use Committee (IACUC) of Chung-Ang University (IACUC number: 201800044, start date: 4 May 2018). Nine- to ten-week-old male C57BL/6 mice were purchased from Orient Co., Ltd. (Seoul, Korea). Mice were housed in microisolator cages on individually ventilated cage racks with ad libitum access to an autoclaved standard rodent diet (LabDiet 5008, Purina, St. Louis, MO, USA) and were kept under a 12:12 h light/dark cycle. Anesthesia was performed via an intraperitoneal injection of ketamine hydrochloride (100 mg/kg body weight) and xylazine hydrochloride (6 mg/kg body weight). The pupils of the anesthetized mice were dilated with topical drops of 1% tropicamide (Santen, Osaka, Japan).

2.6. Mouse Model of Laser-Induced Choroidal Neovascularization (CNV)

Immediately after mice were anesthetized and their pupils dilated, experimental CNV lesions (four spots per eye) were created at the 3, 6, 9, and 12 o'clock positions of the posterior pole of the fundus at equal distances from the optic nerve head with the following parameters: 532 nm wavelength, 50 μm diameter, 70 ms duration, and 220 mW intensity (Micron IV image-guided laser system, Phoenix Research Laboratories, Pleasanton, CA, USA). Only mice with cavitation bubbles, which indicated the disruption of Bruch's membrane, were included in the study. Immediately after CNV induction, the mice were given an intravitreal injection of rivoceranib-loaded PLGA microspheres (10 μg rivoceranib/10% RG502H–2.0k in 1 μL PBS), PLGA microspheres (10% RG502H–2.0k in 1 μL PBS), or PBS (1 μL). Two weeks later, the mice were euthanized for further analysis.

2.7. Quantification of Laser-Induced CNV

The eyes were enucleated and fixed in 4% paraformaldehyde solution in PBS. The posterior eyecups comprising the retinal pigmented epithelium, choroid, and sclera were microdissected from the surrounding tissues and prepared as flat mounts. The flat mounts were then stained with Alexa Fluor[®] 594-conjugated Griffonia simplicifolia isolectin B4 (IB4; 1:100 dilution; Invitrogen, Carlsbad, CA, USA) overnight at 4 °C. Images of CNV lesions were obtained using a fluorescence microscope (Olympus, Tokyo, Japan); the exposure and gain were kept constant for all samples. In each whole-mount image, the numbers of pixels in the CNV areas were measured using ImageJ software (National Institute of Health, Bethesda, MD, USA).

2.8. Statistical Analysis

All data are expressed as the mean \pm standard error of mean (SEM) of indicated *n* values. One-way analysis of variance was used to determine the significance of differences between groups. Data were analyzed using the Bonferroni correction for multiple comparisons. Differences were considered significant when $p < 0.05$.

3. Results

3.1. Preparation and Characterization of Rivoceranib Microspheres

The rivoceranib microspheres were prepared using an oil-in-water emulsification process, in which the manufacturing parameters, including the molecular weight and terminal functional group of PLGA polymers, and the emulsifying speeds for the formation of the oil-in-water emulsions were varied to observe the effect of the parameters on the release behavior of rivoceranib. The formulation parameters of the microspheres are summarized in Table 1. The fabrication parameters such as polymer end group did not significantly affect the efficiency of drug loading, suggesting there may be no interactions between the polymer end groups and rivoceranib.

Table 1. Rivoceranib microsphere formulations.

Sample	Polymer Molecular Weight (Mw) ^a	Polymer end Group	Emulsification Rate (rpm)	Drug Loading Content (%)	Encapsulation Efficiency (%)
502–1.5k	7000–17,000	Hydroxyl	1500	7.94	79.4
502–2.0k	7000–17,000	Hydroxyl	2000	7.38	73.8
502H–1.5k	7000–17,000	Carboxyl	1500	8.25	82.5
502H–2.0k	7000–17,000	Carboxyl	2000	7.89	78.9
503H–1.5k	24,000–38,000	Carboxyl	1500	7.80	78.0
503H–2.0k	24,000–38,000	Carboxyl	2000	8.77	87.7

^a as described in the manufacturer's specification.

The rivoceranib microspheres showed a spherical morphology with a smooth surface, as observed in a scanning electron microscope (SEM) (Figure 1). The microspheres prepared at 2000 rpm of the emulsifying speed were smaller in size than those prepared at 1500 rpm (Figure 2). However, the viscosity of the polymer due to the difference in molecular weight seemed not to be significant.

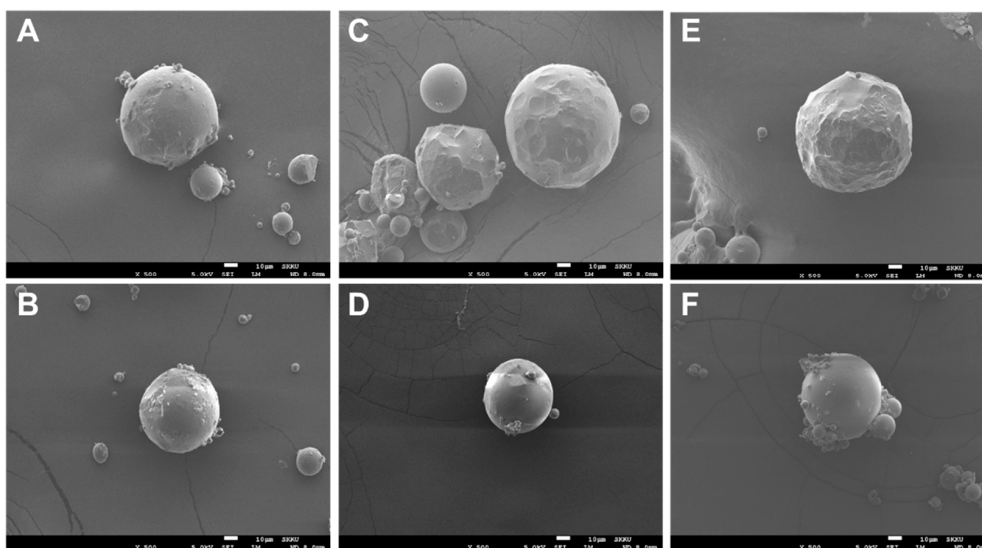


Figure 1. SEM images of rivoceranib microspheres. (A,B) microspheres were fabricated using PLGA RG502, (C,D) microspheres were from PLGA RG502H, (E,F) microspheres were from PLGA RG503H. Microspheres (A,C,E) were prepared at the emulsifying speed of 1500 rpm. Microspheres (B,D,F) were prepared at 2000 rpm. Scale bars = 10 μ m.

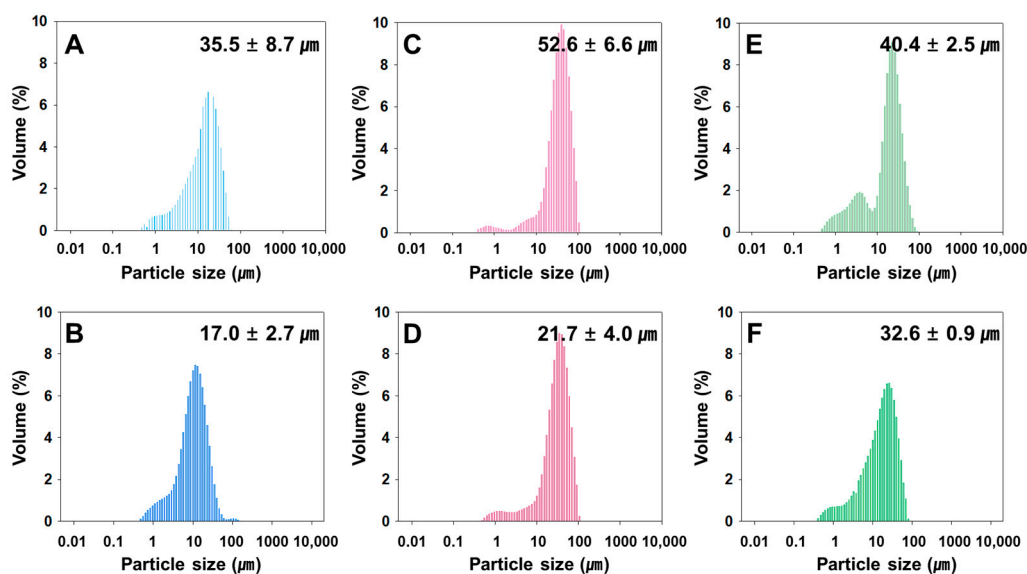


Figure 2. Size distribution of rivoceranib microspheres, determined by a light scattering method. (A,B) microspheres were fabricated using PLGA RG502, (C,D) microspheres were from PLGA RG502H, (E,F) microspheres were from PLGA RG503H. Microspheres (A,C,E) were prepared at the emulsifying speed of 1500 rpm. Microspheres (B,D,F) were prepared at 2000 rpm.

3.2. Polymer–Drug Interactions

Interactions between a polymer matrix and a drug compound in a formulation are considered important since the interactions may affect the physicochemical properties and bioavailability of the drug [23]. The possibilities of polymer–drug interactions are often studied using the thermal and spectroscopic methods using DSC and FTIR, respectively [24]. The thermal behaviors of PLGA (RG502), rivoceranib, a physical mixture of PLGA and the drug (1:1, *w/w*), and polymer–drug blend films (1:1, *w/w*) are shown in Figure 3. PLGA RG502 and rivoceranib showed endothermic peaks at 38.5 °C and 194.5 °C, respectively (Figure 3A,B). It should be noted that the melting peak of rivoceranib appears in the polymer–drug physical mixture (Figure 3C) and the polymer–drug blend films (Figure 3D–F) with minor shifts in position, suggesting the absence of significant interactions that affect the crystalline nature of rivoceranib. The minor changes in the peak position may be due to the blending process, which decreases the purity of each component and, therefore, and do not indicate the polymer–drug interactions [25]. The effect of polymer–drug interactions on the thermal behaviors of the components was also observed in the rivoceranib-loaded microspheres. As shown in the blend films, no significant changes in the thermograms of the microspheres were observed, although the endothermic peak for rivoceranib was not detectable, possibly due to the low quantity of the drug (Figure S1).

The potential polymer–drug interactions were further investigated using FTIR spectral analysis. The shifts of frequency and bandwidth of interacting groups indicate the changes in oscillation of the molecular dipoles in a polymer–drug mixture [26]. The characteristic peaks of PLGA (C=O at 1750–1705 cm^{-1} ; OH at 3500–3400 cm^{-1}) and rivoceranib (–COOH at 1750–1700 cm^{-1} ; –NH at 700–600 cm^{-1} ; –C≡N at 2250–2200 cm^{-1}) are shown in Figure 4A. The FTIR spectra of the polymer–drug physical blend films as well as the polymer–drug physical mixture did not show any absence of peaks of the functional groups in the spectra. In addition, no new bands were detected in the polymer–drug blend film. These results suggest that there are no significant chemical interactions, and the formation of new chemical linkages between PLGA and rivoceranib, demonstrating the significant compatibility between the two compounds.

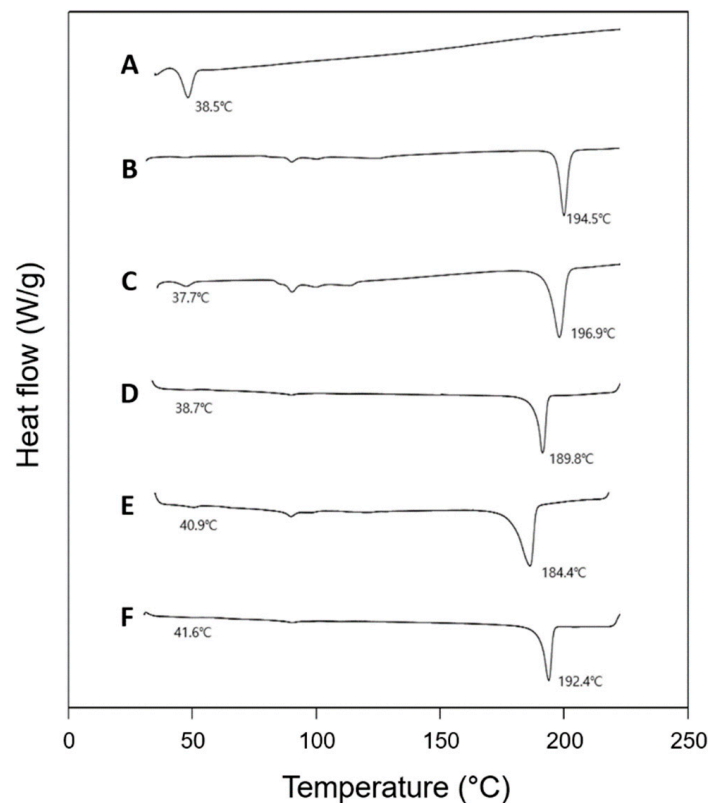


Figure 3. Differential scanning calorimetry (DSC) thermograms of (A) PLGA RG 502; (B) rivoceranib; (C) physical mixture (1:1) of PLGA RG502 and rivoceranib; (D) PLGA RG502 and rivoceranib (1:1) blend film; (E) PLGA RG502H and rivoceranib (1:1) blend film; (F) PLGA RG503H and rivoceranib (1:1) blend film. The downward peaks in the diagrams represent the endothermic behavior.

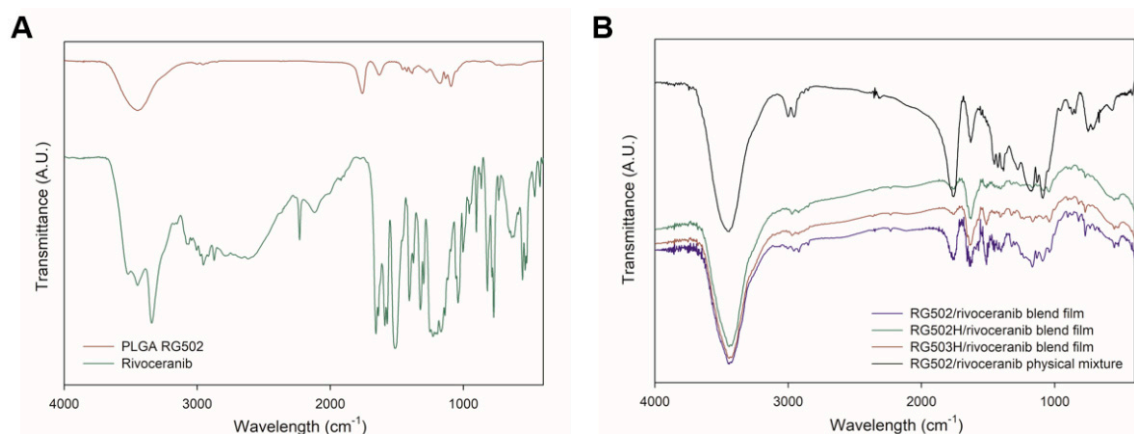


Figure 4. Fourier transform infrared (FTIR) spectrum of (A) PLGA RG502 polymer and rivoceranib; (B) PLGA RG502 and rivoceranib (1:1) blend film, PLGA RG502H and rivoceranib (1:1) blend film, PLGA RG503H and rivoceranib (1:1) blend film, and physical mixture (1:1) of PLGA RG502 and rivoceranib.

3.3. Sustained Drug Release Profiles of Rivoceranib Microspheres

In vitro rivoceranib release profiles from the rivoceranib microsphere formulations (Table 1) are shown in Figure 5. The release of free rivoceranib followed a zero-order kinetics with the cumulative drug release of 84% for 5 days. This result agrees with a previous observation with the release profile of a hydrophobic drug, paclitaxel, in an aqueous medium [27]. The microsphere formulations exhibited a burst release in a range from 1.4 to 5.7% over the initial 1 h. After the initial burst, the microsphere formulations

achieved sustained drug release for 50 days. The relatively low initial burst and slow drug release profiles would be due to the hydrophobic nature of rivoceranib. The RG502–2.0k and RH502H–2.0k microspheres exhibited a similar drug release profile that resulted in 89.0 and 85.9% release during the experimental period, respectively. This indicated that the polar hydroxyl- and the ionizable carboxyl-end group of RG502 and RG502H did not significantly affect the drug release behaviors of the microspheres, suggesting the lack of significant interactions between the end group of the polymer chain and rivoceranib. The molecular weight of PLGA and the emulsification speed in the microsphere fabrication process significantly influence the release kinetics of the drug. The smaller microspheres prepared at a higher emulsification speed (2000 rpm), including 502–2.0k, 502H–2.0k, and 503H–2.0k, exhibited much faster drug release profiles than ones prepared at a lower speed, owing to the increased surface area [28].

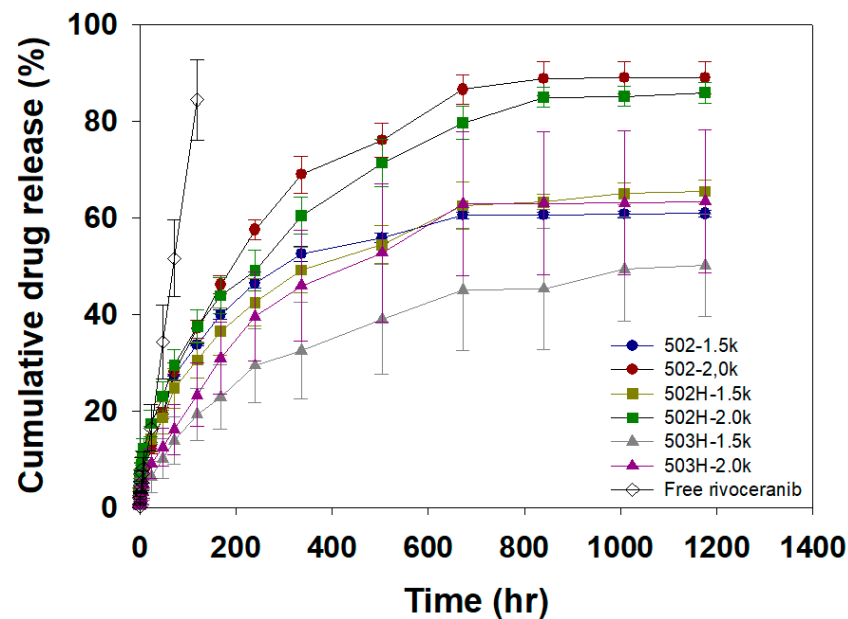


Figure 5. In vitro release curves of free rivoceranib and rivoceranib-loaded microspheres. The drug release profiles were represented as a mean \pm SEM ($n = 3$).

3.4. Suppression of CNV Formation in Mice by Intravitreal Administration of Rivoceranib Microspheres

To evaluate the ability of rivoceranib microspheres to suppress CNV formation in vivo, a mouse with laser-induced CNV was used. This model induced a rupture of Bruch's membrane via laser photocoagulation, which causes the aberrant growth of new vessels from the choroid into the subretinal space [29]. The least effective dose of rivoceranib was determined as 1.0 μg , based on our previous results [30]. Immediately after laser photocoagulation, RG502H–2.0k microspheres containing 10 μg rivoceranib, RG502H–2.0k microspheres without the drug (blank microspheres), or PBS were intravitreally injected into mice. Two weeks later, the eyes were harvested and the area of CNV lesions was evaluated (Figure 6A). The posterior eyecups comprising retinal pigment epithelium (RPE), choroid, and sclera were flat-mounted and stained with isolectin B4 (IB4, stained in red). The CNV area was quantified by measuring the fluorescence intensity of images with isolectin B4-positive areas. Representative images of the IB4-stained CNV lesions show that the area of CNV lesions in RG502H–2.0k microsphere-treated mice was much smaller than those in PBS- or blank microsphere-treated controls (Figure 6B). Quantitative analysis showed that the area of CNV lesions in mice treated with RG502H–2.0k microspheres was $2.78 \pm 0.21 \times 10^3 \mu\text{m}^2$, which was $2.12 \pm 0.27 \times 10^3 \mu\text{m}^2$ and $1.35 \pm 0.24 \times 10^3 \mu\text{m}^2$ lower than those in mice treated with blank microsphere and PBS, respectively. These

results indicate that RG502H-2.0k microspheres efficiently block laser-induced pathological neovascularization in the choroid of mice.

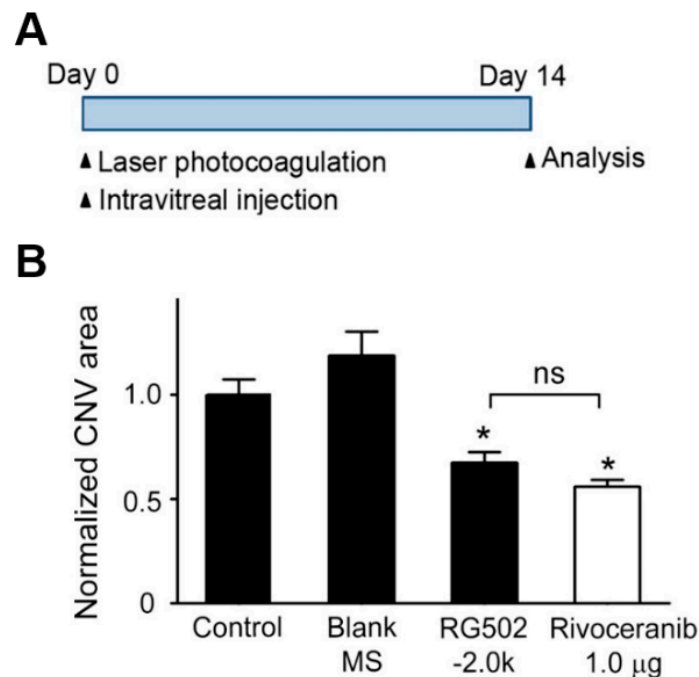


Figure 6. Inhibitory effect of rivoceranib-loaded PLGA microspheres and rivoceranib on laser-induced CNV formation in mice. (A) In vivo treatment schedule for the laser-induced choroidal neovascularization (CNV) experiment. (B) Immediately after laser photocoagulation, the mice received a single intravitreal injection of PBS (1 µL; $n = 10$ mice, Control), drug free RG502H microspheres (10% microsphere in 1 µL PBS, $n = 4$ mice, Blank MS), and rivoceranib-loaded PLGA 502H microspheres (10 µg rivoceranib/10% 502H–2.0k in 1 µL PBS, $n = 10$ mice). Two weeks later, the CNV area was analyzed. Rivoceranib (1.0 µg rivoceranib in 1 µL DMSO, $n = 4$ mice) and PBS (1 µL; $n = 10$ mice, Control). Two weeks later, the CNV area was analyzed. The CNV area was quantified by measuring the fluorescence intensity of images with isolectin IB4-positive areas. CNV areas of samples were expressed relative to that of control (one-way ANOVA with Bonferroni post hoc multiple comparison test, ns = not significant, * $p < 0.05$ vs. blank MS). Data are presented as the mean \pm SEM.

4. Conclusions

In wet-type age-related macular degeneration (AMD), VEGF and its receptors have been recognized as primary disease targets, in which the increased expression of VEGF contributes to aberrant angiogenesis and vascular leakage, leading to vision impairment and loss. In this regard, we investigated the possibility of repurposing an anticancer drug, rivoceranib, as a therapeutic intervention for AMD, and the effect of biodegradable microsphere-based sustained delivery of the drug on pathological angiogenesis in the eye using a laser-induced CNV model that is a common animal model of wet-type AMD. The rivoceranib microsphere achieved sustained in vitro drug release for 50 days. The intravitreal administration of the microsphere effectively suppressed the abnormal blood vessel formation of the foveal avascular zone (subfoveal CNV). Considering the biocompatibility and clinical significance of PLGA microspheres, the rivoceranib microspheres could be considered as an economical and effective alternative to antiangiogenic antibody therapy for AMD.

Supplementary Materials: The following are available online at <https://www.mdpi.com/article/10.3390/pharmaceutics13101548/s1>, Figure S1: Differential scanning calorimetry (DSC) thermograms of (A) PLGA RG502 microsphere (drug free); (B) PLGA RG502/rivoceranib microsphere (502–2.0k); (C) PLGA RG502H microsphere (drug free); (D) PLGA RG502H/rivoceranib microsphere (502H–2.0k); (E) PLGA RG503H microsphere (drug free); (F) PLGA RG503H/rivoceranib microsphere (503H–2.0k). The downward peaks in the diagrams represent the endothermic behavior.

Author Contributions: Conceptualization, J.H.J. and W.S.; methodology, E.S.K., M.S.L., H.J., S.Y.L., D.K. (Doha Kim), D.K. (Dahwun Kim), J.J., S.L., H.J.C. and D.M.K.; software, E.S.K., M.S.L. and H.J.; validation, E.S.K., M.S.L., J.J., S.L., H.J.C. and D.M.K.; formal analysis, E.S.K., M.S.L., H.J. and S.Y.L.; investigation, E.S.K., M.S.L., H.J., S.Y.L., D.K. (Doha Kim), D.K. (Dahwun Kim), J.J., S.L., H.J.C. and D.M.K.; resources, J.H.J.; data curation, E.S.K., M.S.L.; writing—original draft preparation, E.S.K. and M.S.L.; writing—review and editing, J.H.J.; supervision, J.H.J.; project administration, J.H.J.; funding acquisition, J.H.J. and W.S. All authors have read and agreed to the published version of the manuscript.

Funding: This research was supported by the National Research Foundation of Korea (NRF) grants (2018M3A9B502131913, 2020R1A4A4079931, 2020R1A2C2010449) funded by the Ministry of Science and ICT (MSIT).

Institutional Review Board Statement: The protocols were approved by the Institutional Animal Care and Use Committees (IACUC) of Chung-Ang University (IACUC number: 201800044, start date: 4 May 2018).

Informed Consent Statement: Not applicable.

Acknowledgments: This research was supported by the National Research Foundation of Korea (NRF) grants (2018M3A9B502131913, 2020R1A4A4079931, 2020R1A2C2010449) funded by the Ministry of Science and ICT (MSIT).

Conflicts of Interest: The authors declare no conflict of interest. The authors alone are responsible for the content and writing of this article.

References

1. Klaver, C.C.; Wolfs, R.C.; Vingerling, J.R.; Hofman, A.; de Jong, P.T. Age-specific prevalence and causes of blindness and visual impairment in an older population: The rotterdam study. *Arch. Ophthalmol.* **1998**, *116*, 653–658. [CrossRef] [PubMed]
2. Fleckenstein, M.; Keenan, T.D.; Guymer, R.H.; Chakravarthy, U.; Schmitz-Valckenberg, S.; Klaver, C.C.; Wong, W.T.; Chew, E.Y. Age-related macular degeneration. *Nat. Rev. Dis. Primers* **2021**, *7*, 31. [CrossRef]
3. Bird, A.C.; Bressler, N.M.; Bressler, S.B.; Chisholm, I.H.; Coscas, G.; Davis, M.D.; de Jong, P.T.; Klaver, C.C.; Klein, B.E.; Klein, R.; et al. An international classification and grading system for age-related maculopathy and age-related macular degeneration. The international arm epidemiological study group. *Surv. Ophthalmol.* **1995**, *39*, 367–374. [CrossRef]
4. Holz, F.G.; Wolfensberger, T.J.; Piguat, B.; Gross-Jendroska, M.; Wells, J.A.; Minassian, D.C.; Chisholm, I.H.; Bird, A.C. Bilateral macular drusen in age-related macular degeneration. Prognosis and risk factors. *Ophthalmology* **1994**, *101*, 1522–1528. [CrossRef]
5. Soubrane, G.; Bressler, N.M. Treatment of subfoveal choroidal neovascularisation in age related macular degeneration: Focus on clinical application of verteporfin photodynamic therapy. *Br. J. Ophthalmol.* **2001**, *85*, 483–495. [CrossRef]
6. Ferrara, N.; Gerber, H.P.; LeCouter, J. The biology of vegf and its receptors. *Nat. Med.* **2003**, *9*, 669–676. [CrossRef]
7. van Wijngaarden, P.; Coster, D.J.; Williams, K.A. Inhibitors of ocular neovascularization: Promises and potential problems. *JAMA* **2005**, *293*, 1509–1513. [CrossRef] [PubMed]
8. Jager, R.D.; Mieler, W.F.; Miller, J.W. Age-related macular degeneration. *N. Engl. J. Med.* **2008**, *358*, 2606–2617. [CrossRef] [PubMed]
9. Mandal, A.; Pal, D.; Agrahari, V.; Trinh, H.M.; Joseph, M.; Mitra, A.K. Ocular delivery of proteins and peptides: Challenges and novel formulation approaches. *Adv. Drug Deliv. Rev.* **2018**, *126*, 67–95. [CrossRef]
10. Wang, Y.; Wang, V.M.; Chan, C.C. The role of anti-inflammatory agents in age-related macular degeneration (amd) treatment. *Eye* **2011**, *25*, 127–139. [CrossRef]
11. Edelhauser, H.F.; Rowe-Rendleman, C.L.; Robinson, M.R.; Dawson, D.G.; Chader, G.J.; Grossniklaus, H.E.; Rittenhouse, K.D.; Wilson, C.G.; Weber, D.A.; Kuppermann, B.D.; et al. Ophthalmic drug delivery systems for the treatment of retinal diseases: Basic research to clinical applications. *Investig. Ophthalm. Vis. Sci.* **2010**, *51*, 5403–5420. [CrossRef]
12. Haller, J.A.; Bandello, F.; Belfort, R.; Blumenkranz, M.S.; Gillies, M.; Heier, J.; Loewenstein, A.; Yoon, Y.H.; Jiao, J.; Li, X.Y.; et al. Dexamethasone intravitreal implant in patients with macular edema related to branch or central retinal vein occlusion. *Ophthalmology* **2011**, *118*, 2453–2460. [CrossRef]

13. Campochiaro, P.A.; Brown, D.M.; Pearson, A.; Chen, S.; Boyer, D.; Ruiz-Moreno, J.; Garretson, B.; Gupta, A.; Hariprasad, S.M.; Bailey, C.; et al. Sustained delivery fluocinolone acetonide vitreous inserts provide benefit for at least 3 years in patients with diabetic macular edema. *Ophthalmology* **2012**, *119*, 2125–2132. [CrossRef]
14. Herrero-Vanrell, R.; Bravo-Osuna, I.; Andres-Guerrero, V.; Vicario-de-la-Torre, M.; Molina-Martinez, I.T. The potential of using biodegradable microspheres in retinal diseases and other intraocular pathologies. *Prog. Retin. Eye Res.* **2014**, *42*, 27–43. [CrossRef]
15. Prajapati, V.D.; Jani, G.K.; Kapadia, J.R. Current knowledge on biodegradable microspheres in drug delivery. *Expert Opin. Drug Del.* **2015**, *12*, 1283–1299. [CrossRef] [PubMed]
16. Saishin, Y.; Silva, R.L.; Saishin, Y.; Callahan, K.; Schoch, C.; Ahlheim, M.; Lai, H.; Kane, F.; Brazzell, R.K.; Bodmer, D.; et al. Periocular injection of microspheres containing ptk412 inhibits choroidal neovascularization in a porcine model. *Investig. Ophthalmol. Vis. Sci.* **2003**, *44*, 4989–4993. [CrossRef]
17. Mietzner, R.; Kade, C.; Froemel, F.; Pauly, D.; Stamer, W.D.; Ohlmann, A.; Wegener, J.; Fuchshofer, R.; Breunig, M. Fasudil loaded plga microspheres as potential intravitreal depot formulation for glaucoma therapy. *Pharmaceutics* **2020**, *12*, 706. [CrossRef]
18. Carrasquillo, K.G.; Ricker, J.A.; Rigas, I.K.; Miller, J.W.; Gragoudas, E.S.; Adamis, A.P. Controlled delivery of the anti-vegf aptamer eye001 with poly(lactic-co-glycolic)acid microspheres. *Investig. Ophthalmol. Vis. Sci.* **2003**, *44*, 290–299. [CrossRef] [PubMed]
19. Olsson, A.K.; Dimberg, A.; Kreuger, J.; Claesson-Welsh, L. Vegf receptor signalling—in control of vascular function. *Nat. Rev. Mol. Cell Biol.* **2006**, *7*, 359–371. [CrossRef]
20. Kang, H.; Ho, A.L.; Muzaffar, J.; Bowles, D.W.; Kim, S.B.; Ahn, M.J.; Hanna, G.J.; Worden, F.P.; Yun, T.; Norton, S.; et al. A phase ii open-label, multicenter, study to evaluate the efficacy and safety of rivocecanib in subjects with recurrent or metastatic adenoid cystic carcinoma. *J. Clin. Oncol.* **2020**, *38*, TPS6597. [CrossRef]
21. Jeong, J.H.; Nguyen, H.K.; Lee, J.E.; Suh, W. Therapeutic effect of apatinib-loaded nanoparticles on diabetes-induced retinal vascular leakage. *Int. J. Nanomed.* **2016**, *11*, 3101–3109.
22. Lee, J.E.; Kim, K.L.; Kim, D.; Yeo, Y.; Han, H.; Kim, M.G.; Kim, S.H.; Kim, H.; Jeong, J.H.; Suh, W. A patinib-loaded nanoparticles suppress vascular endothelial growth factor-induced angiogenesis and experimental corneal neovascularization. *Int. J. Nanomed.* **2017**, *12*, 4813–4822. [CrossRef]
23. Kumar, N.; Goindi, S.; Saini, B.; Bansal, G. Thermal characterization and compatibility studies of itraconazole and excipients for development of solid lipid nanoparticles. *J. Therm. Anal. Calorim.* **2014**, *115*, 2375–2383. [CrossRef]
24. Mohamed, A.I.; Abd-Motagaly, A.M.; Ahmed, O.A.; Amin, S.; Ali, A.I. Investigation of drug-polymer compatibility using chemometric-assisted uv-spectrophotometry. *Pharmaceutics* **2017**, *9*, 7. [CrossRef]
25. Botha, S.A.; Lotter, A.P. Compatibility study between naproxen and tablet excipients using differential scanning calorimetry. *Drug Dev. Ind. Pharm.* **1990**, *16*, 673–683. [CrossRef]
26. Qiao, M.X.; Chen, D.W.; Ma, X.C.; Liu, Y.J. Injectable biodegradable temperature-responsive plga-peg-plga copolymers: Synthesis and effect of copolymer composition on the drug release from the copolymer-based hydrogels. *Int. J. Pharm.* **2005**, *294*, 103–112. [CrossRef]
27. Zhang, Z.; Wang, X.; Li, B.; Hou, Y.; Yang, J.; Yi, L. Development of a novel morphological paclitaxel-loaded plga microspheres for effective cancer therapy: In vitro and in vivo evaluations. *Drug Deliv.* **2018**, *25*, 166–177. [CrossRef]
28. Chen, W.; Palazzo, A.; Hennink, W.E.; Kok, R.J. Effect of particle size on drug loading and release kinetics of gefitinib-loaded plga microspheres. *Mol. Pharm.* **2017**, *14*, 459–467. [CrossRef]
29. Gong, Y.; Li, J.; Sun, Y.; Fu, Z.; Liu, C.H.; Evans, L.; Tian, K.; Saba, N.; Fredrick, T.; Morss, P.; et al. Optimization of an image-guided laser-induced choroidal neovascularization model in mice. *PLoS ONE* **2015**, *10*, e0132643. [CrossRef]
30. Kim, K.L.; Suh, W. Apatinib, an inhibitor of vascular endothelial growth factor receptor 2, suppresses pathologic ocular neovascularization in mice. *Investig. Ophthalmol. Vis. Sci.* **2017**, *58*, 3592–3599. [CrossRef] [PubMed]

Article

Comprehensive Evidence of Carrier-Mediated Distribution of Amantadine to the Retina across the Blood–Retinal Barrier in Rats

Yusuke Shinozaki, Shin-ichi Akanuma , Yuika Mori, Yoshiyuki Kubo and Ken-ichi Hosoya * 

Department of Pharmaceutics, Graduate School of Medicine and Pharmaceutical Sciences, University of Toyama, 2630 Sugitani, Toyama 930-0194, Japan; m2061220@ems.u-toyama.ac.jp (Y.S.); akanumas@pha.u-toyama.ac.jp (S.-i.A.); s1860308@ems.u-toyama.ac.jp (Y.M.); kubo.yoshiyuki.jf@teikyo-u.ac.jp (Y.K.)

* Correspondence: hosoyak@pha.u-toyama.ac.jp; Tel.: +81-76-434-7505

Abstract: Amantadine, a drug used for the blockage of NMDA receptors, is well-known to exhibit neuroprotective effects. Accordingly, assessment of amantadine transport at retinal barriers could result in the application of amantadine for retinal diseases such as glaucoma. The objective of this study was to elucidate the retinal distribution of amantadine across the inner and outer blood–retinal barrier (BRB). In vivo blood-to-retina [³H]amantadine transport was investigated by using the rat retinal uptake index method, which was significantly reduced by unlabeled amantadine. This result indicated the involvement of carrier-mediated processes in the retinal distribution of amantadine. In addition, in vitro model cells of the inner and outer BRB (TR-iBRB2 and RPE-J cells) exhibited saturable kinetics (K_m in TR-iBRB2 cells, 79.4 μ M; K_m in RPE-J cells, 90.5 and 9830 μ M). The inhibition of [³H]amantadine uptake by cationic drugs/compounds indicated a minor contribution of transport systems that accept cationic drugs (e.g., verapamil), as well as solute carrier (SLC) organic cation transporters. Collectively, these outcomes suggest that carrier-mediated transport systems, which differ from reported transporters and mechanisms, play a crucial role in the retinal distribution of amantadine across the inner/outer BRB.

Keywords: amantadine; blood–retinal barrier; drug delivery; retinal disease; NMDA receptor; inner BRB; retinal capillary endothelial cells; outer BRB; retinal pigment epithelial cells; transporter

Citation: Shinozaki, Y.; Akanuma, S.-i.; Mori, Y.; Kubo, Y.; Hosoya, K.-i. Comprehensive Evidence of Carrier-Mediated Distribution of Amantadine to the Retina across the Blood–Retinal Barrier in Rats. *Pharmaceutics* **2021**, *13*, 1339. <https://doi.org/10.3390/pharmaceutics13091339>

Academic Editor: Gert Fricker

Received: 12 July 2021

Accepted: 24 August 2021

Published: 26 August 2021

Publisher's Note: MDPI stays neutral with regard to jurisdictional claims in published maps and institutional affiliations.



Copyright: © 2021 by the authors. Licensee MDPI, Basel, Switzerland. This article is an open access article distributed under the terms and conditions of the Creative Commons Attribution (CC BY) license (<https://creativecommons.org/licenses/by/4.0/>).

1. Introduction

Retinal neurodegenerative diseases, such as glaucoma and diabetic retinopathy, cause progressive visual deficit [1,2]. It is well-known that the progression of the visual deficit involves N-methyl-D-aspartate (NMDA) receptors [3,4]. Previous in vitro and in vivo analyses have indicated the involvement of overactivation of NMDA receptors in the loss of retinal ganglion cells (RGCs) [5,6], which transmit light stimuli from the eye to the brain. Recently, there has been an attempt to block NMDA receptors for the treatment of retinal diseases. For example, it has been reported that memantine, which is an adamantane derivative and an inhibitor of NMDA receptors, has been shown to exhibit neuroprotection in the retina of animal models of retinal diseases, both in vitro and in vivo [7,8]. Moreover, pharmacotherapy with memantine for glaucoma has reached phase III clinical trials [9]. Although a clinical trial of memantine failed [10], it is believed that adamantane derivatives have the potential to treat retinal diseases. Among the adamantane derivatives that are utilized for the blockage of NMDA receptors in clinical practice, amantadine shows the simplest structure. Therefore, scrutiny of the manner of retinal amantadine distribution could contribute to the clinical application of these derivatives.

The blood–retinal barrier (BRB) is known to regulate retinal drug distribution and is composed of retinal capillary endothelial and pigmented epithelial cells, termed the inner

BRB and outer BRB, respectively [11]. Although the paracellular transport of compounds across these barriers is restricted by cellular tight junctions, recent studies have suggested that several ionic nutrients and drugs are supplied by blood-to-retina transport mediated by various plasma membrane transporters and transport systems [12]. As the pKa value of amantadine is 10.1, it is indicated that amantadine exists in the cationic form under physiological conditions (pH ~7.4) [13]. Accordingly, to develop a suitable strategy for efficient retinal amantadine distribution, an understanding of the retinal distribution of amantadine across the BRB would be valuable, in addition to clarifying the involvement of plasma membrane transport systems during this process.

To date, several solute carrier (SLC) transporters have been identified in amantadine transport in vivo and in vitro. As shown in Table 1, the roles of multidrug and toxin extrusion protein 1 (MATE1/Slc47a1) and neutral and basic amino acid transporter (ATB^{0,+}/Slc6a14) at several tissues in amantadine transport have been reported [14,15]. Moreover, amantadine is reportedly a substrate for SLC organic cation transporter 1, abbreviated as OCT1 (Slc22a1), and OCT2 (Slc22a2) [16,17]. Among these transporters, mRNA expression of MATE1 has been observed in the inner and outer BRB model cells [18,19]. In addition to MATE1, the expression of other organic cation transporter subtypes has been documented. For example, plasma membrane monoamine transporter (PMAT/slcl29a4) and organic cation/L-carnitine transporters 1-2 (OCTN1-2/slcl22a4-5) are expressed at the BRB [18,19]. Moreover, putative cationic drug transport systems that accept several cationic and lipophilic drugs, including verapamil, clonidine, and propranolol, are known to exist in the inner BRB [20–23]. In these previous reports, amantadine reportedly exhibited an inhibitory effect on the uptake of these cationic drugs in inner BRB model cells, namely TR-iBRB2 cells [24]. Based on these lines of evidence, it can be speculated that these transporters and putative transport systems at the inner and outer BRB participate in amantadine transport to the retina across the BRB.

The present study aimed to clarify the details underlying the retinal distribution of amantadine. Herein, we used the retinal uptake index (RUI) experiment to elucidate the role of carrier-mediated processes in the retinal transfer of amantadine. In addition, the properties of amantadine transport across the inner and outer BRB were determined by using TR-iBRB2 cells and a conditionally immortalized rat RPE cell line (RPE-J cells) [25].

Table 1. Candidates of amantadine transporter and transport system in the retina.

Name		Is Amantadine Accepted as a Substrate?	Is It Expressed in the Retina?
Slc6a14	ATB ^{0,+}	Yes [15]	N.D.
Slc22a1	OCT1	Yes [16]	N.D.
Slc22a2	OCT2	Yes [17]	N.D.
Slc22a3	OCT3	N.D.	N.D.
Slc22a4	OCTN1	N.D.	Yes (mRNA) [18]
Slc22a5	OCTN2	N.D.	Yes (mRNA) [18]
Slc29a4	PMAT	N.D.	Yes (mRNA) [19]
Slc47a1	MATE1	Yes [14]	Yes (mRNA) [19]
Putative transport systems	Verapamil Clonidine Propranolol	N.D.	Yes [20–23]

N.D., not determined.

2. Materials and Methods

2.1. Animals and Reagents

The animal experiments performed in this study were approved by the Animal Care Committee of the University of Toyama with the registration numbers of A2017PHA-6 and A2020PHA-1. Male Wistar/ST rats (approximately 200 g; Japan SLC, Hamamatsu, Japan) were maintained under controlled conditions (12/12 h dark/light cycle; temperature, ~23 °C; humidity, around 50%). Male rats present an advantage for the comparison of

previous reports of in vivo retinal distribution, as quantitative data of compound distribution to the retina have been obtained by using male rats [26]. A total of 13 rats were used for the assessment of in vivo blood-to-retina transport (control, $n = 5$; co-administration of unlabeled amantadine, $n = 4$; co-administration of PAH, $n = 4$). Amantadine HCl, [^3H]- ([^3H]amantadine; 0.3 Ci/mmol) was obtained from Moravek (Brea, CA, USA). From American Radiolabeled Chemicals (St. Louis, MO, USA), n -[1- ^{14}C]butanol ([^{14}C]n-butanol; $2.0 \times 10^3 \mu\text{Ci/mmol}$) and verapamil [N-methyl- ^3H] hydrochloride ([^3H]verapamil; 80 Ci/mmol) were purchased. Unlabeled drugs and compounds used in this study were commercially available.

2.2. Assessment of In Vivo Blood-to-Retina Transport

Rats were anesthetized by an intraperitoneal injection of pentobarbital sodium at 50 mg/kg. Using the rats, intracarotid artery injection was performed by following the method given in previous manuscripts [20–22,26], and the details of the procedure are given in the Supplementary Materials. The functional retinal compound distribution as a percentage of the in vivo retinal transfer of [^{14}C]n-butanol (RUI) was determined by using Equation (1).

$$\text{RUI (\%)} = ([^3\text{H}]\text{amantadine}/[^{14}\text{C}]n\text{-butanol (in retina)})/([^3\text{H}]\text{amantadine}/[^{14}\text{C}]n\text{-butanol (in the injected solution)}) \times 100 \quad (1)$$

2.3. In Vitro Transport Study

In 10% fetal bovine serum (FBS; Merck, Darmstadt, Germany)-containing Dulbecco's modified Eagle's medium (DMEM; Nissui Pharmaceutical, Tokyo, Japan) with 20 mM NaHCO_3 , 0.19 mM benzylpenicillin potassium, and 0.14 mM streptomycin sulfate, TR-iBRB2 cells (passage number 32–60) were cultured according to previous reports [20–22,24]. As described previously [25,27], RPE-J cells (passage number 79–92) were cultured in DMEM with 4% FBS, 20 mM NaHCO_3 , and 0.1 mM non-essential amino acid (FUJIFILM Wako Pure Chemical, Osaka, Japan) containing 0.16 mM benzylpenicillin potassium and 0.17 mM streptomycin sulfate. In accordance with established protocols for the uptake study [20–22], the cells were seeded at a density of 1.0×10^5 cells/well onto a collagen I-coated 24-well plate (BioCoat™ Collagen I Cellware, Corning, Corning, NY, USA) and cultured for 2 days, at 33 °C, under 5% CO_2 /air. Referring to the previous reports [20–23,28,29], we started the uptake reaction, and the details of the procedure are included in the Supplemental Materials.

The uptake activities for [^3H]amantadine and [^3H]verapamil were calculated as the cell/medium ratio, using Equation (2).

$$\text{Cell/medium ratio} = [^3\text{H}]\text{compound (dpm) per cell protein (mg)}/[^3\text{H}]\text{compound (dpm) per medium (\mu\text{L})} \quad (2)$$

Kinetic parameters for cell uptake, such as the maximal uptake rate (V_{\max}), Michaelis–Menten constant (K_m), and non-saturable uptake clearance (K_d), were obtained by using the nonlinear least-squares regression analysis program (MULTI) [30] with Equations (3)–(5), where the uptake rate of the test compound and its concentration were V and S , respectively.

$$V = (V_{\max} \times S)/(K_m + S) \quad (3)$$

$$V = (V_{\max} \times S)/(K_m + S) + K_d \times S \quad (4)$$

$$V = (V_{\max 1} \times S)/(K_{m1} + S) + (V_{\max 2} \times S)/(K_{m2} + S) \quad (5)$$

2.4. Data and Statistical Analyses

All the data are shown as the mean \pm standard deviation (SD). Using the unpaired two-tailed Student's t -test (two groups) or one-way analysis of variance followed by Dunnett's test (more than two groups), statistical differences were evaluated.

3. Results

3.1. In Vivo Blood-to-Retina Transport of [^3H]Amantadine across the BRB

The in vivo RUI was observed to be $129 \pm 13\%$ (Figure 1), indicating that retinal distribution of [^3H]amantadine is 1.29-fold greater than that of [^{14}C]n-butanol. Following co-administration of 50 mM unlabeled amantadine, the RUI value significantly decreased by 44%. To test the effect of compounds at the same concentration, co-administration of 50 mM p -aminohippuric acid (PAH),

which is an anionic compound that is reported to have no effect on the retinal distribution of cationic drugs, such as propranolol and clonidine [21,22], was performed. As a result, no significant effect was observed in the presence of 50 mM PAH (Figure 1).

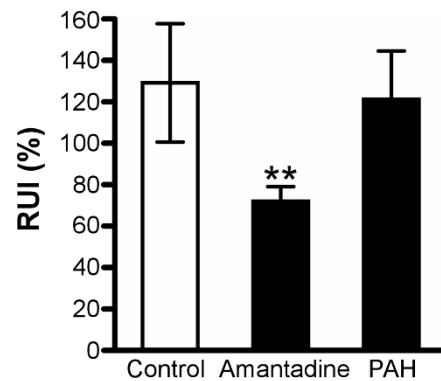


Figure 1. $[^3\text{H}]$ Amantadine RUI in rats. $[^3\text{H}]$ Amantadine (5 $\mu\text{Ci}/\text{rat}$) and $[^{14}\text{C}]n$ -butanol (0.5 $\mu\text{Ci}/\text{rat}$) were injected in the absence (control, $n = 5$) or presence of 50 mM unlabeled amantadine ($n = 4$) or 50 mM PAH ($n = 4$). Each column, expressing $[^3\text{H}]$ amantadine RUI, represents the mean \pm SD; ** $p < 0.01$, significant difference from control. RUI, retinal uptake index; PAH, p -aminohippuric acid.

3.2. Amantadine Uptake Properties in TR-iBRB2 Cells

TR-iBRB2 cells showed a time-dependent increase in $[^3\text{H}]$ amantadine uptake for at least 5 min. The initial uptake rate was presented as $14.0 \pm 4.1 \mu\text{L}/(\text{min} \cdot \text{mg protein})$ (Figure 2A). At 4 $^\circ\text{C}$, the $[^3\text{H}]$ amantadine uptake significantly reduced by 86% (Figure 2A). Concentration-dependent uptake of amantadine by TR-iBRB2 cells exhibited saturable and non-saturable processes, with a V_{max} of $1.36 \pm 0.38 \text{ nmol}/(\text{min} \cdot \text{mg protein})$, a K_m of $79.4 \pm 27.3 \mu\text{M}$, and a K_d of $2.75 \pm 0.58 \mu\text{L}/(\text{min} \cdot \text{mg protein})$ (Figure 2B).

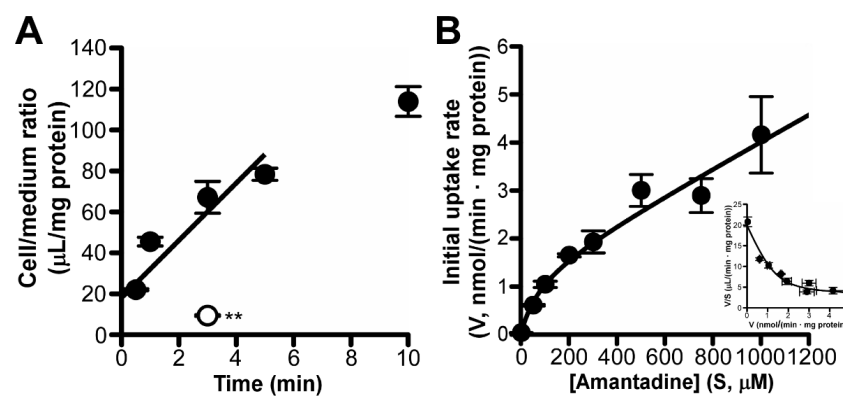


Figure 2. Time-, temperature-, and concentration-dependent uptake of $[^3\text{H}]$ amantadine by TR-iBRB2 cells. (A) Time dependency of $[^3\text{H}]$ amantadine uptake (1.67 μM , 0.1 $\mu\text{Ci}/\text{well}$) by TR-iBRB2 cells at 37 $^\circ\text{C}$ (control; closed circles) and effect of low temperature (4 $^\circ\text{C}$; open circle) on the uptake; ** $p < 0.01$, significant difference from the control. (B) Concentration dependency of amantadine uptake by TR-iBRB2 cells. Amantadine uptake was examined at 37 $^\circ\text{C}$ for 3 min over the concentration range of 1.67 to 1000 μM and analyzed by using Michaelis-Menten and Eadie-Scatchard (inset) plots. Each point in the figure represents the mean \pm SD ($n = 3$).

Furthermore, Na^+ -free and K^+ -replacement buffer had no significant effect on the uptake of $[^3\text{H}]$ amantadine by TR-iBRB2 cells; however, Cl^- -free buffer significantly reduced the uptake of $[^3\text{H}]$ amantadine by 38% (Figure 3A). At an extracellular pH of 6.4, $[^3\text{H}]$ amantadine uptake by TR-iBRB2 cells was significantly reduced by 64% (Figure 3B). At an extracellular pH of 8.4, we noted the tendency of an increase in uptake of $[^3\text{H}]$ amantadine by TR-iBRB2 cells (Figure 3B). A proton ionophore, namely carbonyl cyanide- p -trifluoromethoxyphenylhydrazone (FCCP) [21,27], significantly decreased uptake by 50% at 50 μM (Figure 3C). In previous studies, it was indicated

the acute treatment and pretreatment of NH_4Cl caused alkalinized and acidified intracellular pH in endothelial and epithelial cells, respectively [28,29]. Although acute NH_4Cl treatment also induces the neutralization between the acid endosomal/lysosomal and intracellular compartments [27], we performed a study of $[^3\text{H}]$ amantadine uptake with acute and pretreatment of NH_4Cl to examine the effect of H^+ -gradient on the intra- and extra-cellular compartments. The uptake was significantly decreased by 80% and increased by 90% at alkalinized and acidified intercellular pH, respectively (Figure 3D). Under the experimental conditions in Figure 3, there is a possibility that the cytotoxicity may have affected the results of this uptake, because these experimental conditions are not ideal for the culture of these cells. However, the cellular protein amount after the uptake reaction was not significantly altered in each group compared with the control (Supplementary Materials Figure S1). Therefore, the cytotoxic effect caused by these experimental conditions is considered to be minimal.

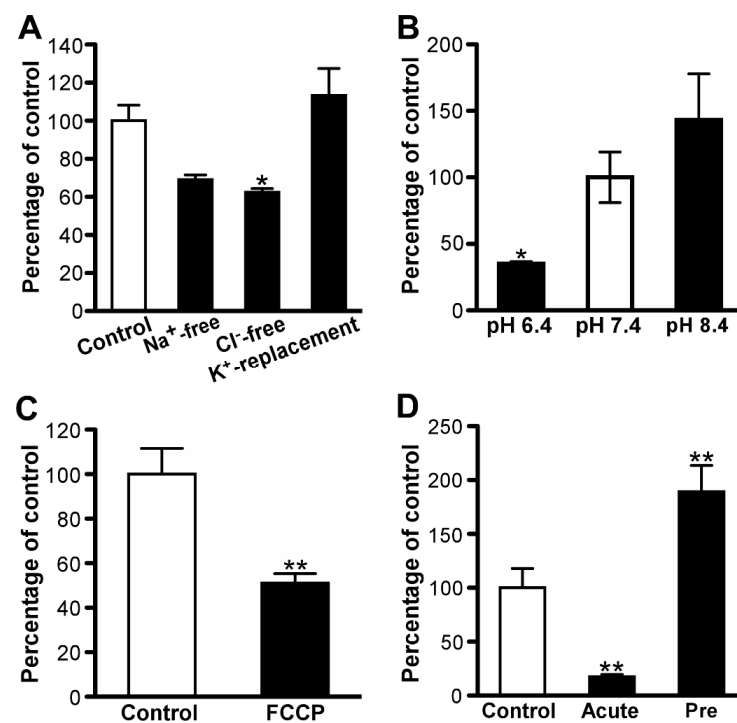


Figure 3. Uptake properties of $[^3\text{H}]$ amantadine by TR-iBRB2 cells. (A) Effect of Na^+ , Cl^- , and membrane potential on $[^3\text{H}]$ amantadine uptake ($1.67 \mu\text{M}$, $0.1 \mu\text{Ci}/\text{well}$) for 3 min at 37°C . (B) Effect of extracellular pH on $[^3\text{H}]$ amantadine uptake by TR-iBRB2 cells. (C) Effect of carbonyl cyanide-*p*-trifluoromethoxyphenylhydrazone (FCCP) treatment at $50 \mu\text{M}$ on $[^3\text{H}]$ amantadine uptake. (D) Effect of intracellular pH on the uptake of $[^3\text{H}]$ amantadine for 15 s by TR-iBRB2 cells at 37°C . Pretreatment (Pre) and acute treatment with 30 mM NH_4Cl were performed to decrease and increase intracellular pH, respectively. Each column in the figure represents the mean \pm SD ($n = 3$); * $p < 0.05$, ** $p < 0.01$, significantly different from the control.

3.3. Amantadine Uptake Properties in RPE-J Cells

In the current study, $[^3\text{H}]$ amantadine was time-dependently incorporated for at least 3 min in RPE-J cells, at an initial uptake rate of $15.9 \pm 0.3 \mu\text{L}/(\text{min}\cdot\text{mg protein})$ (Figure 4A). At 4°C , this uptake was significantly reduced by 87% (Figure 4A). Amantadine uptake by RPE-J cells involved both high- and low-affinity saturable processes (Figure 4B). Following the calculation, K_{m1} and V_{max1} values were $90.5 \pm 49.6 \mu\text{M}$ and $0.914 \pm 0.510 \text{ nmol}/(\text{min}\cdot\text{mg protein})$, respectively, for the high-affinity uptake process. For the low-affinity uptake process, the K_{m2} and V_{max2} values were $9830 \pm 1620 \mu\text{M}$ and $85.3 \pm 11.4 \text{ nmol}/(\text{min}\cdot\text{mg protein})$, respectively.

Na^+ -free, Cl^- -free, and K^+ -replacement buffers had no significant impact on the uptake of $[^3\text{H}]$ amantadine by RPE-J cells (Figure 5A). The uptake of $[^3\text{H}]$ amantadine by RPE-J cells was significantly decreased by 32% and increased by 25% at extracellular pH of 6.4 and 8.4, respectively (Figure 5B). Furthermore, the uptake of $[^3\text{H}]$ amantadine by RPE-J cells was significantly decreased by 78% and increased by 18% at alkalinized and acidified intercellular pH, respectively (Figure 5C). The

cellular protein in each group of Figure 5 also had no significant difference compared with control (Supplementary Materials Figure S2).

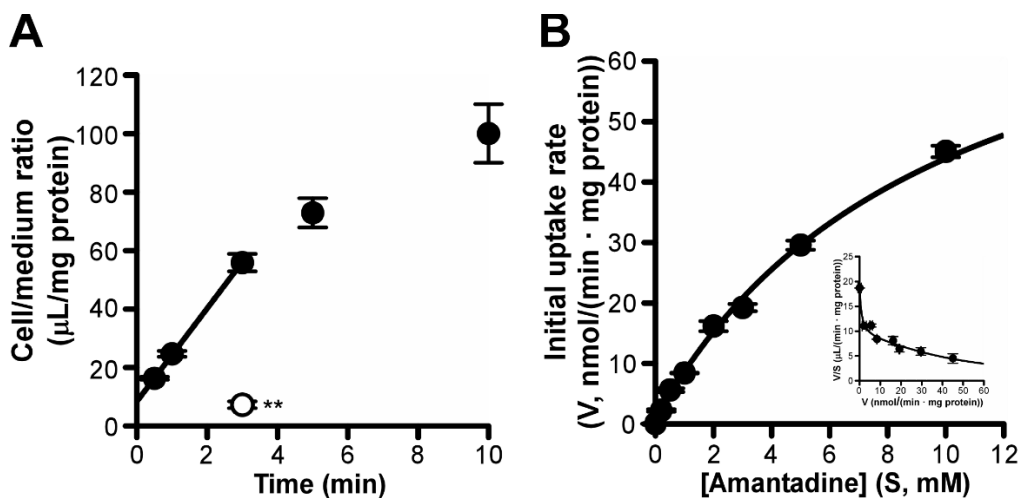


Figure 4. Time-, temperature-, and concentration-dependent uptake of [³H]amantadine by RPE-J cells. (A) Time dependency of [³H]amantadine uptake (1.67 μM, 0.1 μCi/well) by RPE-J cells (37 °C; control, closed circles) and effect of low temperature (4 °C; open circle) on [³H]amantadine uptake; ** *p* < 0.01, significant difference from the control. (B) Concentration-dependent uptake of amantadine (1.67 μM–10 mM) by RPE-J cells was expressed by using Michaelis-Menten and Eadie-Scatchard (inset) plots. Each point in the figure represents the mean ± SD (*n* = 3).

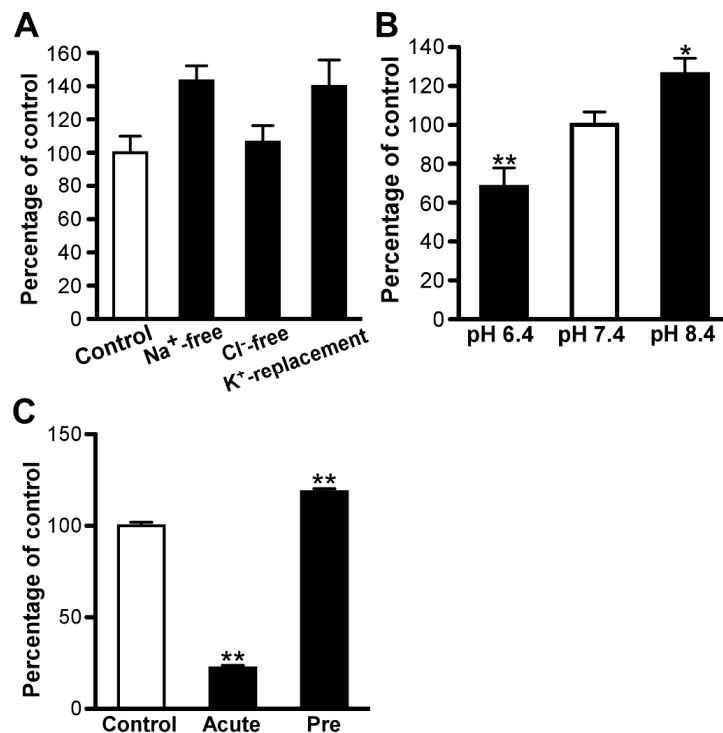


Figure 5. Properties of [³H]amantadine uptake by RPE-J cells. (A) Effect of Na⁺, Cl⁻, and membrane potential on [³H]amantadine uptake (1.67 μM, 0.1 μCi/well) for 3 min at 37 °C. (B) Effect of extracellular pH on the uptake of [³H]amantadine. (C) Effect of intracellular pH on [³H]amantadine uptake for 15 s at 37 °C by RPE-J cells. Pretreatment (Pre) and acute treatment with 30 mM NH₄Cl were performed to decrease and increase intracellular pH, respectively. Each column in the figure represents the mean ± SD (*n* = 3); * *p* < 0.05, ** *p* < 0.01, significantly different from the control.

3.4. Inhibition of [³H]Amantadine Transport by Drugs/Compounds

The inhibitory effects on the in vitro [³H]amantadine uptake are summarized in Table 2. At 0.2 mM, several cationic drugs (desipramine, imipramine, quinidine, and verapamil) strongly inhibited [³H]amantadine uptake by both TR-iBRB2 cells and RPE-J cells.

Table 2. Effect of compounds on the uptake of [³H]amantadine by TR-iBRB2 cells and RPE-J cells.

Compound	Concentration (mM)	% of Control	
		TR-iBRB2	RPE-J
Control		100 ± 12	100 ± 12
Desipramine	0.2	7.05 ± 0.57 **	10.7 ± 5.6 **
Imipramine	0.2	8.37 ± 1.43 **	16.9 ± 5.2 **
Propranolol	0.2	8.61 ± 0.75 **	15.7 ± 5.9 **
Quinidine	0.2	13.7 ± 1.8 **	34.1 ± 3.0 **
Memantine	0.2	16.7 ± 2.2 **	123 ± 38 **
	1.0	N.D.	27.1 ± 2.6 **
Pyrilamine	0.2	20.9 ± 1.8 **	77.8 ± 38.4
	1.0	N.D.	18.2 ± 1.7 **
Verapamil	0.2	22.1 ± 6.2 **	20.5 ± 4.8 **
Amantadine	0.2	34.1 ± 4.1 **	89.9 ± 5.6
	1.0	N.D.	21.3 ± 3.1 **
Timolol	0.2	34.6 ± 10.6 **	59.1 ± 5.1
Clonidine	0.2	42.1 ± 12.1 **	71.6 ± 4.7
	1.0	N.D.	30.8 ± 4.0 **
Pyrimethamine	0.2	44.3 ± 8.8 **	88.9 ± 3.3
PAH	0.2	85.8 ± 10.8	139 ± 33
Acetazolamide	0.2	90.9 ± 3.8	N.D.
Gluconate	0.2	91.7 ± 21.7	86.2 ± 23.4
Cimetidine	0.2	97.6 ± 24.7	106 ± 5
Choline	0.2	101 ± 8	124 ± 39
MPP ⁺	0.2	106 ± 31	75.5 ± 5.0
	1.0	N.D.	91.9 ± 5.6
Decynium-22	0.2	106 ± 31	86.7 ± 41.9
	0.5	N.D.	136 ± 8
L-Carnitine	0.2	111 ± 35	95.1 ± 5.2
	2.5	99.5 ± 2.3	119 ± 28
TEA	0.2	117 ± 45	87.7 ± 11.8
	1.0	N.D.	81.8 ± 10.3
Serotonin	0.2	126 ± 60	158 ± 52 **
L-Glutamic acid	2.5	80.2 ± 10.0	84.5 ± 16.4
L-Aspartic acid	2.5	101 ± 23	79.5 ± 12.7
Glycine	2.5	102 ± 4	116 ± 13
L-Leucine	2.5	112 ± 17	113 ± 16
L-Arginine	2.5	127 ± 15	150 ± 38 **

Uptake of [³H]amantadine (1.67 μM, 0.1 μCi/well) by the indicated cells was performed for 3 min at 37 °C. Each value represents the mean ± SD (*n* = 3–30); ** *p* < 0.01, significantly different from the control. PAH, *p*-aminohippuric acid; MPP⁺, 1-methyl-4-phenylpyridinium; TEA, tetraethylammonium; N.D., not determined.

Memantine, pyrilamine, amantadine, and clonidine (0.2 mM) exhibited a marked inhibition of [³H]amantadine uptake by TR-iBRB2 cells but not RPE-J cells; however, these cationic drugs significantly inhibited [³H]amantadine uptake by RPE-J cells at 1 mM. SLC organic cation/anion transporter substrates, such as PAH, cimetidine, choline, 1-methyl-4-phenylpyridinium (MPP⁺), and decynium-22, did not suppress [³H]amantadine uptake. Similarly, anionic and cationic amino acids, including L-glutamic acid and L-arginine, did not significantly impact [³H]amantadine uptake.

3.5. Mutual Effect of Amantadine and Verapamil on Uptake by TR-iBRB2 Cells

We next examined the involvement of verapamil-sensitive putative transport systems in the inner BRB [20] in amantadine transport. Accordingly, we performed a kinetic analysis of amantadine uptake by TR-iBRB2 cells in the presence of verapamil. On analyzing the Lineweaver–Burk plot, the fitted line of concentration-dependent amantadine uptake by TR-iBRB2 cells in the presence of 10 μM verapamil did not intersect with that in the absence of verapamil, on both the *y*-axis and *x*-axis

(Figure 6A). In the presence of amantadine at 220 μM , the fitted line of concentration-dependent verapamil uptake intersected at the y -axis with that in the absence of amantadine (Figure 6B); this indicated that amantadine competitively inhibits verapamil-sensitive transport mechanisms at the inner BRB.

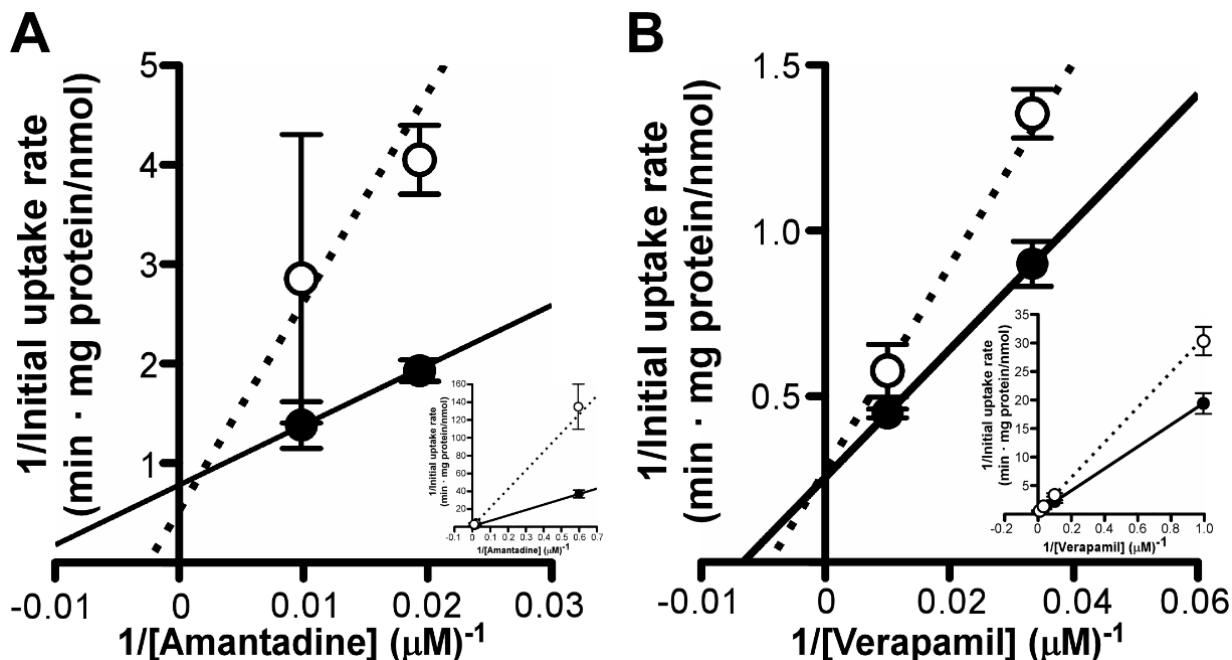


Figure 6. Mutual effect on uptake by TR-iBRB2 cells of amantadine (A) and verapamil (B). (A) The uptake of amantadine at a concentration of 1.67, 50, 100, and 300 μM was assessed at 37 $^{\circ}\text{C}$ for 3 min, with (open circles, dotted line) or without (closed circles, solid line) 10 μM verapamil. (B) The uptake of verapamil at a concentration of 1, 10, 100, and 300 μM was examined at 37 $^{\circ}\text{C}$ for 3 min, with (open circles, dotted line) or without (closed circles, solid line) 220 μM amantadine. Each point in the Lineweaver–Burk plot of all data (inset) and highlighted data at the high concentration range represents the mean \pm SD ($n = 3$).

3.6. Effect of Amantadine on Concentration-Dependent Verapamil Uptake by RPE-J Cells

The effect of amantadine on verapamil-sensitive putative transport systems in the outer BRB was investigated. Herein, we investigated the time-dependent uptake of verapamil by RPE-J cells. RPE-J cells showed a time-dependent increase with an initial uptake rate of $70.4 \pm 5.6 \mu\text{L}/(\text{min} \cdot \text{mg protein})$ in [^3H]verapamil uptake for at least 3 min (Figure 7A). At 1 min, this [^3H]verapamil uptake was reduced with 200 μM unlabeled verapamil by 86% (Figure 7A). In RPE-J cells, verapamil uptake exhibited a saturable process, with a V_{max} value of $6.31 \pm 0.35 \text{ nmol}/(\text{min} \cdot \text{mg protein})$ and a K_m value of $55.6 \pm 5.2 \mu\text{M}$ (Figure 7B). In the Lineweaver–Burk plot analysis, the fitted line of concentration-dependent verapamil uptake by RPE-J cells in the presence of 200 μM amantadine did not intersect with that in the absence of verapamil, at both the y -axis and x -axis (Figure 7B); this suggested that amantadine does not competitively or non-competitively inhibit verapamil transport at the outer BRB.

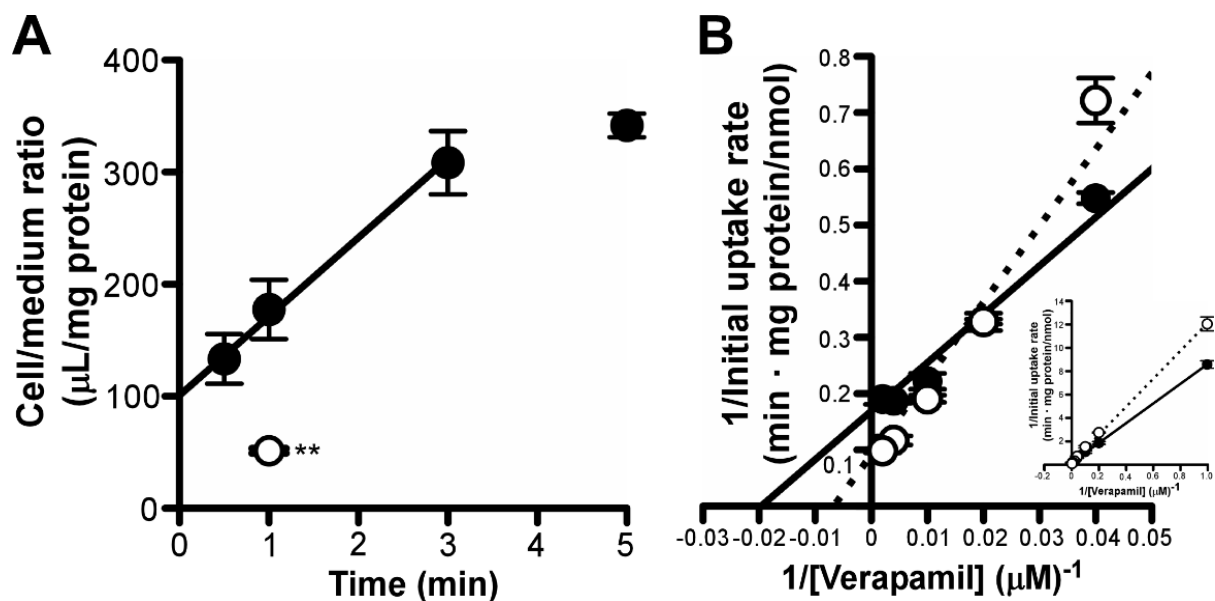


Figure 7. Effects of amantadine on uptake of [³H]verapamil by RPE-J cells. (A) Time dependency and self-inhibition of [³H]verapamil uptake by RPE-J cells. RPE-J cells were incubated with [³H]verapamil (6.25 nM, 0.1 μCi/well), in the presence (open circle) or absence (control, closed circles) of 200 μM verapamil at 37 °C. (B) Lineweaver-Burk plot of all data (inset) and highlighted data at the concentration of 5, 10, 25, 50, 100, 250, and 500 μM verapamil uptake at 37 °C for 3 min, in the absence (closed circles, solid line) or presence (open circles, dotted line) of 100 μM amantadine by RPE-J cells. Each point in the Figure represents the mean ± SD (*n* = 3); ** *p* < 0.01, significant difference from the control.

4. Discussion

We assessed the inner and outer BRB-mediated transport of amantadine, as well as the carrier-mediated transport of amantadine in the inner and outer BRB. Detailed *in vitro* analyses clarified characteristics of amantadine transport mechanisms at the BRB; however, the involvement of typical organic cation transporters and putative cationic drug transport systems in the carrier-mediated amantadine transport at the BRB is not suggested.

The *in vivo* retinal drug transfer study (Figure 1) indicated that amantadine underwent active retinal distribution from the circulating blood. Previously, we reported the correlation between *in vivo* retinal distribution of drugs transported by passive diffusion and lipophilic properties, indicated as log *D* {RUI = 46.2 × exp(0.515 × log *D*)} [26]. The log *D* value of amantadine is 0.176 [31]. Therefore, if amantadine is only transported to the rat retina by passive diffusion across the *in vivo* BRB, the RUI value of amantadine can be estimated as 50.4% (= 46.2 × exp(0.515 × 0.176)). Compared with this estimated value, the RUI value of [³H]amantadine in the present study was 2.5-fold greater (129%). In addition, unlabeled amantadine at 50 mM showed a significant reduction in the [³H]amantadine RUI; however, PAH at the same concentration demonstrated a minimal impact. Based on these findings, it can be suggested that carrier-mediated transport at the inner and outer BRB promotes the retinal distribution of amantadine.

Furthermore, transport studies using *in vitro* models of the inner and outer BRB detected carrier-mediated amantadine transport at these barriers. In TR-iBRB2 cells, both saturable and non-saturable components were involved in the uptake of amantadine, with a *K_m* value of 79.4 μM (Figure 2B). As the contribution ratio of the saturable component was 86% (= $V_{max}/K_m \div (V_{max}/K_m + K_d) \times 100$), carrier-mediated processes of amantadine uptake could play an important role in amantadine transport at the inner BRB. In terms of the kinetic analysis of amantadine uptake by RPE-J cells, it was observed that this uptake was composed of two saturable processes, with *K_m* values of 90.5 and 9830 μM for high- and low-affinity processes, respectively (Figure 4B). The contributions of high- and low-affinity processes were calculated as 54% (= $V_{max1}/K_{m1} \div (V_{max1}/K_{m1} + V_{max2}/K_{m2}) \times 100$) and 46% (= $V_{max2}/K_{m2} \div (V_{max1}/K_{m1} + V_{max2}/K_{m2}) \times 100$), respectively; this indicated that the involvement of the high-affinity process in carrier-mediated amantadine transport at the outer BRB is equal to that of the low-affinity process. Collectively, these results suggest that carrier-mediated processes play a major role in amantadine transport across the inner and outer BRB.

As described in the previous section, the *K_m* value for the saturable process of amantadine uptake by TR-iBRB2 cells (79.4 μM) is similar to that determined for the high-affinity process of

amantadine uptake by RPE-J cells (90.5 μM). However, the contribution ratios of saturable kinetics (50–100 μM) in TR-iBRB2 and RPE-J cells were 86% and 54%, respectively. This difference may influence the properties of net amantadine transport at the inner and outer BRB. For example, TR-iBRB2 cells exhibited Cl^- -sensitive [^3H]amantadine uptake; this effect was not observed in RPE-J cells (Figures 3A and 5A). Moreover, several cationic compounds, such as memantine, pyrillamine, and clonidine, demonstrated a lower inhibitory effect (0.2 mM) on [^3H]amantadine uptake by RPE-J cells than that on uptake by TR-iBRB2 cells (Table 2). The characteristics of high- and low-affinity processes need to be individually evaluated to clarify the differences. Nevertheless, our study, including kinetic analyses, implies that the net transport of amantadine at the inner BRB differs from that at the outer BRB.

Although several transporters reportedly accept amantadine as a substrate, our study indicates a minor contribution of these transporters and putative transport systems in terms of amantadine transport at the inner and outer BRB. We observed no inhibitory effect of OCTs and/or $\text{ATB}^{0,+}$ inhibitors, such as decynium-22, TEA, MPP^+ , glycine, and L-arginine, on [^3H]amantadine uptake by both model cells (Table 2) [32–38]; this indicates that OCTs and $\text{ATB}^{0,+}$ were not involved in amantadine transport at the inner and outer BRB. In addition, typical organic cation transporters that are expressed in the inner and outer BRB, such as OCTN1-2, MATE1, and PMAT, play a minor role in amantadine transport because substrates of these transporters (cimetidine, L-carnitine, TEA, MPP^+ , and serotonin [39–46]) did not significantly reduce [^3H]amantadine uptake by these cells (Table 2). Regarding unidentified cationic drug transport systems for clonidine, propranolol, and verapamil at the BRB [20–22], amantadine transport mechanisms at the inner and outer BRB appear distinct from these cationic drug transport systems based on our results. The K_m values for clonidine and propranolol uptake by TR-iBRB2 cells are 286 and 237 μM , respectively [21,22]. As [^3H]amantadine uptake by TR-iBRB2 cells was reduced by more than 58% in the presence of clonidine and propranolol (0.2 mM), which is lower than the K_m values described above, it is unlikely that putative cationic drug transport systems for clonidine and propranolol participate in amantadine transport at the inner BRB. Reportedly, novel verapamil transport systems have been identified in the rat inner BRB *in vitro* [20]. In addition, the uptake study of verapamil using RPE-J cells indicated the existence of carrier-mediated verapamil transport in the rat outer BRB (Figure 7), as well as human RPE cells [23]. However, it is strongly suggested that amantadine transport systems at the inner and outer BRB are distinct from the verapamil transport systems considering the mutual effect of amantadine and verapamil on uptake by TR-iBRB2 and RPE-J cells (Figures 6A and 7B). Collectively, the results of the functional study suggest that retinal distribution of amantadine across the inner and outer BRB occurs via carrier-mediated transport systems that do not consist of known organic cation transporters and putative organic cation transport systems for cationic drugs, including verapamil.

Parsons et al. reported that amantadine inhibits NMDA receptors, with an IC_{50} of 20 μM [47]. During pharmacotherapy for Parkinson's disease, the plasma concentration range of 0.6–29 μM for amantadine has been established [48]. As the K_m values for the relatively high-affinity process of amantadine transport in the *in vitro* inner and outer BRB model cells (50–100 μM) were greater than the concentrations related to the pharmacology and pharmacetics of amantadine, carrier-mediated amantadine transport at the inner/outer BRB is critical for understanding retinal amantadine distribution. Hence, identifying amantadine transport systems at the BRB could help establish an appropriate pharmaceutical strategy for amantadine applications in retinal diseases. For the identification of the molecule involved in the relatively high-affinity process of amantadine uptake, TR-iBRB2 cells may afford an advantage, as the relatively high-affinity process was the only observed carrier-mediated process of amantadine transport.

5. Conclusions

In the current study, we demonstrated the process of retinal amantadine transport. The RUI experiment indicated the retinal distribution of amantadine. Moreover, the uptake study using *in vitro* model cells suggested the involvement of transport systems in amantadine blood-to-retina transport across the inner and outer BRB. Furthermore, it can be suggested that transport systems for amantadine at the inner/outer BRB are independent of cationic drug transport systems for verapamil, as well as SLC organic cation and amino acid transporters. These transport systems for amantadine at the BRB promote amantadine distribution to the retina. Therefore, the characteristics of amantadine transport at the BRB identified in this study can provide an in-depth understanding of amantadine-sensitive transport mechanisms at the BRB and, thus, the utilization of adamantane derivatives, such as amantadine, for retinal diseases.

Supplementary Materials: The Supplemental Materials are available online at <https://www.mdpi.com/article/10.3390/pharmaceutics13091339/s1>. Figure S1. The cellular protein amount in the group of Figure 3. Each column represents the mean \pm S.D. ($n = 3$). In the tested group, the significant difference from the control was not observed ($p > 0.05$). Figure S2. The cellular protein amount in the group of Figure 5. Each column represents the mean \pm S.D. ($n = 3$). In the tested group, the significant difference from the control was not observed ($p > 0.05$).

Author Contributions: Conception, Y.S., S.-i.A., Y.K. and K.-i.H.; collection, assembly of data, and interpretation, Y.S., S.-i.A. and Y.M.; writing the manuscript, Y.S., S.-i.A. and K.-i.H. All authors have read and agreed to the published version of the manuscript.

Funding: This study was supported by Grant-in-Aids from the Japan Society for Promotion of Science, KAKENHI (Scientific Research (B), 16H05110 and 20H03403; Scientific Research (C), 19K07160).

Institutional Review Board Statement: The animal study was conducted according to the guidelines of the Animal Care Committee of the University of Toyama and approved by the Committee (A2017PHA-6 (date of approval: 14 March 2017) and A2020PHA-1 (date of approval: 9 March 2020)).

Informed Consent Statement: Not applicable.

Data Availability Statement: The data of this study are available from the corresponding author upon reasonable request.

Conflicts of Interest: The authors declare no conflict of interest.

References

- McMonnies, C.W. Glaucoma history and risk factors. *J. Optom.* **2017**, *10*, 71–78. [CrossRef]
- Lechner, J.; O’Leary, O.E.; Stitt, A.W. The pathology associated with diabetic retinopathy. *Vis. Res.* **2017**, *139*, 7–14. [CrossRef]
- Fechtner, R.D.; Weinreb, R.N. Mechanisms of optic nerve damage in primary open angle glaucoma. *Surv. Ophthalmol.* **1994**, *39*, 23–42. [CrossRef]
- Lipton, S.A. Possible role for memantine in protecting retinal ganglion cells from glaucomatous damage. *Surv. Ophthalmol.* **2003**, *48*, S38–S46. [CrossRef]
- Luo, X.; Heidinger, V.; Picaud, S.; Lambrou, G.; Dreyfus, H.; Sahel, J.; Hicks, D. Selective excitotoxic degeneration of adult pig retinal ganglion cells in vitro. *Invest. Ophthalmol. Vis. Sci.* **2001**, *42*, 1096–1106.
- Chidlow, G.; Osborne, N.N. Rat retinal ganglion cell loss caused by kainate, NMDA and ischemia correlates with a reduction in mRNA and protein of Thy-1 and neurofilament light. *Brain Res.* **2003**, *963*, 298–306. [CrossRef]
- Hare, W.A.; Wheeler, L. Experimental glutamatergic excitotoxicity in rabbit retinal ganglion cells: Block by memantine. *Invest. Ophthalmol. Vis. Sci.* **2009**, *50*, 2940–2948. [CrossRef]
- Hare, W.; WoldeMussie, E.; Lai, R.; Ton, H.; Ruiz, G.; Feldmann, B.; Wijono, M.; Chun, T.; Wheeler, L. Efficacy and safety of memantine, an NMDA-type open-channel blocker, for reduction of retinal injury associated with experimental glaucoma in rat and monkey. *Surv. Ophthalmol.* **2001**, *45*, S284–S289. [CrossRef]
- Weinreb, R.N.; Liebmann, J.M.; Cioffi, G.A.; Goldberg, I.; Brandt, J.D.; Johnson, C.A.; Zangwill, L.M.; Schneider, S.; Badger, H.; Bejani, M. Oral memantine for the treatment of glaucoma: Design and results of 2 randomized, placebo-controlled, phase 3 studies. *Ophthalmology* **2018**, *125*, 1874–1885. [CrossRef]
- Bucolo, C.; Platania, C.B.M.; Drago, F.; Bonfiglio, V.; Reibaldi, M.; Avitabile, T.; Uva, M. Novel therapeutics in glaucoma management. *Curr. Neuropharmacol.* **2018**, *16*, 978–992. [CrossRef]
- Cunha-Vaz, J.G. The blood-retinal barriers system. Basic concepts and clinical evaluation. *Exp. Eye Res.* **2004**, *78*, 715–721. [CrossRef]
- Liu, L.; Liu, X. Roles of drug transporters in blood-retinal barrier. *Adv. Exp. Med. Biol.* **2019**, *1141*, 467–504. [PubMed]
- Aoki, F.Y.; Sitar, D.S.; Ogilvie, R.I. Amantadine kinetics in healthy young subjects after long-term dosing. *Clin. Pharmacol. Ther.* **1979**, *26*, 729–736. [CrossRef] [PubMed]
- Muller, F.; Weitz, D.; Deraud, V.; Sandvoss, M.; Mertsch, K.; Konig, J.; Fromm, M.F. Contribution of MATE1 to renal secretion of the NMDA receptor antagonist memantine. *Mol. Pharm.* **2017**, *14*, 2991–2998. [CrossRef] [PubMed]
- Kooijmans, S.A.; Senyschyn, D.; Mezhiselvam, M.M.; Morizzi, J.; Charman, S.A.; Weksler, B.; Romero, I.A.; Couraud, P.O.; Nicolazzo, J.A. The involvement of a Na(+)- and Cl(-)-dependent transporter in the brain uptake of amantadine and rimantadine. *Mol. Pharm.* **2012**, *9*, 883–893. [CrossRef] [PubMed]
- Goralski, K.B.; Lou, G.; Prowse, M.T.; Gorboulev, V.; Volk, C.; Koepsell, H.; Sitar, D.S. The cation transporters rOCT1 and rOCT2 interact with bicarbonate but play only a minor role for amantadine uptake into rat renal proximal tubules. *J. Pharmacol. Exp. Ther.* **2002**, *303*, 959–968. [CrossRef]
- Busch, A.E.; Karbach, U.; Miska, D.; Gorboulev, V.; Akhoundova, A.; Volk, C.; Arndt, P.; Ulzheimer, J.C.; Sonders, M.S.; Baumann, C.; et al. Human neurons express the polyspecific cation transporter hOCT2, which translocates monoamine neurotransmitters, amantadine, and memantine. *Mol. Pharmacol.* **1998**, *54*, 342–352. [CrossRef]

18. Tachikawa, M.; Takeda, Y.; Tomi, M.; Hosoya, K. Involvement of OCTN2 in the transport of acetyl-L-carnitine across the inner blood-retinal barrier. *Invest. Ophthalmol. Vis. Sci.* **2010**, *51*, 430–436. [CrossRef]
19. Kubo, Y.; Yamamoto, M.; Matsunaga, K.; Usui, T.; Akanuma, S.I.; Hosoya, K.I. Retina-to-blood transport of 1-methyl-4-phenylpyridinium involves carrier-mediated process at the blood-retinal barrier. *J. Pharm. Sci.* **2017**, *106*, 2583–2591. [CrossRef]
20. Kubo, Y.; Kusagawa, Y.; Tachikawa, M.; Akanuma, S.; Hosoya, K. Involvement of a novel organic cation transporter in verapamil transport across the inner blood-retinal barrier. *Pharm. Res.* **2013**, *30*, 847–856. [CrossRef]
21. Kubo, Y.; Shimizu, Y.; Kusagawa, Y.; Akanuma, S.; Hosoya, K. Propranolol transport across the inner blood-retinal barrier: Potential involvement of a novel organic cation transporter. *J. Pharm. Sci.* **2013**, *102*, 3332–3342. [CrossRef] [PubMed]
22. Kubo, Y.; Tsuchiyama, A.; Shimizu, Y.; Akanuma, S.; Hosoya, K. Involvement of carrier-mediated transport in the retinal uptake of clonidine at the inner blood-retinal barrier. *Mol. Pharm.* **2014**, *11*, 3747–3753. [CrossRef] [PubMed]
23. Han, Y.H.; Sweet, D.H.; Hu, D.N.; Pritchard, J.B. Characterization of a novel cationic drug transporter in human retinal pigment epithelial cells. *J. Pharmacol. Exp. Ther.* **2001**, *296*, 450–457.
24. Hosoya, K.; Tomi, M.; Ohtsuki, S.; Takanaga, H.; Ueda, M.; Yanai, N.; Obinata, M.; Terasaki, T. Conditionally immortalized retinal capillary endothelial cell lines (TR-iBRB) expressing differentiated endothelial cell functions derived from a transgenic rat. *Exp. Eye. Res.* **2001**, *72*, 163–172. [CrossRef] [PubMed]
25. Nabi, I.R.; Mathews, A.P.; Cohen-Gould, L.; Gundersen, D.; Rodriguez-Boulan, E. Immortalization of polarized rat retinal pigment epithelium. *J. Cell. Sci.* **1993**, *104*, 37–49. [CrossRef]
26. Hosoya, K.; Yamamoto, A.; Akanuma, S.; Tachikawa, M. Lipophilicity and transporter influence on blood-retinal barrier permeability: A comparison with blood-brain barrier permeability. *Pharm. Res.* **2010**, *27*, 2715–2724. [CrossRef]
27. Kubo, Y.; Yamada, M.; Konakawa, S.; Akanuma, S.I.; Hosoya, K.I. Uptake study in lysosome-enriched fraction: Critical involvement of lysosomal trapping in quinacrine uptake but not fluorescence-labeled verapamil transport at blood-retinal barrier. *Pharmaceutics* **2020**, *12*, 747. [CrossRef] [PubMed]
28. Tega, Y.; Tabata, H.; Kurosawa, T.; Kitamura, A.; Itagaki, F.; Oshitari, T.; Deguchi, Y. Structural requirements for uptake of diphenhydramine analogs into hCMEC/D3 cells via the proton-coupled organic cation antiporter. *J. Pharm. Sci.* **2021**, *110*, 397–403. [CrossRef]
29. Lin, H.; Miller, S.S. pHi regulation in frog retinal pigment epithelium: Two apical membrane mechanisms. *Am. J. Physiol.* **1991**, *261*, C132–C142. [CrossRef]
30. Yamaoka, K.; Tanigawara, Y.; Nakagawa, T.; Uno, T. A pharmacokinetic analysis program (multi) for microcomputer. *J. Pharmacobiodyn.* **1981**, *4*, 879–885. [CrossRef]
31. Grabowski, T.; Gumulka, S.W.; Borucka, B.; Raszewski, W. Analysis relationships between pharmacokinetic parameters in silico/in vivo of selected antiviral drugs based on structural analysis. *Adv. Clin. Exp. Med.* **2008**, *17*, 285–292.
32. Grundemann, D.; Gorboulev, V.; Gambaryan, S.; Veyhl, M.; Koepsell, H. Drug excretion mediated by a new prototype of polyspecific transporter. *Nature* **1994**, *372*, 549–552. [CrossRef]
33. Urakami, Y.; Okuda, M.; Masuda, S.; Saito, H.; Inui, K.I. Functional characteristics and membrane localization of rat multispecific organic cation transporters, OCT1 and OCT2, mediating tubular secretion of cationic drugs. *J. Pharmacol. Exp. Ther.* **1998**, *287*, 800–805. [PubMed]
34. Grundemann, D.; Babin-Ebell, J.; Martel, F.; Ording, N.; Schmidt, A.; Schomig, E. Primary structure and functional expression of the apical organic cation transporter from kidney epithelial LLC-PK1 cells. *J. Biol. Chem.* **1997**, *272*, 10408–10413. [CrossRef] [PubMed]
35. Kekuda, R.; Prasad, P.D.; Wu, X.; Wang, H.; Fei, Y.J.; Leibach, F.H.; Ganapathy, V. Cloning and functional characterization of a potential-sensitive, polyspecific organic cation transporter (OCT3) most abundantly expressed in placenta. *J. Biol. Chem.* **1998**, *273*, 15971–15979. [CrossRef] [PubMed]
36. Wu, X.; Kekuda, R.; Huang, W.; Fei, Y.J.; Leibach, F.H.; Chen, J.; Conway, S.J.; Ganapathy, V. Identity of the organic cation transporter OCT3 as the extraneuronal monoamine transporter (uptake2) and evidence for the expression of the transporter in the brain. *J. Biol. Chem.* **1998**, *273*, 32776–32786. [CrossRef]
37. Sloan, J.L.; Mager, S. Cloning and functional expression of a human Na(+) and Cl(-)-dependent neutral and cationic amino acid transporter B(0+). *J. Biol. Chem.* **1999**, *274*, 23740–23745. [CrossRef] [PubMed]
38. Nakanishi, T.; Hatanaka, T.; Huang, W.; Prasad, P.D.; Leibach, F.H.; Ganapathy, M.E.; Ganapathy, V. Na+- and Cl--coupled active transport of carnitine by the amino acid transporter ATB(0,+) from mouse colon expressed in HRPE cells and Xenopus oocytes. *J. Physiol.* **2001**, *532*, 297–304. [CrossRef]
39. Yabuuchi, H.; Tamai, I.; Nezu, J.; Sakamoto, K.; Oku, A.; Shimane, M.; Sai, Y.; Tsuji, A. Novel membrane transporter OCTN1 mediates multispecific, bidirectional, and pH-dependent transport of organic cations. *J. Pharmacol. Exp. Ther.* **1999**, *289*, 768–773.
40. Wu, X.; George, R.L.; Huang, W.; Wang, H.; Conway, S.J.; Leibach, F.H.; Ganapathy, V. Structural and functional characteristics and tissue distribution pattern of rat OCTN1, an organic cation transporter, cloned from placenta. *Biochim. Biophys. Acta.* **2000**, *1466*, 315–327. [CrossRef]
41. Wu, X.; Huang, W.; Prasad, P.D.; Seth, P.; Rajan, D.P.; Leibach, F.H.; Chen, J.; Conway, S.J.; Ganapathy, V. Functional characteristics and tissue distribution pattern of organic cation transporter 2 (OCTN2), an organic cation/carnitine transporter. *J. Pharmacol. Exp. Ther.* **1999**, *290*, 1482–1492. [PubMed]

42. Tamai, I.; Ohashi, R.; Nezu, J.; Yabuuchi, H.; Oku, A.; Shimane, M.; Sai, Y.; Tsuji, A. Molecular and functional identification of sodium ion-dependent, high affinity human carnitine transporter OCTN2. *J. Biol. Chem.* **1998**, *273*, 20378–20382. [CrossRef] [PubMed]
43. Otsuka, M.; Matsumoto, T.; Morimoto, R.; Arioka, S.; Omote, H.; Moriyama, Y. A human transporter protein that mediates the final excretion step for toxic organic cations. *Proc. Natl. Acad. Sci. USA* **2005**, *102*, 17923–17928. [CrossRef] [PubMed]
44. Ohta, K.Y.; Inoue, K.; Hayashi, Y.; Yuasa, H. Molecular identification and functional characterization of rat multidrug and toxin extrusion type transporter 1 as an organic cation/H⁺ antiporter in the kidney. *Drug. Metab. Dispos.* **2006**, *34*, 1868–1874. [CrossRef] [PubMed]
45. Ito, S.; Kusuhara, H.; Yokochi, M.; Toyoshima, J.; Inoue, K.; Yuasa, H.; Sugiyama, Y. Competitive inhibition of the luminal efflux by multidrug and toxin extrusions, but not basolateral uptake by organic cation transporter 2, is the likely mechanism underlying the pharmacokinetic drug-drug interactions caused by cimetidine in the kidney. *J. Pharmacol. Exp. Ther.* **2012**, *340*, 393–403. [CrossRef]
46. Engel, K.; Wang, J. Interaction of organic cations with a newly identified plasma membrane monoamine transporter. *Mol. Pharmacol.* **2005**, *68*, 1397–1407. [CrossRef]
47. Parsons, C.G.; Panchenko, V.A.; Pinchenko, V.O.; Tsyndrenko, A.Y.; Krishtal, O.A. Comparative patch-clamp studies with freshly dissociated rat hippocampal and striatal neurons on the NMDA receptor antagonistic effects of amantadine and memantine. *Eur. J. Neurosci.* **1996**, *8*, 446–454. [CrossRef]
48. Nishikawa, N.; Nagai, M.; Moritoyo, T.; Yabe, H.; Nomoto, M. Plasma amantadine concentrations in patients with Parkinson's disease. *Parkinsonism. Relat. Disord.* **2009**, *15*, 351–353. [CrossRef]



Article

Investigating Ex Vivo Animal Models to Test the Performance of Intravitreal Liposomal Drug Delivery Systems

Gustav Christensen ¹, Leon Barut ¹, Dileep Urimi ², Nicolaas Schipper ² and François Paquet-Durand ^{1,*}

¹ Institute for Ophthalmic Research, University of Tübingen, Elfriede-Aulhorn Straße 5-7, 72076 Tübingen, Germany; gustav.christensen@uni-tuebingen.de (G.C.); leon.barut@student.uni-tuebingen.de (L.B.)

² Division Bioeconomy and Health, Chemical Process and Pharmaceutical Development, RISE Research Institutes of Sweden, Forskargatan 18, 151 36 Södertälje, Sweden; dileep.urimi@ri.se (D.U.); nicolaas.schipper@ri.se (N.S.)

* Correspondence: francois.paquet-durand@klinikum.uni-tuebingen.de; Tel.: +49-7071-29-87430

Abstract: There is a strong need for innovative and efficient drug delivery systems for ocular therapy development. However, testing intravitreal drug delivery systems without using live animals is challenging. Ex vivo animal models offer an interesting alternative. We analyzed the potential of using fresh porcine eyes obtained from the local slaughterhouse as a model for testing the intravitreal biodistribution and retention of liposomes with or without polyethylene glycol (PEG) conjugation and with different surface charges. The histology of the eyes was analyzed to localize the liposomes, and it was found that liposomes with PEG absorbed rapidly on the retina (within 1 h), with positively charged and PEG-coated liposomes being retained for at least 24 h. In parallel, fluorophotometry was employed on intact eyes, to determine the pharmacokinetics of the fluorophore calcein, as a substitute for a small hydrophilic therapeutic compound. We found a 4.5-fold increase in the vitreous half-life of calcein loaded in liposomes, compared with the free solution. Retinal toxicity was addressed using murine-derived retinal explant cultures. Liposomes were non-toxic up to 500 µg/mL. Toxicity was observed at 5 mg/mL for anionic and cationic liposomes, with 2-fold and 2.5-fold increased photoreceptor cell death, respectively. Overall, we could show that important ocular drug delivery considerations such as pharmacokinetics and biodistribution can be estimated in ex vivo porcine eyes, and may guide subsequent in vivo experiments.

Citation: Christensen, G.; Barut, L.; Urimi, D.; Schipper, N.; Paquet-Durand, F. Investigating Ex Vivo Animal Models to Test the Performance of Intravitreal Liposomal Drug Delivery Systems. *Pharmaceutics* **2021**, *13*, 1013. <https://doi.org/10.3390/pharmaceutics13071013>

Academic Editors: Francisco Javier Otero-Espinar and Anxo Fernández Ferreiro

Received: 31 May 2021

Accepted: 25 June 2021

Published: 2 July 2021

Publisher's Note: MDPI stays neutral with regard to jurisdictional claims in published maps and institutional affiliations.



Copyright: © 2021 by the authors. Licensee MDPI, Basel, Switzerland. This article is an open access article distributed under the terms and conditions of the Creative Commons Attribution (CC BY) license (<https://creativecommons.org/licenses/by/4.0/>).

Keywords: liposomes; intravitreal; ocular drug delivery; retinal explants

1. Introduction

Treating retinal diseases with injections into the vitreous body of the eye is common practice in the clinic. Repeated intravitreal administration is part of the treatment of certain diseases like age-related macular degeneration [1] and diabetic retinopathy. However, in addition to being unpleasant and a reason for patient non-compliance, intravitreal injections can lead to complications, such as retinal detachment, vitreous hemorrhage, and endophthalmitis [2]. Encapsulation of drugs in drug delivery systems can extend the vitreous retention time of the drug, and reduce the injection frequency [3]. In this regard, nano-sized liposomes offer promising potential. They are composed of usually well-tolerated lipids, and less material is required to form the liposomes as compared to other colloidal drug delivery systems (such as lipid-nanoparticles and polymersomes), which restricts scattering of in-coming light through the vitreous [4]. Liposomes can encapsulate hydrophilic and hydrophobic compounds simultaneously and the surface can be easily modified, e.g., the surface charge can be fine-tuned or targeting ligands to certain cell types can be conjugated [4–7]. In addition, they are biodegradable, and potentially more safe for repeated applications than non-degradable drug delivery systems like metallic nanoparticles [5].

The vitreous is a gel-like substance and provides the structural integrity of the eyeball. It consists mostly of water (98–99%), whereas the dry materials include fibers (mainly collagen type II), hyalocytes, and sugars [8]. The high water content means that in particular small hydrophilic molecules (<1000 Da) diffuse rapidly through the vitreous with a half-life typically not more than a few hours [9–13]. In general, it is understood that liposomes with a positive surface potential diffuse slower in the vitreous than those with negative or neutral surface potentials [14], due to the presence of negatively charged components such as hyaluronic acid and heparan sulfate [8]. Grafting polyethylene glycol (PEG) polymers on the liposome surface is a common technique to diminish immune responses, otherwise induced by the nanocarriers [15]. This results in an improved circulating half-life of systemically administered PEGylated liposomes. In the vitreous, immunological activity is limited compared to the rest of the body, and there is evidence that PEG enhances the vitreous diffusion of liposomes by shielding electrostatic interaction of the liposomes with vitreal components [7,16,17]. This could mean that the vitreous retention time of PEGylated liposomes is less than their non-PEGylated counterpart.

Testing viable intravitreal drug delivery systems in preclinical studies is often restricted to *in vivo* experimentation in live animals [16,17], which is usually expensive, time-consuming, and carries ethical considerations. Moreover, often rabbits are used [18], although the volume of the rabbit vitreous is only around 1.5 mL, while it is 3–4 mL for humans [16]. Interestingly, an *in vitro* eye model (PK-Eye™) has been developed to estimate human pharmacokinetics of intravitreal therapeutic compounds and formulations, which are cleared through the anterior route [13,19]. The model has similar dimensions to human eyes, and the rate of clearance between two compartments can be measured. However, the model does not address the tissue absorption of the injected formulations. Porcine eyes obtained from leftover carcasses at slaughterhouses could provide an alternative, as the porcine vitreous is large (4 mL), and histological sections can be prepared to localize fluorescently labelled drug delivery systems within the eyes [20]. Porcine *ex vivo* organs have previously been used as a surrogate for *in vivo* systems. For instance, cornea absorption of nanoparticles has been tested [21], and porcine skin has been used to obtain pharmacokinetic parameters of topical drug delivery systems [22].

Here, we investigated the potential of using *ex vivo* porcine eyes obtained from the slaughterhouse as a model for testing intravitreally administered drug delivery systems. Liposomes with positive, neutral, or negative surface potentials, with or without surface-grafted PEG were chosen as delivery systems, as the vitreous diffusion of similar formulations is available from the literature. Non-invasive ocular fluorophotometry was used to measure the spread of intravitreally injected liposomes loaded with a hydrophobic fluorophore. To further assess the tissue distribution within the eye, a full histological workup was performed and correlated with the non-invasive imaging data. The intravitreal pharmacokinetics were then evaluated for a hydrophilic fluorophore encapsulated in the most promising liposome formulation. Lastly, the potential retinal cytotoxicity of these liposomes was assessed using organotypic murine retinal explant cultures.

2. Materials and Methods

2.1. Materials

A total of 99% chloroform with 0.5–1% ethanol, 1-palmitoyl-2-oleoyl-sn-glycero-3-phosphocholine (POPC), cholesterol, 1,2-dioleoyl-3-trimethylammonium-propane (chloride salt) (DOTAP), 1,2-distearoyl-sn-glycero-3-phosphoethanolamine-*N*-[amino (polyethylene glycol)-2000] (ammonium salt) (DSPE-PEG₂₀₀₀), 1-palmitoyl-2-oleoyl-sn-glycero-3-phospho-L-serine (sodium salt) (POPS), dioctadecyl-3,3,3,3 Tetramethylindodicarbocyanine (DiO), calcein, sodium chloride, hydrogen chloride, sodium hydroxide, disodium hydrogen phosphate dihydrate, sodium dihydrogen phosphate monohydrate, paraformaldehyde, (4-(2-hydroxyethyl)-1-piperazineethanesulfonic acid) (HEPES), proteinase K, fetal bovine serum, polycarbonate membranes (0.1 µm pore size), and filter supports were obtained from Sigma Aldrich (Darmstadt, Germany). R16 medium and

dialysis cassettes (Slide-A-Lyzer, cellulose, 100K molecular weight cut-off) were obtained from Thermo Fisher Scientific (Waltham, MA, USA).

2.2. Methods

2.2.1. Preparation of Liposomes

Liposomes were produced using the thin-film hydration method [23]. All lipids were dissolved in chloroform and mixed in the respective molar ratios summarized below in Table 1 in a round-bottom flask. For DiO-labelled liposomes, 0.2 mol% DiO was added. The solvent was evaporated using a rotary evaporator (model RC600, KNF Neuberger, Trenton, NJ, USA) at 50 °C, 105 rpm and 300 mbar for at least 1 h, until a thin film of dried lipids was left. For samples characterized with dynamic light scattering, the film was hydrated in 10 mM HEPES buffer (pH 7, adjusted with NaOH). For other formulations, phosphate-buffered saline (PBS) was added. The lipid suspension was extruded with a mini-extruder (Avanti Polar Lipids, Alabaster, AL, USA) through a polycarbonate membrane with 100 nm pore sizes between two filter supports, for at least 11 times, and stored at 4 °C.

Table 1. Molar percentages of lipid components in the liposomes.

Formulation	POPC	Cholesterol	DOTAP	POPS	DSPE-PEG ₂₀₀₀
An-Lp	44.4%	33.3%		22.2%	
An-PEG-Lp	63.3%	31.7%			5%
Cat-Lp	44.4%	33.3%	22.2%		
Cat-PEG-Lp	42.2%	31.7%	21.1%		5%
Neu-Lp	66.6%	33.3%			
Neu-PEG-Lp	58.3%	31.7%	5%		5%

An: anionic, Cat: cationic, Neu: neutral, PEG: polyethylene glycol, Lp = liposome.

The liposome size and size distribution were measured using dynamic light scattering at a detection angle of 173°. Samples were analyzed in a disposable low volume cuvette at a sample refractive index of 1.47 at 25 °C. The ζ -potential of the samples was obtained by measuring the electrophoretic mobility of the particles under the influence of an applied electric field. Both size and ζ -potential measurements were carried out on Zetasizer Nano ZS (Malvern Instruments, Malvern, UK) using the Zetasizer Software version 7.13 (Malvern Instruments, Malvern, UK). Liposome concentrations of 0.3 mg/mL in 10 mM HEPES were used for the analysis.

2.2.2. Distribution of Liposomes in Porcine Vitreous Assessed with Fluorophotometry

Fresh porcine eyes were obtained from the slaughterhouse. Before use, the eyes were washed briefly with PBS buffer. Background fluorescence was measured on an ocular fluorometer (FM-2 Fluorotron Master, OcuMetrics, CA, USA), which records green fluorescent signal along the axial length. Triplicate recordings were obtained for each measurement. A total of 50 μ L liposomes encapsulating the fluorophore dioctadecyl-3,3,3,3 Tetramethylindodicarbocyanine (DiO) (12.5 mg/mL, PBS) was injected with a 22-gauge needle (Hamilton 1705 RN syringe, Hamilton, Reno, NV, USA) into the center of the eye (roughly 11 mm axially from the optic nerve). The signal from DiO-labelled liposomes was measured immediately after injection ($t = 0$). Subsequently, the eyes were submerged in PBS buffer and put on a platform shaker (Heidolph Instruments, Schwabach, Germany) at 45 rpm to simulate eye movement. This speed corresponds to the average or lower end of saccadic movements [24,25]. The signal was measured after 1, 2, 6, and 24 h. Eyes without liposome injection were used to determine the amount of auto-fluorescence.

2.2.3. Histological Evaluation of Liposomes Intravitreally Injected in Porcine Eyes

After injection of DiO-loaded liposomes in porcine eyes and incubation for either 1 or 24 h, the eyes were fixed in 4% paraformaldehyde in PBS (PFA). Eyes that were not injected were used as control. The fixation protocol was adapted from a published protocol [20] with

a few changes. Firstly, a 27-gauge needle was used to puncture 4 holes in roughly equal distance around the limbus. Secondly, 200 μ L PFA was intravitreally injected just below the limbus. Eyes were submerged to PFA and left at 4 °C for 5 days. Afterwards, the eyes were washed twice in PBS for 10 min, transferred to an embedding medium (Tissue-Tek O.C.T. Compound, Sakura Finetek Europe, Alphen aan den Rijn, Netherlands) and snap frozen with liquid N₂. The frozen eyes were sectioned on a cryostat (NX50, Thermo Fisher, Waltham, MA, USA) to produce 40 μ m thick sections on Superfrost Plus™ object slides (R. Langenbrinck, Emmendingen, Germany). The sections were dried for at least 1 h at 37 °C and rehydrated with PBS. Mounting medium with DAPI (Vectashield with DAPI, Vector laboratories, Burlingame, CA, USA) was added to the sections, and they were kept at 4 °C for at least 30 min prior to imaging with fluorescent microscopy (Axio Imager Z2 with ApoTome function, Zeiss, Oberkochen, Germany). A CCD camera with a 20 \times objective was used. Ex./Em. wavelengths of 483/501 nm were used to detect the green DiO signal. Image acquisition was done by recording 30 z-stacks 1 μ m apart and projecting the images using the Maximum Intensity Projection function in the acquisition software (ZEN 2.6, Zeiss). The same software was used to measure the mean fluorescent signal from the green channel. For the analysis, 3 eyes were measured per condition ($n = 3$). For each condition, 10–15 z-stacks were recorded at different areas on the retina and around 10 z-stacks were obtained from the vitreous, using 3 different microscopy slides (30–45 images for the retina, and 30 images for the vitreous per condition). The green DiO signal from all images were averaged. The background signal was obtained from un-injected eyes. The average background value was subtracted from all the other values. One-way ANOVA with Tukey's post-hoc test was calculated with GraphPad Prism 8 (GraphPad Software, San Diego, CA, USA) to assess statistical significance within the dataset.

2.2.4. Assessment of Pharmacokinetic Parameters

The most promising liposome formulation in the previous distribution experiment was chosen to encapsulate the hydrophilic fluorophore calcein (622.55 g/mol). Liposomes (25 mg/mL) with 2 mM calcein (pH 7, adjusted with NaOH) in PBS were prepared as described above, and excess calcein was removed with dialysis against 150 mM NaCl at a volume 2000X that of the sample. The dialysate was exchanged after 2 h, 4 h, and then left overnight. The liposomes were sterile-filtered (Millex-GP, 0.22 μ m, polyethersulfon, Merck Milipore, Darmstadt, Germany) and the fluorescent intensity at 530 nm was measured on a microplate reader (Tecan Spark 10M, Tecan, Männedorf, Switzerland) to determine the concentration of encapsulated calcein with a standard curve (Supplemental data, Figure S1A). Before injection, the calcein concentration was diluted to 90 μ M. The same concentration of free calcein was used as control. As the porcine eyes used in this experiment were intended for extended use (>24 h), they were cleaned with 70% ethanol, kept at sterile conditions, and only handled using sterile tools. The eyes were washed in 70% ethanol and sterile-filtered PBS every day. Excess tissue were dissected from the eyes before injection. A 27-gauge needle was used to inject 50 μ L of the liposome/calcein or free calcein solution into the vitreous through the *pars plana* (roughly 5 mm from the limbus). The calcein signal was measured using fluorophotometry (FM-2 Fluorotron Master, OcuMetrics, CA, USA), and the signal across the vitreous was averaged. Only data points where the calcein signal was observed to be constant across the vitreous were used. This was done to account for a potential uneven distribution. A standard curve of free calcein in extracted porcine vitreous (Supplemental data, Figure S1B) was obtained and used to determine the calcein concentration in the intact porcine vitreous.

2.2.5. Retina Viability Assay

Animals

The C3H wild-type mouse line was used in all studies [26]. Animals were used irrespective of gender and were housed with free access to food and water under standard white light with 12 h light/dark cycles. They were sacrificed at postnatal day 13 by CO₂ as-

phyxiation, followed by cervical dislocation. All procedures were performed in accordance with §4 of the German law on animal protection and approved by the animal protection committee of the University of Tübingen (Einrichtung für Tierschutz, Tierärztlichen Dienst und Labortierkunde; Registration No. AK02/19M, 3. April 2019).

Explanation and Culturing of Mouse Retinas

Retinas from mice eyes were isolated following a previously published protocol [27]. First, the eyes were pretreated in proteinase K to dissolve layers around the retina. Incubation in 20% fetal bovine serum stopped the proteinase reaction. Then, they were dissected under sterile conditions to separate the retina together with its retinal pigment epithelium. The retina was cut in a four-leaf clover shape, so that it could be placed flatly in a Transwell polycarbonate membrane (0.4 μm , Corning-Costar, New York, NY, USA) with the epithelium facing the membrane. Serum-free R16 medium, which was free of antibiotics and contained essential nutrients for retinal cultures [28], was used. Medium was exchanged every second day. After two days, a 20 μL solution of sterile-filtered liposomes were added on top of the cultures and incubated with the retinas for 24 h, after which the retina cultures were fixed in PFA. For cryoprotection, the cultures were incubated at room temperature in rising concentrations of sucrose (10, 20, and 30%) in PBS for 10 min, 20 min, and overnight at 4 $^{\circ}\text{C}$, respectively. The retinas were submerged in embedding medium and frozen with liquid N_2 . They were sectioned to produce 14 μm thick sections on Superfrost PlusTM slides.

Assessing Cell Death in Retinal Sections Using the TUNEL Assay

To detect dying cells in the retina cultures after addition of liposomes, a terminal deoxynucleotidyl transferase dUTP nick end labeling (TUNEL) assay was used. The protocol is available elsewhere [29,30]. The detection kit TMR red, Product No. 12156792910 (Sigma Aldrich, Darmstadt, Germany) was used. Retinal explant cultures incubated with PBS buffer (control) or increasing concentrations of the liposome formulations An-PEG-Lp or Cat-PEG-Lp (see Table 1) were tested. DAPI was used as nuclear counterstain. Fluorescent microscopy with red (Ex./Em. 548/561 nm) and blue (Ex./Em. 353/465 nm) channels to detect the TUNEL-induced labelling of dying cells and DAPI staining, respectively, was used. A total of 12 z-stacks 1 μm apart were recorded, and the relative amount of TUNEL-positive cells were manually counted and averaged for each retinal culture (representing one animal). The results were analyzed with one-way ANOVA and Dunnett's multiple comparisons test ($\alpha = 0.05$).

3. Results

3.1. Liposome Characterization

To confirm the successful formation of liposomes, all formulations were analyzed with dynamic light scattering (Table 2). In this study, the effect of charge and PEGylation of the liposomes in the porcine vitreous distribution and retention was tested. Therefore, liposomes that were either anionic, cationic, or more neutrally charged were prepared either with or without surface-grafted PEG. The charge of each formulation was determined by measuring the ζ -potential.

Table 2. Characterization of liposomes. Data are presented as mean \pm SD for $n = 3$.

Formulation	φ (nm)	PDI	ζ -potential (mV)
An-Lp	131 \pm 2	0.046 \pm 0.00	−55 \pm 3
An-PEG-Lp	127 \pm 2	0.051 \pm 0.01	−34 \pm 3
Cat-Lp	135 \pm 5	0.078 \pm 0.01	42 \pm 2
Cat-PEG-Lp	129 \pm 2	0.054 \pm 0.02	41 \pm 1
Neu-Lp	163 \pm 4	0.166 \pm 0.03	−12 \pm 1
Neu-PEG-Lp	154 \pm 17	0.164 \pm 0.03	29 \pm 2

PDI: polydispersity index.

Similar sizes were observed for all formulations with narrow size distributions, except for the more neutrally charged liposomes, which were slightly larger (20–30 nm) and shown more polydispersity. The Neu-PEG-Lp formulation were more positively charged than expected (around 29 mV), probably due to insufficient shielding of the positive charges by the PEG chains.

3.2. Liposome Distribution in Ex Vivo Porcine Eyes

Fluorophotometry was used to analyze the vitreous distribution of liposome in intact ex vivo porcine eyes. The distribution kinetics of the formulations summarized in Table 1 were measured to identify comparative differences and establish an initial framework for further experiments. A green hydrophobic fluorophore (DiO) was introduced into the formulations to measure the signal only from the liposomes themselves as little or no DiO was expected to be released. The liposomes were intravitreally injected into the center of the porcine eyes (Figure 1A). The detected signal was normalized to the initial signal measured at $t = 0$ (immediately after injection). A standard curve of DiO-liposomes dissolved in extracted vitreous fluid was obtained and a linear relationship ($R^2 = 0.97$) was found between liposome concentration and fluorescence intensity, allowing normalization (Supplemental data, Figure S1C). The time-dependent signal decrease was measured for each formulation (Figure 1B–D) to estimate the time required to obtain a complete distribution of the liposomes in the pig eye (i.e., when baseline was reached). The area under the curves (AUC) depicted in Figure 1B–D were used as a single value to compare differences in the distribution dynamics of the liposomes (Figure 1E). Except for the cationic liposomes (Cat-Lp), all formulations were almost completely distributed in the vitreous after 24 h. The formulations without PEG (except Neu-Lp) diffused slower than the ones with PEG, and Cat-Lp diffused the slowest. Negatively charged liposomes with PEG (An-PEG-Lp) seemed to diffuse the fastest, although there was no statistically significant difference with the other PEGylated liposomes.

The diffusion coefficient of liposomes with different charges has been quantified for ex vivo vitreous dissected from porcine eyes [13]; however, fluorophotometry allowed us to measure liposome signal from completely intact eyes. Overall, a signal decrease over time was consistently observed, indicating that the system can be used to measure the spread of the injected formulation over time (Figure 1). In general, PEG-coated liposomes had a more rapid signal decrease in the vitreous compared with formulations without PEG, indicating a faster rate of diffusion. Cationic liposomes without PEG diffused slowest in the vitreous. However, PEGylation of this formulation decreased the AUC around 70%. This increased vitreal distribution of PEGylated cationic liposomes is consistent with previously known studies [7,17,31]. Somewhat surprising was the observation that anionic liposomes without PEG seemed to diffuse slower than neutral liposomes without PEG. This observation could be attributed to the inclusion of serine phospholipids (POPS) in the An-Lp formulation, which contain carboxylate in the head group. Although anionic, the carboxylate group could hinder the diffusion in the vitreous as it is a donor for hydrogen bonds and can interact with collagen fibers and hyaluronic acid [32]. Similarly, a study on the diffusion dynamics of polystyrene (PS) particles showed no statistical significant difference between cationic PS particles and carboxyl-coated PS particles in the porcine vitreous [33].

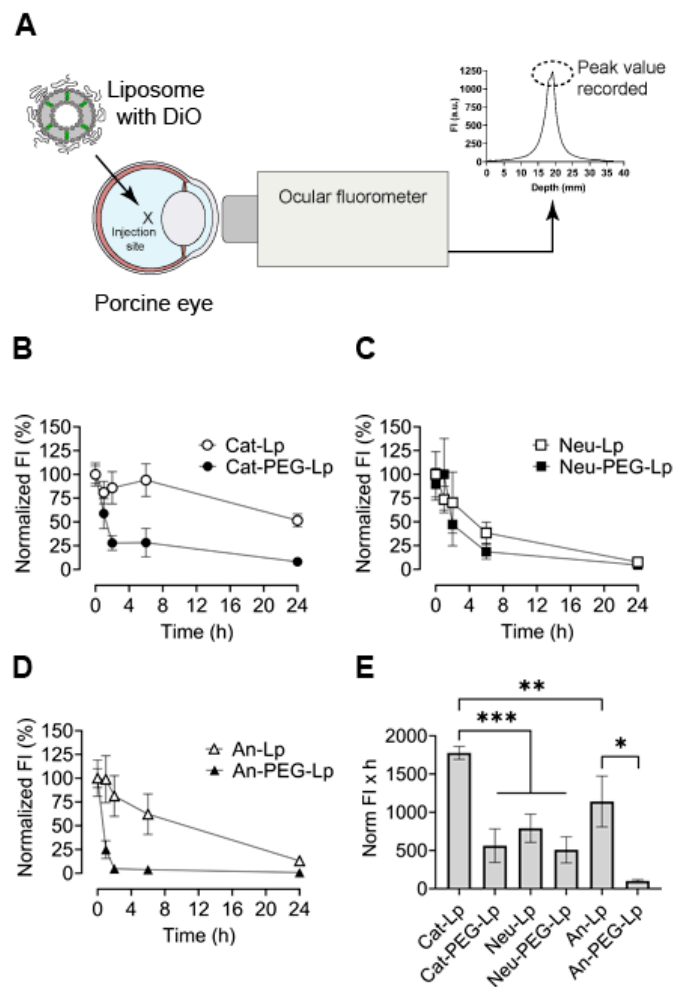


Figure 1. Diffusion dynamics of liposomes (Lp) intravitreally administered to intact ex vivo porcine eyes. (A) Liposomes were loaded with a hydrophobic green fluorophore (DiO), injected into the center of eyes. DiO signal was recorded non-invasively after specific time-points on an ocular fluorophotometer. (B–D) Peak signal was used to plot the normalized fluorescent intensity (FI) over time for cationic (Cat), neutrally charged (Neu), and anionic (An) formulations with or without poly(ethylene glycol) (PEG) grafted on the liposome surface. (E) The area under the normalized FI-time curves (B–D) was determined for each formulation. Results represent mean \pm SEM for $n = 4$ –6. * = $p < 0.05$, ** = $p < 0.01$, *** = $p < 0.001$. Statistical analysis: One-way ANOVA with Tukey’s post-hoc test.

3.3. Histological Analysis

The direct transport of liposomes to the retina is an important consideration when delivering hydrophobic compounds or macromolecules with an intracellular target (like genetic material). To determine the retinal absorption of DiO-labelled liposomes, histological sections were obtained from porcine eyes, which were fixed either 1 or 24 h post-injection (Figure 2). The 24 h time-point was chosen as most formulations seemed to have spread evenly in the vitreous (Figure 1B–D). Sections from the porcine vitreous (Figure 2A) and retina (Figure 2B) were analyzed for DiO signal. To assess the retinal distribution, the average fluorescent intensity from the retinal layers was measured using the acquisition software (Figure 2C).

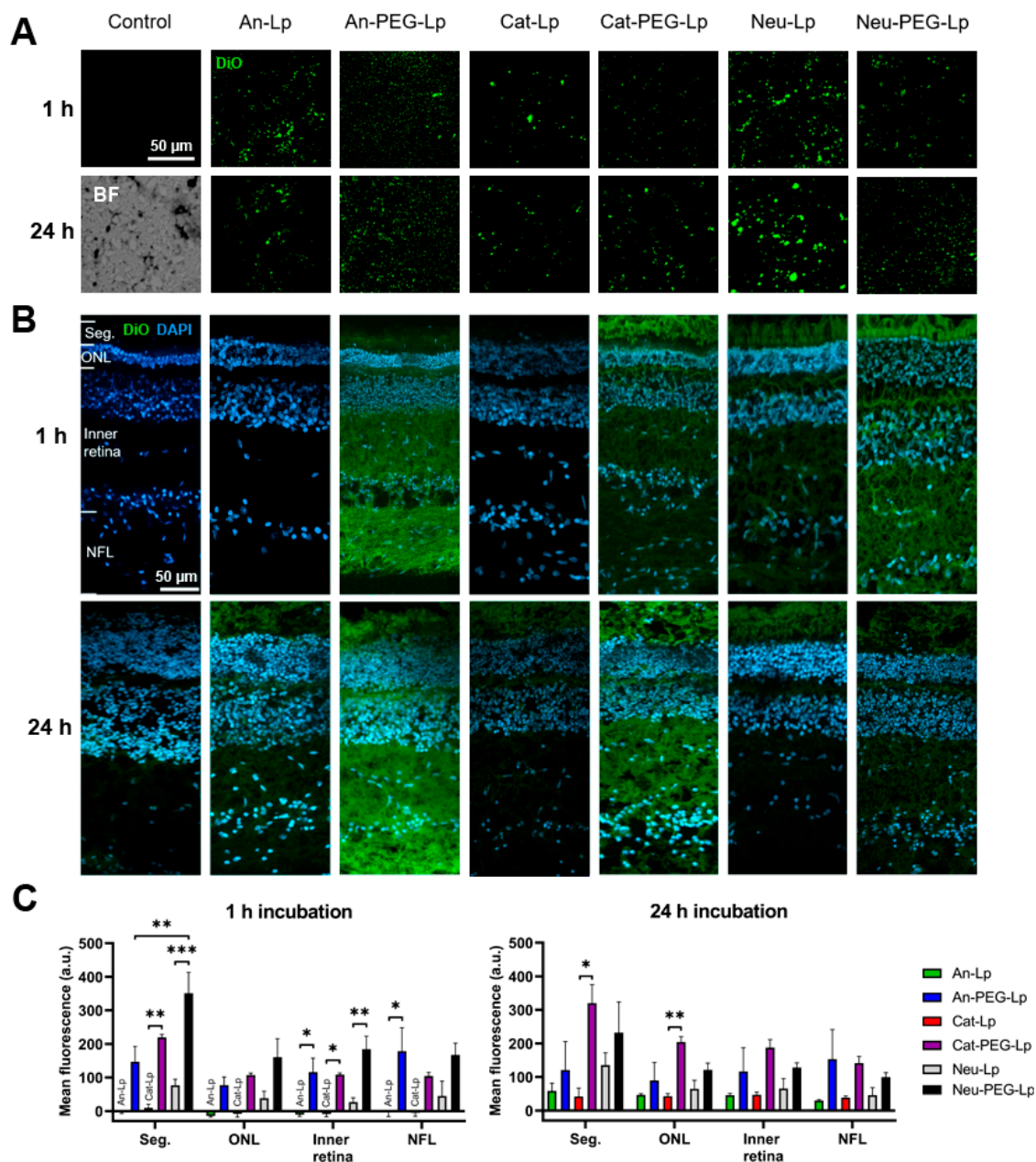


Figure 2. Histological analysis of ex vivo porcine vitreous and retinas from eyes that were fixed either 1 or 24 h after injection with liposome formulations. A green hydrophobic dye (DiO) was encapsulated in the formulations. (A) Images from vitreous sections after injection. Control = no liposomes injected. BF = bright-field image showing the structure of the vitreous. (B) Retina sections after injection. To analyze the retinal distribution of the fluorescent dye, the fluorescent intensity of different layers in the retina was quantified on the microscope software. The layers are depicted in the first image in the top right and are: photoreceptor inner and outer segments (Seg.), outer nuclear layer (ONL), inner retina (from the ganglion cell layer to the outer plexiform layer), and the nerve fiber layer (NFL). (C) Quantification of average fluorescent signal from retinal layers after 1 or 24 h post-injection into ex vivo porcine eyes. Control sections were used to obtain the background signal, which was subtracted from the other conditions. Results represent mean \pm SEM for $n = 3$. * = $p < 0.05$, ** = $p < 0.01$, *** $p < 0.001$. Statistical analysis: One-way ANOVA with Tukey’s post-hoc test.

On sections of the vitreous, the liposomes can be observed as green dots. In general, vitreous distribution seemed to be more even for PEGylated formulations, while more aggregations could be seen for non-PEGylated liposomes. The An-PEG-Lp formulation expressed the lowest degree of aggregation (smallest dots), while the more positively charged formulations (Cat-Lp and Cat-PEG-Lp) appeared to aggregate more in the vit-

reous. Although slightly anionic, the Neu-Lp formulation also showed a high degree of aggregation. This indicates that PEG is an important factor in the stability of liposomes in the vitreous.

From the analysis of the DiO signal in the retina, it is clear that charge and PEGylation affect the retinal uptake. All PEGylated formulations seemed to be taken up earlier when compared to non-PEGylated liposomes. The positively charged and PEGylated formulations (Cat-PEG-Lp and Neu-PEG-Lp) showed the highest uptake, with the highest signal coming from the photoreceptor segments. However, the Cat-Lp formulation, while showing a similar ζ -potential (Table 2), did not interact strongly with the retina, during the first 24 h, likely because the vitreous distribution was slower (Figure 1). Similarly, the An-Lp formulation diffused slowly in the vitreous, resulting in no signal at the retina after 1 h. Its PEGylated counter-part (An-PEG-Lp), on the other hand, showed high early-state absorption.

3.4. Pharmacokinetic Evaluation

We then determined whether the ex vivo porcine eyes could be used to estimate the pharmacokinetic parameters of a hydrophilic fluorophore, calcein, and to what extent liposome encapsulation would improve the pharmacokinetics. Calcein was chosen as it is released slowly from the liposomes [31]. The Cat-Lp formulation showed the slowest vitreous diffusion (Figure 1) and was thus expected to provide the longest retention time. When calcein was encapsulated in this liposome formulation, we observed a 4.5-fold increase in the vitreous half-life (Figure 3). To accurately evaluate the pharmacokinetic profiles with fluorophotometry, a homogenous distribution along the visual axis is required [34], i.e., an even signal throughout the vitreous. For free calcein, such a distribution was observed already after 1 h. For calcein encapsulated in Cat-Lp, it was only observed after more than 2 days.

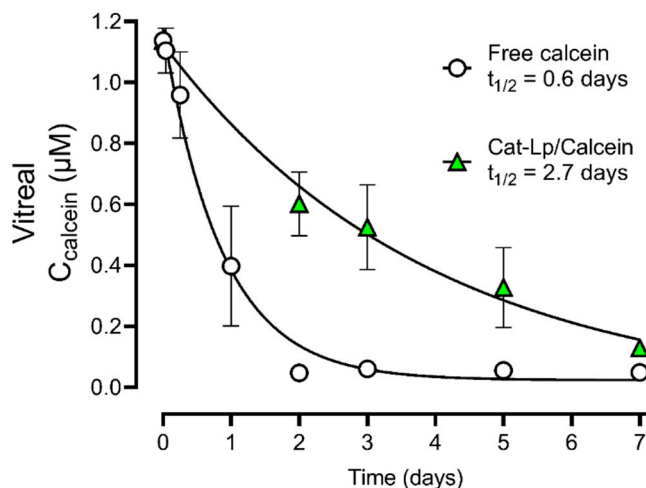


Figure 3. Estimation of the vitreal half-life ($t_{1/2}$) of free calcein and calcein encapsulated in cationic liposomes (Cat-Lp/Calcein) after intravitreal injection into ex vivo porcine eyes. Vitreal calcein concentration was obtained from ocular fluorophotometry. The data shows a 4.5-fold increase in vitreal half-life when calcein was encapsulated. Data points were fitted to a one-phase exponential decay model ($R^2 = 0.92$ for calcein and $R^2 = 0.72$ for Cat-Lp/Calcein) calculated with GraphPad Prism 8 and represent mean \pm SEM, for $n = 3$ (calcein) and $n = 6$ (Cat-Lp/Calcein).

3.5. Retina Viability Assay

The toxicity of the formulations to retinal cells was evaluated using a well-established organotypic retinal explant culture system [27]. As PEGylated liposomes were shown to reach the retina in the porcine eye model to a greater extent, formulations without PEG were not tested on murine retina. In addition, as the cationic liposomes included the

lipid DOTAP, which has been shown to exhibit some cytotoxicity to HeLa cells [35], the formulations Cat-PEG-Lp and An-PEG-Lp were chosen for the analysis, to assess whether the addition of cationic lipids would cause more cell death to retinal cultures. The amount of dying retinal cells were quantified using the TUNEL assay (Figure 4). We found that the formulations were only toxic at high concentrations (5 mg/mL), with cationic liposomes causing more cell death than anionic liposomes. This effect was seen in cells of the inner nuclear layer, composed predominantly of second order neurons, and was even more evident in the outer nuclear layer, where the photoreceptors reside.

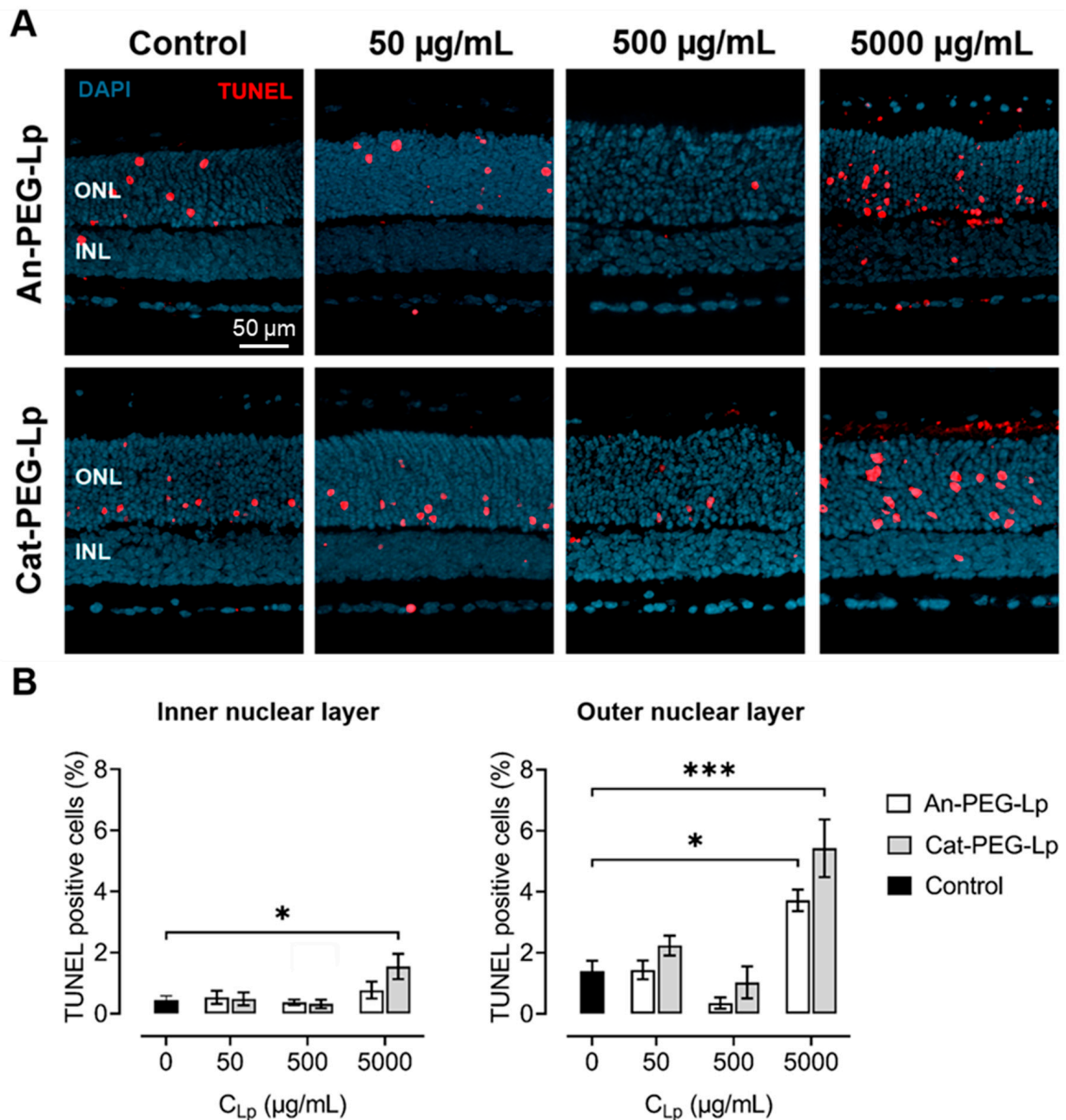


Figure 4. Retina viability assay. (A) TUNEL assay (red) was used to evaluate death of retinal cells from the inner nuclear layer (INL) and the outer nuclear layer (ONL) of retinal explant cultures after addition of anionic (An-PEG-Lp) and cationic (Cat-PEG-Lp) PEGylated liposomes at incremental concentrations. Control = no liposomes added. DAPI (blue) was used as nuclear counterstain. (B) Quantification of dying cells expressed as the percentage of TUNEL positive cells in the tissue sections. Results represent mean \pm SEM for $n = 3-6$. * = $p < 0.05$, *** $p < 0.001$. Statistical analysis: One-way ANOVA with Dunnett's post-hoc test.

4. Discussion

In this study, we provide a new framework for testing the ocular distribution and retention of ocular drug delivery systems using ex vivo porcine eyes as a model. The ex vivo system along with ocular fluorophotometry and histology could give an early-state assessment of the behavior of liposomal drug delivery systems, in terms of distribution time, tissue interactions, and estimating relevant pharmacokinetic parameters of a model drug. The differences of the tested liposomes are summarized in Table 3. Interestingly, the PEG-coated formulations reach the retina faster than the non-PEG-coated counterparts, which could be accounted for by the vitreous diffusion. Although the An-PEG-Lp formulation diffuses the fastest, it does not absorb on the retina faster than the PEG-coated and positively charged liposomes, illustrating that these liposomes could be better suited for direct retinal transport. On the other hand, a possible limitation of positively charged liposomes could be the higher degree of toxicity.

Table 3. Overview of relevant properties of the investigated liposomes.

Formulation	Vitreous Diffusion	Vitreous Retention	Retinal Absorption	Retinal Toxicity
An-Lp	Slow	High	Very slow	
An-PEG-Lp	Very fast	Very low	Fast	Low
Cat-Lp	Very slow	Very high	Very slow	
Cat-PEG-Lp	Fast	Low	Very fast	Intermediate
Neu-Lp	Fast	Low	Intermediate	
Neu-PEG-Lp	Fast	Low	Very fast	

Apart from a comparative analysis of different liposomes, non-invasive ocular fluorophotometry also allowed us to estimate the pharmacokinetics of a small hydrophilic fluorophore (calcein) in the intact eyeball (Figure 3). The use of fluorophotometry to assess ocular pharmacokinetics has previously been established [34,36]. For ex vivo porcine eyes, degeneration of the tissue limits long-term analysis. After day five, the vitreous became more and more liquefied, which could be observed by deflation of the eyeball. This happened even under sterile conditions. Liquefaction has been associated with increased flow, which would increase vitreous drug clearance [18]. To mitigate the issue in future experiments, medium-perfused ex vivo eyes have been used for a duration of up to 14 days [37], and could potentially keep the tissue fresh for longer. From the histological porcine retina sections (Figure 3), it appears that the retina is degenerating, which is worse after 24 h than after 1 h. This is obvious when comparing the structure with cultured retinas from mice (Figure 4).

Viability of the tissue in the ex vivo model may influence the pharmacokinetic data obtained in the current study. Active transport processes and cell uptake of liposomes may decrease over time. Surprisingly, however, the vitreous half-life of calcein that was obtained ex vivo here (0.6 days) agrees well with that of a recent in vivo rabbit study, which measured the intravitreal calcein pharmacokinetics [38]. Although the rabbit vitreous is smaller than the porcine, it is generally understood that the vitreous diffusion is not the rate-limiting step for retention of small molecules [3]. Our data suggests that at least the short-term pharmacokinetics may be comparable to the in vivo situation. In the aforementioned study, the half-life of calcein loaded in liposomes was extended to seven days, which is more than in our case (2.7 days). The composition of the liposomes in the two studies were different and the release of calcein from the liposomes used in the in vivo rabbit study is expected to be slower. In the latter study lipids with a high transition temperature were used (hydrogenated L- α -phosphatidylcholine), while lipids with a low transition temperature (POPC) were used in the current study. Calcein is released from POPC liposomes approximately three times quicker than from the hydrogenated counterpart, as shown by Maherani et al. [31]. This would thus affect the vitreous half-life of calcein.

The diffusion and vitreal half-life of intravitreally administered drugs are not only very dependent on the liposome system used, but also on the properties of the drug. For instance, liposomal 5-Fluorouridine 5'MP was reported to have a half-life of 5.2 days while for liposomal Gentamicin this was less than two days [4]. With the ex vivo, non-invasive imaging approached used here, a comparable analysis between the encapsulated and non-encapsulated compound is possible. We obtained an extension of 4.5 times the intravitreal half-life when calcein was encapsulated in liposomes, which is within the range of what would be expected from in vivo studies. The previously mentioned liposomal Gentamicin system only extended the half-life by a factor of 1.2, and for a liposomal Amikacin system [11], the half-life was extended by 1.8. However, liposomal 5-Fluorouridine 5'MP saw a 27-fold increase in intravitreal half-life.

The limitation of pharmacokinetic evaluation using fluorophotometry is that only fluorescent markers can be detected, i.e., only the retention of fluorescent drugs or fluorescently-labelled drugs can be tested. Labelling of the drug molecule has the disadvantage that it changes the chemistry and potentially the release profile of the drug. The major advantage of fluorophotometry, however, is that intact eyes can be used, and the only intervention required is the injection. Different routes of applications (e.g., intravitreal, topical, subconjunctival) can be compared. The real-time pharmacokinetics can be measured, which is especially relevant for in vivo studies, since there is no need for sampling the vitreous or aqueous humor fluid or sacrificing the animal for every measurement. Even further, the very same methodology may be used to non-invasively study the pharmacokinetics of drug delivery systems in clinical trials. In other words, fluorophotometry may provide for a direct comparison between ex vivo models, preclinical in vivo models, and clinical trials, using the same methodology and instrumentation.

In the ex vivo porcine eye model, the biodistribution of the formulations is another parameter, which can be tested and give insight into the potential of a given drug delivery system. Liposome-mediated delivery of macromolecules such as peptides and genetic materials (e.g., plasmids [39] and siRNA [40]), which have an intracellular target, requires direct transport to the cells. We have shown that the ex vivo model can answer whether the delivery system is able to reach the target of interest (e.g., the retina) by passive diffusion and offers an estimate about how much time would be required. It is, however, questionable whether the retinal cells of the ex vivo model take up the drug delivery system through active processes. Active cell uptake would have to be confirmed with cell or tissue cultures.

According to our results, PEGylated liposomes diffused to the retina within 1 h (Figure 2), and could be detected in the outer retina. Previously, PEGylated liposomes have been shown to improve retinal transport compared with non-PEGylated liposomes [41]. Since cationic liposomes interact stronger with the retinal tissue, we obtained a higher signal for these liposomes (Cat-PEG-Lp and Neu-PEG-Lp), especially in the deeper parts of the retina (outer nuclear layer and photoreceptor segments). Whether the DiO signal coming from the outer retina is from intact liposomes or unbound DiO transported throughout the retina, possibly in extracellular vesicles, is not clear from these tests. Nevertheless, the results show that a hydrophobic model drug can be transported throughout the retina. We tried to analyze the histology of eyes injected with calcein-loaded liposomes, but no signal was detected (data not shown). This could be due to substantial calcein release and elimination caused by the histological preparation procedure, which include freezing and washing steps. DiO, on the contrary, is not expected to be released from liposomes dissolved in the vitreous.

For ocular drug delivery systems with a retinal target, there is a strict requirement of safety, since retinal cells are predominantly post-mitotic cells that cannot be replaced once lost. We found that the retina can safely tolerate up to 500 µg/mL of liposomal formulations, even for positively charged liposomes. Although only two formulations were tested here, similar toxicity profiles would be expected for the other formulations investigated in this study. In retinal cultures, more dying cells were observed in the outer nuclear layer, where the cell bodies of photoreceptors reside, compared to the inner nuclear layer. However,

this is not necessarily an effect of the formulation, since the control condition, where cell death is primarily caused by the explanation procedure, showed a similar trend. The observation that in murine explant cultures photoreceptors are more sensitive than second order neurons in the inner retina is consistent with previous data [30,42].

In summary, we provide a first systematic overview of the intravitreal behavior of different liposomal formulations in the ex vivo porcine eye. This approach can supply important information about ocular drug delivery systems, especially regarding their intravitreal pharmacokinetics and biodistribution, without requiring the use of experimental animals. Importantly, the non-invasive imaging approach used here can be directly transferred to corresponding pre-clinical in vivo studies and even clinical studies, allowing a direct comparison of measurement parameters across different systems and species.

Supplementary Materials: The following are available online at <https://www.mdpi.com/article/10.3390/pharmaceutics13071013/s1>, Figure S1: standard curves of calcein and DiO.

Author Contributions: Conceptualization, G.C. and F.P.-D.; methodology, G.C., L.B. and D.U.; formal analysis, G.C. and L.B.; data curation, G.C.; writing—original draft preparation, G.C.; writing—review and editing, G.C., L.B., D.U., N.S. and F.P.-D.; visualization, G.C. and L.B.; supervision, N.S. and F.P.-D.; funding acquisition, N.S. and F.P.-D. All authors have read and agreed to the published version of the manuscript.

Funding: This work was financially supported by the German Research Council (DFG) grant no. PA1751/10-1.

Institutional Review Board Statement: The study was conducted according to §4 of the German law on animal protection and approved by the Ethics Committee of the University of Tübingen (Einrichtung für Tierschutz, Tierärztlichen Dienst und Labortierkunde; Registration No. AK02/19M, 3 April 2019).

Informed Consent Statement: Not applicable.

Data Availability Statement: Not applicable.

Acknowledgments: We are grateful to Sven Schnichels for guidance and help regarding fluorophotometry and to Katharina-Henriette Rasp for providing the porcine eyes used in this study.

Conflicts of Interest: The authors declare no conflict of interest. The funders had no role in the design of the study; in the collection, analyses, or interpretation of data; in the writing of the manuscript, or in the decision to publish the results.

References

- García-Quintanilla, L.; Luaces-Rodríguez, A.; Gil-Martínez, M.; Mondelo-García, C.; Maroñas, O.; Mangas-Sanjuan, V.; González-Barcia, M.; Zarra-Ferro, I.; Aguiar, P.; Otero-Espinar, F.J.; et al. Pharmacokinetics of Intravitreal Anti-VEGF Drugs in Age-Related Macular Degeneration. *Pharmaceutics* **2019**, *11*, 365. [CrossRef] [PubMed]
- Shima, C.; Sakaguchi, H.; Gomi, F.; Kamei, M.; Ikuno, Y.; Oshima, Y.; Sawa, M.; Tsujikawa, M.; Kusaka, S.; Tano, Y. Complications in patients after intravitreal injection of bevacizumab. *Acta Ophthalmol.* **2008**, *86*, 372–376. [CrossRef] [PubMed]
- Amo, E.M.d.; Rimpelä, A.-K.; Heikkinen, E.; Kari, O.K.; Ramsay, E.; Lajunen, T.; Schmitt, M.; Pelkonen, L.; Bhattacharya, M.; Richardson, D.; et al. Pharmacokinetic aspects of retinal drug delivery. *Prog. Retin. Eye Res.* **2017**, *57*, 134–185. [PubMed]
- Bochot, A.; Fattal, E. Liposomes for intravitreal drug delivery: A state of the art. *J. Control. Release* **2012**, *161*, 628–634. [CrossRef] [PubMed]
- Khiev, D.; Mohamed, Z.A.; Vichare, R.; Paulson, R.; Bhatia, S.; Mohapatra, S.; Lobo, G.P.; Valapala, M.; Kerur, N.; Passaglia, C.L.; et al. Emerging Nano-Formulations and Nanomedicines Applications for Ocular Drug Delivery. *Nanomaterials* **2021**, *11*, 173. [CrossRef] [PubMed]
- Vighi, E.; Trifunović, D.; Veiga-Crespo, P.; Rentsch, A.; Hoffmann, D.; Sahaboglu, A.; Strasser, T.; Kulkarni, M.; Bertolotti, E.; van den Heuvel, A.; et al. Combination of cGMP analogue and drug delivery system provides functional protection in hereditary retinal degeneration. *Proc. Natl. Acad. Sci. USA* **2018**, *115*, 2997–3006. [CrossRef]
- Lee, J.; Goh, U.; Lee, H.-J.; Kim, J.; Jeong, M.; Park, J.-H. Effective Retinal Penetration of Lipophilic and Lipid-Conjugated Hydrophilic Agents Delivered by Engineered Liposomes. *Mol. Pharm.* **2017**, *14*, 423–430. [CrossRef]
- Le Goff, M.M.; Bishop, P.N. Adult vitreous structure and postnatal changes. *Eye* **2008**, *22*, 1214–1222. [CrossRef] [PubMed]
- Bourlaist, C.L.; Chevanne, F.; Ropert, P.; Bretagne, G.; Acar, L.; Zia, H.; Sado, P.A.; Needham, T.; Leverge, R. Release kinetics of liposome-encapsulated ganciclovir after intravitreal injection in rabbits. *J. Microencapsul.* **1996**, *13*, 473–480. [CrossRef]

10. Alghadyan, A.; Peyman, G.A.; Khoobehi, B.; Liu, K.-R. Liposome-bound cyclosporine: Retinal toxicity after intravitreal injection. *Int. Ophthalmol.* **1988**, *12*, 105–107. [CrossRef] [PubMed]
11. Zeng, S.; Hu, C.; Wei, H.; Lu, Y.; Zhang, Y.; Yang, J.; Yun, G.; Zou, W.; Song, B. Intravitreal Pharmacokinetics of Liposome-encapsulated Amikacin in a Rabbit Model. *Ophthalmology* **1993**, *100*, 1640–1644. [CrossRef]
12. Zhang, R.; He, R.; Qian, J.; Guo, J.; Xue, K.; Yuan, Y.-f. Treatment of Experimental Autoimmune Uveoretinitis with Intravitreal Injection of Tacrolimus (FK506) Encapsulated in Liposomes. *Investig. Ophthalmol. Vis. Sci.* **2010**, *51*, 3575–3582. [CrossRef]
13. Awwad, S.; Day, R.M.; Khaw, P.T.; Brocchini, S.; Fadda, H.M. Sustained release ophthalmic dexamethasone: In vitro in vivo correlations derived from the PK-Eye. *Int. J. Pharm.* **2017**, *522*, 119–127. [CrossRef] [PubMed]
14. Eriksena, A.Z.; Brewer, J.; Andresena, T.L.; Urquhart, A.J. The diffusion dynamics of PEGylated liposomes in the intact vitreous of the ex vivo porcine eye: A fluorescence correlation spectroscopy and biodistribution study. *Int. J. Pharm.* **2017**, *522*, 90–97. [CrossRef] [PubMed]
15. Nosova, A.S.; Koloskova, O.O.; Nikonova, A.A.; Simonova, V.A.; Smirnov, V.V.; Kudlay, D.; Khaitov, M.R. Diversity of PEGylation methods of liposomes and their influence on RNA delivery. *MedChemComm* **2019**, *10*, 369–377. [CrossRef] [PubMed]
16. Bakri, S.J.; Snyder, M.R.; Reid, J.M.; Pulido, J.S.; Ezzat, M.K.; Singh, R.J. Pharmacokinetics of intravitreal ranibizumab (Lucentis). *Ophthalmology* **2007**, *114*, 2179–2182. [CrossRef]
17. Amo, E.M.d.; Vellonen, K.-S.; Kidron, H.; Urtti, A. Intravitreal clearance and volume of distribution of compounds in rabbits: In silico prediction and pharmacokinetic simulations for drug development. *Eur. J. Pharm. Biopharm.* **2015**, *95*, 215–226. [PubMed]
18. Del Amo, E.M.; Urtti, A. Rabbit as an animal model for intravitreal pharmacokinetics: Clinical predictability and quality of the published data. *Exp. Eye Res.* **2015**, *137*, 111–124. [CrossRef]
19. Awwad, S.; Al-Shohani, A.; Khaw, P.T.; Brocchini, S. Comparative Study of In Situ Loaded Antibody and PEG-Fab NIPAAM Gels. *Macromol. Biosci.* **2018**, *18*. [CrossRef]
20. Smet, M.D.d.; Valmaggia, C.; Zarranz-Ventura, J.; Willekens, B. Microplasmin: Ex Vivo Characterization of Its Activity in Porcine Vitreous. *Retina* **2009**, *50*, 814–819. [CrossRef]
21. Alvarez-Trabado, J.; López-García, A.; Martín-Pastor, M.; Diebold, Y.; Sanchez, A. Sorbitan ester nanoparticles (SENS) as a novel topical ocular drug delivery system: Design, optimization, and in vitro/ex vivo evaluation. *Int. J. Pharm.* **2018**, *546*, 20–30. [CrossRef] [PubMed]
22. Herkenne, C.; Naik, A.; Kalia, Y.N.; Hadgraft, J.; Guy, R.H. Pig Ear Skin ex Vivo as a Model for in Vivo Dermatopharmacokinetic Studies in Man. *Pharm. Res.* **2006**, *23*, 1850–1856. [CrossRef]
23. Zhang, H. Thin-Film Hydration Followed by Extrusion Method for Liposome Preparation. In *Liposomes: Methods and Protocols*; D'Souza, G.G.M., Ed.; Springer: New York, NY, USA, 2017; pp. 17–22.
24. Harwood, M.R.; Mezey, L.E.; Harris, C.M. The spectral main sequence of human saccades. *J. Neurosci.* **1999**, *19*, 9098–9106. [CrossRef]
25. Gibaldi, A.; Sabatini, S.P. The saccade main sequence revised: A fast and repeatable tool for oculomotor analysis. *Behav. Res. Methods* **2021**, *53*, 167–187. [CrossRef]
26. Sanyal, S.; Bal, A.K. Comparative light and electron microscopic study of retinal histogenesis in normal and rd mutant mice. *Z. Anat. Entwickl.* **1973**, *142*, 219–238. [CrossRef]
27. Belhadj, S.; Tolone, A.; Christensen, G.; Das, S.; Chen, Y.; Paquet-Durand, F. Long-Term, Serum-Free Cultivation of Organotypic Mouse Retina Explants with Intact Retinal Pigment Epithelium. *J. Vis. Exp.* **2020**, e61868. [CrossRef]
28. Caffé, A.R.; Ahuja, P.; Holmqvist, B.; Azadi, S.; Forsell, J.; Holmqvist, I.; Söderpalm, A.K.; van Veen, T. Mouse retina explants after long-term culture in serum free medium. *J. Chem. Neuroanat.* **2002**, *22*, 263–273. [CrossRef]
29. Loo, D.T. In situ detection of apoptosis by the TUNEL assay: An overview of techniques. *Methods Mol. Biol.* **2011**, *682*, 3–13. [PubMed]
30. Prajapati, M.; Christensen, G.; Paquet-Durand, F.; Loftsson, T. Cytotoxicity of β -Cyclodextrins in Retinal Explants for Intravitreal Drug Formulations. *Molecules* **2021**, *26*, 1492. [CrossRef] [PubMed]
31. Maherani, B.; Arab-Tehrany, E.; Kheirloomoom, A.; Geny, D.; Linder, M. Calcein release behavior from liposomal bilayer; influence of physicochemical/mechanical/structural properties of lipids. *Biochimie* **2013**, *95*, 2018–2033. [CrossRef] [PubMed]
32. Suh, K.Y.; Yang, J.M.; Khademhosseini, A.; Berry, D.; Tran, T.-N.T.; Park, H.; Langer, R. Characterization of chemisorbed hyaluronic acid directly immobilized on solid substrates. *J. Biomed. Mater. Res.* **2005**, *72*, 292–298. [CrossRef]
33. Käs Dorf, B.T.; Arends, F.; Lieleg, O. Diffusion Regulation in the Vitreous Humor. *Biophys. J.* **2015**, *109*, 2171–2181. [CrossRef]
34. Dickmann, L.J.; Yip, V.; Li, C.; Abundes, J.; Maia, M., Jr.; Young, C.; Stainton, S.; Hass, P.E.; Joseph, S.B.; Prabhu, S.; et al. Evaluation of Fluorophotometry to Assess the Vitreal Pharmacokinetics of Protein Therapeutics. *Investig. Ophthalmol. Vis. Sci.* **2015**, *56*, 6991–6999. [CrossRef] [PubMed]
35. De Leo, V.; Milano, F.; Paiano, A.; Bramato, R.; Giotta, L.; Comparelli, R.; Ruscigno, S.; Agostiano, A.; Bucci, C.; Catucci, L. Luminescent CdSe@ZnS nanocrystals embedded in liposomes: A cytotoxicity study in HeLa cells. *Toxicol. Res.* **2017**, *6*, 947–957. [CrossRef] [PubMed]
36. Ghate, D.; Brooks, W.; McCarey, B.E.; Edelhauser, H.F. Pharmacokinetics of Intraocular Drug Delivery by Periocular Injections Using Ocular Fluorophotometry. *Investig. Ophthalmol. Vis. Sci.* **2007**, *48*, 2230–2237. [CrossRef] [PubMed]

37. Loewen, R.T.; Roy, P.; Park, D.B.; Jensen, A.; Scott, G.; Cohen-Karni, D.; Fautsch, M.P.; Schuman, J.S.; Loewen, N.A. A Porcine Anterior Segment Perfusion and Transduction Model with Direct Visualization of the Trabecular Meshwork. *Investig. Ophthalmol. Vis. Sci.* **2016**, *57*, 1338–1344. [CrossRef]
38. Blazaki, S.; Pachis, K.; Tzatzarakis, M.; Tsilimbaris, M.; Antimisiaris, S.G. Novel Liposome Aggregate Platform (LAP) system for sustained retention of drugs in the posterior ocular segment following intravitreal injection. *Int. J. Pharm.* **2020**, *576*, 118987. [CrossRef]
39. Levine, R.M.; Pearce, T.R.; Adil, M.; Kokkoli, E. Preparation and Characterization of Liposome-Encapsulated Plasmid DNA for Gene Delivery. *Langmuir* **2013**, *29*, 9208–9215. [CrossRef]
40. Blazaki, S.; Pachis, K.; Tzatzarakis, M.; Tsilimbaris, M.; Antimisiaris, S.G. Liposomes as siRNA delivery vectors. *Curr. Drug Metab.* **2014**, *15*, 882–892.
41. Tavakoli, S.; Peynshaert, K.; Lajunen, T.; Devoldere, J.; Amo, E.M.d.; Ruponen, M.; De Smedt, S.C.; Remaut, K.; Urtti, A. Ocular barriers to retinal delivery of intravitreal liposomes: Impact of vitreoretinal interface. *J. Control. Release* **2020**, *328*, 952–961. [CrossRef]
42. Paquet-Durand, F.; Hauck, S.M.; Van Veen, T.; Ueffing, M.; Ekström, P. PKG activity causes photoreceptor cell death in two retinitis pigmentosa models. *J. Neurochem.* **2009**, *108*, 796–810. [CrossRef] [PubMed]



Article

Distribution of Gold Nanoparticles in the Anterior Chamber of the Eye after Intracameral Injection for Glaucoma Therapy

Tobias Sonntag^{1,†}, Franziska Froemel^{2,†}, W. Daniel Stamer³, Andreas Ohlmann⁴, Rudolf Fuchshofer² and Miriam Breunig^{1,*}

¹ Department of Pharmaceutical Technology, University of Regensburg, Universitaetsstrasse 31, 93040 Regensburg, Germany; tobias.sonntag@chemie.uni-regensburg.de

² Department of Human Anatomy and Embryology, University of Regensburg, Universitaetsstrasse 31, 93040 Regensburg, Germany; franziska.froemel@vkl.uni-regensburg.de (F.F.); rudolf.fuchshofer@vkl.uni-regensburg.de (R.F.)

³ Department of Ophthalmology, Duke University, Durham, NC 27710, USA; william.stamer@dm.duke.edu

⁴ Department of Ophthalmology, Ludwig-Maximilians-University Munich, Mathildenstrasse 8, 80336 Muenchen, Germany; andreas.ohlmann@med.uni-muenchen.de

* Correspondence: miriam.breunig@chemie.uni-regensburg.de; Tel.: +49-(0)-941-943-4828

† Both authors contributed equally.

Citation: Sonntag, T.; Froemel, F.; Stamer, W.D.; Ohlmann, A.; Fuchshofer, R.; Breunig, M. Distribution of Gold Nanoparticles in the Anterior Chamber of the Eye after Intracameral Injection for Glaucoma Therapy. *Pharmaceutics* **2021**, *13*, 901. <https://doi.org/10.3390/pharmaceutics13060901>

Academic Editors: Francisco Javier Otero-Espinar and Anxo Fernández Ferreiro

Received: 21 May 2021
Accepted: 15 June 2021
Published: 17 June 2021

Publisher's Note: MDPI stays neutral with regard to jurisdictional claims in published maps and institutional affiliations.



Copyright: © 2021 by the authors. Licensee MDPI, Basel, Switzerland. This article is an open access article distributed under the terms and conditions of the Creative Commons Attribution (CC BY) license (<https://creativecommons.org/licenses/by/4.0/>).

Abstract: In glaucoma therapy, nanoparticles (NPs) are a favorable tool for delivering drugs to the outflow tissues of the anterior chamber of the eye where disease development and progression take place. In this context, a prerequisite is an efficient enrichment of NPs in the trabecular meshwork with minimal accumulation in off-target tissues such as the cornea, lens, iris and ciliary body. We evaluated the optimal size for targeting the trabecular meshwork by using gold NPs of 5, 60, 80 and 120 nm with a bare surface (AuNPs) or coated with hyaluronic acid (HA-AuNPs). NPs were compared regarding their colloidal stability, distribution in the anterior chamber of the eye ex vivo and cellular uptake in vitro. HA-AuNPs demonstrated an exceptional colloidal stability. Even after application into porcine eyes ex vivo, the HA coating prevented an aggregation of NPs inside the trabecular meshwork. NPs with a diameter of 120 nm exhibited the highest volume-based accumulation in the trabecular meshwork. Off-target tissues in the anterior chamber demonstrated an exceptionally low gold content. Our findings are particularly important for NPs with encapsulated anti-glaucoma drugs because a higher particle volume would be accompanied by a higher drug payload.

Keywords: glaucoma; gold nanoparticles; anterior chamber; distribution; stability; intracameral injection; trabecular meshwork; hyaluronic acid

1. Introduction

With an estimated 60.5 million cases, glaucoma is one of the leading causes of irreversible blindness worldwide [1]. Primary open-angle glaucoma (POAG) is the most prevalent form of glaucomatous diseases [2]. Eye drops are applied as first-line treatment to reduce the intraocular pressure (IOP), which is the major risk factor of the disease. However, bioavailability of topically applied drugs in the anterior chamber is only about 1 to 5% [3]. Another fundamental problem is that most conventional drugs do not target the causal pathological changes occurring in the outflow tissues [4]. Here, the trabecular meshwork and Schlemm's canal are affected by an increased production of extracellular matrix and a significant stiffening of cells [4]. Therefore, it is crucial to develop new causative options to drastically improve the therapeutic outcome. Recently, new drugs have been approved that interfere with the fundamental pathological processes of POAG development, such as Rho-associated protein kinase inhibitors (e.g., netarsudil and ripasudil) [5] or nitric oxide donors (e.g., latanoprostene bunod) [6]. In addition to these small-molecule drugs, macromolecules, such as small interfering RNA (siRNA), are discussed as an innovative

alternative to intervene disease progression [7,8]. However, their high molecular weight, inherent instability and strong negative charge currently prevent nucleic acids to reach a sufficiently high bioavailability in the anterior chamber of the eye [9].

To significantly boost the availability of drugs in the outflow tissues, we and others recently proposed nanoparticles (NPs) as a delivery system to the anterior eye [10–12]. NPs are expected to follow the physiological outflow pathway of the aqueous humor, thereby reaching the trabecular meshwork and Schlemm's canal [13]. Aqueous humor is secreted by the ciliary epithelial cells and drains from the posterior to the anterior chamber. A minor part exits the eye through the uveoscleral pathway, while the major part of the aqueous humor leaves the eye through the trabecular meshwork into Schlemm's canal [14]. The outflow resistance, responsible for the IOP, is located within the juxtacanalicular tissue and the endothelium of Schlemm's canal [14]. The cells of this tissues represent the target cells of the NPs. Once arrived at the target cells, NPs have the great advantage that they allow for an efficient cellular uptake of their therapeutic freight [15]. Macromolecular drugs in particular, such as siRNA, would otherwise be highly unstable and not be able to cross cellular membranes [16]. Different types of NPs for intracameral injection have been evaluated, such as inorganic silica NPs [17] or polymer NPs like poly(lactic-co-glycolic acid) (PLGA) [10]. A critical parameter is the size of the particles as it influences their transport through the tissue and uptake into target cells [18]. However, in contrast to other tissues [19], there has been no systematic approach to determine which NP size may be optimal to maximize the amount of drug that arrives at its final destination within the anterior chamber of the eye. A detailed characterization of the specific NP features would be of utmost importance to create a specific and effective drug delivery system that targets the outflow tissues. Equally important is if the NPs are eventually distributed to off-target tissues in the anterior eye, such as the cornea, lens, iris or ciliary body.

Therefore, in this study, we systematically examined the size-dependent distribution of NPs in the anterior eye, with a particular focus on the outflow tissues after intracameral injection. Model gold NPs of different sizes of 5, 60, 80 and 120 nm were evaluated. Particles with a bare surface (AuNPs) were compared to gold NPs that were modified with hyaluronic acid (HA-AuNPs). Hyaluronic acid (HA) was chosen because it may improve the colloidal stability of the NPs and because it is a widely used excipient in ocular drug delivery [20,21]. The surface- and size-dependent distribution of the NPs after intracameral injection was examined after *ex vivo* perfusion of porcine eyes. Additionally, to evaluate the successful cellular uptake of the NPs, *in vitro* cell culture experiments were performed.

2. Materials and Methods

2.1. Materials

Spherical AuNPs with a citric acid coated surface and a size of 5, 60, 80 and 120 nm were purchased from Nanopartz (Loveland, CO, USA). Dulbecco's modified Eagle's medium (DMEM) containing 4.5 g/L glucose and 1 g/L glucose for cell culture was obtained from Merck (Darmstadt, Germany) and fetal bovine serum (FBS) was bought from Biowest (Nuaille, France). Dialysis membranes (molecular weight cut-off = 25,000 and 3500 Da) were purchased from Carl Roth (Karlsruhe, Germany) and sodium hyaluronate (HA; 13 kDa) from Lifecore Biomedicals (Chaska, Minnesota, USA). All other chemicals were purchased from Merck (Darmstadt, Germany). 3-(4,5-Dimethylthiazol-2-yl)-2,5-diphenyltetrazolium bromide (MTT) was obtained from PanReac AppliChem (Darmstadt, Germany).

2.2. Cell Culture

Primary human trabecular meshwork (hTM) cells and Schlemm's canal (SC) cells were fully characterized according to standard methods (PMIDs: 9727403, 29526795) and used until passage number 8. Primary fibroblasts were used until passage 13. All procedures for collecting human tissue were according to the Declaration of Helsinki. hTM cells, SC cells and fibroblasts were cultivated in DMEM (supplemented with 4.5 g/L glu-

cose for fibroblasts and 1 g/L glucose for hTM and SC cells) containing 10% (*v/v*) FBS, 100 units/mL penicillin and 100 µg/mL streptomycin. Immortalized human TM cells (HTM-N) were obtained from Iok-Hou Pang and Louis DeSantis (Alcon Research Laboratories, Fort Worth, TX, USA). They were cultured in DMEM high glucose (4.5 g/L) with L-glutamine (0.584 g/L) and 1 mM sodium pyruvate. Human umbilical vein endothelial cells (HUVECs) were grown in Endothelial Cell Growth Medium MV + supplements (PromoCell, Heidelberg, Germany) with 10% FBS, 100 units/mL penicillin and 100 µg/mL streptomycin.

2.3. Preparation of HA-Modified AuNPs

Preparation of thiolated HA: Thiol end-modified HA (HA-SH) was prepared by reductive amination as previously described [22]. In brief, 100 mg HA (13 kDa) and 60 mg cystamine dihydrochloride were dissolved in 10 mL 0.1 M borate buffer (pH = 8.5) containing 0.4 M NaCl and stirred for 2 h. NaBH₃CN was added to the solution for a final concentration of 200 mM and stirred at 40 °C for 5 days. Afterwards, 100 mM dithiothreitol was added and stirred again for 12 h. The resulting HA-SH was dialyzed using a dialysis membrane (MWCO = 3500 Da) against 5 L of 100 mM NaCl solution for 2 days followed by 25% ethanol for 1 day and pure water for 1 day to remove the unreacted chemicals. Finally, the product was freeze-dried for 5 days. HA-SH was characterized using an Avance 300 NMR-spectrometer (Bruker Bio Spin, Ettlingen, Germany).

Preparation of AuNPs with a hyaluronic acid surface (HA-AuNPs): Thiol-gold chemistry was used for the modification of AuNPs with HA: 248 µL HA-SH solution (1 mg/mL) was added to 2 mL AuNP dispersion and stirred for 48 h. HA-AuNPs were purified using a dialysis membrane (MWCO = 25,000) against purified water for 72 h.

2.4. Characterization of Gold NPs

Transmission electron microscopy (TEM): To evaluate the size and the presence of aggregates, all particle species were imaged using a 100 kV Zeiss Libra 120 electron microscope (Carl Zeiss AG, Oberkochen, Germany) at a magnification of 80,000×. For analysis, samples were pipetted onto carbon-coated copper grids (300 mesh; Plano, Wetzlar, Germany) and incubated for 3 min. Excess NP dispersion was removed with a filter paper. All grids were air-dried and stored in a desiccator until TEM analysis.

Hydrodynamic diameter and zeta potential: The size and zeta potential of all NP species were measured with a Malvern Zetasizer Nano ZS (Malvern, Herrenberg, Germany). All samples were measured with a 633 nm He-Ne laser at an angle of 173° backward scatter (25 °C) in 10% Dulbecco's Phosphate-Buffered Saline liquid (DPBS) using either polystyrene semi-microcuvettes (dynamic light scattering; Sarstedt, Nuembrecht, Germany) or folded capillary cells (zeta potential; Malvern, Herrenberg, Germany), respectively.

UV-Vis spectroscopy: UV-Vis spectroscopic measurements were performed with a FluoStar Omega (BMG Labtech, Ortenberg, Germany). UV-Vis spectra of all particle types were taken in DPBS ($\lambda = 400$ to 800 nm).

2.5. Colloidal Stability of Gold NPs

For stability analysis, gold NPs were prepared as used for the in vitro and ex vivo experiments. For the in vitro stability test of gold NPs, particles were dispersed in DMEM with pyruvate containing 0.35% FBS for a final gold concentration of 2750 ppb Au. For the ex vivo stability test, gold NPs were diluted with DPBS containing 5 mM glucose for a final gold concentration of 9390 ppb Au. The hydrodynamic diameter (z-average size) was measured for every particle type after 0, 0.5, 4, 6 and 20 h.

2.6. Uptake of Gold NPs in Different Cell Types In Vitro

Uptake experiments were performed using all cell types and particle species. Six-well plates were used to perform the uptake experiments. All experiments were performed at pH 7.4. First, NP dispersions in DMEM containing 0.35% fetal bovine serum were prepared

at a final gold concentration of 0, 550, 2750 and 5500 ppb. All samples were pre-incubated for 1 h to induce the formation of the protein corona. Afterwards, the NP dispersions were added to the cells. For the SC and hTM cells, the number of different concentrations was reduced due to the rarity of these cells. Sizes of 80 nm and 120 nm gold NPs with both surfaces were used at a concentration of $c(\text{Au}) = 5500$ ppb. After 6 h of incubation (37 °C, 5% CO₂), the NP dispersion was removed, and the cells were washed twice with DPBS. Afterwards, 3 mL of aqua regia was added to each well and incubated at 60 °C for 6 h. Each sample was diluted to a final volume of 10 mL with 5% nitric acid (*v/v*) and Scandium as an internal standard was added. The final concentration of the internal standard was 1 µg/mL. Inductively coupled plasma–mass spectrometry (ICP-MS) measurements were performed with an ELAN 6000 (Perkin Elmer, Waltham, MA, United States). Experiments were performed in independent triplicates.

2.7. Perfusion Experiments of Porcine Eyes Ex Vivo

Fresh enucleated porcine eyes were obtained from a local butcher. Eyes with visible damage to the cornea were excluded. After removal of extraocular tissue, the porcine eyes were submerged into the limbus in 0.89% NaCl at 35 °C. The perfusion procedure was performed as previously described [10]. Particles were diluted in DPBS containing 5 mM glucose to a final gold concentration of 9390 ppb Au. The perfusion system consisted of a perfusion chamber and a collection chamber. The infusion needle was inserted into the anterior chamber via the cornea and connected to the perfusion chamber. The needle was moved through the pupil and the tip of the needle was placed in the posterior chamber. A second needle was positioned into the anterior chamber and connected to the collection reservoir. This drain was closed during the perfusion except during the exchange periods. First, a volume of 4 mL gold NPs ($c(\text{Au}) = 9390$ ppb) was exchanged over a time period of about 10–15 min. The NP concentration for ex vivo testing was based on analytical considerations and was determined using spiked tissue samples. Higher gold concentrations resulted in a non-linear increase of the signal, while lower gold concentrations revealed results below the detection limit of the ICP-MS method. Afterwards, the collection drain was closed, and the eyes were perfused with NPs at a constant pressure of 10 mmHg for 3 h. Then, a second exchange of perfusion solution with 4 mL of a 5 mM glucose solution was performed to remove the remaining NPs. Afterwards, unbound NPs were washed away by perfusion with 5 mM glucose solution for 2 h. The anterior chamber of the eye was dissected into ciliary body, cornea, iris, lens and trabecular meshwork. All tissue samples were freeze-dried for 3 days to obtain the dry weight of each tissue sample. Experiments were performed at least in independent triplicates. For the evaluation of NP distribution by electron microscopy, small samples of cornea-scleral slices, containing the trabecular meshwork, were withheld.

2.8. Electron Microscopy Examination of the Trabecular Meshwork

Porcine eyes were obtained from the ex vivo perfusion experiments. For TEM analysis, cornea-scleral slices from one quadrant per eye were fixed in Karnovsky's solution (2.5% glutaraldehyde and 2.5% paraformaldehyde in a 0.1 M cacodylate buffer) for 24 h [23]. After rinsing in the 0.1 M cacodylate buffer, postfixation was accomplished in a mixture of 1% OsO₄ and 0.8% potassium ferrocyanide in a 0.1 M cacodylate buffer for 3.5 h at 48 °C. The eyes were then dehydrated in a graded series of ethanol and embedded in Epon (Serva, Heidelberg, Germany). Semithin sections (1 µm) were collected on uncoated glass slides and stained with methylene blue/azure II (LIT). Ultrathin sections were mounted on uncoated copper grids, stained with uranyl acetate and lead citrate, and examined on a Zeiss Libra transmission electron microscope (Carl Zeiss AG). The number of NPs in the trabecular meshwork was quantified and related to an area of 1000 µm². Particles were counted in the entire trabecular meshwork and divided into the outer and inner part of the trabecular meshwork. Particles that did not penetrate deeply into the trabecular meshwork were attributed to the outer trabecular meshwork, while particles that were

found deeper in the trabecular meshwork were assigned to the inner trabecular meshwork. Images were analyzed with ImageSP (TRS, Moorenweis, Germany) and QuPath (version 0.2.3, University of Edinburgh, Edinburgh, UK).

2.9. Gold Content of the Cells and Tissue Samples

For ICP-MS measurements, each tissue sample was subjected to a microwave digestion for 1 h at 140 to 190 °C in aqua regia. Subsequently, each sample was diluted to 10 mL with 5% (v/v) nitric acid and Scandium as an internal standard at a final concentration of 1 µg/mL was added. ICP-MS-measurements were performed with an ELAN 6000 (Perkin Elmer, Waltham, MA, USA).

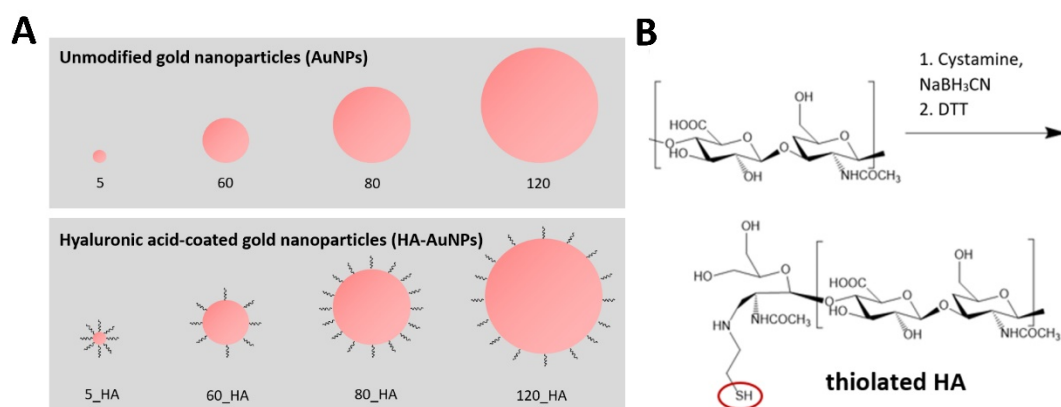
2.10. Statistical Analysis

All reported data were calculated as the mean ± standard deviation of at least three independent samples. When necessary, standard deviations were calculated according to the rules of propagation of errors. Unpaired, two-tailed Welch's t-tests for statistical analyses were performed with GraphPad PRISM 6.01 software (San Diego, CA, USA) to assess statistical significance ($p < 0.05$).

3. Results

3.1. Modification and Physicochemical Characterization of Gold NPs

In this study, commercially available gold NPs of different sizes were applied for cellular uptake studies in vitro and perfusion of porcine eyes ex vivo (Scheme 1A). In all experiments, unmodified AuNPs were compared to gold NPs carrying HA on their surface (HA-AuNPs).



Scheme 1. Schematic drawing of gold NPs and their modification. (A) For in vitro and ex vivo experiments, gold NPs with a nominal size of 5, 60, 80 and 120 nm were applied. Particles were decorated with hyaluronic acid (HA-AuNPs) to determine their physicochemical properties, cellular uptake and distribution in the anterior chamber of the eye in comparison to AuNPs with an unmodified surface. (B) For modification, end-thiol-modified HA was synthesized and coupled to the particles using thiol-gold chemistry.

In a first step, HA was immobilized on the surface of unmodified AuNPs. To this end, a terminal thiol group was introduced into HA, resulting in thiolated HA. The reaction was performed using reductive amination (Scheme 1B) [22]. ¹H-NMR-spectroscopy validated the successful conversion to thiolated HA (see Supplementary Material Figure S1). Thiolated HA was then coupled to the AuNPs via thiol-gold chemistry [24], resulting in a partially covalent chemical bond between the thiol of HA-SH and the AuNP surface.

TEM visualized the spherical shape of all particle species. The diameters of the AuNPs were determined to be 5.7 ± 3.7 nm, 60.8 ± 3.4 nm, 78.2 ± 4.6 nm and 119.0 ± 7.1 nm, respectively (Figure 1A). The diameter of the modified HA-AuNPs was similar. The HA coating did not cause any visible changes of HA-AuNPs like aggregation. As expected,

TEM did not visualize HA on the gold surface. For simplicity reasons, in the following, the AuNPs and HA-AuNPs are denoted with a size of 5, 60, 80 and 120 nm, respectively.

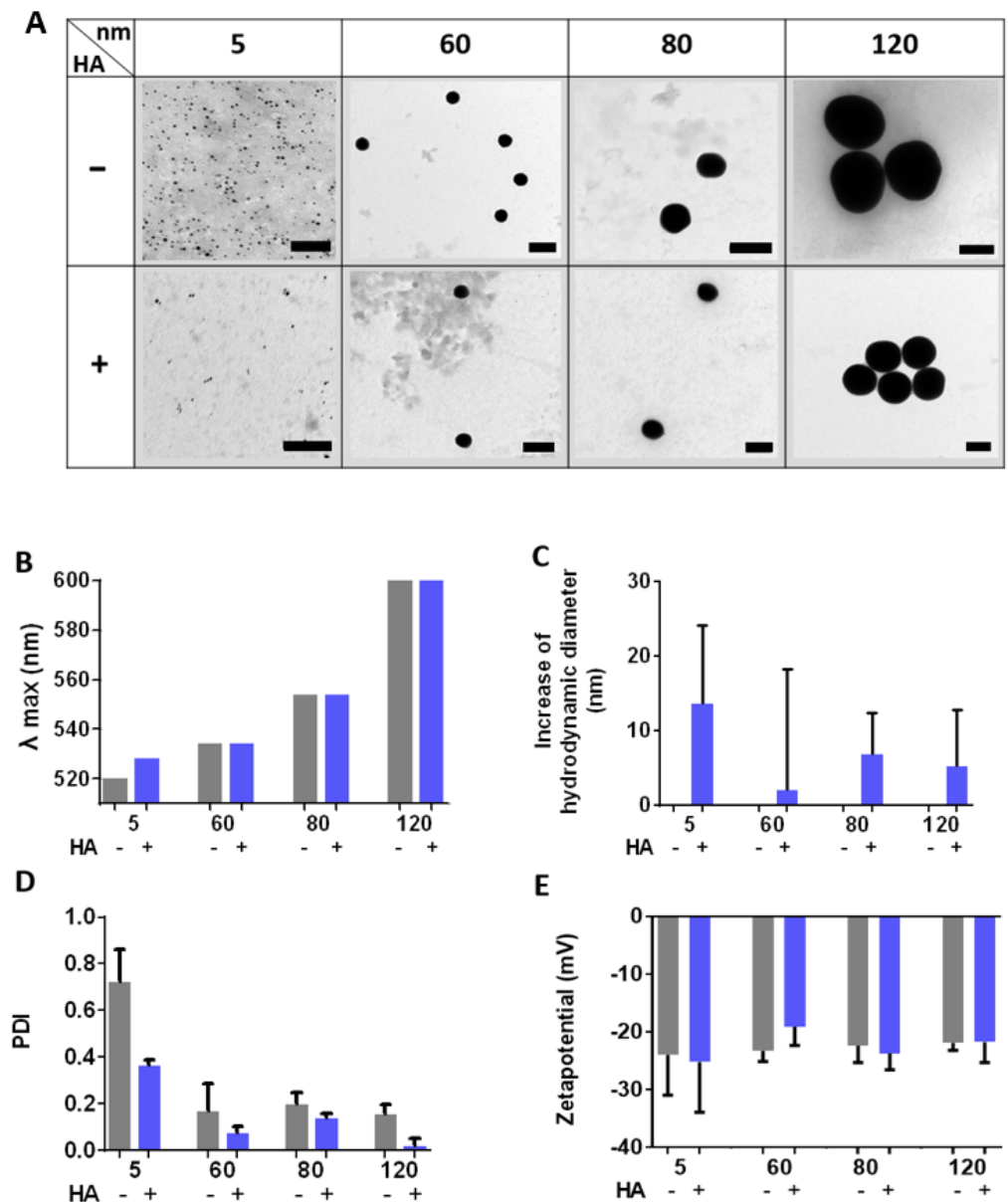


Figure 1. Physicochemical characterization of the AuNPs and HA-AuNPs. (A) TEM images demonstrated a spherical shape of all particles. The sizes of the AuNPs were 5.7 ± 3.7 nm, 60.8 ± 3.4 nm, 78.2 ± 4.6 nm and 119.0 ± 7.1 nm, respectively. The sizes of the HA-AuNPs were 5.1 ± 2.4 nm, 64.7 ± 2.5 nm, 88.6 ± 10.2 nm and 125.1 ± 9.3 nm, respectively. There was no considerable difference between the AuNPs and HA-AuNPs. The scale bar indicates 100 nm. (B) The SPR absorbance maximum of the particles showed a right shift with increasing particle size. For the AuNPs, the UV-maxima were 520 nm, 534 nm, 554 nm and 604 nm, respectively. For the HA-AuNPs, the UV-maxima were 528 nm, 534 nm, 554 nm and 606 nm. HA surface modification caused a right-shift of the UV-maximum only in case of the 5 nm AuNPs. (C) To illustrate the size increase after coating with HA, the difference in the hydrodynamic diameter between the HA-AuNPs and AuNPs was calculated. The hydrodynamic diameter differed by about 2 to 14 nm and was not statistically significantly different. (D) The polydispersity index (PDI) decreased with increasing size and after HA coating. (E) The zeta potential of all particle types was negative (−20 to −25 mV).

Gold NPs have a characteristic surface plasmon resonance (SPR) absorbance in the visible spectrum depending on their size and dielectric constant of the surrounding medium [25]. As expected, the SPR peak shifted towards larger wavelengths with increasing particle size for both AuNPs and HA-AuNPs (Figure 1B). For 5 nm AuNPs, also a shift in the SPR peak from 520 to 528 nm was determined after coating, indicating a successful deposition of HA. For other particle sizes, a shift after coating with HA was not detectable.

To verify the HA coating, the hydrodynamic diameter of the particles was determined. Values after and before coating were subtracted and expressed as size increase. As expected, the HA coating led to a slight size increase between 2 and 14 nm (Figure 1C). It seemed that particularly the 5 nm particles showed a larger size increase after coating. The polydispersity index (PDI) of the NPs decreased with increasing size (Figure 1D), which means that the size distribution of the particles became narrower. In addition, HA-AuNPs had a lower PDI compared to AuNPs. The surface zeta potential of all particle species was around -20 to -25 mV (Figure 1E).

3.2. Colloidal Stability of Gold NPs

Another important factor for further application is the stability of the NPs in physiological media because aggregation can significantly alter the physicochemical properties. To assess the colloidal stability, AuNPs and HA-AuNPs were incubated in cell culture or perfusion medium as it will be used subsequently either for in vitro or ex vivo studies, respectively. Then, the hydrodynamic diameter of the particles was monitored over time (Figure 2). In cell culture medium, HA-AuNPs did not show any significant change in the hydrodynamic diameter, even after 20 h of incubation, while the AuNPs showed a tremendous increase in size, indicating the presence of large aggregates (Figure 2A). In contrast, in the perfusion medium, there was no discernable difference between the AuNPs and HA-AuNPs (Figure 2B). Instead, both particle species demonstrated excellent colloidal stability in the perfusion medium with the exception of 5 nm AuNPs. The enormous size increase of 5 nm AuNPs indicated the presence of larger aggregates. To corroborate the higher colloidal stability of the HA-AuNPs, the protein adsorption on the NP surface in serum containing medium was investigated by using SDS-PAGE. HA-AuNPs revealed a significantly lower protein adsorption compared to AuNPs (see Supplementary Material Figure S2).

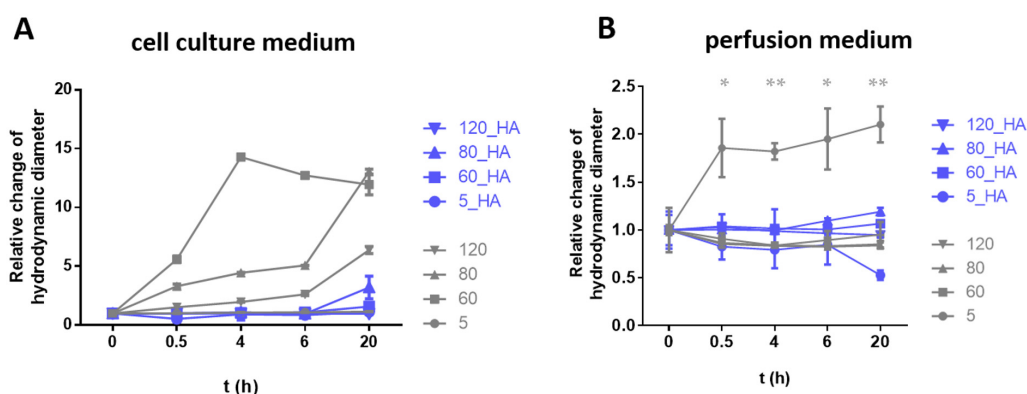


Figure 2. Colloidal stability of NPs in cell culture and perfusion media. The stability of AuNPs (grey lines) and HA-AuNPs (blue lines) was tested in cell culture medium (A) and in perfusion medium (B) over a time period of 20 h. The hydrodynamic diameter after certain time points was related to the initial hydrodynamic diameter ($t = 0$ h) and reported as the relative hydrodynamic diameter. Measurements were taken after 0, 0.5, 4, 6 and 20 h. AuNPs showed a significant increase in size after incubation in the cell culture medium. HA-AuNPs did not show an increase in size, indicating a higher stability in the cell culture medium. In perfusion medium, none of the particles showed a significant increase in size, indicating a sufficient stability. An exception was the 5 nm AuNPs. Statistically significant differences between 5 nm AuNPs and 5 nm HA-AuNPs are denoted by * or ** ($p < 0.05$ or $p < 0.01$, respectively).

3.3. Perfusion of Porcine Eyes with Gold NPs Ex Vivo

Ex vivo perfusion of porcine eyes was performed to determine the distribution of gold NPs in their anterior chambers. A total of 6 h after injection of the gold NPs, the anterior chamber was dissected and the ciliary body, cornea, iris, lens and trabecular meshwork were prepared. The gold content of each tissue sample was determined by ICP-MS and related to the dry weight of the tissue (Figure 3). A general trend was that with increasing particle size a higher gold content was measured. The gold content directly correlates to the NPs' volume. This means that with an increasing size of the applied gold NPs, the overall particle volume in the tissue increased. An exception was the 5 nm AuNPs. Within one particle size and surface modification, the gold content was particularly pronounced in the trabecular meshwork and higher than in other tissues such as the cornea, iris, lens and ciliary body. In the cornea and lens, almost no gold was detected. These observations were true for all particle sizes of AuNPs and HA-AuNPs.

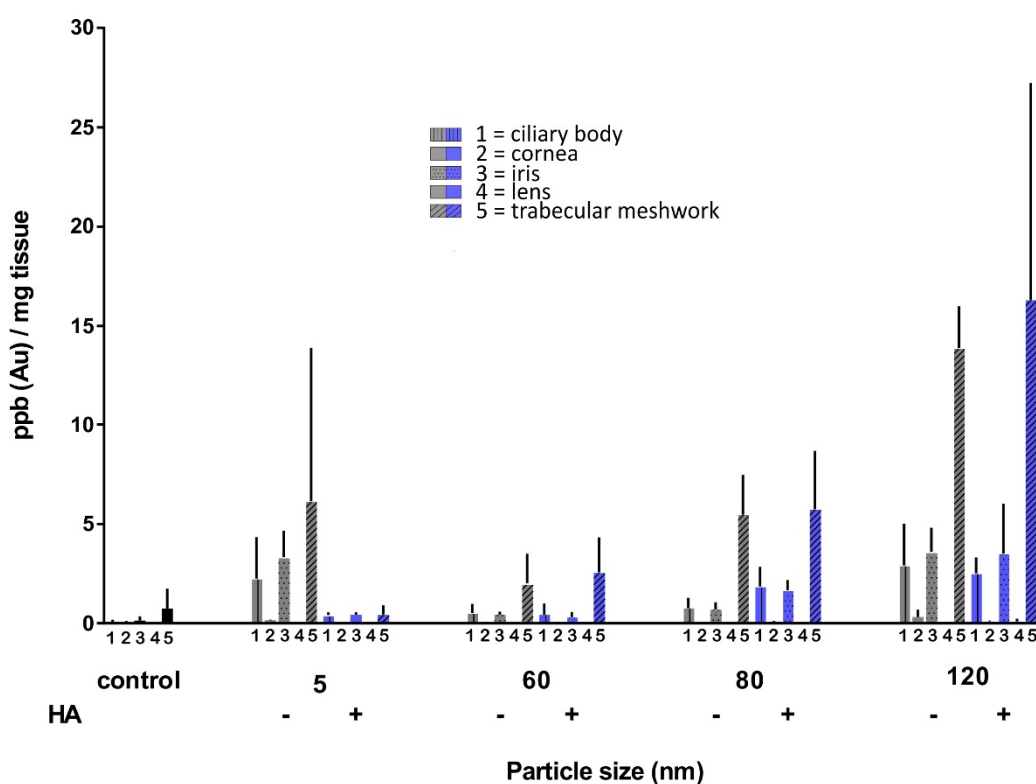


Figure 3. Perfusion of porcine eyes with gold NPs ex vivo. Freshly enucleated porcine eyes were used for ex vivo perfusion. Perfusion was performed with 5, 60, 80 and 120 nm AuNPs (grey bars) and HA-AuNPs (blue bars), respectively. The applied particle concentrations were normalized to a total gold concentration of 9390 ppb. Afterwards, the eyes were dissected into the ciliary body (1), cornea (2), iris (3), lens (4) and trabecular meshwork (5). Each tissue sample was dried, weighed, dissolved in aqua regia and analyzed separately. The amount of gold in parts per billion per mg tissue was analyzed by using ICP-MS. Control experiments (black bars) were conducted with perfusion medium without any gold NPs.

Because the trabecular meshwork is of particular interest, we had a closer look and directly compared the gold amount after application of the different particle types (Figure 4A). It was even more obvious that an increasing size led to a significantly higher gold content. Again, the 5 nm AuNPs did not follow this pattern. There was no statistically significant difference between the AuNPs and HA-AuNPs. Having a look at the number instead of the volume of gold NPs in the trabecular meshwork, the trend was vice versa. Then, the number of particles decreased with increasing particle size (Figure 4B). Comparing Figure 4A,B one must keep in mind that even if a much lower number of larger particles was delivered to the trabecular meshwork, their overall particle volume was much higher.

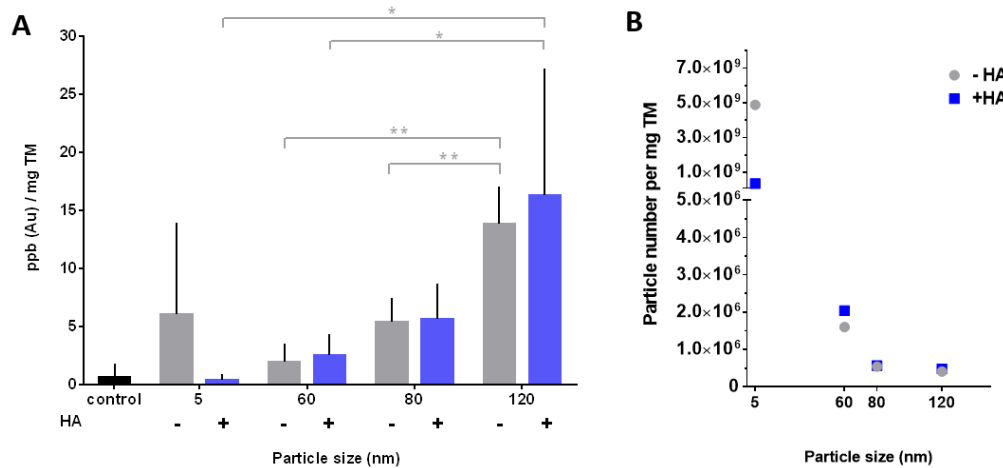


Figure 4. Gold content and the particle number in the trabecular meshwork (TM) after ex vivo perfusion with gold NPs. (A) The amount of gold per mg tissue in the trabecular meshwork was analyzed using the data from Figure 3. Grey bars represent the trabecular meshwork samples perfused with AuNPs, and blue bars represent the samples perfused with HA-AuNPs. The control is shown in the black bar. Larger particles led to a significantly higher gold content in the trabecular meshwork than smaller particles, except for the 5 nm AuNPs. Statistically significant differences are denoted by * or ** ($p < 0.05$ or $p < 0.01$, respectively). (B) The gold content per mg trabecular meshwork was calculated to obtain the particle number per mg trabecular meshwork. The smallest gold NPs showed the highest number of incorporated particles, but larger particles reflect the higher overall particle volume.

3.4. Distribution Pattern of Gold NPs in the Outflow Tissue

Thereafter, the distribution of 60 and 120 HA-AuNPs within the trabecular meshwork was carefully investigated by TEM (Figure 5). Both particle species showed an extracellular and intracellular distribution pattern. Extracellular NPs were detected within the extracellular matrix (Figure 5 upper left panel) and in the so called “open spaces” of the fluid egress pathways (Figure 5 upper right panel). Intracellular NPs were only observed in trabecular meshwork cells, but not in endothelial cells of the aqueous plexus. The porcine aqueous plexus is the anatomical correlate to the human Schlemm’s canal.

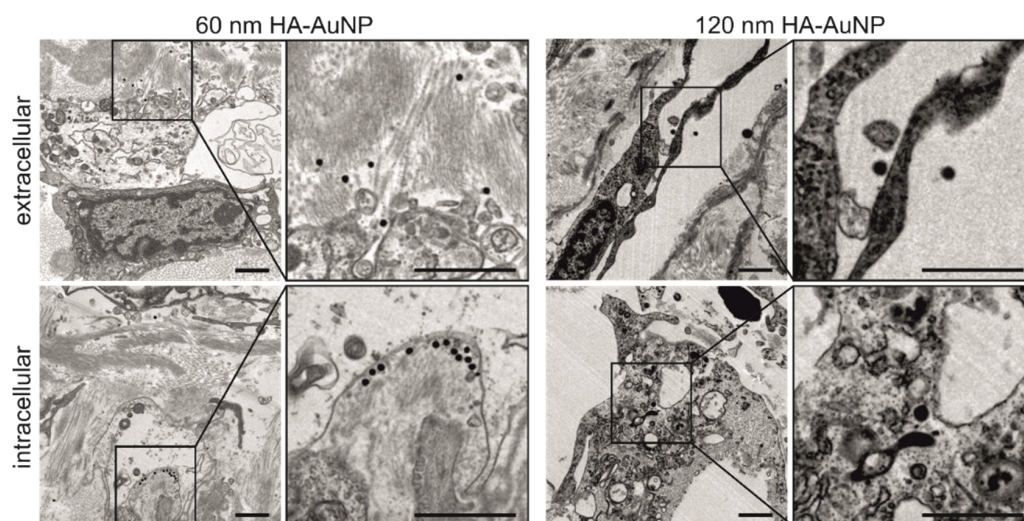


Figure 5. NP distribution within the trabecular meshwork after ex vivo perfusion with gold NPs. Both the 60 and 120 nm HA-AuNPs were located within the trabecular meshwork. Extracellular NPs were found in the extracellular matrix (**upper panel, overview image left**) and in the fluid egress pathway (**upper panel, magnification image right**). Intracellular NPs were detected in trabecular meshwork cells. Right-hand images are enlargements of the indicated areas of the left-hand images; scale bars represent 1 μm .

The quantification of the NPs showed a uniform distribution in the entire trabecular meshwork (Table 1). The comparison of distribution in the different regions revealed no significant differences between both particle sizes. In addition, both NP sizes were found intracellular in trabecular meshwork cells, in a similar amount (Figure 5). A difference between both particle sizes was that the 120 nm HA-AuNPs were rather taken up by cells in the outer trabecular meshwork, while the 60 nm HA-AuNPs were also taken up by cells in the inner trabecular meshwork. An interesting observation was that nearly all HA-AuNPs remained single in the tissue and did not aggregate (Table 1 and Supplementary Material Figure S3).

Table 1. Quantitative evaluation of distribution of 60 or 120 nm HA-AuNPs in TEM images. Three independent experiments were conducted. TM = trabecular meshwork.

Criteria	60 nm	120 nm	Statistics
particles per 1000 μm^2			
–of total TM (\pm SEM)	1.18 \pm 0.75	1.71 \pm 0.62	$p = 0.61$
–of outer TM (\pm SEM)	1.55 \pm 1.12	1.05 \pm 0.61	$p = 0.66$
–of inner TM (\pm SEM)	1.02 \pm 0.14	2.12 \pm 0.87	$p = 0.37$
aggregated NPs	0 of 125	2 of 73	

3.5. Cellular Uptake of Gold NPs In Vitro

To test if a certain gold NP size is also preferably taken up by their target cells, we performed cellular uptake studies. Cultured cells from the trabecular meshwork and Schlemm’s canal were tested (Table 2). Due to its convoluted structure, it was technically not possible to isolate the aqueous plexus after ex vivo perfusion. Nevertheless, we included human Schlemm’s canal cells for in vitro studies due to their importance for glaucoma development and progression [26]. HTM-N cells were used as a trabecular meshwork cell line. In addition, primary hTM cells from two different donors were used. According to the literature, human umbilical vein endothelial cells (HUVECs) were used as surrogate for Schlemm’s canal cells [27,28]. In addition, primary human cells of the Schlemm’s canal (SC) from two different donors were applied. Last but not least, primary human fibroblasts served as a disease model for glaucomatous cells due to the fact that cells in the trabecular meshwork increasingly acquire the phenotype of contractile myofibroblasts during glaucoma development [14].

Table 2. Cell types used for the cellular uptake of NPs in vitro.

Tissue/Condition	Immortalized Cell Lines	Primary Cells
trabecular meshwork	HTM-N	hTM (no. 134 and 136)
endothelial cells	–	SC (no. 74 and 79) HUVEC
disease model	–	fibroblasts

The four different sizes of gold NPs were added to the cells at three different concentrations for 6 h. In the case of primary cells of the trabecular meshwork and Schlemm’s canal, only 80 and 120 nm gold NPs at the highest concentration were evaluated. The cellular gold content was measured by using ICP-MS (Figure 6). The gold content correlated again to the particle volume. In the trabecular meshwork cell line, the gold content increased with the size and the concentration of the NPs for both AuNPs and HA-AuNPs (Figure 6A). In hTM cells, this trend was not as clear (Figure 6B,C). In HUVECs that served as a surrogate for cells of the Schlemm’s canal, the cellular gold content increased with the size and concentration of AuNPs, but not in the case of HA-AuNPs (Figure 6D). In contrast, when using primary SC cells, the cellular gold content increased with the size irrespective of the surface modification (Figure 6E,F). The fibroblast also nicely followed the pattern of a higher gold content of the cells with increasing particle size and concentration (Figure 6G).

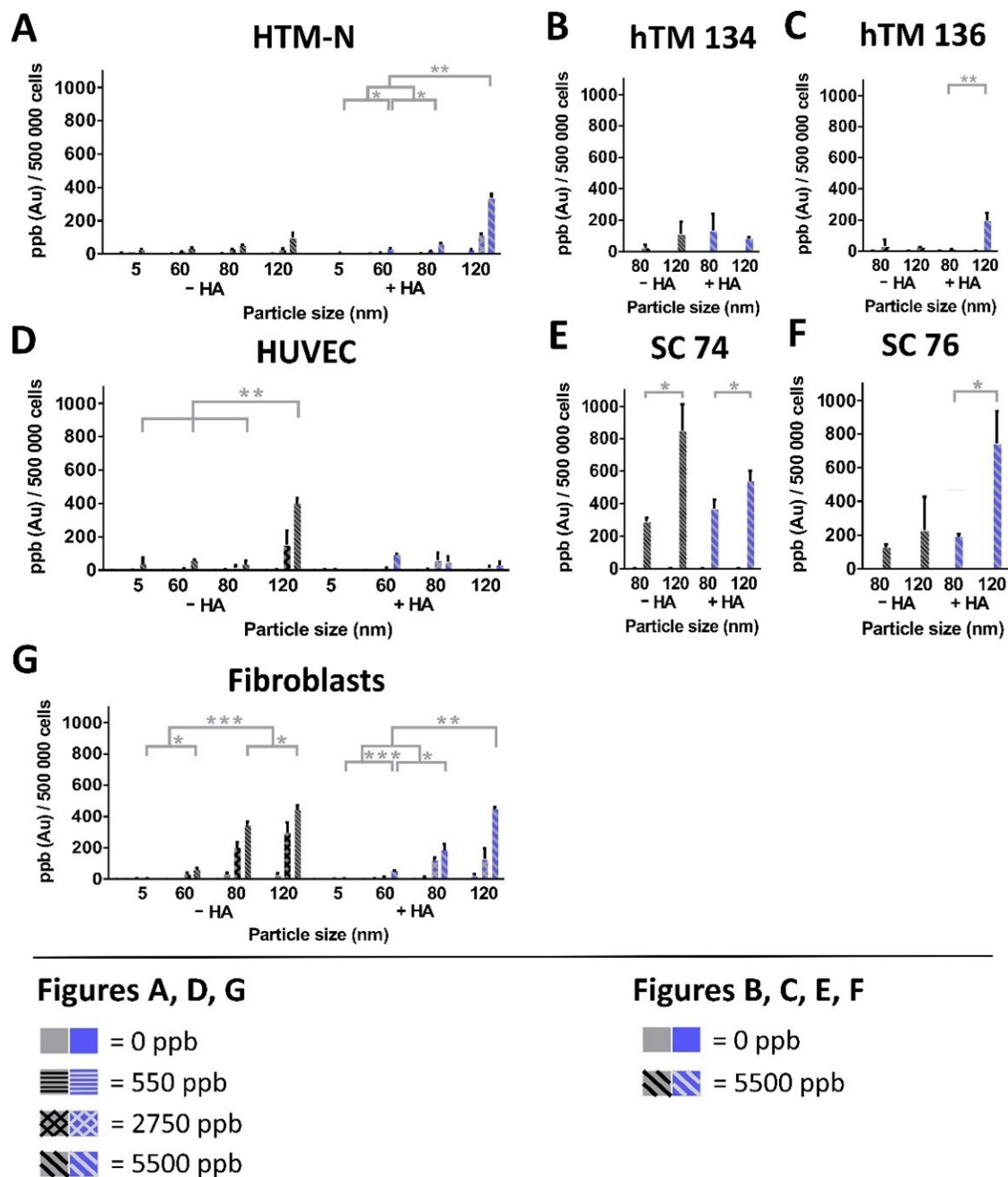


Figure 6. Uptake of AuNPs and HA-AuNPs into different cell types. Different cell types were used to determine the amount of uptake of AuNPs versus HA-AuNPs. Grey bars represent the AuNPs, and blue bars represent the HA-AuNPs. For HTM-N cells, HUVECs and fibroblasts (A,D,G), three different NP concentrations were applied (550, 2750 and 5500 ppb). For primary hTM and SC cells (B,C,E,F), only the highest NP concentration was evaluated (5500 ppb). Larger particles seemed to increase the uptake of gold. (A) For HTM-N cells, the gold content increased with the NP concentration and the uptake of HA-AuNPs was tendentially higher compared to AuNPs. (B) Primary hTM134 cells did not exhibit any significant tendency between the different particle species. (C) Primary hTM136 cells demonstrated a higher uptake for the 120 nm HA-AuNPs. (D) HUVEC cells showed a lower uptake of HA-AuNPs compared to AuNPs. The 120 nm AuNPs were taken up significantly better than smaller AuNPs. (E) Primary SC74 cells displayed higher uptake rates for 120 nm AuNPs or HA-AuNPs, compared to the corresponding 80 nm particles, respectively. (F) Primary SC79 cells showed a higher uptake of 120 nm HA-AuNPs compared to 80 nm HA-AuNPs. (G) Fibroblasts featured a tendency to have larger particles for both surface modifications and several particle sizes. Statistically significant differences are denoted by *, ** or *** ($p < 0.05$, $p < 0.01$ or $p < 0.001$, respectively).

Finally, the safety of the NPs is of utmost importance for possible therapeutic application. Therefore, the toxicity of the NPs was evaluated in an MTT assay and clearly demonstrated no significant adverse effects for all applied particle types (see Supplementary Material Figure S4).

4. Discussion

Glaucoma is a leading cause of acquired blindness and is linked to pathologic changes in the trabecular meshwork and Schlemm's canal [29]. For successful glaucoma treatment and to avoid adverse events, it will be of utmost importance to deliver therapeutic agents effectively and selectively to the trabecular meshwork. NPs may be an optimal tool for drug delivery to the anterior eye [30], particularly when the delivery of high molecular weight drugs is envisioned [10,17]. Because it is not known which NP size is optimal for this purpose, in this study, we systematically analyzed the uptake and distribution of AuNPs of different surface modifications (unmodified vs. hyaluronic acid) and sizes (5, 60, 80 and 120 nm) in the anterior chamber of the eye.

NPs for drug delivery to the anterior eye can be composed of different materials. As yet, fluorescently labelled PLGA NPs [10] and functionalized silica NPs [17] have been applied for intracameral injection. Polymeric NPs have the advantage that they can be tailored to be biodegradable [31]. In contrast, inorganic NPs are usually not degradable [32]. We hypothesize that NPs that leave the anterior chamber will enter the venous circulation via Schlemm's canal. Depending on their size, the NPs will then be eliminated from the circulation via the kidney or by the mononuclear phagocyte system [33]. We chose gold NPs as a model in this study because of several advantages, including their easy surface modification using thiol-gold chemistry, availability in different sizes, high biocompatibility with cells and tissues [34] and low detection limits using ICP-MS. Spherical and not rod-shaped AuNPs were used in this study because the results may then be better transferred to lipid or polymer NPs that also have a spherical shape. Different methods were chosen for the characterization of the particles because each one provided different information about their physico-chemical properties. The increase in the particle size was nicely corroborated by UV-Vis spectroscopy, which revealed a right shift of the SPR maximum with increasing particle size. This right shift was expected due to the fact that optical absorption and scattering is dependent on particle size and is described theoretically by Mie theory [25]. Because the SPR maximum also changes with the dielectric constant of the surrounding medium, one could have expected a difference between the coated and uncoated particles of the same size. However, this was only possible for the 5 nm particles. For other particle sizes, this difference was not detected, most likely because the SPR peak broadens with increasing particle size and then the small differences between AuNPs and HA-AuNPs cannot be detected reliably anymore. However, with the help of dynamic light scattering, the expected size increase of AuNPs after coating with HA was clearly demonstrated. At the same time, the PDI of the gold NPs was reduced after coating with HA, indicating a separation of the particles due to shielding effects [20]. 60, 80 and 120 nm particles had a PDI of 0.2 or even lower, accounting for a narrow size distribution of the particles, especially after HA coating. The PDI is calculated as the square of the absolute standard deviation divided by the mean particle diameter. Consequently, size variations cause a disproportionately higher PDI for smaller particles. The lower PDI of the HA-AuNPs might indicate a protective effect of HA against aggregation. The surface zeta potential is an important property of NPs as it influences unspecific binding [35]. It was negative for both surfaces of the gold NPs, which was expected because both citrate ions on unmodified AuNPs and HA carry negative charges.

The colloidal stability is of utmost importance for NP application. A lack of colloidal stability leads to aggregation of NPs. Consequently, decisive properties of the particles, such as cellular uptake, toxicity or biodistribution, can be altered significantly [36]. The consequence of protein adsorption on the surface of NPs cannot be easily predicted because it may influence the colloidal stability in either a positive or negative manner [37]. In

contrast, a high ionic strength of the surrounding media usually negatively influences the colloidal stability [38]. After incubation in cell culture medium containing 0.35% serum, which is equal to the concentration of proteins in the aqueous humor [39], HA-AuNPs did not show any sign of aggregation. In contrast, AuNPs did not withstand these conditions and showed a severe tendency towards aggregation. This indicates a stabilizing effect of HA and is also well known for polyethylene glycol (PEG)-functionalized gold NPs [40]. In contrast, in perfusion medium, there was only a significant increase in the 5 nm AuNPs detectable. This can be attributed to the high specific surface area of these small particles. All other particles were more or less stable, irrespective of their size and surface modification. Generally, bare AuNPs are more stable in phosphate buffer than in serum-containing culture medium [38]. This finding was confirmed by our study, where the unmodified AuNPs demonstrated a higher stability in the perfusion buffer than in the cell culture medium. In addition, the adsorbed proteins to both particle types were semi-quantitatively compared by SDS-PAGE. This brought further evidence for the shielding effects of HA, and because it was clearly demonstrated that the HA coating reduced the protein adsorption significantly on the surface of the gold NPs.

The perfusion of porcine eyes was performed to study the optimal NP size for targeting the trabecular meshwork. The results clearly illustrate that larger particles deliver a much higher overall particle volume to the trabecular meshwork. All other tissues of the anterior eye showed lower concentrations of gold. Particularly, the cornea and the lens demonstrated exceptionally low gold concentrations and were comparable to the control. This distribution pattern is beneficial for targeting the trabecular meshwork as it minimizes the risk of off target effects, especially to the cornea, which is a natural anatomical barrier and is therefore not expected to take up NPs at a significant level [41]. Studies assessing the ocular biodistribution of topically applied polymeric NPs revealed a relatively low distribution to the iris and the cornea [42]. In addition, if too many NPs end up in the cornea or the lens, it may interfere with vision due to scattering effects [25]. Further *in vivo* studies will be necessary to confirm and substantiate the results of this study. A potential distribution of NPs from the anterior chamber to the retina and/or vitreous body seems highly unlikely due to the physiology of the aqueous humor dynamics [43] and was therefore not investigated in this study. In fact, the velocity of posterior fluid movement is negligible compared to the aqueous humor flow in the anterior chamber [44]. Therefore, drugs applied to the anterior chamber are primarily eliminated through the aqueous humor [45,46]. For targeting the trabecular meshwork, larger particles regardless of their surface showed favorable properties. Unfortunately, unmodified 5 nm AuNPs were prone to aggregation and therefore acted like larger particles. The uncontrolled tendency towards aggregation makes them useless for drug delivery purposes. Even though there was no difference between the AuNPs and HA-AuNPs for 60, 80 and 120 nm particles, one would choose HA-AuNPs for therapeutic application due to their significantly higher colloidal stability. Electron microscopy of tissue samples corroborated that HA coating is beneficial because even in the trabecular meshwork the particles remained single and did not aggregate. In our *in vitro* and *ex vivo* experiments, the measured gold concentration directly correlated to the particle volume. Consequently, larger gold NPs lead to a higher overall particle volume delivered to the trabecular meshwork. Generally, active pharmaceutical ingredients can either be attached to the surface of NPs or encapsulated into the particles' matrix. Our findings are particularly important for NPs with encapsulated drugs because a higher particle volume offers much more space for the drug and allows for a much higher drug content per particle. Consequently, even if fewer larger particles have arrived at the target tissue, they would lead to an overall higher drug amount.

The *ex vivo* perfusion experiments confirmed that the NPs preferentially arrived in the target tissue in a high amount and that the 120 nm particles showed a slight superiority compared to the smaller sizes. Many drugs, such as siRNA, have their place of action inside cells. An intracellular location of the NPs after perfusion was confirmed by TEM. Once arrived at the target cells, NPs have the great advantage to allow for an efficient cellular

uptake of their therapeutic freight [8]. Macromolecular drugs in particular, such as siRNA, would otherwise be highly unstable and not be able to cross cellular membranes [9]. In a next step, we substantiated and quantified the cellular uptake *in vitro*. In addition to trabecular meshwork cells, we also chose cells of Schlemm's canal, because these cells are equally important for disease development and progression [47]. The trend of a higher uptake of larger particles was demonstrated in most, but not all cell types. It was very remarkable that primary cells showed an efficient uptake of NPs and that particularly Schlemm's cells showed the highest uptake rate amongst the primary cell types, which is of utmost importance for drug delivery. Another fact of importance was the favorable uptake of gold NPs into fibroblasts. Trabecular meshwork cells show a transformation to myofibroblasts in the course of the disease [14]. According to our experiments, this transformation will not impede NP uptake. However, one must keep in mind that at late-stage glaucoma there is a significant loss of trabecular meshwork cells [48]. For application of NPs that are envisioned to target the outflow tissues, two options are conceivable. The NPs are injected into the anterior chamber of the eye, thereby avoiding the significant barrier of the cornea. Regarding this application route, there is only limited literature and clinical experience so far compared to intravitreal injections [4,49]. However, because drug delivery devices for intracameral injection are gaining increasing attention [50,51], guidelines on intracameral injection techniques have been provided recently [49]. Another limitation is that frequent application intervals would be necessary because the aqueous humor has a rapid turnover [4]. To cope with this shortcoming, a depot formulation containing the NPs would be ideal in the long run. Such a depot would be applied intraocularly, for example, into the vitreous body [52]. After release from the depot, the NPs would reach the anterior chamber and be distributed to the trabecular meshwork. Such a formulation would be more patient friendly and most likely associated with a much higher compliance because it would reduce the application frequency dramatically. Another location for a depot formulation would be the supraciliary space or the anterior chamber [4].

5. Conclusions

We successfully investigated the relevance of NP size for targeting the trabecular meshwork after intracameral injection *ex vivo*. Particles with a diameter of 120 nm exhibited the highest volume-based accumulation rate in the trabecular meshwork, while smaller particles were superior regarding the delivered particle number. This fact is useful for drug delivery as it enables particles to selectively target the trabecular meshwork by choosing the optimal size and thereby reducing off-target effects. Our results additionally suggest that NPs of about 120 nm can be a useful tool for glaucoma therapy due to their higher drug encapsulation capacity. Consequently, a lower number of particles will be needed to elicit a therapeutic effect.

Supplementary Materials: The following are available online at <https://www.mdpi.com/article/10.3390/pharmaceutics13060901/s1>, Figure S1: ¹H-NMR-spectra of hyaluronic acid and thiolated hyaluronic acid in comparison, Figure S2: Determination of protein adsorption by using SDS-PAGE, Figure S3: Aggregated HA-AuNPs, Figure S4: MTT-Assay to determine the cell toxicity.

Author Contributions: T.S. and F.F. are candidates from the University of Regensburg; M.B. and R.F. are professors at the University of Regensburg; A.O. is a group leader at the Ludwig-Maximilians-University Munich; and W.D.S. is professor at Duke University. Conceptualization, M.B.; particle preparation, analytics and *in vitro*-studies, T.S., M.B.; perfusion of porcine eyes and TEM analysis of outflow tissue, F.F., R.F.; resources, M.B., R.F., A.O. and W.D.S.; data curation, T.S. and F.F.; writing—original draft preparation, T.S. and M.B.; writing—review and editing, R.F., M.B., critical revision for important intellectual content, A.O., W.D.S., supervision, M.B. and R.F.; project administration, M.B., R.F.; funding acquisition, R.F., M.B. All authors have read and agreed to the published version of the manuscript.

Funding: This research was supported by Deutsche Forschungsgemeinschaft (DFG; Grant BR3566/3-1 and FU734/4-1).

Institutional Review Board Statement: Not applicable.

Informed Consent Statement: Not applicable.

Data Availability Statement: Not applicable.

Acknowledgments: The authors thank Labor Kneissler GmbH & Co. KG for support with microwave digestions. Furthermore, the authors thank Renate Liebl, Margit Schimmel, Angelika Pach and Joachim Rewitzer for excellent technical support.

Conflicts of Interest: The authors declare no conflict of interest.

References




1. Tham, Y.-C.; Li, X.; Wong, T.Y.; Quigley, H.A.; Aung, T.; Cheng, C.-Y. Global Prevalence of Glaucoma and Projections of Glaucoma Burden through 2040. *Ophthalmology* **2014**, *121*, 2081–2090. [CrossRef]
2. Kapetanakis, V.V.; Chan, M.P.Y.; Foster, P.J.; Cook, D.G.; Owen, C.G.; Rudnicka, A.R. Global variations and time trends in the prevalence of primary open angle glaucoma (POAG): A systematic review and meta-analysis. *Br. J. Ophthalmol.* **2015**, *100*, 86–93. [CrossRef]
3. Jünemann, A.G.; Chorągiewicz, T.; Ozimek, M.; Grieb, P.; Rejdak, R. Drug bioavailability from topically applied ocular drops. Does drop size matter? *Ophthalmol. J.* **2016**, *1*, 29–35. [CrossRef]
4. Mietzner, R.; Breunig, M. Causative glaucoma treatment: Promising targets and delivery systems. *Drug Discov. Today* **2019**, *24*, 1606–1613. [CrossRef]
5. Honjo, M.; Tanihara, H. Impact of the clinical use of ROCK inhibitor on the pathogenesis and treatment of glaucoma. *Jpn. J. Ophthalmol.* **2018**, *62*, 109–126. [CrossRef] [PubMed]
6. Fingeret, M.; Gaddie, I.B.; Bloomstein, M. Latanoprostene bunod ophthalmic solution 0.024%: A new treatment option for open-angle glaucoma and ocular hypertension. *Clin. Exp. Optom.* **2019**, *102*, 541–550. [CrossRef] [PubMed]
7. Guter, M. Layer-By-Layer Nanoparticles for Glaucoma Therapy. Ph.D. Thesis, Universität Regensburg, Regensburg, Germany, 2018.
8. Cassidy, P.S.; Kelly, R.A.; Reina-Torres, E.; Sherwood, J.M.; Humphries, M.M.; Kiang, A.-S.; Farrar, G.J.; O'Brien, C.; Campbell, M.; Stamer, W.D.; et al. siRNA targeting Schlemm's canal endothelial tight junctions enhances outflow facility and reduces IOP in a steroid-induced OHT rodent model. *Mol. Ther. Methods Clin. Dev.* **2021**, *20*, 86–94. [CrossRef]
9. Baran-Rachwalska, P.; Torabi-Pour, N.; Sutera, F.M.; Ahmed, M.; Thomas, K.; Nesbit, M.A.; Welsh, M.; Moore, C.T.; Saffie-Siebert, S.R. Topical siRNA delivery to the cornea and anterior eye by hybrid silicon-lipid nanoparticles. *J. Control. Release* **2020**, *326*, 192–202. [CrossRef] [PubMed]
10. Dillinger, A.E.; Guter, M.; Froemel, F.; Weber, G.R.; Perkumas, K.; Stamer, W.D.; Ohlmann, A.; Fuchshofer, R.; Breunig, M. Intracameral Delivery of Layer-by-Layer Coated siRNA Nanoparticles for Glaucoma Therapy. *Small* **2018**, *14*, e1803239. [CrossRef] [PubMed]
11. Janagam, D.R.; Wu, L.; Lowe, T.L. Nanoparticles for drug delivery to the anterior segment of the eye. *Adv. Drug Deliv. Rev.* **2017**, *122*, 31–64. [CrossRef]
12. Diebold, Y.; Calonge, M. Applications of nanoparticles in ophthalmology. *Prog. Retin. Eye Res.* **2010**, *29*, 596–609. [CrossRef]
13. Breunig, M.; Babl, S.; Liebl, R.; Guter, M. Layer-by-layer coated nanoparticles for glaucoma therapy: Focusing on the transport and cellular uptake in the trabecular meshwork. *Acta Ophthalmol.* **2016**, *94*, 94. [CrossRef]
14. Braunger, B.M.; Fuchshofer, R.; Tamm, E.R. The aqueous humor outflow pathways in glaucoma: A unifying concept of disease mechanisms and causative treatment. *Eur. J. Pharm. Biopharm.* **2015**, *95*, 173–181. [CrossRef]
15. Tatiparti, K.; Sau, S.; Kashaw, S.K.; Iyer, A.K. siRNA Delivery Strategies: A Comprehensive Review of Recent Developments. *Nanomaterials* **2017**, *7*, 77. [CrossRef]
16. Dowdy, S.F. Overcoming cellular barriers for RNA therapeutics. *Nat. Biotechnol.* **2017**, *35*, 222–229. [CrossRef]
17. Liao, Y.-T.; Lee, C.-H.; Chen, S.-T.; Lai, J.-Y.; Wu, K.C.-W. Gelatin-functionalized mesoporous silica nanoparticles with sustained release properties for intracameral pharmacotherapy of glaucoma. *J. Mater. Chem. B* **2017**, *5*, 7008–7013. [CrossRef]
18. Jiang, W.; Kim, B.Y.; Rutka, J.T.; Chan, W.C.W. Nanoparticle-mediated cellular response is size-dependent. *Nat. Nanotechnol.* **2008**, *3*, 145–150. [CrossRef]
19. Tabish, T.A.; Dey, P.; Mosca, S.; Salimi, M.; Palombo, F.; Matousek, P.; Stone, N. Smart Gold Nanostructures for Light Mediated Cancer Theranostics: Combining Optical Diagnostics with Photothermal Therapy. *Adv. Sci.* **2020**, *7*, 1903441. [CrossRef]
20. Apaolaza, P.; Busch, M.; Asin-Prieto, E.; Peynshaert, K.; Rathod, R.; Remaut, K.; Dünker, N.; Göpferich, A. Hyaluronic acid coating of gold nanoparticles for intraocular drug delivery: Evaluation of the surface properties and effect on their distribution. *Exp. Eye Res.* **2020**, *198*, 108151. [CrossRef]
21. Guter, M.; Breunig, M. Hyaluronan as a promising excipient for ocular drug delivery. *Eur. J. Pharm. Biopharm.* **2017**, *113*, 34–49. [CrossRef]

22. Lee, M.-Y.; Yang, J.-A.; Jung, H.S.; Beack, S.; Choi, J.E.; Hur, W.; Koo, H.; Kim, K.; Yoon, S.K.; Hahn, S.K. Hyaluronic Acid–Gold Nanoparticle/Interferon α Complex for Targeted Treatment of Hepatitis C Virus Infection. *ACS Nano* **2012**, *6*, 9522–9531. [CrossRef]
23. Karnovsky, M.J. A formaldehyde-glutaraldehyde fixative of high osmolality for use in electron-microscopy. *J. Cell Biol.* **1965**, *27*, 137–138.
24. Wang, W.; Wei, Q.-Q.; Wang, J.; Wang, B.-C.; Zhang, S.-H.; Yuan, Z. Role of thiol-containing polyethylene glycol (thiol-PEG) in the modification process of gold nanoparticles (AuNPs): Stabilizer or coagulant? *J. Colloid Interface Sci.* **2013**, *404*, 223–229. [CrossRef] [PubMed]
25. Huang, X.; El-Sayed, M.A. Gold nanoparticles: Optical properties and implementations in cancer diagnosis and photothermal therapy. *J. Adv. Res.* **2010**, *1*, 13–28. [CrossRef]
26. Allingham, R.R.; de Kater, A.W.; Ethier, R.C. Schlemm’s Canal and Primary Open Angle Glaucoma: Correlation Between Schlemm’s Canal Dimensions and Outflow Facility. *Exp. Eye Res.* **1996**, *62*, 101–109. [CrossRef]
27. Ashpole, N.E.; Overby, D.R.; Ethier, C.R.; Stamer, W.D. Shear Stress-Triggered Nitric Oxide Release from Schlemm’s Canal Cells. *Investig. Ophthalmol. Vis. Sci.* **2014**, *55*, 8067–8076. [CrossRef]
28. McDonnell, F.; Perkumas, K.M.; Ashpole, N.E.; Kalnitsky, J.; Sherwood, J.M.; Overby, D.R.; Stamer, W.D. Shear Stress in Schlemm’s Canal as a Sensor of Intraocular Pressure. *Sci. Rep.* **2020**, *10*, 1–11. [CrossRef]
29. Wang, K.; Read, A.T.; Sulchek, T.; Ethier, C.R. Trabecular meshwork stiffness in glaucoma. *Exp. Eye Res.* **2017**, *158*, 3–12. [CrossRef]
30. Occhiutto, M.L.; Maranhão, R.C.; Costa, V.P.; Konstas, A.G. Nanotechnology for Medical and Surgical Glaucoma Therapy—A Review. *Adv. Ther.* **2019**, *37*, 155–199. [CrossRef]
31. Karlsson, J.; Vaughan, H.J.; Green, J.J. Biodegradable Polymeric Nanoparticles for Therapeutic Cancer Treatments. *Ann. Rev. Chem. Biomol. Eng.* **2018**, *9*, 105–127. [CrossRef]
32. Yang, G.; Phua, S.Z.F.; Bindra, A.K.; Zhao, Y. Degradability and Clearance of Inorganic Nanoparticles for Biomedical Applications. *Adv. Mater.* **2019**, *31*, e1805730. [CrossRef] [PubMed]
33. Dawidczyk, C.M.; Kim, C.; Park, J.H.; Russell, L.; Lee, K.H.; Pomper, M.G.; Searson, P.C. State-of-the-art in design rules for drug delivery platforms: Lessons learned from FDA-approved nanomedicines. *J. Control. Release* **2014**, *187*, 133–144. [CrossRef] [PubMed]
34. Kang, M.S.; Lee, S.Y.; Kim, K.S.; Han, D.-W. State of the Art Biocompatible Gold Nanoparticles for Cancer Theragnosis. *Pharmaceutics* **2020**, *12*, 701. [CrossRef] [PubMed]
35. Verma, A.; Stellacci, F. Effect of Surface Properties on Nanoparticle Cell Interactions. *Small* **2010**, *6*, 12–21. [CrossRef]
36. Moore, T.L.; Rodriguez-Lorenzo, L.; Hirsch, V.; Balog, S.; Urban, D.; Jud, C.; Rothen-Rutishauser, B.; Lattuada, M.; Petri-Fink, A. Nanoparticle colloidal stability in cell culture media and impact on cellular interactions. *Chem. Soc. Rev.* **2015**, *44*, 6287–6305. [CrossRef] [PubMed]
37. Larson, T.A.; Joshi, P.P.; Sokolov, K. Preventing Protein Adsorption and Macrophage Uptake of Gold Nanoparticles via a Hydrophobic Shield. *ACS Nano* **2012**, *6*, 9182–9190. [CrossRef]
38. Barreto, Â.; Luis, L.G.; Girão, A.V.; Trindade, T.; Soares, A.; Oliveira, M. Behavior of colloidal gold nanoparticles in different ionic strength media. *J. Nanoparticle Res.* **2015**, *17*, 1–13. [CrossRef]
39. Tripathi, R.C.; Millard, C.B.; Tripathi, B.J. Protein composition of human aqueous humor: SDS-PAGE analysis of surgical and post-mortem samples. *Exp. Eye Res.* **1989**, *48*, 117–130. [CrossRef]
40. Mansori, J.; Kumar, D.; Meenan, B.J.; Dixon, D. Polyethylene glycol functionalized gold nanoparticles: The influence of capping density on stability in various media. *Gold Bull.* **2011**, *44*, 99–105. [CrossRef]
41. Lin, S.; Ge, C.; Wang, D.; Xie, Q.; Wu, B.; Wang, J.; Nan, K.; Zheng, Q.; Chen, W. Overcoming the Anatomical and Physiological Barriers in Topical Eye Surface Medication Using a Peptide-Decorated Polymeric Micelle. *ACS Appl. Mater. Interfaces* **2019**, *11*, 39603–39612. [CrossRef]
42. Swetledge, S.; Jung, J.P.; Carter, R.; Sabliov, C. Distribution of polymeric nanoparticles in the eye: Implications in ocular disease therapy. *J. Nanobiotechnol.* **2021**, *19*, 1–19. [CrossRef]
43. Goel, M.; Picciani, R.G.; Lee, R.K.; Bhattacharya, S.K. Aqueous Humor Dynamics: A Review. *Open Ophthalmol. J.* **2010**, *4*, 52–59. [CrossRef]
44. del Amo, E.M.; Rimpelä, A.-K.; Heikkinen, E.; Kari, O.K.; Ramsay, E.; Lajunen, T.; Schmitt, M.; Pelkonen, L.; Bhattacharya, M.; Richardson, D.; et al. Pharmacokinetic aspects of retinal drug delivery. *Prog. Retin. Eye Res.* **2017**, *57*, 134–185. [CrossRef]
45. Agrahari, V.; Mandal, A.; Agrahari, V.; Trinh, H.M.; Joseph, M.; Ray, A.; Hadji, H.; Mitra, R.; Pal, D.; Mitra, A.K. A comprehensive insight on ocular pharmacokinetics. *Drug Deliv. Transl. Res.* **2016**, *6*, 735–754. [CrossRef]
46. Tojo, K.J.; Ohtori, A. Pharmacokinetic model of intravitreal drug injection. *Math. Biosci.* **1994**, *123*, 59–75. [CrossRef]
47. Overby, D.R.; Zhou, E.H.; Vargas-Pinto, R.; Pedrigi, R.M.; Fuchshofer, R.; Braakman, S.T.; Gupta, R.; Perkumas, K.M.; Sherwood, J.M.; Vahabikashi, A.; et al. Altered mechanobiology of Schlemm’s canal endothelial cells in glaucoma. *Proc. Natl. Acad. Sci. USA* **2014**, *111*, 13876–13881. [CrossRef]
48. Vingolo, E.M.; Chabib, A.; Anselmucci, F. Regeneration of trabecular meshwork in primary open angle glaucoma by stem cell therapy: A new treatment approach. *Transpl. Res. Risk Manag.* **2019**, *11*, 11–16. [CrossRef]
49. Liebmann, J.M.; Barton, K.; Weinreb, R.N.; Eichenbaum, D.A.; Gupta, P.K.; McCabe, C.M.; Wolfe, J.D.; Ahmed, I.; Sheybani, A.; Craven, E.R. Evolving Guidelines for Intracameral Injection. *J. Glaucoma* **2020**, *29*, S1–S7. [CrossRef]

50. Shah, T.J.; Conway, M.D.; Peyman, G.A. Intracameral dexamethasone injection in the treatment of cataract surgery induced inflammation: Design, development, and place in therapy. *Clin. Ophthalmol.* **2018**, *12*, 2223–2235. [CrossRef]
51. Braga-Mele, R.; Chang, D.F.; Henderson, B.A.; Mamalis, N.; Talley-Rostov, A.; Vasavada, A. Intracameral antibiotics: Safety, efficacy, and preparation. *J. Cataract. Refract. Surg.* **2014**, *40*, 2134–2142. [CrossRef]
52. Mietzner, R.; Kade, C.; Froemel, F.; Pauly, D.; Stamer, W.D.; Ohlmann, A.; Wegener, J.; Fuchshofer, R.; Breunig, M. Fasudil Loaded PLGA Microspheres as Potential Intravitreal Depot Formulation for Glaucoma Therapy. *Pharmaceutics* **2020**, *12*, 706. [CrossRef]

Review

Factors Affecting Posterior Capsule Opacification in the Development of Intraocular Lens Materials

Grace Cooksley^{1,2,*}, Joseph Lacey², Marcus K. Dymond¹ and Susan Sandeman^{1,*}

¹ School of Pharmacy and Biomolecular Sciences, University of Brighton, Brighton BN2 4GJ, UK; m.dymond@brighton.ac.uk

² The Ridley Innovation Centre, Rayner Intraocular Lenses Limited, Worthing BN14 8AG, UK; josephlacey@rayner.com

* Correspondence: g.cooksley@brighton.ac.uk (G.C.); s.sandeman@brighton.ac.uk (S.S.)

Abstract: Posterior capsule opacification (PCO) is the most common complication arising from the corrective surgery used to treat cataract patients. PCO arises when lens epithelial cells (LEC) residing in the capsular bag post-surgery undergo hyper-proliferation and transdifferentiation into myofibroblasts, migrating from the posterior capsule over the visual axis of the newly implanted intraocular lens (IOL). The developmental pathways underlying PCO are yet to be fully understood and the current literature is contradictory regarding the impact of the recognised risk factors of PCO. The aim of this review is firstly to collate the known biochemical pathways that lead to PCO development, providing an up-to-date chronological overview from surgery to established PCO formation. Secondly, the risk factors of PCO are evaluated, focussing on the impact of IOLs' properties. Finally, the latest experimental model designs used in PCO research are discussed to demonstrate the ongoing development of clinical PCO models, the efficacy of newly developed IOL technology, and potential therapeutic interventions. This review will contribute to current PCO literature by presenting an updated overview of the known developmental pathways of PCO, an evaluation of the impact of the risk factors underlying its development, and the latest experimental models used to investigate PCO. Furthermore, the review should provide developmental routes for research into the investigation of potential therapeutic interventions and improvements in IOL design in the aid of preventing PCO for new and existing patients.

Citation: Cooksley, G.; Lacey, J.; Dymond, M.K.; Sandeman, S. Factors Affecting Posterior Capsule Opacification in the Development of Intraocular Lens Materials. *Pharmaceutics* **2021**, *13*, 860. <https://doi.org/10.3390/pharmaceutics13060860>

Academic Editors: Francisco Javier Otero-Espinar and Anxo Fernández Ferreiro

Keywords: posterior capsule opacification; pathophysiology; wound healing; lens epithelial cells; intraocular lenses; experimental models; clinical studies

Received: 9 May 2021
Accepted: 7 June 2021
Published: 10 June 2021

Publisher's Note: MDPI stays neutral with regard to jurisdictional claims in published maps and institutional affiliations.



Copyright: © 2021 by the authors. Licensee MDPI, Basel, Switzerland. This article is an open access article distributed under the terms and conditions of the Creative Commons Attribution (CC BY) license (<https://creativecommons.org/licenses/by/4.0/>).

1. Introduction

Despite the histopathology of posterior capsule opacification (PCO) being well characterised, the molecular mechanisms underlying the pathology are still unknown [1–4]. In addition to this, current literature contains contradictions regarding the extent to which established risk factors impact PCO development. Herein, the known biomolecular pathways in PCO development are reviewed and a chronological overview of the mechanisms underlying the pathophysiology of PCO formation are presented. Moreover, this review explores the risk factors for PCO and considers their impact on PCO development. Lastly, this review examines the latest experimental models in PCO research used to investigate the next generation of medical and technological advancements for patients with PCO.

PCO is the most common complication arising from corrective surgery to treat cataracts [1,5–7]. In 2018, the World Health Organisation [WHO] estimated that 90 million people worldwide still live with cataract-associated blindness [8]. Each year, an additional 1–2 million people become blind, of which 75% are treatable [9]. This number is only expected to rise due to an increasingly expanding and ageing global population [9]. The Royal National Institute of Blind People (RNIB) estimated that by 2020, 695,000 people would be living with cataracts in the United Kingdom, a number that would increase by

30% between 2020 and 2030. In England alone, 330,000 cataract surgeries are performed per year [10]. Whilst in the UK cataract surgery is a routine, outpatient surgical procedure, a number of complications can occur for a subsection of patients. Approximately 20–50% of patients develop PCO and require further corrective treatment [11].

PCO presents as a secondary cataract, an agglomeration of cells over the visual axis causing a loss of acuity. During surgery, the surgeon will create an opening in the capsular bag, known as capsulorhexis, and use phacoemulsification to remove the diseased, opaque lens and lens epithelial cells (LEC) from the capsular bag before implanting an artificial intraocular lens (IOL) [12,13]. The extent of LEC removal influences the propensity towards PCO development [14,15]. The initial inflammation caused by the surgical trauma may incite the hyper-proliferation, transdifferentiation, and migration of residual LECs [16]. The transformed LECs migrate along the posterior capsule towards the anterior chamber to accumulate over the visual axis, forming a secondary cataract [1,17].

1.1. Pathophysiology of Posterior Capsule Opacification

The wound healing response of LECs post-cataract surgery is believed to be the first key developmental stage of PCO. Ocular inflammation is triggered as a result of the opening incision and subsequent lens cell removal [18,19]. Jiang et al. [16] showed that within the first 24 h post-surgery, the LEC transcriptome differentially expresses 19 of the 27 cataract-associated genes, some of which are markers of mesenchymal cell fate and are associated with chronic inflammatory conditions. The genes with the greatest upregulation in expression are *CXCL1*, *S100a9*, *CSF3/G-CSF*, *COX-2*, *CCL2*, *LCN2*, and *HMOX1* [20]. Some of these genes are involved in the production of proinflammatory chemokines such as *CXCL1*, alarmin *S100a9*, and *G-CSF* [16]. This response may be initiated by the surgically induced break in the blood-aqueous barrier and subsequent leakage of plasma protein into the aqueous humour (Figure 1A) [16,19]. At 48 h post operation, the elevated levels of inflammatory mediators interleukin (IL)-6, IL-1 β , and IL-8 expressed by the LECs initiate and promote chronic inflammation pathways (Figure 1B) [5,21–25]. Migrating neutrophils and macrophages attracted by the secreted chemokines cleave the inactive precursor of the latent transforming growth factor beta (TGF- β) via proteinases in the aqueous humour [26,27]. The activated TGF- β binds to LECs via type I and type II receptor serine-threonine kinases on the cell surface [2]. This begins a cascade of SMAD proteins signalling, the messengers activated via TGF β signalling [28,29]. These signalling pathways lead to TGF- β -gene transcription, activation of Rho GTPases, and stimulation of the PI3/Akt and MAPK pathways (Figure 1C). These events are associated with myofibroblast formation, epithelial-mesenchymal-transition (EMT)-related matrix contraction, cell differentiation, and inhibition of normal LEC pathways [2]. As a result, the LECs are stimulated to hyper-proliferate and differentiate into myofibroblasts, leading to their eventual migration over the visual axis of the IOL (Figure 1D).

From current literature, the hypothesised key mediators involved in PCO development are IL-1 β , IL-8, IL-6, and TGF- β . IL-1 β can be synthesised by retinal pigment epithelial cells, LECs, corneal epithelial cells, and to some extent, corneal stromal cells when triggered during inflammatory processes [25,30,31]. IL-1 β promotes inflammation by acting as a proinflammatory mediator, stimulating the secretion of other cytokines such as IL-8 [24,25,32]. IL-8 can be produced by peripheral blood monocytes, endothelial cells, fibroblasts, and epithelial cells [25]. A study conducted by Ferrick [25] exemplifies the interconnectivity of IL-1 β and IL-8 in augmenting the inflammatory response. Rat eye models were first injected with IL-1 β . At 20 h post injection, IL-8-activated neutrophils were detected. The rat neutrophils levels then subsided after 48 h. However, this inflammatory resolution may not occur as quickly in humans. The study concluded that IL-1 β produces a stronger inflammatory response with long-lasting effects due to the cascade of pathways it initiates such as activating leukocytes, instigating proinflammatory mechanisms in local cells and promoting the synthesis of cytokines such as IL-8, whereas IL-8 acts as a specific chemoattractant for neutrophils.

The presence of IL-6 during PCO development is supported by the study conducted by Nishi [23]. The authors found IL-6 expression to be significantly higher in the aqueous humour of LECs obtained during cataract surgery in comparison to medium controls. IL-6 is believed to be involved in the upregulation of extracellular matrix (ECM) synthesis, the contraction of the capsular bag, and EMT of LECs, as shown by Ma [5]. Within 24 h of IL-6 stimulation, the human LEC-B3 (HLE-B3) line initiated a significant increase in ECM synthesis and activation of the JAK/STAT3 pathway was observed [5]. Cells treated with JAK/STAT3 inhibitor WP1066 showed significantly inhibited expression of collagen, fibronectin, and TGF- β 2 ($p > 0.01$). This suggests that the JAK/STAT3 pathway influences the expression of ECM proteins in HLE-B3 cells. The authors also showed that IL-6 works in synergy with TGF- β to promote EMT, since HLE-B3 cells treated with IL-6 and TGF- β 2 showed significantly increased expression of the markers of EMT, alpha smooth muscle actin (α -SMA), collagen, and fibronectin in comparison to cells treated with either IL-6 or TGF- β 2.

TGF- β is a well-established key mediator within PCO development [1,6,16,17,29,33,34]. The isoforms TGF- β 1 and - β 2 are found in ciliary processes and within the limbal epithelium where they are hypothesised to be involved in the transdifferentiation of conjunctival to corneal epithelium. As a consequence, it is believed these isoforms are locally synthesised due to their predominance in the aqueous humour [6,35]. Moreover, Nishi [36] found that LECs express TGF- β 2. The binding of TGF- β to its receptor activates kinase domains within the receptor, augmenting phosphorylation cascades which initiate SMAD3 transcription factors [2,28]. The TGF- β receptor kinase has many roles within the ocular tissue, in both normal and pathological conditions [37,38]. TGF- β is important in maintaining corneal integrity, in tissue repair, and in the regulation of cell proliferation and death [37,38]. Nevertheless, hyper-activation of the growth factor can lead to an exaggerated wound-healing response and increased ECM deposition by cells, which may cause fibrotic corneal disease, fibrosis of lens and retinal epithelium, and loss of vision [6,28,35,37].

Short-term exposure to TGF- β can lead to long-term impact. Possible mechanisms behind this are the positive feedback loop on the upregulation of TGF- β gene expression stimulated by the exposure to TGF- β or the ability of TGF- β to bind to collagen IV, a predominant component of the capsular bag. In PCO development, TGF- β is also involved in the activation of the EMT pathway in LEC; the differentiation of the epithelial cells to migratory spindle-like myofibroblasts [29,39–42]. The activation of TGF- β inhibits the proliferation of LECs in favour of initiating transdifferentiation by upregulating the expression of α -SMA genes [6,28,43]. Therefore, α -SMA can be used as a biomarker for myofibroblasts [44]. Furthermore, TGF- β has been shown to increase the secretion of ECM components by LECs. In this process, ECM turnover is disturbed; the upregulation of fibronectin, collagen I and IV, and inhibitors of matrix metalloproteinases (MMPs) cause a greater production of ECM with reduced degradation. The increased ECM leads to capsule wrinkling and thickening of the posterior capsule [6,43,45]. The presentation of PCO can differ between individuals, depending on patient specific risk factors affecting the patients.

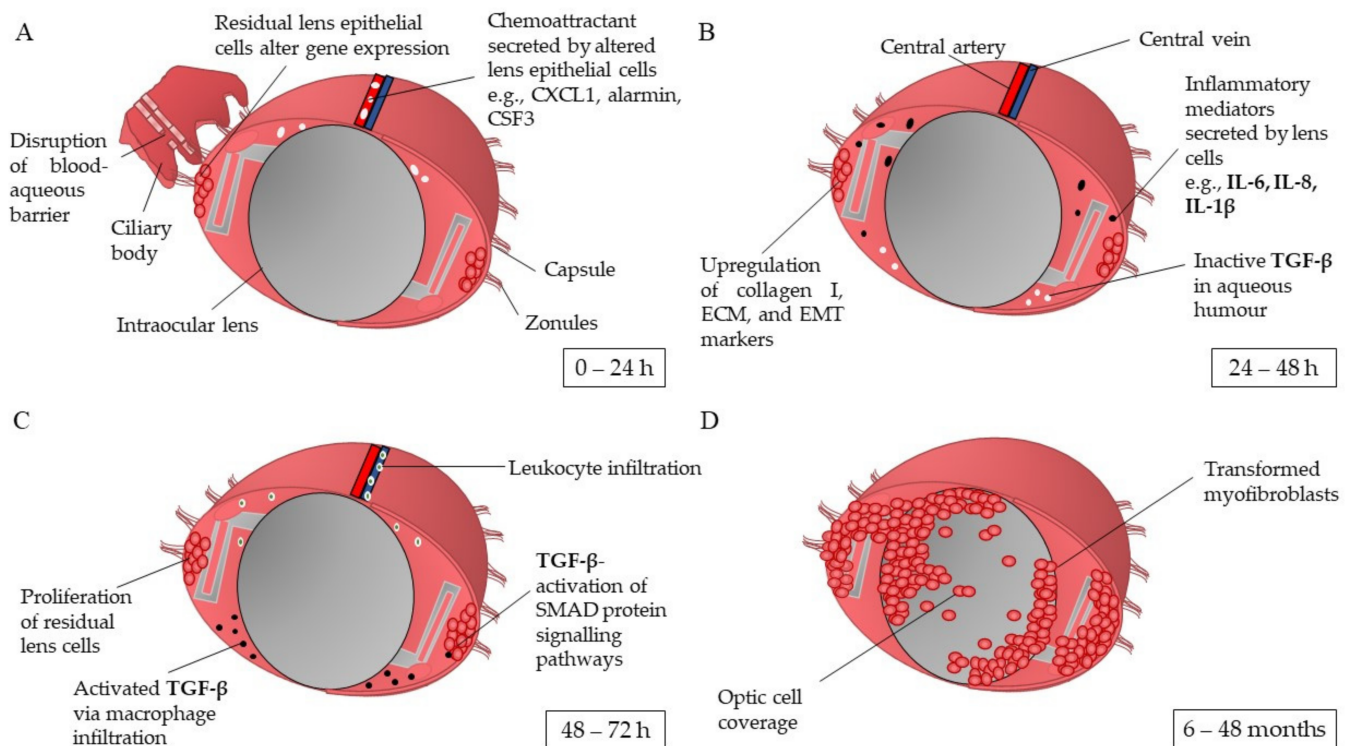


Figure 1. Schematic overview of the capsular bag post cataract surgery in the development of posterior capsule opacification. (A) Stimulated by surgery trauma, residual lens epithelial cells undergo the wound healing response, alteration of gene transcriptome and expression of chemoattractants targeting inflammatory mediators and innate immune cells. (B) Upregulation of inflammatory mediators, i.e., IL-1 β expressed by lens cells undergoes autocrine signalling to initiate the synthesis of collagen I, extracellular matrix (ECM), and epithelial-mesenchymal transition (EMT), proteins and markers. (C) Residual lens epithelial cells start to proliferate; leukocyte infiltration attracted by the high levels of chemoattractants and inflammatory mediators activate dormant transforming growth factor beta (TGF- β) residing in the aqueous humour. TGF- β activates SMAD3 signalling pathways in the lens cells, stimulating PI3/Akt, Rho GTPases, and MAPK pathways. (D) The transdifferentiated lens cells migrate over the intraocular lens' optic. IL: interleukin; TGF- β : transforming growth factor beta [2,5,6,16,17,20,21,25,26,37,46].

1.2. Risk Factors for Developing Posterior Capsule Opacification

PCO typically develops in the first 2–5 years post-surgery [7,11,14,47,48]. There are several risk factors that can make patients more susceptible to developing PCO. These are patient-associated risk, surgical-associated risk, and IOL-associated risk, as discussed.

1.2.1. Patient-Associated Risk Factors

Studies show that patient age alters the propensity of the LECs to proliferate [7,14,47]. The younger the patient, the more LECs are within the capsular bag with greater proliferative potential [47]. Children undergoing cataract surgery can expect a 100% risk of developing PCO [49]. LECs in patients less than 40 years of age grow three times quicker than in patients less than 60 years of age [50]. Patients with diabetes have shown significant PCO development after a year follow-up. However, the severity does not differ between diabetic and non-diabetic patients over a long-term duration, suggesting that diabetes may only increase the rate of PCO development due to the initial protein-rich and inflamed tissue [14,47,51,52]. Pre-existing ocular diseases in patients such as dry-eye disease and uveitis can lead to an increased rate of PCO development and a greater likelihood of experiencing vision-threatening PCO [53].

1.2.2. Surgical-Associated Risk Factors

The outcome of cataract surgery can influence the propensity towards PCO development. The removal of LECs is fundamental in preventing PCO. However, this is a difficult achievement and any number of residual LECs can mount a full PCO response [2,14,15,47]. Nevertheless, surgical interventions such as hydrodissection-enhanced cortical clean-up to remove lens substance and in-the-bag fixation to ensure IOL centralisation for optimal barrier effect can reduce PCO incidence [14,54]. An additional surgical intervention to prevent PCO development for paediatric patients is known as optic capture. Optic capture involves implanting the IOL optic through the posterior capsulorhexis opening [55,56]. This technique effectively prevents PCO as it locks the IOL in a central position preventing lateral movement and delays LEC migration due to the fusion of the anterior and posterior capsulorhexis [57]. A study conducted by Davidson [15] exemplifies how surgical technique can impact cell growth over the IOL. The surgical techniques extracapsular cataract extraction (ECCE), phacoemulsification, and phacoemulsification with capsule vacuuming were evaluated on cadaver eyes. The cell growth density over the anterior capsule was 31.6%, 16.1%, and 7.7%, respectively. When cultured in serum-free media, the phacoemulsification with capsule vacuuming group took 5.3 days longer to reach confluence. Polishing of the posterior capsule showed a reduction in PCO development as shown by Paik [58] who found that the surgeon who routinely polished the posterior capsule had a 20% PCO rate, in comparison to 30% for the surgeon who did not. Nevertheless, the impact of polishing is highly controversial and application relies on the surgeon's preference [59,60]. Although surgical technique alone is not enough to prevent PCO, the surgeon's skill and commitment to removal of LECs via phacoemulsification can influence severity and rate of onset.

1.2.3. Intraocular Lens-Associated Risk Factors

The process of selecting the appropriate IOL is patient-specific. The choice of material, design, and function of the IOL can greatly impact risk of developing PCO. A prospective study conducted by Joshi [61] exemplifies the importance of IOL selection for patients with pre-existing conditions. A total of 1400 eyes undergoing cataract surgery with peripheral pre-existing PCO (PPPCO) were either implanted with a hydrophobic or hydrophilic IOL. PPPCO is often seen in the developing world due to the late presentation of patients and in some cases of blunt ocular trauma [61,62]. The study found PPPCO patients implanted with a hydrophilic IOL had a higher propensity towards PCO development than those implanted with a hydrophobic IOL. The author concluded that patients with PPPCO should be considered for hydrophobic IOL implantation only. Current literature offers little consensus to the impact of IOL composite material on PCO development.

Lens Material

IOLs have been typically constructed from polymethylmethacrylate (PMMA), silicone, or acrylic, which is further divided into hydrophobic and hydrophilic due to their differing composite monomers [63]. PMMA IOLs were the first implantable material used in the early generation of IOL technology by Ridley [64]. The biostability, low inflammatory response, compatibility with injection moulding protocols, and refractive index of 1.49 made PMMA the preferred material over glass [63,65,66]. Nevertheless, the rigidity, intolerance to elevated pressure levels, lower biocompatibility relative to silicone and acrylic, and brittleness of PMMA has led to the replacement of PMMA with more flexible materials. One driving force for this change is the surgical procedure as more flexible IOLs require smaller incision sizes, leading to a faster recovery period [19,65,66]. Silicone is a flexible hydrophobic material with a refractive index of 1.41–1.46 [63]. In the early generation of silicone IOLs, the low refractive index of silicone required thicker optics to achieve the same optical power as PMMA. However, later developments using copolymers of silicone and other monomers increased the refractive index and reduced IOL thickness [63,65]. PCO rates for silicone IOLs are reduced compared to other IOL material types due to the lower

cell deposition. Nevertheless, as the capsular bag wall cannot adhere to silicone, the barrier effect of a square edge design is prevented (discussed in Lens Design) [63,66]. Another disadvantage of silicone is that the material favours bacterial adhesion increasing infection risk [63,65,67]. Alternatively, hydrophobic acrylic-based IOLs, composed of copolymers of acrylate and methacrylate, can be used. These IOLs have a high refractive index of 1.44–1.55, flexibility, and uveal biocompatibility [19,63,65]. However, these acrylic-based IOLs are easy to mark or scratch during implantation and require more attention to centre in the capsular bag when implanted [19,63]. Hydrophilic acrylic IOLs are soft, flexible, have a low tendency to scratch, and a refractive index of 1.43 [63]. Despite this, the hydrophilic composite monomers of these IOLs promote cell adhesion and some studies have suggested higher PCO rates as a result of this [63,65,67].

The extent to which IOL composite material, more specifically material wettability, impacts the onset of PCO is controversial. Recent review articles comparing hydrophobic and hydrophilic IOLs have shown some consensus on the conclusion that hydrophobic IOLs show lower PCO rates in comparison to hydrophilic IOLs [19,51,66,68,69]. Nevertheless, these clinical studies used small sample sizes and the trend of PCO development may be less disparate between hydrophobic and hydrophilic IOLs if a larger cohort size is used. Using clinical studies with smaller sample sizes may show a trend of PCO development between hydrophobic and hydrophilic which may not be valid as the impact of a single individual can greatly influence the overall conclusion. Moreover, the patients' associated risk is not accounted for as it would be in a larger population; separating impact of the material alone would be impossible. This exemplifies an important limitation in using studies with smaller sample sizes in a meta-analysis on factors influencing PCO development. The validity of such studies can be easily questioned and can lead to misdirection of clinicians.

Examples of reviews using studies with large participant cohorts include Auffarth [69] who conducted a retrospective cohort design review to compare PCO and neodymium-doped yttrium aluminium garnet (Nd:YAG) capsulotomy rates between patients implanted with PMMA, silicone, and hydrophobic and hydrophilic acrylic IOLs. Patients were aged 50–80 years and were followed up for a minimum of 3 years. A total of 1525 patients were included ($n = 384$ PMMA; $n = 426$ silicone; $n = 421$ hydrophobic acrylic; $n = 294$ hydrophilic acrylic). The review found an overall PCO rate of 22.8% (28.3%, 21.6%, 8.9%, and 37.0%, respectively) and an overall Nd:YAG rate of 17.3% (19.3%, 16.2%, 7.1%, and 31.1%, respectively). It was concluded by the authors that hydrophobic acrylic IOLs show significantly lower PCO and Nd:YAG laser ablation rates. Another study supporting the argument that hydrophobic IOLs show lower PCO rates is a retrospective review conducted by Boureau et al. [52] who analysed patient charts to determine the requirement for Nd:YAG capsulotomy between hydrophilic IOLs (XL-Stabi, Zeiss-Ioltech, Ioltech, France) and hydrophobic IOLs (SA60AT, AcrySof, Alcon, Fort Worth, Tex or AR40E, Advanced Medical Optics Inc, Santa Ana, CA, USA). A total of 767 patients fulfilled the inclusion criteria ($n = 263$, XL-Stabi; $n = 250$, AcrySof SA60AT; $n = 254$, AR40E). The patients were aged 50–85 years and were followed up for a minimum of 36 months. The study showed a PCO rate of 52.9%, 13.6%, and 26.8%, respectively and a ND:YAG capsulotomy rate of 51.0%, 12.0%, and 25.2%, respectively. Other studies have concluded differently. Mathew [70] assessed the outcome of 3461 eyes implanted with a hydrophilic IOL (Rayner C-flex 570C). The patients were 39–93 years of age and the follow-up period ranged 5.3–29.0 months. This study found a Nd:YAG capsulotomy rate of 0.6% at 12 months and 1.7% at 24 months. Nevertheless, studies have also found there to be no difference in PCO development between hydrophobic and hydrophilic IOLs. A clinical study conducted by Bai [71] showed 60 patients implanted with a 360-degree square edge hydrophilic acrylic IOL (Rayner C-flex 570C) or a square edge hydrophobic acrylic IOL (Sensar AR40E) had no statistically significant difference in PCO grade after 24 months. There is sufficient evidence to suggest that IOL material can influence the propensity towards PCO development. However, the influence of material

wettability on patient's susceptibility to PCO cannot be fully established until additional targeted clinical studies with larger population sizes are performed.

Lens Design

The optic edge and haptic configuration of an IOL can influence its in-the-bag stability and the likelihood of developing PCO. The optic edge refers to the edge structure of an IOL, which is typically curved (or rounded) or square-cut (square-edge) (Figure 2A). IOLs with a square-edge design have shown a reduction in PCO development, regardless of material [2,52,71–75]. The square edge design is most effective when present 360° around the optic to ensure no cell growth at optic–haptic junctions [73,76]. The current theory explaining how this works is known as the barrier effect, derived from sandwich theory. Sandwich theory states that PCO development is reduced when there is maximum contact between the IOL and the posterior capsular bag wall [77,78]. The square optic edge allows the IOL to achieve the required contact with the capsular bag, preventing the migration of LECs. However, the square edge design is not effective for all patients. The design relies on contraction of the posterior capsule to meet the optic edge of the IOL establishing the barrier. This does not occur in some patients [19]. Additionally, a study conducted by Vock [79] reviewed 143 eyes over 10 years to determine Nd:YAG laser ablation rates between a round-edge silicone and a sharp-edged hydrophobic acrylic intraocular lens. The study found that 10 years post surgery, patients fitted with a sharp-edged IOL had significantly greater cumulative Nd:YAG rates than those fitted with a round-edge IOL. This unanticipated finding may be a result of late barrier failure, the delayed redivision of the capsule leaves caused by Soemmerring ring formation establishing a collagenous sealing of the capsule leaves to the optic rim. Moreover, an increase in haptic number and configuration can disturb the square edge design [80,81]. Single-piece IOLs show greater in-the-bag stability. However, they have slightly higher rates of PCO development in comparison to three-piece IOLs (Figure 2B) [81–83].

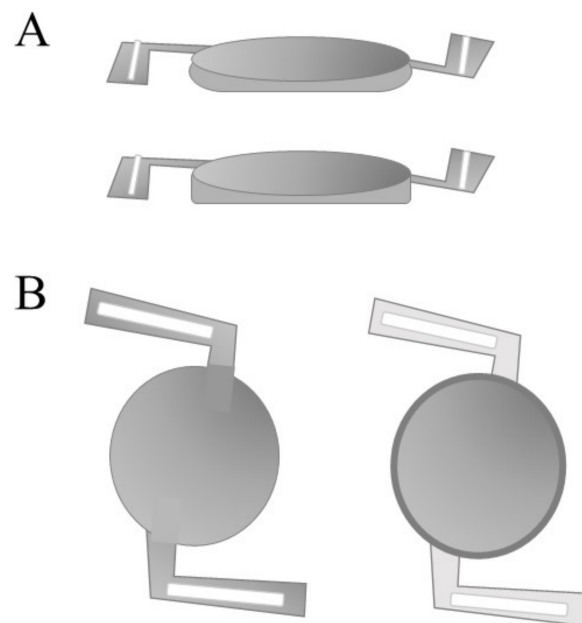


Figure 2. (A) Schematic design of an intraocular lens with a rounded optic edge (top) and squared optic (bottom). (B) Schematic design of the single-piece IOL (left) and three-piece IOL (right) [75,84].

Lens Function

The function of an IOL determines the post-operative outcome in terms of visual acuity, range of vision, and likelihood of developing long-term complications. Monofocal IOLs improve visual acuity for patients. However, patients remain with one focal point

and still require spectacles for near vision [65,85]. Multifocal IOLs utilise bifocal or trifocal points, allowing near, intermediate, and distance vision. However, they are consequently more likely to experience dysphotopsias and post-operative complications [63,65,85,86]. Toric IOLs are given to cataract patients with astigmatism. However, if the lenses become misaligned, the patient may experience blurred vision and require glasses [65,85,86]. In the next generation of IOL technology, the development of accommodative IOL (AIOL) will provide patients with improved visual acuity and dynamic changes in focus [65,86,87]. Nevertheless, the current commercially available AIOLs increase PCO incidence [12,88]. This is demonstrated by Sadoughi [12] who found that there was a 23% increase in PCO development for patients fitted with the AIOL Crystalens HD in comparison to patients fitted with monofocal lenses. The influence of IOL material, design, and surgical technique on the onset and severity of PCO development is too complex to differentiate each factor's sole impact. Producing an effective treatment for all patient types is a challenging process considering the complex pathology and multitude of risk factors underlying PCO development.

1.3. Therapeutic Interventions for Posterior Capsule Opacification

PCO is managed with Nd:YAG laser capsulotomy. The agglomerated cells are targeted, creating an opening which restores visual acuity. A retrospective study of 806 patients found the requirement for Nd:YAG capsulotomy was 10.6% after one year, 14.8% after two, and 28.6% after four years [89]. The procedure can lead to complications such as retinal detachment, cystoid macular oedema, IOL displacement, mild anterior uveitis, and transient intraocular pressure [90]. Developing preventative measures to inhibit the biomolecular pathways of PCO could reduce the risk to patients, lower the requirement for additional treatment post cataract surgery, and ease the burden on healthcare services. Thus far, improvements in surgical technique and the square edge optic design have shown a reduction in PCO incidence [4,9,72,76,91]. Non-pharmacological methods to reduce PCO development include gene therapy and inducing osmotic changes in LECs [2]. Pharmacological approaches to preventing PCO include cytostatic drugs, anti-inflammatory drugs, and antagonists to key molecules within the developmental pathways of PCO as exemplified by Shao [92]. Shao [92] stimulated the HLE-B3 cell line SRA01/04 with TGF- β 2 to induce EMT then treated the cells with fasudil, an inhibitor of the Rho-kinase activated during TGF- β signalling. Fasudil significantly reduced cell proliferation and migration, down-regulated α -SMA expression, and prevented the suppression of epithelial marker Connexin43. Nevertheless, despite extensive research into therapeutic solutions for PCO, no clinical treatment exists other than Nd:YAG.

1.4. Capsular Devices to Prevent Posterior Capsule Opacification Development

Capsular devices were developed to facilitate cataract surgery by improving capsular bag stability and intraocular lens centration [93,94]. The introduction of the capsular device by Hara [95] in 1991 has since led to the evolution of endocapsular devices that have aided capsular support and stability leading to a subsequent reduction in PCO development. The equator ring (E-ring) introduced by Hara [95] was a closed silicone circle with square-edge design and an inner groove to allow IOL fixation. The squared edges were hypothesised to delay PCO formation. Hara [96] compared 51 eyes, 14 of which were implanted with the E-ring, and found the E-ring significantly reduced PCO development. This design was built upon by Nishi who developed a capsular tension ring (CTR) made from PMMA with sharp rectangular edges. Although the implantation of a CTR has shown reduced PCO formation in comparison to patients implanted with an IOL alone, the discontinuous capsular bend created allows the possibility for LEC migration [93,97,98]. This CTR design was adapted into an open-capsule device for the purpose of expanding and opening the capsular bag, separating the anterior and posterior capsules [93,99]. The open-capsule device can be made of hydrophobic or hydrophilic material and is a closed ring with a square-edge design. Alon [100] showed that the open-

capsule ring reduced PCO development, regardless of base material. New Zealand white rabbits were assigned either to two control groups, each implanted with hydrophobic or hydrophilic IOLs without an open-capsule ring, or to four study groups, each implanted with a hydrophobic or hydrophilic IOL and a hydrophobic or hydrophilic open-capsule ring. A clinical evaluation found a 69% reduction in the eyes implanted with the device relative to the control eyes. This reduction has been linked to the 360° squared edge and the delivery of aqueous humour to the capsule equator through windows in the rim of the device that prevents LEC migration and proliferation, respectively [93]. An additional endocapsular device was developed by Sharklet Technologies, Inc. (Aurora, CO, USA) to act as an artificial capsular bag. The protective silicone membrane has a square-edge haptic ring which provides a ridge for the IOL haptics. The signature feature of this design is the composite sharkskin-inspired microtopography which inhibits bioadhesion and has been hypothesised to prevent LEC migration [93,101]. These capsular devices, in addition to the other risk factors discussed, present the complexity of understanding and treating PCO. Experimental models are utilised in PCO research for insight into the underlying pathophysiology, testing newly developed IOL technology in aid of device optimisation, and investigating potential therapeutic interventions.

2. Experimental Models to Investigate Posterior Capsule Opacification

2.1. *In Vitro* Models

Whilst *in vitro* models are not representative of the physiological environment they have been used as a rapid and cost-effective route to ascertain the molecular mechanisms underlying PCO formation. Additionally, cell models are typically used in the first stage of investigating possible therapeutic interventions due to the reduced ethical constraints and ability to provide fundamental toxicology data prior to using relatively more expensive *in vivo* and *ex vivo* models. Cell culture models have shown the role of fibronectin, growth factors such as TGF- β , and enzymes including aldose reductase in the development of PCO [102–104]. The creation of three-dimensional cell culture models has broadened the application of *in vitro* models to encompass structural replicability.

2.1.1. Two-Dimensional *In Vitro* Models

Cell cultures are used as *in vitro* models as the cultures provide a dynamic growing system [17]. Cultures are comprised of primary or immortalised cell lines. Chick primary cell cultures derived from chick lenses have been used to model the lens fibre cell differentiation that occurs during the development of Soemmerring's ring in PCO and the early stages of growth factor signalling. This is demonstrated by VanSlyke [102] who used a chick primary cell line to examine the role of fibronectin within the transformation of lens cells post-surgery. Chick embryonic lens cells from primary cell cultures were either plated on laminin-control or fibronectin-coated wells. Western blot analysis was conducted to quantify the expression of SMAD isoforms, markers of TGF- β signalling. The study showed the cells incubated with the fibronectin coating expressed pSMAD3 at 1.9 ± 0.23 -fold increase (mean \pm SEM; $n = 5$; $p = 0.001$) in comparison to the laminin-control at day 3. This study suggests the potential involvement of fibronectin in TGF- β signalling.

In addition to primary cell lines, the human lens epithelial cell line HLEB3 is one of the most established cell lines for research into the development and treatment of PCO [1,105–107]. HLE-B3 cells possess receptors for growth factors and when incubated with these factors, elicit fibrotic pathways shown during PCO development. Wertheimer [103] used the HLE-B3 cell line to investigate the use of erlotinib, an inhibitor of epithelial growth factor (EGF) signalling. The study used tetrazolium dye-reduction assay (MTT) and Live-Dead assay to determine the toxicity of different concentrations of erlotinib on the cells. Erlotinib became toxic to the lens cell line at 100 μ M. Chemotactic migration assessed by Boyden chamber assay and chemokinetic migration assessed by time lapse microscopy found that Erlotinib significantly reduced cell migration ($p = 0.004$ and $p = 0.001$, respectively). Wertheimer [108] continued this work by submerging IOLs within solutions

of erlotinib and found that after 24 h exposure, complete cell coverage took 5.9 to 8 days longer than the control IOL.

2.1.2. Three-Dimensional In Vitro Models

The development of three-dimensional in vitro models of PCO provides greater functional and structural applicability as shown by Plüss [106] who created a three-dimensional in vitro model of HLE-B3 cells by seeding the cells within 96-well plates and centrifuging to aggregate the cells. The spheroid structure was established by day 1 and was maintained up to day 26 (Figure 3). The expression of key epithelial markers N-cadherin (CDH2) and $\alpha\beta$ -crystallin (CRYAB), as defined by the study, were confirmed by reverse transcription-quantitative polymerase chain reaction (rt-PCR). The study confirmed the expression of these markers was stable over a period of 15 days. Their gene expression analysis showed the repression of Ephrin type-A receptor (EphA2), involved in maintaining lens transparency, and the significant upregulation of ACTA2, a marker of EMT during PCO development.

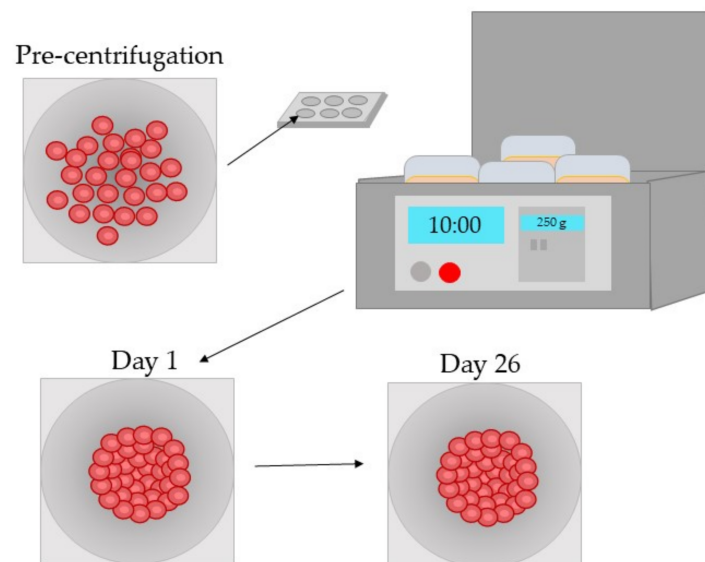


Figure 3. Three-dimensional in vitro spheroids formed by human lens epithelial cell line. Cells were centrifuged at $250\times g$ for 10 min immediately post-seeding in a microplate. The spheroids were maintained for 26 days. Stable expression of key markers N-cadherin (Hs00983056_mL) and $\alpha\beta$ -crystallin (Hs00157107_mL) was seen up to day 26 as determined by reverse transcription-quantitative polymerase chain reaction [106].

In summary, cell cultures as an in vitro model provide insight into the molecular mechanisms of PCO whilst being easily accessible for all laboratories due to their lack of reliance on the limited and often expensive supply of donor tissue. However, despite the development of 3D cell models, there is still restricted applicability of isolated cell cultures to in vivo and ex vivo models. The in vivo models used in PCO research administer treatment or surgical interventions on animal donor eyes and examine the impact on the donor pre- and post-dissection. Unlike in vitro models, in vivo models allow real-time inflammatory responses and provide insight into the impact of surrounding tissue.

2.2. In Vivo Models

In vivo models can be exploited in many aspects of PCO research. Such applications include the investigation of intraocular lenses, underlying biomolecular mechanisms, and the efficacy of surgical interventions, and the testing of therapeutic inhibitors of developmental pathways [17,109–112]. Animal donors include murine, rabbit, and porcine species. However, caution is required when comparing and extrapolating pathological responses

between animals and humans due to differences in species biology [1,17]. Furthermore, each animal donor type has its own limitations.

2.2.1. Murine

Murine models include rat and mice donors. These models cannot be utilised to evaluate IOL technology due to size restriction. Nevertheless, mice models include transgenic variations. Knock-out mice show the involvement of key molecules in the pathophysiology of PCO which can be built upon to develop inhibitory treatments [113]. Kubo [114] exploited murine models to show the role of tropomyosin in PCO development. Extracapsular lens extraction was performed on mice and rat eyes and the expression of tropomyosin (Tpm) isoforms was examined. The study used SDS-PAGE and Western blot analysis to quantify Tpm1 and Tpm2 expression. For the eyes with cataracts, the bands were stronger and immunohistochemistry showed that Tmp1/2 was found predominantly in the cytoplasm and surface lens fibre. The study continued by relating a higher level of Tmp isoforms to the induction of fibroblastic changes and up-regulation of EMT marker, α -SMA. The study concluded that Tpm1 α /2 β could be used as markers for EMT in LECs. In addition to providing insight into unknown molecular mechanisms, murine models can be used to investigate inhibitory therapeutic interventions as demonstrated by Lois [41] who used rat models to investigate the role of TGF- β 2 and anti-TGF- β 2 antibody. The rat eyes were injected with either solutions of 1 ng/mL TGF- β 2, 1 mg/mL human monoclonal TGF- β 2 antibody, or 5.2 mg/mL control IgG4 antibody. Post-operative clinical evaluation and immunohistochemistry analysis showed no significant difference in PCO development or α -SMA staining between the conditions. The authors suggested this to be due to the other isoforms of TGF- β compensating for the blocked TGF- β 2 activity.

2.2.2. Rabbit

Rabbit models can be used to examine the pathophysiology of PCO as demonstrated by the study conducted by Gerhart [111] who investigated the prevalence of Myo/Nog cells, involved in normal morphogenesis of the lens and retina, within the ciliary process and posterior capsule following cataract surgery. Cataract surgery was performed on the rabbit eyes and the PCO grade was evaluated at day 30. At 24 h post surgery, the number of Myo-Nog cells had significantly increased in the equatorial region of the lens [$p = 0.0001$], the ciliary processes ($p = 0.0002$), and some of the zonule fibres. At day 30, a correlation between the elevated Myo/Nog cell density and the average PCO grade of 2.1 ± 0.8 ($n = 13$ eyes) was found. The Myo/Nog cells overlying the capsule wrinkling expressed α -SMA, a biomarker of myofibroblastic cells involved in PCO [44]. The study concluded that Myo/Nog cells contributed to PCO development for some adults and children and could be targeted to prevent capsule wrinkling and PCO.

Rabbit models can also be used to investigate potential treatments and unlike murine models, can be used to test new IOL technology [17]. This is exemplified by Han [109] who used a rabbit model to evaluate the treatment of an antiproliferative-drug-eluting IOL. IOLs were coated with doxorubicin-loaded chitosan nanoparticles layered with heparin, to decrease cell proliferation and adhesion, respectively. The IOLs were implanted into eight-week-old male rabbits and euthanised by air embolism at 10 weeks. The severity of PCO development was assessed from grade 0 to 3 via slit lamp micrographs. The findings showed that the coating was able to reduce Soemmering's ring formation and cell proliferation. Despite the insight that rabbit models have provided, many studies have shown the different responses between rabbit and human models [17,115,116]. Rabbit immune responses are quicker and have different key pathways; therefore, these animals may respond to therapeutic interventions that would not reflect in humans [17,116]. As such, testing newly developed IOL technology and treatments in rabbit models requires the confirmation that the molecules under investigation are present in humans and rabbits.

2.2.3. Porcine

Porcine models present similar anatomical, physiological, and functional features to those found in humans, providing a niche intermediate between mice and humans [117–119]. The porcine genome is three times closer to the human in comparison to the mouse [119]. Porcine models have been used to elicit underlying biomolecular mechanisms as shown by Ma [113] who used a porcine capsular bag model to determine the role of gremlin within PCO development to establish its potential role as a preventative treatment. Gremlin has been shown to play a role in some fibrotic diseases. However, the mechanisms underlying gremlin's ability to induce EMT and ECM production by LEC are still unknown [113]. In the study, ten pig eyes were treated with either 200 µg/L gremlin or control media for 14 days and cell proliferation was observed via inverted microscope and immunocytochemistry. The study showed that gremlin induces expression of α -SMA, promoting the EMT pathway. Porcine models can be used to further investigate newly developed IOL technology and preventative therapeutics prior to human models. Nevertheless, the use of pig eye donors are not as established as murine, canine, and primate models and have yet to be utilised fully within PCO research [117–119]. Despite the crossover of many of the applications of each animal donor type, there are important distinctions between the types. Murine, rabbit, and porcine models can all provide insight into the key molecules contributing to PCO development and be used to test therapeutic interventions. However, rabbit and porcine models alone allow IOL implantation. In addition, pig tissue is the closest structural and functional match to human tissue than any of the other animal donors.

2.3. Ex Vivo Models

Ex vivo models have a benefit over in vivo models as the explant system maintains the natural structure of the surrounding tissue; therefore, these models provide insight into the localised impact of treatments with less stringent ethical constraints [17,120]. A study conducted by Kassumeh [121] exemplifies this as this study investigated slow-releasing methotrexate (MTX)-loaded poly (lactic-co-glycolic) biomatrices as a IOL coating to reduce PCO. MTX was selected as the best candidate from a review of potential pharmacological drugs that were cross-referenced against those approved by the FDA or EMA. The study found no toxic effects on the corneal cell line CEC-SV40. Moreover, the study performed open-sky cataract surgery on twelve cadaver eyes then implanted the coated IOLs. The capsular bags were kept pinned in culture flasks and kept under standard cell culture conditions. At 9.3 days, the control IOLs showed full cell coverage whereas at this time point, the MTX-coated IOLs showed residual LECs were only visible at the outer edges and took 51.0–51.3 days to achieve full coverage. The application of ex vivo models is further supported by D'Antin [122] who used human eye donor tissue to investigate the treatment of hydrogen peroxide and distilled water to prevent cell proliferation within PCO development. The capsule bag-ciliary body complex was dissected from the donor eyes and transferred to sterile petri dishes onto a silicone ring mould where the iris was removed. Continuous circular capsulorrhexis, hydrodissection, and hydroexpression was performed before individual treatment using a silicone irrigation ring (Figure 4). The study found that both treatments significantly delayed cell growth by day 28 whereas the control donor eyes reached cell confluence by day 11.

In contrast, Taiyab [29] used rat ex vivo models to investigate the role of TGF- β in the EMT pathway within PCO development. In their first study, the explant models were treated with TGF- β with or without SIS3, a SMAD3 inhibitor. The untreated samples showed no α -SMA and stress F-actin fibre expression whereas lens explants treated with TGF- β displayed a greater staining of these markers. The explants treated with TGF- β and SIS3 reduced the expression of α -SMA and stress F-actin fibre expression which corresponded with the positive control ICG-001, an inhibitor of TGF- β -induced EMT. Following on from this work, the study investigated the E-cadherin/ β -cadherin complex within the cell periphery that undergoes rearrangement during EMT-related PCO. On treating the explants with TGF- β , a reduction in E-cadherin and increased nuclear translocation of

β -catenin was observed which led to a loss in cell structure. With the addition of SIS3, the staining of E-cadherin did not alter in comparison to the untreated control explants and only a partial reduction in β -catenin nuclear translocation was seen.

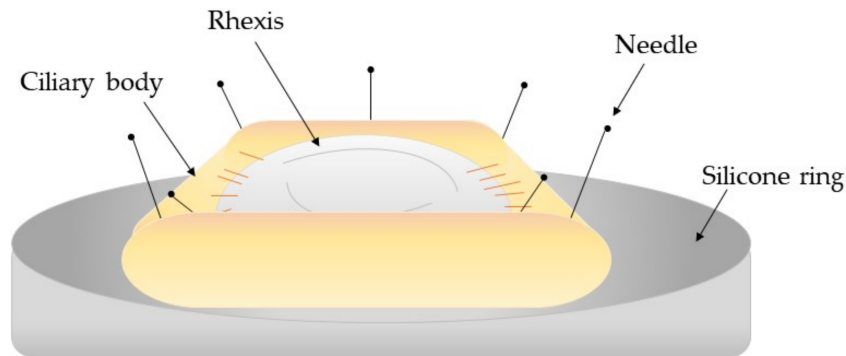


Figure 4. Schematic diagram of the capsule-ciliary body complex attached to a silicone ring mount [122].

Ex vivo models have also been used to improve the reproduction of the clinical environment of PCO as shown by Eldred [123] who used a graded culture media in a human capsular bag model to assess the impact of IOL design on its propensity to initiate PCO development. Mock surgeries were completed on donor human eye tissue after which the eyes were implanted with either Hoya Vivinex or Alcon Acrysof lenses. The capsular bag and surrounding ciliary tissue were secured to a silicone ring within a culture disk. The capsular bag was kept in a graded culture system to reflect the clinical environment, beginning with 5% human serum and 10 ng/mL TGF- β 2 and reducing to serum-free media by day 15–28. A matched pair design was used to assess the implanted IOL and graded culture serum. The findings showed that the graded culture produced quicker posterior coverage, matrix contraction, and significantly increased light scatter. Cell growth over the central optic was greater in the Alcon Acrysof and significantly increased light scatter occurred.

Experimental models provide inexpensive, readily available replicas of the ocular tissue environment to reproduce the pathology of PCO and investigate therapeutic interventions and new IOL technology. Nevertheless, the differences in the wound-healing response and inflammation pathways between species prevents direct comparison to human studies. Experimental models can be exploited prior to clinical studies and present alternative, easily accessible methods for scientific investigation; however, clinical studies utilise a longitudinal design to provide important insight into the dissemination of PCO and the long-term risk factors of novel medical devices and treatments.

2.4. Clinical Studies

Building upon the evidence of preliminary experimental models, clinical studies provide a final evaluation of newly developed IOL technology or therapeutic interventions by using human participants and longitudinal reviews [124]. Clinical studies have been used in PCO research not only for the previously discussed applications but also in determining distribution of PCO and Nd:YAG capsulotomy rates. Nevertheless, these studies also present their own limitations and their specific scope or population demographic can be difficult to translate to the general population, preventing broad applicability. The different study designs and outcomes of recent clinical studies are discussed hereafter.

2.4.1. Surgical Technique and Nd:YAG Laser Ablation Rates

Clinical studies can be important in determining the efficacy of a new surgical technique as shown by Kelkar [125] who evaluated the precision pulse capsulotomy (PPC) technique during phacoemulsification. The study included 99 patients, 123 eyes in the final

analysis. This study did not state the nationality of the patients and a high percentage of the patients were in one age group, of a disproportionately older age range. Moreover, the use of two surgeons presented variability in the performance of the surgical technique under investigation, which is not discussed further. Nevertheless, the study reports on all complications that arose during surgery. The study also discusses previously reported analysis of this technique and provides an in-depth comparison between their findings and previously published data. Although the conclusion on the use of PPC in achieving a “perfectly round capsulorrhexis” is encouraging, the small population size limits this finding, as acknowledged by the authors.

Clinical trials can also provide insight into the epidemiology of Nd:YAG laser capsulotomy rates. This insight provided by clinical trials is an important tool in determining populations most at risk of developing PCO. However, clinical studies that have a median follow-up of less than 2 years do not provide a sufficient timeframe for PCO development [47]. Therefore, these studies would not accurately determine Nd:YAG laser ablation rates as sufficient time has not passed for PCO to develop in the participants. This is exemplified by Ursell [11] who presented a retrospective study to determine three-year incidence of Nd:YAG capsulotomy in relation to the IOL biomaterial; AcroSof hydrophobic (SN60AT/WF, MA30/60AC, MA50/60BM), non-AcroSof hydrophobic (TECNIS ZCB00/ZA9003) or non-AcroSof hydrophilic (AKREOS Mics MI60/Adapt, SOFTEC HD/1, C-FLEX 970C, SUPERFLEX 920H, INCISE, 570H Rayner). Data were collected using Medisoft electronic medical records. The study presented the baseline characteristics of each study group, which was accounted for in the logistic regression analysis. Their results showed the overall Nd:YAG laser ablation incidence rate over the three years was 6.4%. The incidence was two times lower for eyes implanted with AcrySof (2.2–2.7%, $n = 322$) relative to the Non-AcrySof hydrophobic (4.1–4.7%, $n = 843$) and four times lower for eyes implanted with Non-AcrySof hydrophilic (10.5–11.3%, $n = 2157$). The study’s experimental design was limited as patients who were ≤ 65 years were excluded, preventing any generalisation to younger cataract patients. However, the study had a three-year follow up period, establishing sufficient time for PCO to develop in the eye dataset, and the large cohort size of over 50,000 eyes presented a representative population for generalisation of the study’s findings.

2.4.2. Evaluation of Intraocular Lenses

In addition to providing insight into the demographics affected by PCO, clinical studies have additional applications in evaluating newly developed IOL technology when released to a large population. Nevertheless, with the different brands and suppliers of IOL technology, finding a large cohort size is difficult as shown by Van [126] who completed an observational study of 143 patients, 226 eyes at final analysis to investigate the requirement for Nd:YAG for patients implanted with an enVista[®]MX60 IOL. The study did present appropriate exclusion criteria including the exclusion of patients with <24-month follow-up. However, the participant cohort was not representative due to the disproportionate representation of females (29.4/70.6% M/F) and mean age of 80.7 ± 8.3 years. Their primary outcome measures included requirement for Nd:YAG laser ablation and formation rate of glistenings; microvacuoles filled with aqueous humour trapped in the IOL. They found a 3-year cumulative incidence of Nd:YAG laser ablation of 2.2% and no reports of glistenings development. However due to their participant cohort, the results lack validity to represent the larger population.

In comparison to Van [126], Zhao [68] conducted a meta-analysis from a variety of databases to determine a correlation between the wettability of an IOL material and the propensity towards PCO development. Meta-analysis requires a variety of sources to collate findings; therefore, overcoming the challenge of a small participant size. The analysis investigated PCO rates between hydrophobic and hydrophilic acrylic IOLs. The meta-analysis included only age-related cataracts and excluded any case reports and personal communications. The authors used the Cochrane Collaboration tool to report any bias of

the studies included. The review selected 55 eligible studies out of a possible 503 studies, which presented a final total of 889 eyes/patients. Of this group, a broad age range and follow-up period (1–9 years) was included. Their findings suggested hydrophobic IOLs may have lower Nd:YAG rates and PCO score. Nevertheless, the metaanalysis included studies with small participant sizes and studies with different IOL designs, which has been shown to impact PCO development. The authors acknowledged these limitations and suggested further analysis should use long-term randomized controlled studies with large sample sizes to ensure the study design does not influence the findings reported.

2.4.3. Investigating Potential Therapeutic Interventions

Clinical studies can be further used to determine the effectiveness of treatments although there are a limited number of effective therapeutics to date. Hecht [127] presented a retrospective cohort study of 13,368 patients to examine the impact of steroids and NSAID therapy on PCO rates. The mean follow-up was 22.8 ± 15.7 months; a sufficient time period for PCO to develop. The results were confirmed against a second independent dataset. The participants' variables were accounted for and were included within the dataset presented. However, a large number of surgeons were used and their referral of steroid treatment or NSAID therapy introduced subjectivity into the findings. Nevertheless, the study presented a detailed discussion and acknowledged limitations of the retrospective design of the study. The conclusion that post-treatment of steroids alone can significantly decrease PCO development, with no difference found for the additional use of NSAID therapy, could be generalised to a larger population due to the large cohort and time period of investigation within this study. Alongside the restricted availability of treatments, clinical studies are limited to small population cohorts due to the stringent exclusion criteria used specifically in human clinical trials when investigating new treatments. This is exemplified by the study conducted by Rabsilber [128] who investigated the long-term outcomes of the treatment of sealed capsule irrigation with distilled water. Only 17 patients were not excluded, and the follow-up period was 24 months. The treatment was administered to one eye and the other was used as a control. The study found the treatment did not significantly prevent PCO development. However, as in any study with a small population size, further work is required to support the conclusion.

In the last 20 years, PCO research has facilitated a decrease in patients affected by PCO as a result of the introduction of a square-edge design and improvements in surgical techniques. The experimental models discussed in this review have provided insight into the complex developmental pathways of PCO and advancements in IOL technology, allowing long-term restoration of visual acuity and lens function post surgery. A summary of the experimental model design types with their current applications to investigate PCO is shown in Table 1. In future studies, care should be taken to ensure appropriately powered studies and follow-up periods. A minimum of ≥ 2 years is required to ensure sufficient time has passed for PCO presentation to have begun. Moreover, there is a need for studies with a ≥ 10 year follow-up to show unexpected long-term complications such as the late barrier failure, an urgent requirement considering that these complications are more likely to occur as life expectancy rises and cataract surgery is performed earlier in patients [79]. The use of these study design requirements will avoid the dissemination of invalid conclusions, leading to contradictions of known PCO pathways and risk factors. These challenges can be overcome by using retrospective or metaanalysis designs which collate a larger population cohort from multiple studies and provide conclusions that can be used by clinicians to improve the treatment of cataracts and IOL selection in the aid of preventing PCO development for new and existing patients.

Table 1. Overview of the applications of the experimental models of posterior capsule opacification. TGF- β : transforming growth factor beta; EMT: epithelial-mesenchymal transition; LEC: lens epithelial cells.

Model Type	Tissue Donors	Application	References
In vitro	Chick, rat, human, mouse	• Three-dimensional modelling	[106,107,123,129]
		• Role of cytokines and inflammation	[5,16,102]
		• Investigation of intraocular lenses	[105,108,109,130]
		• Inhibition of molecular pathways	[92,103,121,131,132]
		• Surgical technique evaluation	[15]
In vivo	Porcine, murine, human, rabbit	• Investigation of EMT pathway	[114,133]
		• Investigation of intraocular lenses	[109]
		• Investigation of molecular pathways	[110,111]
		• Inhibition of molecular pathways	[41,112,132,134]
		• Role of cytokines	[25]
		• Surgical technique evaluation	[99,100]
Ex vivo	Human, rat, porcine, canine, chick	• Inhibition of molecular pathways	[112,121,132,134,135]
		• Investigation of molecular pathways	[29,136]
		• Investigation of intraocular lenses	[108,137,138]
Clinical studies	n/a	• Identifying risk factors	[47,89]
		• Investigation of therapeutic interventions	[127]
		• Investigation of intraocular lenses	[11,12,53,68–70,121]
		• Surgical technique evaluation	[58,125]

3. Conclusions

In conclusion, this review presented a revised overview of the developmental pathways of PCO, from the initial wound-healing response of the LEC to the formation of a secondary cataract. Additionally, the review examined the individual impact of the risk factors underlying PCO development, establishing the square optic edge as an effective design to prevent PCO and provided clarity on the current understanding on the impact of the IOL material's wettability. Finally, this review demonstrated the latest experimental models used in PCO research and how the model types can be exploited for different applications. Future work should focus on developing current understanding of the pathophysiology

of PCO, providing in-depth analysis of the risk factors leading to PCO, specifically IOL design and function and conducting clinical studies with larger population sizes to ensure reviews provide valid and appropriate conclusions.

Author Contributions: Conceptualisation, Methodology, Software, G.C.; Validation, Formal Analysis, G.C., J.L., M.K.D., S.S.; Investigation, Resources, Data Curation G.C.; Writing—original draft preparation, G.C.; Writing—review and editing, G.C., J.L., M.K.D., S.S.; Visualisation, G.C.; Supervision, J.L., M.K.D., S.S.; Project administration, S.S.; Funding Acquisition, S.S. All authors have read and agreed to the published version of the manuscript.

Funding: This work was supported by University of Brighton Scholarship with the Doctoral Training Alliance Bioscience Programme. Grant Number G2059.

Institutional Review Board Statement: The manuscript did not require ethical approval as it did not use animal nor human participants and is a review of current literature. The manuscript did not require the use of human participants.

Informed Consent Statement: The manuscript did not require the use of human participants, therefore, did not require informed consent.

Data Availability Statement: A full list of references is compiled and attached to this manuscript.

Acknowledgments: This work was supported by a University of Brighton and Doctoral Training Alliance Grant (G2059). The authors would like to acknowledge the Rayner Intraocular Lenses, Ltd. Grant that supported this open access publication.

Conflicts of Interest: The authors report no conflict of interest.

References

1. Wormstone, I.M.; Wang, L.; Liu, C.S.C. Posterior capsule opacification. *Exp. Eye Res.* **2009**, *88*, 257–269. [CrossRef] [PubMed]
2. Nibourg, M.L.; Gelens, E.; Kuijwe, R.; Hooymans, J.M.M.; Kooten Gvan, T.; Koopmans, A.S. Prevention of posterior capsular opacification. *Exp. Eye Res.* **2015**, *136*, 100–115. [CrossRef] [PubMed]
3. Goshe, J.; Awh, C.; Houser, K. Posterior Capsule Opacification. *Am. J. Ophthalmol.* **2020**, *1*. Available online: https://eyewiki.aao.org/w/index.php?title=Posterior_capsule_opacification&oldid=58906 (accessed on 13 September 2020).
4. Sinha, R.; Shekhar, H.; Sharma, N.; Titiyal, J.S.; Vajpayee, R.B. Posterior capsular opacification: A review. *Indian J. Ophthalmol.* **2013**, *61*, 371–376. [CrossRef]
5. Ma, B.; Yang, L.; Jing, R.; Liu, J.; Quan, Y.; Hui, Q.; Li, J.; Qin, L.; Pei, C. Effects of Interleukin-6 on posterior capsular opacification. *Exp. Eye Res.* **2018**, *172*, 94–103. [CrossRef]
6. Meacock, W.R.; Spalton, D.J.; Stanford, M.R. Role of cytokines in the pathogenesis of posterior capsule opacification. *Br. J. Ophthalmol.* **2000**, *84*, 332–336. [CrossRef]
7. Awasthi, N.; Guo, S.; Wagner, B.J. Posterior capsular opacification: A problem reduced but not yet eradicated. *JAMA Ophthalmol.* **2009**, *127*, 555–562. [CrossRef]
8. Trent, N. Global intraocular Lens market 2019: Size, share, demand, trends, growth and 2022 forecasts explored in latest research. *Wise Guy Rep.* **2018**, 1–2.
9. Vasavada, A. Cataract and surgery for cataract. *Br. Med. J.* **2006**, *333*, 128–132.
10. Laser Eye Surgery Hub. Cataract Statistics & Resources. 2018, p. 1. Available online: <https://www.lasereyesurgeryhub.co.uk/cataract-statistics/> (accessed on 9 November 2020).
11. Ursell, P.G.; Dhariwal, M.; Majirska, K.; Ender, F.; Klason-Ray, S.; Venerus, A.; Miglio, C.; Bouchet, C. Three-year incidence of Nd:YAG capsulotomy and posterior capsule opacification and its relationship to monofocal acrylic IOL biomaterial: A UK real world evidence study. *Eye* **2018**, *32*, 1579–1589. [CrossRef]
12. Sadoughi, M.; Einollahi, B.; Roshandel, D.; Sarimohammadli, M.; Feizi, S. Visual and refractive outcomes of phacoemulsification with implantation of accommodating versus standard monofocal intraocular lenses. *J. Ophthalmic Vis. Res.* **2015**, *10*, 370–374. [CrossRef]
13. Jaffe, N.S. History of cataract surgery. *Ophthalmology.* **1996**, *103*, 5–16. [CrossRef]
14. Raj, M.S.; Vasavada, A.R.; Johar, S.R.V.; Vasavadam, A.V.; Vasavada, A.V. Post-operative capsular opacification: A review. *Int. J. Biomed. Sci.* **2007**, *3*, 237–250.
15. Davidson, M.G.; Morgan, D.K.; McGahan, M.C. Effect of surgical technique on in vitro posterior capsule opacification. *J. Cataract Refract. Surg.* **2000**, *26*, 1550–1554. [CrossRef]
16. Jiang, J.; Shihan, M.H.; Wang, Y.; Duncan, M.K. Lens epithelial cells initiate an inflammatory response following cataract surgery. *Investig. Ophthalmol. Vis. Sci.* **2018**, *59*, 4986–4997. [CrossRef]

17. Wormstone, I.M.; Eldred, J.A. Experimental models for posterior capsule opacification research. *Exp. Eye Res.* **2016**, *142*, 2–12. [CrossRef]
18. Mohammadpour, M.; Jafarinasab, M.R.; Javadi, M.A. Outcomes of acute postoperative inflammation after cataract surgery. *Eur. J. Ophthalmol.* **2007**, *17*, 20–28. [CrossRef]
19. Perez-Vives, C. Biomaterial influence on intraocular lens performance: An overview. *J. Ophthalmol.* **2018**, *15*, 2687385. [CrossRef]
20. Rouillard, A.; Gunderson, G.; Fernandez, N.; Wang, Z.; Monteiro, C.; McDermott, M.; Ma'ayan, A. The harmonizome: A collection of processed datasets gathered to serve and mine knowledge about genes and proteins. *Database* **2016**, *2016*, baw100. [CrossRef]
21. Lewis, A.C. Interleukin-6 in the pathogenesis of posterior capsule opacification and the potential role for interleukin-6 inhibition in the future of cataract surgery. *Med. Hypotheses* **2013**, *80*, 466–474. [CrossRef]
22. Dinarello, C.A. Overview of the IL-1 family in innate inflammation and acquired immunity. *Immunol. Rev.* **2018**, *281*, 8–27. [CrossRef] [PubMed]
23. Nishi, O.; Nishi, K.; Ohmoto, Y. Synthesis of interleukin-1, interleukin-6, and basic fibroblast growth factor by human cataract lens epithelial cells. *J. Cataract Refract. Surg.* **1996**, *22*, 852–858. [CrossRef]
24. Basu, A.; Krady, J.K.; Levison, S.W. Interleukin-1: A master regulator of neuroinflammation. *J. Neurosci. Res.* **2004**, *78*, 151–156. [CrossRef] [PubMed]
25. Ferrick, M.R.; Thurau, S.R.; Oppenheim, M.H.; Herbort, C.P.; Ni, M.; Zachariae, C.O.C.; Matsushima, K.; Chan, C.C. Ocular inflammation stimulated by intravitreal interleukin-8 and interleukin-1. *Investig. Ophthalmol. Vis. Sci.* **1991**, *32*, 1534–1539.
26. Xiong, W.; Frasch, S.C.; Thomas, S.M.; Bratton, D.L.; Henson, P.M. Induction of TGF- β 1 synthesis by macrophages in response to apoptotic cells requires activation of the scavenger receptor CD36. *PLoS ONE* **2013**, *8*, e72772. [CrossRef]
27. Wallentin, N.; Wickström, K.; Lundberg, C. Effect of cataract surgery on aqueous TGF- β and lens epithelial cell proliferation. *Investig. Ophthalmol. Vis. Sci.* **1998**, *39*, 1410–1418.
28. Walton, K.L.; Johnson, K.E.; Harrison, C.A. Targeting TGF- β mediated SMAD signaling for the prevention of fibrosis. *Front. Pharmacol.* **2017**, *8*, 461. [CrossRef]
29. Taiyab, A.; Holms, J.; West-Mays, J.A. β -Catenin/Smad3 interaction regulates transforming growth factor- β -induced epithelial to mesenchymal transition in the lens. *Int. J. Mol. Sci.* **2019**, *20*, 2078. [CrossRef]
30. Nishi, O.; Nishi, K.; Ohmoto, Y. Effect of interleukin 1 receptor antagonist on the blood-aqueous barrier after intraocular lens implantation. *Br. J. Ophthalmol.* **1994**, *78*, 917–920. [CrossRef]
31. Wilson, S.E.; Esposito, A. Focus on molecules: Interleukin-1: A master regulator of the corneal response to injury. *Exp. Eye Res.* **2009**, *89*, 124–125. [CrossRef]
32. Ooi, K.G.J.; Galatowicz, G.; Calder, V.L.; Lightman, S.L. Cytokines and chemokines in uveitis—Is there a correlation with clinical phenotype? *Clin. Med. Res.* **2006**, *4*, 294–309. [CrossRef]
33. Kubo, E.; Shibata, S.; Shibata, T.; Kiyokawa, E.; Sasaki, H.; Singh, D.P. FGF2 antagonizes aberrant TGF β regulation of tropomyosin: Role for posterior capsule opacity. *J. Cell Mol. Med.* **2017**, *21*, 916–928. [CrossRef]
34. Kubo, E.; Shibata, T.; Singh, P.D.; Sasaki, H. Roles of TGFB and FGF signals in the lens: Tropomyosin regulation for posterior capsule opacification. *Int. J. Mol. Sci.* **2018**, *19*, 3093. [CrossRef]
35. Tandon, A.; Tovey, J.C.K.; Sharma, A.; Gupta, R.; Mohan, R.R. Role of transforming growth factor beta in corneal function, biology and pathology. *Curr. Mol. Med.* **2012**, *10*, 565–578.
36. Nishi, O.; Nishi, K.; Wada, K.; Ohmoto, Y. Expression of transforming growth factor (TGF)- α , TGF- β 2 and interleukin 8 messenger RNA in postsurgical and cultured lens epithelial cells obtained from patients with senile cataracts. *Graefe's Arch. Clin. Exp. Ophthalmol.* **1999**, *237*, 806–811. [CrossRef]
37. Saika, S. TGFbeta pathobiology in the eye. *Lab. Investig.* **2006**, *86*, 106–115. [CrossRef]
38. Yamashita, H. Functions of the transforming growth factor- β superfamily in eyes. *J. Jpn. Ophthalmol. Soc.* **1997**, *101*, 927–947.
39. Pei, C.; Ma, B.; Kang, Q.-Y.; Qin, L.; Cui, L.-J. Effects of transforming growth factor beta-2 and connective tissue growth factor on induction of epithelial mesenchymal transition and extracellular matrix synthesis in human lens epithelial cells. *Int. J. Ophthalmol.* **2013**, *6*, 752–757.
40. Cho, H.J.; Baek, K.E.; Saika, S.; Jeong, M.J.; Yoo, J. Snail is required for transforming growth factor-beta-induced epithelial-mesenchymal transition by activating PI3 kinase/Akt signal pathway. *Biochem. Biophys. Res. Commun.* **2007**, *353*, 337–343. [CrossRef]
41. Lois, N.; Taylor, J.; McKinnon, A.D.; Smith, G.C.; Van't Hof, R.; Forrester, J.V. Effect of TGF- β 2 and anti-TGF- β 2 antibody in a new in vivo rodent model of posterior capsule opacification. *Investig. Ophthalmol. Vis. Sci.* **2005**, *46*, 4260–4266. [CrossRef]
42. Gotoh, N.; Perdue, N.R.; Matsushima, H.; Sage, E.H.; Yan, Q.; Clark, J.I. An in vitro model of posterior capsular opacity: SPARC and TGF- β 2 minimize epithelial-to-mesenchymal transition in lens epithelium. *Investig. Ophthalmol. Vis. Sci.* **2007**, *48*, 4679–4687. [CrossRef]
43. Amoozgar, B.; Fitzpatrick, S.D.; Sheardown, H. Effect of anti-TGF- β 2 surface modification of polydimethylsiloxane on lens epithelial cell markers of posterior capsule opacification. *J. Bioact. Compat. Polym.* **2013**, *28*, 637–651. [CrossRef]
44. Kurosaka, D.; Kato, K.; Nagamoto, T. Presence of alpha smooth muscle actin in lens epithelial cells of aphakic rabbit eyes. *Br. J. Ophthalmol.* **1996**, *80*, 906–910. [CrossRef]
45. Wormstone, I.M.; Tamiya, S.; Anderson, I.; Duncan, G. TGF- β 2-induced matrix modification and cell transdifferentiation in the human lens capsular bag. *Investig. Ophthalmol. Vis. Sci.* **2002**, *43*, 2301–2308.

46. Weizman Institute of Science. S100A9 gene S100 calcium binding protein A9. *Hum. Gene Database* **2020**. Available online: <https://www.ncbi.nlm.nih.gov/gene?Db=gene&Cmd=DetailsSearch&Term=6280> (accessed on 9 November 2020).
47. Wu, S.; Tong, N.; Pan, L.; Jiang, X.; Li, Y.; Guo, M.; Li, H. Retrospective analyses of potential risk factors for posterior capsule opacification after cataract surgery. *J. Ophthalmol.* **2018**, *2018*, 9089285. [CrossRef]
48. Spalton, D.J. Posterior capsular opacification after cataract surgery. *Eye* **1999**, *13*, 489–492. [CrossRef]
49. Batur, M.; Gül, A.; Seven, E.; Can, E.; Yaşar, T. Posterior capsular opacification in preschool- and school-age patients after pediatric cataract surgery without posterior capsulotomy. *Turk. Oftalmoloji Derg.* **2016**, *46*, 205–208. [CrossRef]
50. Wormstone, I.M.; Liu, C.S.; Rakic, J.M.; Marcantonio, J.M.; Vrenson, G.F.; Duncan, G. Human lens epithelial cell proliferation in a protein-free medium. *Investig. Ophthalmol. Vis. Sci.* **1997**, *38*, 396–404.
51. Praveen, M.R.; Vasavada, A.R.; Shah, G.D.; Shah, A.R.; Khamar, B.M.; Dave, K.H. A prospective evaluation of posterior capsule opacification in eyes with diabetes mellitus: A case-control study. *Eye* **2014**, *28*, 720–727. [CrossRef]
52. Boureau, C.; Lafuma, A.; Jeanbat, V.; Berdeaux, G.; Smith, A.F. Incidence of Nd:YAG laser capsulotomies after cataract surgery: Comparison of 3 square-edged lenses of different composition. *Can. J. Ophthalmol.* **2009**, *44*, 165–170. [CrossRef]
53. Chen, H.-C.; Lee, C.-Y.; Sun, C.-C.; Huang, J.-Y.; Lin, H.-Y.; Yang, S.-F. Risk factors for the occurrence of visual threatening posterior capsule opacification. *J. Transl. Med.* **2019**, *17*, 1. [CrossRef] [PubMed]
54. Ram, J.; Brar, S.G. Posterior capsule opacification: An overview. *DOS Times* **2006**, *12*, 285–288.
55. Keintzel, M.; Kohnen, T. Anterior Optic Capture. *Encycl. Ophthalmol.* **2018**, *2018*. [CrossRef]
56. Menapace, R. Mastering the posterior capsule and optic capture: Elimination of secondary cataract. *Am. J. Ophthalmol.* **2020**, *2020*, 10.
57. Vasavada, A.; Vasavada, V. Pediatric posterior optic capture. *CRST Eur.* **2019**, *2019*, 7–46.
58. Paik, J.; Shiloach, M.; Macsai-Kaplan, M. The effect of posterior capsule polishing on posterior capsule opacification. *Investig. Ophthalmol. Vis. Sci.* **2012**, *53*, 6668.
59. Biswas, P.; Batra, S. Commentary: Anterior capsule polishing: The present perspective. *Indian J. Ophthalmol.* **2020**, *68*, 785–786. [CrossRef]
60. Wang, D.; Yu, X.; Li, Z.; Ding, X.; Lian, H.; Mao, J.; Zhao, Y.; Zhao, Y.-E. The effect of anterior capsule polishing on capsular contraction and lens stability in cataract patients with high myopia. *J. Ophthalmol.* **2018**, *2018*, 8676451. [CrossRef]
61. Joshi, R.S. Incidence of primary peripheral posterior capsular opacification after cataract surgery and posterior capsular opacification in the patients implanted with foldable intraocular lenses. *Nepal. J. Ophthalmol.* **2017**, *9*, 149–155. [CrossRef]
62. Nanavaty, M.A.; Mehta, P.A.; Raj, S.M.; Vasavada, A.R. Diagnosis of pre-existing posterior capsule defect in traumatic white mature cataract with intact anterior capsule. *Eye* **2006**, *20*, 949–951. [CrossRef]
63. Bellucci, R. An introduction to intraocular lenses: Material, optics, haptics, design and aberration. *Cataract* **2013**, *3*, 38–55.
64. Ridley, H. Intra-ocular acrylic lenses—Past, present and future. *Trans. Ophthalmol. Soc. UK* **1964**, *84*, 5–14.
65. Yu, N.; Fang, F.; Wu, B.; Zeng, L.; Cheng, Y. State of the art of intraocular lens manufacturing. *Int. J. Adv. Manuf. Technol.* **2018**, *98*, 1103–1130. [CrossRef]
66. Özyol, P.; Özyol, E.; Karel, F. Biocompatibility of intraocular lenses. *Turk Oftalmoloji Derg.* **2017**, *47*, 221–225. [CrossRef]
67. Saika, S. Relationship between posterior capsule opacification and intraocular lens biocompatibility. *Prog. Retin. Eye Res.* **2004**, *23*, 283–305. [CrossRef]
68. Zhao, Y.; Yang, K.; Li, J.; Huang, Y.; Zhu, S. Comparison of hydrophobic and hydrophilic intraocular lens in preventing posterior capsule opacification after cataract surgery An updated meta-analysis. *Medicine* **2017**, *96*, e8301. [CrossRef]
69. Auffarth, G.U.; Brezin, A.; Caporossi, A.; Lafuma, A.; Mendicute, J.; Bordeaux, G.; Smith, A.F. Comparison of Nd:YAG capsulotomy rates following phacoemulsification with implantation of PMMA, silicone, or acrylic intra-ocular lenses in four European countries. *Ophthalmic Epidemiol.* **2004**, *11*, 319–329. [CrossRef]
70. Mathew, R.G.; Coombes, A.G.A. Reduction of Nd:YAG capsulotomy rates after implantation of a single-piece acrylic hydrophilic intraocular lens with 360° squared optic edge: 24-Month results. *Ophthalmic Surg. Lasers Imaging* **2010**, *41*, 651–655. [CrossRef]
71. Bai, L.; Zhang, J.; Chen, L.; Ma, T.; Liang, H.C. Comparison of posterior capsule opacification at 360-degree square edge hydrophilic and sharp edge hydrophobic acrylic intraocular lens in diabetic patients. *Int. J. Ophthalmol.* **2015**, *8*, 725–729.
72. Werner, L.; Mamalis, N.; Pandey, S.K.; Izak, A.M.; Nilson, C.D.; Davis, B.L.; Weight, C.; Apple, D.J. Posterior capsule opacification in rabbit eyes implanted with hydrophilic acrylic intraocular lenses with enhanced square edge. *J. Cataract Refract. Surg.* **2004**, *30*, 2403–2409. [CrossRef]
73. HariPriya, A.; Chang, D.F.; Vijayakumar, B.; Niraj, A.; Shekhar, M.; Tanpreet, S.; Aravind, S. Long-term posterior capsule opacification reduction with square-edge polymethylmethacrylate intraocular lens: Randomized controlled study. *Ophthalmology* **2017**, *124*, 295–302. [CrossRef]
74. Kohnen, T.; Fabian, E.; Gerl, R.; Hunold, W.; Hütz, W.; Strobel, J.; Hoyer, H.; Mester, U. Optic edge design as long-term factor for posterior capsular opacification rates. *Ophthalmology* **2008**, *115*, 1308–1314. [CrossRef]
75. Nishi, O.; Nishi, K.; Akura, J.; Nagata, T. Effect of round-edged acrylic intraocular lenses on preventing posterior capsule opacification. *J. Cataract Refract. Surg.* **2001**, *27*, 608–613. [CrossRef]
76. Mencucci, R.; Favuzza, E.; Boccalini, C.; Gicquel, J.J.; Raimondi, L. Square-edge intraocular lenses and epithelial lens cell proliferation: Implications on posterior capsule opacification in an in vitro model. *BMC Ophthalmol.* **2015**, *15*, 1–5. [CrossRef]

77. Linnola, R.J.; Sund, M.; Ylönen, R.; Pihlajaniemi, T. Adhesion of soluble fibronectin, laminin, and collagen type IV to intraocular lens materials. *J. Cataract Refract. Surg.* **1999**, *25*, 1486–1491. [CrossRef]
78. Linnola, R.J. Sandwich theory: Bioactivity-based explanation for posterior capsule opacification. *J. Cataract Refract. Surg.* **1997**, *23*, 1539–1542. [CrossRef]
79. Vock, L.; Menapace, R.; Stifter, E.; Georgopoulos, M.; Sacu, S.; Buhl, W. Posterior capsule opacification and neodymium:YAG laser capsulotomy rates with a round-edged silicone and a sharp-edged hydrophobic acrylic intraocular lens 10 years after surgery. *J. Cataract Refract. Surg.* **2009**, *35*, 459–465. [CrossRef]
80. Dawes, L.J.; Illingworth, C.D.; Wormstone, I.M. A fully human in vitro capsular bag model to permit intraocular lens evaluation. *Invest. Ophthalmol. Vis. Sci.* **2012**, *53*, 23–29. [CrossRef]
81. Mylonas, G.; Prskavec, M.; Baradaran-Dilmaghani, R.; Karnik, N.; Buehl, W.; Wirtitsch, M. Effect of a single-piece and a three-piece acrylic sharp-edged IOL on posterior capsule opacification. *Curr. Eye Res.* **2013**, *38*, 86–90. [CrossRef]
82. Bilge, A.H.; Aykan, U.; Akin, T.; Unsal, U. The effects of three-piece or single-piece acrylic intraocular lens implantation on posterior capsule opacification. *Eur. J. Ophthalmol.* **2004**, *14*, 375–380. [CrossRef]
83. Wallin, T.R.; Hinckley, M.; Nilson, C.; Olson, R.J. A clinical comparison of single-piece and three-piece truncated hydrophobic acrylic intraocular lenses. *Am. J. Ophthalmol.* **2003**, *136*, 614–619. [CrossRef]
84. Hayashi, K.; Hayashi, H.; Nakao, F.; Hayashi, F. Comparison of decentration and tilt between one piece and three piece polymethyl methacrylate intraocular lenses. *Br. J. Ophthalmol.* **1998**, *82*, 419–422. [CrossRef] [PubMed]
85. Zvornicanin, J.; Zvornicanin, E. Premium intraocular lenses: The past, present and future. *J. Curr. Ophthalmol.* **2018**, *30*, 287–296. [CrossRef] [PubMed]
86. Buckhurst, P.J.; Naroo, S.A.; Shah, S. Advanced intraocular lens designs. *Eur. Ophthalmic Rev.* **2010**, *4*, 82–86. [CrossRef]
87. Alió, J.L.; Barrio, J.L.A.; Vega-Estrada, A. Accommodative intraocular lenses: Where are we and where we are going. *Eye Vis.* **2017**, *4*, 1–12. [CrossRef]
88. Takakura, A.; Iyer, P.; Adams, J.R.; Pepin, S.M. Functional assessment of accommodating intraocular lenses versus monofocal intraocular lenses in cataract surgery: Metaanalysis. *J. Cataract Refract. Surg.* **2010**, *36*, 380–388. [CrossRef]
89. Elgohary, M.A.; Dowler, J.G. Incidence and risk factors of Nd:YAG capsulotomy after phacoemulsification in non-diabetic and diabetic patients. *Clin. Exp. Ophthalmol.* **2006**, *34*, 526–534. [CrossRef]
90. Burq, M.A.; Taqui, A.M. Frequency of retinal detachment and other complications after neodymium:YAG capsulotomy. *J. Cataract Refract. Surg.* **2008**, *58*, 550–552.
91. Nixon, D.R.; Woodcock, M.G. Pattern of posterior capsule opacification models 2 years postoperatively with 2 single-piece acrylic intraocular lenses. *J. Cataract Refract. Surg.* **2010**, *36*, 929–934. [CrossRef]
92. Shao, J.Z.; Qi, Y.; Du, S.S.; Du, W.W.; Li, F.Z.; Zhang, F.Y. In vitro inhibition of proliferation, migration and epithelial-mesenchymal transition of human lens epithelial cells by fasudil. *Int. J. Ophthalmol.* **2018**, *11*, 1253–1257.
93. Kramer, G.D.; Werner, L.; Mamalis, N. Prevention of postoperative capsular bag opacification using intraocular lenses and endocapsular devices maintaining an open or expanded capsular bag. *J. Cataract Refract. Surg.* **2016**, *42*, 469–484. [CrossRef]
94. Hasanee, K.; Butler, M.; Ahmed, I.I.K. Capsular tension rings and related devices: Current concepts. *Curr. Opin. Ophthalmol.* **2006**, *17*, 31–41.
95. Hara, T.; Hara, T.; Yamada, Y. “Equator ring” for maintenance of the completely circular contour of the capsular bag equator after cataract removal. *Ophthalmic Surg.* **1991**, *22*, 358–359.
96. Hara, T.; Hara, T.; Narita, M. Long-term study of posterior capsular opacification prevention with endocapsular equator rings in humans. *Arch Ophthalmol.* **2011**, *129*, 855–863. [CrossRef]
97. Menapace, R.; Sacu, S.; Georgopoulos, M.; Findl, O.; Rainer, G.; Nishi, O. Efficacy and safety of capsular bending ring implantation to prevent posterior capsule opacification: Three-year results of a randomized clinical trial. *J. Cataract Refract. Surg.* **2008**, *34*, 1318–1328. [CrossRef]
98. Nishi, O.; Nishi, K.; Menapace, R.; Akura, J. Capsular bending ring to prevent posterior capsule opacification: 2 year follow-up. *J. Cataract Refract. Surg.* **2001**, *27*, 1359–1365. [CrossRef]
99. Slutzky, L.; Kleinmann, G. Further enhancement of intraocular open-capsule devices for prevention of posterior capsule opacification. *Transl. Vis. Sci. Technol.* **2018**, *7*, 21. [CrossRef]
100. Alon, R.; Assia, E.I.; Kleinmann, G. Prevention of posterior capsule opacification by an intracapsular open capsule device. *Lens* **2014**, *55*, 4005–4013. [CrossRef]
101. Chung, K.K.; Schumacher, J.F.; Sampson, E.M.; Burne, R.; Antonelli, P.J.; Brennan, A.B.; Reddy, S.T. Impact of engineered surface microtopography on biofilm formation of *Staphylococcus aureus*. *Biointerphases* **2007**, *2*, 89–94. [CrossRef]
102. VanSlyke, J.K.; Boswell, B.A.; Musil, L.S. Fibronectin regulates growth factor signaling and cell differentiation in primary lens cells. *J. Cell Sci.* **2018**, *131*, 22. [CrossRef]
103. Wertheimer, C.; Liegl, R.; Kernt, M.; Mayer, W.; Docheva, D.; Kampik, A.; Eibl-Lindner, K.H. EGF receptor inhibitor erlotinib as a potential pharmacological prophylaxis for posterior capsule opacification. *Graefes Arch. Clin. Exp. Ophthalmol.* **2013**, *251*, 1529–1540. [CrossRef]
104. Zukin, L.M.; Pedler, M.G.; Groman-Lupa, S.; Pantcheva, M.; Ammar, D.A.; Mark Petrash, J. Aldose reductase inhibition prevents development of posterior capsular opacification in an in vivo model of cataract surgery. *Investig. Ophthalmol. Vis. Sci.* **2018**, *59*, 3591–3598. [CrossRef] [PubMed]



105. Cooke, C.A.; McGimpsey, S.; Mahon, G.; Best, R.M. An in vitro study of human lens epithelial cell adhesion to intraocular lenses with and without a fibronectin coating. *Invest. Ophthalmol. Vis. Sci.* **2006**, *47*, 2985–2989. [CrossRef] [PubMed]
106. Plüss, C.J.; Kustermann, S. A Human Three-Dimensional In Vitro Model of Lens Epithelial Cells as a Model to Study Mechanisms of Drug-Induced Posterior Subcapsular Cataracts. *J. Ocul. Pharmacol. Ther.* **2019**, *36*, 56–64. [CrossRef] [PubMed]
107. Joseph, R.; Bales, K.; Srivastava, K.; Srivastava, O. Lens epithelial cells-induced pluripotent stem cells as a model to study epithelial-mesenchymal transition during posterior capsular opacification. *Biochem. Biophys. Rep.* **2019**, *20*, 100696. [CrossRef]
108. Wertheimer, C.; Kueres, A.; Siedlecki, J.; Braun, C.; Kassumeh, S.; Wolf, A.; Mayer, W.; Priglinger, C.; Priglinger, S.; Eibl-Lindner, K. The intraocular lens as a drug delivery device for an epidermal growth factor–Receptor inhibitor for prophylaxis of posterior capsule opacification. *Acta Ophthalmol.* **2018**, *96*, e874–e882. [CrossRef]
109. Han, Y.; Tang, J.; Xia, J.; Wang, R.; Qin, C.; Liu, S.; Zhao, X.; Chen, H.; Lin, Q. Anti-adhesive and antiproliferative synergistic surface modification of intraocular lens for reduced posterior capsular opacification. *Int. J. Nanomed.* **2019**, *14*, 9047–9061. [CrossRef]
110. Shihan, M.H.; Kanwar, M.; Wang, Y.; Jackson, E.E.; Faranda, A.P.; Duncan, M.K. Fibronectin has multifunctional roles in posterior capsular opacification (PCO). *Matrix Biol.* **2020**, *90*, 79–108. [CrossRef]
111. Gerhart, J.; Withers, C.; Gerhart, C.; Werner, L.; Mamalis, N.; Bravo-Nuevo, A.; Scheinfeld, V.; FitzGerald, P.; Getts, R.; George-Weinstein, M. Myo/Nog cells are present in the ciliary processes, on the zonule of Zinn and posterior capsule of the lens following cataract surgery. *Exp. Eye Res.* **2018**, *171*, 101–105. [CrossRef]
112. Sternberg, K.; Terwee, T.; Stachs, O.; Guthoff, R.; Lobler, M.; Schmitz, K.P. Drug-induced secondary cataract prevention: Experimental ex vivo and in vivo results with disulfiram, methotrexate and actinomycin. *D. Ophthalmic Res.* **2010**, *44*, 225–236. [CrossRef]
113. Ma, B.; Jing, R.; Liu, J.; Qi, T.; Pei, C. Gremlin is a potential target for posterior capsular opacification. *Cell Cycle* **2019**, *18*, 1714–1726. [CrossRef]
114. Kubo, E.; Hasanova, N.; Fatma, N.; Sasaki, H.; Singh, D.P. Elevated tropomyosin expression is associated with epithelial-mesenchymal transition of lens epithelial cells. *J. Cell. Mol. Med.* **2013**, *17*, 212–221. [CrossRef]
115. Chang, P.; Lin, L.; Zheng, Q.; Yu, F.; Yu, X.; Zhao, Y.; Ding, X.; Zhu, W.; Li, J.; Zhao, Y. An optical section-assisted in vivo rabbit model for capsular bend and posterior capsule opacification investigation. *PLoS ONE* **2016**, *2*, e0148553. [CrossRef]
116. Duncan, G.; Wang, L.; Neilson, G.J.; Wormstone, I.M. Lens cell survival after exposure to stress in the closed capsular bag. *Investig. Ophthalmol. Vis. Sci.* **2007**, *48*, 2701–2707. [CrossRef]
117. Dawson, H.D.; Smith, A.D.; Chen, C.; Urban, J.F. An in-depth comparison of the porcine, murine and human inflammasomes; lessons from the porcine genome and transcriptome. *Vet. Microbiol.* **2017**, *202*, 2–15. [CrossRef]
118. Meurens, F.; Summerfield, A.; Nauwynck, H.; Saif, L.; Gerdts, V. The pig: A model for human infectious diseases. *Trends Microbiol.* **2012**, *20*, 50–57. [CrossRef]
119. Walters, E.M.; Prather, R.S. Advancing swine models for human health and diseases. *Mo. Med.* **2013**, *110*, 212–215.
120. Wormstone, I.M. The human capsular bag model of posterior capsule opacification. *Eye* **2019**, *34*, 225–231. [CrossRef]
121. Kassumeh, S.A.; Wertheimer, C.M.; von Studnitz, A.; Hillenmayer, A.; Priglinger, C.; Wolf, A.; Mayer, W.J.; Teupser, D.; Holdt, L.M.; Priglinger, S.G.; et al. Poly(lactic-co-glycolic) Acid as a slow-release drug-carrying matrix for methotrexate coated onto intraocular lenses to conquer posterior capsule opacification. *Curr. Eye Res.* **2018**, *43*, 702–708. [CrossRef]
122. D’Antin, J.C.; Barraquer, R.I.; Tresserra, F.; Michael, R. Prevention of posterior capsule opacification through intracapsular hydrogen peroxide or distilled water treatment in human donor tissue. *Sci. Rep.* **2018**, *8*, 1–10. [CrossRef]
123. Eldred, J.A.; Zheng, J.; Chen, S.; Wormstone, I.M. An in vitro human lens capsular bag model adopting a graded culture regime to assess putative impact of iols on pco formation. *Investig. Ophthalmol. Vis. Sci.* **2019**, *60*, 113–122. [CrossRef]
124. Aronson, J.K. What is a clinical trial? *Br. J. Clin. Pharmacol.* **2004**, *58*, 1–3. [CrossRef] [PubMed]
125. Kelkar, J.; Mehta, H.; Kelkar, A.; Agarwal, A.; Kothari, A.; Kelkar, S. Precision pulse capsulotomy in phacoemulsification: Clinical experience in Indian eyes. *Indian J. Ophthalmol.* **2018**, *66*, 1272–1277. [CrossRef]
126. Ton Van, C.; Tran, T.H.C. Incidence of posterior capsular opacification requiring Nd:YAG capsulotomy after cataract surgery and implantation of enVista®MX60 IOL. *J. Français Ophthalmol.* **2018**, *41*, 899–903. [CrossRef]
127. Hecht, I.; Karesvuo, P.; Achiron, A.; Elbaz, U.; Laine, I.; Tuuminen, R. Anti-inflammatory Medication After Cataract Surgery and Posterior Capsular Opacification. *Am. J. Ophthalmol.* **2020**, *215*, 104–111. [CrossRef]
128. Rabsilber, T.M.; Limberger, I.J.; Reuland, A.J.; Holzer, M.P.; Auffarth, G.U. Long-term results of sealed capsule irrigation using distilled water to prevent posterior capsule opacification: A prospective clinical randomised trial. *Br. J. Ophthalmol.* **2007**, *91*, 912–915. [CrossRef]
129. Jun, J.H.; Sohn, W.-J.; Lee, Y.; Chang, S.D.; Kim, J.-Y. Experimental lens capsular bag model for posterior capsule opacification. *Cell Tissue Res.* **2014**, *357*, 101–108. [CrossRef]
130. van Kooten, T.G.; Koopmans, S.; Terwee, T.; Norrby, S.; Hooymans, J.M.M.; Busscher, H.J. Development of an accommodating intra-ocular lens-In vitro prevention of re-growth of pig and rabbit lens capsule epithelial cells. *Biomaterials* **2006**, *27*, 5554–5560. [CrossRef]
131. Awasthi, N.; Wang-Su, S.T.; Wagner, B.J. Downregulation of MMP-2 and -9 by proteasome inhibition: A possible mechanism to decrease LEC migration and prevent posterior capsular opacification. *Invest. Ophthalmol. Vis. Sci.* **2008**, *49*, 1998–2003. [CrossRef]

132. Malecaze, F.; Decha, A.; Serre, B.; Penary, M.; Duboue, M.; Berg, D.; Levade, T.; Lubsen, N.H.; Kremer, E.J.; Couderc, B. Prevention of posterior capsule opacification by the induction of therapeutic apoptosis of residual lens cells. *Gene Ther.* **2006**, *13*, 440–448. [CrossRef] [PubMed]
133. Shirai, K.; Tanaka, S.I.; Lovicu, F.J.; Saika, S. The murine lens: A model to investigate in vivo epithelial–mesenchymal transition. *Dev. Dyn.* **2018**, *247*, 340–345. [CrossRef] [PubMed]
134. Yadav, U.C.S.; Ighani-Hosseini, F.; van Kuijk, F.J.G.M.; Srivastava, S.K.; Ramana, K. Prevention of posterior capsular opacification through aldose reductase inhibition. *Investig. Ophthalmol. Vis. Sci.* **2009**, *50*, 752–759. [CrossRef] [PubMed]
135. Ongkasin, K.; Masmoudi, Y.; Wertheimer, C.M.; Hillenmayer, A.; Eibl-Lindner, K.H.; Badens, E. Supercritical fluid technology for the development of innovative ophthalmic medical devices: Drug loaded intraocular lenses to mitigate posterior capsule opacification. *Eur. J. Pharm. Biopharm.* **2020**, *149*, 248–256. [CrossRef] [PubMed]
136. Chandler, H.L.; Haeussler, D.J.; Gemensky-Metzler, A.J.; Wilkie, D.A.; Lutz, E.A. Induction of posterior capsule opacification by hyaluronic acid in an ex vivo model. *Investig. Ophthalmol. Vis. Sci.* **2012**, *53*, 1835–1845. [CrossRef] [PubMed]
137. Hillenmayer, A.; Wertheimer, C.; Kassumeh, S.; von Studnitz, A.; Luft, N.; Ohlmann, A.; Priglinger, S.; Mayer, W. Evaluation of posterior capsule opacification of the Alcon Clareon IOL vs the Alcon Acrysof IOL using a human capsular bag model. *BMC Ophthalmol.* **2020**, *20*, 1–7. [CrossRef]
138. Pot, S.A.; Chandler, H.L.; Colitz, C.M.H.; Bentley, E.; Dubielzig, R.R.; Mosley, T.S.; Reid, T.W.; Murphy, C.J. Selenium functionalized intraocular lenses inhibit posterior capsule opacification in an ex vivo canine lens capsular bag assay. *Exp. Eye Res.* **2009**, *89*, 728–734. [CrossRef]



Article

Permeability of the Retina and RPE-Choroid-Sclera to Three Ophthalmic Drugs and the Associated Factors

Hyeong Min Kim ^{1,†}, Hyoungkoo Han ^{2,†}, Hye Kyoung Hong ¹, Ji Hyun Park ¹, Kyu Hyung Park ¹,
Hyuncheol Kim ^{2,*}  and Se Joon Woo ^{1,*} 

¹ Department of Ophthalmology, Seoul National University College of Medicine, Seoul National University Bundang Hospital, Seongnam 13620, Korea; hmkim3@gmail.com (H.M.K.); alpaomega@hanmail.net (H.K.H.); park9845@hanmail.net (J.H.P.); jiani4@snu.ac.kr (K.H.P.)

² Department of Chemical and Biomolecular Engineering, Sogang University, Seoul 04107, Korea; 507513@hanmail.net

* Correspondence: hyuncheol@sogang.ac.kr (H.K.); sejoon1@snu.ac.kr (S.J.W.); Tel.: +82-2-705-8922 (H.K.); +82-31-787-7377 (S.J.W.); Fax: +82-2-3273-0331 (H.K.); +82-31-787-4057 (S.J.W.)

† These authors contributed equally to this work.

Abstract: In this study, Retina-RPE-Choroid-Sclera (RCS) and RPE-Choroid-Sclera (CS) were prepared by scraping them off neural retina, and using the Ussing chamber we measured the average time-concentration values in the acceptor chamber across five isolated rabbit tissues for each drug molecule. We determined the outward direction permeability of the RCS and CS and calculated the neural retina permeability. The permeability coefficients of RCS and CS were as follows: ganciclovir, 13.78 ± 5.82 and 23.22 ± 9.74 ; brimonidine, 15.34 ± 7.64 and 31.56 ± 12.46 ; bevacizumab, 0.0136 ± 0.0059 and 0.0612 ± 0.0264 ($\times 10^{-6}$ cm/s). The calculated permeability coefficients of the neural retina were as follows: ganciclovir, 33.89 ± 12.64 ; brimonidine, 29.83 ± 11.58 ; bevacizumab, 0.0205 ± 0.0074 ($\times 10^{-6}$ cm/s). Between brimonidine and ganciclovir, lipophilic brimonidine presented better RCS and CS permeability, whereas ganciclovir showed better calculated neural retinal permeability. The large molecular weight drug bevacizumab demonstrated a much lower permeability than brimonidine and ganciclovir. In conclusion, the ophthalmic drug permeability of RCS and CS is affected by the molecular weight and lipophilicity, and influences the intravitreal half-life.

Keywords: permeability; retina; retinal pigment epithelium; Ussing chamber; intravitreal half-life

Citation: Kim, H.M.; Han, H.; Hong, H.K.; Park, J.H.; Park, K.H.; Kim, H.; Woo, S.J. Permeability of the Retina and RPE-Choroid-Sclera to Three Ophthalmic Drugs and the Associated Factors. *Pharmaceutics* **2021**, *13*, 655. <https://doi.org/10.3390/pharmaceutics13050655>

Academic Editors: Francisco Javier Otero-Espinar and Anxo Fernández Ferreiro

Received: 6 April 2021

Accepted: 1 May 2021

Published: 4 May 2021

Publisher's Note: MDPI stays neutral with regard to jurisdictional claims in published maps and institutional affiliations.



Copyright: © 2021 by the authors. Licensee MDPI, Basel, Switzerland. This article is an open access article distributed under the terms and conditions of the Creative Commons Attribution (CC BY) license (<https://creativecommons.org/licenses/by/4.0/>).

1. Introduction

The advancement of ophthalmic drug delivery to the posterior segment requires extensive knowledge of intraocular pharmacokinetics (PK). Representative intraocular PK parameters, such as intravitreal half-life, mean residence time, observed maximum concentration, and clearance rate, were considered as the substantial indicators of drug efficacy [1,2]. Thus, numerous investigations have been conducted to establish better drug efficacy with intravitreal half-life prolongation by reducing the elimination rate and controlling drug release [3–5]. Regarding the elimination/clearance process, retinal pigment epithelium (RPE) is considered as a major barrier in the posterior segment ocular delivery, which is located between the neural retina and choroid [1,6]. After intravitreal injection of newly developed anti-vascular endothelial growth factor (VEGF) drugs or small molecular drugs, the molecules diffuse in the intraocular space. These are eliminated via the anterior (aqueous humor) and posterior (retina-RPE-choroid) pathways across the blood-ocular barriers, including the blood-aqueous barrier (BAB) and blood-retinal barrier (BRB), which consists of the retinal pigment epithelium (RPE) and endothelium of the retinal vessels [7–9]. In addition, the inner limiting membrane (ILM), which is composed of a fine meshwork with nanopores, and tight junctions in the RPE, are considered to restrict drug permeation [10,11]. Therefore, drug permeability in the posterior segment, specifically the neural retina, RPE, and choroid, is important to achieve better drug efficacy.

Since retinal permeability is crucial for intraocular pharmacokinetics and dynamics, numerous experiments have been conducted previously, which found that RPE drug permeability was largely affected by molecular physicochemical properties such as molecular weight (MW) and lipophilicity [12–14]. These permeability studies were performed with *ex vivo* ocular tissues using a special diffusion apparatus known as the “Ussing chamber”, which is widely adopted for the evaluation of molecular transport across epithelia [15]. The ionic transport mechanisms in the fresh isolated tissues were identified and the retinal permeability was estimated by measuring the drug concentration in the chamber and recording the transepithelial resistance/potential. However, most of the previous investigations have focused on the trans-scleral delivery of ophthalmic drugs, from beta-blockers to immunoglobulin and fluorescein isothiocyanate (FITC)-labeled dextrans [12,16,17]. Currently, a few permeability studies have used intravitreal injection drugs [18,19], but experimental data are insufficient to keep up with the rapid advancement of posterior segment ocular drug delivery.

Thus, the purpose of our study was to provide systematic data on the pre-clinically measured permeability coefficients in posterior segment tissues, and to help clinicians and researchers to assess the intraocular pharmacokinetics of three substantial drug compounds being investigated and engineered for the advancement of ocular drug delivery systems. Prior investigations concentrating on the retinal permeability and its effect on intraocular PK parameters have not been adequate, especially the measurement or calculation of the experimental values. Therefore, in this study, we experimented with three ophthalmic drugs, including ganciclovir, brimonidine, and bevacizumab, to evaluate retinal and RPE-choroid-sclera permeability from the vitreous to the systemic blood circulation (outward direction) in New Zealand white rabbit eyes. As mentioned above, both ganciclovir and brimonidine are small molecular weight drugs, and sustained-release intravitreal implants have been developed. Bevacizumab is a representative large molecular weight anti-VEGF drug that has been applied to various retinal diseases. Then, together with seven different small drug molecules studied in previous literature, we analyzed the association between intravitreal half-life and retinal permeability in various ophthalmic drugs.

2. Materials and Methods

2.1. Isolation and Preparation of Ocular Tissues

Approval was obtained from the Seoul National University Bundang Hospital Institutional Animal Care and Use Committee, and animal experiments were conducted in accordance with the guidelines of the Association for Research in Vision and Ophthalmology for animal use in research.

A total of 30 eyes from 15 healthy New Zealand white rabbits weighing 1.5–2.0 kg and aged 8–10 weeks were used for the study; five eyes each for the three ophthalmic drugs (brimonidine, ganciclovir, and bevacizumab) with two different ocular tissues (retina-RPE-choroid-sclera and RPE-choroid-sclera). The rabbits were anesthetized with 15 mg/kg tiletamine hydrochloride/zolazepam hydrochloride (Zoletil, Virbac Laboratories, Carros Cedex, France) and 5 mg/kg of xylazine hydrochloride (Rompun, Bayer Healthcare, Seoul, Korea), and the rabbit eyes were enucleated immediately after euthanization and stored in ice-cold Ringer buffer until use. We then removed the adherent muscles and fats on the outer sclera, divided the anterior and posterior segments by circumferential cutting behind the limbus, and gently separated the lens and vitreous from the neural retina to obtain retina-RPE-choroid-sclera tissues. Finally, we carefully detached the neural retina using forceps to obtain RPE-choroid-sclera tissues. Isolated tissues were stored in phosphate-buffered saline (PBS; pH 7.4). To minimize the damage to tissue integrity, the extracted tissues were used immediately.

2.2. Permeability Studies with the Ussing Chamber

Two different ocular tissues (retina-RPE-choroid-sclera and RPE-choroid-sclera) were placed in a tissue insert with ring-shaped silicone adapters and a circular diffusion area of

0.19625 cm² which was enclosed with micropore membranes (0.22 µm, nitrocellulose; MIL-LIPORE, Darmstadt, Germany), and mounted in the Ussing chamber (Navicyte, Harvard Apparatus, Holliston, MA, USA). Both sides of the chamber (left, donor chamber; right, acceptor chamber) were filled with 4 mL of PBS solution, with drug concentrations of ganciclovir and brimonidine (Sigma-Aldrich, St. Louis, MO, USA) dissolved at 0.244 mg/mL, and bevacizumab (Avastin; Genentech, Inc., San Francisco, CA, USA) at 4.469 mg/mL on the donor side. Both compartments in the Ussing chamber were filled with oxygen or a mixture of 95% O₂ and 5% CO₂. Permeability was measured only in the outward direction, which resembles the elimination pathway from the vitreous to the choroid to the systemic blood circulation.

Samples (0.1 mL) were taken from the acceptor chambers at eight different time points (0.5, 1, 1.5, 2, 2.5, 3, 3.5, and 4 h) and replaced with fresh buffer of the same volume. For the small molecular weight drugs, ganciclovir and brimonidine, drug concentrations from acceptor chambers were quantified by high-performance liquid chromatography (YL9100 HPLC system, Youngin, Korea). Zorbax Eclipse Plus C18 (4.6 mm × 250 mm, 5 µm; Agilent Technologies, Santa Clara, CA, USA) was used for the separation of brimonidine. The flow rate was 1.0 mL/min, and elution of the mobile phase of acetonitrile:buffer (10:90, *v/v*) was isocratic. The buffer consisted of 10 mM trimethylamine, adjusted to pH 3.2 with phosphoric acid. The UV detector was set to 248 nm, and the retention time was 6 min. Symmetry C18 (4.6 × 250 mm, 5 µm; Waters, Milford, MA, USA) was used for the separation of ganciclovir. The flow rate was 1.0 mL/min, and the mobile phase of methanol:buffer (20:80, *v/v*) was isocratic. The buffer was prepared by diluting 1 mL of trifluoroacetic acid in 1000 mL distilled water, and the pH was adjusted to 2.5.

For the large molecular weight drug bevacizumab, an indirect enzyme-linked immunosorbent assay (ELISA) was performed to measure the drug concentrations. The specific immunoassay procedure was previously described in multiple articles published by our group [20–24]. In brief, the human 165-amino-acid variant of recombinant VEGF (R&D systems, Minneapolis, MN, USA) was diluted to 1.0 µg/mL in 50 mM carbonate buffer (pH 9), immobilized on 96-well flat-bottom plates (NUNC, Roskilde, Denmark), and aliquoted at 100 µL/well. Then, the plates were incubated overnight at 4 °C, washed with 1 × PBS, and blocked for 2 h at 4 °C with 1% BSA in 1X PBS. After the final washing process, the plates were stored at 4 °C until further use. Subsequently, the samples acquired from the acceptor chambers at different time points were diluted with 0.1% BSA in 1X PBS to be within the range of the assay, aliquoted into the rVEGF-coated plates (100 µL/well), and incubated overnight at 4 °C. In each individual plate, known bevacizumab concentrations ranging from 0.049–3.125 ng/mL were included to generate a standard curve. Bevacizumab was detected using an anti-human immunoglobulin G horseradish peroxidase antibody (GE Healthcare, Pittsburgh, PA, USA). Finally, the optical density was measured by detecting the absorbance after treating the 3,3',5,5'-tetramethyl benzidine substrate with hydrogen peroxide. Standard curves were generated using SoftMax Pro 5.4.1. software (Molecular Devices, Sunnyvale, CA, USA).

2.3. Selection of Ophthalmic Drugs for Permeability Experiments

In this study, three ophthalmic drugs, including ganciclovir, brimonidine, and bevacizumab, were selected for permeability measurements. Brimonidine is an α₂-adrenergic agonist that is widely used in glaucoma treatment. Brimonidine is currently highlighted for its neuroprotective benefit by promoting retinal ganglion cell survival [25]. Moreover, as previously mentioned, a brimonidine intravitreal implant (Brimo DDS[®], Allergan plc, Dublin, Ireland) is currently under human clinical trial and showed positive results in improving geographic atrophy in neovascular AMD eyes [26]. Thus, we decided to measure the posterior segment tissue permeability of brimonidine, since the drug might be used in the near future not only as a topical agent, but also for intravitreal administration. Ganciclovir is an antiviral drug for the treatment of cytomegalovirus (CMV) retinitis via an intravitreal injection [27]. Ganciclovir attracted our attention because we could assess

the association of drug permeation and molecular physicochemical properties between brimonidine and ganciclovir, also considering that ganciclovir itself features a similar molecular weight, but is hydrophilic compared to brimonidine. In addition, ganciclovir has also been developed as an intravitreal implant (Vitrasert[®], Bausch & Lomb, Rochester, NY, USA). Lastly, we selected bevacizumab to determine the effects of a large molecular weight on permeation. Identifying the permeability of these three ophthalmic drugs is crucial for posterior segment drug delivery to treat various retinal diseases.

2.4. Determination of Permeability Coefficients

The apparent permeability coefficients (P_{app}) of the three ophthalmic drug molecules (ganciclovir, brimonidine, and bevacizumab) were calculated from the slope of the compound amount versus time profile on the acceptor side.

$$P_{app} = \left(\frac{dC}{dt} \right) \times V / (A \times C_0) \quad (1)$$

$\frac{dC}{dt}$: Change in the acceptor concentration calculated from the slope of the time–concentration curve between two time points

V: Buffer volume in the donor compartment (4 mL)

A: Diffusional area of the membrane (exposed surface area: 0.19625 cm²)

C_0 : Initial donor chamber concentration

The slope of the time–concentration curve was derived from the concentration differences between the final time point (4 h) and the initial time point at the presumed steady-state, in this case, 30 min for brimonidine and ganciclovir, and 1.5 h for bevacizumab.

Since we conducted permeability studies with two different ocular tissues (retina-RPE-choroid-sclera (RCS) and RPE-choroid-sclera (CS) scraped off the neural retina), we calculated the neural retina permeability coefficients according to the equation below, which presents the overall contribution to the total permeability with multiple barriers and various permeation resistances.

$$\frac{1}{P_{RCS}} = \frac{1}{P_R} + \frac{1}{P_{CS}} \quad (2)$$

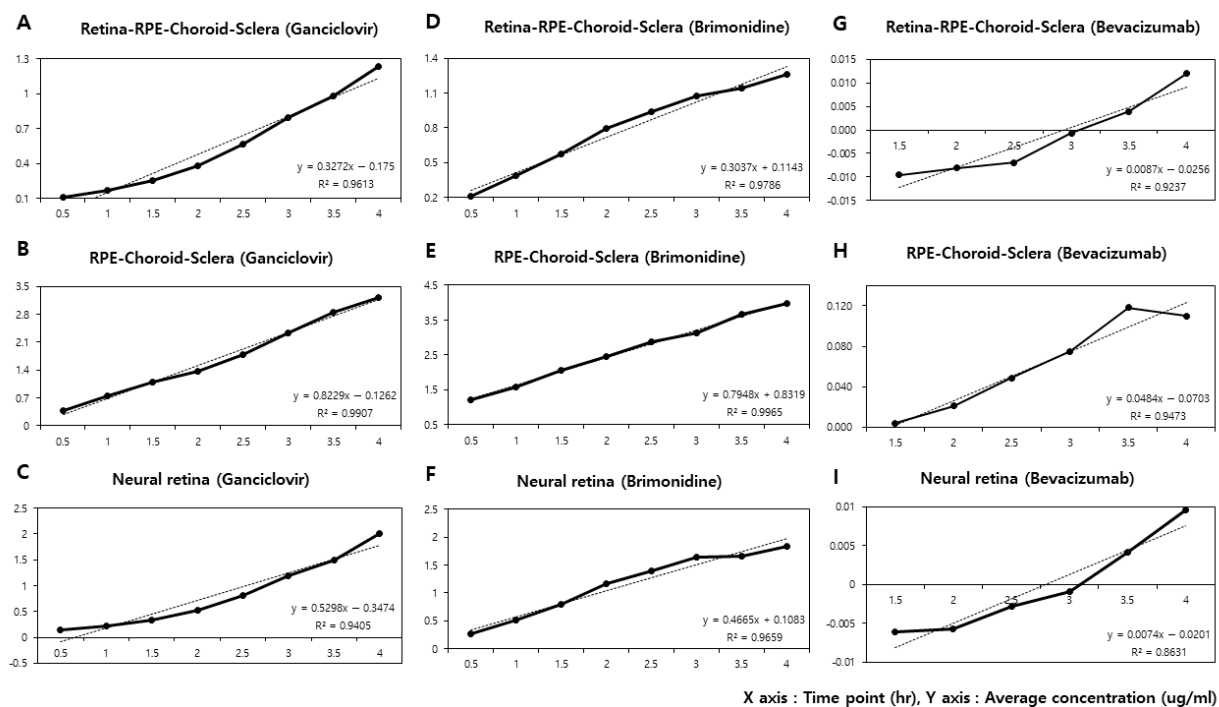
3. Results

The average time–concentration values ($\mu\text{g}/\text{mL}$) of retina-RPE-choroid-sclera (RCS) and RPE-choroid-sclera (CS) rabbit ocular tissues in the acceptor chamber are shown in Table 1. For each ophthalmic drug in two separate tissues, five rabbit eyes (total 30 eyes) were sacrificed to measure the concentrations at eight different time points, from 30 min to 4 h. Then, we depicted the average time–concentration curves as in Figure 1, and calculated $\frac{dC}{dt}$ to derive the permeability coefficients using the equation. Regarding the linear fit in the time point versus average drug concentration plots, a correlation coefficient (R^2) of over 0.9 was obtained. For the retina-RPE-choroid-sclera tissues, the linear fit model of ganciclovir was $y = 0.3272x - 0.175$ ($R^2 = 0.9613$), brimonidine $y = 0.3037x + 0.1143$ ($R^2 = 0.9786$), and bevacizumab $y = 0.0087x - 0.0256$ ($R^2 = 0.9237$). For the RPE-choroid-sclera tissues, the linear fit model of ganciclovir was $y = 0.8229x - 0.1262$ ($R^2 = 0.9907$), brimonidine $y = 0.7948x + 0.8319$ ($R^2 = 0.9965$), and bevacizumab $y = 0.0484x - 0.0703$ ($R^2 = 0.9473$). In this way, to derive every permeability coefficient for three ophthalmic drugs with two different ocular tissues, we calculated each $\frac{dC}{dt}$ value from the steady-state of the linear fit model in 30 rabbit eyes.

Table 1. Average time–concentration values and average change of drug concentration at the acceptor chamber.

Time Point (h)	Ganciclovir (n = 5)		Brimonidine (n = 5)		Bevacizumab (n = 5)	
	RCS ($\mu\text{g/mL}$)	CS ($\mu\text{g/mL}$)	RCS ($\mu\text{g/mL}$)	CS ($\mu\text{g/mL}$)	RCS ($\mu\text{g/mL}$)	CS ($\mu\text{g/mL}$)
0.5 h	0.108	0.382	0.215	1.216	−0.009	−0.009
1.0 h	0.172	0.753	0.386	1.578	−0.007	−0.10
1.5 h	0.254	1.084	0.571	2.057	−0.010	0.004
2.0 h	0.383	1.375	0.793	2.465	−0.008	0.021
2.5 h	0.562	1.792	0.937	2.873	−0.007	0.049
3.0 h	0.793	2.341	1.074	3.124	−0.001	0.075
3.5 h	0.981	2.859	1.146	3.681	0.004	0.118
4.0 h	1.237	3.217	1.258	3.967	0.012	0.110
$\frac{dC}{dt}$ ($\mu\text{g/mL}\cdot\text{h}$)	0.3272	0.8229	0.3037	0.7948	0.0087	0.0484

RCS: Retina-RPE-Choroid-Sclera; CS: RPE-Choroid-Sclera.

**Figure 1.** The average time–concentration curves of three ophthalmic drugs in two different rabbit ocular tissues: Retina-PRE-Choroid-Sclera (RCS) and RPE-Choroid-Sclera (CS), and the calculated data of the neural retina. The slope $\frac{dC}{dt}$ indicates the change in the acceptor concentration between two time points, and the linear fit models and correlation coefficients (R^2) are documented. (A) RCS, brimonidine: $y = 0.3037x + 0.1143$ ($R^2 = 0.9786$); (B) CS, brimonidine: $y = 0.7948x + 0.8319$ ($R^2 = 0.9965$); (C) Neural retina, brimonidine: $y = 0.4665x + 0.1083$ ($R^2 = 0.9659$); (D) RCS, ganciclovir: $y = 0.3272x - 0.175$ ($R^2 = 0.9613$); (E) CS, ganciclovir: $y = 0.8229x - 0.1262$ ($R^2 = 0.9907$); (F) Neural retina, ganciclovir: $y = 0.5298x - 0.3474$ ($R^2 = 0.9405$); (G) RCS, bevacizumab: $y = 0.0087x - 0.0256$ ($R^2 = 0.9237$); (H) CS, bevacizumab: $y = 0.0484x - 0.0703$ ($R^2 = 0.9473$); (I) Neural retina, bevacizumab: $y = 0.0074x - 0.0201$ ($R^2 = 0.8631$).

The representative physicochemical properties, molecular weight, lipophilicity ($\log P$ and water solubility), and the measured permeability coefficients from the experimental and calculated data (Table 1 and Figure 1) are summarized in Table 2. The permeability data are presented as the mean \pm standard deviation. The permeability coefficients (P_{app}) ($\times 10^{-6}$ cm/s) of ganciclovir in retina-RPE-choroid-sclera and RPE-choroid-sclera were 13.78 ± 5.82 and 23.22 ± 9.74 , brimonidine 15.34 ± 7.64 and 31.56 ± 12.46 , and bevacizumab 0.0136 ± 0.0059 and 0.0612 ± 0.0264 , respectively. Between the two small molecular weight

drugs, brimonidine, which is more lipophilic with a higher log P and lower water solubility than ganciclovir, showed better permeability in RCS and CS tissues. On the other hand, bevacizumab, a much larger molecular weight drug compared to both ganciclovir and brimonidine, presented much worse permeability in RCS and CS tissues. According to the experimental data, we could estimate the permeability coefficients of the neural retina: ganciclovir 33.89 ± 12.64 , brimonidine 29.83 ± 11.58 , and bevacizumab 0.0205 ± 0.0074 ($\times 10^{-6}$ cm/s). Unlike the RCS and CS, neural retinal permeability is greater in ganciclovir than in brimonidine, suggesting that rather than lipophilicity, the molecular weight might be the main pharmacokinetic (PK) parameter that affects drug molecule transport in the neural retinal layer.

Table 2. Permeability coefficients from the Ussing chamber experiments with rabbit eye tissues.

Parameters	Ganciclovir (n = 5)	Brimonidine (n = 5)	Bevacizumab (n = 5)
Molecular weight (Da)	255.23	292.13	149,000
Log P	−1.66	1.7	-
Water solubility (mg/mL)	4.3	1.5	-
Intravitreal half-life ($t_{1/2}$, h)	2.83^{\ddagger} [28]	9.9^{\dagger} [29]	181.4^{\ddagger} [30]
Permeability coefficients (P_{app}) ($\times 10^{-6}$ cm/s)			
Retina-RPE-Choroid-Sclera (RCS)	13.78 ± 5.82	15.34 ± 7.64	0.0136 ± 0.0059
RPE-Choroid-Sclera (CS)	23.22 ± 9.74	31.56 ± 12.46	0.0612 ± 0.0264
Neural Retina (R) *	33.89 ± 12.64	29.83 ± 11.58	0.0205 ± 0.0074

Data are expressed as the mean \pm standard deviation. [†] Dutch belted rabbit; [‡] New Zealand White rabbit. * Calculated by the equation of $1/P_{RCS} = 1/P_R + 1/P_{CS}$.

In addition, using the experimental data of three ophthalmic drugs from this study, we evaluated the association between intravitreal half-life and posterior segment ocular tissue permeability. The log scale graph is shown in Figure 2, and we propose that the large molecule of bevacizumab with a longer intravitreal half-life, showed a lower permeability coefficient than brimonidine and ganciclovir. Experimental data with different species in the previous literature are presented in Table 3.

Table 3. Physicochemical properties, intravitreal half-lives, and permeability coefficients of ophthalmic drug molecules in previous literature.

Molecules	Molecular Weight (Da)	Log P	Intravitreal Half-Life ($t_{1/2}$, h) *	Permeability Coefficients (P_{app}) ($\times 10^{-6}$ cm/s) #	Species	Reference
Aztreonam	434.44	−4.4	7.5 [31]	5.37 ± 5.19	Bovine	Ramsay et al., 2019 [19]
Methotrexate	454.45	−0.241	7.6 [32]	9.39 ± 2.74	Bovine	Ramsay et al., 2019 [19]
Ciprofloxacin	331.3	1.313	4.41 [33]	9.52 ± 5.28	Bovine	Ramsay et al., 2019 [19]
Fluconazole	306.27	0.5	3.18 [34]	15.64 ± 4.66	Bovine	Ramsay et al., 2019 [19]
Voriconazole	349.31	0.927	2.5 [35]	25.00 ± 6.12	Bovine	Ramsay et al., 2019 [19]
Dexamethasone	472	0.65	3.5 [36]	8.90 ± 1.6	Porcine	Loch et al., 2012 [18]
Ketorolac	376.41	2.1	3.09 [37]	69.21 ± 31.9	Bovine	Ramsay et al., 2019 [19]

Data are expressed as the mean \pm standard deviation. * Experimental intravitreal half-life data were from New Zealand white rabbit eyes.

Experimental permeability coefficients were measured as RPE-choroid ocular tissues.

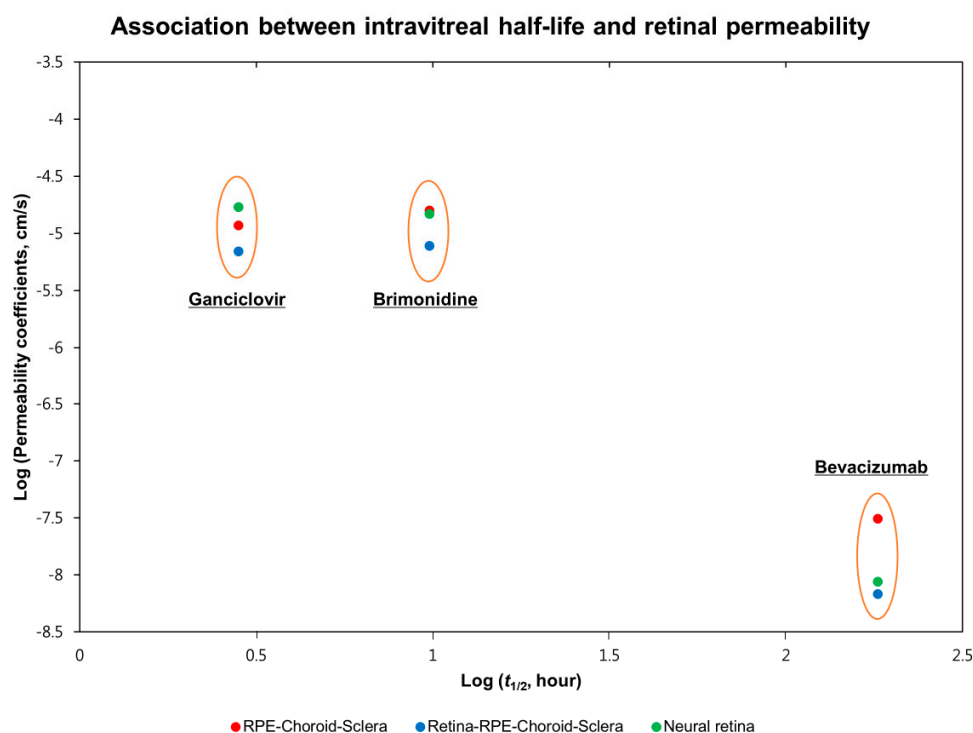


Figure 2. The association between intravitreal half-life and retinal permeability. The experimental data values are documented in Table 2, and then presented as a graph in log scale. Bevacizumab showed low permeability in the ocular tissues due to its high molecular weight compared to brimonidine and ganciclovir.

4. Discussion

In this study, we measured the retina-RPE-choroid-sclera and RPE-choroid-sclera permeability coefficients of three ophthalmic drugs, including ganciclovir, brimonidine, and bevacizumab, from rabbit ocular tissues, and calculated the neural retinal permeability coefficients. As a result, the large molecular weight biologic drug bevacizumab showed very restricted permeation across the posterior segment compared to small molecular weight drugs. Between ganciclovir and brimonidine, a more lipophilic drug, brimonidine, demonstrated better permeation through the RPE-choroid-sclera, even though its molecular weight is slightly larger than that of ganciclovir. However, ganciclovir was estimated to have better neural retinal permeability than brimonidine. Therefore, we propose that molecular weight might be the main factor affecting permeability in the neural retina, whereas both molecular weight and lipophilicity influence permeation through the retinal pigment epithelium (RPE) barrier. In addition, we could postulate that a longer intravitreal half-life might be negatively associated with posterior segment permeability, especially in the neural retina (Figure 2).

The retinal pigment epithelium (RPE) layer separates the neural retina from the choroid and exhibits intercellular tight junctions, working as a part of the blood-retinal barrier and restricting molecular transport. Therefore, numerous studies have focused on the mechanism of drug delivery across the RPE layer. To determine the RPE function for transport and permeation, the Ussing chamber was introduced as two separate baths divided by the epithelium, and electric potentials and concentrations were recorded to investigate the transepithelial ion transport [15]. Kimural et al. experimented in rabbit tissues with the Ussing chamber and suggested that the outward carboxyfluorescein movement through the RPE-choroid showed both passive and carrier-mediated active transport, despite the inward movement by passive diffusion [16]. Xhang et al. investigated brimonidine transport in RPE in bovine ocular tissues with the Ussing chamber, and discovered

the temperature- and energy-dependent uptake of the drug molecules, which might be considered as evidence of a carrier-mediated transport process [38]. Skarphedinsdottir et al. examined the ion transport of mouse retina-choroid-sclera tissues with the Ussing chamber and concluded that Na–K adenosine triphosphatase (ATP) and Na–K-2Cl cotransporters are accountable for transepithelial ion transport [39].

Together with the RPE function of molecular transport, considerable efforts have been made to determine the relationship between molecular physicochemical properties and diffusion/permeation in the posterior segment of ocular tissues. Ambati et al. investigated the *in vitro* scleral permeability of high molecular weight compounds in rabbit eyes with the Ussing chamber, and proposed that the scleral permeability was negatively correlated with molecular weight and radius [12]. Pitkanen et al. experimented with RPE-choroid bovine eye tissues and found that the molecular weight and lipophilicity were relevant to the molecular permeability. The authors suggested that the RPE layer might be a major barrier in the posterior segment drug delivery through the trans-scleral route [13]. Kadam et al. evaluated RPE-choroid-sclera (CS) transport of eight β -blockers in human and various animal ocular tissues. According to this study, RPE-choroid permeability is affected mostly by molecular weight and lipophilicity, while additional factors include tissue thickness and melanin content among different species. Loch et al. compared the permeability coefficients of four ophthalmic drugs: lidocaine, ciprofloxacin, timolol, and dexamethasone, through multiple tissue layers in rabbit, porcine, and bovine eyes with Ussing chambers [18], and found that the experimental retina-RPE-choroid-sclera permeability data of porcine ocular tissues were as follows: lidocaine, 8.9 ± 2.1 ; ciprofloxacin, 1.4 ± 0.2 ; timolol, 2.4 ± 0.5 ; dexamethasone, 2.2 ± 0.4 ; mean \pm standard error of the mean, $\times 10^{-6}$ cm/s). The smaller molecular weight and lipophilic drug lidocaine (288.8 Da, $\log P = 1.54$) revealed the highest permeability, whereas the larger molecular weight and hydrophilic drug ciprofloxacin (367.8 Da, $\log P = -0.54$) exhibited the lowest permeability. Recently, Ramsay et al. measured the bovine RPE-choroid permeability of eight small molecular weight drugs and bevacizumab antibody, and found that the outward permeability for ganciclovir was 9.70 ± 7.90 , and bevacizumab was 0.0035 ± 0.0020 (mean \pm standard error, $\times 10^{-6}$ cm/s) [19].

Other than experimental data, some researchers have developed a simulated model to focus on the retinal permeability and clearance mechanism. Hutton-Smith et al. established a three-compartment (aqueous, vitreous, and retina) semi-mechanistic model to interpret the intraocular distribution and elimination process, including the ILM and RPE permeability [40]. In this study, we derived the prediction values of ocular half-life and retinal permeabilities with reference to the intravitreal injection of therapeutic antibodies in rabbit eyes. The authors suggested that the estimated PK parameters were dependent on the molecule sizes presented as hydrodynamic radii, which was consistent with the *ex vivo* bovine eye measurements. In addition, Haghjou et al. designed a simulated intraocular pharmacokinetics best-fit model to determine the retina-choroid-sclera (RCS) permeability for ophthalmic drugs in the outward direction from the vitreous to systemic circulation [41]. The authors suggested that the prediction of RCS permeability using molecular physicochemical properties might be useful in drug development.

This study had some limitations. First, we should be cautious in extrapolating these data because the estimated neural retina permeability data might not coincide with the real values; because we calculated the neural retina permeability indirectly by the equation with experimental values of retina-RPE-choroid-sclera (RCS) and RPE-choroid-sclera (CS). As the neural retinal layer is very difficult to separate accurately from the RPE-choroid, our method of scraping off the neural retina and measuring the permeability of RCS and CS was an inevitable option. Second, we performed experiments using only three ophthalmic drugs from one animal species. Previous studies have used larger numbers of drug molecules and different species, such as rabbit, porcine, and bovine ocular tissues. Accordingly, we could not derive a statistical correlation between the molecular physicochemical properties and permeability. Moreover, instead of using rabbit eyes, previous studies have analyzed the

association between intravitreal half-life and permeability using bovine and porcine eyes to measure the permeability coefficients; thus, direct comparison might be difficult. Finally, since we experimented only in the outward (vitreous to choroid) direction of permeation, there might be a measurement error, even though we assessed the drug concentration after reaching the steady-state time points.

Nonetheless, our study has some strengths that need to be addressed. To the best of our knowledge, this is the first study to analyze and document the neural retinal permeability of ophthalmic drugs. Almost all prior experiments performed permeability studies with RPE-choroid tissues; therefore, in this study, we determined the permeability differences of the neural retina and RPE-choroid tissues. Another strength of our study is that we demonstrated a negative association between intravitreal half-life and permeability in 10 different ophthalmic drug molecules, including the large molecular weight biologic drug bevacizumab, even though the experimental values were obtained for different animal species. To be comprehensive, we will extend the permeability studies with diverse molecules and ex vivo experiments examining both outward and inward directions in bovine, porcine, and rabbit eyes.

In conclusion, we evaluated the RCS and CS permeability of three ophthalmic drugs and calculated the neural retinal permeability. As a result, both molecular weight and lipophilicity are important PK parameters in the posterior segment drug clearance; however, drug transport and permeation in the neural retinal layer are likely to be affected largely by molecular weight. In addition, the intravitreal half-lives of these molecules may be negatively associated with the permeability coefficients. Subsequent studies should be carried out to determine the exact correlation between molecular physicochemical properties, drug permeation, and intraocular pharmacokinetics, represented as intravitreal half-lives.

Author Contributions: Conceptualization, H.K. and S.J.W.; writing—original draft preparation, H.M.K. and H.H.; writing—review and editing, H.M.K., H.H., H.K.H. and J.H.P.; supervision, K.H.P., H.K. and S.J.W.; project administration, S.J.W.; funding acquisition, S.J.W. All authors have read and agreed to the published version of the manuscript.

Funding: This research was supported by the Bio & Medical Technology Development Program (No. 2018M3A9B5021319) of the National Research Foundation (NRF) and an NRF grant (No. 2020R1F1A1072795, 2020R1A2B5B02001733) funded by the Korean government (MSIT). The funding organization had no role in the design or conduct of this study.

Institutional Review Board Statement: Approval was obtained from the Seoul National University Bundang Hospital Institutional Animal Care and Use Committee, and animal experiments were conducted in accordance with the guidelines of the Association for Research in Vision and Ophthalmology for animal use in research.

Informed Consent Statement: Not applicable.

Data Availability Statement: The datasets used and/or analyzed during the current study are available from the corresponding author on reasonable request.

Conflicts of Interest: The authors declare no conflict of interest.

References


1. Geroski, D.H.; Edelhauser, H.F. Drug delivery for posterior segment eye disease. *Investig. Ophthalmol. Vis. Sci.* **2000**, *41*, 961–964.
2. Novack, G.D.; Robin, A.L. Ocular pharmacology. *J. Clin. Pharmacol.* **2015**, *56*, 517–527. [CrossRef] [PubMed]
3. Nayak, K.; Misra, M. A review on recent drug delivery systems for posterior segment of eye. *Biomed. Pharmacother.* **2018**, *107*, 1564–1582. [CrossRef] [PubMed]
4. Delplace, V.; Ortin-Martinez, A.; Tsai, E.L.S.; Amin, A.N.; Wallace, V.; Shoichet, M.S. Controlled release strategy designed for intravitreal protein delivery to the retina. *J. Control. Release Off. J. Control. Release Soc.* **2019**, *293*, 10–20. [CrossRef] [PubMed]
5. Kang-Mieler, J.J.; Rudeen, K.M.; Liu, W.; Mieler, W.F. Advances in ocular drug delivery systems. *Eye* **2020**, *34*, 1371–1379. [CrossRef]
6. Cunha-Vaz, J.G. The blood–retinal barriers system. Basic concepts and clinical evaluation. *Exp. Eye Res.* **2004**, *78*, 715–721. [CrossRef]

7. Gaudreault, J.; Fei, D.; Beyer, J.C.; Ryan, A.; Rangell, L.; Shiu, V.; Damico, L.A. Pharmacokinetics and Retinal Distribution of Ranibizumab, A Humanized Antibody Fragment Directed Against Vegf-A, Following Intravitreal Administration In Rabbits. *Retina* **2007**, *27*, 1260–1266. [CrossRef] [PubMed]
8. I Sinapis, A.; Sinapis, C.I.; Sinapis, D.I.; Routsias, J.G.; Pantopoulou, A.; Baltatzis, S.; Patsouris, E.; Perrea, D. Pharmacokinetics of intravitreal bevacizumab (Avastin[®]) in rabbits. *Clin. Ophthalmol.* **2011**, *5*, 697–704. [CrossRef] [PubMed]
9. Del Amo, E.M.; Vellonen, K.-S.; Kidron, H.; Urtti, A. Intravitreal clearance and volume of distribution of compounds in rabbits: In silico prediction and pharmacokinetic simulations for drug development. *Eur. J. Pharm. Biopharm.* **2015**, *95*, 215–226. [CrossRef] [PubMed]
10. Caldwell, R.B. Extracellular matrix alterations precede vascularization of the retinal pigment epithelium in dystrophic rats. *Curr. Eye Res.* **1989**, *8*, 907–921. [PubMed]
11. Nishihara, H. Studies on the ultrastructure of the inner limiting membrane of the retina—distribution of anionic sites in the inner limiting membrane of the retina. *Nippon. Ganka Gakkai zasshi* **1991**, *95*, 951–958.
12. Ambati, J.; Canakis, C.S.; Miller, J.W.; Gragoudas, E.S.; Edwards, A.; Weissgold, D.J.; Kim, I.; Delori, F.C.; Adamis, A.P. Diffusion of high molecular weight compounds through sclera. *Investig. Ophthalmol. Vis. Sci.* **2000**, *41*, 1181–1185.
13. Pitkänen, L.; Ranta, V.-P.; Moilanen, H.; Urtti, A. Permeability of Retinal Pigment Epithelium: Effects of Permeant Molecular Weight and Lipophilicity. *Investig. Ophthalmol. Vis. Sci.* **2005**, *46*, 641–646. [CrossRef] [PubMed]
14. Kim, H.M.; Park, K.H.; Chung, J.Y.; Woo, S.J. A Prediction Model for the Intraocular Pharmacokinetics of Intravitreally Injected Drugs Based on Molecular Physicochemical Properties. *Ophthalmic Res.* **2019**, *63*, 41–49. [CrossRef] [PubMed]
15. Ussing, H.H. Transport of Water and Solutes through Living Membranes. *Clin. Sci.* **1972**, *42*, 23–24. [CrossRef]
16. Kimura, M.; Araie, M.; Koyano, S. Movement of Carboxyfluorescein across Retinal Pigment Epithelium–Choroid. *Exp. Eye Res.* **1996**, *63*, 51–56. [CrossRef]
17. Kadam, R.S.; Cheruvu, N.P.S.; Edelhofer, H.F.; Kompella, U.B. Sclera–Choroid–RPE Transport of Eight β -Blockers in Human, Bovine, Porcine, Rabbit, and Rat Models. *Investig. Ophthalmol. Vis. Sci.* **2011**, *52*, 5387–5399. [CrossRef]
18. Loch, C.; Zakelj, S.; Kristl, A.; Nagel, S.; Guthoff, R.; Weitschies, W.; Seidlitz, A. Determination of permeability coefficients of ophthalmic drugs through different layers of porcine, rabbit and bovine eyes. *Eur. J. Pharm. Sci.* **2012**, *47*, 131–138. [CrossRef]
19. Ramsay, E.; Hagström, M.; Vellonen, K.-S.; Boman, S.; Toropainen, E.; del Amo, E.M.; Kidron, H.; Urtti, A.; Ruponen, M. Role of retinal pigment epithelium permeability in drug transfer between posterior eye segment and systemic blood circulation. *Eur. J. Pharm. Biopharm. Off. J. Arb. Pharm.* **2019**, *143*, 18–23. [CrossRef]
20. Ahn, J.; Kim, H.; Woo, S.J.; Park, J.H.; Park, S.; Hwang, D.J.; Park, K.H. Pharmacokinetics of Intravitreally Injected Bevacizumab in Vitrectomized Eyes. *J. Ocul. Pharmacol. Ther. Off. J. Assoc. Ocul. Pharmacol. Ther.* **2013**, *29*, 612–618. [CrossRef]
21. Ahn, S.J.; Ahn, J.; Park, S.; Kim, H.; Hwang, D.J.; Park, J.H.; Park, J.Y.; Chung, J.Y.; Park, K.H.; Woo, S.J. Intraocular Pharmacokinetics of Ranibizumab in Vitrectomized Versus Nonvitrectomized Eyes. *Investig. Ophthalmol. Vis. Sci.* **2014**, *55*, 567–573. [CrossRef]
22. Park, S.J.; Oh, J.; Kim, Y.-K.; Park, J.H.; Hong, H.K.; Park, K.H.; Lee, J.-E.; Kim, H.M.; Chung, J.Y.; Woo, S.J. Intraocular pharmacokinetics of intravitreal vascular endothelial growth factor-Trap in a rabbit model. *Eye* **2015**, *29*, 561–568. [CrossRef]
23. Park, S.J.; Choi, Y.; Na, Y.M.; Hong, H.K.; Park, J.Y.; Park, K.H.; Chung, J.Y.; Woo, S.J. Intraocular Pharmacokinetics of Intravitreal Aflibercept (Eylea) in a Rabbit Model. *Investig. Ophthalmol. Vis. Sci.* **2016**, *57*, 2612–2617. [CrossRef]
24. Joo, K.; Park, S.J.; Choi, Y.; Lee, J.E.; Na, Y.M.; Hong, H.K.; Park, K.H.; Kim, H.M.; Chung, J.-Y.; Woo, S.J. Role of the Fc Region in the Vitreous Half-Life of Anti-VEGF Drugs. *Investig. Ophthalmol. Vis. Sci.* **2017**, *58*, 4261–4267. [CrossRef] [PubMed]
25. Wheeler, L.; WoldeMussie, E.; Lai, R. Role of Alpha-2 Agonists in Neuroprotection. *Surv. Ophthalmol.* **2003**, *48*, S47–S51. [CrossRef]
26. Kuppermann, B.D.; Patel, S.S.; Boyer, D.S.; Augustin, A.J.; Freeman, W.R.; Kerr, K.J.; Guo, Q.; Schneider, S.; López, F.J. Phase 2 study of the safety and efficacy of brimonidine drug delivery system (brimo dds) generation 1 in patients with geographic atrophy secondary to age-related macular degeneration. *Retina* **2021**, *41*, 144–155. [CrossRef]
27. Henderly, D.E.; Freeman, W.R.; Causey, D.M.; Rao, N.A. Cytomegalovirus Retinitis and Response to Therapy with Ganciclovir. *Ophthalmology* **1987**, *94*, 425–434. [CrossRef]
28. Macha, S.; Mitra, A.K. Ocular Disposition of Ganciclovir and Its Monoester Prodrugs following Intravitreal Administration Using Microdialysis. *Drug Metab. Dispos.* **2002**, *30*, 670–675. [CrossRef] [PubMed]
29. Shen, J.; Durairaj, C.; Lin, T.; Liu, Y.; Burke, J. Ocular Pharmacokinetics of Intravitreally Administered Brimonidine and Dexamethasone in Animal Models with and Without Blood–Retinal Barrier Breakdown. *Investig. Ophthalmol. Vis. Sci.* **2014**, *55*, 1056–1066. [CrossRef]
30. Bakri, S.J.; Snyder, M.R.; Reid, J.M.; Pulido, J.S.; Singh, R.J. Pharmacokinetics of Intravitreal Bevacizumab (Avastin). *Ophthalmology* **2007**, *114*, 855–859. [CrossRef] [PubMed]
31. Barza, M.; McCue, M. Pharmacokinetics of aztreonam in rabbit eyes. *Antimicrob. Agents Chemother.* **1983**, *24*, 468–473. [CrossRef]
32. Velez, G.; Yuan, P.; Sung, C.; Tansey, G.; Reed, G.F.; Chan, C.-C.; Nussenblatt, R.B.; Robinson, M.R. Pharmacokinetics and toxicity of intravitreal chemotherapy for primary intraocular lymphoma. *Arch. Ophthalmol.* **2001**, *119*, 1518–1524. [CrossRef]
33. Liu, W.; Liu, Q.F.; Perkins, R.; Drusano, G.; Louie, A.; Madu, A.; Mian, U.; Mayers, M.; Miller, M.H. Pharmacokinetics of Sparfloxacin in the Serum and Vitreous Humor of Rabbits: Physicochemical Properties That Regulate Penetration of Quinolone Antimicrobials. *Antimicrob. Agents Chemother.* **1998**, *42*, 1417–1423. [CrossRef] [PubMed]

34. Gupta, S.K.; Velpandian, T.; Dhingra, N.; Jaiswal, J. Intravitreal Pharmacokinetics of Plain and Liposome-Entrapped Fluconazole in Rabbit Eyes. *J. Ocul. Pharmacol. Ther. Off. J. Assoc. Ocul. Pharmacol. Ther.* **2000**, *16*, 511–518. [CrossRef] [PubMed]
35. Shen, Y.-C.; Wang, M.-Y.; Wang, C.-Y.; Tsai, T.-C.; Tsai, H.-Y.; Lee, Y.-F.; Wei, L.-C. Clearance of Intravitreal Voriconazole. *Investig. Ophthalmol. Vis. Sci.* **2007**, *48*, 2238–2241. [CrossRef]
36. Kwak, H.W. Evaluation of the Retinal Toxicity and Pharmacokinetics of Dexamethasone after Intravitreal Injection. *Arch. Ophthalmol.* **1992**, *110*, 259–266. [CrossRef] [PubMed]
37. Komarowska, I.; Heilweil, G.; Rosenfeld, P.J.; Perlman, I.; Loewenstein, A. Retinal toxicity of commercially available intravitreal ketorolac in albino rabbits. *Retina* **2009**, *29*, 98–105. [CrossRef]
38. Zhang, N.; Kannan, R.; Okamoto, C.T.; Ryan, S.J.; Lee, V.H.L.; Hinton, D.R. Characterization of Brimonidine Transport in Retinal Pigment Epithelium. *Investig. Ophthalmol. Vis. Sci.* **2006**, *47*, 287–294. [CrossRef] [PubMed]
39. Skarphedinsdottir, S.B.; Eysteinnsson, T.; Árnason, S.S. Mechanisms of Ion Transport across the Mouse Retinal Pigment Epithelium Measured In Vitro. *Investig. Ophthalmol. Vis. Sci.* **2020**, *61*, 31. [CrossRef]
40. Hutton-Smith, L.A.; Gaffney, E.A.; Byrne, H.M.; Maini, P.K.; Gadkar, K.; Mazer, N.A. Ocular Pharmacokinetics of Therapeutic Antibodies Given by Intravitreal Injection: Estimation of Retinal Permeabilities Using a 3-Compartment Semi-Mechanistic Model. *Mol. Pharm.* **2017**, *14*, 2690–2696. [CrossRef] [PubMed]
41. Haghjou, N.; Abdekhodaie, M.J.; Cheng, Y.-L. Retina-Choroid-Sclera Permeability for Ophthalmic Drugs in the Vitreous to Blood Direction: Quantitative Assessment. *Pharm. Res.* **2012**, *30*, 41–59. [CrossRef] [PubMed]

Article

Comparative Analysis of Morphological and Release Profiles in Ocular Implants of Acetazolamide Prepared by Electrospinning

Mariana Morais ¹, Patrícia Coimbra ^{2,3} and Maria Eugénia Pina ^{1,3,*} 

¹ Faculty of Pharmacy of University Coimbra, Pólo das Ciências da Saúde, Azinhaga de Santa Comba, 3000-548 Coimbra, Portugal; marymorais@gmail.com

² Department of Chemical Engineering, University Coimbra, CIEPQPF, Rua Sílvio Lima, Pólo II—Pinhal de Marrocos, 3030-790 Coimbra, Portugal; patricia@eq.uc.pt

³ FFUC, Pólo das Ciências da Saúde, Azinhaga de Santa Comba, University Coimbra, CIEPQPF, 3000-548 Coimbra, Portugal

* Correspondence: epina@ff.uc.pt; Tel.: +351-239-488-400

Abstract: The visual impairment that often leads to blindness causes a higher morbidity rate. The goal of this work is to create a novel biodegradable polymeric implant obtained from coaxial fibers containing the dispersed drug—acetazolamide—in order to achieve sustained drug release and increase patient compliance, which is of the highest importance. Firstly, during this work, uncoated implants were produced by electrospinning, and rolled in the shape of small cylinders that were composed of uniaxial and coaxial fibers with immobilized drug inside. The fibers were composed by PCL (poly ϵ -caprolactone) and Lutrol F127 (poly (oxyethylene-*b*-oxypropylene-*b*-oxyethylene)). The prepared implants exhibited a fast rate of drug release, which led to the preparation of new implants incorporating the same formulation but with an additional coating film prepared by solvent casting and comprising PCL and Lutrol F127 or PCL and Luwax EVA 3 ((poly (ethylene-co-vinyl acetate))). Implants were characterized and in vitro release profiles of acetazolamide were obtained in phosphate buffered saline (PBS) at 37 °C. The release profile of the acetazolamide from coated implant containing Luwax EVA 3 is considerably slower than what was observed in case of coated implants containing Lutrol F127, allowing a sustained release and an innovation relatively to other ocular drug delivery systems.

Keywords: ocular implants; electrospinning technique; glaucoma; sustained drug release; poly ϵ -caprolactone; electrospun fibers

Citation: Morais, M.; Coimbra, P.; Pina, M.E. Comparative Analysis of Morphological and Release Profiles in Ocular Implants of Acetazolamide Prepared by Electrospinning. *Pharmaceutics* **2021**, *13*, 260. <https://doi.org/10.3390/pharmaceutics13020260>

Academic Editors: Francisco Javier Otero-Espinar and Anxo Fernández Ferreiro

Received: 16 December 2020

Accepted: 11 February 2021

Published: 15 February 2021

Publisher's Note: MDPI stays neutral with regard to jurisdictional claims in published maps and institutional affiliations.



Copyright: © 2021 by the authors. Licensee MDPI, Basel, Switzerland. This article is an open access article distributed under the terms and conditions of the Creative Commons Attribution (CC BY) license (<https://creativecommons.org/licenses/by/4.0/>).

1. Introduction

Visual impairment that often leads to blindness is among the diseases that causes a higher morbidity rate. According to World Health Organization (WHO) data, in 2014, 285 million people suffer from visual impairment, of which 39 million are blind and about 90% live in developing countries [1].

The conditions related to those diseases are often silent, and therefore, it is estimated that 82% of the blind are over 50 years old. Thus, "prevention" is such a fundamental role that, according to the same organization, 40% of childhood blindness is preventable or treatable.

The causes of the most common visual disabilities are refractive errors (nearsightedness, farsightedness and astigmatism), around 43% of the population. Glaucoma, macular degeneration related to age, cataracts and ocular infections are other causes of visual impairment that can lead to blindness if not properly treated [2]. The number of patients with vision-threatening conditions has been steadily increasing in recent years, largely driven by the growth and ageing of the world's population [1].

In 2013, the WHO approved the action plan 2014–2019 for universal access to eye health, a road map for the member states, the WHO secretariat and international partners in order to achieve a measurable reduction of 25% of avoidable visual impairment in 2019.

However, the implementation and enforcement of these measures (which have difficulty getting off the paper) have not reached the best results. Improvements exist but are in amount and follow-up still limited. Given these forecasts and expectations, it has become urgent to develop systems for the diagnosis, treatment and/or maintenance of the visual system. Many of the major eye diseases of non-refractive nature are treated/controlled with drugs acting in the anterior segment of the eye, administered topically and formulated into eye drops and ointments [3,4].

Nevertheless, in the last decade, intravitreal injections of steroids have been increasingly used in the treatment of non-inflammatory diseases of the eye, which include macular edema, macular degeneration and age-related proliferative diabetic retinopathy. With respect to ocular injection, rapid movement to the posterior segment of the eye leads to decreased half-life time of the drug and concentration on site. Periodic injections are required, which not only lead to patient discomfort but also cause other complications [5], such as vitreous hemorrhage, infections, cataracts and detachment of the retina. These diseases, of which the frequency will increase in the future due to aging and lifestyle, are also chronic diseases on which traditional treatment proves ineffective [6]. It is necessary to develop alternatives to out-of-date formulations, such as sustained release systems for drugs that can be implanted close to the target tissue.

Micro- and nanoparticles, such as microspheres and liposomes, are not a viable option because its accumulation in the vitreous cavity is likely to cause blurring of vision and hinder the examination of fundus by an ophthalmologist [7]. For all this, recently, implants were developed capable of promoting the sustained release of drugs into the eye; these implants are divided into intraocular lenses for refractive error correction and drug delivery systems [8,9].

Electrospinning is a versatile methodology by which a variety of constructs can be obtained with several applications [10–13]. In the field of drug delivery, electrospun fibers evidence several advantages, such as relatively easy drug entrapment, the obtention of high drug loading and specific morphology during the process. An additional advantage is represented by the possibility of their post-treatment (which can include coating) with the possibility of modulate drug delivery, constituting an important innovation.

Acetazolamide, a carbonic anhydrase inhibitor, is still the most effective drug for the treatment of glaucoma for many years [14]. Recent attempts were made in order to develop an effective formulation that include incorporation of drug in dendritic nanoarchitectures [15] and nanoemulsions [16]. However, these efforts did not exempt the toxicity of its components, mainly in nanoemulsion formulations [17].

Regarding the previous considerations, the aim of this experimental study was to formulate novel acetazolamide polymeric implants that allow a higher sustained drug release than other drug delivery ocular systems, in order to decrease side effects and increase patient compliance.

2. Materials and Methods

2.1. Materials

Acetazolamide, purity 99%, was purchased from Alfa Aesar (Heysham, UK). Poly (ϵ -caprolactone), Lutrol F127 (poly (oxyethylene-*b*-oxypropylene-*b*-oxyethylene)) with 70% oxyethylene and molar mass of 9.8 to 14.6 g/mol and Luwax EVA 3 (poly (ethylene-co-vinyl acetate)) with 13–15% of vinyl acetate were purchased from BASF (Prior Velho, Portugal). Chloroform (CLF), dimethylformamide (DMF), methanol (MeOH), tetrahydrofuran (THF) and ethanol (EtOH), analytical reagents grade, were obtained from Fisher Scientific (Loughborough, UK). Reagents used in the preparation of phosphate buffered saline (PBS) were acquired from Sigma (Lisboa, Portugal).

2.2. Preparation of the Formulations for Electrospinning Fibrous and Coaxial Fibers

The preparation of the implant begins with the production of electrospun fibrous mats with coaxial or uniaxial fibers. Coaxial fibers consisted of a shell of PCL and a core of acetazolamide (ACZ) and Lutrol F127. The shell solutions were prepared by dissolving 1.2 g of PCL in 8 mL of CLF: DMF: 3:1 (*v/v*) mixture. Two solvent systems were used to prepare the cores mixtures: MeOH:DMF: 3:1 (*v/v*), which dissolves Lutrol F127 but only partially dissolves ACZ, and EtOH:DMF:H₂O 2:1:1 (*v/v/v*), able to completely dissolve both Lutrol F127 and ACZ. The coaxial fibers resultant of these two different core formulations were designated as MD and EDW, following the initials of the solvents used (Table 1). Mats with fibers with a uniaxial structure were also prepared, by blending PCL and Lutrol F127 in a mixture of CLF:DMF 7:3 (*v/v*) (Table 1).

Table 1. Composition of the formulations used to produce the core of the coaxial fibers and the uniaxial fibers inner.

Type	Formulation	Polymer (Mass)	ACZ (Mass)	Solvent	Volume
Coaxial	MD	0.3 g Lutrol	75 mg	MeOH:DMF 3:1	2 mL
Coaxial	EDW	0.3 g Lutrol	75 mg	EtOH:DMF:H ₂ O 2:1:1	2 mL
Uniaxial	Blending	0.3 g Lutrol +1.2 g PCL	75 mg	CLF:DMF 7:3	10 mL

2.3. Preparation of Membranes Using an Electrospinning Setup

The electrospinning apparatus includes a high-voltage generator SL 10–300 W from Spellman, a system of coaxial needles, a copper square collector and two syringe pumps loaded with PCL solution, to form the fibers shell, and the core mixture, consisting of dissolved Lutrol F127 and dissolved or dispersed ACZ. The applied voltage, flow rate or flow delivered by each syringe and the distance between syringe tip and collector [18,19] applied are presented in Table 2.

Table 2. Electrospinning parameters for each formulation.

Formulation	Lutrol F127 (Flow Rate)	PCL (Flow Rate)	Voltage	Distance to the Collector
MD	0.5 mL/h	2.0 mL/h	16 kV	20 cm
EDW	0.5 mL/h	2.0 mL/h	15 kV	20 cm
Blending		2.5 mL/h	11 kV	20 cm

2.4. Implant Preparation/Preparation of Coated Films Implants

The membranes obtained above were cut into rectangles with 4 cm long by 1.5 cm wide, approximately. The implants were obtained by rolling the referred rectangles into cylinders of 1.5 cm high. Small amounts of chloroform were used, for sealing the ends of the cylinders (the two bases) and the side part.

Some of the implants were coated with polymeric films, composed of blends of PCL and Lutrol 127 or PCL and Luwax EVA 3. The films were prepared by solvent casting, according to the formulations presented in Table 3. The solutions were subjected to stirring until completely dissolved. In case of solutions with Luwax EVA 3, it was necessary to resort to heating (50 °C) until achieve complete dissolution. Finally, the solutions were poured into petri dishes and placed to dry under a fume hood for 24 h to form the films.

Table 3. Coating films composition (THF: tetrahydrofuran; Lt: Lutrol F127; Lw: Luwax EVA 3).

Form	Polymers		Total (mg)	Solvent	Lt/Lw (%)	PCL (%)
500 Lut	125 mg Lutrol F127	375 mg PCL	500	THF	25%	75%
500 Luw	125 mg Luwax EVA 3	375 mg PCL	500	THF	25%	75%
1000 Lut	250 mg Lutrol F127	750 mg PCL	1000	THF	25%	75%
1000 Luw	250 mg Luwax EVA 3	750 mg PCL	1000	THF	25%	75%

The formed films were cut into rectangles with sufficient area to cover the entire cylinder. Then, the largest edge of the rectangle was swabbed with chloroform facilitating cylinder adhesion. Finally, part of the MD and EDW implants were coated by the respective film by having their ends rolled up and sealed with heat in according with Figure 1.

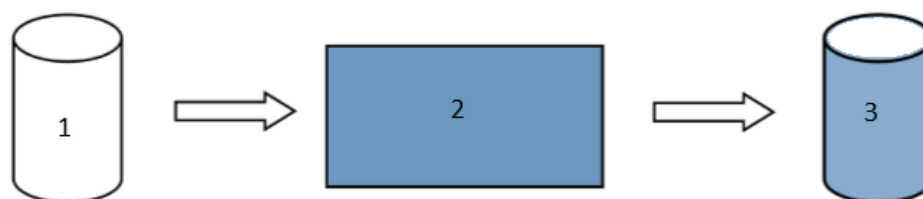


Figure 1. General scheme of implants coating. **1**—MD, EDW and blending implants obtained from electrospinning membranes; **2**—Polymeric films for coating composed by PCL and Lutrol F127 or Luwax EVA 3; **3**—final scheme of coated implants.

2.5. Characterization of Implants

In the morphological and physicochemical characterization of the prepared implant, methods were used to examine the morphological characteristics of the fibers and implants, for analyzing the content of fibers and to study the hydrophilicity degree of the implants.

2.5.1. Scanning Electronic Microscopy (SEM)

This method was used to access the morphology of the produced fibers, transversal surface of the coated implants and lateral surface of the same implants. Cylindrical implants were immersed in liquid nitrogen and then cut in half with a scalpel, and both sides were used in the analysis by SEM: one to observe the cross section and the other to analyze the lateral surface. The samples were glued to a holder with carbon tape, coated with gold for 10 s and analyzed on a Gemini Geiss Field Emission SEM.

2.5.2. Infrared Spectroscopy (FTIR)

FTIR spectra of fibrous mats, coating films and its individual polymeric components were recorded. The solutions were poured into petri dishes and placed in the hood for 24 h. The spectra were acquired in ATR mode on a spectrometer Jasco FT/IR-4200 equipped with a Golden Gate Single Reflection Diamond ATR. The spectra were obtained at 64 scans with resolution of 4 cm^{-1} , between $600\text{ and }4000\text{ cm}^{-1}$.

2.5.3. Contact Angle

The hydrophilicity of the fibrous mats and coating films was evaluated by water contact angle measurements. This technique measures the angle formed between the surface under study and a water droplet. Thus, it assesses the affinity degree between the surface and water and allows conclude about the hydrophilicity degree of the surface.

Measurements were made with a Dataphysics OCA-20 contact angle analyzer (Data-Physics Instruments, Filderstadt, Germany) using the sessile drop method.

2.5.4. Simultaneous Thermal Analysis

This technique refers to the application of Differential Scanning Calorimetry (DSC) coupled with Thermogravimetric Analysis (TGA) and allows to identify thermal events and to determine the glass transition, melting and degradation (onset) temperatures of the polymers. Samples with a weight between 5 and 10 mg were placed in porcelain dishes and analyzed on a Q600 SDT TA Instruments, from room temperature to 500 °C, using a heating rate of 10 °C/min.

2.5.5. In Vitro Drug Release Study

Each implant was placed in individual glass vials containing 4 mL of phosphate buffered saline solution (PBS) identically to others authors [20]. The flasks were kept at 37 °C in an oven with temperature control and at predetermined intervals the release medium was completely removed and replaced by the same amount of fresh PBS. These collected samples were stored in a refrigerator (± 2 °C) until quantification.

Samples were quantified by UV/VIS spectrophotometric method at a wavelength of 266 nm [20]. The calibration curve was obtained by preparing several solutions containing different drug concentrations that ranged from 5.3 ug/mL to 26.5 ug/mL in PBS.

3. Results

3.1. Obtained Implants

The implants prepared in accordance with previous description (Section 2.4) are described in Table 4. The considered parameters were: type of fibers, fiber core, fiber inner, coating and total polymer mass.

Table 4. Types of implants and their composition.

Name	Type of Fibers	Fiber Core	Fiber Inner	Coating	Total Polymer Mass
MD	Coaxial	PCL	Lutrol F127 and ACZ in Methanol and dimethylformamide (DMF)	No	—
EDW	Coaxial	PCL	Lutrol F127 and ACZ in Ethanol, DMF and water	No	—
MD Lut500	Coaxial	PCL	Lutrol F127 and ACZ in Methanol and DMF	Lutrol F127 and PCL polymer	500 mg
MD Luw500	Coaxial	PCL	Lutrol F127 and ACZ in Methanol and DMF	Luwx EVA 3 and PCL polymer	500 mg
EDW Lut1000	Coaxial	PCL	Lutrol F127 and ACZ in Ethanol, DMF and water	Lutrol F127 and PCL polymer	1000 mg
EDW Luw1000	Coaxial	PCL	Lutrol F127 and ACZ in Ethanol, DMF and water	Luwx EVA 3 and PCL polymer	1000 mg
Blending	Uniaxial	Lutrol F127 and ACZ			No

3.2. Characterization of Implants

3.2.1. Composition/Thickness of the Coating

Table 5 shows the values of thickness of each coating film. The polymers were dissolved in the same volume of solvent (THF) and the solutions were placed in identical glass plates. Thus, solutions with more polymer mass present thicker films, which confirms the information presented in Table 5.

Table 5. Composition and thickness of coating films.

Solutions	Polymers (Weight)	Total (Weight)	Thickness (μm)	
500 Lut	125 mg Lutrol F127	375 mg PCL	500 mg	52.5 ± 12.6
500 Luw	125 mg Luwax EVA 3	375 mg PCL	500 mg	50.0 ± 8.1
1000 Lut	250 mg Lutrol F127	750 mg PCL	1000 mg	168.5 ± 6.2
1000 Luw	250 mg Luwax EVA 3	750 mg PCL	1000 mg	271.3 ± 6.3

3.2.2. SEM

Figure 2A,B represent the blending and EDW electrospun mats, respectively. It is noted that the uniaxial fibers from the blending mat have some surface beads, probably due to the accumulation of undissolved drug. The solvents of this formulation, chloroform and dimethylformamide, have a slightly hydrophobic nature, which makes it difficult to achieve complete dissolution of the drug. The possible presence of undissolved drug accumulations can cause erratic and inconstant drug release. On the other hand, the coaxial fibers from EDW implant have smooth surfaces without irregularities.

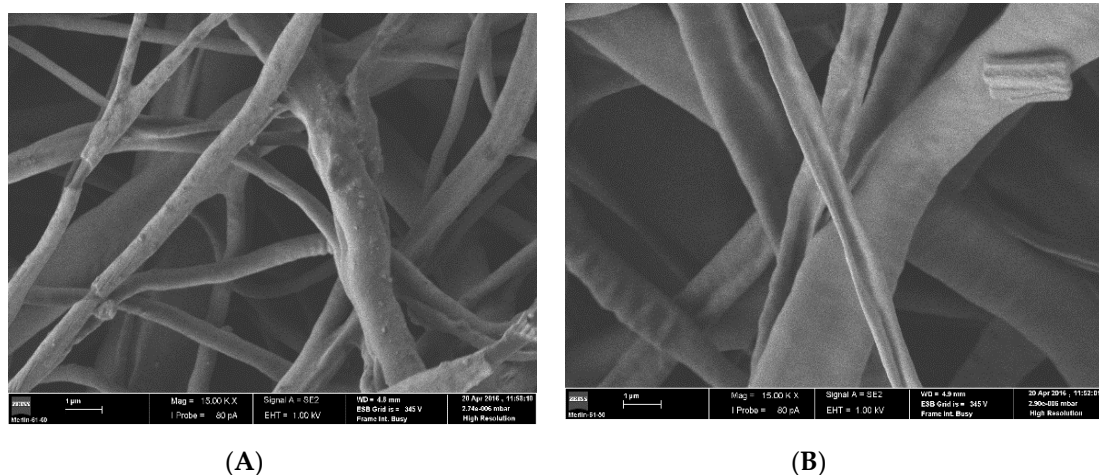


Figure 2. Images obtained by SEM. (A) Blending implant fibers, (B) EDW implant fibers.

Figure 3 shows a cross-section and the coating surface of the MD 500 Lut and the 500 Luw MD implant, respectively. If we look at Figure 3B,D it is observed that the coating surface containing Lutrol F127 presents less porosity relative to the coating containing Luwax EVA 3, in spite of different magnification. The film containing Luwax EVA 3 had to be heated due to its low solubility in THF to achieve complete dissolution. In the cooling process, phase separation occurred: one rich in polymer and another rich in solvent. The extraction solvent by slow evaporation gave a porous structure, as can be seen in Figure 3D.

Regarding the cross-sectional view of the implant, Figure 3A,C have the same morphology: several concentric layers inside, corresponding to the wrapped fibrous membrane, and an outer layer corresponding to the coating. As for the thickness of the coating, there are no significant differences, which coincides with the results obtained through direct measurement of the thickness of the coatings shown in Table 5.

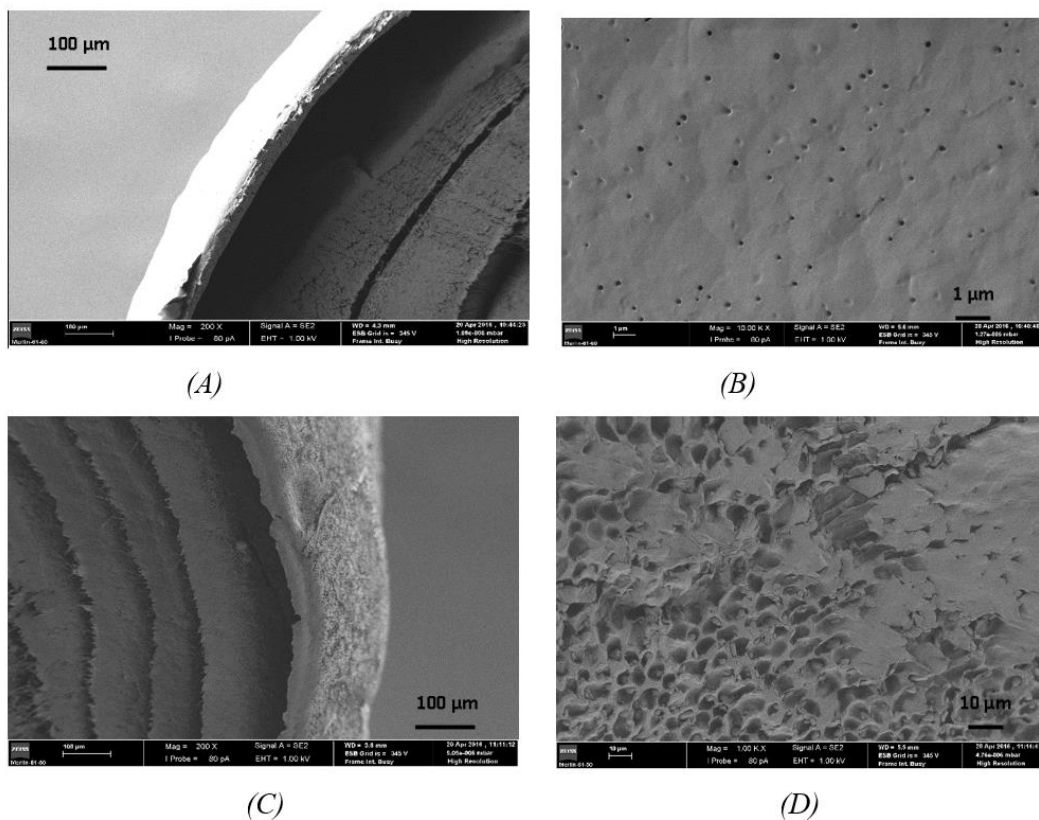


Figure 3. Images obtained by SEM. Cross-section view (A) and coating surface (B) of the MD 500 Lut implant and cross-section view (C) and coating surface (D) of the MD 500 Luw implant.

Figure 4 shows the cross-section and the coating surface of the EDW 1000 Lut and EDW 1000 Luw implants, respectively. Figure 4C,D suggest that the implant coating surface have a more extensive pore network and tubules than in the MD500 Lut and MD 500 Luw implants. In the case of the EDW 1000 Luw implant during the coating film formation, a more extensive separation occurred because of the increase in the mass of the polymer, resulting in a more irregular porous structure.

Regarding the cross-sectional view of the implants, the results are similar to earlier: several concentric layers within as a result of rolled membrane and a thicker outer coating in the case of the EDW 1000 Lut and EDW 1000 Luw implants.

3.2.3. FTIR

Figures 5–7 show the FTIR spectra of each implant compared with the spectra of each separate component. By analyzing the spectra, it is verified that the characteristic peaks of each isolated component are visible in the spectra of the implants. It is also noticeable that the most prominent peak in the implant spectra correspond to PCL, since this is the component present in greater quantities. The results evidenced the absence of drug–polymer interactions.

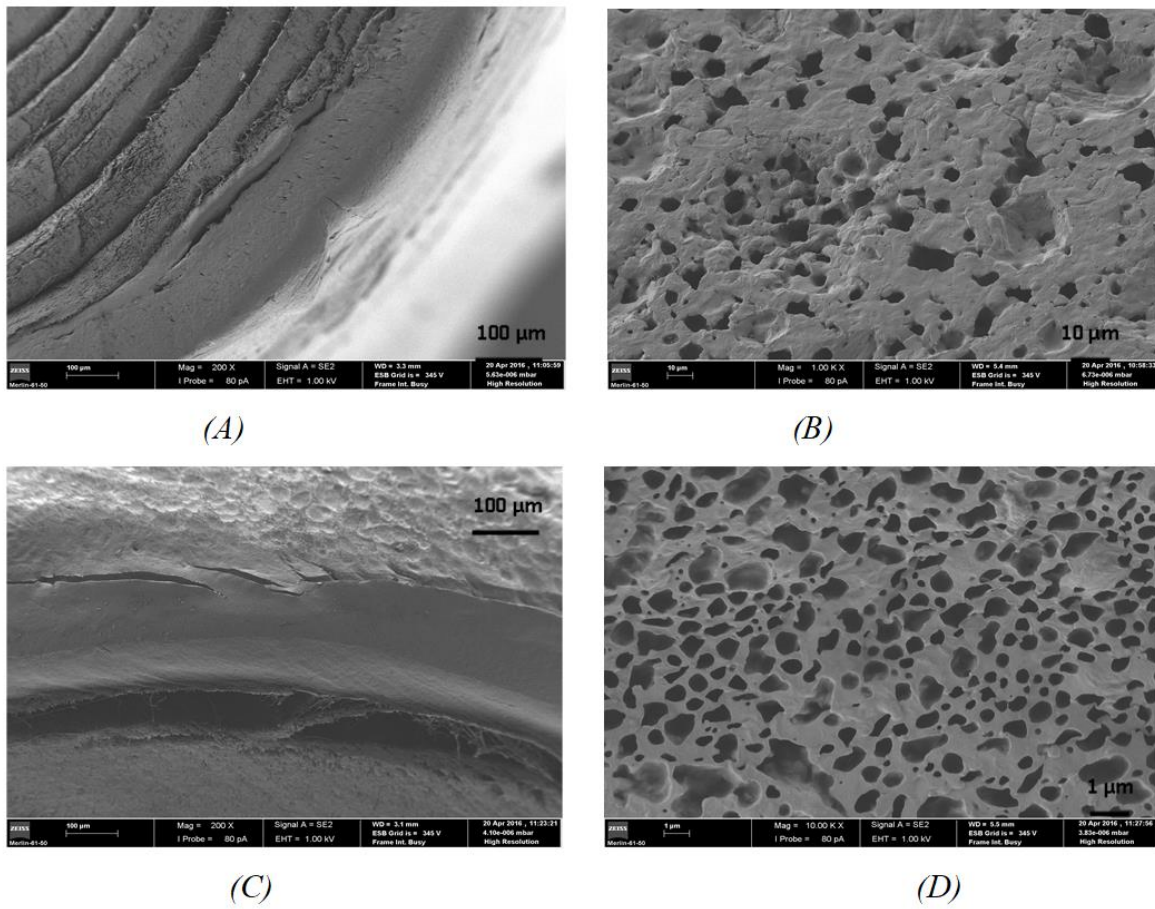


Figure 4. Images obtained by SEM. Cross section view (A) and coating surface (B) of the EDW 100 Lut implant and cross-section view (C) and coating surface (D) of the EDW 1000 Luw implant.

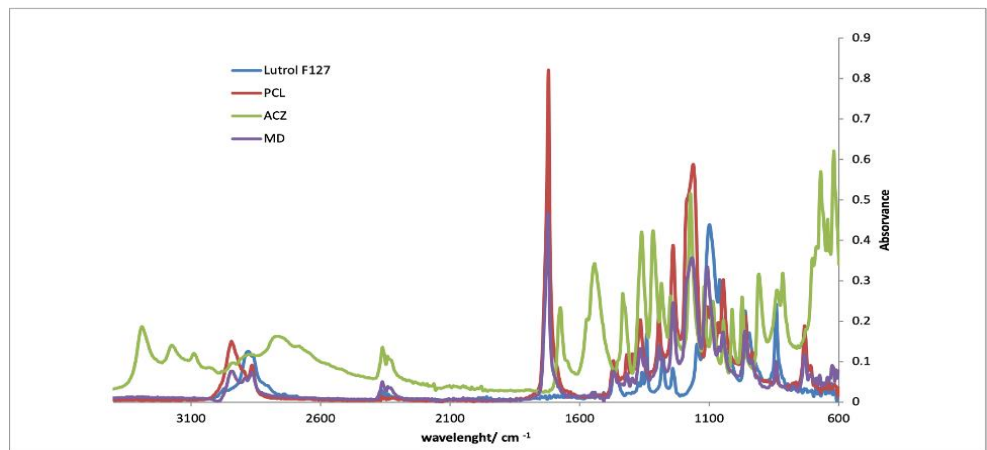


Figure 5. FTIR spectra of MD implants compared with PCL, Lutrol F127 and acetazolamide.

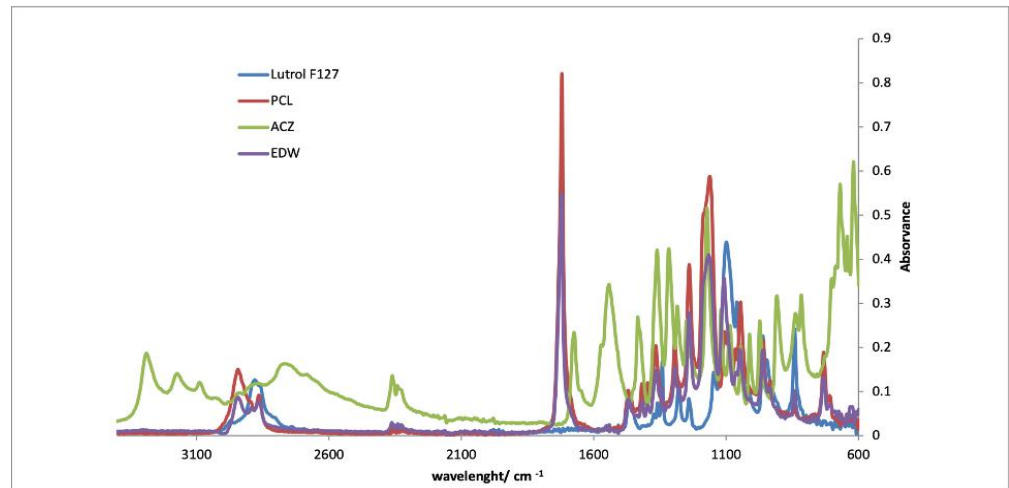


Figure 6. FTIR spectra of EDW implants compared with PCL, Lutrol F127 and acetazolamide.

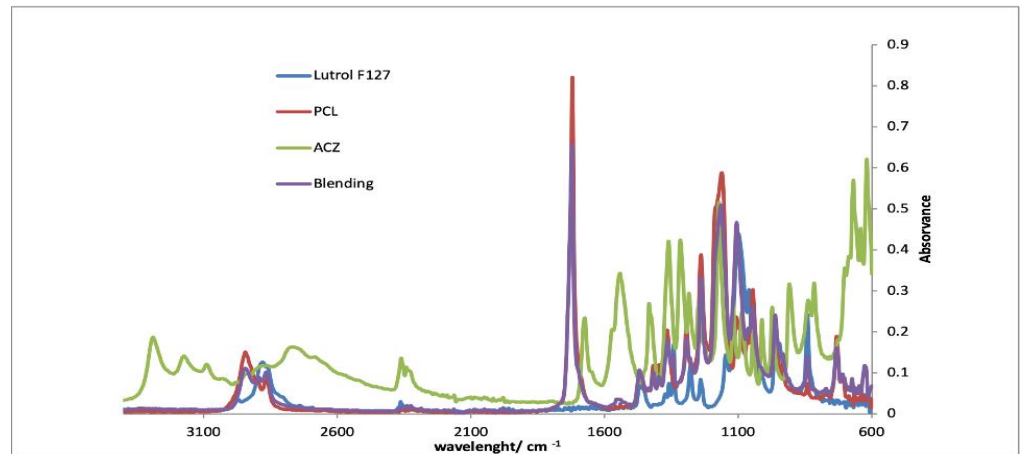


Figure 7. FTIR spectra of blending implants compared with PCL, Lutrol F127 and acetazolamide.

3.2.4. Contact Angles of Implants Surface

Analyzing Tables 6 and 7, it appears that the contact angles vary according to the physical-chemical characteristics of materials: hydrophilic surfaces in contact with water cause the spreading of the droplet, resulting in low contact angles; on the other hand, hydrophobic surfaces in contact with water decrease the area of the contact surface, resulting in higher angles.

In Table 6, by comparing the two blending membranes, the hydrophilic character of acetazolamide is observed, causing a decrease of the contact angle.

The coaxial fibers have a higher angle than the uniaxial fibers with the drug due to the presence of PCL coating, which isolates the hydrophilic insides of the fibers.

Table 6. Water membrane contact angles (Mean ± SD, n = 3).

Blending without ACZ	Membranes		
	Blending	MD without ACZ	MD
Angle/ 58.84 ± 10.60	Angle/ 38.08 ± 12.16	Angle/ 100.35 ± 4.58	Angle/ 50.75 ± 4.45

Table 7. Water-coating contact angles (Mean \pm SD, $n = 3$). Simultaneous Thermal Analysis of the Implants.

Coating	
PCL-Lut 75:25	PCL-Luw 75:25
Angle/ 37.22 \pm 4.40	Angle/ 102.60 \pm 3.40

In Table 7, it can be seen that the two coatings have different contact angles, explained by the hydrophilicity of Lutrol F127 and hydrophobicity of Luwax of EVA 3, although they represent only 25% of the coating.

3.2.5. Simultaneous Thermal Analysis of the Implants

Table 8 describes the obtained parameters by analyzing the thermograms related to pure substances: acetazolamide, Lutrol F127 and PCL and membranes (EDW, MD and blending), respectively. It is noted that acetazolamide has a state transition (melting) at 274.84 °C, which is not found in the thermograms of membranes. Thus, it can be inferred that in EDW, MD and blending implants, the drug interacts strongly with Lutrol F127, which is in amorphous form or the drug amount (about 5%) is so low that the peak regarding the transition is unnoticeable.

Table 8. Melting temperature, onset degradation temperature and variation of melting enthalpy of pure substances: acetazolamide, Lutrol F127, PCL and the membrane formulations: EDW, MD and blending.

Substance/ Membrane	Melting Temperature (°C)	Variation of Melting Enthalpy (J/g)	Onset Degradation Temperature (°C)
Acetazolamide	274.84	−132.20	271.25
Lutrol F127	60.43	−123.50	370.30
PCL	67.47	−67.34	388.27
EDW	61.03	−54.36	379.89
MD	61.85	−57.71	380.03
Blending	61.78	−61.30	382.79

The melting temperatures of membranes have intermediate values between the melting temperature of Lutrol F127 (60.43 °C) and PCL (67.47 °C). The same is applied to the degradation temperatures. These results suggest that the thermal events of membranes are close to the thermal events of its two major components (Lutrol F127 and PCL).

3.2.6. Drug Release Assay of Implants with and without Coating

Through the analysis of Figure 8, it is observed that MD, EDW and blending implants without coating exhibit very similar release rates, despite previous studies showing a clear difference in release patterns between blending and coaxial fibers [18,21]. Therefore, it is concluded that, under these conditions, the type of fiber (blending or coaxial) does not affect the release of the drug. The implants without coating had the fastest release rates, i.e., during the first 48 h, they released almost all pharmacological content of the systems. It is worth noting the fact that MD implants exhibit a percentage of cumulative drug release of more than 100%, which can be explained by the acetazolamide not being totally encapsulated and instantaneously “released” and/or by the saturation of the PBS medium, with no observation of sink conditions [20].

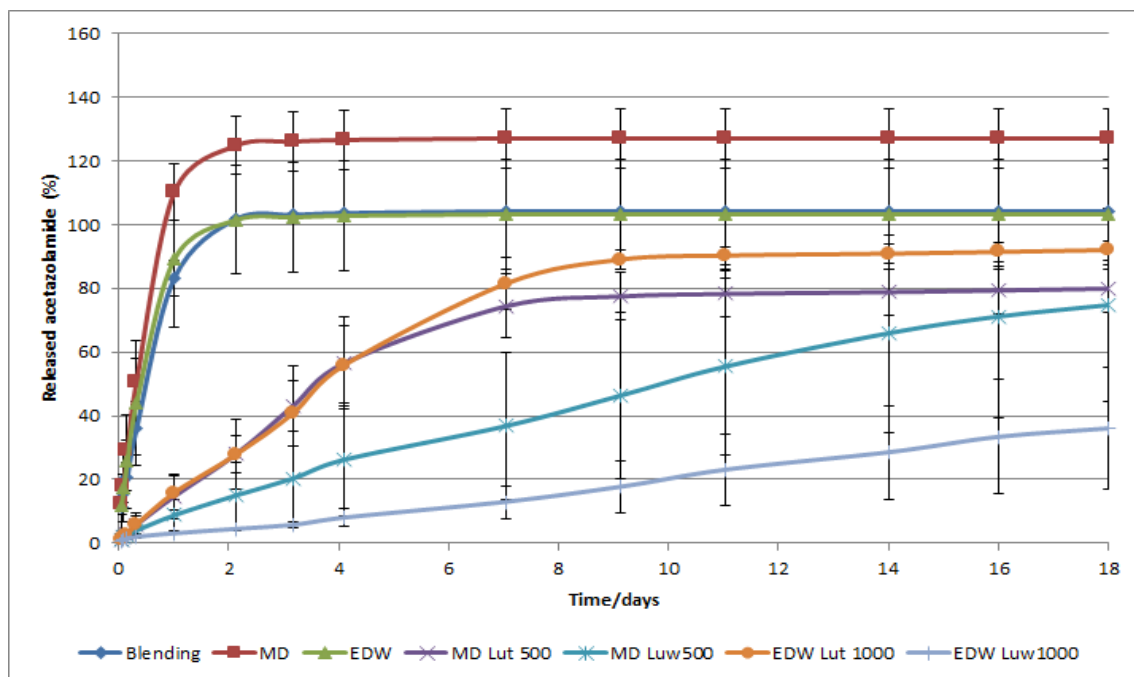


Figure 8. Percentage of drug release through time regarding implants with and without coating.

With regard to coated implants, it is apparent that the coating containing Lutrol F127 had a faster release rate than coated implants containing Luwax EVA 3. This is explained because Lutrol F127, one hydrophilic polymer, shows higher affinity with saline medium and the diffusion of the drug through swollen polymer layer is faster; in the case of Luwax EVA 3, there is less affinity with saline medium, and its penetration in the pores with subsequent erosion and drug diffusion occurs more slowly [22].

The coating thickness strongly affects the release kinetics in case of Luwax EVA 3, as discernible in Figure 8, since the distance traveled by the drug until it reaches the implant—the diffusional distance—is greater, and therefore, the diffusion is delayed. On the other hand, the thickness of coating containing Lutrol F127 does not influence the release rate, which is explained by its swelling.

The coated implants have a more favorable release rate of acetazolamide and, indeed, suggest a promisor alternative to nanoparticles used in previous studies [23,24], whose content was released in less than 24 h.

4. Discussion

Summing up, seven polymeric types of acetazolamide ocular implants (with and without coating) were prepared by electrospinning/solvent casting method, respectively, in accordance with the previous description.

The characterization of prepared implants includes several studies: SEM analyses revealed some differences in structure related to the composition; however, the thickness of the coating coincides with the results obtained through direct measurements. FTIR results indicate compatibility drug-polymers. Contact angles of implants surface change according to the nature of surface (hydrophilic or hydrophobic) in contact with water. Thermal analysis of the implants suggested that the observed thermal events are related to the thermal events of its two major polymers (Lutrol 127 and PCL). These results are in line with the results obtained by other researchers [20].

In order to mimic the pH value of 7.4 of the human eye, the devices were placed in falcons with PBS, and for the test to take place at body temperature and consequently the human eye, the falcons were placed in an oven at 37 °C; at pre-determined intervals, the entire volume of PBS was removed from the falcons, and replaced with a new solution of PBS, to mimic the *in vivo* simulated condition for the drug release study from ocular

implants. All implants have been subjected to release tests for 18 days. Through the release profile of each type of implant and their morphological and physicochemical features, it was concluded that the implants exhibiting an effective performance in drug release are constituted of PCL and Lutrol F127 dissolved in ethanol, dimethylformamide and water-EDW formulation—and coated with Luwax EVA 3. The presence of water as a solvent of Lutrol F127 and acetazolamide caused a more effective dissolution leading to a more uniform and gradual release rate. Moreover, the hydrophobicity of Luwax EVA 3 is related to polymer degradation by erosion, which retards the drug release. On the other hand, the devices with thicker coating, namely, the obtained film by dissolving 1000 mg of Luwax EVA 3 in 10 mL of THF, led to a slower release, since the distance that separates the drug from the saline medium is greater, motivating a delay in its diffusion.

The coated implants have a more favorable release rate of acetazolamide than nanoparticles used in previous studies, in which the content was released in less than 24 h [23,24].

Previous studies have demonstrated that these drug delivery systems can be used *in vivo*; examples are the approved FDA Iluvien[®] and Ozurdex[®] systems. The core-shell fibers appear as an improvement of this system combining the erosion (phenomenon that mainly happens in the Ozurdex[®]) with the diffusion (phenomenon that mainly happens in Iluvien[®]) [5]. By controlling the thickness of the implant cover, we may in the future modulate the drug release in according with the required objectives.

We cannot fail to mention that sterilization of ocular implants is inevitable to avoid infection after surgery. However, sterilization methods have to be reliable and chosen according to the used materials properties. In one recent study carried out by Cassan et al. [25], the impact of three different sterilization techniques (β , γ and X-ray) on electrospun PCL scaffolds was evaluated. It was shown that material properties of PCL in electrospun fiber mats were affected by all three sterilization techniques, although electron beam had less of an effect on PCL than γ -irradiation, being recommended for PCL fiber mats.

Another experimental work [26] compared different sterilization/disinfection methods (gamma irradiation, UV-irradiation, *in situ* generated chlorine gas, low-temperature argon plasma) on various properties (drug stability, solid state, mechanical properties, swelling and biodegradation, drug release) of electrospun drug-loaded matrices. Two different polymeric compositions were studied—polycaprolactone (PCL) alone or in combination with polyethylene oxide (PEO)—with the model antibacterial drug chloramphenicol (CAM). Although no changes in the morphology were seen, the most crucial was the effect of sterilization on the polymer crystallinity, which is also directly changing the mechanical properties and polymer degradation behavior. The authors concluded that no single sterilization method can be considered appropriate for all materials and formulations; thus, a case-by-case approach needs to be taken when developing a novel electrospun drug delivery system as a drug product.

Paying attention to these considerations, in the near future, we will dedicate our research work to the selection of the most appropriate sterilization method for the prepared ocular implants.

5. Conclusions

Electrospinning is a simple and versatile method to produce fibers using charged polymer solutions. As drug delivery systems, electrospun fibers are an excellent choice because of easy drug entrapment, high surface area, morphology control and biomimetic characteristics. Various drugs and biomolecules can be easily encapsulated inside or on the fiber surface, either during electrospinning or through post-processing of the fibers. Multicomponent fibers have attracted special attention because new properties and morphologies can be easily obtained through the combination of different polymers.

Considering that acetazolamide, by inhibiting a large-scale enzyme, carbonic anhydrase, fell into disuse, mainly because of renal side effects, we can conclude that the use of these local and specialized systems allowed the application of this drug, which is effective

and safe when directly administered to the vitreous humor. The continued apprehension of these systems leads to visible improvements in the quality of life of people with glaucoma.

In future studies, acetazolamide polymeric implants prepared by electrospinning and coated by a solvent casting method could be successfully used for ocular administration for the treatment of ocular affections, increasing patient compliance and resulting in visible improvements in their quality of life.

Author Contributions: Conceptualization: M.E.P. and P.C.; methodology: M.M.; software: M.M. and P.C.; Validation: M.M., P.C. and M.E.P.; formal analysis: M.M.; investigation, M.M.; resources: experiments and trials were performed in the CIEPQPF. The morphological analysis by SEM was performed at Pedro Nunes Institute (IPN), Coimbra, Portugal; data curation: M.E.P., writing—original draft preparation: M.M. and P.C.; writing—review and editing: M.E.P.; visualization: P.C.; supervision: P.C. and M.E.P.; project administration: M.E.P. All authors have read and agreed to the published version of the manuscript.

Funding: This research received no external funding.

Institutional Review Board Statement: Not applicable.

Informed Consent Statement: Informed consent was obtained from all subjects involved in the study.

Data Availability Statement: Not applicable.

Acknowledgments: This study was carried out under the master's program in Drug Technologies, Faculty of Pharmacy, University of Coimbra. All experiments and trials were performed in the CIEPQPF. The morphological analysis by SEM was performed at Pedro Nunes Institute (IPN), Coimbra, Portugal.

Conflicts of Interest: The authors declare no conflict of interest.








References

- Bourne, R.; Flaxman, S.; Braithwaite, T.; Cicinelli, M.; Das, A.; Jonas, J.; Keeffe, J.; Kempen, J.; Leasher, J.; Limburg, H.; et al. Magnitude, temporal trends, and projections of the global prevalence of blindness and distance and near vision impairment: A systematic review and meta-analysis. *Lancet Glob. Health* **2017**, *5*, e888–e897. [CrossRef]
- Molokhia, S.A.; Thomas, S.C.; Garff, K.J.; Mandell, K.J.; Wirostko, B.M. Anterior eye segment drug delivery systems: Current treatments and future challenges. *J. Ocul. Pharmacol. Ther.* **2013**, *29*, 92–105. [CrossRef]
- Moosa, R.M.; Choonara, Y.E.; Du Toit, L.C.; Kumar, P.; Carmichael, T.; Tomar, L.K.; Tyagi, C.; Pillay, V. A review of topically administered mini-tablets for drug delivery to the anterior segment of the eye. *J. Pharm. Pharmacol.* **2014**, *66*, 490–506. [CrossRef] [PubMed]
- Del Amo, E.M.; Rimpela, A.K.; Heikkinen, E.; Kari, O.K.; Ramsay, E.; Lajunen, T.; Schmitt, M.; Pelkonen, L.; Bhattacharya, M.; Richardson, D.; et al. Pharmacokinetic aspects of retinal drug delivery. *Prog. Retin. Eye Res.* **2017**, *57*, 134–185. [CrossRef]
- Hazirolan, D.; Pleyer, U. Think global-act local: Intravitreal drug delivery systems in chronic noninfectious uveitis. *Ophthalmic Res.* **2013**, *49*, 59–65. [CrossRef] [PubMed]
- Obstbaum, S.A.; Cioffi, G.A.; Krieglstein, G.K.; Fennerty, M.B.; Alm, A.; Araie, M.; Carassa, R.G.; Greve, E.L.; Hitchings, R.A.; Kaufman, P.T.; et al. Gold standard medical therapy for glaucoma: Defining the criteria identifying measures for an evidence-based analysis. *Clin. Ther.* **2004**, *26*, 2102–2120. [CrossRef]
- Fialho, S.L.; Rego, M.G.; Cardillo, J.A.; Siqueira, R.C.; Jorge, R.A., Jr. Implantes biodegradáveis destinados à administração intra-ocular. *Arq. Bras. Oftalmol.* **2003**, *66*, 891–896.
- Karimian, F.; Baradaran-Rafii, A.; Hashemian, S.J.; Hashemloo, A.; Jafari, M.E.; Yaseri, M.; Ghahari, E.; Akbarian, S. Comparison of three phakic intraocular lenses for correction of myopia. *J. Ophthalmic Vis. Res.* **2014**, *9*, 427–433. [CrossRef] [PubMed]
- Instituto de Oftalmologia de Curitiba. Implante de Lentes Intraoculares (LIO). Available online: <http://www.ioc.med.br/especialidades/implante-de-lentes-intraoculares-lio> (accessed on 27 February 2019).
- Hunley, M.T.; Long, T.E. Electrospinning functional nanoscale fibers: A perspective for the future. *Polym. Int.* **2008**, *57*, 385–389. [CrossRef]
- Huang, Z.M.; Zhang, Y.Z.; Kotaki, M.; Ramakrishna, S. A review on polymer nanofibers by electrospinning and their applications in nanocomposites. *Sci. Technol.* **2003**, *63*, 2223–2253. [CrossRef]
- Angkawinitwong, U.; Awwad, S.; Khaw, P.; Brocchini, S.; Williams, G.R. Electrospun nanofibers—A promising solid in-situ gelling alternative for ocular drug delivery. *Acta Biomater.* **2020**, *126*, 125–132.
- Rodrigues Da Silva, G.; Limab, T.H.; Fernandes-Cunha, G.M.; Oréficeb, R.L.; Silva-Cunha, A.; Zhaod, M.; Behar-Cohend, F. Ocular biocompatibility of dexamethasone acetate loaded poly(ϵ -caprolactone) nanofibers. *Eur. J. Pharm. Biopharm.* **2019**, *142*, 20–30. [CrossRef] [PubMed]

14. Kauri, P.; Singh, M.; Kanwar, M. Formulation and evaluation of ophthalmic preparations of acetazolamide. *Int. J. Pharm.* **2000**, *199*, 119–127. [CrossRef]
15. Mishra, V.; Jain, N.K. Acetazolamide encapsulated dendritic nano-architectures for effective glaucoma management in rabbits. *Int. J. Pharm.* **2014**, *461*, 380–390. [CrossRef]
16. Morsi, N.; Ibrahim, M.; Refai, H.; Sorogy, H. Nanoemulsions-based electrolyte triggered in situ gel for ocular delivery of acetazolamide. *Eur. J. Pharm. Sci.* **2017**, *104*, 302–314. [CrossRef] [PubMed]
17. Saifullah, M.; Ahsan, A.; Shishir, M.R. Production, stability and application of micro and nanoemulsion in food production and the food processing industry. In *Emulsions: Nanotechnology in the Agri-Food Industry*; Grumezescu, A.M., Ed.; Academic Press: London, UK; Elsevier Inc.: London, UK, 2016; Chapter 12; pp. 405–442.
18. Ji, W.; Yang, F.; van den Beucken, J.J.; Bian, Z.; Fan, M.; Chen, Z.; Jansen, J.A. Fibrous scaffolds loaded with protein prepared by blend or coaxial electrospinning. *Acta Biomater.* **2010**, *6*, 4199–4207.
19. Arinstein, A.; Avrahami, R.; Zussman, E. Buckling behaviour of electrospun microtubes: A simple theoretical model and experimental observations. *J. Phys. D Appl. Phys.* **2008**, *42*, 1–7. [CrossRef]
20. Natu, M.V.; Sousa, H.; Gil, M.H. Effects of drug solubility, state and loading on controlled release in biocomponent electrospun fibers. *Int. J. Pharm.* **2010**, *397*, 50–58.
21. Tiwari, S.K.; Tzezana, R.; Zussman, E.; Venkatraman, S.S. Optimizing partition-controlled drug release from electrospun core-shell fibers. *Int. J. Pharm.* **2010**, *392*, 209–217. [CrossRef] [PubMed]
22. Martínez-Pérez, C.; Olivas-Armendariz, I.; Castro-Carmona, J.; García-Casillas, P. Scaffolds for tissue engineering via thermally induced phase separation. *Adv. Regen. Med.* **2011**, *13*, 275–294.
23. Singh, J.; Chhabra, G.; Pathak, K. Development of acetazolamide-loaded, pH-triggered polymeric nanoparticulate in situ gel for sustained ocular delivery: In vitro, ex vivo evaluation and pharmacodynamics study. *Drug Dev. Ind. Pharm.* **2013**, *9*, 1223–1232.
24. Verma, P.; Gupta, R.N.; Jha, A.K.; Pandey, R. Development, in vitro and in vivo characterization of Eudragit RL 100 nanoparticles for improved ocular bioavailability of acetazolamide. *Drug Deliv.* **2013**, *20*, 269–276. [CrossRef] [PubMed]
25. Cassan, D.; Hoheisel, A.L.; Glasmacher, B.; Menzel, H. Impact of sterilization by electron beam, gamma radiation and Xrays on electrospun poly-(ϵ -caprolactone) fiber mats. *J. Mater. Sci. Mater. Med.* **2019**, *30*, 1–11. [CrossRef] [PubMed]
26. Preema, L.; Vaarmetsa, E.; Meosa, A.; Jõgib, I.; Putrinšč, M.; Tensonc, T.; Kogermanna, K. Effects and efficacy of different sterilization and disinfection methods on electrospun drug delivery systems. *Int. J. Pharm.* **2019**, *567*, 118450. [CrossRef] [PubMed]

Article

Development and Characterization of a Tacrolimus/Hydroxypropyl- β -Cyclodextrin Eye Drop

Xurxo García-Otero ^{1,2}, Victoria Díaz-Tomé ^{1,3}, Rubén Varela-Fernández ^{1,4}, Manuel Martín-Pastor ⁵, Miguel González-Barcia ³, José Blanco-Méndez ^{1,6}, Cristina Mondelo-García ³, María A. Bermudez ⁷, Francisco Gonzalez ^{8,9}, Pablo Aguiar ^{2,*}, Anxo Fernández-Ferreiro ^{3,*} and Francisco J. Otero-Espinar ^{1,6,*}

- ¹ Pharmacology, Pharmacy and Pharmaceutical Technology Department, Faculty of Pharmacy, University of Santiago de Compostela (USC), 15705 Santiago de Compostela, Spain; xurxo.garcia@rai.usc.es (X.G.-O.); victoria.diaz@rai.usc.es (V.D.-T.); ruben.varela.fernandez@rai.usc.es (R.V.-F.); jose.blanco.mendez@usc.es (J.B.-M.)
- ² Molecular Imaging Group, University Clinical Hospital, Health Research Institute of Santiago de Compostela (IDIS), 15706 Santiago de Compostela, Spain
- ³ Clinical Pharmacology Group, University Clinical Hospital, Health Research Institute of Santiago de Compostela (IDIS), 15706 Santiago de Compostela, Spain; miguel.gonzalez.barcia@sergas.es (M.G.-B.); cristina.mondelo.garcia@sergas.es (C.M.-G.)
- ⁴ Clinical Neurosciences Group, University Clinical Hospital, Health Research Institute of Santiago de Compostela (IDIS), 15706 Santiago de Compostela, Spain
- ⁵ Nuclear Magnetic Resonance Unit, Research Infrastructures Area, University of Santiago de Compostela (USC), 15782 Santiago de Compostela, Spain; manuel.martin@usc.es
- ⁶ Paraquasil Group, University Clinical Hospital, Health Research Institute of Santiago de Compostela (IDIS), 15706 Santiago de Compostela, Spain
- ⁷ Physiology Department–CIMUS, University of Santiago de Compostela (USC), 15782 Santiago de Compostela, Spain; maria.alvarez.bermudez@udc.es
- ⁸ Ophthalmology Department, Clinical University Hospital Santiago de Compostela (SERGAS), 15706 Santiago de Compostela, Spain; francisco.gonzalez@usc.es
- ⁹ Department of Surgery and Medical-Surgical Specialties and CIMUS, University of Santiago de Compostela (USC), 15782 Santiago de Compostela, Spain
- * Correspondence: pablo.aguiar.fernandez@sergas.es (P.A.); anxo.fernandez.ferreiro@sergas.es (A.F.-F.); francisco.otero@usc.es (F.J.O.-E.); Tel.: +34-881814878 (F.J.O.-E.)

Citation: García-Otero, X.; Díaz-Tomé, V.; Varela-Fernández, R.; Martín-Pastor, M.; González-Barcia, M.; Blanco-Méndez, J.; Mondelo-García, C.; Bermudez, M.A.; Gonzalez, F.; Aguiar, P.; et al. Development and Characterization of a Tacrolimus/Hydroxypropyl- β -Cyclodextrin Eye Drop. *Pharmaceutics* **2021**, *13*, 149. <https://doi.org/10.3390/pharmaceutics13020149>

Received: 20 December 2020

Accepted: 19 January 2021

Published: 23 January 2021

Publisher's Note: MDPI stays neutral with regard to jurisdictional claims in published maps and institutional affiliations.



Copyright: © 2021 by the authors. Licensee MDPI, Basel, Switzerland. This article is an open access article distributed under the terms and conditions of the Creative Commons Attribution (CC BY) license (<https://creativecommons.org/licenses/by/4.0/>).

Abstract: Uveitis is a vision inflammatory disorder with a high prevalence in developing countries. Currently, marketed treatments remain limited and reformulation is usually performed to obtain a tacrolimus eye drop as a therapeutic alternative in corticosteroid-refractory eye disease. The aim of this work was to develop a mucoadhesive, non-toxic and stable topical ophthalmic formulation that can be safely prepared in hospital pharmacy departments. Four different ophthalmic formulations were prepared based on the tacrolimus/hydroxypropyl- β -cyclodextrin (HP β CD) inclusion complexes' formation. Phase solubility diagrams, Nuclear Magnetic Resonance (NMR) and molecular modeling studies showed the formation of 1:1 and 1:2 tacrolimus/HP β CD inclusion complexes, being possible to obtain a 0.02% (*w/v*) tacrolimus concentration by using 40% (*w/v*) HP β CD aqueous solutions. Formulations also showed good ophthalmic properties in terms of pH, osmolality and safety. Stability studies proved these formulations to be stable for at least 3 months in refrigeration. Ex vivo bioadhesion and in vivo ocular permanence showed good mucoadhesive properties with higher ocular permanence compared to the reference pharmacy compounding used in clinical settings ($t_{1/2}$ of 86.2 min for the eyedrop elaborated with 40% (*w/v*) HP β CD and Liquifilm[®] versus 46.3 min for the reference formulation). Thus, these novel eye drops present high potential as a safe alternative for uveitis treatment, as well as a versatile composition to include new drugs intended for topical ophthalmic administration.

Keywords: tacrolimus; hydroxypropyl- β -cyclodextrin; topical ophthalmic administration; eye drops; uveitis; PET/CT imaging

1. Introduction

Uveitis is a sight-threatening inflammatory disorder that affects a wide range of ages in the world population, being the main cause of 5–20% of blindness in Europe and United States and over 25% in developing countries [1,2]. This affection can lead to other types of complications, including cataract, increased intraocular pressure (IOP), macular edema (ME) or glaucoma, compromising visual loss [3–5]. Therefore, it causes a great clinical and socioeconomic impact on the life quality of patients [6–8] and early diagnosis and treatment are important to prevent complications.

Uveitis is a recurrent and common ophthalmic disease that has an idiopathic etiology, caused by a complication of an infection or associated with a systemic disease (infectious or autoimmune disorder) [3,9]. The pathogenesis of uveitis is often caused by an autoimmune response. Inflammatory cytokines promote the activation of T cells and trigger recruitment of large numbers of circulation inflammatory leukocytes into the eye. This process may cause irreversible tissue damage and visual impairment. Topical corticosteroids constitute the first therapeutic line to treat the disease, but remarkable adverse effects can appear due to continuous treatment with these drugs. The use of immunosuppressants in uveitis is indicated in corticosteroid-refractory eye disease or after systemic side effects' appearance.

Tacrolimus is a macrolide with a high molecular weight (804.02 g/mol) isolated from *Streptomyces tsukubaensis*, with a great immunosuppressive activity (100 times more potent than cyclosporine A) [10,11] that inhibits T cell proliferation and suppresses the release of inflammatory cytokines; it can theoretically be used to reduce inflammatory activity in uveitis patients [3]. This drug has been used in different ocular diseases including corneal graft rejection [12–14], vernal keratoconjunctivitis (VKC) [15–17], dry eye [11,18], uveitis [5,19,20], scleritis [21,22] or graft-versus-host disease [23–25], among others. Additionally, clinical studies have shown tacrolimus' high effectivity compared to other immunosuppressants such as cyclosporine, at lower concentrations [26].

Nowadays, tacrolimus eye drops are not marketed and all its use rests in the elaboration in hospital pharmacy departments (HPDs). The preparation of ophthalmic tacrolimus formulations is limited by its poor water solubility (1–12 µg/mL) [27,28] due to the hydrolytic mechanism [29]. For this reason, 0.03% (*w/v*) tacrolimus eye drops are being obtained by reformulation from intravenous drug presentation (Prograf®) [15]. However, in this formulation, tacrolimus is solubilized in ethanol, containing irritating compounds that usually cause discomfort and unpleasantness to the patient. Based on these statements, it would be interesting to design new topical ophthalmic formulations with the lowest possible toxic potential and better tolerability. Several types of tacrolimus formulations such as niosomes [30], nanoemulsions [5], microspheres [31], nanocapsules [32], micelles [33], emulsions [34] or liposomes [35] have also been described by other authors. Nonetheless, if these are not synthesized to be marketed, their elaboration in HPDs will be complicated.

The need to increase the solubility and stability of the drug becomes a task of extreme necessity. There are several types of β -cyclodextrin (β CD) derivatives, although most of them have not been authorized or there are not enough preclinical studies to support their use at the topical ophthalmic level [36]. Some β -cyclodextrins have been used by other authors as complexing agents with several drugs [27,37,38]. The oligosaccharide 2-hydroxypropyl- β -cyclodextrin (HP β CD) is a cyclic oligosaccharide formed by seven units of α -1,4-linked glucose and a hydroxypropylated group, with a lipophilic central cavity and a hydrophilic outer surface. The rigid doughnut-shaped structure makes it a natural complexing agent, being able to form inclusion complexes with several drugs, where their structure (or part of it) may fit in the cyclodextrin cavity [39]. The complexation between drugs and cyclodextrin affects many drugs' physicochemical properties, including their chemical stability and aqueous solubility [39]. Therefore, this hydrophilic cyclodextrin derivative can form highly water-soluble complexes with lipophilic drugs, as it happens with tacrolimus. There are few reports on the use of cyclodextrins to improve the pharmaceutical characteristics of tacrolimus [37]. However, HP β CD has been chosen in this work due to the fact that, according to the European Medicines Agency (EMA), it

is the safest and most appropriated cyclodextrin for topical ophthalmic administration, proving that it was not toxic [40]; this fact becomes important when transferring research to the clinic. Hence, there is already a commercialized formulation (Indocollyre[®] 0.1% ophthalmic solution) complexing HP β CD and indomethacin [41]. The improvement of aqueous tacrolimus eye drops is still a challenge because of its low chemical stability and solubility in particular [27].

The aim of this work was based on the design and development of different topical ophthalmic formulations containing tacrolimus as an alternative to the reformulated Prograf[®] intravenous solution (REF). The characterization of these tacrolimus-loaded ophthalmic formulations incorporating the improvements that cyclodextrin (HP β CD) properties can provide in terms of tacrolimus solubility and stability in aqueous solution was also carried out. Cyclodextrin properties may also improve the mucoadhesive characteristics of the formulations, leading to a retention time increase on the ocular surface. In addition, the use of new molecular imaging techniques such as positron emission tomography/computed tomography imaging (PET/CT imaging) was incorporated into the present study in order to better understand the *in vivo* formulations' permanence on the corneal surface. On the other hand, the evaluation of the eye drops' safety was necessary to verify that there were no corneal surface alterations. Based on this background, the novelty of this work relies on the obtention of a consistent preclinical base for a new safe, stable and bioadhesive tacrolimus eye drop designed for appropriate preparation by HPDs. Besides, additional goals were also pre-established such as ease of preparation, scalability from the laboratory scale to HPDs and patient comfort improvement.

2. Materials and Methods

Tacrolimus powder was acquired from Guinama[®] S.L.U. (La Pobla de Vallbona, Spain), 2-hydroxypropyl- β -cyclodextrin Kleptose[®] HPB (HP β CD; $M_w = 1399$ Da, substitution degree = 0.65 molar ratio) was provided from Roquette Laisa S.A.[®] (Valencia, Spain), Liquifilm[®] was purchased from Allergan[®] Pharmaceuticals Ireland (Mayo, Ireland), Balanced Salt Solution (BSS[®]) was acquired from Alcon[®] laboratories (Fort Worth, TX, USA) and Prograf[®] (5 mg/mL, ampoules) was purchased from Astellas Pharma S.A.[®] (Madrid, Spain). Ultrapure water MilliQ[®] (Millipore Iberica; Madrid, Spain) was used throughout the whole work. All other chemicals and reagents were of the highest purity grade commercially available.

2.1. Tacrolimus/HP β CD Solubilization Study

2.1.1. Phase Solubility Diagram

A phase solubility diagram was used to estimate the stability constant (K) of the tacrolimus/HP β CD inclusion complex. The solubility measurements were carried out following the previous work of our research group, described by Anguiano-Igea et al. [42]. This protocol was adjusted to the Higuchi and Connors phase solubility model [43]. A solubility study was carried out by adding an excess amount of the tacrolimus powder to MilliQ[®] aqueous solutions containing increasing concentrations of HP β CD (from 0 to 400 mg/mL). The vials containing these suspensions were then shaken in a VWR incubated mini-shaker (VWR International, Radnor, PA, USA) at 25 °C and 250 rpm for 7 days until reaching an equilibrium. Subsequently, each aliquot was centrifuged for 30 min at 15,300 rcf (Centrifuge 5804 R; Eppendorf[®], Hamburg, Germany) and 100 μ L of the supernatant was diluted with 400 μ L of MilliQ[®] water (1:5 dilution) prior to measurement. Each HP β CD concentration was assayed in quintuplicate.

Tacrolimus concentration was determined for each sample using an HPLC system (Agilent 1260 series; Agilent Technologies[®], Santa Clara, CA, USA) equipped with a Diode Array Detector HS, a solvent delivery quaternary pump system, 400 bar maximum pressure and an autosampler. The software model OpenLAB CDS 3D UV (PDA) was used for the data processing. The analysis was performed under an isocratic method. The column used was a Poroshell 120, EC-C18 (4.6 \times 100 mm, 4 μ m) and at a temperature of 60 °C.

The mobile phase was water-acetonitrile (35:65 (v/v)) using a 1.5 mL·min⁻¹ flow rate. A 210-nm wavelength was employed for the tacrolimus quantification. The volume of the injected sample was 10 µL and the retention time was 3 min. The analytical method was validated according to International Conference on Harmonization (ICH) guideline recommendations [44] and the mathematical adjustments were made in GraphPad Prism® 8 v.8.2.1 software (GraphPad Software, San Diego, CA, USA, 2019).

A_P phase solubility types are usually observed when a drug molecule forms a complex with more than one CD molecule, assuming a consecutive complexation. A quadratic model equation allows the estimation of both stability constants ($K_{1:1}$ and $K_{1:2}$). The value of $K_{1:2}$ is often lower than that of $K_{1:1}$.

These constants values were calculated using the following Equation (1):

$$S = S_0 + (K_{1:1} \cdot S_0 + K_{1:1} \cdot K_{1:2} \cdot S_0 \cdot [\text{HP}\beta\text{CD}]) \cdot [\text{HP}\beta\text{CD}], \quad (1)$$

where S is the total solubility, S_0 is the free drug solubility and $K_{1:1}$ and $K_{1:2}$ are the stability constants of the complex tacrolimus/HPβCD. $K_{1:1}$ and $K_{1:2}$ values were calculated by non-linear regression using GraphPad Prism® 8 v.8.2.1 software.

2.1.2. NMR Studies and Molecular Modeling

NMR experiments were conducted at two different temperature conditions, 278 and 298 K, on a Bruker NEO 17.6 T spectrometer (proton resonance 750 MHz) (Billerica, MA, USA), equipped with a ¹H/¹³C/¹⁵N triple resonance PA-TXI probe with a deuterium lock channel and a shielded Pulse Field Gradient (PFG) z-gradient. The spectrometer control software was TopSpin 4.0 (Billerica, MA, USA, 2020). The reported chemical shifts are referenced to the lock deuterium solvent. Spectra were processed and analyzed using Mestrenova v14.0 software (Mestrelab Research S.L., Santiago de Compostela, Spain, 2019).

One-dimensional saturation transfer difference ¹H spectra (STD) [45] were measured. The experiment consisted of a selective saturation pulse train, a WET selective solvent suppression module and a 90-degree hard-pulse followed by *fid* (*free induction decay*) acquisition. The selective saturation consisted of a train of soft Gaussian-shaped pulses of 50-ms duration with a 1-ms interpulse delay. The selective saturation was applied during 2 s at a specific frequency of the ¹H spectrum, covering a region of the spectrum of ± 125 Hz around the chosen frequency (i.e., ± 0.17 ppm in a 750 spectrometer). The STD^{off} saturation was applied at 20 ppm. The STD^{on} saturation was applied at the frequency of one specific signal of tacrolimus separated by more than 300 Hz from any signals of the HPβCD. The STD^{on} and STD^{off} scans were measured in alternate scans and subtracted by the phase cycling, providing the subtracted STD^{off-on} spectra. Three STD spectra were obtained by STD^{on} saturation of the tacrolimus signals at 6.30, 6.12 and 2.12 ppm, respectively. Each spectrum was acquired in 15 min with 128 scans and a 6.75-s total scan duration consisting of a 2-s pre-scan d_1 , a 2-s STD saturation time and a 2.75-s *fid* acquisition.

Molecular modeling was also performed to have an orientation of which is the most likely interaction between tacrolimus and HPβCD molecules using an MM+ force field in HyperChem®. The HPβCD used in this work (Kleptose® HPB) was a mixture of hydroxypropylated-β-CDs with a substitution mean degree of 0.65 (0.58–0.68; a mean of 4.2 hydroxypropyl groups per cyclodextrin molecule). An HPβCD molecule type with an average of four hydroxypropyl groups per native CD unit was used to obtain the molecular model.

2.1.3. Vehicle Solubility Study

In addition to conducting a MilliQ® water solubility study, it was studied whether the tacrolimus solubility varied in different media in which the final tacrolimus eye drops could be formulated. The tacrolimus solubility was tested in two different vehicles besides MilliQ® water, these being BSS® and Liquifilm®.

Three HPβCD proportions (20%, 30% and 40% (w/v)) were used sixfold with each vehicle and a two-way ANOVA was subsequently applied to compare the formulations'

solubility and to check for significant differences among them. This assay was carried out as a way to select the formulations to be tested for further analysis.

2.2. Formulation Preparation Procedure

The 2-hydroxypropyl- β -cyclodextrin (HP β CD) solutions were prepared by dissolving them in the two vehicles studied in the previous assay (BSS[®] and Liquifilm[®]); these were selected because they are ophthalmic vehicles that are frequently used in HPDs for eye drop formulation. BSS[®] is an isotonic salt solution for use in irrigating eye tissues, with pH 7.5 and a \approx 300 mOsm/kg osmolality [46]. Furthermore, Liquifilm[®] is an artificial eye tear that contains 1.4% polyvinyl alcohol (PVA) and a benzalkonium chloride preservative as well as different salts [47].

Based on the vehicle solubility study results (see Section 2.1. Tacrolimus solubilization with HP β CD results), the HP β CD and tacrolimus concentrations were chosen. The formulations were labeled as TBS 20 (20% (*w/v*) HP β CD and 0.01% (*w/v*) of tacrolimus in BSS[®]), TBS 40 (40% (*w/v*) HP β CD and 0.02% (*w/v*) of tacrolimus in BSS[®]), TLI 20 (20% (*w/v*) HP β CD and 0.01% (*w/v*) of tacrolimus in Liquifilm[®]) and TLI 40 (40% (*w/v*) HP β CD and 0.02% (*w/v*) of tacrolimus in Liquifilm[®]) (see Table 1). Once the cyclodextrin was dissolved, tacrolimus powder was added under magnetic stirring (>750 rpm) until all the tacrolimus powder was dissolved.

Table 1. Tacrolimus eye drops composition.

Formulation	Composition		
	HP β CD (<i>w/v</i> , %)	Tacrolimus (<i>w/v</i> , %)	Vehicles
TBS 20	20	0.01	BSS [®]
TLI 20	20	0.01	Liquifilm [®]
TBS 40	40	0.02	BSS [®]
TLI 40	40	0.02	Liquifilm [®]
REF	-	0.03	Liquifilm [®]

The reference formulation was prepared just as it is formulated in an HPD; a mixture of 0.03% (*w/v*) tacrolimus in Liquifilm[®] was prepared by a Prograf[®] (5 mg/mL) intravenous ampoule dilution as it was done in previous work [15], instead of using the tacrolimus powder. All formulations were kept under refrigeration conditions (4 ± 2 °C) to avoid degradation processes of the drug when they were prepared. Tacrolimus concentrations used in clinical practice are very variable (0.005% to 0.1% range) [11,17,48,49]; it should be noted that the selection of the designated tacrolimus concentration has been carried out on the basis of previous experimental studies (see Section 2.1.3. Vehicle solubility study).

2.3. Optimization Procedure: Tacrolimus Solubilization Time

The purpose of this assay was to know the required tacrolimus solubilization time in the eye drops so that when the formulation has to be replicated in an HPD, the drug will not be removed when performing the sterilizing filtration, ensuring quality, final product efficacy and patient safety.

This study was designed to establish the minimum stirring time of the tacrolimus powder to achieve the desired concentration in the solution media. HP β CD dissolution was carried out in triplicate (10 mL per formulation), and the amount of tacrolimus powder was added once all the cyclodextrin was dissolved. The solutions were shaken in a Cimarec I multipoint magnetic stirrer (ThermoFisher[®] Scientific; Waltham, MA, USA) at 900 rpm and 30 °C during the whole study period.

At predetermined times (24, 40, 48, 67, 72, 90 and 96 h), samples were collected without stopping the stirring, thus achieving the dissolution homogeneity. Samples were centrifuged (Centrifuge 5804 R; Eppendorf[®], Germany) at 15,300 rcf and 25 °C for 30 min

to remove any undissolved particles. Subsequently, 400 µL of the supernatant was taken to measure the tacrolimus concentration by HPLC (Agilent 1260 series; Agilent Technologies[®], Santa Clara, CA, USA) with the method described above (see Section 2.1.1. Phase solubility diagram). The tacrolimus concentration was corrected in each measure according to the volume that was left (0.5 mL less in each sample). Resulting data were compared and a statistical analysis was performed using a two-way ANOVA to analyze the influence of the solubilization time and the composition of the formulations. The analysis was carried out using GraphPad Prism[®] 8 v.8.2.1 software.

2.4. Physicochemical Characterization

2.4.1. pH and Osmolality Determination

The osmolality measurements were performed with an OsmoSpecial 1 osmometer (Astori Tecnica[®]; Poncarale, Italy), while the pH was measured using a pH meter (HI5221 HANNA[®], Italy) at 25 ± 0.5 °C. Each determination was carried out in triplicate.

2.4.2. Surface Tension Determination

Surface tension at the surface-to-air interface was measured using the du Nöuy ring method [50]. A Lauda TD1 tensiometer (LAUDA Scientific GmbH[®], Lauda-Königshofen, Germany) fitted with a platinum ring (2-cm diameter) was used to measure the surface tension of the tacrolimus formulations. A platinum du Nöuy ring was immersed into the liquid and then lifted to obtain tension values. The measurements were made at room temperature.

All glassware used for the surface tension measurements was washed with MilliQ[®] water and then dried in a clean oven before use. The platinum du Nöuy ring was washed with alcoholic KOH, rinsed in MilliQ[®] water and flamed until red-hot before each measurement. The determinations were carried out in triplicate.

2.4.3. Squeezing Force Determination

The squeezing force test evaluates the force needed to dispense a drop from 5-mL polypropylene eyedropper bottles that are commonly used in HPDs. A comparison of the cyclodextrin formulations with each other and between the reference one was made in order to assess the presence or absence of significant differences depending on their composition.

This method was performed following the method established by Charles H. Cox, with minor modifications [51], in a Shimadzu[®] texturometer (Kyoto, Japan). Figure 1 describes in detail the protocol followed to obtain the squeeze force measurements. The eyedropper bottle containing 5 mL of formulation was placed on a plate with a 45° inclination just below the load cell (1000 N maximum force). Test parameters were set after the method optimization; the upper probe moved down at a speed of 0.5 mm/s and an assessment of the required force to spill one drop of the formulation was performed. Five eyedropper bottles of each formulation were tested in quintuplicate (25 measurements per formulation). A one-way ANOVA was carried out to find out if there were significant differences. Tukey's multiple comparisons test was subsequently performed in order to compare all formulations.

2.5. Corneal Mucoadhesion

Tacrolimus formulations' mucoadhesion was measured following a method designed and developed by our research group using a Shimadzu[®] texturometer [52]. Corneal bioadhesion was used to quantitatively determine the interaction between the formulation and the corneal bovine surface. As presented in Figure 2, fresh bovine corneas were adjusted to a cornea mold made of clay and subsequently fixed to a texturometer load cell (20 N maximum force). Formulations were dropped in a glass bottle (40 mm diameter, 20 mm height) and placed in the lower part of the analyzer.

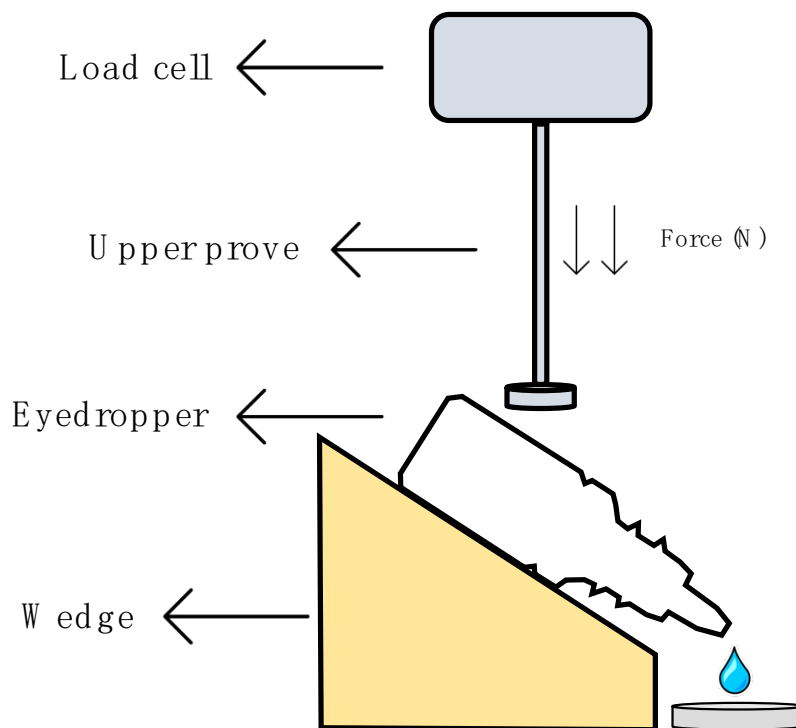


Figure 1. Scheme of the squeezing force determination.

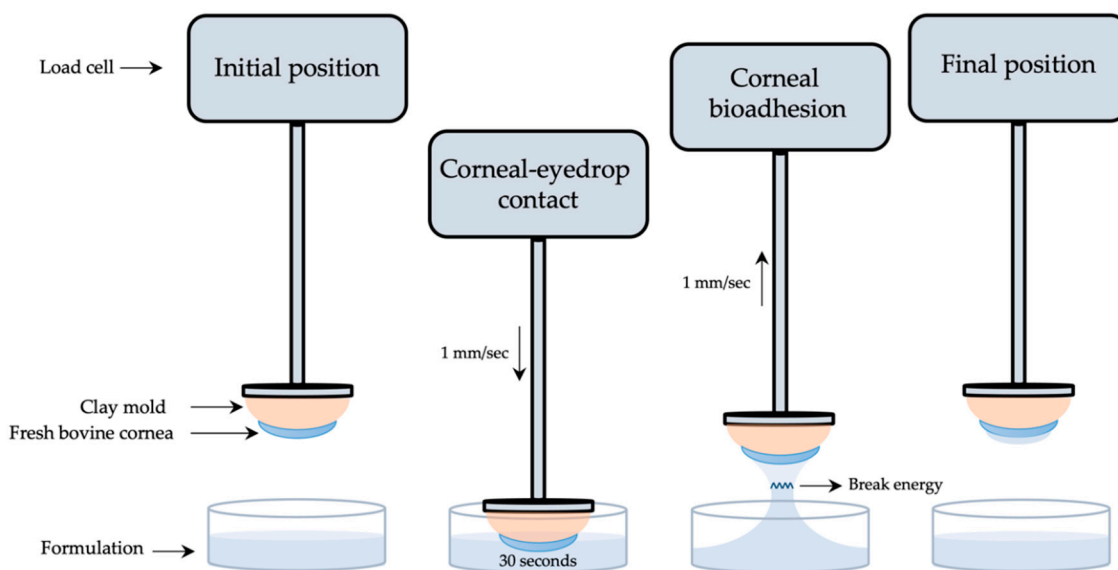


Figure 2. Scheme of the corneal mucoadhesion method.

Corneas were immersed 2 mm deep into the formulation at a 1 mm/s speed and force data (N) were obtained. Then, corneas were kept in touch with the formulation for 30 s, and just after returning to the starting point at a 1 mm/s speed, work (mJ) was measured. Mucoadhesion work was calculated from the area under the curve (AUC) of the force–displacement curve. All method parameters were previously studied and subsequently applied. Each measurement was carried out in triplicate.

2.5.1. Bovine Corneal Opacity and Permeability Test (BCOP)

The Bovine Corneal Opacity and Permeability test (BCOP) is an organotypic assay used to identify potential ocular corrosives and severe irritants. This method was carried

out using slaughterhouse materials (fresh bovine corneas), allowing the animal replacement compliance and avoiding the use of laboratory animals. This assay was founded on the method established by Tchao et al. [53] and adapted by Gautheron et al. [54], with minor modifications.

Freshly excised eyes were obtained from a local slaughterhouse and transported to the laboratory in optimal conditions. A macroscopic inspection of the eyes was performed, and only free-of-defects corneas were dissected and used for the test. Fresh corneas were mounted in Franz diffusion cells with the corneal epithelial surface facing upwards, dividing the two different chambers of the diffusion cell (donor and receptor). A thermostatic bath with a controlled temperature (37 ± 2 °C) and under stirring (100 rpm) during the whole assay was used to incubate all Franz diffusion cells.

Corneal opacity changes were measured by two different techniques, these being photometry and UV–Vis spectrophotometry. Photometry was assessed using a luxmeter (Gossen® Mavolux 5032C USB; Nürnberg, Germany), where corneas were placed between two cylindrical supporting black holders (fabricated with polylactic acid filaments using a 3D printer, Witbox® BQ, Madrid, Spain) and illuminated with a pipe light (Olympus® Highlight 200, Tokyo, Japan) with fixed brightness values [55]. Corneal transparency was measured in transmittance values by UV–Vis spectrophotometry (from 200 to 800 nm), allowing the light to pass through the corneas, from the source to the receiver of the spectrophotometer (Cary 60 UV-Vis, Agilent Technologies®; Santa Clara, CA, USA). Each formulation was tested in triplicate.

The following protocol was performed for formulations' addition and opacity measurements: (I) determination of the initial opacity values for freshly excised corneas by photometry and UV–Vis spectrophotometry; a corneal blank was made before photometry determination in order to remove basal light, while the cornea itself was used as a blank (800-nm wavelength) before spectrophotometry determination; (II) addition of 1 mL Phosphate-Buffered Saline (PBS) into the donor chamber of the vertical diffusion cells and cornea incubation were performed for 10 min, followed by opacity determination; (III) an amount of 1 mL of the formulation was then added to the upper chamber for 10 min, followed by its subtraction and further addition of PBS for 120 min; after this time, the opacity determination was repeated.

Once the opacity was measured, the same corneas were used to evaluate the corneal permeability changes, so 1 mL of 0.4% (*w/v*) fluorescein aqueous solution was added in the donor compartment, keeping in touch with the corneal epithelium side. After 90 min, the corneal permeability determination was evaluated by measuring the optical density (OD) in the medium (PBS) of the lower compartment at a 490-nm wavelength.

An *in vitro* irritation score (IVIS) can be calculated with the measurements of corneal opacity and permeability. The IVIS was determined by the following Equation (2):

$$\text{IVIS} = \text{mean opacity value} + (15 \times \text{mean permeability OD}_{490} \text{ value}), \quad (2)$$

2.5.2. Hen's Egg Test on the Chorioallantoic Membrane (HETCAM)

The hen's egg test on the chorioallantoic membrane (HETCAM) assay is one of the new organotypic models that allows the identification of irritative reactions, and it has become the international standard assay for acute eye irritation and corrosion (OECD TG 405, 2002; EC B.5). This assay was performed to evaluate possible acute ocular irritation caused by the present tacrolimus formulations.

Fertilized Broiler eggs (50–60 g weight) were obtained from the regional hatchery technology center and incubated for nine days in specific conditions (37 ± 0.5 °C and $65\% \pm 5\%$ RH). The eggs were automatically rotated in an automatic rotational incubator every 2 h until the eighth day, where rotation was stopped, and the eggs were kept in the axial position during 24 h for the proper placement of the chorioallantoic membrane (CAM). The protocol used was adapted from the procedure described by Spielmann and Liebsch [56].

At the ninth day of incubation, embryonated eggs were opened by their upper part with a tiny drill (Dremel®, Madrid, Spain) and the inner membrane was moistened with

0.9% (*w/v*) NaCl aqueous solution so that it could be removed later. Briefly, 300 μ L of 0.9% (*w/v*) NaCl solution (negative control), 0.1% (*w/v*) NaOH solution (positive control) and tacrolimus formulations (TBS 20, TLI 20, TBS 40, TLI 40 and REF) were directly instilled onto the CAM (2 eggs per compound). The membrane was observed over a 5-min period using an Olympus[®] SZ61TR Stereomicroscope and Olympus[®] CellSens Entry software.

Hemorrhage, lysis and coagulation of the CAM were measured; these reactions can be quantified through an irritation score (IS) following the Kalweit et al. criteria [57]. Based on this, they can be classified as follows: 0–0.9, no irritation; 1–4.9, slight irritation; 5–8.9, moderate irritation; and 9–21, severe irritation.

2.6. Stability Study

The stability study was only carried out with the formulations containing the greatest amount of drugs due to the fact that all the formulations have the same composition, the formulations with 40% (*w/v*) HP β CD being the most representative, as they have a greater amount of the components with activity and based on the clinical common usability and the drug concentration similarity at present.

Based on this, both formulations (TBS 40 and TLI 40) were aseptically prepared under laminar air flow. Briefly, 2 mL of each gel was conditioned into a 5-mL polypropylene eyedropper, previously sterilized, and the dropper was closed with a polypropylene cap. Three batches of each formulation were prepared and subjected to a double filtration with 0.22- μ m PES (polyethersulfone) filters.

The stability of each eyedrop was studied in unopened multidose eyedroppers for 4 months at three different temperature conditions: in refrigeration (4 ± 2 °C), at room temperature (25 ± 2 °C) and at oven temperature (40 ± 2 °C), protected from light exposure in all cases. Three units per formulation were subjected to tacrolimus quantification, osmolality determination, pH measurements and microbiological control growth at predetermined times (0, 15, 30, 45, 78 and 120 days). All samples were also visually inspected for any macroscopic changes (e.g., color, turbidity and precipitation).

2.6.1. Quantification of Tacrolimus Amount

The determination of tacrolimus was performed as previously mentioned (see Section 2.1.1. Phase solubility diagrams). Refrigerated and accelerated samples were kept at room temperature for 20 minutes before quantification. Each sample was assayed in triplicate. The analytical method was validated according to International Conference on Harmonization (ICH) guideline recommendations [44].

2.6.2. Osmolality, pH and Microbiological Control Growth

The pH and osmolality measurements were performed following the same experimental procedure previously described (see Section 2.4.1. pH and osmolality determination). In order to study the microbiological stability, 1 mL of each formulation was added in blood agar plates, Sabouraud/Chloranphenicol agar plates and liquid thioglycate medium plates. These samples were grown at 37 °C for predetermined periods (48 h, 15 days and 10 days, respectively). Once each incubation period ended, microbiological growth was observed and determined.

2.6.3. Statistical Analysis

Pharmaceutical Codex [58] has established the margins of the expiration period of the formulations as being once the concentration of active ingredient is reduced by 10% concerning the initial concentration. The percentage of unaltered drug versus time was fitted to a first order kinetics using GraphPad Prism[®] 8 v.8.2.1 software and the degradation constant (K), expiration time (t_{90}) and determination coefficient (R^2) were calculated. pH and osmolality monitoring were performed to observe the presence of any changes. Microbiological stability was considered adequate when no microbial growth was pro-

vided in the cultured samples. The presence of any abnormal macroscopic particles in the formulations was not considered acceptable.

2.7. *In Vivo* Evaluation of the Residence Time on the Ocular Surface

In vivo studies were carried out on male Sprague-Dawley rats with an average weight of 250 g supplied by the animal facility at the University of Santiago Compostela (Spain). The animals were kept in individual cages under controlled temperature (22 ± 1 °C) and humidity ($60 \pm 5\%$), with day–night cycles regulated by artificial light (12/12 hours) and feeding *ad libitum*. The animals were treated according to the ARVO statement for the use of animals in ophthalmic and vision research as well as the approved guidelines for laboratory animals [59,60]. Experiments (idis12072017) were approved by the Institutional Committee of the Health Research Institute of Santiago de Compostela (IDIS) following the Galician Network Committee for Ethics Research, the Spanish and European Union (EU) rules (86/609/CEE, 2003/65/CE, 2010/63/EU, RD 1201/2005 and RD53/2013).

The positron emission tomography (PET) and computed tomography (CT) procedures for conducting the radiolabeling of the formulations and the quantitative ocular permanence study were described in our previous works [15,61,62]. Briefly, PET and CT images were acquired using the Albira PET/CT Preclinical Imaging System (Bruker Biospin®; Woodbridge, Connecticut, USA). Anesthetized animals (2.5% (*v/v*) isoflurane/oxygen) were positioned into the imaging bed, monitoring the respiration frequency. Afterward, 7.5 µL of each tacrolimus formulation, previously radiolabeled with ^{18}F -fluorodeoxyglucose (^{18}F -FDG), was instilled into the conjunctival sac of both eyes using a micropipette. The administered radioactivity was 0.20–0.25 MBq per eye. After the instillation, static PET frames at different times (0, 30, 75, 120, 240 and 300 min) were acquired as a way to evaluate the pharmacokinetics behavior. To prevent the rats from scratching their eyes by removing the instilled formulations, an Elizabethan collar was placed between PET studies. Two animals (4 eyes) were tested for each formulation in order to accomplish the 3Rs regulatory frameworks [63].

Image analysis was performed using the Amide's Medical Image Data Analysis Tool [64]. Regions of interest (ROIs) were manually drawn for the different frames by delimiting the total radiotracer uptake of each eye using a spherical volume of 1767.1 m^3 ($15 \times 15 \times 15 \text{ mm}$). The radiotracer uptake over time was corrected by the radioisotope decay (^{18}F half-life: 109.7 min). Subsequently, a clearance rate for each formulation was obtained in terms of the ocular remaining radioactivity uptake over time after instillation. The data were fitted using a non-compartmental analysis in order to calculate the elimination constant (K), the half-life ($t_{1/2}$) and the zero and first moment pharmacokinetic parameters, area under curve (AUC_0^∞) and mean residence time (MRT) using GraphPad Prism® 8 v.8.2.1 software.

3. Results and Discussion

3.1. Tacrolimus/HPβCD Solubilization Study

The phase solubility diagram of tacrolimus in aqueous HPβCD solutions at 25 °C is shown in Figure 3. The resulting profile indicates an A_p -type diagram that shows a positive deviation from characteristic linearity, this being supported by previous studies [27,37]. Thus, the formation of a soluble complex in the aqueous media with the formation of high-order drug/CD complexes at high cyclodextrin concentrations is assumed. It must be taken into account that the formation of 1:1 and 1:2 drug/CD complexes and both $K_{1:1}$ and $K_{1:2}$ stability constants were calculated. Tacrolimus aqueous solubility in the absence of cyclodextrins was $4 \pm 0.67 \mu\text{g/mL}$, and $K_{1:1}$ and $K_{1:2}$ values were 143.1 ± 10.3 and $2.1 \pm 0.6 \text{ M}^{-1}$, respectively.

The low values of stability constant indicate that tacrolimus and HPβCD interactions were weak, especially in the 1:2 complex. The main reason for this weak interaction between the drug and cyclodextrin may be the high molecular weight and the complex molecular structure of tacrolimus that hampered an adequate adaptation to the cyclodextrin

cavity. This study was made only with HP β CD because according to the EMA, it is the safest cyclodextrin and most appropriated for topical ophthalmic administration together with sulfobutylether- β -cyclodextrin (SBE β CD), proving that it is not toxic [40]. This fact becomes important when transferring research to the clinic. Thus, NMR studies were performed in order to study the part of the drug and cyclodextrin structure involved in the complex formation.

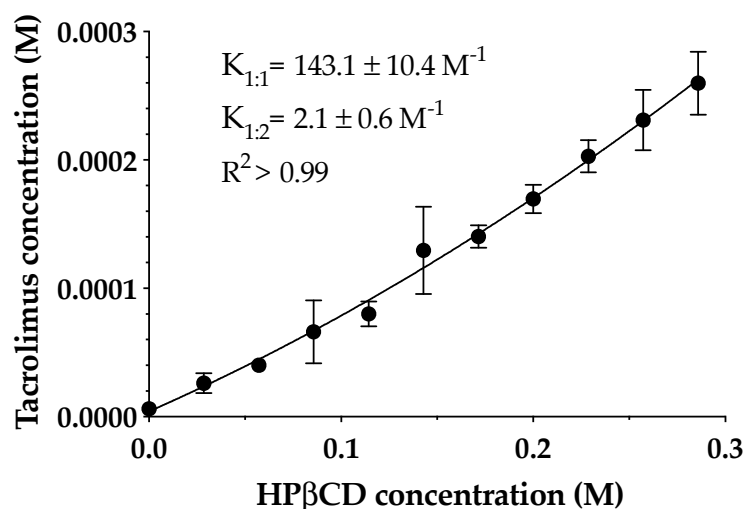


Figure 3. The phase solubility diagram of tacrolimus/hydroxypropyl- β -cyclodextrin (HP β CD) at 25 °C in purified water. Stability constants values represent the mean \pm SD ($n = 5$).

The intermolecular interaction between tacrolimus and HP β CD in aqueous solution was studied by NMR in the tacrolimus/HP β CD mixture prepared in D₂O at a 200 mM HP β CD concentration and tacrolimus saturation (0.2 mM). The ¹H spectrum of the mixture at 278 K (Figure 4a) shows resonances at the chemical shifts expected for tacrolimus signals (a reference spectrum of pure tacrolimus in MeOD is given in Figure 4d) with a considerable broadening, a possible indication that the tacrolimus is forming a large aggregate or self-aggregate in the water solution due to its very low polar characteristics. To test for binding between the tacrolimus and HP β CD in the mixtures, a one-dimensional saturation transfer difference spectrum (STD) was used, being a well-known NMR technique for screening ligands binding to protein receptors [45,65]. STD spectra were measured with auto-subtraction of alternate scans acquired with off- and on-irradiation providing the so-called STD^{on-off} spectra [45]. In these STD spectra, the on-irradiation was placed in a certain proton signal of tacrolimus that is sufficiently separated in frequency from any HP β CD signal to prevent them being directly saturated. Three STD^{on-off} spectra were measured at 278 and 298 K under otherwise identical conditions. Interestingly, only the STD^{on-off} spectra measured at the lower temperature (278 K, but not at 298 K) provided STD signal responses for the HP β CD species, as can be seen in Figure 4b–d. This is due to the partial transfer of saturation from the tacrolimus signal being irradiated to the HP β CD resonances, which reflects that there is a binding equilibrium between these two molecules (Figure 4). The fact that the STD responses are only obtained in the spectra measured at 278 K and not at 298 K could indicate that there is low affinity between the two molecules at 298 K (i.e., binding equilibrium with $K_d > 10 \text{ mM}$ [66]), while the affinity is notably enhanced at 278 K (i.e., $K_d < 1 \text{ mM}$ [66]). Overall, these NMR results strongly suggest that tacrolimus is forming a large self-aggregate in the water solution and it is partially solubilized by forming a complex with HP β CD.

The molecular modeling of the tacrolimus/HP β CD interaction of 1:1 and 1:2 stoichiometry inclusion complexes is shown in Figure 5. The molecular docking studies indicated the higher probability of tacrolimus inclusion by its 4-hydroxy-3-methoxycyclohexyl group.

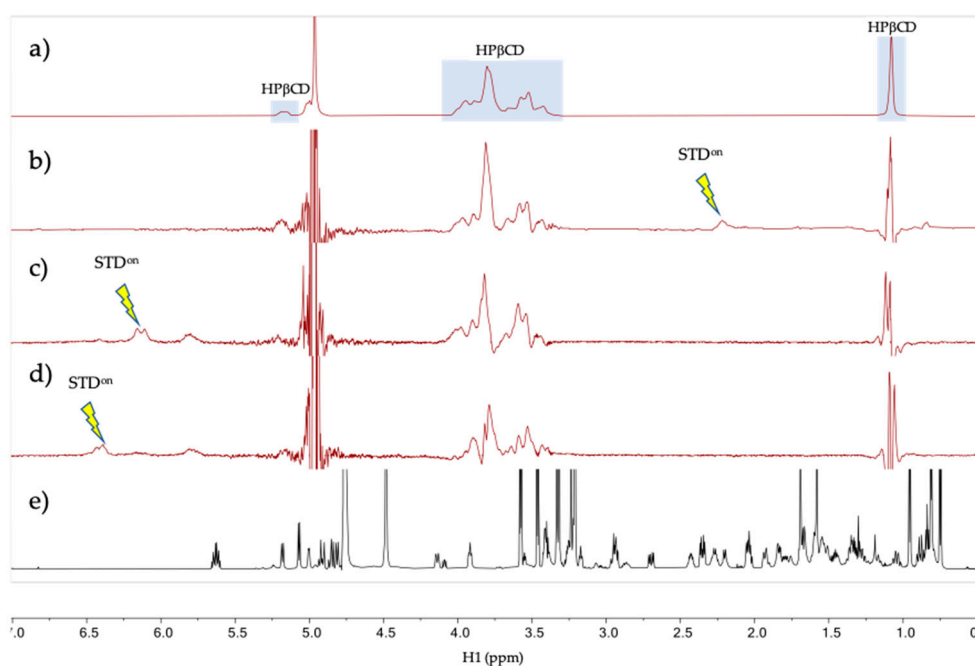


Figure 4. NMR spectra of tacrolimus/HP β CD interaction. (a–d) NMR spectra of the mixture tacrolimus/HP β CD in D₂O at 278 K. (a) HP β CD ¹H spectrum; (b) STD^{on-off} spectrum with on-irradiation at 2.12 ppm; (c) STD^{on-off} spectrum with on-irradiation at 6.12 ppm; (d) STD^{on-off} spectrum with on-irradiation at 6.30 ppm and (e) Reference ¹H spectrum of pure tacrolimus in MeOD. The arrows indicate the approximate position of the on-saturation applied. Signals of HP β CD are indicated in spectrum (a).

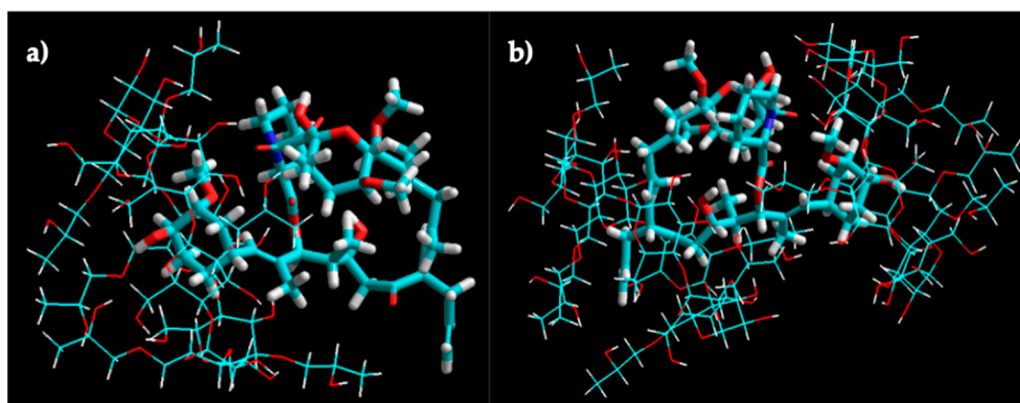


Figure 5. Molecular modeling of tacrolimus/HP β CD interaction. Molecular modeling of the 1:1 (a) and 1:2 (b) complex structures for tacrolimus and HP β CD obtained by manual docking and energy minimization using an MM+ force field in HyperChem[®].

The effect of BSS and Liquifilm[®] (as ophthalmic vehicles) on the complexation was also studied (Figure 6). Hence, a vehicle solubility study was experimentally carried out to determine the tacrolimus behavior with increasing HP β CD concentration media. As presented in Figure 6, a proportional increase in the tacrolimus solubility was observed by increasing the amount of cyclodextrin included into the vehicle. A two-way ANOVA was subsequently performed to compare all the media and assess the inclusion complexes' formation. The resulting data showed no significant differences between the 20% (*w/v*) and 30% (*w/v*) HP β CD in all vehicles; nonetheless, statistically significant differences ($\alpha < 0.05$) were found between 20% (*w/v*) and 30% (*w/v*) HP β CD solutions compared to the 40% (*w/v*) HP β CD solutions in all the vehicles. According to these results, the 30% (*w/v*) HP β CD

formulations were discarded and only 20% (*w/v*) and 40% (*w/v*) HP β CD solutions were used in further studies.

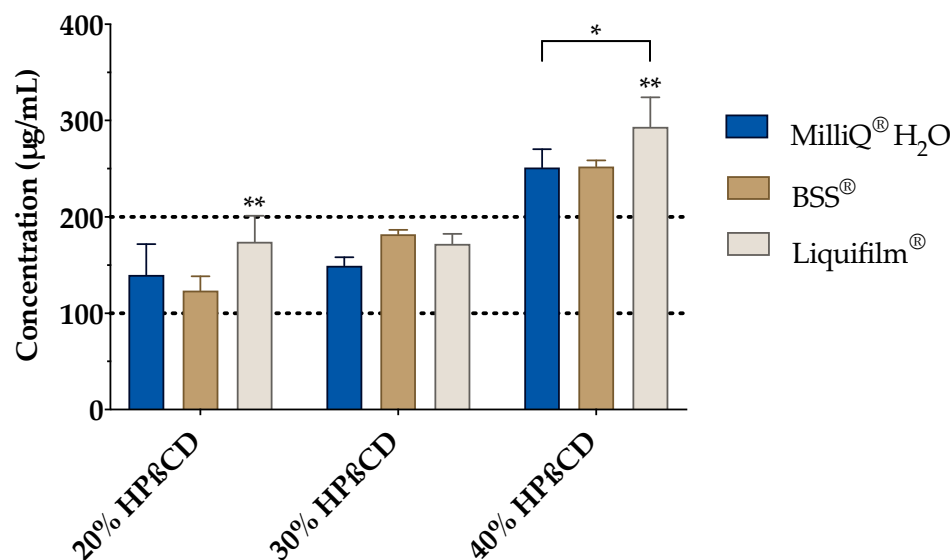


Figure 6. Tacrolimus solubility with 20%, 30% and 40% (*w/v*) of HP β CD in Balanced Salt Solution (BSS[®]) and Liquifilm[®] vehicles. Statistical analysis: two-way ANOVA followed by Tukey's multiple comparison test (* $\alpha < 0.05$ compared with 20% (*w/v*) and 30% (*w/v*) HP β CD in all vehicles); one-way ANOVA followed by Tukey's multiple comparison test (** $\alpha < 0.05$ compared with the other two vehicles (MilliQ[®] water and BSS[®])).

The resulting data also showed significant differences ($\alpha < 0.05$) among all the formulations for both HP β CD concentrations. Tukey's multiple comparison test was then performed, and significant differences were also observed between Liquifilm[®] and the other two vehicles (MilliQ[®] water and BSS[®]) but there were none found between MilliQ[®] water and BSS[®]. The tacrolimus solubility in Liquifilm[®]-diluted formulations may be attributed to the ternary complex formation (tacrolimus/HP β CD/PVA), increasing tacrolimus solubility by a synergistic solubilization effect [67].

Formulations were successfully prepared by an inclusion complex/dissolution technique. Tacrolimus was incorporated into the HP β CD hydrophobic cavity, leading to an increase in its water solubility. The solubilization time was determined in order to know the time necessary to completely dissolve the required dose (Figure 7).

The time needed to prepare the aforementioned tacrolimus topical ophthalmic formulations will be a key preparation parameter in HPDs. As presented in Figure 7, 20% (*w/v*) HP β CD formulations containing tacrolimus reached 100% solubilization in a 90-h period, while 40% (*w/v*) HP β CD formulations containing tacrolimus showed different solubilization time, being quicker for the TLI 40 (72-h period, against the 90-h period for TBS 40). A two-way ANOVA was further carried out to study differences in tacrolimus solubilization time among the formulations. The resulting data showed statistically significant differences between TLI and TBS formulations ($\alpha < 0.05$) from 40 h onwards. Nevertheless, no differences were found between TLI 20 and TLI 40, nor between TBS 20 and TBS 40.

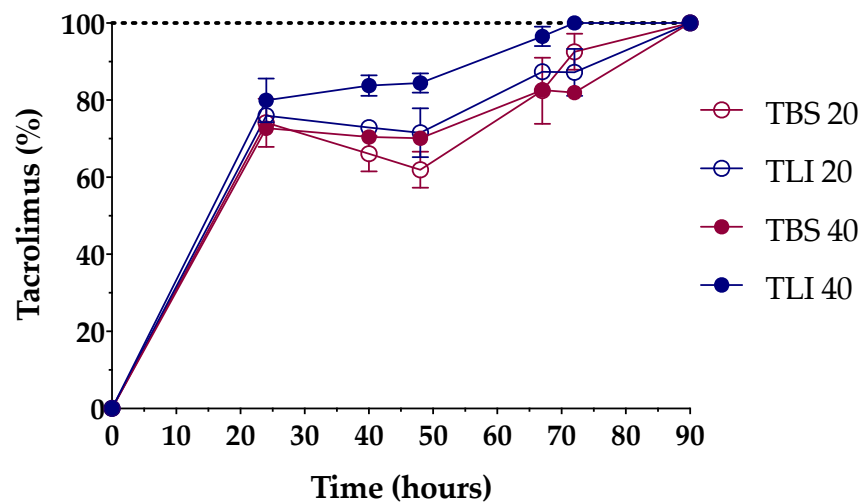


Figure 7. Dissolution time comparison among the different tacrolimus formulations. The 100% tacrolimus concentration corresponds to 0.01% (*w/v*) tacrolimus for TBS 20 and TLI 20 and 0.02% (*w/v*) tacrolimus for TBS 40 and TLI 40.

3.2. Physicochemical Characterization

3.2.1. pH, Osmolality and Surface Tension

pH and osmolality determinations were carried out in order to ensure that the formulations show values within the ocular physiological range. As presented in Table 2, all formulations met the pH and osmolality specifications described for topical ophthalmic administration. These results support the idea that these new formulations could be used without generating adverse effects in the ocular surface, compared to the control formulation (REF) [15] where, despite showing a pH value within the physiological range (pH 4 to 8) [68], the osmolality values (1220.5 mOsm/kg) were four times higher than the limit value for topical ophthalmic administration. Likewise, hypertonic topical ophthalmic formulations may alter the tear osmolality and, thus, induce ocular inflammation, as described by Dutescu et al. [69].

Table 2. pH, osmolality and surface tension results of tacrolimus/HP β CD formulations.

Formulations	pH		Osmolality (mOsm/kg)		Surface Tension (mN/m)	
	Mean	SD	Mean	SD	Mean	SD
TBS 20	7.036	0.021	359.3	5.86	54.63	0.93
TLI 20	6.986	0.005	283.6	2.52	58.46	1.10
TBS 40	7.203	0.005	628	6.93	51.5	0.61
TLI 40	6.933	0.005	383	18.08	58.43	0.21
REF	7.3	0.014	1220.5	18.57	47.5	0.2

Surface tension determination constitutes a key assay for a topical ophthalmic formulation. Appropriate surface tension values guarantee that a formulation may be spread evenly over the entire corneal surface, ensuring the drug optimal ocular penetration and also enhancing the comfort of the user when applying eye drops [70]. The ideal eye drop will have a surface tension similar to the tear film fluid (42–46 mN/m) [71]. Nonetheless, Han et al. previously studied the surface tension of commercialized ophthalmic formulations and the results showed that these topical ophthalmic solutions had surface tensions greater than that of tears (34.3–70.9 mN/m), most likely increasing the tear film stability and allowing for a greater lubrication of the eye [72].

Therefore, in the case of the designed formulations (TBS 20, TLI 20, TBS 40 and TLI 40), the surface tension values were slightly higher than physiological parameters, but

they were still at an optimal value (see Table 2). These surface tension values can be given by HP β CD, which shows values of 54.8–57.5 mN/m in solution, as it was previously mentioned by Saokham et al. [67]. However, the reference formulation (REF) showed lower surface tension values than the others, being associated to the presence of ethanol in its composition.

A one-way ANOVA was applied to determine the surface tension of each formulation, and statistically significant differences were observed ($\alpha < 0.05$). Tukey's multiple comparison test was also performed, and no statistically significant differences were found between the TLI 20 and TLI 40 formulations, but significant differences were observed between the rest of the formulations ($\alpha < 0.05$).

3.2.2. Squeezing Force Determinations

Figure 8 show the squeezing force test results for the studied formulations. Based on the research of Conner et al. [73], a large percentage of patients (>50%) receiving local ophthalmic treatments reported that self-management is difficult due to the need to apply force to the eyedropper in order to get the preparation out. Besides, high doses may cause the patient to suffer from side effects, while underdosing may cause damage or prolonged drug therapy. The volume and structure uniformity of the formulation drops are also important properties to ensure accurate drug dosage and avoid treatment variability.

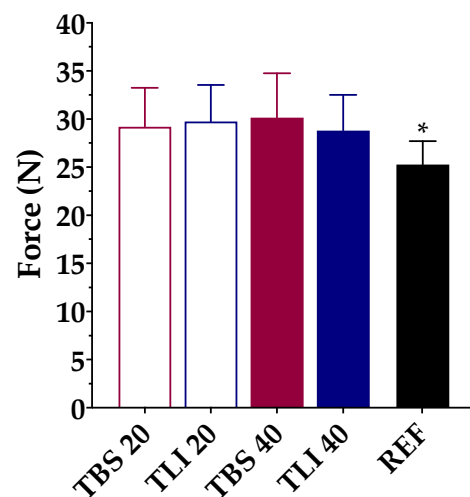


Figure 8. Comparison of squeeze force (N) values among different tacrolimus formulations (TBS 20, TLI 20, TBS 40, TLI 40 and REF). Statistical analysis: one-way ANOVA followed by Tukey's multiple comparison test (* $\alpha < 0.05$ compared with prepared formulations).

The squeezing force test may be affected by different factors such as the formulation viscosity, surface tension or dropper tip design [74]. Therefore, the same type of packaging for testing was used. A one-way ANOVA was applied to determine the required force to dispense a drop of each formulation, and statistically significant differences were observed ($\alpha < 0.05$). Tukey's multiple comparison test was also applied, and no statistically significant differences were found between the tacrolimus/HP β CD formulations, but significant differences were observed between the reference formulation (REF) and the prepared formulations ($\alpha < 0.05$).

3.3. Corneal Mucoadhesion

Knowing that the mucoadhesion properties of the topical ophthalmic formulations will give an approximate idea of the permanence time on the ocular surface, bioadhesion work measurements were performed with the studied topical ophthalmic formulations. All data were assessed through breaking strength (N) and bioadhesion work (mJ) measurements (Figure 9).

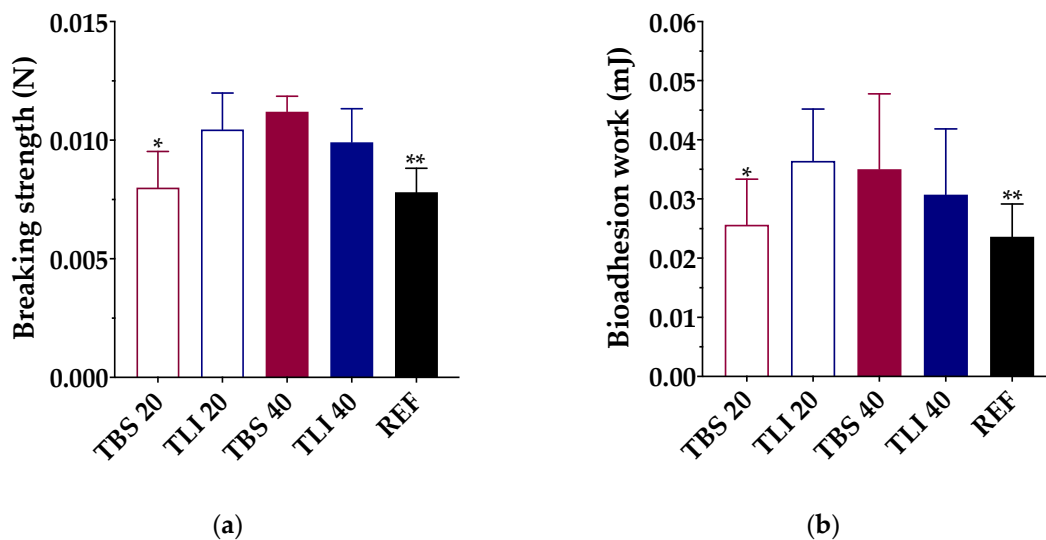


Figure 9. (a) Maximum breaking strength (N) and (b) bioadhesion work (mJ) obtained for each formulation using bovine cornea as a substrate. Statistical analysis: (a) one-way ANOVA followed by Tukey's multiple comparison test (* $\alpha < 0.05$ compared with TLI 20, TBS 40 and TLI 40 and ** $\alpha < 0.05$ compared with TLI 20, TBS 40 and TLI 40); (b) one-way ANOVA followed by Tukey's multiple comparison test (* $\alpha < 0.05$ compared with TLI 20 and ** $\alpha < 0.05$ compared with TLI 20 and TBS 40).

A one-way ANOVA was performed to define the bioadhesion work of the studied formulations, and statistically significant differences were observed ($\alpha < 0.05$). Tukey's multiple comparison test was also applied, and statistically significant differences were found between the TBS 20 and TLI 20 formulations and between the REF and TLI 20 and TBS 40, but no significant differences were observed between the rest of the formulations ($\alpha > 0.05$).

The highest bioadhesion work values were obtained for the TLI 20 (0.036 ± 0.009 mJ) and TBS 40 (0.035 ± 0.013 mJ) formulations, and the lowest values were obtained for TBS 20 (0.026 ± 0.008 mJ) and REF (0.023 ± 0.005 mJ). In the case of TLI 40 (0.031 ± 0.011 mJ), no statistically significant differences were observed compared with TLI 20 and TBS 40. It was observed that during the separation stage of the cornea from the formulation, a formulation film remained adhered to the cornea when the load cell was lifted. It can be assumed, then, that the formulation interacts with the corneal surface with more intensity than the own cohesive forces of the formulation. Therefore, the adhesive bond fails due to the formulation fracture, making the viscosity and consistency play a fundamental role.

An in vivo ocular permanence study was subsequently performed using a PET/CT imaging technique to confirm the bioadhesive behavior of the formulations.

3.4. Ocular Irritancy and Toxicity

Some eye irritation and toxicity assessment tests have shown considerable potential to eliminate procedures that were historically performed by animal experimentation, such as the Draize rabbit eye irritation test which presents one of the most criticized and contested animal tests [75]. The efficacy of these in vitro and ex vivo procedures has been well studied by pharmaceutical industries and some national regulatory agencies [76]. The replacement of the Draize rabbit eye test with alternative models includes physicochemical tests, cell and tissue culture systems or organotypic models as eye components or isolated eyes [76–78].

The strategy to replace the Draize test by combining several animal-free methods has raised expectations [75]. The combination of two different methods has been proposed in this work. The Bovine Corneal Opacity and Permeability test (BCOP), which allows to detect whether the tested compounds cause a moderate, severe or very severe irritation,

combined with the hen's egg test on the chorioallantoic membrane assay (HETCAM) covers the whole spectrum of irritation, since mild or very mild irritation signs can be detected.

3.4.1. Bovine Corneal Opacity and Permeability Test (BCOP)

Transmittance values of opacity and permeability assays were studied to assess whether formulations induce corrosivity or irritation (see Figures 10 and 11). No significant structural changes were observed in terms of corneal opacity and fluorescein permeability when comparing all formulations to the negative control solution (PBS) but were observed with regard to the positive control (ethanol) ($\alpha < 0.05$).

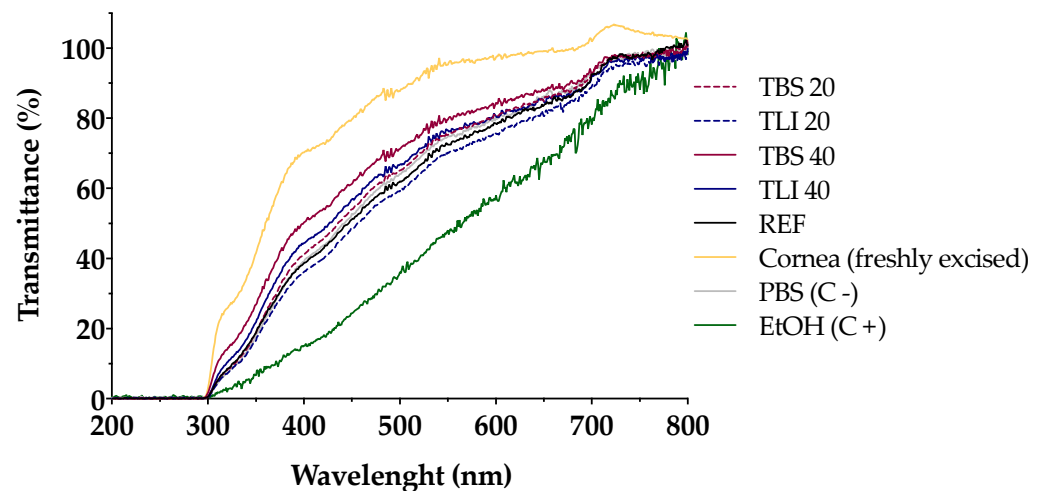


Figure 10. Ultraviolet-visible (UV-Vis) scan (from 200 to 800 nm) of corneal transmittance (%) values of bovine corneas treated with TBS 20, TLI 20, TBS 40, TLI 40, REF, PBS (negative control) and ethanol (positive control) after 10 min tacrolimus formulation treatment and 120 min PBS treatment.

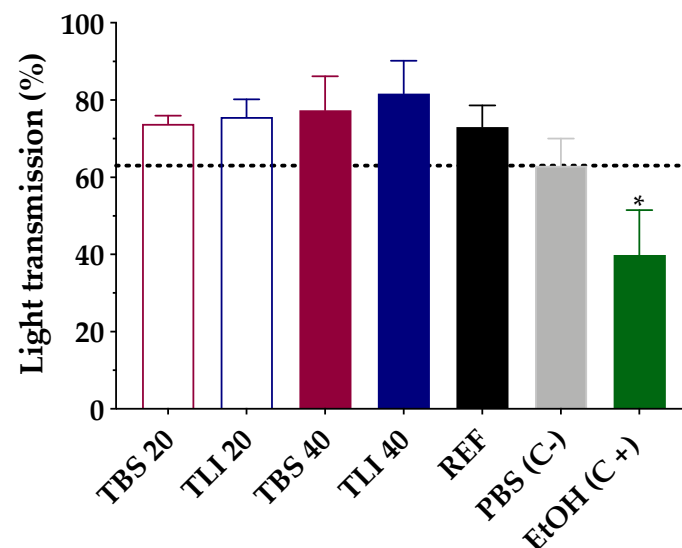


Figure 11. Opacity values of bovine corneas treated with TBS 20, TLI 20, TBS 40, TLI 40, REF, PBS (negative control) and ethanol (positive control) after 10 min tacrolimus formulation treatment and 120 min PBS treatment. Here, 63% light transmission corresponds to the total light transmitted through bovine corneas incubated in PBS. Statistical analysis: one-way ANOVA followed by Tukey's multiple comparison test (* $\alpha < 0.05$ compared with prepared formulations, reference formulation and negative control).

Similarly, opacity and permeability data were corrected for background or control values prior to further statistical determinations being estimated. The IVIS score was

then calculated and all formulations resulted in an *in vitro* irritation score of 0 (IVIS = 0), showing no toxic effects compared to control formulations.

Likewise, the fluorescein permeability test was further applied on the corneas previously treated with the tested formulations. The resulting data showed no statistically significant differences between all the formulations; however, significant differences ($\alpha < 0.05$) were observed between the studied formulation and the positive control (ethanol).

3.4.2. Hen's Egg Test on the Chorioallantoic Membrane (HETCAM)

All tacrolimus eyedrops were tested on the egg's CAM as well as two controls, NaCl as a negative control (C-) and NaOH as a positive control (C+). All formulations were evaluated, and data were compared to the NaCl and NaOH solutions' results. All formulations showed no toxic effects (irritation score = 0) compared them with the positive control formulation (see Figure 12). This agrees with previously described BCOP test results.

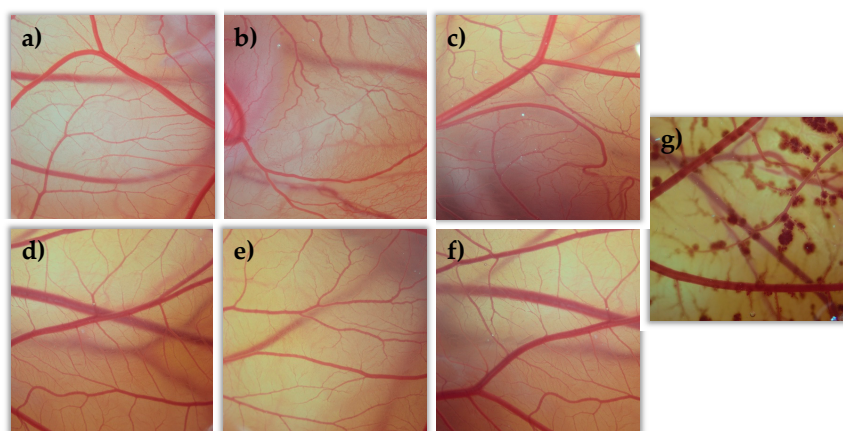


Figure 12. Hen's egg test on the chorioallantoic membrane (HETCAM) images 5 min post-instillation for the different formulations. (a) NaCl (C-); (b) TBS 20; (c) TLI 20; (d) TBS 40; (e) TLI 40; (f): REF; (g) NaOH (C+).

3.5. Stability Study

Stability studies of pharmaceutical compounds are essential to ensure drug efficacy [79,80] as well as to know if degradation products can cause toxic side effects and other undesired effects [27]. In this assay, only TBS 40 and TLI 40 were studied due to all formulations containing the exact same qualitative composition; thus, the formulations with the highest tacrolimus concentrations were tested as representative; these formulations were chosen based on the clinical common usability and the drug concentration similarity at present. As presented in Figure 13, it can be seen that temperature was an important factor in the stability under storage of tacrolimus/HP β CD ophthalmic formulations. TBS 40 and TLI 40 showed the same tacrolimus degradation pattern for each storage condition and no statistically significant differences were found between them ($\alpha > 0.05$).

Table 3 shows the degradation constant (K), expiration time (t_{90}) and determination coefficient (R^2) values for both tacrolimus eye drops. It must be taken into account that TBS 40 showed a higher degradation rate (1.23 times) than TLI 40 for the oven temperature condition, though significant degradation rate variations were not observed for the other two storage conditions.

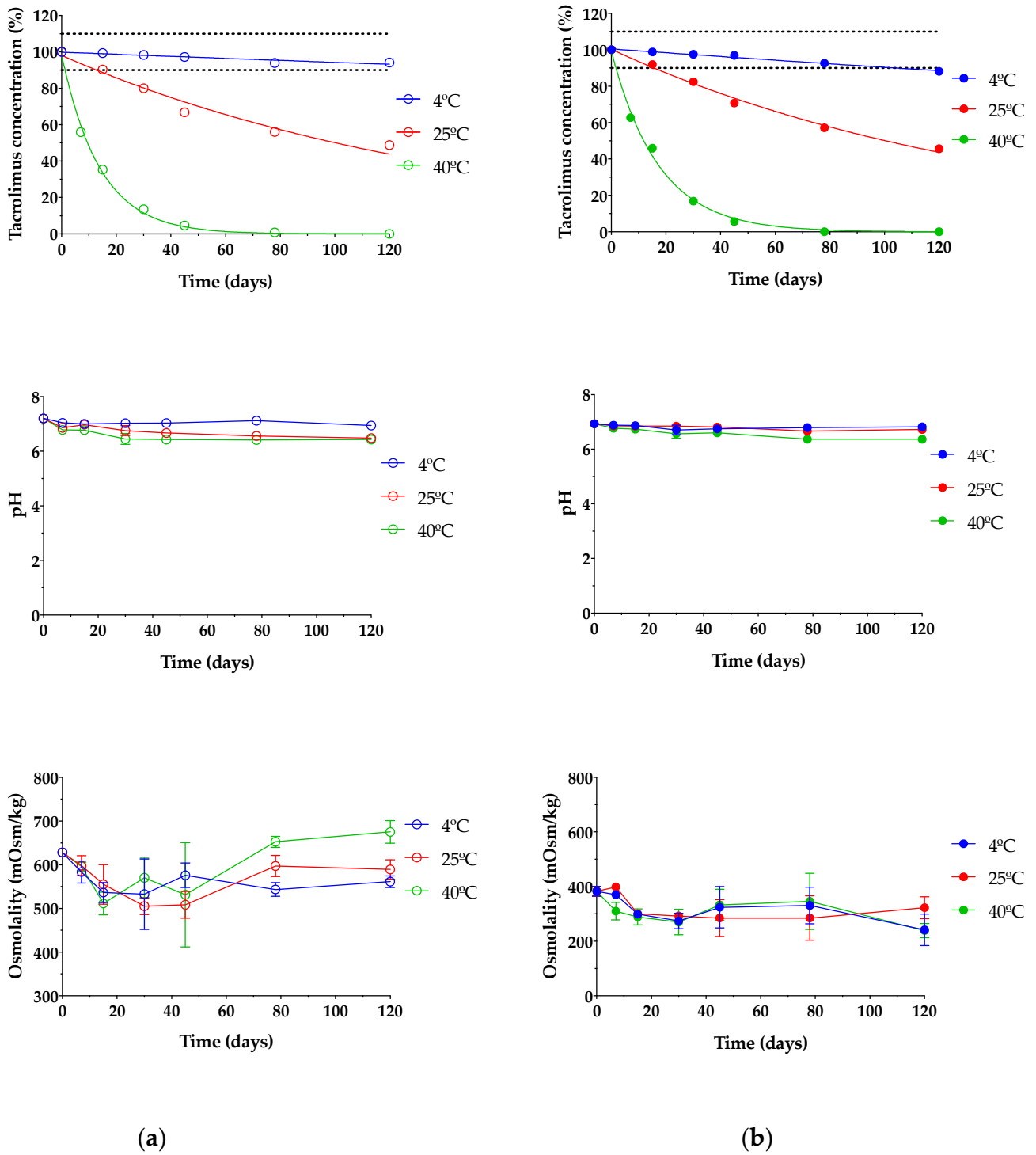


Figure 13. Tacrolimus concentration, pH and osmolality stability of (a) TBS 40 and (b) TLI 40 stored under three different temperature conditions: in refrigeration (4 ± 2 °C), at room temperature (25 ± 2 °C) and at oven temperature (40 ± 2 °C) during a 4-month stability test.

Table 3. The degradation constant K , t_{90} and R^2 of two tacrolimus eye drops (TBS 40 and TLI 40) obtained by interpolation of the calculated regression line (% of remaining tacrolimus concentration vs time).

Formulations	Storage Condition	K (days ⁻¹)		t_{90} (days)		R^2	
		Mean	SD	Mean	SD	Mean	SD
TBS 40	Refrigeration (4 °C)	0.0006	4.3×10^{-5}	184.32	13.5	0.8890	0.0179
	Room temperature (25 °C)	0.0067	0.0002	15.72	0.53	0.9645	0.0057
	Oven temperature (40 °C)	0.0713	0.0016	1.48	0.03	0.9966	0.0012
TLI 40	Refrigeration (4 °C)	0.0011	5.8×10^{-5}	98.50	5.2	0.9410	0.040
	Room temperature (25 °C)	0.0067	0.0002	15.66	0.40	0.9867	0.0035
	Oven temperature (40 °C)	0.0577	0.0004	1.82	0.01	0.9959	0.0007

Eye drops stored at oven temperature (40 ± 2 °C) were not stable in the first 7 days of the study, observing a rapid tacrolimus degradation process. In the case of eye drops kept at room temperature (25 ± 2 °C), the tacrolimus degradation was not so abrupt, but from day 15 of the study, the tacrolimus concentration was reduced to below 90% of the initial concentration, so the formulation was no longer stable. Nonetheless, both eye drops preserved in refrigeration (4 ± 2 °C) were stable beyond the 3-month period; specifically, the initial concentration of tacrolimus previously fell below 90% in the TLI 40 formulation compared to the TBS 40 formulation. Therefore, the optimal storage condition for tacrolimus topical ophthalmic formulations was at 4 °C.

In this way, it was determined that eye drops kept in refrigeration condition have an available period of at least 3 months. In the case of TLI 40, the presence of benzalkonium chloride may be beneficial to the stability of tacrolimus once opened by minimizing microbial contamination.

Prajapati et al. studied tacrolimus degradation in aqueous HP β CD solutions [27]. Their results showed an inversely proportional correlation between tacrolimus degradation rate and HP β CD concentration values, with a maximum degradation value where no HP β CD was included into the formulations. The presence of 40% (*w/v*) HP β CD in the formulations used in the present study suggested that the increased stability of tacrolimus was due to the inclusion of complex formation between HP β CD and tacrolimus.

Likewise, pH and osmolality measurements showed no significant changes over the course of the study regardless of storage condition ($\alpha > 0.05$). The results guaranteed that all tested formulations were also in the appropriate range for topical ophthalmic administration, ensuring suitability for an accurate tacrolimus ocular penetration.

Furthermore, microbiological control growth is a test to take into account the quality control of the prepared formulations since it ensures the sterility of the preparations and, therefore, the conditions of asepsis in the production process. Sterility is one of the most important requirements when preparing ophthalmic formulations as it reduces the risk of eye infections. In this study, an adequate conservation of the eye drops was observed for each condition since no presence of microorganisms was found in any of the studied samples. In addition, no macroscopic changes (e.g., color, turbidity and precipitation) were observed during the whole study period. Thus, the absence of microorganisms and suspended particles was in good agreement with the preparation of this type of topical ophthalmic formulations in HPDs, by a simple technique with non-strict equipment requirements.

3.6. In Vivo Evaluation of the Residence Time on the Ocular Surface

The development of new ophthalmic topical vehicles for increasing drugs' permanence on the ocular surface is important to improve drug bioavailability in the eye as well as the treatment adherence by patients [81]. PET/CT imaging is a relatively new imaging modality that provides a quantifiable signal on the pharmacokinetic profile of the topically administered radiopharmaceutical. In this way, it allows to obtain a signal in the eye after an eye drop instillation and its subsequent follow-up at different study times, and to be

able to follow the biodistribution of the formulation in the nasolacrimal duct and nasal cavity [62].

In this study, the PET/CT imaging technique was used to determine the residence times of the proposed tacrolimus topical ophthalmic formulations on the ocular surface, and they were compared with the tacrolimus eye drop (REF) elaborated by HPDs.

In Figure 14, the permanence of the studied eye drops at different times can be seen more visually, with PET/CT images showing both coronal planes (rat eyes and nasolacrimal duct).

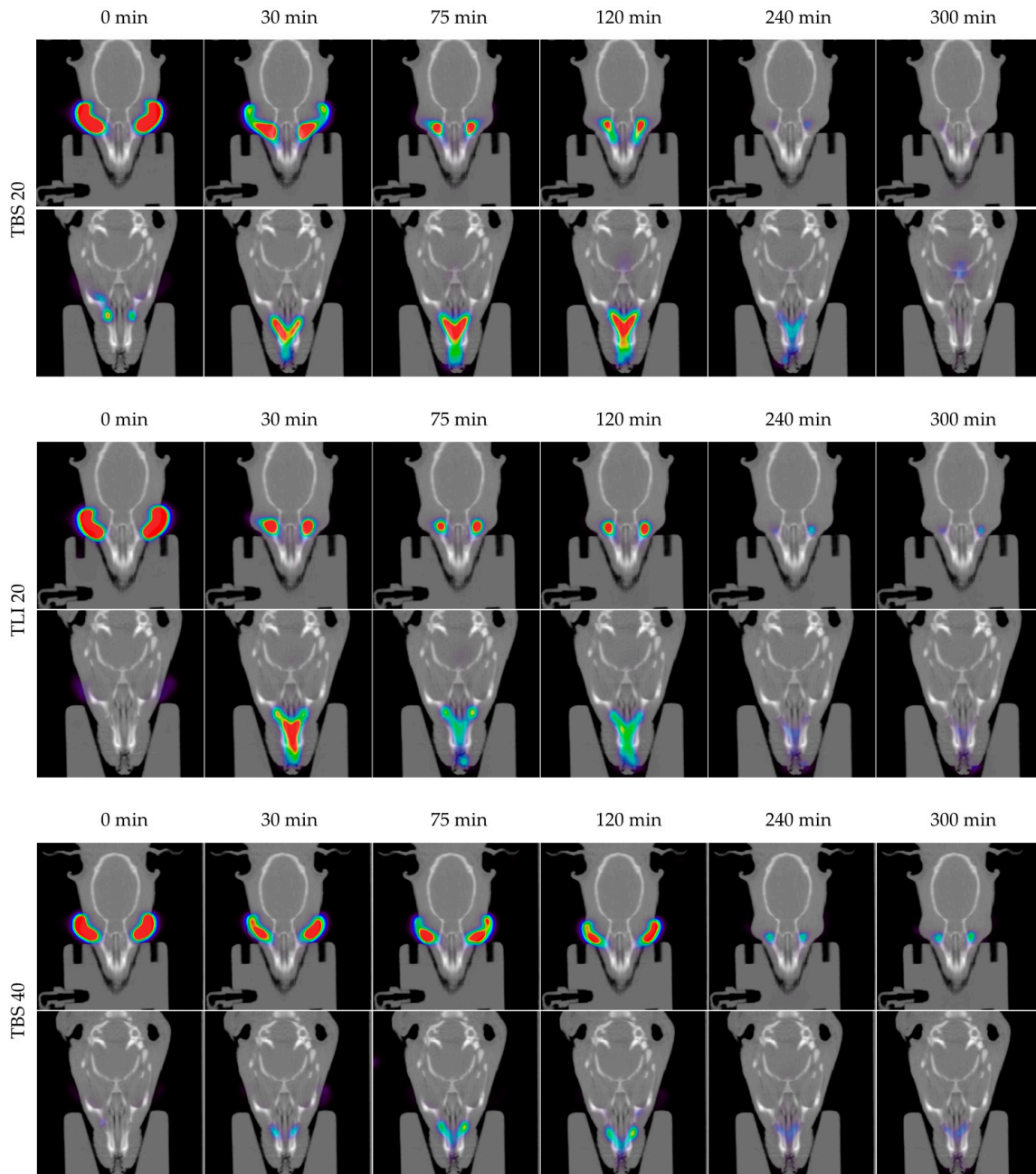


Figure 14. Cont.

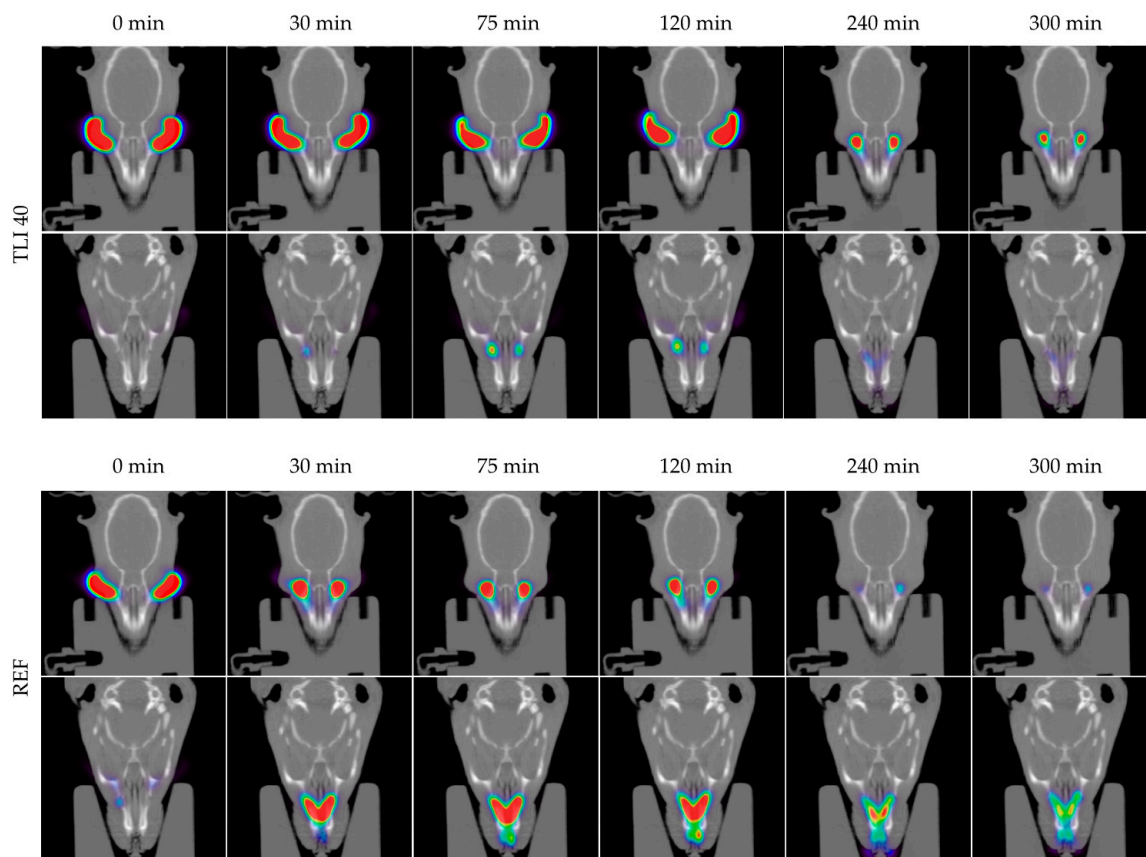


Figure 14. Fused positron emission tomography (PET)/computed tomography (CT) images displayed in coronal plane representing rat eyes (above) and nasolacrimal duct (below) with TBS 20, TLI 20, TBS 40, TLI 40 and REF at 0, 30, 75, 120, 240 and 300 minutes post-administration. The formulation signal on the eye surface is coded on a color scale: blue areas show low radioactive activity whereas red areas show high radioactive activity.

Figure 15 shows the clearance rate for each tested formulation compared to the tacrolimus eye drop (REF) elaborated by HPDs. The clearance rate was represented in terms of the ocular remaining radioactivity uptake over time after instillation and the corresponding fits in order to estimate all pharmacokinetic parameters (K , $t_{1/2}$, AUC_0^∞ and MRT) and the remaining formulation at 75 min (%), which are represented in Table 4. All the parameters indicated a significant increase in the ocular retention time for the TBS 40 and TLI 40 formulations compared to TBS 20 and TLI 20; the best formulation result was obtained for TLI 40. The results from the ocular permanence assays showed that formulations containing higher concentrations of HP β CD had a longer eye residence time, regardless of the vehicle used. Adding HP β CD to formulations, apart from increasing the solubility and stability of tacrolimus, also gave a more viscous and stickier characteristic to the solution. This feature helps the eye drop to spread and be more retained on the eye surface as it can be seen during eye drop instillation. PET/CT studies showed that the formulations were mucoadhesive and had an adequate consistency to remain on the ocular surface for a long time.

A two-way ANOVA was applied to the % of remaining formulation on the ocular surface parameter in order to evaluate the influence of the time and the formulation in its clearance to determine whether there were differences in the permanence of the formulations on the corneal surface. No statistically significant differences were observed between 20% (*w/v*) HP β CD formulations compared to REF. Nevertheless, statistically significant differences were observed ($\alpha < 0.05$) between 20% (*w/v*) HP β CD formulations and 40% (*w/v*) HP β CD formulations as well as between 40% (*w/v*) HP β CD formulations and REF for times beyond 30 min post-administration.

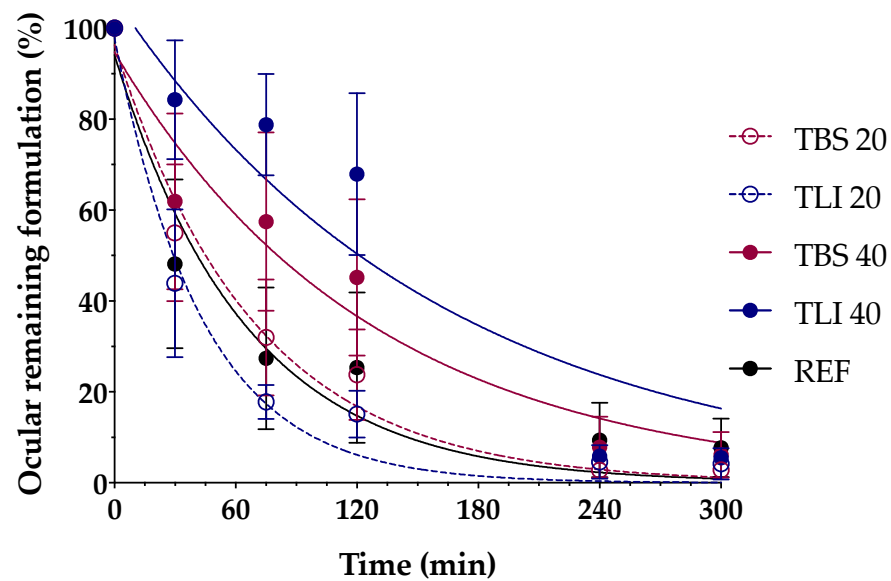


Figure 15. Tacrolimus eyedrop clearance rate (TBS 20, TLI 20, TBS 40, TLI 40 and REF) from the ocular surface determined by PET. Resulting data are represented in eye remaining radioactivity uptake (%) vs time after instillation.

Table 4. Pharmacokinetics parameters (K , $t_{1/2}$, AUC_0^∞ , mean residence time (MRT) and % remaining formulation at 75 min) of the tacrolimus eye drops obtained by the fitting of the percentage formulation remaining on ocular surface.

Formulations	K (min^{-1})		$t_{1/2}$ (min)		AUC_0^∞ ($\% \times \text{min}$)		MRT (min)		Remaining Formulation at 75 min (%)	
	Mean	SD	Mean	SD	Mean	SD	Mean	SD	Mean	SD
TBS 20	0.014	0.003	49.70	10.34	74.96	7.70	72.90	6.02	31.99	12.79
TLI 20	0.025	0.008	29.40	8.51	59.16	11.18	73.94	22.62	17.79	3.74
TBS 40	0.024	0.023	61.79	46.16	89.61	57.41	76.43	35.70	57.46	19.65
TLI 40	0.011	0.007	86.22	38.93	123.31	51.18	90.51	17.67	78.82	11.15
REF	0.018	0.010	46.34	22.88	82.22	30.2	93.28	37.55	27.44	15.65

The TLI 40 vehicle (Liquifilm[®]) is composed of PVA; this polymer has a mechanism based on the interdiffusion of polymer chains across the bioadhesive interface that produces entanglements and physical bonds between the polymer and the substrate. The intimate contact and the presence of hydroxyl radicals in the polymer can promote the establishment of weak interactions with the mucin layer (i.e., hydrogen bonds) [82]. The mucoadhesion study assumptions related to TLI 40 formulation were confirmed by the PET/CT imaging technique.

The conventional pharmacological treatments for uveitis are associated with strict patient compliance, limited efficacy due to the appearance of refractory processes and different severe side effects. HPDs have resorted to a reformulation process of intravenous formulations as a way to obtain new topical ophthalmic pharmacy compounding as a pharmacological alternative. One of the most used pharmacy compounding products was based on Prograf[®] reformulation, this being an hydroalcoholic eye drop containing 0.03% (w/v) tacrolimus. Nevertheless, this type of treatment has shown different disadvantages, including high osmolality and patient discomfort due to the eye drop composition.

Different formulations are proposed in the present work as new pharmacological alternatives, specifically intended for topical ophthalmic administration for uveitis treatment. These formulations have proven to be adequate for this administration pathway, showing several advantages compared to the currently used treatments, including I) patient comfort

improvement, II) great efficacy with a simple preparation method, III) easy translational research to HPDs and IV) a health expenditure reduction in uveitis treatment.

4. Conclusions

In this work, a consistent tacrolimus solubilization study was carried out as a way to deeply understand this drug behavior in future topical ophthalmic formulations. Tacrolimus/HP β CD interaction in solution was confirmed by phase solubility diagram, NMR and molecular modeling studies, and the influence of the vehicle was also studied. The use of 40% (*w/v*) HP β CD allowed to prepare eye drop solutions with a 0.02% (*w/v*) tacrolimus concentration that could be in the therapeutic range for uveitis treatment.

The developed HP β CD-based formulations showed pH, osmolality, surface tension and safety values in the optimum range for topical ophthalmic administration. Stability studies showed no changes in the eye drops kept in refrigeration condition for at least 3 months, which could facilitate the preparation programming and improve the patient comfort.

Additionally, *ex vivo* mucoadhesion and *in vivo* ocular permanence studies showed good mucoadhesive properties and lower ocular clearance for TBS 40 and TLI 40, almost doubling the permanence half-life time in the ocular surface compared to the REF pharmacy compounding.

Taking into account all of the obtained results, TLI 40 was proposed as the best candidate. This eye drop allowed reaching a 0.02% (*w/v*) drug dose, which was safe and showed the best mucoadhesive and ocular permanence properties. In addition, the presence of benzalkonium chloride in Liquifilm[®] could help to prevent microbial growth once the eye drops were opened.

Author Contributions: Conceptualization, X.G.-O., M.G.-B., A.F.-F. and F.J.O.-E.; methodology, X.G.-O., V.D.-T., R.V.-F. and M.M.-P.; formal analysis, X.G.-O.; investigation, X.G.-O.; resources, M.G.-B., J.B.-M. and P.A.; data curation, X.G.-O., V.D.-T., R.V.-F. and M.M.-P.; writing—original draft preparation, X.G.-O.; writing—review and editing, X.G.-O., V.D.-T., R.V.-F., M.M.-P., M.G.-B., J.B.-M., C.M.-G., M.A.B., F.G., P.A., A.F.-F. and F.J.O.-E.; supervision, A.F.-F. and F.J.O.-E.; funding acquisition, M.G.-B., P.A., A.F.-F. and F.J.O.-E. All authors have read and agreed to the published version of the manuscript.

Funding: This research was partially supported by the Spanish Ministry of Science, Innovation and Universities (RTI2018-099597-B-100), the ISCIII (PI17/00940, RETICS Oftared, RD16/0008/0003 and RD12/0034/0017) and by Xunta de Galicia, grant numbers GPC2013/015 and GRC2017/015.

Institutional Review Board Statement: Not applicable.

Informed Consent Statement: Not applicable.

Data Availability Statement: Not applicable.

Acknowledgments: X.G.-O. and R.V.-F. acknowledge the financial support of the IDIS (Health Research Institute of Santiago de Compostela) (predoctoral research fellowships). P.A. acknowledges the support of RYC-2015/17430 (Ramón y Cajal). A.F.-F. acknowledges the support received from the Instituto de Salud Carlos III (ISCIII) through its Juan Rodes grant (JR18/00014).

Conflicts of Interest: The authors declare no conflict of interest.

References

- De Smet, M.D.; Taylor, S.R.; Bodaghi, B.; Miserocchi, E.; Murray, P.I.; Pleyer, U.; Zierhut, M.; Barisani-Asenbauer, T.; LeHoang, P.; Lightman, S. Understanding uveitis: The impact of research on visual outcomes. *Prog. Retin. Eye Res.* **2011**, *30*, 452–470. [CrossRef] [PubMed]
- Bodaghi, B.; Cassoux, N.; Wechsler, B.; Hannouche, D.; Fardeau, C.; Papo, T.; Huong, D.L.T.; Piette, J.-C.; LeHoang, P. Chronic Severe Uveitis. *J. Clin. Med.* **2001**, *80*, 263–270. [CrossRef] [PubMed]
- Zhai, J.; Gu, J.; Yuan, A.P.J.; Chen, P.J. Tacrolimus in the Treatment of Ocular Diseases. *BioDrugs* **2011**, *25*, 89–103. [CrossRef] [PubMed]
- Rothova, A.; Van Veenendaal, W.; Linssen, A.; Glasius, E.; Kijlstra, A.; De Jong, P. Clinical Features of Acute Anterior Uveitis. *Am. J. Ophthalmol.* **1987**, *103*, 137–145. [CrossRef]

5. Garg, V.; Jain, G.K.; Nirmal, J.; Kohli, K. Topical tacrolimus nanoemulsion, a promising therapeutic approach for uveitis. *Med. Hypotheses* **2013**, *81*, 901–904. [CrossRef] [PubMed]
6. Fabiani, C.; Vitale, A.; Orlando, I.; Capozzoli, M.; Fusco, F.; Rana, F.; Franceschini, R.; Sota, J.; Frediani, B.; Galeazzi, M.; et al. Impact of Uveitis on Quality of Life: A Prospective Study from a Tertiary Referral Rheumatology-Ophthalmology Collaborative Uveitis Center in Italy. *Isr. Med. Assoc. J. IMAJ* **2017**, *19*, 478–483. [PubMed]
7. Thorne, J.E.; Skup, M.; Tundia, N.; Macaulay, D.; Revol, C.; Chao, J.; Joshi, A.; Dick, A.D. Direct and indirect resource use, healthcare costs and work force absence in patients with non-infectious intermediate, posterior or panuveitis. *Acta Ophthalmol.* **2016**, *94*, e331–e339. [CrossRef]
8. Chu, D.S.; Johnson, S.; Mallya, U.; Davis, M.R.; Sorg, R.A.; Duh, M.S. Healthcare costs and utilization for privately insured patients treated for non-infectious uveitis in the USA. *J. Ophthalmic Inflamm. Infect.* **2013**, *3*, 64. [CrossRef]
9. Taddio, A.; Cimaz, R.; Caputo, R.; DeLibero, C.; Di Grande, L.; Simonini, G.; Mori, F.; Novembre, E.; Pucci, N. Childhood chronic anterior uveitis associated with vernal keratoconjunctivitis (VKC): Successful treatment with topical tacrolimus. Case series. *Pediatr. Rheumatol. Online J.* **2011**, *9*, 34. [CrossRef]
10. Jewett, A.; Tseng, H.-C. 35-Immunotherapy. In *Pharmacology and Therapeutics for Dentistry*, 7th ed.; Dowd, F.J., Johnson, B.S., Mariotti, A.J., Eds.; Mosby: Maryland Heights, MO, USA, 2017; pp. 504–529. ISBN 978-0-323-39307-2.
11. Moscovici, B.K.; Holzchuh, R.; Chiacchio, B.B.; Santo, R.M.; Shimazaki, J.; Hida, R.Y. Clinical Treatment of Dry Eye Using 0.03% Tacrolimus Eye Drops. *Cornea* **2012**, *31*, 945–949. [CrossRef]
12. Joseph, A.; Raj, D.; Shanmuganathan, V.; Powell, R.J.; Dua, H.S. Tacrolimus immunosuppression in high-risk corneal grafts. *Br. J. Ophthalmol.* **2006**, *91*, 51–55. [CrossRef] [PubMed]
13. Hikita, N.; Lopez, J.S.; Chan, C.C.; Mochizuki, M.; Nussenblatt, R.B.; De Smet, M.D. Use of topical FK506 in a corneal graft rejection model in Lewis rats. *Investig. Ophthalmol. Vis. Sci.* **1997**, *38*, 901–909.
14. Mills, R.; Jones, D.B.; Winkler, C.R.; Wallace, G.W.; Wilhelmus, K.R. Topical FK-506 prevents experimental corneal allograft rejection. *Cornea* **1995**, *14*, 157–160. [CrossRef] [PubMed]
15. Luaces-Rodríguez, A.; Touriño-Peralba, R.; Alonso-Rodríguez, I.; García-Otero, X.; González-Barcia, M.; Rodríguez-Ares, M.T.; Martínez-Pérez, L.; Aguiar, P.; Gómez-Lado, N.; Silva-Rodríguez, J.; et al. Preclinical characterization and clinical evaluation of tacrolimus eye drops. *Eur. J. Pharm. Sci.* **2018**, *120*, 152–161. [CrossRef] [PubMed]
16. Astellas Pharma Inc. A Randomized, Placebo-Controlled, Double-Masked Study of 0.1% Tacrolimus (FK506) Ophthalmic Suspension in Vernal Keratoconjunctivitis. Available online: <https://www.clinicaltrials.gov/ct2/show/NCT00567762> (accessed on 21 January 2021).
17. Shoughy, S.S.; Jaroudi, M.O.; Tabbara, K.F. Efficacy and safety of low-dose topical tacrolimus in vernal keratoconjunctivitis. *Clin. Ophthalmol.* **2016**, *10*, 643–647. [CrossRef] [PubMed]
18. Moawd, P. Evaluation of the Effect of Topical Application of Tacrolimus 0.03% (FK506) Eye Drops Versus Cyclosporine 0.05% Eye Drops in Treatment of Dry Eye in Secondary Sjogren Syndrome. Available online: <https://www.clinicaltrials.gov/ct2/show/NCT03865888webpage> (accessed on 21 January 2021).
19. Whitcup, S.M.; Pleyer, U.; Lai, J.C.; Lutz, S.; Mochizuki, M.; Chan, C.-C. Topical liposome-encapsulated FK506 for the treatment of endotoxin-induced uveitis. *Ocul. Immunol. Inflamm.* **1998**, *6*, 51–56. [CrossRef] [PubMed]
20. Ishioka, M.; Ohno, S.; Nakamura, S.; Isobe, K.; Watanabe, N.; Ishigatsumo, Y.; Tanaka, S.-I. FK506 Treatment of Noninfectious Uveitis. *Am. J. Ophthalmol.* **1994**, *118*, 723–729. [CrossRef]
21. Young, A.L.; Wong, S.; Leung, A.T.; Leung, G.Y.; Cheng, L.L.; Lam, D.S. Clinical Case Notes. Successful treatment of surgically induced necrotizing scleritis with tacrolimus. *Clin. Exp. Ophthalmol.* **2005**, *33*, 98–99. [CrossRef]
22. Lee, Y.J.; Kim, S.W.; Seo, K.Y. Application for Tacrolimus Ointment in Treating Refractory Inflammatory Ocular Surface Diseases. *Am. J. Ophthalmol.* **2013**, *155*, 804–813.e1. [CrossRef]
23. Ryu, E.H.; Kim, J.M.; Laddha, P.M.; Chung, E.-S.; Chung, T.-Y. Therapeutic Effect of 0.03% Tacrolimus Ointment for Ocular Graft versus Host Disease and Vernal Keratoconjunctivitis. *Korean, J. Ophthalmol.* **2012**, *26*, 241–247. [CrossRef]
24. Tam, P.M.K.; Young, A.L.; Cheng, L.L.; Lam, P.T.H. Topical 0.03% tacrolimus ointment in the management of ocular surface inflammation in chronic GVHD. *Bone Marrow Transplant.* **2009**, *45*, 957–958. [CrossRef] [PubMed]
25. Jung, J.W.; Lee, Y.J.; Yoon, S.; Kim, T.-I.; Kim, E.K.; Seo, K.Y. Long-term Result of Maintenance Treatment with Tacrolimus Ointment in Chronic Ocular Graft-Versus-Host Disease. *Am. J. Ophthalmol.* **2015**, *159*, 519–527.e1. [CrossRef] [PubMed]
26. Murphy, C.C.; Greiner, K.; Plskova, J.; Duncan, L.; Frost, N.A.; Forrester, J.V.; Dick, A.D. Cyclosporine vs Tacrolimus Therapy for Posterior and Intermediate Uveitis. *Arch. Ophthalmol.* **2005**, *123*, 634–641. [CrossRef] [PubMed]
27. Prajapati, M.; Eiriksson, F.F.; Loftsson, T. Stability characterization, kinetics and mechanism of tacrolimus degradation in cyclodextrin solutions. *Int. J. Pharm.* **2020**, *586*, 119579. [CrossRef] [PubMed]
28. Patel, P.V.; Patel, H.K.; Mehta, T.A.; Panchal, S.S. Self micro-emulsifying drug delivery system of tacrolimus: Formulation, in vitro evaluation and stability studies. *Int. J. Pharm. Investig.* **2013**, *3*, 95–104. [CrossRef] [PubMed]
29. Siegl, C.; König-Schuster, M.; Nakowitsch, S.; Koller, C.; Graf, P.; Unger-Manhart, N.; Schindlegger, Y.; Kirchoff, N.; Knecht, C.; Prieschl-Grassauer, E.; et al. Pharmacokinetics of topically applied tacrolimus dissolved in Marinosolv, a novel aqueous eye drop formulation. *Eur. J. Pharm. Biopharm.* **2019**, *134*, 88–95. [CrossRef]

30. Zeng, W.; Li, Q.; Wan, T.; Liu, C.; Pan, W.; Wu, Z.; Zhang, G.; Pan, J.; Qin, M.; Lin, Y.; et al. Hyaluronic acid-coated niosomes facilitate tacrolimus ocular delivery: Mucoadhesion, precorneal retention, aqueous humor pharmacokinetics, and transcorneal permeability. *Colloids Surf. B* **2016**, *141*, 28–35. [CrossRef]
31. Lamprecht, A.; Yamamoto, H.; Takeuchi, H.; Kawashima, Y. A pH-sensitive microsphere system for the colon delivery of tacrolimus containing nanoparticles. *J. Control. Release* **2005**, *104*, 337–346. [CrossRef]
32. Nassar, T.; Rom, A.; Nyska, A.; Benita, S. A Novel Nanocapsule Delivery System to Overcome Intestinal Degradation and Drug Transport Limited Absorption of P-glycoprotein Substrate Drugs. *Pharm. Res.* **2008**, *25*, 2019–2029. [CrossRef]
33. Wang, Y.; Wang, C.; Fu, S.; Liu, Q.; Dou, D.; Lv, H.; Fan, M.; Guo, G.; Luo, F.; Qian, Z. Preparation of Tacrolimus loaded micelles based on poly(ϵ -caprolactone)–poly(ethylene glycol)–poly(ϵ -caprolactone). *Int. J. Pharm.* **2011**, *407*, 184–189. [CrossRef]
34. Uno, T.; Yamaguchi, T.; Li, X.K.; Suzuki, Y.; Hashimoto, H.; Harada, Y.; Kimura, T.; Kazui, T. The pharmacokinetics of water-in-oil-in-water-type multiple emulsion of a new tacrolimus formulation. *Lipids* **1997**, *32*, 543–548. [CrossRef] [PubMed]
35. Janicki, J.J.; Chancellor, M.B.; Kaufman, J.; Gruber, M.A.; Chancellor, D.D. Potential Effect of Liposomes and Liposome-Encapsulated Botulinum Toxin and Tacrolimus in the Treatment of Bladder Dysfunction. *Toxins* **2016**, *8*, 81. [CrossRef] [PubMed]
36. Gao, S.; Sun, J.; Fu, D.; Zhao, H.; Lan, M.; Gao, F. Preparation, characterization and pharmacokinetic studies of tacrolimus-dimethyl- β -cyclodextrin inclusion complex-loaded albumin nanoparticles. *Int. J. Pharm.* **2012**, *427*, 410–416. [CrossRef] [PubMed]
37. Arima, H.; Yunomae, K.; Miyake, K.; Irie, T.; Hirayama, F.; Uekama, K. Comparative Studies of the Enhancing Effects of Cyclodextrins on the Solubility and Oral Bioavailability of Tacrolimus in Rats. *J. Pharm. Sci.* **2001**, *90*, 690–701. [CrossRef] [PubMed]
38. Mahmoudi, A.; Malaekhe-Nikouei, B.; Hanafi-Bojd, M.Y.; Toloei, M.; Hosseini, M.; Nikandish, M. Preliminary In Vivo Safety Evaluation of a Tacrolimus Eye Drop Formulation Using Hydroxypropyl Beta Cyclodextrin After Ocular Administration in NZW Rabbits. *Clin. Ophthalmol.* **2020**, *14*, 947–953. [CrossRef]
39. Loftsson, T.; Björnsdóttir, S.; Pálsdóttir, G.; Bodor, N. The effects of 2-hydroxypropyl- β -cyclodextrin on the solubility and stability of chlorambucil and melphalan in aqueous solution. *Int. J. Pharm.* **1989**, *57*, 63–72. [CrossRef]
40. European Medicines Agency (EMA). Cyclodextrins Used as Excipients. Available online: <https://www.ema.europa.eu/en/cyclodextrins> (accessed on 17 December 2020).
41. Chauvin, L. INDOCOLLYRE 0,1% collyre sol en récipient unidose. Available online: <https://www.vidal.fr/medicaments/indocollyre-0-1-collyre-sol-en-recipient-unidose-8613.html> (accessed on 21 January 2021).
42. Anguiano-Igea, S.; Otero-Espinar, F.; Vila-Jato, J.; Blanco-Méndez, J. Interaction of clofibrate with cyclodextrin in solution; Phase solubility, 1H NMR and molecular modelling studies. *Eur. J. Pharm. Sci.* **1997**, *5*, 215–221. [CrossRef]
43. Higuchi, T.; Connors, K.; Connors, S. Phase Solubility Techniques. Available online: <https://www.scienceopen.com/document?vid=76f1d8c7-413c-40f2-aa7f-227482d5d1ad> (accessed on 17 November 2020).
44. Q2 (R1) Validation of Analytical Procedures: Text and Methodology. Available online: <https://www.fda.gov/regulatory-information/search-fda-guidance-documents/q2-r1-validation-analytical-procedures-text-and-methodology> (accessed on 21 January 2021).
45. Mayer, M.; Meyer, B. Mapping the Active Site of Angiotensin-Converting Enzyme by Transferred NOE Spectroscopy. *J. Med. Chem.* **2000**, *43*, 2093–2099. [CrossRef]
46. FDA BSS[®] Sterile Irrigating Solution (Balanced Salt Solution). Available online: <https://dailymed.nlm.nih.gov/dailymed/fda/fdaDrugXsl.cfm?setid=4bd4d59c-eb3b-4a5e-9eb7-ae95b0a92bea&type=display> (accessed on 9 December 2020).
47. AEMPS Ficha Técnica Liquifilm[®]. Available online: https://cima.aemps.es/cima/pdfs/es/ft/60226/FT_60226.pdf (accessed on 21 January 2021).
48. Zanjani, H.; Aminifard, M.N.; Ghafourian, A.; Pourazizi, M.; Maleki, A.; Arish, M.; Shahrakipoor, M.; Rohani, M.R.; Abrishami, M.; Zare, E.K.; et al. Comparative Evaluation of Tacrolimus Versus Interferon Alpha-2b Eye Drops in the Treatment of Vernal Keratoconjunctivitis. *Cornea* **2017**, *36*, 675–678. [CrossRef]
49. Fukushima, A.; Ohashi, Y.; Ebihara, N.; Uchio, E.; Okamoto, S.; Kumagai, N.; Shoji, J.; Takamura, E.; Nakagawa, Y.; Namba, K.; et al. Therapeutic effects of 0.1% tacrolimus eye drops for refractory allergic ocular diseases with proliferative lesion or corneal involvement. *Br. J. Ophthalmol.* **2014**, *98*, 1023–1027. [CrossRef]
50. Macy, R. Surface tension by the ring method. Applicability of the du Nouy apparatus. *J. Chem. Educ.* **1935**, *12*, 573. [CrossRef]
51. Cox, C.H. Squeeze Force Measuring System. Patent US007441468B2, 28 October 2008. Available online: <https://patentimages.storage.googleapis.com/b3/43/bc/d55228f30c3e35/US7441468.pdf> (accessed on 21 January 2021).
52. Díaz-Tomé, V.D.; García-Otero, X.; Blanco-Fernández, G.; Fernández-Ferreiro, A.; Otero-Espinar, F.J.; Varela-Fernández, R. In Vitro and in Vivo Ophthalmic Bioadhesion and Ocular Safety Characterization of Cyclodextrin Based Solution. The 1st International Electronic Conference on Pharmaceutics session Cyclodextrins in Pharmaceutics. *Conf. Online* **2020**. [CrossRef]
53. Salem, H.; Katz, S.A.; Katz, S.A. *Alternative Toxicological Methods*; CRC Press: Boca Raton, FL, USA, 2003; ISBN 978-0-429-21420-2.
54. Eskes, C.; Bessou, S.; Bruner, L.; Curren, R.; Harbell, J.; Jones, P.; Kreiling, R.; Liebsch, M.; McNamee, P.; Pape, W.; et al. 1 Subgroup 3. Eye Irritation. Available online: </paper/1-Subgroup-3.-Eye-Irritation-Eskes-Bessou/6dc8084ae36a6c2ab4ca59586e230776bafd8f5d> (accessed on 15 November 2020).
55. Fernández-Ferreiro, A.; Santiago-Varela, M.; Gil-Martínez, M.; González-Barcia, M.; Luaces-Rodríguez, A.; Díaz-Tomé, V.; Pardo, M.; Blanco-Méndez, J.; Piñeiro-Ces, A.; Rodríguez-Ares, M.T.; et al. In Vitro Evaluation of the Ophthalmic Toxicity Profile of Chlorhexidine and Propamidine Isethionate Eye Drops. *J. Ocul. Pharmacol. Ther.* **2017**, *33*, 202–209. [CrossRef] [PubMed]

56. Spielmann, H.; Kalweit, S.; Liebsch, M.; Wirnsberger, T.; Gerner, I.; Bertram-Neis, E.; Krauser, K.; Kreiling, R.; Miltenburger, H.; Pape, W.; et al. Validation study of alternatives to the Draize eye irritation test in Germany: Cytotoxicity testing and HET-CAM test with 136 industrial chemicals. *Toxicol. Vitro*. **1993**, *7*, 505–510. [CrossRef]
57. Kalweit, S.; Besoke, R.; Gerner, I.; Spielmann, H. A national validation project of alternative methods to the Draize rabbit eye test. *Toxicol. Vitro*. **1990**, *4*, 702–706. [CrossRef]
58. Lund, W. *The Pharmaceutical CODEX: Principles & Practice of Pharmaceutics*; 12e (HB); CBS Publishers & Distributors: DaRyaganj, New Delhi, India, 2009; ISBN 978-81-239-1650-7.
59. The Association for Research in Vision and Ophthalmology Statement for the Use of Animals in Ophthalmic and Visual Research. Available online: http://www.arvo.org/About_ARVO/Policies/Statement_for_the_Use_of_Animals_in_Ophthalmic_and_Visual_Research/ (accessed on 21 January 2021).
60. National Research Council (US) Committee for the Update of the Guide for the Care and Use of Laboratory Animals. *Guide for the Care and Use of Laboratory Animals*, 8th ed.; The National Academies Collection: Reports funded by National Institutes of Health; National Academies Press (US): Washington, DC, USA, 2011; ISBN 978-0-309-15400-0.
61. Fernández-Ferreiro, A.; Silva-Rodríguez, J.; Otero-Espinar, F.J.; González-Barcia, M.; Lamas, M.J.; Ruibal, A.; Luaces-Rodríguez, A.; Vieites-Prado, A.; Moreira, T.S.; Herranz, M.; et al. Positron Emission Tomography for the Development and Characterization of Corneal Permanence of Ophthalmic Pharmaceutical Formulations. *Investig. Ophthalmology Vis. Sci.* **2017**, *58*, 772–780.
62. Castro-Balado, A.; Mondelo-García, C.; González-Barcia, M.; Zarra-Ferro, I.; Otero-Espinar, F.J.; Ruibal, Á.; Aguiar, P.; Fernández-Ferreiro, A. Ocular Biodistribution Studies Using Molecular Imaging. *Pharmaceutics* **2019**, *11*, 237. [CrossRef]
63. Burden, N.; Aschberger, K.; Chaudhry, Q.; Clift, M.J.D.; Doak, S.H.; Fowler, P.; Johnston, H.J.; Landsiedel, R.; Rowland, J.; Stone, V. The 3Rs as a framework to support a 21st century approach for nanosafety assessment. *Nano Today* **2017**, *12*, 10–13. [CrossRef]
64. Loening, A.M.; Gambhir, S.S. AMIDE: A Free Software Tool for Multimodality Medical Image Analysis. *Mol. Imaging* **2003**, *2*, 131–137. [CrossRef]
65. Meyer, B.; Peters, T. NMR Spectroscopy Techniques for Screening and Identifying Ligand Binding to Protein Receptors. *Angew. Chem. Int. Ed.* **2003**, *42*, 864–890. [CrossRef]
66. Furukawa, A.; Konuma, T.; Yanaka, S.; Sugase, K. Quantitative analysis of protein–ligand interactions by NMR. *Prog. Nucl. Magn. Reson. Spectrosc.* **2016**, *96*, 47–57. [CrossRef] [PubMed]
67. Saokham, P.; Muankaew, C.; Jansook, P.; Loftsson, T. Solubility of Cyclodextrins and Drug/Cyclodextrin Complexes. *Molecules* **2018**, *23*, 1161. [CrossRef] [PubMed]
68. Baranowski, P.; Karolewicz, B.; Gajda, M.; Pluta, J. Ophthalmic Drug Dosage Forms: Characterisation and Research Methods. *Sci. World J.* **2014**, *2014*, 1–14. [CrossRef] [PubMed]
69. Dutescu, R.M.; Panfil, C.; Schrage, N. Osmolarity of Prevalent Eye Drops, Side Effects, and Therapeutic Approaches. *Cornea* **2015**, *34*, 560–566. [CrossRef] [PubMed]
70. Dabrowski, H.P.; Salpekar, A.; Jr, O.W.L. Ophthalmic Solution for Artificial Tears 1997. Patent US005591426A, 7 January 1997. Available online: <https://patentimages.storage.googleapis.com/6e/1b/c3/0718a34b45e98c/US5591426.pdf> (accessed on 21 January 2021).
71. Nagyová, B.; Tiffany, J. Components responsible for the surface tension of human tears. *Curr. Eye Res.* **1999**, *19*, 4–11. [CrossRef] [PubMed]
72. Han, K.; Woghiren, O.E.; Priefer, R. Surface tension examination of various liquid oral, nasal, and ophthalmic dosage forms. *Chem. Central. J.* **2016**, *10*, 31. [CrossRef] [PubMed]
73. Connor, A.J.; Severn, P.S. Force requirements in topical medicine use—the squeezability factor. *Eye* **2011**, *25*, 466–469. [CrossRef] [PubMed]
74. Van Santvliet, L.; Ludwig, A. Determinants of eye drop size. *Surv. Ophthalmol.* **2004**, *49*, 197–213. [CrossRef]
75. Luechtefeld, T.; Maertens, A.; Russo, D.P.; Rovida, C.; Zhu, H.; Hartung, T. Analysis of Draize eye irritation testing and its prediction by mining publicly available 2008–2014 REACH data. *ALTEX-Altern. Animal Exp.* **2016**, *33*, 123–134. [CrossRef]
76. Balls, M.; Botham, P.; Bruner, L.; Spielmann, H. The EC/HO international validation study on alternatives to the draize eye irritation test. *Toxicol. Vitro*. **1995**, *9*, 871–929. [CrossRef]
77. Christian, M.S.; Diener, R.M. Soaps and Detergents: Alternatives to Animal Eye Irritation Tests. *J. Am. Coll. Toxicol.* **1996**, *15*, 1–44. [CrossRef]
78. Chamberlain, M.; Gad, S.; Gautheron, P.; Prinsen, M. Irag Working Group 1: Organotypic models for the assessment/prediction of ocular irritation. *Food Chem. Toxicol.* **1997**, *35*, 23–37. [CrossRef]
79. Garnero, C.; Zoppi, A.; Aloisio, C.; Longhi, M.R. Chapter 7-Technological delivery systems to improve biopharmaceutical properties. In *Nanoscale Fabrication, Optimization, Scale-Up and Biological Aspects of Pharmaceutical Nanotechnology*; Grumezescu, A.M., Ed.; William Andrew Publishing: Norwich, NY, USA, 2018; pp. 253–299. ISBN 978-0-12-813629-4.
80. Campos, M.S.T.; Fialho, S.L.; Pereira, B.G.; Yoshida, M.I.; De Oliveira, M.A. Kinetics studies of the degradation of sirolimus in solid state and in liquid medium. *J. Therm. Anal. Calorim.* **2017**, *130*, 1653–1661. [CrossRef]
81. Thompson, A.C.; Thompson, M.O.; Young, D.L.; Lin, R.C.; Sanislo, S.R.; Moshfeghi, D.M.; Singh, K. Barriers to Follow-Up and Strategies to Improve Adherence to Appointments for Care of Chronic Eye Diseases. *Investig. Ophthalmology Vis. Sci.* **2015**, *56*, 4324–4331. [CrossRef] [PubMed]
82. Peppas, N.A.; Mongia, N.K. Ultrapure poly (vinyl alcohol) hydrogels with mucoadhesive drug delivery characteristics. *Eur. J. Pharm. Biopharm.* **1997**, *43*, 51–58. [CrossRef]

Article

Formulation and Stability of Ataluren Eye Drop Oily Solution for Aniridia

Celia Djayet ¹, Dominique Bremond-Gignac ^{2,3} , Justine Touchard ¹, Philippe-Henri Secretan ^{1,4}, Fabrice Vidal ¹, Matthieu P. Robert ² , Alejandra Daruich ^{2,3}, Salvatore Cisternino ^{1,5}  and Joël Schlatter ^{1,*} 

¹ Assistance Publique-Hôpitaux de Paris, AP-HP, Hôpital Universitaire Necker-Enfants Malades, Service de Pharmacie, Université de Paris, 75015 Paris, France; celia.djayet@aphp.fr (C.D.); justine.touchard@aphp.fr (J.T.); phsecretan@yahoo.fr (P.-H.S.); fabrice.vidal@aphp.fr (F.V.); salvatore.cisternino@aphp.fr (S.C.)

² Assistance Publique-Hôpitaux de Paris, AP-HP, Hôpital Universitaire Necker-Enfants Malades, Service d'ophtalmologie, CRMR OPHTARA, Université de Paris, 75015 Paris, France; dominique.bremond@aphp.fr (D.B.-G.); matthieu.robert@aphp.fr (M.P.R.); alejandra.daruich-matet@aphp.fr (A.D.)

³ INSERM UMRS 1138, Team 17, Centre de Recherche des Cordeliers, Université Sorbonne Paris Cité, 75006 Paris, France

⁴ Matériaux et Santé, Université Paris-Saclay, 92296 Chatenay-Malabry, France

⁵ INSERM UMRS 1144, Optimisation Thérapeutique en Neuropsychopharmacologie, Faculté de Pharmacie, Université de Paris, 75006 Paris, France

* Correspondence: joel.schlatter@aphp.fr; Tel.: +33-1-44-49-25-11

Abstract: Congenital aniridia is a rare and severe panocular disease characterized by a complete or partial iris defect clinically detectable at birth. The most common form of aniridia occurring in around 90% of cases is caused by PAX6 haploinsufficiency. The phenotype includes ptosis, nystagmus, corneal limbal insufficiency, glaucoma, cataract, optic nerve, and foveal hypoplasia. Ataluren eye drops aim to restore ocular surface PAX6 haploinsufficiency in aniridia-related keratopathy (ARK). However, there are currently no available forms of the ophthalmic solution. The objective of this study was to assess the physicochemical and microbiological stability of ataluren 1% eye drop in preservative-free low-density polyethylene (LDPE) bottle with an innovative insert that maintains sterility after opening. Because ataluren is a strongly lipophilic compound, the formulation is complex and involves a strategy based on co-solvents in an aqueous phase or an oily formulation capable of totally dissolving the active ingredient. The visual aspect, ataluren quantification by a stability-indicating chromatographic method, and microbiological sterility were analyzed. The oily formulation in castor oil and DMSO (10%) better protects ataluren hydrolysis and oxidative degradation and permits its complete solubilization. Throughout the 60 days period, the oily solution in the LDPE bottle remained clear without any precipitation or color modification, and no drug loss and no microbial development were detected. The demonstrated physical and microbiological stability of ataluren 1% eye drop formulation at 22–25 °C might facilitate clinical research in aniridia.

Keywords: aniridia; ataluren; ophthalmic solution; rare disease; stability

Citation: Djayet, C.; Bremond-Gignac, D.; Touchard, J.; Secretan, P.-H.; Vidal, F.; Robert, M.P.; Daruich, A.; Cisternino, S.; Schlatter, J. Formulation and Stability of Ataluren Eye Drop Oily Solution for Aniridia. *Pharmaceutics* **2021**, *13*, 7. <https://dx.doi.org/10.3390/pharmaceutics13010007>

Received: 18 November 2020

Accepted: 17 December 2020

Published: 22 December 2020

Publisher's Note: MDPI stays neutral with regard to jurisdictional claims in published maps and institutional affiliations.



Copyright: © 2020 by the authors. Licensee MDPI, Basel, Switzerland. This article is an open access article distributed under the terms and conditions of the Creative Commons Attribution (CC BY) license (<https://creativecommons.org/licenses/by/4.0/>).

1. Introduction

Congenital aniridia is a rare and severe ocular disease. This panocular disease is characterized by a complete or partial iris defect clinically detectable at birth [1–3]. The disease is commonly associated with nystagmus, low vision, ptosis, corneal limbal insufficiency, glaucoma, cataract, optic nerve, and foveal hypoplasia. Congenital aniridia affects equally males and females and has a prevalence of 1:100,000 to 1:40,000 [1]. The most common form of aniridia occurring in around 90% of cases is caused by PAX6 haploinsufficiency due to intragenic mutation or chromosomal rearrangement in the PAX6 gene at 11p13. An autosomal dominant transmission is present in up to 90% of cases. Sporadic congenital

aniridia may consist of 13% to 33% of cases as family forms consist of around two-third of cases. Congenital aniridia may be part of a syndrome as in WAGR contiguous gene syndrome (Wilms tumor, aniridia, genitourinary anomalies, and mental retardation) or in the rare Gillespie syndrome (cerebellar ataxia and mental retardation) [1–3]. A minority of different gene mutations may also be observed in congenital aniridia due to other gene anomalies [1,4]. The visual prognosis of aniridia is severe, with congenital low vision due to foveal hypoplasia and occasionally optic nerve hypoplasia. The severe evolution results from keratopathy associated with corneal opacification, glaucoma, and cataract [1–6]. In the corneal limbus, the loss of the stem cell niche in Vogt's palisades progresses and causes corneal opacity called aniridia-related keratopathy (ARK), which can finally lead to blindness [7]. Therefore, a new approach for aniridia treatment has been proposed involving nonsense mutation suppression therapies, such as ataluren, which could limit aniridia disease progression and corneal damage [8–10]. As a result of the study, a phase 2 clinical trial was designed to evaluate the effect of oral ataluren in participants with nonsense mutation aniridia [11].

Ataluren, chemically known as 3-(5-(2-fluorophenyl)-1,2,4-oxadiazol-3-yl)benzoic acid, is a drug having nonsense codon suppression activity approved by the FDA and European agencies for the treatment of Duchenne muscular dystrophy in ambulatory patients aged 2 years and older [12]. Ataluren enables ribosomal read-through of mRNA containing such as a premature stop codon, resulting in the production of a full-length protein [13,14]. Currently, ataluren granules for oral suspension (Translarna[®] 125 mg, 250 mg, and 1000 mg, PTC Therapeutics International Limited, Dublin, Ireland) are the only marketed form.

The formulation of an ataluren eye drops solution could be advantageous for the repositioning of ataluren in the ocular treatment of aniridia. Eye drops allow more effective corneal exposure while limiting systemic body exposure. Ataluren is a small and lipophilic molecule soluble in organic solvents, such as dimethylsulfoxide (DMSO), and very slightly soluble in water [15]. Ataluren (1% *m/v*) suspension in 0.9% saline vehicle containing 1% tween 80 as a co-solvent, and 1% carboxymethylcellulose to increase viscosity, also known as the 'START' formulation, was shown to rescue the corneal deficit in Pax6-deficient mice model of aniridia [10]. Although this preclinical study suggests a benefit of the topical administration of ataluren, its chemical stability over time, as well as its sterility, were not assessed to our knowledge [10]. The objective of our study was to develop a 1% ataluren solution free of particles and chemically and microbiologically stable at least over 2 months when stored at 25 ± 3 °C.

2. Materials and Methods

2.1. Chemicals and Materials

The pharmaceutical ingredient of ataluren was obtained from Sigma-Aldrich (St. Quentin Fallavier, France). DMSO USP grade was provided from Wak-Chemie Medical GmbH (Cryosure, Steinbach, Germany). Pharmaceutical grade castor oil was provided from Cooper (Melun, France). Pharmaceutical hydroxypropylcellulose and tween 80 were provided from Inresa-Pharma (Bartenheim, France). Other chemicals were of analytical grade. Titanium dioxide (99.5% Aeroxide[®] P25, nanopowder, average primary particle size 21 nm) came from Sigma Aldrich (St. Quentin Fallavier, France). All solvents used were HPLC grade from Merck (Darmstadt, Germany). Cationorm[®] was obtained from Santen (Evry, France) and contained mineral oils, cetalkonium chloride, tyloxapol, poloxamer 188, glycerin, buffer system (Tris-HCl/trometamine), and water for injection. The sterile preservative-free low-density polyethylene (LDPE) multidose opaque eyedropper Novelia[®] was obtained from Nemera (La Verpillere, France) and distributed by CAT laboratory (Montereau, France). It was chosen for its capacity to maintain sterility in normal use and under conditions of misuse and extended use, including an anti-return valve system with a silicone membrane.

2.2. Formulation Development Assay and Preparation of Ataluren Eye Drops

Aqueous formulation of ataluren (1%) compounded with 0.9% sodium chloride, 1% tween 80, 1% ataluren (*m/v*), and 1% hydroxypropylcellulose (STAR) was prepared. This ataluren suspension was stored at 25 ± 3 °C, and the chemical stability was assessed during 21 days.

Other experiments were carried out by dissolving ataluren (1%) in pure castor oil and in a ready-to-use ophthalmic Cationorm[®] solution, also known as hydrating and lubricating eye drops. Although the ophthalmic solution obtained was limpid, precipitates were formed in less than 3 weeks without the possibility of resuspension/dissolution despite manual shaking (data not shown).

Alternative ataluren (1% *m/v*) eye drops formulations using DMSO as co-solvent in castor oil were evaluated [16]. Ataluren 1% (*m/v*) compounded with 10% (*v/v*) DMSO and 90% (*v/v*) castor oil allowed its complete solubilization. First, ataluren powder should be mixed in DMSO until completely dissolved. Second, castor oil should be added, and the resulting oily solution was mixed by inversion for 1 min. The obtained ataluren solution was filtered through a 0.22 µm polyethersulfone filter (Millex, Merck Millipore, Fontenay-sous-Bois, France) and then sterilely distributed into the eyedropper vials (10 mL per unit) in a vertical laminar B-class airflow hood of the microbiological safety cabinet.

2.3. Analyses Performed on the Ataluren Formulations

2.3.1. Visual Inspection

At each sample time, a visual inspection of the eye drop solution was made by the same operator, looking for a change in coloring, particles, or precipitate, compared with a control consisting of castor oil.

2.3.2. Instrumentation

For each unit, ataluren was quantified using the liquid chromatography (HPLC) method adapted from the method described by Kong et al. [17]. Analyses were performed on a Thermo Scientific Ultimate 3000 chromatogram system (Villebon-sur-Yvette, France), including a quaternary pump (LPG 3400A), an automatic sampler (WPS 3000TSL), a diode array detector (DAD 3000RS) with 5 cm flow cell, and the associated software used to record and interpret chromatograms (Chromeleon[®], Version 7.2.8, Thermo Scientific, 2018). The stationary phase consisted of a Kinetex[®] C18 column (250 × 4.6 mm; 5 µm, Phenomenex, Le Pecq, France). The mobile phase was a gradient mixture of 0.1% formic acid (A) and acetonitrile (B). The flow rate was maintained at 1 mL/min, and the gradient profile was as follows: t₀–11 min: A = 30% B = 70%; t₁₁–15 min A = 70% B = 30%. The injection volume was 50 µL. The drug absorbance for quantification was obtained at 276 nm.

2.3.3. Method Validation

The HPLC method was validated for specificity, the limit of detection (LOD), the limit of quantification (LOQ), linearity, precision, accuracy, according to ICH Q2 validation guidelines [18].

Linearity was determined by preparing one calibration curve daily for three days using five concentrations of ataluren at 50, 60, 70, 80, and 90 µg/mL, diluted in acetonitrile. For each calibration, the slope, intercept, and regression coefficient (*r*) were calculated as regression parameters by the least square method. ANOVA tests were applied to determine applicability. The accuracy for the active compound was determined by analyzing three replicates of samples prepared at 80%, 100%, and 120% of the target concentration. Accuracy was expressed as the percentage of recovery determined by experimental concentration/theoretical concentration × 100. The acceptance criterion was ± 2% deviation from the normal value for the recovery of ataluren. To verify the method's precision, repeatability was estimated by calculating the relative standard deviation (RSD) of intraday analysis, and the intermediate precision was evaluated using RSD of inter-day analysis. Both RSDs should be less than 2%. For that, each day for three days, six solutions of ataluren 1%

were prepared, analyzed, and quantified using a calibration curve prepared the same day. The limit of detection (LOD) and limit of quantification (LOQ) for ataluren assay were determined by calibration curve method using the following equations:

$$LOD = \frac{3.3 \times SD \text{ of } y - \text{intercept}}{\text{Slope of calibration curve}}; LOQ = \frac{10 \times SD \text{ of } y - \text{intercept}}{\text{Slope of calibration curve}}$$

The matrix effect was evaluated by reproducing the previous methodology with the presence of all excipients present in the formulation and by comparing curves and intercepts.

The specificity was assessed by subjecting the ataluren 1% solubilized in DMSO (10%) and castor oil solutions to various forced degradation conditions: 0.1 M hydrochloric acid (HCl), 0.1 M sodium hydroxide (NaOH), 0.3% and 15% hydrogen peroxide (H₂O₂) for 24 h, 48 h, and 72 h at 60 °C. To mimic the potential photodegradation occurring prior to or after drug administration, photolytic studies were carried out by exposing the drug solutions to direct UV-visible light with and without photocatalyst or photosensitizer (i.e., titanium oxide 1 g L⁻¹, riboflavin 100 mg L⁻¹). Photolysis experiments were performed using a QSUN-XE-1 (Q-Lab, Bolton, UK) light chamber equipped with a xenon lamp, which simulates natural sunlight in a wavelength range of 300–800 nm. A Daylight-Q filter was used to simulate CIE Standard Illuminant D65 (Q-Lab), and the irradiance was maintained constant (1.5 W m⁻² at 420 nm). The measurements corresponded to a visible intensity of ~119,600 lx and a UVA intensity at 300–400 nm of 66.5 W m⁻². For all the experiments, the temperature was controlled and set at 25.0 ± 0.5 °C.

2.3.4. Sterility Assay

Sterility is an absolute requirement of ophthalmic formulations. In order to evaluate the sterility of the eye drop in ophthalmic bottles, a test for sterility was carried out using the technique of membrane filtration with the product to be examined according to the European pharmacopeia [19].

To ensure applicability of the sterility test, sterility and fertility of media with and without the formulation were controlled. Six collection type strains were included corresponding to four bacteria (*Pseudomonas aeruginosa* ATCC 9027, *Staphylococcus aureus* ATCC 6538, *Clostridium sporogenes* ATCC 19404, and *Bacillus subtilis* ATCC 6633) and two fungi (*Candida albicans* ATCC 10231, *Aspergillus brasiliensis* ATCC 16404). Fluid thioglycollate medium and soya-bean casein digest medium were used as culture media. For each reference strain, 10 mL of formulations with and without the drug were filtered using the Steritest™ device (Steritest™ NEO, Merck Millipore, Guyancourt, France).

To validate the sterility applicability test, microbial growth clearly observable and visually comparable to that observed without product was observed each day for 5 days. To assess the sterility test of eye drops ataluren oily solution, the same procedure was applied, and the potential microbial growth was observed each day for 14 days.

2.4. Stability Study

Six bottles of the ataluren formulation were prepared and stored at 25 ± 3 °C. Physical and chemical examinations were performed in triplicate immediately after preparation (Day 0) and at Day 1, 3, 7, 14, 30, 60, and 90 to define drug stability throughout its period of storage except for the STAR ataluren suspension (Day 0, 7, and 21).

The chemical stability of the extemporaneous preparation was defined by the drug content that contained not less than 90% and not more than 110% of the labeled amount of ataluren [20].

2.5. Data Analysis-Acceptability Criteria

Data analyses were performed using Prism (GraphPad Software, version 7.04, San Diego, CA, USA, 2017). Descriptive statistics for continuous variables were expressed as mean ± SD.

The study was conducted following methodological guidelines issued by the International Conference on Harmonisation (ICH) for stability studies [18]. The instability of ataluren solutions was considered by a variation of concentration outside the 90–110% range of initial concentration of drug and the presence of degradation products. The observed solutions must be limpid, of unchanged color, and clear of visible signs of precipitation.

3. Results

3.1. Subsection

The retention time of ataluren was observed to be about 11.6 min (Figure 1).

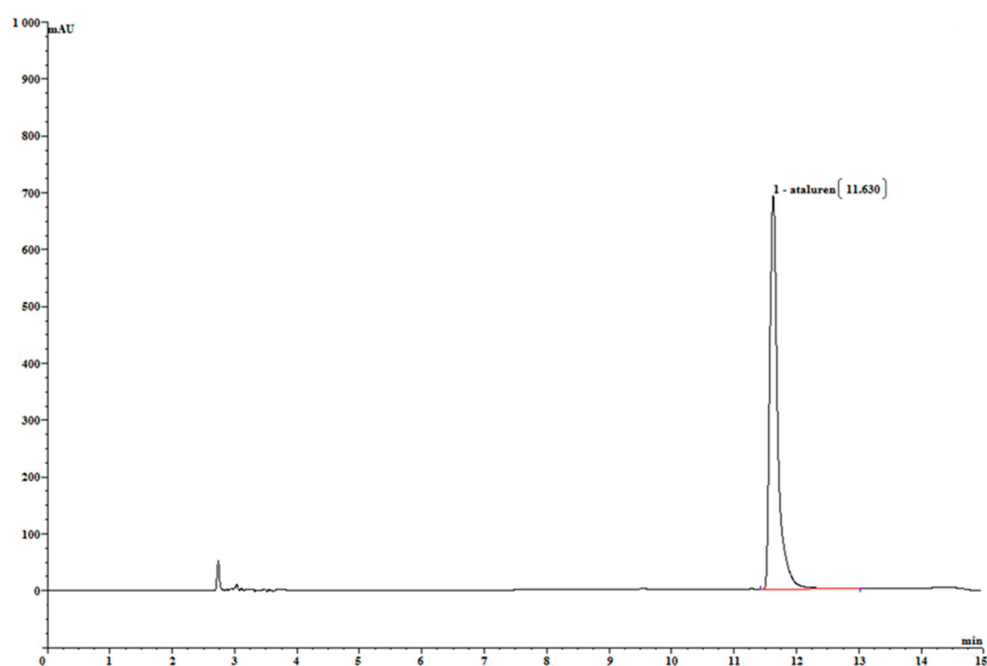


Figure 1. Reference chromatogram of ataluren at 276 nm in the oily solution.

The chromatographic method used was found linear for concentrations ranging from 50 to 90 $\mu\text{g}/\text{mL}$. The calculated regression parameters are given in Table 1 and are within the linearity acceptance criteria. An average regression equation was $y = 2.074 (\pm 0.017) x + 10.250 (\pm 1.271)$, where x is the ataluren concentration, and y is the surface area, and the average determination coefficient R^2 of three calibration curves was 0.9995. No matrix effect was detected.

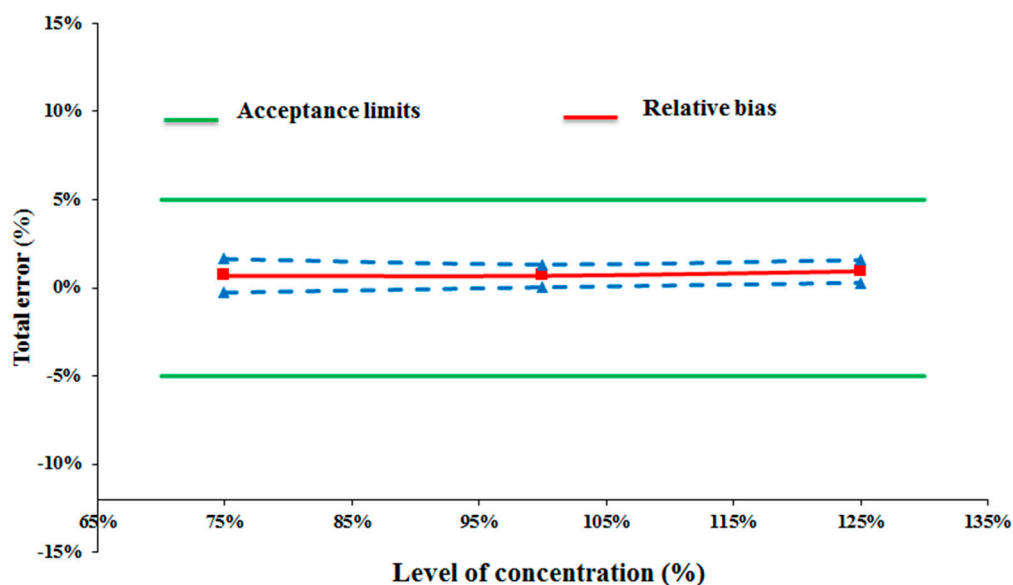
Table 1. Linearity study of the stability-indicating analytic method.

Nominal Concentration ($\mu\text{g}/\text{mL}$)	Mean Peak Area \pm SD ($n = 45$)	Calculated Amount ($\mu\text{g}/\text{mL}$)	Accuracy (%)
50	114.44 \pm 0.76	50.2 \pm 0.7	100.5
60	134.05 \pm 0.81	59.7 \pm 0.5	99.5
70	155.69 \pm 0.79	70.1 \pm 0.6	100.2
80	175.69 \pm 1.50	79.8 \pm 1.2	99.7
90	197.32 \pm 0.63	90.2 \pm 0.6	100.2

Results for intra-day precision and inter-day precision were less than 2.1%, as shown in Table 2. The 95% accuracy profile was within the predefined acceptance limits (Figure 2).

Table 2. Relative standard deviation values (%) for repeatability and intermediate precision (IQC). Definition: relative standard deviation (RSD).

Theoretical Concentration ($\mu\text{g/mL}$)	Mean Calculated Concentration ($\mu\text{g/mL}$)	% RSD Repeatability ($n = 6$)	% RSD Intermediate Precision ($n = 3$)
55	55.4 \pm 0.6	0.57	0.79
70	70.5 \pm 0.9	0.81	1.13
85	85.8 \pm 1.8	1.46	2.02

**Figure 2.** The 95% accuracy profile according to the ataluren level.

The determined values of LOD and LOQ were 6.8 $\mu\text{g/mL}$ and 11.1 $\mu\text{g/mL}$, respectively, calculated using slope and Y-intercept.

When exposed to strong acidic, basic, or 0.3% H_2O_2 conditions, ataluren was not degraded after 7 days of exposure (Table 3).

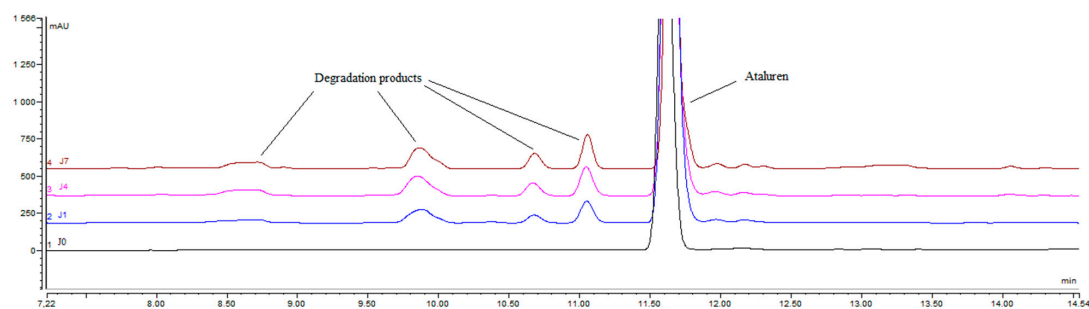
Table 3. Forced degradation studies of 1% eye drop oily formulation.

Stress Conditions	% Remaining (Degradation)		
	Day 1	Day 3	Day 7
Acidic stress (0.1 M HCl, 60 °C)	100.1 (+0.1)	100.3 (+0.3)	100.4 (+0.4)
Alkaline stress (1 M NaOH, 60 °C)	100.2 (+0.2)	99.9 (−0.1)	100.1 (+0.1)
Oxidative stress (0.3% H_2O_2 , 60 °C)	100.2 (+0.2)	99.2 (−0.8)	98.1 (−1.9)
Oxidative stress (15% H_2O_2 , 60 °C)	99.4 (−0.6)	89.7 (−10.3)	74.1 (−25.9)

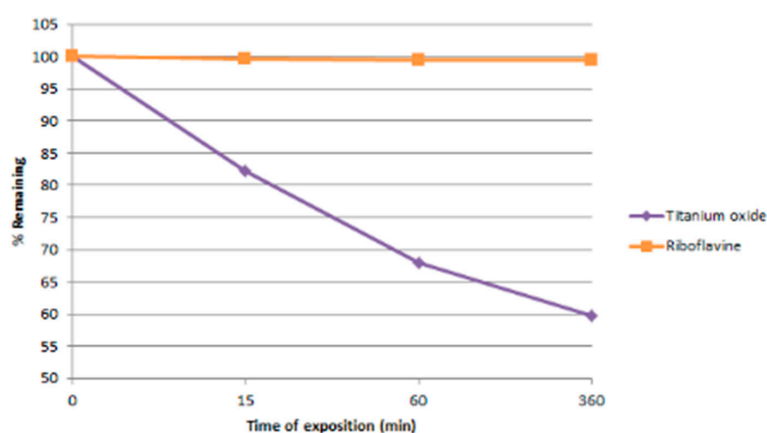
Degradation products appeared only for 15% hydrogen peroxide (H_2O_2) exposure and are highlighted in Figure 3a.

In the direct photolytic stress condition, ataluren was not degraded (Table 4).

However, in the presence of a photocatalyst agent (titanium oxide), ataluren was rapidly degraded (Figure 3b). This was not the case when exposing the drug to light in the presence of riboflavin. Our method is stability-indicating as it enables separation between ataluren and its degradation products without peak interferences.



(a)



(b)

Figure 3. (a) Chromatograms of ataluren obtained at day 0 (black, control), 1 day (blue), 4 days (pink), and 7 days (orange) and its degradation products when exposed to 15% H₂O₂; (b) Indirect photolysis of ataluren.

Table 4. Direct photolysis of ataluren. The measurements corresponded to a visible intensity of ~119,600 lx and an ultraviolet (UVA) intensity at 300–400 nm (66.5 W m⁻²).

Time of Exposition (min)	Mean Peak Area ± SD	% Remaining
30	240.2 ± 2.5	100.1
60	246.0 ± 1.9	102.4
180	240.4 ± 0.6	100.1
360	248.4 ± 2.1	103.4

3.2. Chemical Stability of Ataluren Aqueous Suspension

The chemical stability of the STAR ataluren suspension ($n = 6$) showed a loss of the chemical stability greater than 10% at day 21 (Table 5).

Table 5. Chemical stability of the STAR ataluren suspension eye drops (0.9% Sodium chloride, 1% Tween 80, 1% Ataluren, 1% hydroxypropylcellulose) stored at 25 ± 3 °C ($n = 3$ in triplicate).

Bottles	Actual Concentration (100 mg/10 mL)	Mean ± SD % Ataluren Concentration Remaining	
	Day 0	Day 7	Day 21
A	100.4 ± 1.2	98.7 ± 1.1	84.0 ± 1.3
B	101.2 ± 1.5	97.9 ± 1.3	84.5 ± 1.4
C	99.8 ± 1.3	99.4 ± 1.1	84.0 ± 1.1

3.3. Stability of Ataluren Oily Solution in Eyedroppers

3.3.1. Physical Stability

There were no detectable visual changes in color and limpidity and no appearance of any visible particulate matter during the study period.

3.3.2. Chemical Stability

The ataluren 1% eye drop oily solution stored in LDPE ophthalmic bottles at 22–25 °C demonstrated chemical stability for up to 60 days (Table 6). Ataluren retained at least 99% of its initial concentration at 60 days. Chromatograms showed no sign of degradation products throughout the study.

Table 6. Chemical stability of ataluren 1% eye drop castor oil and dimethylsulfoxide formulation stored at 22–25 °C in low-density polyethylene (LDPE) ophthalmic bottles and over time.

Eyedropper	Actual Concentration (100 mg/10 mL)	Mean ± SD% Ataluren Concentration Remaining				
		Day 0	Day 5	Day 15	Day 21	Day 30
1	100.7 ± 1.3	99.7 ± 1.3	99.2 ± 1.2	99.2 ± 1.3	100.8 ± 1.2	100.9 ± 1.4
2	100.4 ± 1.7	97.8 ± 1.2	99.4 ± 1.4	99.4 ± 1.5	101.5 ± 1.5	101.0 ± 1.9
3	100.3 ± 1.5	99.4 ± 1.3	98.6 ± 1.5	99.0 ± 1.1	100.1 ± 1.2	100.9 ± 1.5

3.3.3. Sterility Assay

The sterility applicability of the method was validated according to the European Pharmacopeia sterility assay [19]. The visual microbial growth in the control fertility experiments was clearly observed and comparable in the presence and absence of the product to be tested. No microbial growth was observed for any eye drop samples analyzed with this method over 14 days. Because the microbiological tests showed the absence of bacterial or fungal contamination of the preparation over time, the use of a preservative agent was not considered in the castor oil and DMSO eye drop formula.

4. Discussion

Our study reports new data on the stability of ataluren in ophthalmic solutions. The use of diverse co-solvent strategies (i.e., tween 80; cationorm[®]) only allowed partial ataluren solubilization, chemically stable less than 2–3 weeks. The use of castor oil and DMSO allowed us to obtain a 1% ataluren ophthalmic solution—exempt of suspended particles, sterile, and chemically stable. All parameters of the tested oily formulation were in favor of physicochemical and microbiological stability over 60 days.

Oxidation was shown critical in ataluren degradation, which is enhanced in aqueous media. The lack of water in the optimized formulation, combined with the use of pharmaceutical-grade castor oil controlled for its peroxide content, could also explain the enhanced stability of ataluren in the oily solution. In addition, the presence of DMSO, well-known for its antioxidant properties, may also have contributed to the absence of degradation perceived in the final formulation [21].

Simulated light experiments provided some insights into the propensity of ataluren to degrade both prior to and after administration. Ataluren concentration did not decrease upon direct light exposure, pointing out that the drug may resist to the light in the proposed formulation. Further, when riboflavin, a natural photosensitizing agent constituent of the eye, was added, no degradation was observed, which indicates that ataluren may not degrade through the photosensitized process naturally occurring in the eye [22]. Still, precaution should be taken as ataluren concentration decreased upon exposure when nanoparticles of titanium dioxide P25, a powerful photocatalyst, were added [23]. This

points out that ataluren may degrade in the presence of a strong oxidizing agent, such as hydroxyl radical ($\bullet\text{OH}$), which was detected in the context of nuclear cataract [24,25].

The sterility assay did not reveal any microbial contamination over the study time. The closure system eyedropper (Novelia[®]), which does not allow unfiltered air to penetrate the eyedropper, provided a further guarantee for sterility preservation of the content more than one month of simulated use [25]. Unlike a suspension, the sterilizing filtration process of removing microorganisms using a 0.22 μm filter can be performed with ataluren eye drops solution.

The ataluren eye drops concentration at 1% was selected according to a preclinical study showing its efficacy in a Pax6-deficient mouse model of aniridia [9]. In this study, the ataluren eye drop formulation was a suspension, which is less suitable than a solution in eye topical treatment. Indeed, some studies demonstrate the limitations of ophthalmic suspensions to deliver the proper dose after shaking because of the ineffective redispersion of particle sediment, also known as 'cake' or inappropriate manual shaking [26–28]. As suggested for steroids eye drops suspensions studies, some preclinical and clinical data show that reducing the drug particle size to the nanometer range in diameter provides effective ocular tissue penetration and more effective symptoms efficacy, even with reduced drug concentration and dosing frequency [29]. Ophthalmic suspensions are also known to cause ocular adverse effects, such as irritation, redness of the eye, and interference with vision [30]. Ataluren suspension caused marked ocular irritation, and the suspension formulation, referred to as START, abolished the irritation response seen with other formulations only apparently in mice [10].

DMSO is a drug characterized by anti-inflammatory, analgesic, and weak bacteriostatic properties and the ability to have radical scavenging activity [31,32]. It is also known as a well-tolerated penetration enhancing agent of drugs through biological membranes, including the cornea [33]. Based on these considerations, ophthalmic applications of DMSO have been already proposed and used in humans. Indeed, DMSO, known for its great solvating properties, is a well-known treatment for some eye diseases and is FDA-approved in some drug products like Onyx[®] injection, Viadur[®] implant, or Pennsaid[®] topical gel [34–36]. DMSO, in association with various drugs, was safely used for ophthalmic applications in humans or animals [32,37,38]. Administration of up to 50% of DMSO in eye drops demonstrated the well acceptance of DMSO for ophthalmic use with no sign of irritation or toxicity [37–43]. In a recent study, the irritation potential and ocular tolerance of brinzolamide ophthalmic DMSO solution were evaluated when administered to the rabbit eye according to the OECD guidelines for acute eye irritation testing [43,44]. In all examined formulations of brinzolamide in DMSO for ophthalmic use, no sign of irritation or toxicity was observed [43]. In addition, DMSO has been used at 10–15% as a cryopreservation agent, safely used to freeze mammalian cells, including cornea, to guarantee cell viability after thawing [45]. Castor oil is a natural derivative of the *Ricinus communis* plant that possesses anti-inflammatory, anti-nociceptive, antioxidant, and antimicrobial properties [43,46–48]. Castor oil eye drops have been administered safely in several eye disorders like mild dry eye, blepharitis, contact lens discomfort, refractory Meibomian gland dysfunction [49–51].

5. Conclusions

In view of its physicochemical stability and its preservation of sterility, this study confirms 60 days stability of 1% ataluren eye drop solution when stored at 25 ± 3 °C in LDPE ophthalmic bottles. Ataluren eye drops aim to restore ocular surface PAX6 haploinsufficiency in congenital aniridia, and this new formulation opens to further clinical studies and innovative treatment for patients.

Author Contributions: Conceptualization, D.B.-G., A.D., M.P.R., S.C., and J.S.; methodology, P.-H.S., S.C., and J.S.; data curation, C.D., J.T., P.-H.S., F.V., and J.S.; software, F.V. and J.S.; validation, P.-H.S., F.V., and J.S.; formal analysis, C.D., J.T., F.V., and J.S.; investigation, C.D., J.T., P.-H.S., F.V., and J.S.; writing—original draft preparation, S.C. and J.S.; writing—review and editing, D.B.-G., S.C., and J.S.;

supervision, P.-H.S., S.C., and J.S.; project administration, S.C. and J.S.; funding acquisition, S.C. and J.S. All authors have read and agreed to the published version of the manuscript.

Funding: This research received no external funding.

Institutional Review Board Statement: Not applicable.

Informed Consent Statement: Not applicable.

Data Availability Statement: Data is contained within the article.

Conflicts of Interest: The authors declare no conflict of interest.



References

- Hingorani, M.; Hanson, I.; van Heyningen, V. Aniridia. *Eur. J. Hum. Genet.* **2012**, *20*, 1011–1017. [CrossRef] [PubMed]
- Brémond-Gignac, D.; Gérard-Blanluet, M.; Copin, H.; Bitoun, P.; Baumann, C.; Crolla, J.A.; Benzacken, B.; Verloes, A. Three patients with hallucal polydactyly and WAGR syndrome, including discordant expression of Wilms tumor in MZ twins. *Am. J. Med. Genet. A* **2005**, *134*, 422–425. [CrossRef] [PubMed]
- Gerber, S.; Alzayady, K.J.; Burglen, L.; Brémond-Gignac, D.; Marchesin, V.; Roche, O.; Rio, M.; Funalot, B.; Calmon, R.; Durr, A.; et al. Recessive and Dominant De Novo ITPR1 Mutations Cause Gillespie Syndrome. *Am. J. Hum. Genet.* **2016**, *98*, 971–980. [CrossRef] [PubMed]
- Chrystal, P.W.; Walter, M.A. Aniridia and Axenfeld-Rieger Syndrome: Clinical presentations, molecular genetics and current/emerging therapies. *Exp. Eye. Res.* **2019**, *189*, 107815. [CrossRef]
- Brémond-Gignac, D. Congenital aniridia in children. *Rev. Prat.* **2019**, *69*, 67–70.
- Lim, H.T.; Kim, D.H.; Kim, H. PAX6 aniridia syndrome: Clinics, genetics, and therapeutics. *Curr. Opin. Ophthalmol.* **2017**, *28*, 436–447. [CrossRef]
- Lagali, N.; Edén, U.; Utheim, T.P.; Chen, X.; Riise, R.; Dellby, A.; Fagerholm, P. In vivo morphology of the limbal palisades of vogt correlates with progressive stem cell deficiency in aniridia-related keratopathy. *Investig. Ophthalmol. Vis. Sci.* **2013**, *54*, 5333–5342. [CrossRef]
- Liu, X.; Zhang, Y.; Zhang, B.; Gao, H.; Qiu, C. Nonsense suppression induced readthrough of a novel PAX6 mutation in patient-derived cells of congenital aniridia. *Mol. Genet. Genom. Med.* **2020**, *3*, e1198. [CrossRef]
- Wang, X.; Gregory-Evans, K.; Wasan, K.M.; Sivak, O.; Shan, X.; Gregory-Evans, C.Y. Efficacy of Postnatal In Vivo Nonsense Suppression Therapy in a Pax6 Mouse Model of Aniridia. *Mol. Ther. Nucleic Acids* **2017**, *7*, 417–428. [CrossRef]
- Gregory-Evans, C.Y.; Wang, X.; Wasan, K.M.; Zhao, J.; Metcalfe, A.L.; Gregory-Evans, K. Postnatal manipulation of Pax6 dosage reverses congenital tissue malformation defects. *J. Clin. Investig.* **2014**, *124*, 111–116. [CrossRef]
- PTC Therapeutics. STAR: A Phase 2, Multicenter, Randomized, Double-Masked, Placebo-Controlled Study of the Safety and Efficacy of Ataluren (PTC124) for the Treatment of Nonsense Mutation Aniridia. ClinicalTrials.gov: NCT02647359. Available online: <https://clinicaltrials.gov/ct2/show/NCT02647359#contactlocation> (accessed on 19 October 2020).
- European Medicines Agency. Translarna™ (Ataluren) Summary of Product Characteristics (2019). Available online: www.ema.europa.eu/en/documents/product-information/translarna-epar-product-information_en.pdf (accessed on 19 October 2020).
- Peltz, S.W.; Morsy, M.; Welch, E.M.; Jacobson, A. Ataluren as an agent for therapeutic nonsense suppression. *Annu. Rev. Med.* **2013**, *64*, 407–425. [CrossRef] [PubMed]
- Roy, B.; Friesen, W.J.; Tomizawa, Y.; Leszyk, J.D.; Zhuo, J.; Johnson, B.; Dakka, J.; Trotta, C.R.; Xue, X.; Mutyam, V.; et al. Ataluren stimulates ribosomal selection of near-cognate tRNAs to promote nonsense suppression. *Proc. Natl. Acad. Sci. USA* **2016**, *113*, 12508–12513. [CrossRef] [PubMed]
- Drug Bank Database. Ataluren. Available online: <https://go.drugbank.com/drugs/DB05016> (accessed on 4 December 2020).
- Yeh, M.K.; Chang, L.C.; Chiou, A.H. Improving tenoxicam solubility and bioavailability by cosolvent system. *AAPS PharmSciTech* **2009**, *10*, 166–171. [CrossRef] [PubMed]
- Kong, R.; Laskin, O.L.; Kaushik, D.; Jin, F.; Ma, J.; McIntosh, J.; Souza, M.; Almstead, N. Ataluren Pharmacokinetics in Healthy Japanese and Caucasian Subjects. *Clin. Pharmacol. Drug Dev.* **2019**, *8*, 172–178. [CrossRef]
- European Medicines Agency. ICH Topic Q1A(R2): Stability Testing of New Drug Substances and Products. Available online: https://www.ema.europa.eu/en/documents/scientific-guideline/ich-q-1-r2-stability-testing-new-drug-substances-products-step-5_en.pdf (accessed on 20 October 2020).
- EDQM (European Directorate for the Quality of Medicines & Healthcare). *European Pharmacopoeia 10.5; 2020, 5.1.4 Sterility Assay 04/2011:20601*; EDQM Council of Europe: Strasbourg, France, 2020.
- Food Drug and Administration. Guidance for Industry: Drug Stability Guidelines. Available online: <https://www.fda.gov/media/69957/download> (accessed on 20 October 2020).
- Sanmartín-Suárez, C.; Soto-Otero, R.; Sánchez-Sellero, I.; Méndez-Álvarez, E. Antioxidant properties of dimethyl sulfoxide and its viability as a solvent in the evaluation of neuroprotective antioxidants. *J. Pharmacol. Toxicol. Methods* **2011**, *63*, 209–215. [CrossRef]
- Challier, C.; Mártire, D.O.; García, N.A.; Criado, S. Visible light-mediated photodegradation of imidazoline drugs in the presence of Riboflavin: Possible undesired effects on imidazoline-based eye drops. *J. Photochem. Photobiol. A Chem.* **2017**, *332*, 399–405. [CrossRef]

23. Sangchay, W.; Sikonga, L.; Kooptarnond, K. Comparison of photocatalytic reaction of commercial P25 and synthetic TiO₂-AgCl nanoparticles. *Procedia Eng.* **2012**, *32*, 590–596. [CrossRef]
24. Garner, B.; Davies, M.J.; Truscott, R.J. Formation of hydroxyl radicals in the human lens is related to the severity of nuclear cataract. *Exp. Eye Res.* **2000**, *70*, 81–88. [CrossRef]
25. Roche, M.; Lannoy, D.; Bourdon, F.; Danel, C.; Labalette, P.; Berneron, C.; Simon, N.; Odou, P. Stability of frozen 1% voriconazole eye-drops in both glass and innovative containers. *Eur. J. Pharm. Sci.* **2020**, *141*, 105102. [CrossRef]
26. Nourry, H.; Viard, C.; Cambourieu, C.; Warnet, J.M. A relevant choice for corticoid eye drops: Solution or suspension? *J. Fr. Ophthalmol.* **2011**, *34*, 691–696. [CrossRef]
27. Diestelhorst, M.; Kwon, K.A.; Süverkrup, R. Dose uniformity of ophthalmic suspensions. *J. Cataract. Refract. Surg.* **1998**, *24*, 672–677. [CrossRef]
28. Kwon, K.A.; Diestelhorst, M.; Süverkrup, R. Dosage problems in suspension eyedrops. *Klin. Monbl. Augenheilkd.* **1996**, *209*, 144–149. [CrossRef] [PubMed]
29. Salinger, C.L.; Gaynes, B.I.; Rajpal, R.K. Innovations in topical ocular corticosteroid therapy for the management of postoperative ocular inflammation and pain. *Am. J. Manag. Care* **2019**, *25* (Suppl. 12), S215–S226. [PubMed]
30. Pelletier, J.; Capriotti, K.; Stewart, K.; Barone, S.; Capriotti, J. A Novel Transdermal ophthalmic preparation for blepharitis in a dilute povidone-iodine and dimethyl sulfoxide (DMSO) system: A case series. *EC Ophthalmol.* **2018**, *9*, 129–134.
31. Brayton, C.F. Dimethyl sulfoxide (DMSO): A review. *Cornell. Vet.* **1986**, *76*, 61–90.
32. Balicki, I. Clinical study on the application of tacrolimus and DMSO in the treatment of chronic superficial keratitis in dogs. *Pol. J. Vet. Sci.* **2012**, *15*, 667–676. [CrossRef]
33. Furrer, P.; Mayer, J.M.; Plazonnet, B.; Gurny, R. Ocular tolerance of absorption enhances in ophthalmic preparations. *AAPS Pharm. Sci.* **2002**, *4*, E2. [CrossRef]
34. Hanna, C.; Fraunfelder, F.T.; Meyer, S.M. Effects of dimethyl sulfoxide on ocular inflammation. *Ann. Ophthalmol.* **1977**, *9*, 61–65.
35. Mckim, A.; Strub, R. Dimethyl sulfoxide USP, Ph.Eur in approved pharmaceutical products and medical devices. *Pharm. Technol.* **2008**, *32*, 74–85.
36. Mckim, S.; Strub, R. Advances in the regulated pharmaceutical use of dimethyl sulfoxide USP, Ph. Eur. *Pharmaceut. Technol.* **2016**, *3*, 30–35.
37. Patel, A.; Cholkar, K.; Agrahari, V.; Mitra, A.K. Ocular drug delivery systems: An overview. *World J. Pharmacol.* **2013**, *2*, 47–64. [CrossRef]
38. Skrypuch, O.W.; Tokarewicz, A.C.; Willis, N.R. Effects of dimethyl sulfoxide on a model of corneal alkali injury. *Can. J. Ophthalmol.* **1987**, *22*, 17–20.
39. Yoshizumi, M.O.; Niizawa, J.M.; Meyers-Elliott, R. Ocular toxicity of intravitreal vidarabine solubilized in dimethyl sulfoxide. *Arch. Ophthalmol.* **1986**, *104*, 426–430. [CrossRef] [PubMed]
40. Yoshizumi, M.O.; Banihashemi, A.R. Experimental intravitreal ketoconazole in DMSO. *Retina* **1988**, *8*, 210–215. [CrossRef] [PubMed]
41. Altan, S.; Sağsöz, H.; Oğurtan, Z. Topical dimethyl sulfoxide inhibits corneal neovascularization and stimulates corneal repair in rabbits following acid burn. *Biotech. Histochem.* **2017**, *92*, 619–636. [CrossRef] [PubMed]
42. Altan, S.; Oğurtan, Z. Dimethyl sulfoxide but not indomethacin is efficient for healing in hydrofluoric acid eye burns. *Burns* **2017**, *43*, 232–244. [CrossRef] [PubMed]
43. Bhalerao, H.; Koteswara, K.B.; Chandran, S. Brinzolamide dimethyl sulfoxide In Situ Gelling Ophthalmic Solution: Formulation Optimisation and In Vitro and In Vivo Evaluation. *AAPS PharmSciTech* **2020**, *21*, 69. [CrossRef]
44. OECD Guideline for Testing of Chemical, Acute Eye Irritation/Corrosion 405: 2017. Available online: <https://www.oecd.org/env/test-no-405-acuteeye-irritation-corrosion-9789264185333-en.htm> (accessed on 8 December 2020).
45. Suh, L.H.; Zhang, C.; Chuck, R.S.; Stark, W.J.; Naylor, S.; Binley, K.; Chakravarti, S.; Jun, A.S. Cryopreservation and lentiviral-mediated genetic modification of human primary cultured corneal endothelial cells. *Investig. Ophthalmol. Vis. Sci.* **2007**, *48*, 3056–3061. [CrossRef]
46. Medhi, B.; Kishore, K.; Singh, U.; Seth, S.D. Comparative clinical trial of castor oil and diclofenac sodium in patients with osteoarthritis. *Phyther. Res.* **2009**, *23*, 1469–1473. [CrossRef]
47. Oloyede, G.K. Antioxidant activities of methyl ricinoleate and ricinoleic acid dominated *Ricinus communis* seeds extract using lipid peroxidation and free radical scavenging methods. *Res. J. Med. Plants* **2012**, *6*, 511–520. [CrossRef]
48. Jena, J.; Gupta, A.K. *Ricinus communis* linn: A phytopharmacological review. *Int. J. Pharm. Pharm. Sci.* **2012**, *4*, 25–29.
49. Sandford, E.C.; Muntz, A.; Craig, J.P. Therapeutic potential of castor oil in managing blepharitis, meibomian gland dysfunction and dry eye. *Clin. Exp. Optom.* **2020**. [CrossRef] [PubMed]
50. Maissa, C.; Guillon, M.; Simmons, P.; Vehige, J. Effect of castor oil emulsion eyedrops on tear film composition and stability. *Contact Lens Anterior Eye* **2010**, *33*, 76–82. [CrossRef] [PubMed]
51. Muntz, A.; Sandford, E.; Classen, M.; Curd, L.; Jackson, A.K.; Watters, G.; Wang, M.T.M.; Craig, J.P. Randomized trial of topical periocular castor oil treatment for blepharitis. *Ocul. Surf.* **2020**, in press. [CrossRef] [PubMed]

Article

Quantification of Drugs in Distinctly Separated Ocular Substructures of Albino and Pigmented Rats

Anna-Kaisa Rimpelä , Michel Garneau, Katja S. Baum-Kroker, Tanja Schönberger, Frank Runge and Achim Sauer * 

Department of Drug Discovery Sciences, Boehringer Ingelheim Pharma GmbH & Co. KG, 88397 Biberach, Germany; anna-kaisa.rimpelae@boehringer-ingelheim.com (A.-K.R.); michel.garneau@boehringer-ingelheim.com (M.G.); katja.baum-kroker@boehringer-ingelheim.com (K.S.B.-K.); tanja.schoenberger@boehringer-ingelheim.com (T.S.); frank.runge@boehringer-ingelheim.com (F.R.)
* Correspondence: achim.sauer@boehringer-ingelheim.com; Tel.: +49-7351-54-5023

Received: 13 November 2020; Accepted: 28 November 2020; Published: 2 December 2020

Abstract: The rat is a commonly used species in ocular drug research. Detailed methods of separating rat ocular tissues have not been described in literature. To understand the intraocular drug distribution, we developed a robust method for the separation of individual anterior and posterior substructures of pigmented Brown Norway (BN) and albino Wistar Han (WH) rat eyes, followed by quantification of drug concentration in these substructures. A short formalin incubation, which did not interfere with drug quantification, enabled the preservation of individual tissue sections while minimizing cross-tissue contamination, as demonstrated by histological analysis. Following oral administration, we applied the tissue separation method, in order to determine the ocular concentrations of dexamethasone and levofloxacin, as well as two in-house molecules BI 113823 and BI 1026706, compounds differing in their melanin binding. The inter-individual variability in tissue partitioning coefficients (K_p) was low, demonstrating the reproducibility of the separation method. K_p values of individual tissues varied up to 100-fold in WH and up to 46,000-fold in BN rats highlighting the importance of measuring concentration directly from the ocular tissue of interest. Additionally, clear differences were observed in the BN rat tissue partitioning compared to the WH rat. Overall, the developed method enables a reliable determination of small molecule drug concentrations in ocular tissues to support ocular drug research and development.

Keywords: ocular; drug delivery; pharmacokinetics; tissue isolation; rat; eye; drug concentration; method; pigment; melanin

1. Introduction

Diseases of the posterior segment of the eye are the leading causes of blindness in many western countries [1,2]. Treating these diseases, however, remains challenging, due to limitations in available drugs and drug delivery methods. For many posterior segment diseases, such as the dry form of age-related macular degeneration (AMD) and normotensive glaucoma, there are no treatments available. For others, such as the wet form of AMD, diabetic retinopathy and macular edema, treatments are delivered through frequent intravitreal injections. So far, no clinical successes have been seen in developing oral or other less invasive treatments for these diseases. Therefore, there is a tremendous need to develop new therapies and improve drug delivery methods for posterior segment diseases. These challenges are being addressed with a wide variety of academic and industrial research efforts in exploring new delivery routes and developing improved formulations to deliver the drug to the posterior segment less invasively [3–5]. In addition, new therapeutic concepts are being evaluated in

various animal models [6,7] and attempts are being made to repurpose old active molecules for ocular indications [8].

Ocular drug research requires information on local ocular drug concentrations, whether it is to assess drug release from formulations, in order to evaluate pharmacokinetics of ocular drugs or to assess their efficacy in animal models. An important pre-requisite for developing a successful new treatment is to deliver the drug to the target tissue at therapeutic concentrations. The eye is a pharmacokinetically complex organ, with a multitude of tissue barriers and uneven drug distribution into its substructures. For small molecule drugs, accumulation caused by melanin binding in the highly pigmented retinal pigment epithelium (RPE) and choroid in the posterior segment, as well as the iris and ciliary body (CB) in the anterior segment of the eye can result in large concentration differences between pigmented and non-pigmented tissues [9,10]. As targets for posterior segment diseases are located in both, the pigmented and non-pigmented tissues (neural retina, RPE and choroid), it is crucial to evaluate the concentration of the drug in the specific target tissue, enabling a thorough assessment and refinement of pharmacokinetic/pharmacodynamic (PK/PD) relationships of ocular drug candidates.

Despite its small eye size, the rat is a commonly used model species in ocular drug research [11]. Due to wide availability, easy handling, relatively low cost and ethical reasons, various disease models have been developed in the rat. For the same reasons, the rat is also used for early ocular pharmacokinetic evaluations. To date, only limited literature is available on the methods of tissue separation of the rat eye. Previous studies on ocular concentrations in the rat, either consider the eyes as a whole [12], differentiate only between a few ocular tissues [13–15] or refrain from describing tissue separation methods in detail [9]. The rabbit is another frequently used species in ocular studies, but the information on the methodology used for tissue separation of the rabbit eye is also limited [16]. Due to the small size of the rat eye, the separation process is more delicate compared to the rabbit eye and the risk of cross-tissue contamination is higher. For melanin-binding drugs, a contamination originating from the pigmented tissues, can lead to considerable overestimation of drug concentration in non-pigmented tissues. To the best of our knowledge, this contamination has not been considered in the literature in any animal species previously. For the various reasons listed above, there is a significant need for a reliable and reproducible method to separate the distinct substructures of the rat eye, overcoming the limitations and lack of method description of previously reported studies.

The aim of the present study was to develop a method for the separation of rat ocular tissues and their processing for quantification of small molecule drug concentrations. As both albino and pigmented rats are used in pre-clinical research, understanding the impact of melanin binding on ocular distribution is highly important for small molecule drugs. Consequently, we developed the method in albino Wistar Han (WH) and pigmented Brown Norway (BN) rats and demonstrated its functionality in vivo with four compounds. The method enables the quantification of drug concentrations from individual ocular tissues of the rat eye while the obtained results emphasize the importance of measuring tissue-specific concentrations.

2. Materials and Methods

2.1. Chemicals

Dexamethasone (purity $\geq 97\%$) and levofloxacin (purity $\geq 98\%$) were obtained from Sigma Aldrich (St. Louis, MO, USA) and BI 113823, as well as BI 1026706 from the in-house dispensary at Boehringer Ingelheim (BI). Melanin from *Sepia officinalis* and synthetic melanin were obtained from Sigma Aldrich together with sodium hydroxide (NaOH), bovine serum albumin (BSA) and formalin solution (10%, neutral buffered). Dimethyl sulfoxide (DMSO) was purchased from Merck Millipore (Burlington, MA, USA). Phosphate buffered saline (PBS) was made from one vial of phosphate buffer powder (pH 6.6, Sigma Aldrich) and 34.2 g of NaCl (Sigma Aldrich) by mixing both in purified water (Milli-Q, MilliporeSigma, Burlington, MA, USA) in a total volume of 3.8 L. The pH was adjusted to 6.5 with

HCl. Ethanol (EtOH) was obtained from Carl Roth GmbH (Karlsruhe, Germany). Acetonitrile (ACN) was purchased from Honeywell (Charlotte, NC, USA). Tween-80 (Polysorbat 80) and hydroxyethyl cellulose (Natrosol) for the oral suspension formulation of the drugs were obtained from Dr. W. Kolb AG (Hedingen, Switzerland) and Ashland Industries Deutschland (Düsseldorf, Germany), respectively.

2.2. Animals

All animal experiments were conducted in accordance with the German and European Animal Welfare Act and authorized by the Regierungspräsidium Tübingen as the responsible local German authority under reference numbers 14-009-G (25 June 2014) and 19-004-G (04 June 2019). Animal experiments were performed in male Wistar Han (Crl:WI(Han)) and Brown Norway (BN/Crl) rats (Charles River Research Models and Services Germany GmbH). The average weight of the animals was 220 g (range 204–260 g). The animals were housed under a 12-h light/dark cycle with free access to standardized pelleted food (Granovit AG) and water.

2.3. Ocular Tissue Distribution Study

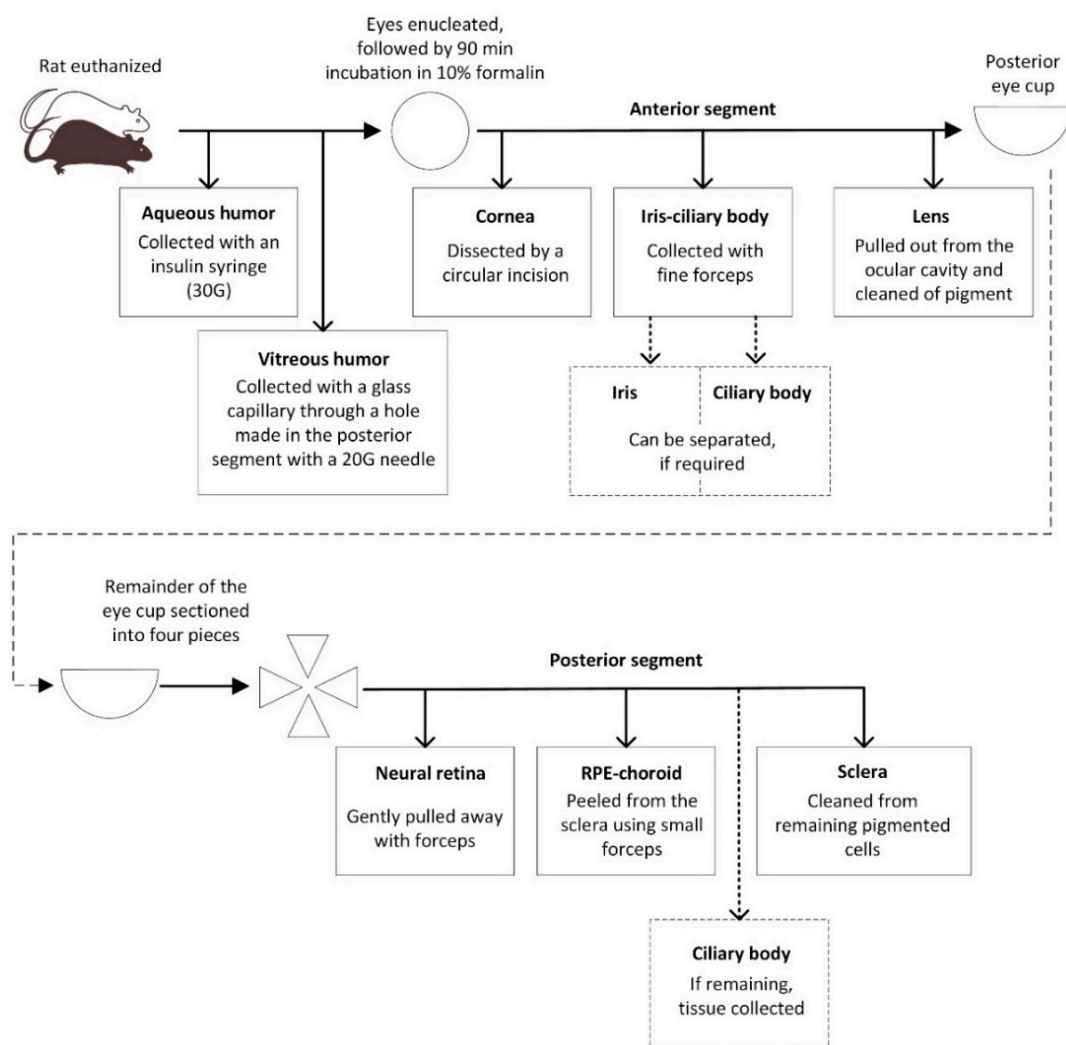
Cocktails of either dexamethasone (4 mg/kg) and levofloxacin (7 mg/kg) (cocktail 1) or the two internal Boehringer Ingelheim compounds BI 113823 (10 mg/kg) and BI 1026706 (10 mg/kg) (cocktail 2) were administered to the rats via oral gavage ($n = 3$ rats/strain for cocktail 1 and $n = 2$ rats/strain for cocktail 2) at a dose volume of 2 mL/kg. The compounds were dosed as a suspension in a vehicle consisting of 0.015% Tween-80 and 0.5% hydroxyethyl cellulose in water. Blood samples were obtained under isoflurane anesthesia at 0.25, 0.5, 1, 2, 4, and 8 h. Blood was collected from the sublingual vein into K₃EDTA coated vials (Sarstedt, Nümbrecht, Germany) and plasma was obtained by centrifugation for 5 min at approximately 3500× *g*. At 8 h, the anesthetized animals were euthanized by anesthetic overdose followed by exsanguination, and ocular tissues were collected, as described below. In addition, a small piece of the femoral muscle was excised as a reference tissue for tissue distribution as previously described by Cui et al. [17].

2.4. Ocular Tissue Separation and Sampling

Ocular tissue separation was performed under microscope control (Carl Zeiss f-170 Stereoscope, Oberkochen, Germany). Immediately following euthanasia, the aqueous and vitreous humor were collected. The aqueous humor was sampled via an insulin syringe (30 G) introduced through the cornea into the anterior chamber, transferred to a vial and frozen pending analysis. A sample from the vitreous humor was collected via a glass capillary using a modification of the mousetrap technique [18]. A 20 G needle was used to puncture the posterior segment of the eye (2 mm posterior to the limbus). A glass microelectrode with a broken tip (borosilicate glass, wall thickness 0.225 mm, outside diameter 1.5 mm; Hilgenberg GmbH, Malsfeld, Germany; pulled with a DMZ-Universal Puller, Zeitz-Instruments GmbH, Munich, Germany) was inserted posterior to the lens. Approximately 6 µL of vitreous humor was slowly aspirated into the glass microelectrode via silicone tubing, connected to a low volume syringe, placed in a vial and frozen.

The eye was then carefully enucleated, any extraocular material was removed, and the eye was fixed in 2 mL of 10% formalin for 90 min at room temperature. After fixation, the eye was blotted dry to remove excess formalin and placed on a holding block with the cornea facing up. Under the dissection microscope, the cornea was dissected by a circular incision in the limbus region. It was then removed and cleaned of other tissues. The iris and pieces of the ciliary body were separated from other tissues (cornea and/or lens) using a pair of fine forceps. The lens was pulled out of the ocular cavity and freed of any remaining contaminating tissue. The remainder of the eye cup was placed on a flat surface. Starting from the optic nerve toward the ora serrata, the eye was carefully sectioned into four pieces using a scalpel. If any vitreous humor was still present, it was carefully removed. Using a pair of fine forceps, the neural retina was detached from the eye at the optical nerve junction and at the ora serrata. The neural retina was gently pulled away from the eye. Heavily contaminated retinal sections

were discarded and any residual pigmented tissues removed with fine forceps. The RPE-choroid was peeled from the sclera using small forceps. Care was taken not to collect the remaining part of the ciliary body that might have been left attached to the eye; the remaining ciliary body was collected and added to the iris-CB sample. The remaining scleral tissue was cleaned from adherent pigmented cells by wiping with a cotton swap. All the dissected tissues were placed in pre-weighed tubes. All tubes were weighed and the tissue weights recorded. The step-by-step tissue separation process is described in Scheme 1 and illustrated in Figure S1.



Scheme 1. Ocular tissue separation procedure. RPE = retinal pigmented epithelium.

2.5. Effect of Formalin Fixation on Drug Recovery

We tested the effect of formalin fixation on drug recovery by performing an additional ocular distribution study with cocktail 1 compounds (same study design as described above) in both rat strains ($n = 3$ rats/strain). At the 8 h timepoint, aqueous and vitreous humor collection followed by enucleation was performed as described above. The right eye was immediately separated in the distinct ocular tissues (cornea, iris-CB and lens). The posterior part of the eye was kept intact (retina, RPE-choroid and sclera), as a clean separation of the tissues from the fresh eye was not achievable. All tissues were weighed and frozen until analysis. The entire left eye was immediately added to 2 mL of 10% formalin. Following the 90-min formalin incubation, the cornea, iris-CB and lens of the left eye were isolated as described above while the posterior section (retina, RPE-choroid and sclera) was kept as a whole. All tissues were weighed and frozen pending analysis.

2.6. Melanin Binding and Drug Extraction from Melanin

We measured the melanin binding of the compounds *in vitro* with melanin from *Sepia officinalis* applying a previously described method [19]. The compounds (1 μM) were incubated with Sepia melanin (1 mg/mL in PBS pH 6.5) in a volume of 500 μL . After 2 h of incubation, the tubes were centrifuged at $20,000\times g$ for 15 min to pellet the melanin with the bound drug, and the supernatant was sampled for quantification of the unbound drug concentration. We measured the extraction of the compounds from the melanin-drug pellets, first with a standard tissue extraction solvent (EtOH:H₂O (4:1)), and thereafter, with a basic solvent (100 mM NH₄OH in EtOH:H₂O (4:1)) in case the extraction was low with the first solvent. The supernatant was fully removed and the pellet was resuspended in 500 μL of the solvent. The suspension was then moved to a 2-mL Precellys[®] homogenization tube (CKMix, Bertin Instruments, Montigny-le-Bretonneux, France) and homogenized with a Precellys[®] Evolution homogenizer (Bertin Instruments, Montigny-le-Bretonneux, France) at 5500 rpm (three cycles of 40 s with a 30 s break in between) to replicate the process to be used for the *in vivo* tissue samples. After homogenization, the tubes were centrifuged at $14,200\times g$ for 10 min. A sample from the supernatant was taken for the analysis of the amount extracted from the melanin and subsequent calculation of the extraction rate. For cocktail 1 drugs, this process was repeated twice to assess if more compound could be extracted by repeated washing. Control samples for the analysis of the total drug concentration were incubated in the same manner as in the binding assay, but the melanin suspension was replaced with PBS (pH 6.5) containing 0.1% BSA to prevent nonspecific binding of the compounds to the tube.

The samples were analyzed by high performance liquid chromatography coupled to tandem mass spectrometry (HPLC-MS/MS) with a similar method described later for the tissue samples. The samples were prepared for the analysis by mixing 25 μL of the sample with 50 μL of ACN:H₂O (4:1), 25 μL of an internal standard solution, 25 μL of blank matrix (either PBS with 0.1% BSA or PBS pre-incubated with melanin), and 200 μL of ACN. The prepared samples were then centrifuged at $3200\times g$ for 10 min, and a 120 μL sample of the supernatant was mixed with 120 μL of ACN:H₂O (4:1). The identified extraction solvents were later applied to the *in vivo* tissue samples.

2.7. Tissue Sample Preparation and Analysis

Pre-weighed ocular tissue samples were homogenized with a Precellys[®] Evolution homogenizer in the same manner as for the compound extraction from melanin. The extraction solvent used for each cocktail was selected based on the *in vitro* extraction study described above: 100 mM NH₄OH in EtOH:H₂O (4:1) was used for cocktail 1 (dexamethasone, levofloxacin) and EtOH:H₂O (4:1) for cocktail 2 (BI 113823, BI 1026706). Extraction volume (i.e., extraction ratio) depended on the tissue and ranged from 10 to 250 $\mu\text{L}/\text{mg}$ tissue. Detailed information can be found in Supplementary Material (Table S1). After the homogenization, the samples were centrifuged at $14,200\times g$. Internal standard in ACN or ACN:methanol (1:1) was added to an aliquot of the supernatant before sample analysis. The plasma samples were directly diluted with the internal standard, centrifuged, and further diluted 1:2 with 0.1% formic acid. To avoid unnecessary use of animals, standard curves prepared in WH rat plasma with the same pre-treatment as used for the plasma samples and used for all plasma and tissue samples. To confirm the validity of the standard curve for specific tissue samples, quality control (QC) samples were prepared in appropriate strain-specific tissues at three different concentrations; the tissue was homogenized, as described above for the tissue samples and the homogenate was spiked with the compound.

Drug concentrations in the samples were determined by HPLC-MS/MS. BI 113823 and BI 1026706 were quantified using [¹³C₂D₂]BI 113823 and [¹³CD₂¹⁵N]BI 1026706 as internal standards. Dexamethasone and levofloxacin were quantified without an internal standard. Calibration ranges for each compound are listed in Table S2. The assays comprised sample clean-up by protein precipitation, chromatography with gradient elution on a 1260 Infinity II HPLC-system (Agilent Technologies, Waldbronn, Germany) equipped with a Waters Acquity HSS T3, 2.1 \times 50 mm, 1.8 μm analytical

HPLC column (BI compounds) or a Phenomenex Luna Omega Polar C18, 2.1 × 50 mm, 1.6 μm column (dexamethasone, levofloxacin) and detection and quantification of the analytes by electrospray ionisation in the positive ion mode on a API6500 (AB (SCIEX, Concord, ON, Canada). For quantification, transitions from $m/z = 525.3 \rightarrow 181.2$ and $m/z = 529.3 \rightarrow 181.3$ were recorded for BI 113823 and its internal standard, respectively, $m/z = 536.2 \rightarrow 155.1$ and $m/z = 540.0 \rightarrow 156.1$ for BI 1026706 and its internal standard, respectively. The transitions $m/z = 393.1 \rightarrow 373.1$ and $m/z = 362.1 \rightarrow 318.1$ were recorded for dexamethasone, and levofloxacin, respectively. Concentration results are reported as nmol/L (nM) assuming a tissue density of 1 g/mL.

Tissue/plasma concentration ratios, i.e., tissue partition coefficients (Kp_{tissue}), were calculated of the concentrations based on Equation (1), where C_{tissue} refers to the concentration in the tissue and C_{plasma} to plasma concentration. The ratio of tissue partitioning between BN and WH rat (BN/WH ratio) was calculated according to Equation (2):

$$Kp_{tissue} = C_{tissue} / C_{plasma} \quad (1)$$

$$BN / WHratio = Kp_{tissue,BN} / Kp_{tissue,WH} \quad (2)$$

2.8. Histology

To investigate the level of cross-tissue contamination, we prepared the ocular tissues for histological examination using the above-described protocol. After separation of the different ocular layers, the tissues were cut into smaller pieces and transferred into histology cassettes. To avoid sample loss and to keep the samples flat, sponges and filter paper were used. The samples were fixed in 10% neutral buffered formalin for approximately 24 h, processed with an automated tissue processor (Tissue-Tek[®] VIP[®] 6, Sakura Finetek Europe B.V., Alphen aan den Rijn, the Netherlands), embedded in paraffin and cut in 3 μm sections. Staining with hematoxylin and eosin (HE) was performed according to standard protocols.

2.9. Melanin Contamination in the Neural Retina

To estimate the possible contamination in the neural retina from the underlying, highly pigmented RPE-choroid in the BN rat, we measured the melanin content of pooled retinal samples (two replicates of two pooled retinas) where no measures were taken to avoid contamination in the isolation process (i.e., the retinal tissue sample was not cleaned of remaining pigmented tissue). Melanin content was determined using the sodium hydroxide solubilization method [20–22] with small modifications. The isolated retina was diluted 1:40 (*w:v*) with EtOH:H₂O (4:1) and homogenized with Precellys[®] Evolution homogenizer at 5500 rpm (three cycles of 40 s with a 30 s break in between). The homogenization cycle was run twice to assure a homogeneous melanin concentration. An aliquot of the homogenate was then mixed with 1.5 parts of 1.7 M NaOH:DMSO (9:1) and the samples were heated at 90–95 °C for 30 min to solubilize the tissue and melanin. The absorbance of the sample was immediately measured at 475 nm with SpectraMax 340PC384 microplate reader (Molecular Devices, San Jose, CA, USA) using a Nunc MaxiSorp 96-well plate (Thermo Fisher Scientific, Waltham, MA, USA) with an 80 μL sample volume.

We made a calibration curve for the retinal melanin contamination measurement by spiking albino (WH) rat retina with RPE-choroid from the pigmented BN rat. Both tissues were individually homogenized as mentioned above, and 1.5 parts of 1.7 M NaOH:DMSO (9:1) was added to aliquots of the homogenates. The albino retina was then spiked with pigmented RPE-choroid before heating these spiked calibration samples at 90–95 °C for 30 min and measuring the absorbance as described for the retinal samples above. The lower limits of quantification (LLOQ) and detection (LLOD) were determined from the absorbance of 14 blank samples (albino retina without added RPE-choroid) as follows:

$$LLOQ = mean + 10 \cdot SD \quad (3)$$

$$LLOD = mean + 3.3 \cdot SD \quad (4)$$

3. Results

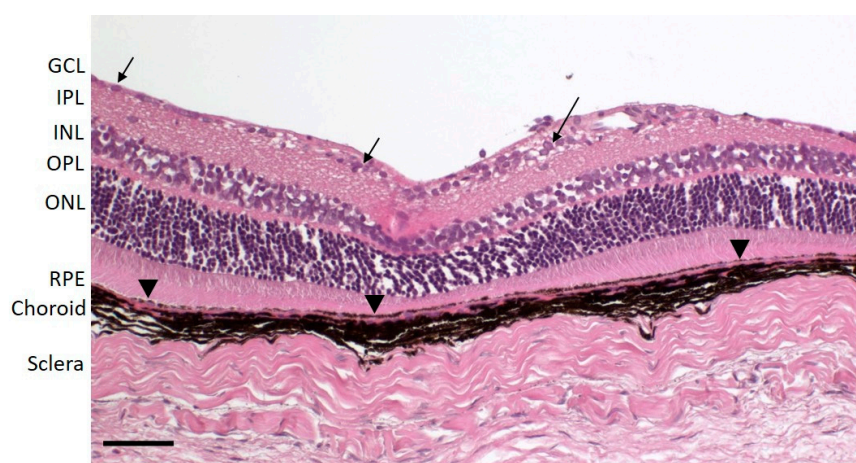
3.1. Ocular Tissue Separation

3.1.1. Separation of Ocular Substructures

For the separation of contamination-free ocular structures of a small rat eye, it is important to maintain the macroscopic structure of the eye as long as possible. We observed that collecting the aqueous and vitreous humor before enucleation of the eye prevented the eye from collapsing during aspiration. Aspirating the aqueous and vitreous humors lead to clear and consistent sample volumes of ca. 10, and 6 μL , respectively, amenable to HPLC-MS/MS analysis.

In our experience, a dissection of the retina without contamination from melanin containing structures was neither possible from freshly withdrawn nor from frozen rat eyes. Introducing a short fixation step allowed an easy separation of the tissues and led to minimal cross-tissue contamination. An optimal fixation was reached after 90 min in 10% formalin. Shorter fixation times resulted in softer tissues that were hard to separate whereas longer fixation times lead to brittle tissues, especially for the RPE-choroid. Applying this technique, we were able to separate the cornea, iris, ciliary body, lens, retina and the sclera. Iris and ciliary body were combined for compound quantification due to low sample volume. A separation of the cell monolayer RPE from the choroid was mechanically impossible; therefore, these two structures had to be sampled together.

Histological images of the anterior and posterior segment tissues are presented in Figure 1. The contamination observed in different tissue sections was very low and showed low variability; the images shown were chosen to describe the level of contamination representatively. Only the sclera shows some visible contamination; this low level of contamination originates from the choroid and can be detected as pigment deposits on the scleral tissue (Figure 1b). As many targets for posterior segment diseases are located in the retina, we were particularly interested in avoiding contamination of the retina by the underlying, highly pigmented RPE-choroid. Figure 2 shows a series of images of the retina; contaminations were rare and essentially negligible in relation to the size of the isolated pieces of retina. These histological data indicate good reproducibility and high-quality separation.



(a)

Figure 1. Cont.

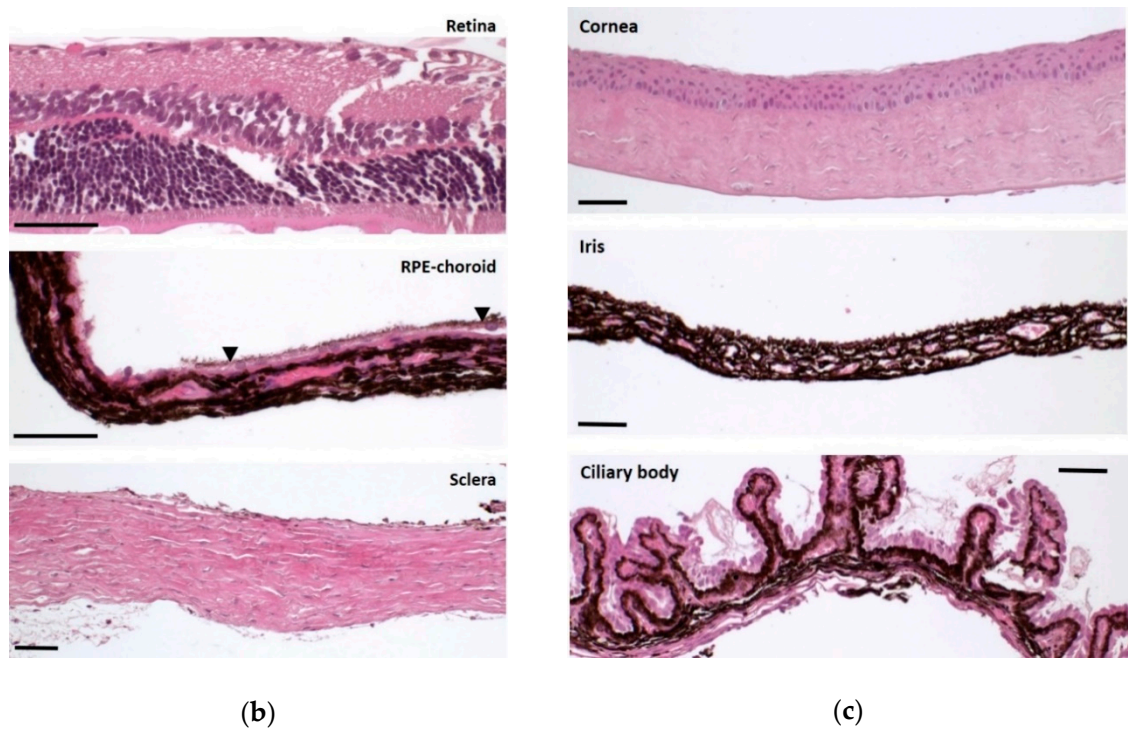


Figure 1. Histology images of BN rat ocular tissues demonstrating the low cross-tissue contamination observed with the presented separation technique. All bars: 50 μm . (a) Posterior segment with ganglion cell layer (GCL, black arrows), inner plexiform layer (IPL), inner nuclear layer (INL), outer plexiform layer (ONL), outer nuclear layer (ONL), retinal pigment epithelium (RPE, black arrow heads), choroid, and sclera. (b) Separated posterior segment tissue layers from top to bottom: retina, RPE-choroid, sclera. (c) Separated anterior segment tissue layers from top to bottom: cornea, iris, ciliary body.

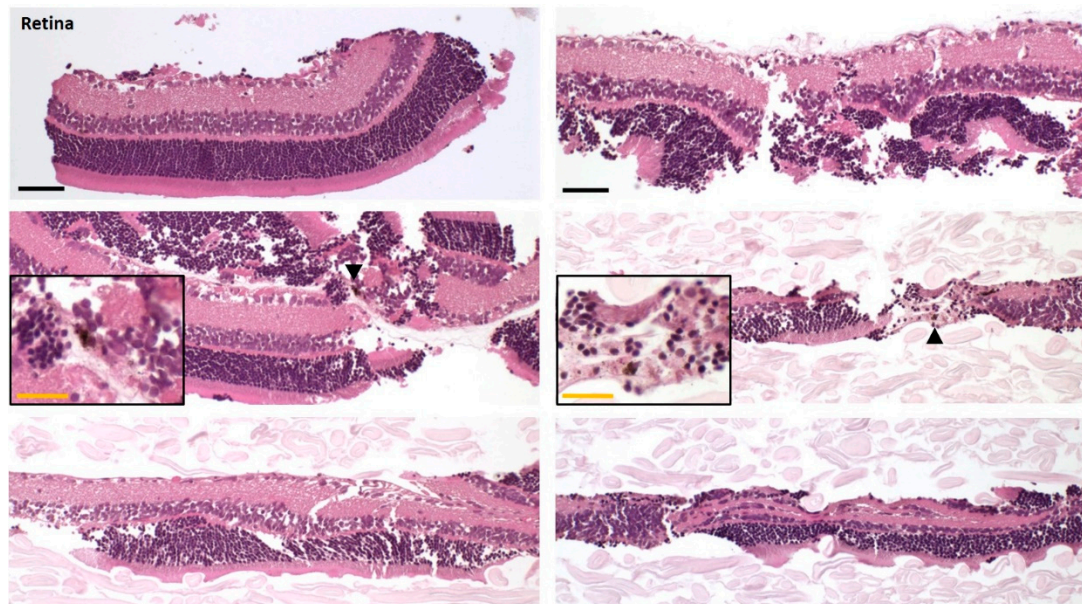


Figure 2. Histology images of retina preparations of several BN rat eyes demonstrating the low cross-tissue contamination observed with the presented separation technique. Black arrowheads show the rarely observed contamination; inserts show these areas magnified. Black bar: 50 μm (applies to all six figures), yellow bar: 25 μm (applies to the insert where shown).

3.1.2. Melanin Contamination in the Neural Retina

To estimate the contamination of the separated neural retina from the underlying RPE-choroid, we measured the RPE-choroid content in the retinal tissue by measuring absorbance originating from melanin in the RPE-choroid. For this purpose, we prepared a calibration curve with albino retina spiked with pigmented (BN) rat RPE-choroid. The LLOD and LLOQ were 1.2%, and 3.3% of RPE-choroid in the retina (*w/w*), respectively.

The melanin content, and thus, the contamination with RPE-choroid of the analyzed pooled retinas was below the LLOD, indicating low contamination. We also attempted to measure the melanin content of the individual retinal samples from which the compound concentration was later determined. Boiling of smaller volumes resulted in high variability in the measurement (data not shown). Therefore, this approach was not suitable to reliably estimate the melanin contamination in the individual retinal samples due to the low sample volume.

3.2. Melanin Binding and Drug Extraction from Melanin

We determined the melanin binding of the compounds *in vitro* with *Sepia* melanin (1 mg/mL melanin, 1 μ M compound). BI 113823 and levofloxacin had clearly higher melanin binding than BI 1026706 and dexamethasone (Table 1). In the same assay, we evaluated the extraction of the compounds from melanin to choose a suitable extraction solvent for the *in vivo* samples. As the *in vivo* tissue distribution study was performed by coadministering two compounds at once, the extraction had to be optimized for the respective compound cocktails. The results are listed in Table 1. Extraction was first determined in EtOH:H₂O (4:1), a solvent commonly used in-house for tissue drug extraction. For the cocktail 1 compounds, dexamethasone extraction was above 50% but levofloxacin extraction was low. Basic conditions (100 mM NH₄OH in EtOH:H₂O (4:1)) improved the extraction of levofloxacin. Repeated washing did not improve the extraction of either of these compounds as less than 10% additional extraction was observed with the second and third washings. Therefore, the level of ca. 50% extraction was accepted, and the basic solvent was selected for the *in vivo* extraction of cocktail 1 compounds. For both compounds in cocktail 2 (BI compounds), the extraction ratio in the original solvent was acceptable and this solvent was used for the *in vivo* extraction.

Table 1. *In vitro* melanin binding and extraction of the studied compounds from *Sepia* melanin (1 mg/mL melanin and 1 μ M compound concentration). Individual values presented if two replicates were studied, mean \pm standard deviation presented if more than two replicates.

Study/Solvent	Fraction Unbound or Extracted (%)			
	In vivo Cocktail 1		In vivo Cocktail 2	
	Dexamethasone	Levofloxacin	BI 1026706	BI 113823
Melanin binding (unbound fraction (%))	58; 59	1.3 \pm 0.5 ¹	33 \pm 5 ²	3.9 \pm 0.7 ²
Extraction EtOH:H ₂ O (4:1)	52; 56	5; 18	43; 48	64; 75
Extraction 100 mM NH ₄ OH in EtOH:H ₂ O (4:1)	51; 53	59 \pm 13 ¹	ns	ns

¹ Four replicates, ² six replicates, ns = Not studied.

3.3. Effect of Formalin Fixation on Compound Recovery

We tested the effect of formalin fixation on the recovery of cocktail 1 compounds by performing an additional ocular distribution study in both rat strains and comparing the recovery of compounds from fixed and fresh eyes. In the BN rat, the fixed vs. fresh recovery of each tissue substructure was within the accepted bioanalytical variation of 70–140%, indicating a low effect of formalin fixation on compound recovery (Table 2). Similar variation was observed in the vitreous and aqueous concentrations of left vs. right eye (these were sampled from the fresh eye in all cases). In the WH rat, the recovery was

again mostly within the 70–140% range, except for the slightly lower recovery observed in the cornea and posterior segment.

Table 2. Recovery of cocktail 1 compounds from substructures of fixed compared to fresh rat eyes. Recovery calculated as percentage of concentration in fixed eye compared to fresh eye. Aqueous and vitreous were sampled from fresh eyes in both cases.

Tissue	Dexamethasone		Levofloxacin	
	BN	WH	BN	WH
Fixed vs. fresh tissue				
Cornea	131 ± 18	66 ± 13	86 ± 20	55 ± 10
Iris-CB	87 ± 7	85 ¹	138 ± 32	95 ± 21
Lens	91 ± 18	145; 102 ¹	109 ± 5	161; 110 ¹
Posterior segment	70 ± 7	49 ± 4	95 ± 16	49 ± 7
Left vs. right eye				
Aqueous	85, 106 ¹	115 ± 21	108 ± 12	104 ± 10
Vitreous	128 ± 8	122 ± 34	153 ± 35	104 ± 3

¹ Individual values as data available from only one or two samples.

3.4. Drug Concentrations in Ocular Tissues

To investigate the ocular distribution of the drugs, the drug cocktails were administered orally (via gavage) to 2–3 rats/strain (n = 4–6 eyes). Blood and tissues samples were collected to monitor systemic exposure as well as ocular tissue distribution (Figure S1). The tissue results are depicted in Figure 3 as Kp values. Kp values for whole eyes were calculated from the individual tissue values based on hypothetical volumes of the individual tissues. The tissue volumes used as well as the measured tissue concentrations and plasma concentrations can be found in Supplementary Material (Figure S2, Tables S3 and S4).

The inter-individual variability of tissue partitioning for a given compound in a given tissue was low (Figure 3 and Table S4), demonstrating the reproducibility of the method. Varying differences were observed between ocular tissues of the same strain (inter-tissue differences, Figure 3). For all four compounds, the lowest concentrations in both WH and BN rat eyes were detected in the aqueous, vitreous and lens. In WH rats, the highest tissue concentrations were found in the RPE-choroid for the two BI compounds. In contrast, levofloxacin showed the highest concentration in the cornea while dexamethasone had very similar concentrations in all non-humorous tissues. The calculated Kp values largely varied across tissues, the difference between the lowest and highest Kp was 6.3-, 12-, 21- and 100-fold, for dexamethasone, levofloxacin, BI 1026706 and BI 113823, respectively. In BN rats, for all tested compounds, the concentrations in the pigmented tissues iris-CB and RPE-choroid were the highest, leading partially to very extensive lowest-to-highest Kp differences of 65-, 1,100-, 290- and 46,000-fold for dexamethasone, levofloxacin, BI 1026706 and BI 113823, respectively. The 6- to 100-fold Kp differences in albino rats and, more profoundly, the 65- to 46,000-fold differences in pigmented rats illustrate the importance of understanding the exposure in the relevant ocular substructures.

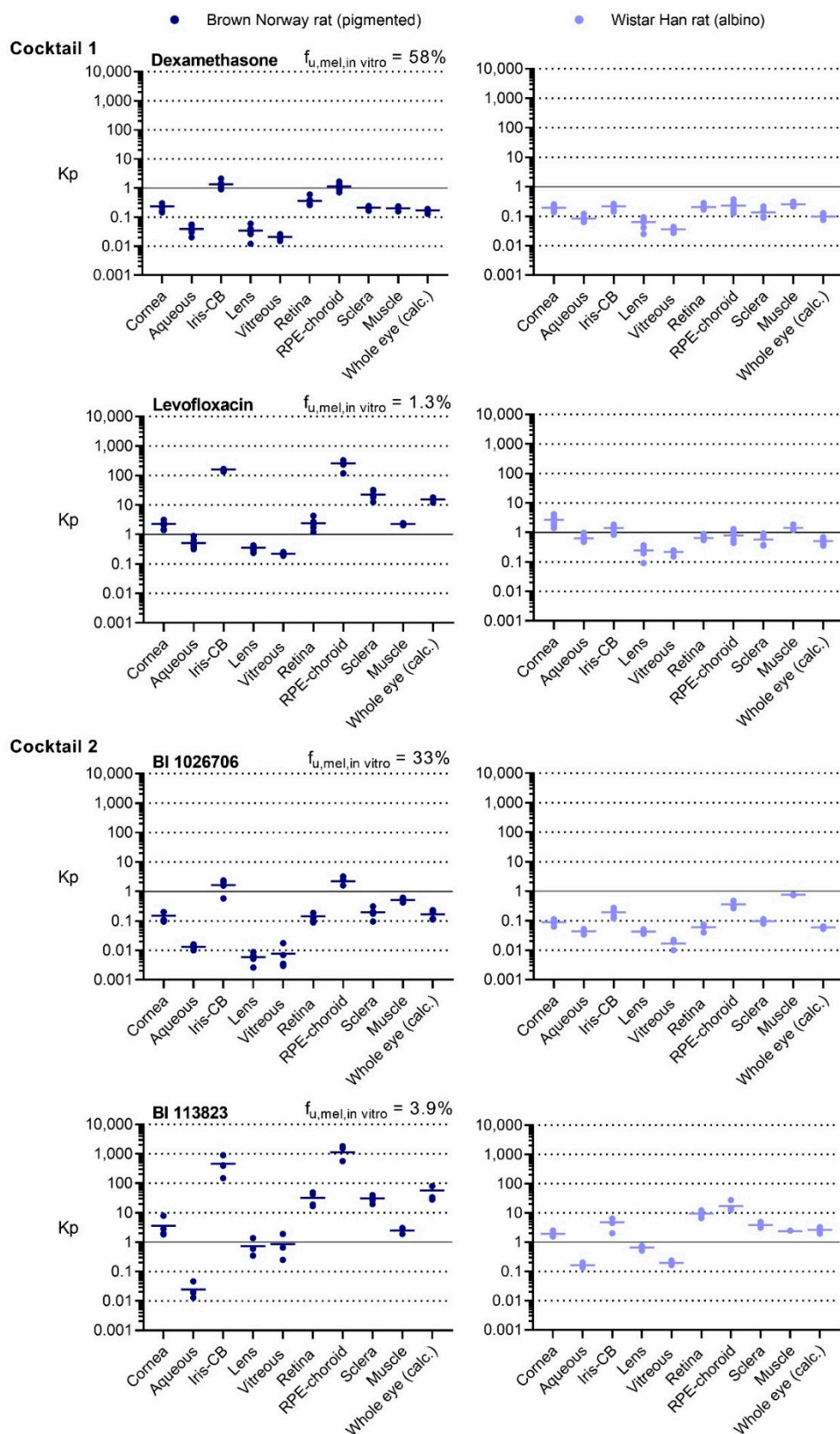


Figure 3. Tissue partitioning (Kp) of the compounds 8 h after oral administration to rats. The individual values for each eye ($n = 4-6$ eyes) are shown and the mean is presented as a line. Whole eye value was calculated (calc.) with hypothetical volumes (Table S3) for the individual tissues. The measured in vitro melanin binding (1 mg/mL melanin, 1 μ M compound) is shown for each compound ($f_{u,meI,in\ vitro}$).

To better understand whether the distribution into non-pigmented ocular structures is comparable between albino and pigmented animals, we calculated Kp ratios between BN and WH rats (BN/WH ratio) (Table 3). For the muscle as a reference tissue, the ratio ranged from 0.68 to 1.6, which is close to the theoretical value of one. As expected, the ratios for iris-CB and RPE-choroid were much higher. There was an apparent link between sclera ratios and the corresponding RPE-choroid ratios, indicating a contamination of this tissue with material from the RPE-choroid which was also visible after tissue separation. Interestingly, the relative concentrations of BI 1026706 were higher in albino than in pigmented animals in the aqueous and vitreous humor and even more pronouncedly in the lens (BN/WH ratios below 1 in Table 3). For BI 113823 we found an increased BN/WH ratio of 4.4 in the vitreous but a low ratio of 0.15 in the aqueous humor. Thus, also non-pigmented ocular tissue partitioning can differ between non-pigmented and pigmented animals.

Table 3. Ratio of Kp values between pigmented BN and albino WH rat (BN/WH ratio). The ratios were calculated from the average Kp values. Whole eye value was calculated (calc.) with hypothetical volumes (Table S3) for the individual substructures.

Tissue	Dexamethasone	Levofloxacin	BI 1026706	BI 113823
Cornea	1.2	0.85	1.7	1.9
Aqueous	0.47	0.80	0.31	0.15
Iris-CB	6.2	113	8.5	96
Lens	0.55	1.4	0.14	1.1
Vitreous	0.57	1.0	0.45	4.4
Retina	1.8	3.7	2.4	3.4
RPE-choroid	5.0	320	6.2	66
Sclera	1.6	40	2.1	8.0
Muscle	0.8	1.6	0.68	1.0
Whole eye (calc.)	1.7	30	2.8	21

4. Discussion

Although, ocular pharmacokinetic studies in rats can be found in the literature [9,12–15,23], they rarely report the methods by which the different ocular tissues were isolated and treated after the isolation. In particular, for species with smaller eyes (rat eye diameter ca. 6 mm), the availability of robust, reproducible separation methods is an important cornerstone to gain better understanding of ocular drug distribution and PK/PD. We describe, here, a method allowing a stepwise separation of the anterior and posterior substructures of the rat eye and quantification of small molecules in the separated structures. The reported method, based on a short fixation of the eye in formalin before tissue separation, offers a simple and refined way to isolate the specific tissues with minimal cross-contamination.

Small molecules exhibit high melanin binding potential, stressing the need for clean separation of the posterior segment tissues, retina and RPE-choroid, since a small contamination of the retina with melanin containing tissue could lead to a considerable over-estimation of retinal drug concentrations. Unfortunately, retina and RPE-choroid of the rat eye are very difficult to distinctly separate from one another. We chose to fix the eye in formalin before the separation process, as formalin is known to induce retinal detachment [24] and preserve tissue structure. A short fixation time of 90 min, considerably shorter than the generally used tissue fixation times for histology purposes (overnight or longer), was optimal for our purpose.

Due to the massive concentration differences possible between pigmented and non-pigmented ocular tissues, we applied two methods to investigate retina contaminations with pigmented tissue. While the low melanin content determined in the pooled retinas via the less sensitive photometry was encouraging, the histology of the separated retinas demonstrated the efficiency of the separation

process leading to essentially no contaminations with RPE-choroid. We consider this achievement of high importance for an accurate quantification of compounds with melanin binding potential in the retinal tissue.

To understand the effect of fixation on compound recovery, we compared the recovery of the cocktail 1 compounds, levofloxacin and dexamethasone, from fresh and fixed eyes in both rat strains (Table 2). For most of the tissues, fixation had no impact on the recovery, as the concentration in the fixed eye relative to the fresh eye was within the typically accepted error range of analytical methods. For the cornea and the posterior segment in the WH rat, however, we saw a lower recovery of 49 to 66% for both compounds. These lower recoveries could be due to the compound diffusing from these substructures to the formalin or to swelling of the collagen-rich tissues cornea and sclera, as collagenous tissues are known to swell during formalin fixation [25]. It appears likely that the sclera, being the largest tissue of the posterior segment and residing on the surface in direct contact with the formalin, is the major source for the observed lower recovery in the posterior segment. Whether this lower recovery is a result of compound loss or weight gain of the tissues, is out of the interest of this study, considering that the sclera is not a typical target tissue for ocular therapies. As our tissues of interest are mainly in the inner parts of the eye, we consider the method suitable for the reliable analysis of ocular concentrations for our purpose. In case the main tissues of interest for the concentration measurement are in the anterior segment, separating the tissues from fresh eyes may be preferred as this method avoids the possible artifacts (tissue swelling and drug diffusion) with respect to the cornea.

HPLC-MS/MS analysis of the tissue drug concentrations requires the drug to be extracted from the tissue before analysis. Melanin binding of drugs occurs reversibly via different types of electrostatic and hydrophobic interactions between the drug and the melanin polymer depending on the molecular properties of the drug [26–28]. It has been observed that some solvents do not extract all of the bound drug from melanin [15,29–31], which is explained by the different effects of solvents on the drug-melanin interactions. We evaluated solvent extraction efficiency from melanin *in vitro*, as direct measurement from *in vivo* samples would require the use of radiolabeled compounds. Apart from levofloxacin, the compounds showed good extraction in EtOH:H₂O (4:1). The low recovery of levofloxacin with this solvent and the improvement of the extraction by increasing the basicity of the solvent demonstrated the importance of considering this technical aspect. To improve the accuracy of *in vivo* concentration measurements, we recommend to optimize compound-specific melanin extraction *in vitro*.

We applied the tissue separation method to determine the ocular concentrations of levofloxacin and dexamethasone, as well as the two proprietary in-house compounds 8 h after oral administration. We could see substantial ocular distribution with BI 113823 and levofloxacin, as most of the ocular tissues had higher concentrations than the concentration in plasma. The two other compounds, BI 1026706 and dexamethasone, had lower ocular distribution with majority of the tissues having lower concentrations than the concentration in plasma. The lower ocular distribution, especially to the non-pigmented tissues, was also linked with a lower distribution to muscle, a well-perfused tissue described generally as a reference for tissue distribution [17]. The effect of melanin binding on the distribution to the pigmented tissues, RPE-choroid and iris-CB, was extremely evident. The highest differences in *K_p* between the corresponding BN and WH tissues were observed for the highest *in vitro* melanin binder levofloxacin in the RPE-choroid (320-fold), whereas the lowest differences (5-fold) were observed for the lowest melanin binder, dexamethasone. The inter-individual variability of the *K_p* values was low, which demonstrates the reproducibility of the method. Due to the limited concentration data from different tissues of the rat eye available in literature, we cannot thoroughly compare our results to existing data with other tissue isolation methods. However, two ocular distribution studies after oral administration of levofloxacin by Tanaka et al. [9,15] measured the concentrations in ocular substructures of pigmented rats. We compared our concentration results from the studied 8-h time point to their 24-h time point. The tissues combined for the concentration determination differed slightly between their two studies and compared to our investigation; in one of the studies, they measured the concentration from the uveal tract (iris, CB, choroid) and in the other study from the

RPE-choroid-sclera. We estimated the concentrations achieved in these tissue combinations, in our study, based on the concentrations from the individual tissues. The good agreement of dose-normalized results between our study and their studies is presented in Figure 4. The differences in concentrations between the corresponding individual tissues are visibly smaller than the differences from one tissue to another. Therefore, considering the different time points used and the different methods employed for the analysis of the concentrations (radioactivity vs. traditional HPLC-MS/MS), the comparison seems very reasonable.

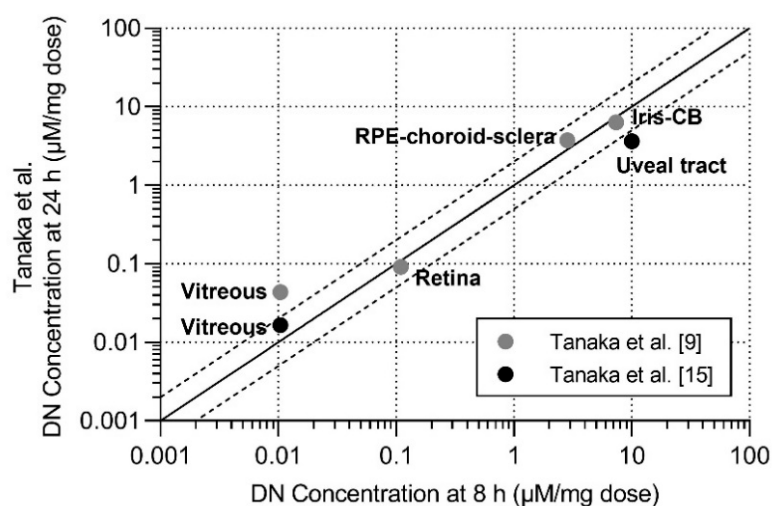


Figure 4. Comparison of dose-normalized (DN) results of levofloxacin ocular distribution between our study (x-axis) and two studies by Tanaka et al. (y-axis) performed with ^{14}C -levofloxacin [9,15]. The solid line is the line of identity and the dashed lines represent two-fold deviation.

The importance of measuring concentrations directly from the tissue of interest is evident from the observed differences in distribution to individual ocular substructures. Whole-eye exposure, commonly used as a surrogate for ocular tissue distribution, does not correctly describe the exposure in the different substructures (Figure 3). Larger differences among the individual substructures and between the whole-eye and individual tissue concentrations can understandably be seen in pigmented rats, where melanin binding increases the concentrations in the pigmented tissues. Nevertheless, up to 100-fold differences between substructures were also seen in albino animals: For BI 113823, we found a 16-fold lower concentration in the aqueous humor and a 6.5-fold higher concentration in the RPE-choroid compared to the whole eye, demonstrating the difficulty of estimating individual tissue concentrations from the whole-eye concentration. Moreover, extrapolating from one ocular tissue to another, for example from the vitreous to the other tissues of the posterior segment, can be misleading. Retina/vitreous ratios varied from 3.5- to 48-fold in the WH rat and from 11- to 37-fold in the BN rat. The RPE-choroid/vitreous ratios varied from 3.7- to 87-fold and from 55- to 1,300-fold in the WH, and BN rats, respectively.

In addition to the expected and already described concentration differences in RPE-choroid and iris-CB of WH and BN rats, there were also clear inter-strain differences in partitioning to other tissues (Table 3). K_p values of the retina were 1.8- to 3.7-fold higher in the BN rat, whereas differences in vitreous K_p values ranged from 0.45- to 4.4-fold. Aqueous humor K_p values, on the other hand, were always lower in BN rats. Additional investigations with more compounds, including time-dependency studies, are needed to increase the understanding of the drivers and mechanisms of ocular drug distribution. Our data, however, clearly indicate that the distribution into the substructures of the eye is compound specific and exposure differences of albino and pigmented rats are not limited to the pigmented tissues. Therefore, quantification of the compounds directly in the ocular substructures of interest, in the relevant animal strain(s), is needed.

5. Conclusions

We have developed a reproducible method for the quantification of drug concentrations in rat ocular tissues by briefly fixing the eye in formalin prior to tissue separation. The method can be applied to both albino and pigmented rats enabling the separation of different ocular tissues with minimal cross-tissue contamination. We investigated possible sources of errors in analyzing concentrations from pigmented eyes and highlighted the importance of analyzing concentrations from individual ocular tissues due to large tissue-specific differences in ocular exposure. Overall, the method facilitates reliable analysis of local drug concentrations in a specific ocular target tissue, an important aspect of estimating PK/PD relationships to support drug discovery and development.

Supplementary Materials: The following are available online at <http://www.mdpi.com/1999-4923/12/12/1174/s1>, Figure S1: Step-by-step rat ocular tissue separation., Table S1: Tissue-dependent extraction ratios used for tissue sample preparation for HPLC-MS/MS analysis., Table S2: Calibration ranges (nmol/L) of HPLC-MS/MS analysis of the in vivo plasma and tissue concentration., Figure S2: Plasma concentration-time profiles of the individual Brown Norway (BN) and Wistar Han (WH) rats after oral delivery (p.o.), Table S3: Tissue volumes used for the calculation of whole eye/plasma concentration ratios., Table S4: Average concentrations measured from ocular tissues and muscle.

Author Contributions: Conceptualization, A.-K.R., M.G., K.S.B.-K. and A.S.; methodology, A.-K.R., M.G., K.S.B.-K., T.S., F.R. and A.S.; validation, A.-K.R., M.G., K.S.B.-K. and A.S.; formal analysis, A.-K.R., M.G. and T.S.; investigation, A.-K.R., M.G., K.S.B.-K. and T.S.; resources, A.S.; writing—original draft preparation, A.-K.R. and M.G.; writing—review and editing, A.-K.R., M.G., K.S.B.-K., F.R. and A.S.; visualization, A.-K.R.; supervision, A.S.; project administration, A.S. All authors have read and agreed to the published version of the manuscript.

Funding: This research was funded by Boehringer Ingelheim Pharma GmbH & Co. KG.

Acknowledgments: We thank Heidi Assfalg, Carmen Hummel, Heike Biesinger and Viktoria Kneer for their excellent technical contribution. Nuvisan GmbH (Grafing, Germany) is acknowledged for performing the bioanalytical measurements of the tissue samples.

Conflicts of Interest: The authors declare no conflict of interest. All authors are employees of Boehringer Ingelheim Pharma GmbH & Co. KG, Biberach, Germany. The company had no role in the design, execution, or interpretation of the study or writing of the manuscript.

References

1. Wong, W.L.; Su, X.; Li, X.; Cheung, C.M.; Klein, R.; Cheng, C.-Y.; Wong, T.Y. Global prevalence of age-related macular degeneration and disease burden projection for 2020 and 2040: A systematic review and meta-analysis. *Lancet Glob. Health* **2014**, *2*, 106–116. [CrossRef]
2. Tham, Y.C.; Li, X.; Wong, T.Y.; Quigley, H.A.; Aung, T.; Cheng, C.Y. Global prevalence of glaucoma and projections of glaucoma burden through 2040: A systematic review and meta-analysis. *Ophthalmology* **2014**, *121*, 2081–2090. [CrossRef] [PubMed]
3. Varela-Fernández, R.; Díaz-Tomé, V.; Luaces-Rodríguez, A.; Conde-Penedo, A.; García-Otero, X.; Luzardo-Álvarez, A.; Fernández-Ferreiro, A.; Otero-Espinar, F.J. Drug delivery to the posterior segment of the eye: Biopharmaceutic and pharmacokinetic considerations. *Pharmaceutics* **2020**, *12*, 269. [CrossRef] [PubMed]
4. Del Amo, E.M.; Rimpelä, A.K.; Heikkinen, E.M.; Kari, O.K.; Ramsay, E.; Lajunen, T.; Schmitt, M.; Hellinen, L.; Bhattacharya, M.; Richardson, D.; et al. Pharmacokinetic aspects of retinal drug delivery. *Prog. Retin. Eye Res.* **2017**, *57*, 134–185. [CrossRef]
5. Souto, E.B.; Dias-Ferreira, J.; Machado, A.L.; Ettcheto, M.; Cano, A.; Camins, A.; Espina, M.; García, M.L.; Sánchez-López, E. Advanced formulation approaches for ocular drug delivery: State-of-the-art and recent patents. *Pharmaceutics* **2019**, *11*, 460. [CrossRef]
6. Smith, S.B.; Wang, J.; Cui, X.; Mysona, B.A.; Zhao, J.; Bollinger, K.E. Sigma 1 receptor: A novel therapeutic target in retinal disease. *Prog. Retin. Eye Res.* **2018**, *67*, 130–149. [CrossRef]
7. Schwarzer, P.; Kokona, D.; Ebnetter, A.; Zinkernagel, M.S. Effect of inhibition of colony-stimulating factor 1 receptor on choroidal neovascularization in mice. *Am. J. Pathol.* **2020**, *190*, 412–425. [CrossRef]

8. Csaky, K.G.; Dugel, P.U.; Pierce, A.J.; Fries, M.A.; Kelly, D.S.; Danis, R.P.; Wurzelmann, J.I.; Xu, C.F.; Hossain, M.; Trivedi, T. Clinical evaluation of pazopanib eye drops versus ranibizumab intravitreal injections in subjects with neovascular age-related macular degeneration. *Ophthalmology* **2015**, *122*, 579–588. [CrossRef]
9. Tanaka, M.; Takashina, H.; Tsutsumi, S. Comparative assessment of ocular tissue distribution of drug-related radioactivity after chronic oral administration of 14c-levofloxacin and 14c-chloroquine in pigmented rats. *J. Pharm. Pharmacol.* **2004**, *56*, 977–983. [CrossRef]
10. Lee, V.H.L.; Robinson, J.R. Disposition of pilocarpine in the pigmented rabbit eye. *Int. J. Pharm.* **1982**, *11*, 155–165. [CrossRef]
11. Shah, M.; Cabrera-Ghayouri, S.; Christie, L.A.; Held, K.S.; Viswanath, V. Translational preclinical pharmacologic disease models for ophthalmic drug development. *Pharm. Res.* **2019**, *36*, 1–34. [CrossRef]
12. Jakubiak, P.; Cantrill, C.; Urtti, A.; Alvarez-Sánchez, R. Establishment of an in vitro-in vivo correlation for melanin binding and the extension of the ocular half-life of small-molecule drugs. *Mol. Pharm.* **2019**, *16*, 4890–4901. [CrossRef]
13. Tan, A.Y.; LeVatte, T.L.; Archibald, M.L.; Tremblay, F.; Kelly, M.E.; Chauhan, B.C. Timolol concentrations in rat ocular tissues and plasma after topical and intraperitoneal dosing. *J. Glaucoma* **2002**, *11*, 134–142. [CrossRef] [PubMed]
14. Acheampong, A.A.; Shackleton, M.; John, B.; Burke, J.; Wheeler, L.; Tang-Liu, D. Distribution of brimonidine into anterior and posterior tissues of monkey, rabbit, and rat eyes. *Drug Metab. Dispos.* **2002**, *30*, 421–429. [CrossRef] [PubMed]
15. Tanaka, M.; Ono, C.; Yamada, M. Absorption, distribution and excretion of 14c-levofloxacin after single oral administration in albino and pigmented rats: Binding characteristics of levofloxacin-related radioactivity to melanin in vivo. *J. Pharm. Pharmacol.* **2004**, *56*, 463–469. [CrossRef] [PubMed]
16. Chockalingam, A.; Xu, L.; Stewart, S.; Lemerdy, M.; Tsakalozou, E.; Fan, J.; Patel, V.; Rouse, R. Protocol for evaluation of topical ophthalmic drug products in different compartments of fresh eye tissues in a rabbit model. *J. Pharmacol. Toxicol. Methods* **2019**, *96*, 9–14. [CrossRef] [PubMed]
17. Cui, Y.; Lotz, R.; Rapp, H.; Klinder, K.; Himstedt, A.; Sauer, A. Muscle to brain partitioning as measure of transporter-mediated efflux at the rat blood-brain barrier and its implementation into compound optimization in drug discovery. *Pharmaceutics* **2019**, *11*, 595. [CrossRef]
18. Fortmann, S.D.; Lorenc, V.E.; Shen, J.; Hackett, S.F.; Campochiaro, P.A. Mousetap, a novel technique to collect uncontaminated vitreous or aqueous and expand usefulness of mouse models. *Sci. Rep.* **2018**, *8*, 6371. [CrossRef]
19. Jakubiak, P.; Reutlinger, M.; Mattei, P.; Schuler, F.; Urtti, A.; Alvarez-Sánchez, R. Understanding molecular Drivers of melanin binding to support rational design of small molecule ophthalmic drugs. *J. Med. Chem.* **2018**, *61*, 10106–10115. [CrossRef]
20. Donatien, P.; Jeffery, G. Correlation between rod photoreceptor numbers and levels of ocular pigmentation. *Investig. Ophthalmol. Vis. Sci.* **2002**, *43*, 1198–1203.
21. Cheruvu, N.P.; Amrite, A.C.; Kompella, U.B. Effect of Eye Pigmentation on Transscleral Drug Delivery. *Investig. Ophthalmol. Vis. Sci.* **2008**, *49*, 333–341. [CrossRef] [PubMed]
22. Durairaj, C.; Chastain, J.E.; Kompella, U.B. Intraocular distribution of melanin in human, monkey, rabbit, minipig and dog eyes. *Exp. Eye Res.* **2012**, *98*, 23–27. [CrossRef] [PubMed]
23. Ono, C.; Yamada, M.; Tanaka, M. Absorption, distribution and excretion of 14C-chloroquine after single oral administration in albino and pigmented rats: Binding characteristics of chloroquine-related radioactivity to melanin in-vivo. *J. Pharm. Pharmacol.* **2003**, *55*, 1647–1654. [CrossRef] [PubMed]
24. Tokuda, K.; Baron, B.; Kuramitsu, Y.; Kitagawa, T.; Tokuda, N.; Morishige, N.; Kobayashi, M.; Kimura, K.; Nakamura, K.; Sonoda, K.H. Optimization of fixative solution for retinal morphology: A comparison with Davidson’s fixative and other fixation solutions. *Jpn. J. Ophthalmol.* **2018**, *62*, 481–490. [CrossRef] [PubMed]
25. Chatterjee, S. Artefacts in histopathology. *J. Oral Maxillofac. Pathol.* **2014**, *18*, 111–116. [CrossRef]
26. Lowrey, A.H.; Famini, G.R.; Loumbev, V.; Wilson, L.Y.; Tosk, J.M. Modeling drug-melanin interaction with theoretical linear solvation energy relationships. *Pigment. Cell Res.* **1997**, *10*, 251–256. [CrossRef]
27. Larsson, B.S. Interaction between chemicals and melanin. *Pigment. Cell Res.* **1993**, *6*, 127–133. [CrossRef]
28. Rimpelä, A.K.; Reinisalo, M.; Hellinen, L.; Grazhdankin, E.; Kidron, H.; Urtti, A.; Del Amo, E.M. Implications of melanin binding in ocular drug delivery. *Adv. Drug Deliv. Rev.* **2018**, *126*, 23–43. [CrossRef]

29. Aula, P.; Kaila, T.; Huupponen, R.; Salminen, L. Timolol binding to bovine ocular melanin in vitro. *J. Ocul. Pharmacol. Ther.* **1988**, *4*, 29–36. [CrossRef]
30. Howells, L.; Godfrey, M.; Sauer, M.J. Melanin as an adsorbent for drug residues. *Analyst* **1994**, *119*, 2691–2693. [CrossRef] [PubMed]
31. Ono, C.; Tanaka, M. Binding characteristics of fluoroquinolones to synthetic levodopa melanin. *J. Pharm. Pharmacol.* **2003**, *55*, 1127–1133. [CrossRef] [PubMed]

Publisher’s Note: MDPI stays neutral with regard to jurisdictional claims in published maps and institutional affiliations.



© 2020 by the authors. Licensee MDPI, Basel, Switzerland. This article is an open access article distributed under the terms and conditions of the Creative Commons Attribution (CC BY) license (<http://creativecommons.org/licenses/by/4.0/>).

MDPI
St. Alban-Anlage 66
4052 Basel
Switzerland
www.mdpi.com

Pharmaceutics Editorial Office
E-mail: pharmaceutics@mdpi.com
www.mdpi.com/journal/pharmaceutics



Disclaimer/Publisher's Note: The statements, opinions and data contained in all publications are solely those of the individual author(s) and contributor(s) and not of MDPI and/or the editor(s). MDPI and/or the editor(s) disclaim responsibility for any injury to people or property resulting from any ideas, methods, instructions or products referred to in the content.



Academic Open
Access Publishing

mdpi.com

ISBN 978-3-0365-8798-1